Karlsruhe Institute of Technology

Amer Baniodeh

Cooperative effects in non-cyclic and cyclic Fe^{III}/4f coordination clusters

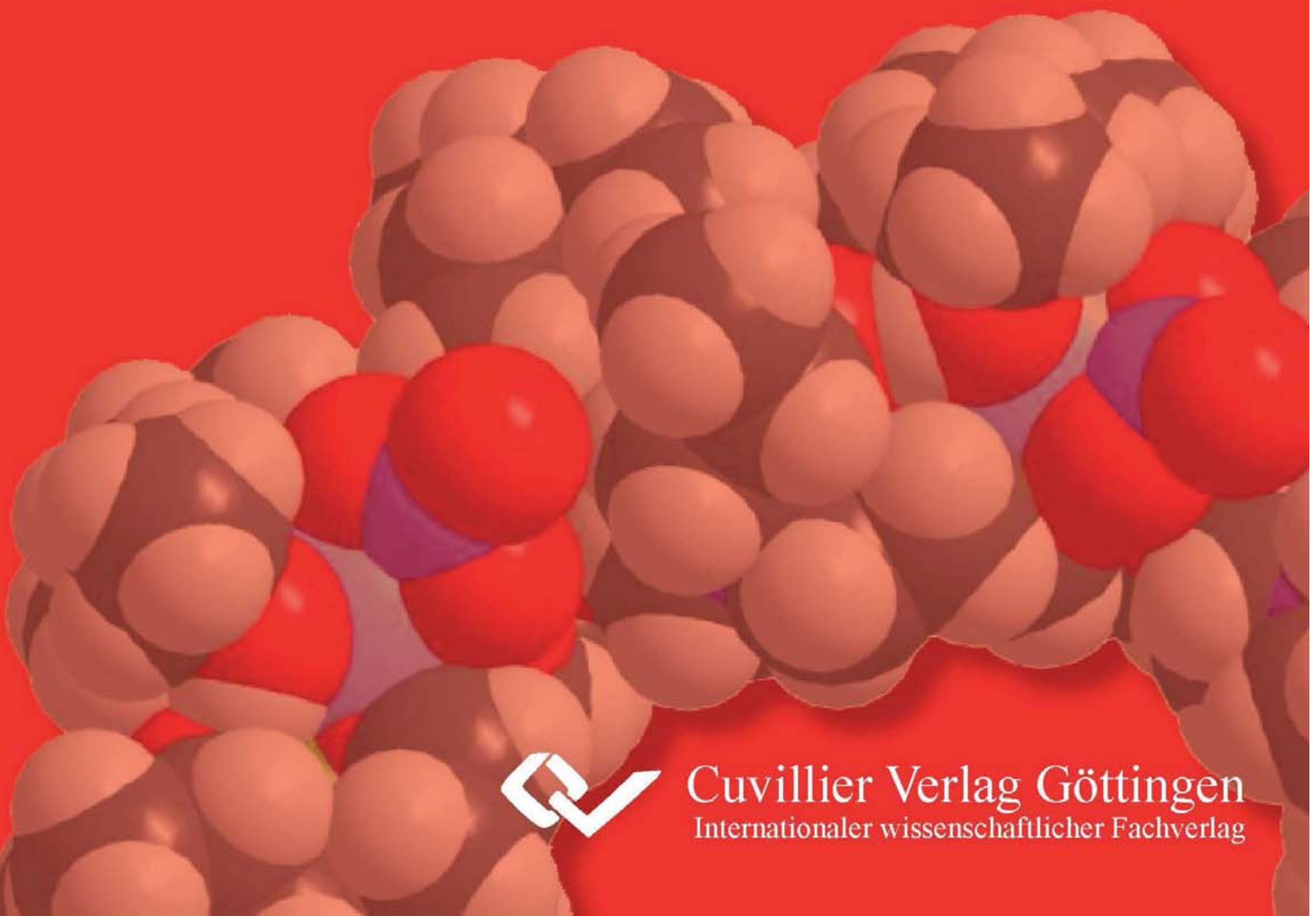

Cuvillier Verlag Göttingen
Internationaler wissenschaftlicher Fachverlag

Cooperative effects in non-cyclic and cyclic Fe^{III}/4f coordination clusters

COOPERATIVE EFFECTS IN NON-CYCLIC AND CYCLIC Fe^{III}/4f COORDINATION CLUSTERS

Zur Erlangung des akademischen Grades eines

DOKTORS DER NATURWISSENSCHAFTEN

(Dr. rer. nat.)

Fakultät für Chemie und Biowissenschaften

Karlsruher Institut für Technologie (KIT) – Universitätsbereich

(genehmigte)

DISSERTATION

von

Dipl.-Chem. Amer J. M. Baniodeh

aus

Tammoun, Palästina

Dekan: Prof. Dr. Martin Bastmeyer

Referent: Prof. Dr. Annie K. Powell

Korreferent: PD Dr. Andreas N. Unterreiner

Tag der mündlichen Prüfung: 19.10.2012

Bibliografische Information der Deutschen Nationalbibliothek
Die Deutsche Nationalbibliothek verzeichnet diese Publikation in der
Deutschen Nationalbibliografie; detaillierte bibliografische Daten sind im Internet
über http://dnb.d-nb.de abrufbar.
1. Aufl. - Göttingen : Cuvillier, 2013
Zugl.: Karlsruhe (KIT), Univ., Diss., 2012

978-3-95404-448-1

Nonnenstieg 8, 37075 Göttingen
Telefon: 0551-54724-0
Telefax: 0551-54724-21
www.cuvillier.de

1. Auflage, 2013
Gedruckt auf säurefreiem Papier

978-3-95404-448-1

Contents

Chapter 1: Introduction

Chapter 2: A Comparative Study of a Tetranuclear {Fe_2Ln_2} Family

Chapter 3: Cyclic Fe^{III}/Ln^{III} Coordination Clusters

Chapter 4: $\{Fe_{10}Ln_{10}\}$ Cooperative Coordination Clusters

Chapter 6: Experimental

Zusammenfassung

Die vorliegende Arbeit beschäftigt sich mit der Grundlagenforschung von molekularem Magnetismus am Beispiel von Fe^{III}/4f-Koordinationsclustern und deren Anwendungsmöglichkeiten. Es wurden in dieser Arbeit zahlreiche Fe^{III}/4f-Verbindungen diskutiert. Dreiwinklige oxo-verbrückte $[Fe^{III}_3O]$-Verbindungen mit verschiedenen Carboxylaten dienten als Vorläufer. Diese halfen den Mechanismus der selbst-organisierten Reaktionen in dieser Arbeit besser zu verstehen. Andere Verbindugen wurden gezielt synthetisiert um als Referenzverbindungen die Eigenschaften der untersuchten Materialien zu verstehen.

Die Diskussion der Ergebnisse wurde in drei Kapiteln aufgeteilt.

Kapitel 2 stellt eine Vergleichsstudie dar. Es beschäftigt sich mit der fundamentalen Größe/Ursache des einzelmolekularmagnetischen Verhaltens, der magnetischen Anisotropie. Darin wurde diskutiert, ob die elektronische Natur von organischen Substituenten die magnetische Anisotropie beeinflusst. Dazu wurde ein tetranuklearer $\{Fe_2Dy_2\}$-Koordinationscluster ausgewählt, der aus einer oxo-verbrückten $\{Fe^{III}_3O\}$-Verbindung mit Benzoatliganden, einem Triethanolaminliganden und Dysprosium(III)-Nitrat synthetisiert wurde. Durch Verwendung der Lanthanoiden(III)-Nitrate konnte eine Serie von $\{Fe_2Ln_2\}$ fast vollständig synthtetisiert werden (Ln= Ce bis Yb und Y). Darüberhinaus wurden über 25 $\{Fe_2Dy_2\}$-Analoge Verbindungen mit verschiedenen Carboxylaten und/ oder Ligand Kombinationen hergestellt. Sowohl die $\{Fe_2Ln_2\}$-Serie als auch die $\{Fe_2Dy_2\}$-Koordinationscluster wurden mittels magnetischer Suszeptibilitätsmessungen, Mössbauer Spektroskopie und Elektronenspinresonanz-Spektroskopie (ESR) untersucht. Sowohl für die Serie als auch für die Substituenten wurden theoretische Rechnungen durchgeführt.

Diese Arbeit kommt zu dem Ergebnis, dass der Substituentenaustausch einen signifikanten Effekt auf die magnetische Anisotropie und somit auf das einzelmolekülmagnetische Verhalten hat. Die magnetische Relaxation und verwandte Prozesse, jedoch nicht das statische magnetische Verhalten (Kollektiver Magnetismus) wurden stark beeinflusst.

Die Ergebnisse dieses Kapitels sollen Forscher in diesem Bereich helfen, die Rolle der Liganden insbesondere deren Einfluss auf die magnetische Anisotropie der Lanthanoide zu nutzen um effektivere Einzelmolkülmagnete zu synthetisieren. Mit Hilfe der Mössbauer Spektroskopie konnten die Substituenten Effekte besser detektieren werden als mit der magnetischen SQUID-Methode. Ein phenomenalogischer Effekt wurde in der Mössbauer Spektroskopie entdeckt.

In Kapitel 3 wurde die Fähigkeit von Triethanolamin oder ähnlichen Liganden basierend auf der Synthesestrategie von $\{Fe_2Ln_2\}$-Komplexen genutzt, um zyklische Fe^{III}/4f - Koordinationscluster mit symmetrischen und asymmetrischen Strukturen zu erhalten.

In diesem Kapitel wurden mittels magnetischen Messungen und Mössbauer Spektroskopie drei Serien von zyklischen Fe^{III}/Ln- (Ln= schwere Lanthanoide, Tm, Yb und Lu) Komplexen untersucht. Die magnetischen Eigenschaften dieser Komplexe sind anspruchsvoll. Die Mössbauer Methode erklärt diese Eigenschaften präziser, vermutlich aufgrund der kürzeren Lebensdauer. Langsame magnetische Relaxation wurde sogar für Fe/Ln-Verbindungen mit Tm^{III} und Yb^{III} detektiert. Weiterhin konnte gezeigt werden, dass diamagnetische Lu^{III} -Ionen an einem magnetischen Hyperfine Transfer teilnehmen können.

Kapitel 4 beschäftigt sich mit der Synthese, den Strukturen, den magnetischen Eigenschaften, dem Mgantokalorischen Effekt, den Mössbauer Spektren und mit dem optischen Verhalten von einzigartigen $\{Fe_{10}Ln_{10}\}$- zyklischen Aggregaten. Das Zusammenspiel zwischen der Chiralität der Liganden und der Wasserbrückenbindungen ist entscheidend über die Stabilität der Struktur. Das $\{Fe_{10}Ln_{10}\}$-Koordinationscluster ist ein ferromagnetisches System. Die *dc* Suszeptibilitäten sind jedoch für jedes Lanthanoid unerwartet unterschiedlich.

Terbium(III)- und Dysprosium(III)-Verbindungen sind Einzelmolekülmagnete. Diese Verbindung sind außerdem magnetische Kühler. Die Frage über die bemerkenswerte Erscheinung der Kristalle und Lösungen wurde mit Hilfe von Steady-State Absorptionsmessungen und Femtoskunden Studie beantwortet. Diese Studie in Kombination mit allen anderen Ergebnissen, die erhalten wurden, deutet darauf hin, dass diese Verbindungen als multifunktionale molekulare Verbindungen bezeichnet werden können. Erste Untersuchungen auf die Halbleiterfähigkeit wurden durchgeführt. Das bemerkenswerte Verhalten dieser Materie in Wasser wurde auch in diesem Kapitel diskutiert. Weiterhin wurde versucht eine blau-violette Materie zu identifizieren, die nach mischen von rotem laugen Salz mit $\{Fe_{10}Ln_{10}\}$ in der Sonne durch Photoreduktion entstehen kann.

Dieses zyklische kooperative Koordinationsclustersystem könnte als mit Lanthanoiden dotiertes (1:1) nanoskaliges molekulares Fe^{III}-Clustersystem verstanden werden.

Weiterhin wurde diskutiert, ob diese Ergebnisse über die magnetischen und elektronischen Eigenschaften eine Analogie zu den Eigenschfaten der Festkörperverbindungen finden und ob eine allgemeinere Erklärung für all diese kooperativen Effekte gegeben werden kann. Nicht zu letzt die Frage ob, eine Korrelation zwischen den magnetischen Eigenschaften und den Ergenbissen aus der Femtosekundenspektroskopie Untersuchungen bestehe? Diese Arbeit soll helfen neue zukünftige Forschungszwege zu öffnen!

Chapter 1

Introduction

1.1 Motivation

Research Philosophy

Major research interest in the Powell group is the synthesis and characterisation of Molecular Nano-Magnets which are described as Single Molecule Magnets (SMMs) when the details of their molecular structures are at atomic resolution. Other research interests are the synthesis of Super Metal Organic Frameworks (SMOFS) and the field of Biomimetics. The knowledge which can be won from these fields can be combined to lead to multifunctional materials, increased fundamental understanding of complex systems and a wide range of possible applications. This is the underlying research philosophy of the group. [1]

General scope

Multifunctional materials can only be discovered when cooperative effects operating within can be understood. At the heart of this endeavour is the aim to measure and understand the nature and mechanisms of cooperative effects in oxo-bridged coordination clusters (CCs) through applying a range of characterization methods. On one hand it will be possible to achieve a more fundamental understanding of the magnetic anisotropy in such systems, which is an essential condition for creating SMMs. On the other hand, there is the important aim of using new chemical syntheses and studying the resulting compounds by applying appropriate physical methods in order to search for new properties and open the way for producing multifunctional materials with a wide range of applications. [1]

In this thesis the term “oxo-bridged SMMs” refers to coordination clusters showing SMM properties in which the metal ions are held together by oxygen atoms deriving from various ligands or variously deprotonated protic solvent molecules. Such coordination clusters, as well as several examples of SMMs [2-5] built using ideas from supramolecular chemistry are structurally related to the basic concepts set-out by Alfred Werner in his Coordination Chemistry Theory. Just taking the example of a CC, in comparison with a coordination complex based on a single metal ion being held in a coordination sphere of lignands, the CC has a central collection of bridged and coupled (cooperating) metal ions encapsulated in a shell of ligands. For oxo-CCs the cooperativity is achieved by information transfer via the oxo groups. Overall, whereas a coordination complex will be a few Ångstroms across, a CC is usually more than 1 nm in cross-section. In a CC or Supramoelcular Coordination Compound (SCC) such as crown-ether complexes, the stabilizing and their influence on the properties are the same as in oxo bridged

CC being Molecular Magnets (MMs).[6-11] Non-covalent interactions in oxo-bridged MMs could be also of major importance for catalysis or other "hot" research areas today.[3,5] In particular CCs which are described as SMMs are realistic candidates for data storage applications.[12-13]

Subject

Normally, when chemists aim to synthesise Single Molecule Magnets (SMMs), they proceed according to the following steps: i) they probe ligands with possible selectivity for complexation of paramagnetic ions (often magnetically anisotropic) which later could lead to a cluster-compound with promising collective magnetism and where they think that this new compound might act as a SMM; ii) the structure of the new compound can be determined to atomic resolution (needs single crystals for X-ray diffraction) although it is mostly impossible to predict its SMM behaviour from the structure; iii) dc and ac magnetic measurements are used to characterise its collective magnetic and possible SMM behaviour ; iv) the discovered magnetic behaviour can be theoretically investigated as long as the system is not too big and thus can provide a benchmark for understanding later systems.[14] It should be noted that whilst it can be more instructive to work-out why a system does not show the desired properties (e.g. SMM behaviour) aimed for in the synthesis, it is generally true that very few of these "failures" are investigated further, which in turn means that often valuable insights are lost.

More than twenty years have passed since the discovery [14] that the Mn_{12}-ac coordination cluster originally reported by Lis [15] shows slow relaxation of magnetization. There have been extensive synthetic efforts aimed at adapting this system and the discovery of new SMM examples. However, very little systematic study has been carried out, so that in manganese CC chemistry only a few families of related CCs have been investigated. The Mn_{12}-system has, understandably, been the most toughly studied and a high number of compounds exist showing similar cores but with different ligands and sometimes different magnetic behaviour.[14] Other SMM families of 3d metal ions are those with the Mn_4[16], Mn_6[17] and Fe_4[18] coordination clusters.[14, 16-18] An enhancement of the energy barrier has been achieved within each family and it was also found that the exchange coupling as well as the ground spin state could be manipulated. However, in most of these cases the effect was related to a specific change in the overall structure influencing the collective magnetism. It was thus largely impossible to register whether any changes in the electronic nature of the encapsulating ligands can affect the overall magnetic behaviour for these systems. Indeed, in general any significant influence from making changes in the electronic donating or withdrawing effects of the ligands has been ignored, possibly as a result of the assumption that this would at most provide very minor perturbations.

Since all the above-mentioned cluster families contain only 3d ions, the assumption that the electronic properties of the ligands will not exert much influence on the resulting magnetism may well be valid since in general the coupling between 3d ions is relatively strong and can be expected to dominate the magnetic properties. However, recently chemists have turned their attention to synthesising CCs as possible SMM systems using lanthanides, mixtures of 3d and 4f ions and also a few examples of other blends of d and f ions such as 4d-4f. There are many examples such compounds from the Powell group with systematic work on 3d/4f systems used to discover the best sets of synthetic parameters needed to target specific types of SMM (see also *Fe/4f chemistry* and refs **[36]** later this chapter*)*. A special area of interest is in 3d/4f compounds where the 3d ion is Fe^{III}, which is an ion which not only produces fascinating SMM systems in 3d CC chemistry, but is also useful as a sensor for anisotropy in 3d/4f compounds via the information gained from using Mössbauer spectroscopy. This is a useful extra handle in this field since the highly anisotropic nature of lanthanide ions complicates the interpretation and understanding of magnetic measurements on these compounds. In general it is thought that the observed magnetic profiles are influenced by spin-orbit coupling to a greater extent than by the ligand field, although this is largely substantiated by studies on solid state compounds rather than the bounded CC systems which are becoming increasingly common. As will be seen in the following chapters of this thesis, a so-called “Paradigm shift” is needed in the description of CC systems incorporating lanthanide ions. The key features here are: i) the significant dipolar coupling effect between highly anisotropic lanthanide ions and between the 4f and 3d ions; ii) the interplay between strengths of super-exchange and dipolar coupling; iii) the significant input of both 3d metal ion and ligand on the overall electronic structure of the 3d/4f metal core and the overall anisotropy of the 4f ion. This third point suggests that in this context the more challenging task is actually to understand the effect of ligands, and maybe also the 3d ions, on the *f*-orbitals. **[19]**

For example, in this work a non-cyclic tetranuclear 3d/4f $\{Fe_2Ln_2\}$[20a] “test-bed” CC system was selected in order to investigate electronic nature of ligands on the magnetic anisotropy.[20b] See thesis overview.

1.2 Molecular Magnetism

History and basics

The phenomenon of magnetism was identified first in the mineral magnetite, which is a mixed valent inverse spinel compound which can be formulated as $\{Fe^{III}(Fe^{II}Fe^{III}O_4)\}$ or ($Fe^{II}O$-$Fe^{III}{}_2O_3$) in order to emphasis its structural and magnetic features. [21] The relationship between magnetism and electricity was later made clear through the development of electromagnetic wave theory. [12, 21] In the 20th century Peter Weiss, developed the theory of ferromagnetism based on the assumption that the interaction between magnetic molecules could be described empirically considering an internal molecular field. Bohr identified the underlying physics from which magnetism results; i.e. the minute spin associated with an unpaired electron. This is the case in many solid state materials for which magnetic theory is mostly applied and discussed. The understanding of the magnetic behaviour of coordination compounds has been developed from the basic principles of the magnetism of bulk materials.[21]

In principle, every material interacts with a magnetic field with two basic types of behaviour: i) magnetism of single atoms or ions, namely diamagnetism and paramagnetism; ii) collective magnetism resulting from the cooperative coupling of centres in the material which can be classified as ferromagnetism, ferrimagnetism and antiferromagnetism. [21] In case the reader needs to refer further information about these basic principles, these can be found in standard textbooks. [21-25]

Since the discovery that Mn_{12}ac can show slow relaxation of magnetization and hysteresis as expected for bulk materials showing long-range ordering, but not for molecules, several other terms and definitions should be considered when discussing the SMM behaviour of CCs. In other words, how can we understand the observation that a single molecule responds to a magnetic field in the way we would expect for an ordered bulk solid? The important features such a molecule should possess for SMM behaviour to be observed are non-zero spin (usually as the ground state) combined with a sufficient degree of magnetic anisotropy to produce hard and easy axes of magnetization. A further feature important at this “Quantum World” level of scale (roughly nanoscale) is that quantum tunnelling (QTM – quantum tunnelling of magnetisation) can be expected and this can be regarded as undesirable if the goal is to store information or desirable if the goal is to process information (quantum computing). These aspects are discussed briefly below since they are important for the discussion of the results in this work, in particular in chapter 2.

Magnetic Anisotropy

A material is magnetically anisotropic when its magnetism becomes orientation dependent. While an isotropic material (in the absence of an applied field) has no preferential direction for its moment, an anisotropic system will align itself along an easy-axis (the energetically favourable direction of spontaneous magnetization). Two physical reasons are known to give rise to this anisotropy. These are dipolar effects (magnetic dipoles) and spin-orbital coupling. For example, in the case of an iron cylinder the cylindrical length is much greater than the circular diameter which means the magnetization will be oriented along its length to give an easy-axis. For an iron disk, the diameter is now the larger metric parameter and the direction of the length defines a hard axis. In the case of a spherical iron-ball, the system is isotropic as there is neither a favourable nor an unfavourable direction. This results from the inner crystallographic structure of the ball or the crystallographic anisotropy. Other forms of anisotropy are the magneto-crystalline anisotropy of the coupling of magnetization and crystal-cell (spin-orbital-coupling) and form-anisotropy which results from the changes in the form of a material. Finally exchange-bias or exchange-anisotropy which arises from the orientation of the magnetization in ferromagnetic materials is as a result of the interaction between it and an antiferromagnetic component.[23,26]

Quantum Tunnelling of Magnetization (QTM)

15 years ago two groups independently proposed an explanation for the unusual step-like features apparent in the magnetic hysteresis loops obtained from samples of Mn_{12}-ac.[23, 26, 27] Fig. 1.1.shows a schematic representation of the hysteresis behaviour of the Mn_{12}-ac SMM (measured at 2.1 K). The behaviour is not the result of thermal activation but caused through the loss of spin polarization in the molecules due to tunnelling of the magnetization through the energy barrier. [23,27a)]

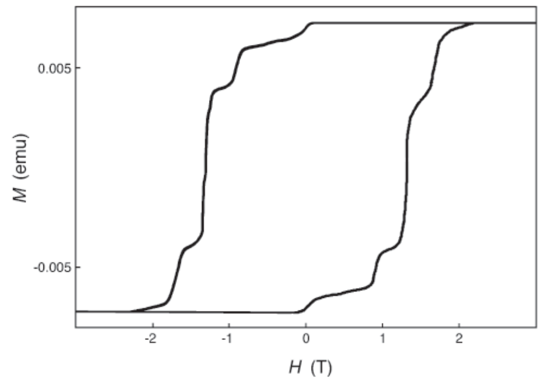

Figure 1.1. Schematic representation of the hysteresis of Mn_{12}-ac. The step-like curves represent the QTM in this compound.

Methods of measuring

For work on CCs in general and SMMs in particular the high sensitivity of the SQUID (Superconducting Quantum Interference Device) Magnetometer makes this the instrument of choice for measuring the magnetic behaviour and has been used in this work.[28] This method is based on the sensitivity the SQUID sensor (which is built from a weak Josephson-contact) on the change in the magnetic flux. Because a SQUID contains a superconductor, there is no electrical resistance at low temperature and thus no magnetic field. However, a circulating current can be induced by applying a field. This causes another magnetic field but in the opposite direction (Lenz-rule) according to the Meissner-Ochsenfeld effect. Theoretically, the BCS (Bardeen Cooper Schreiffer) theory which is about the Cooper-pair helps in understanding how a superconductor works in a SQUID.[28] Two types of SQUID magnetometers are useful, the *DC* and *AC* techniques. This combination in a SQUID is useful for identifying whether a material might be a SMM.[29] The DC measurement gives basic information about the overall magnetic behaviour as a function of temperature while the AC measurement is a more sensitive technique because a current field is applied from which one can determine the magnetic moment. In this case the induced moment sample is time dependent.

The *AC* measurement can give information about the magnetization dynamics [29] and it is possible to split the susceptibility χ and phase shift φ obtained from this measurement into a real part (in-phase, χ`) and imaginary part (out of phase, χ``). These two quantities are very important as aids in understanding SMM behaviour. It is possible to extract the energy barrier to spin inversion using an Arrhenius law analysis of the relaxation data (equ.1.1) and the blocking temperature to onset of slow relaxation of the magnetization can also be estimated from the data. The energy barrier and blocking temperature are related to each other (equ. 1.2). The magnetic measurement can take place at very low temperatures (He cooling) which is currently the temperature region where SMMs operate. The blocking temperature (T_B in K) is defined (according equ. 1.2) as the temperature below which the relaxation of the magnetization becomes slow compared to the time scale of a particular investigation technique. For example a molecule magnetized at 2 K will keep 40% of its magnetization after 2 months and by lowering the temperature to 1.5 K this will correspond to several years.

$$\tau = \tau_0 e^{(Ueff / k_B T)} \quad (1.1)$$

$$T_B = \frac{\Delta E = Ueff}{\ln(\tau / \tau_0) k_B} (1.2)$$

Where U_{eff} is the energy barrier to spin relaxation in cm^{-1} or K, τ_0 the relaxation time for the magnetization in a SMM and τ relaxation attempt frequency in s^{-1}.

Single Molecule Magnets

A Single Molecule Magnet (SMM) is a molecule that shows slow relaxation of the magnetization (magnetic bistability) of purely molecular origin. **[30]** These are coordination clusters which should show hysteresis of the magnetization at low enough temperatures with correct sweeping rates (Fig. 1.2). What can now be regarded as the “classical” criteria for SMM behaviour is a high spin ground state (S) and large negative axial-zero-field splitting parameter (D) to give an intrinsic energy barrier for spin reversal that results in slow relaxation of magnetization. In the meantime, with the study of systems incorporating metal ions which are much more anisotropic than ions such as the widely used high spin Mn^{III} ion, and with the observation that SMM behaviour can be observed in compounds where excited magnetic states are available, this definition needs some modification. An important point in dealing with highly anisotropic systems is that it is no longer possible to invoke a “giant spin” model to describe a collective, additive spin on the molecule (S) but instead the system is better described in terms of parameters which reflect the large contribution from orbital effects and the spin-orbit coupling. In this case, we can categorize a system showing SMM behaviour as one which possesses significant magnetic anisotropy and a non-zero spin state.

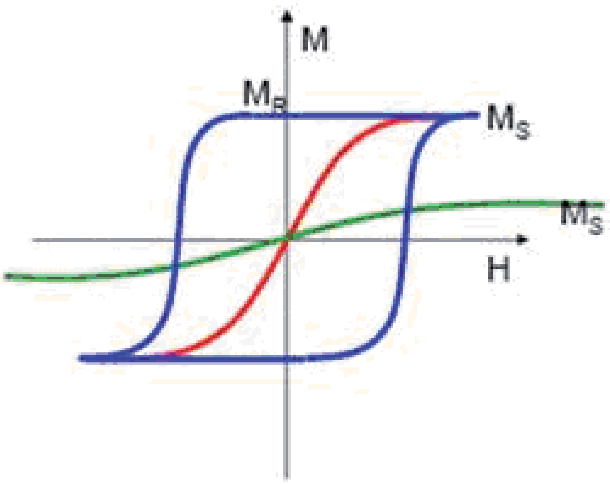

Figure 1.2. Schematic representation for the hysteresis: a ferromagnet or SMM (blue), superparamagnet (red) and paramagnet (green).

Theoretical reflection

Note that only the general equations in chapter 1 will have numbers. In all other chapters equations will not be numbered since they were used to for calculations and they are a part of the results discussion!

The general Hamiltonian which describes a magnetic system is given in equ. 1.3. H_0 is the unperturbed Hamiltonian. The Hamiltonian operator H_0 (equ. 1.3a) describes the two unperturbed potentials (Fig. 1.3) and treats the effect of an applied field parallel to the axis of the cluster and the axial-splitting through the crystal field. It can be expressed through the equations (1.3b) and the energy-levels of the sub-levels through equ. 1.4. H_1 describes the perturbation through the coupling of these two potentials (magnetization or/and applying an external magnetic field) and which leads to the degeneration of the M_s-levels (Fig. 1.3a, b). In addition, a third Hamiltonian H_2 describes the interaction with the surrounding. In Fig. 1.3 c) and is where the system relaxes and the two potentials are again equally occupied.[26, 30]

$$H = H_0 + H_1 + H_2 (1.3a)$$
$$H_0 = D[S^2{}_z - S(S+1)/3] + g\mu_B H_z S_z (1.3b)$$
$$H = D[S^2{}_z - S^2/3] + E[S^2{}_x + S^2{}_y](1.3c)$$
$$E(Ms) = D(M^2{}_s - 110/3) + g\mu_B H_z M_s (1.4)$$

D (negative for SMMs) is the axial and E is the rhombic zero-splitting parameter. The axial term of the Hamilton operator (which is an approximation) gives the energies of the M_s states, while the transversal terms the lead to mixing of the M_s states. This usually influences SMM behaviour negatively since QT becomes active. [26]

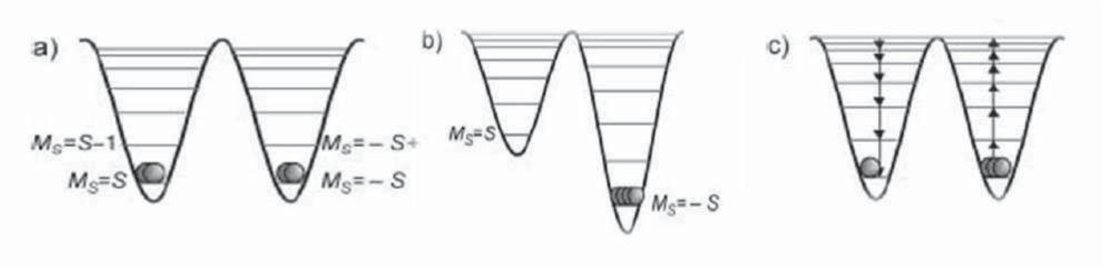

Figure 1.3. a) Undisturbed situation and D is negative so all ±M_s are in lowest states, b) disturbed through coupling, here also can the tunnelling happen and c) relaxation to the original state. [26]

Magnetic Properties of (oxo bridged) Fe^{III} in Complexes

A large ground spin state in CCs with Fe^{III} (d^5, high spin) could be achieved by assembling individual ions ferromagnetically. The high spin ground state of individual ions such as high spin Fe^{III} [31], Mn^{III} [32], Fe^{II} ($S = 2$) [33] is one reason why they are of interest in SMM research. In fact, all three ions can show significant single ion magnetic anisotropies, with the ZFS for the hs d^5 configuration of Fe^{III} resulting from mixing of low lying excited states. Iron(III) turns out to be a useful ion for producing SMMS.[31] A further relevant feature is that ferritin, the iron-storage protein form in most living organisms, can be considered itself as a nanosize magnetic particle. In fact ferritin has been investigated for quantum tunnelling effects of the magnetisation. Many large iron clusters have been reported, ranging from binuclear up to thirty nuclearity species. [31] All synthesized Fe^{III} SMMs so far reported are characterised by antiferromagnetic coupling between the Fe^{III} ions so that large spin in the ground state can only arise if the overall coupling can be described as ferrimagnetic.[read 31a)] Essentially such behaviour for a CC results from different magnitudes of exchange coupling between pairs of iron centres with a result similar to that seen in bulk ferromagnetic materials with antiferromagnetic coupling of spins of unequal magnitude (e.g. magnetite). In the molecular system the effect derives from the many different J-values present and which are responsible for the effect of uncompensated spin ground states. It has been argued that the defect Fe^{III} oxide maghemite, γ-Fe_2O_3 is an example of a bulk ferrimagnet with a similar type of non-compensation of magnetic moments and that ferrimagnetic iron–oxo clusters can be considered as models of this prototype mineral. [31a]

The exchange interactions in oxo-bridged Fe^{III} pairs have been much investigated both theoretically and experimentally. The simplest approach considers two parameters, the average metal–oxygen distance, *P*, and the metal–oxygen–metal angle, α. Magnetic data recorded on a large series of iron complexes suggest that the *P*-dependence of the exchange coupling constant, *J*, is well represented by equ.1.5.[31a]

$$J = 1.753 \times 10^{12} \exp(-12.663\, P)(1.5)$$

Where *J* (sometimes expressed as 2J) is expressed in cm^{-1}, *P* in Å, and the exchange Hamiltonian is in the form $H = JS1 \cdot S2$. The coupling constant is largely insensitive to the Fe–O–Fe angle for $\alpha > 120°$. For smaller angles an effect is clearly observed, *J* becoming smaller as the angle α is reduced. A systematic study has been performed in a series of binuclear complexes with two alkoxo bridges and similar Fe–O distances. The values of the angles range from 102 to 106°, while *J* varies between *ca*. 15 and 21 cm^{-1}. Is the coupling constant negative? so the coupling is antiferromagnetic. The simplest correlation was found to be of the type given by equ. 1.6.

$$J = 1.48\alpha - 135\,(1.6)$$

With *J* being given in cm^{-1} and α in degree. An extrapolation of eqn. (1.6) suggests that for $\alpha \approx 90°$ the coupling should become ferromagnetic. The decrease in the antiferromagnetic coupling constant for $\alpha < 120°$ has been predicted by a complete exchange model recently. **[31a, 34]**

The anisotropy of the pairs depends on the anisotropy of the individual ions (single ion anisotropy) and on an additional term that is brought about by the interaction between the two iron ions (spin-spin anisotropy). High spin Fe^{III} has a d^5 configuration, which yields an orbital singlet ^6S ground term for the free ion. The ground state of the ion in complex is also orbitally non-degenerate; therefore the Zeeman anisotropy is very low, with $g_x \approx g_y \approx g_z \approx 2.0023$. However some admixture with excited states of lower spin multiplicity is allowed by spin–orbit coupling and the ground $S = 5/2$ state does show zero field splitting, which may easily be of the order of 1 cm^{-1}. [31a]

The anisotropy associated with the spin–spin interaction can be described to a good approximation by the interaction between the magnetic points dipoles centred on the two iron ions. For a pair of antiferromagnetically coupled ions the dipolar interaction orients the two spins orthogonal to the vector *r* connecting the two centres. In fact the poles of the same sign would be in contact for an orientation parallel to *r*. Therefore the plane perpendicular to *r* (Fig.1.4) is a hard plane for the magnetisation of the antiferromagnetic dimmer, which is more easily magnetised when the field is applied parallel to the axis connecting the two spins. [31a]

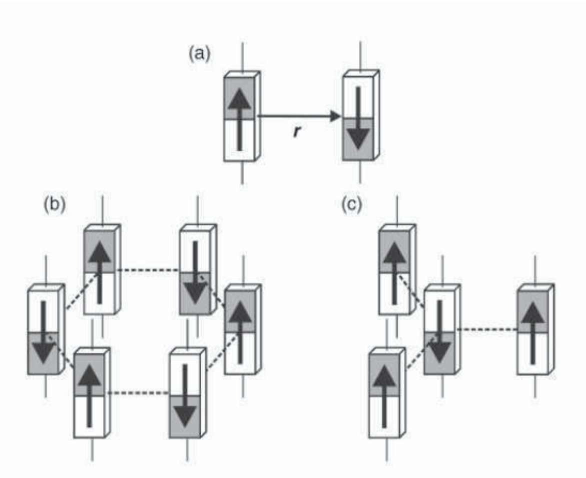

Figure 1.4. Schematic representation of preferred spin orientation due to the dipolar interaction in an antiferromagnetic Fe^{III} dimmer (a), in a cyclic antiferromagnetic Fe^{III} cluster (b), in a ferrimagnetic tetrameric Fe^{III} cluster (c). Adapted from [31a)].

Dipolar interactions thus provide an Ising-type contribution to the magnetic anisotropy. These considerations can be extended to polynuclear systems. In particular, when antiferromagnetically coupled metal ions are arranged in a planar structure with axial symmetry, nearest-neighbour dipolar interactions determine an *XY* anisotropy with an easy plane of magnetisation when the ground state has $S = 0$ (Fig. 1(b)). In fact, in the lowest-energy configuration, the individual spins are antiparallel to their nearest neighbours (owing to exchange interactions) and perpendicular to the average plane through the metal array (dipolar interaction). [31, 34] A ferrimagnetic system, however, exhibits Ising type anisotropy (Fig. 1. c).

Cyclic CCs containing Fe^{III} which have so far been reported are six, eight, ten, twelve and eighteen member. In all the cases the Fe^{III}-Fe^{III} interaction is antiferromagnetic with S=0. Thus, the energies of the lowest states can be expressed according to equ. 1.7.[31a]

$$E(S) = J_{eff} S(S+1)(1.7)$$

Where J_{eff}= 4J/N, with N the number of iron ions. Such rings are non-magnetic at very low temperatures. By increasing the field the excited magnetic states are stabilized, till they become the ground state. Now the S=1 is the ground state and then S=2 and so on. This is result of energy state mixing such as in QT. [31, 34]

The smallest iron cluster (Fe^{III}) which found to exhibit slow relaxation of magnetization became in the meanwhile the first member of a family of {Fe_4} clusters (Fig. 1.5, left). These compounds are ferrimagnets (S=5/2). [18, 31]

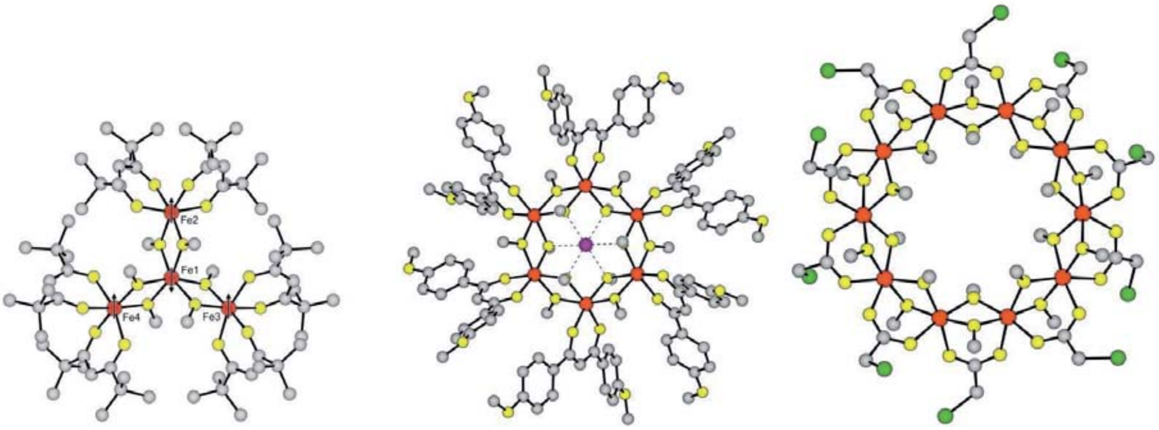

Figure 1.5. Examples: $[Fe_4(OMe)_6(dpm)_6]$ with dpm= 2,2,6,6-tetramethylheptane-3,5-dionate (left), $[NaFe_6(OMe)_{12}(pmdbm)_6]^+$ with pmdbm= 1,3-di(4-methoxyphenyl propane)-1,3-dionate (middle) and $[Fe(OMe)_2(O_2CCH_2Cl)]_{10}$ (right). Fe (red), O (yellow), Cl (green), Na (purple), C (grey). Adapted from [31a].

All members of this family are SMMs except one which has very similar parameters and was prepared with a Schiff-base ligand, which led to the question what makes a SMM?[18] A famous example of an Fe-SMM with high S is the {Fe_{19}} S = 33/2 system.[31b-d)] Very recently, *Gatteschi et. al.* discussed and compared the properties of Molecular Nano-Magnets (MNM) and Magnetic Nano-Particles (MNP), using the Fe SMMs as examples of MNMs and postulating that these provide a bridge between the molecular and the bulk world of magnetism within a quantum regime. This gives hints as to how (if?) size can play a role in the magnetic properties of these two classes of compounds. [31l)]

Magnetic Properties of Ln^{III}

Strictly speaking, the lanthanides are the elements coming immediately after lanthanum in the periodic table where the 4f orbitals become filled with electrons. Lanthanum itself is part of group 3 (modern nomenclature) of the periodic table and sits directly below yttrium. Together with Sc and Ac these metals are known as the rare earths, although none of them are especially scarce. As a result of the size of its ionic radius, Y^{III} actually turns out to be a useful diamagnetic analogue for the later Ln^{III} ions which have substantially reduced ionic radii due to the lanthanide contraction. [19]

The energy levels of the $4f^n$-configurations can be derived using a Russell-Saunders coupling scheme to a fair approximation. Moreover, the spin-orbit coupling constants are very large (*ca.*1000cm^{-1}). As result, the lanthanide (few exceptions) ions feature a ground state with well defined value of total angular *J* with the result that the next *J* state is energetically much higher than k_BT (*ca.* 200 cm^{-1}) and consequently unoccupied. From there, the susceptibility and magnetic moments of lanthanides can be estimated using formulae with well-defined *J* values. In the case of Sm^{III} and Eu^{III} the first excited *J*-state is (as observed) close to the ground state. While anisotropic Ln^{III} ions are excellent candidates for obtaining SMMs, their electronic structures are extremely complex. [19]

This is because electronic spin is no longer the only significant source of angular momentum in the system. The degeneracy of the f orbitals yields large orbital moments (note Ho^{III} has the largest magnetic moment) that must be taken into consideration. Thus, for Dy^{III}, simply defining this as $4f^9$ is far less descriptive than the term symbol for the spin–orbit coupled ground state: $^6H_{15/2}$ (S = 5/2; L =5; J = 15/2) (Fig. 1.6, left). The spin–orbit coupled quantum number, *J*, is highly important since the spin–orbit coupling energy is generally larger than the effect of the crystal field for f-elements.

The ground J state of Dy^{III} is sixteen-fold degenerate ($2J_{Dy}$ + 1 states) and composed of magnetic sub-states, m_J, characterized by m_J= ±15/2,………, ±1/2 (+*J*, *J*-1, …-*J*). These projections of the total angular momentum quantum number can be affected differently by the surrounding crystal field, thereby removing the (2*J* + 1)-fold degeneracy of the ground state. This splitting, in combination with the strong spin–orbit interaction, links the orientation of the spin to the strength and symmetry of the ligand field. The implication for SMMs is that we can increase single-ion anisotropy simply by judiciously choosing the coordination environment of the lanthanide ion. It is becoming clear that the Dy^{III} ion often represents the ideal ion for single-molecule magnetism:[36a] it is a Kramer's ion, so a doubly degenerate m_J ground state must result, and it combines a large-moment $^6H_{15/2}$ ground state with significant anisotropy of the 4f shell.

Recently a perspective article from *Long et. al.*[19] was published. They give a simple model of the f-element electronic structure from which the single ion anisotropy of Ln^{III} ions is mainly discussed. They used the simplest Hamiltonian to describe the 4f ions plus their relation to the ligand field (equ. 1.8). They assume that single-ion anisotropy can be guaranteed when doubly generated m_J states can be largely separated from the excited ones through special ligand types such as the phthalocyanine ligands.

$$H = H_{ion} + H_{cf} \, (1.8)$$

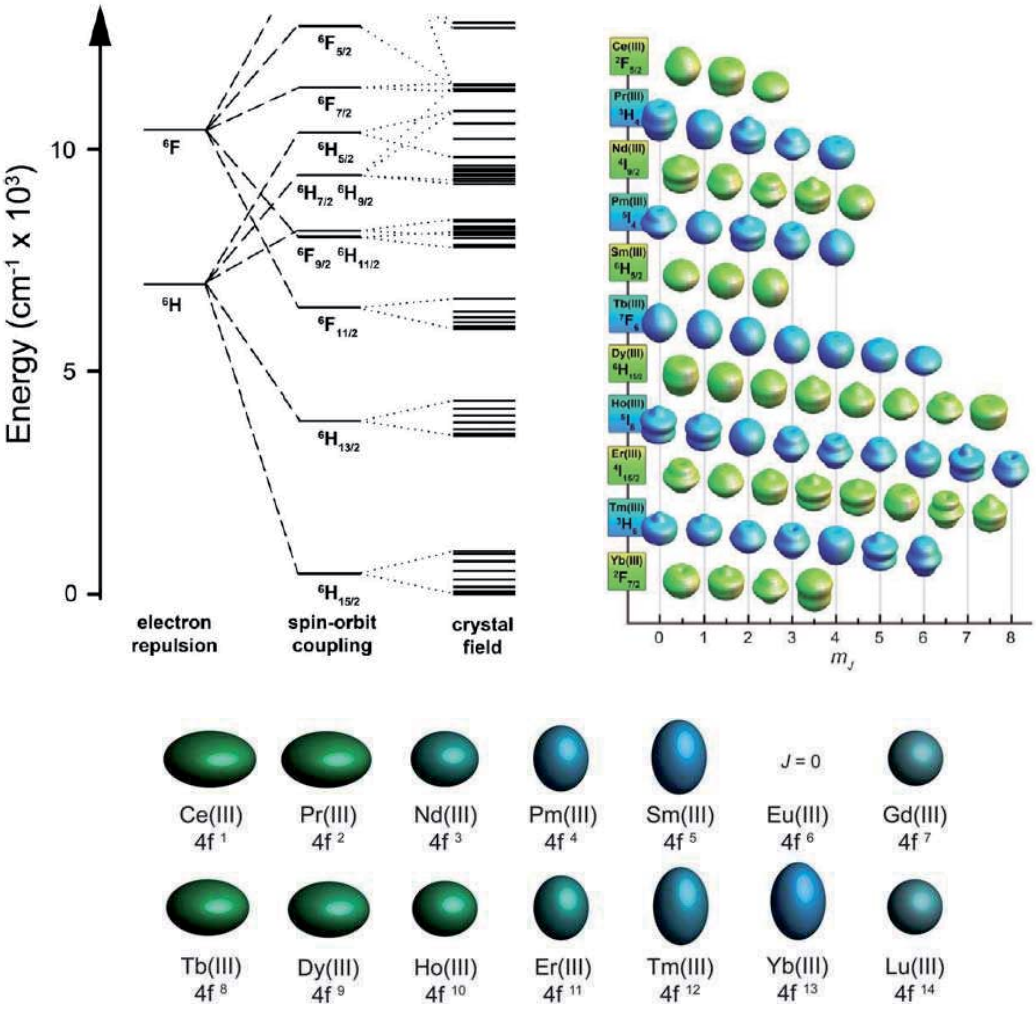

Figure 1.6. (Upper, Left) Low energy electronic structure of Dy^{III} ion with sequential pertubations of electron-electron repulsion (H_{ee}), spin-orbit coupling (H_{so}), and the crystal field (H_{lf}). The crystal field splitting is constructed from a model for the complex $[Dy((Me_3Si)_2N)_3]$. (Upper, Right) Approximation of the angular dependence of the total 4f charge density for m_J states composing the lowest spin-orbit (J) state for each Ln^{III}. In the absence of a crystals field all m_J states are degenerate. (Lower) the quadropule approximations fort he 4f shell distributions. Fore example, Tb^{III} oblate and Tm^{III} prolate. Prolate is axially elongated and oblate is equatorially expanded. Adapted from [19].

In Fig. 1.6 the electronic structure of the Dy^{III} ion (modelled for compound $[Dy((Me_3Si)_2N)_3]$) and the 4f charge density for the m_J states as well as the quadropule appromation for the 4f shell distribution for Ln^{III} ions are illustrated. These Figures are taken for the recently reviewed properties perspective article from *Long et. al.*[19]. They give a simple model of the f-element electronic structure from which the single ion anisotropy of Ln^{III} ions is mainly discussed. They discuss the shape of each ion's 4f-shell (the lowest *J*) (Fig. 1.7, upper and right and lower) as mathematically calculated quadruple approximations (Fig. 1.6, lower). They also discuss the angular dependence of the total 4f charge and how they differ for each ion (Fig. 1.6, upper and right).

However, this model also suggests a less explored method of generating strong single-ion anisotropy for single-molecule magnet synthesis involving strongly prolate ions like Tm^{III} and Yb^{III}. In general the Ln^{III} ions can provide remarkable examples of SMMs and SIMs showing very high energy barriers. [35] However, very fast relaxation rates and QTM effectively remove any possibility of using these high barriers to trap information in one magnetic sublevel state

Fe^{III}/4f chemistry

The strongest solid-state magnets are compounds containing lanthanides in conjunction with 3d metals such as $SmCo_5$ and $Nd_2Fe_{14}B$. In these materials, the electronic structure is usually described differently from the descriptions used for molecular systems and the link between the magnetic properties of CCs and such essentially inter metallic systems is hard to identify at present. However, the fact that such strong magnetism can be produced in these systems suggests that it should be possible to produce molecular-based systems with promising properties.

The number of FeDy SMMs is small and the work in our group is unique in exploring the synthesis of such compounds with the view to performing Magneto-Mössbauer correlation studies as a means of probing bulk and local propertiesFe/4f CCs based on molecular magnetism.[36] The clusters systems so far reported in the literature are: $\{Fe_2Ln_2\}$ (see chapter 2) [20], $\{Fe_5Ln_8\}$ [36b)], $\{Fe_7Dy_3\}$ [36c], $\{Fe_4Ln_2\}$ [36d)], $\{Fe_3Ln\}$[36e], $\{Fe_{16}Ln_4\}$ (see chapter 3) [36f] and $\{Fe_4Dy_4\}$[36g)] as well as $\{Fe_7Dy_4\}$[36h)]. Other groups reporting bulk magnetic studies on Fe/4f compounds have published data on $\{Fe_4Ln_2\}$ and $\{Fe_{12}Ln_4\}$.[37]

1.3 Magneto Caloric Effect (MCE)

3d-4f as well as 3d and 4f MMs are suitable candidates for showing the Magneto-Caloric Effect (MCE) if they possess high total spin. However, no MCE studies have been published so far on Fe/4f systems (see chapter 4). [38]

A thermodynamic interaction of a material with a magnetic field can cause an entropy change. The entropy (non-classical) of a system with a number of quantum states Ω (non-degenerated) is given in equ. 1.9. The relation between the entropy and magnetism can be found in the magnetic moment of a system since it has 2S+1 magnetic levels and this is given in equation 1.10.[39]

$$S_E = k_B \ln(\Omega) \quad (1.9)$$

$$S_E = R \ln(2S+1) \quad (1.10)$$

Fig. 1.7 shows the MCE with adiabatic demagnetization. The system is adiabatic which means that its entropy stays constant by changing the field. Now, if the system is adiabatic and it is in general state $A_i(T_i, H_i)$, also its temperature is T_i and "feels" a magnetic field H_i, and if the any change in the field would cause change in the entropy, so this change should be compensated somehow. In the MCE, the compensation can be by an equal but opposite entropy change associated to with lattice. As result of this the temperature of the system changes. [39]

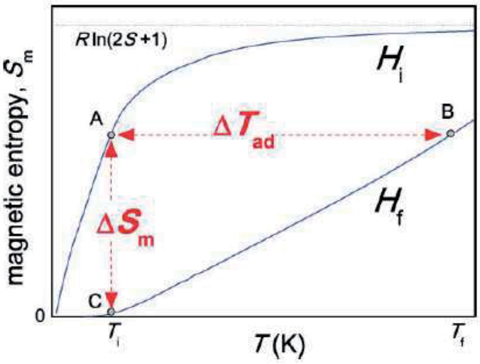

Figure 1.7. Molar magnetic entropy of a (super)paramagnet with spin S per formal unit, as a function of temperature, for magnetic field H_i and $H_f > H_i$. *AB* process: adiabatic magnetization providing ΔT_{ad}. *AC* process: isothermal magnetization providing ΔS_m. [39]

As shown in Fig. 1.7 the field change from *i* to *f* state brings the system to the general state B and the temperature of the material changes to T_f. The change in the entropy ΔS_m. can be achieved by the isothermal change of H_f which brings the system to the general state C. The MCE effect can be understood through the two characteristic parameters ΔT_{ad} and ΔS_m. [39]

Ferromagnetic materials become attracted to a magnet, thus, high spin compounds can show high MCE and particularly so if their spins are isotropically oriented.

This effect has been known since 1881 and is important in magnetic refrigeration; [40] in solid materials (e.g. containing Gd) [41] and in nano-materials [41]. However, only recently have chemists begun to investigate magnetic coordination clusters as systems which could allow access to extremely low temperatures. [38] It is very important to differentiate between the MCE effect for solid state materials and for CCs. *R. Sessoli et. al.* recently discussed this effect but for MM with the title “Chilling with Magnetic Molecules”. [39c)]

1.4 Mössbauer spectroscopy [42]

The Effect

The Mössbauer method will be discussed in more detail since this method is essential in the explanation of the magnetic behaviour of the compounds which are discussed in this work (mainly chapter 2 and 3).

The Mössbauer effect is based on the “recoil-free resonant nuclear-absorption” of gamma (γ) rays by a nucleus, which is emitted by their radioactive isotope source. Although many isotopes are theoretically Mössbauer-active; only a few are commonly investigated as a result of their long life-time and detectable ɣ-energy: ^{57}Fe, ^{119}Sn, ^{121}Sb, ^{151}Eu.

The most used radioactive source is ^{57}Co , which decays via electron capture (EC, Fig.1.9) to the second excited state of ^{57}Fe (I= 5/2) with a γ-energy of 136 keV. 85-91% then relaxes to the first excited state of ^{57}Fe (I= 3/2) with 9-15% relaxing directly to the ground state ^{57}Fe (I= 1/2). In addition, a second relaxation can happen which is from the first excited state to the ground state and generates a γ-ray with energy 14.4 keV and which is used practically to investigate materials containing iron. The detector can be adjusted for the detection of this range of energy. All higher energy levels (such 136 keV) are too broad for detection and thus are subtracted.

To avoid loss of energy (kinetically) because of recoil the sample can be fixed in a matrix (crystal) such as a rhodium matrix which makes the atom massive enough not to recoil. In addition lowering the temperature of the measurement helps in minimizing the vibrations so that a good spectrum can be obtained. In these conditions it is possible to achieve resonant absorption by modulating the energy of the γ- ray beam by oscillating the γ- ray source with the resulting Doppler shift changing the energy of the photons (Fig. 1.10).

The Outputs

From Mössbauer spectrum three outputs can be later analyzed which give information regarding oxidation state, environment and magnetism of the studied matter (table 1.1): i) Isomer shift (δ), ii) Quadruple splitting (ΔE_Q) and iii) Magnetic splitting (ΔE_M). The isomer shift δ results from the difference in the electron densities around the nuclei on both sides (absorber and emitter). The spectra will be also shifted if the number of valence electrons in the absorber is different than that in emitter. This helps in identifying the oxidation state and the spin state. It can be expressed through the follow equation (equ. 1.11):

where, *Z* is the atomic charge, *e* the electronic charge, *R* effective nuclear radius, *c* velocity of light, E_γ energy of γ-ray, and $\rho(0)$ terms are total electron densities at the nuclei for absorber (a) and source (s). ΔR is the difference between *R* (excited) and R (ground).

$$\delta = \left(\frac{Ze^2R^2c}{5\varepsilon 0 E\gamma} \right) \left[\rho_a(0) - \rho_s(0) \right] \left[\frac{\Delta R}{R} \right] mms^{-1} \, (1.11)$$

The 3d orbitals (here Fe; [Ar] $3d^6$ $4s^2$, Fe^{II}; $3d^6$ $4s^0$ and Fe^{III}; $3d^5$ $4s^0$) partially shields the nucleus from the influence of the 3s, and so the ion with the most electrons in the 3d orbital will do the most shielding, i.e. Fe^{2+}. This smaller density gives a greater magnitude of difference between the emitter and absorber, hence a larger isomer shift.

If the surroundings of the nucleus do not have spherically symmetric charge distribution, the nucleus will possess an electric nuclear quadruple moment. This leads to splitting of I= 3/2 to m_I= ± ½ and ± 3/2 (Fig 1.11).

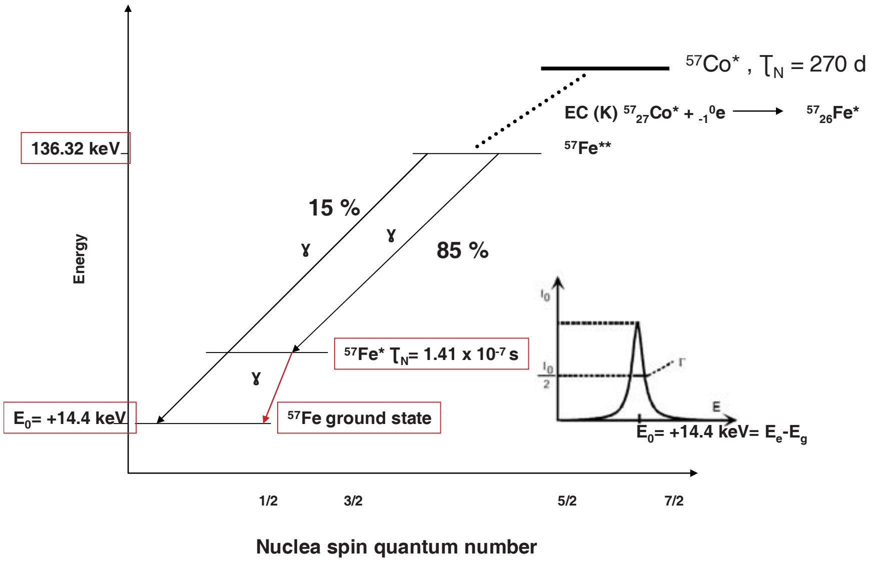

Figure 1.9. Shows a very trivial spectrum for an emitter and absorber in the same surroundings. [42]

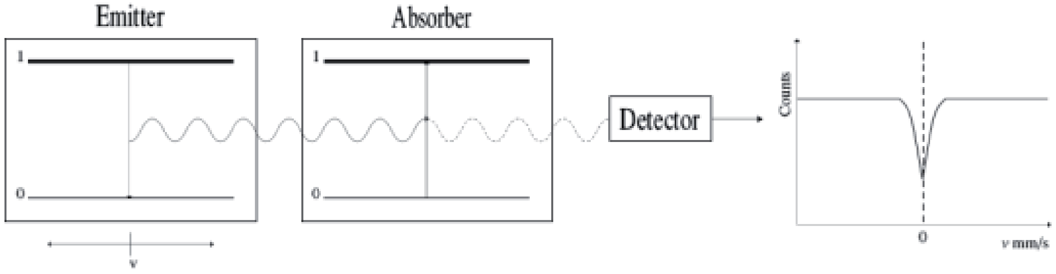

Figure 1.10. Singlet observed when Emitter and Absorber have same environment. [42]

The Spectrum

The splitting of the energy levels through a quadruple can be expressed through the formula (1.12): with the largest field gradient (equ. 1.13).

The angular dependency of the quadruple-term gives the possibility to determine the orientation of spins. The magnetic splitting is directly proportional to the applied magnetic field. In this case the nucleus interacts with the magnetic field and this leads to removing the degeneracy of the sub-states with angular momentum quantum number (I> 0 to 2I+1). The ground state of ^{57}Fe splits into two (-1/2 and 1/2 and the first excited into four (-1/2, +1/2, -3/2, and 3/2). The allowed selection rule is that $\Delta m_I = 0, \pm 1$ and there are thus six maximum obtainable transitions. (Fig. 1.12)

Table 1. 1. Summary of the information which can be gained from Mössbauer measurements.[43]

Interaction	Mössbauer-parameter	Informations
electric monopol-interaction between nuclei and the electrons at nuclei sites.	Isomer shift δ [mm/s]	-oxidations state - bonds - electro-negativity of ligands - spin state
electric quadruple- interaction between electric quadruple moment of a nuclei and inhomogeneous electric field at nuclei sites.	Quadruple splitting ΔE_Q [mm/s]	- molecule symmetry - bonds
magnetic dipole- interaction between magnetic dipole moment of nuclei and magnetic field at nuclei sites.	Internal magnetic splitting ΔE_M [mm/s]	- magnetism of material

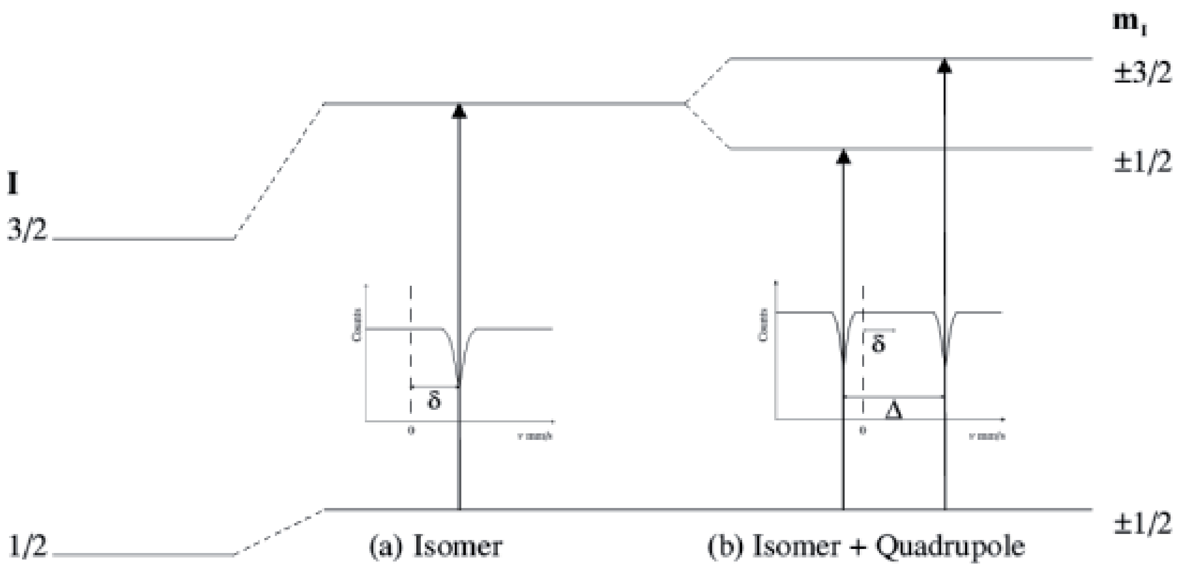

Figure 1.11. Schematic representation of isomer and quadruple splitting to $m_I = \pm 1/2$ and $m_I = \pm 3/2$. [42]

$$\Delta E_Q = eQV_{zz} \quad (1.12)$$

$$V_{zz} = \frac{1}{4\pi\varepsilon_0}\sum_i q_i^{-3}(3\cos^2\theta_i - 1) \quad (1.13)$$

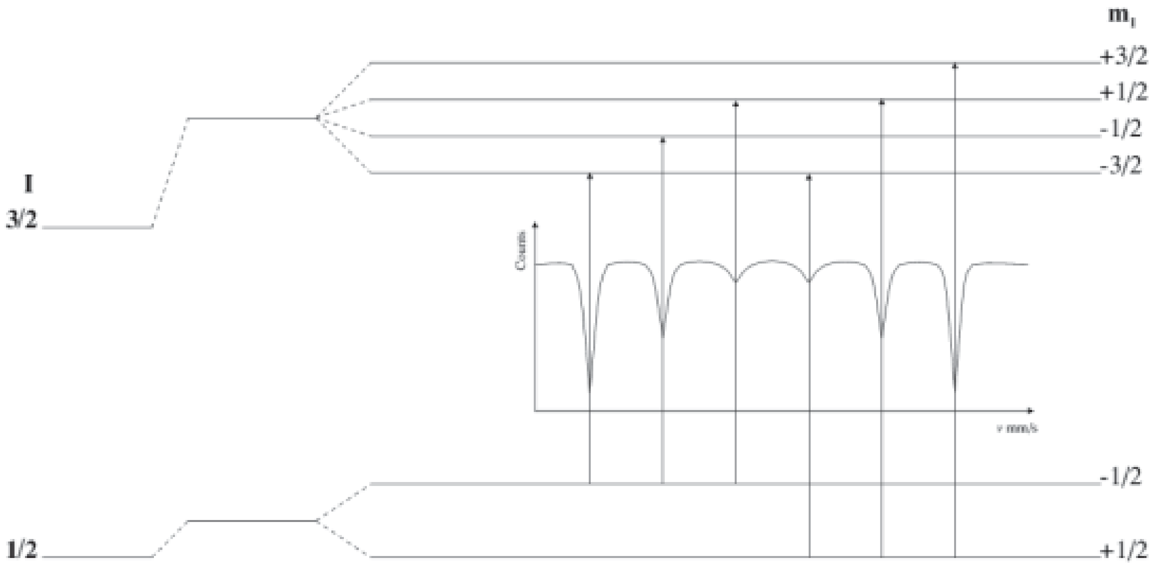

Figure 1.12. Schematic representation of the six allowed lines when magnetic splitting also observed. [42]

The field is actually a combination of applied and hyperfine field. Normally, if all electrons are paired (e.g. antiferromagnetically coupled Fe^{III} ions) then the magnetic splitting is equal to the applied filed? The effective hyperfine field (B_e) resulting from applied field can be expressed through equ. 1.14).

$$B_e = B_c - \left(\frac{3\cos^2\theta - 1}{2}\right)B_d \pm B_a \pm B_{dm} \text{ - - - - - }(1.14)$$

Where B_c contact and B_d dipolar are the terms of the hyperfine field, B_a is the applied and B_{dm} is the demagnetizing field.

The Mössbauer technique is a very sensitive method which can be very helpful in understanding the magnetic behaviour and as a complementary method to magnetism. In our group, we demonstrated how important this method is in order to understand the magnetic anisotropy of Ln^{III} ions in FeLn CCs [36] and additionally for the determination of the ground spin state of high nuclearity Fe^{III} cluster(s) by combined use of magnetic measurements and Mössbauer spectroscopy.[44]

1.5 Electron Paramagnetic Resonance (EPR) spectroscopy

In the presence of magnetic field unpaired electrons absorb microwave energy and this changes their spin ($\Delta m_s = \pm 1$). Unlike susceptibility measurements no signals can be observed from diamagnetic systems. The spin of the electron s and the angular momentum *l* are related through the magnetic moment where g_e is the Landé factor and it is for free electron equal to 2.0023. By applying electromagnetic radiation perpendicular to the static field, transitions between the energy levels will be induced to give resonance and the characteristic spectrum for a free electron. [45]

Transitions are indeed possible if alternating field is perpendicular to the static one. However, if several unpaired electrons are involved, the basic formula for EPR is modified by replacing g_e by g (equ. 1.15), which is reasonable since this effective g- factor described within the context of the Russell-Saunders coupling scheme. [45]

$$h\nu = g\beta H (1.15)$$

Usually, EPR spectroscopy has been used in our group to confirm the value of S obtained from susceptibility measurements using HFEPR. For example, the EPR method (W-band) was used to look at high spin CCs such as Fe_{19} [46a)] and Mn_{19} [46b)]. In general, if the cluster has high symmetry it is easier to study it by the EPR method. However, in the work described here, the much lower frequency technique of X-band EPR was used and although this can give no information regarding S states [47] it is a useful extra method we used to support magnetic, Mössbauer and theoretical data for a full series of Fe_2Ln_2 compounds (chapter 2).

1.6 Femtosecond Spectroscopy

Femtosecond Chemistry

Femtosecond chemistry [48] can be used to study the chemical reactions and properties of chemical compounds on extremely short timescales (10^{-15} s). In particular, the method makes it possible to gain a picture of fast electronic transition processes. This method was used, to study the electron dynamics in a cyclic CC system (chapter 4) in collaboration with the group of PD Dr. Unterreiner (physical chemistry department) at KIT. Some of these results are presented in Chapter 4. More details about the experimental method and physics background can be found in the the work of Dr. Unterreiner with the title (in German) "Ultraschnelle Relaxationsdynamik solvatisierter Elektronen in flüssigem Ammoniak und Wasser" which translates as means "Ultrafast relaxation dynamic of solvated electrons in liquid ammonia and water". In this work, the mode-locking is explained which a necessary technique by which a laser can be made to produce pulses of light of extremely short duration. Furthermore, details about the laser types, many technical details as well as experimental details about the Pump-

Probe technique are given. More physical details about the results of the femtosecond method in this work will be found in the PhD thesis of Yu Liang from this group. [49]

Pumpe-Probe Technique

The "Pump-Probe" technique is probably the one most used in this field since it represents a powerful technique to obtain information on electron dynamics on an ultra short time-scale. The main principle of this method is the use of two or more optical pulses with a variable time delay between them. [49] This means excitation to the first or second excited state of the material can be achieved after the first pulse (pump). A (probe) pulse is used to detect the electron dynamics and the data collected can help in understanding, for example, optical properties. In order to follow the progress in real time, continuous scanning of the time delay between pump and probe is performed. (Fig. 1.13)

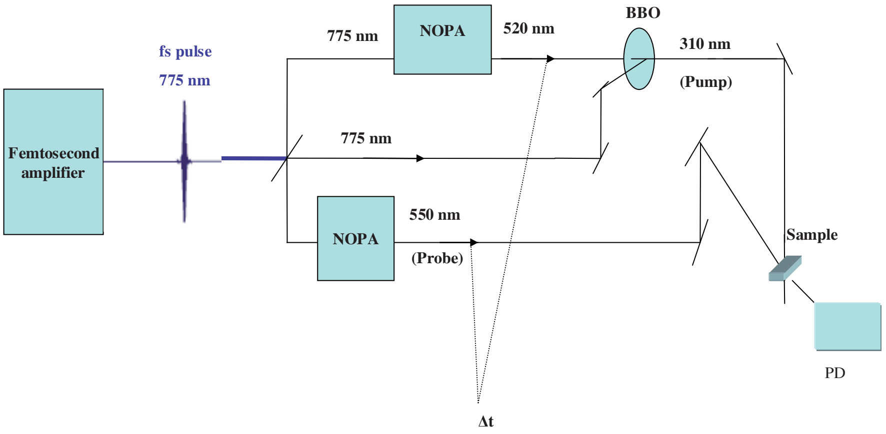

Figure 1.13. A schematic representation for the principle work of Pump-Probe technique. BBO (*ß*-Barium borate), optic active crystal, 775 nm is the central wave length, NOPA the unit for frequences conversion where also the white light becomes produced and Δt is the time delay. PD means detector units. This simple scheme was made by the author of this work. If the reader is interested in more detailed figures which explain the Pump-Probe method in much more details, see ref. [57]

In this particular set-up, the UV-VIS spectroscopic region is investigated, which is in contrast to most other femtosecond set-ups which tend to look in the IR region. As will be seen in

Chapter 4, this has allowed us to gain some remarkable insights into the modification of the electronic behaviour of systems containing Fe and 4f metal ions and is undoubtedly the first time this technique has ever been applied to such molecular systems (notwithstanding the fact that the CCs are completely new species). The femtosecond pulse (life time 100 fs) is specifically used to investigate species in excited states, but also the very fast timescale of the experiment makes it possible to capture snapshots of processes which are simply too fast to register using other techniques. Femtoscond spectroscopy has also been described as 2D-spectroscopy because both the spectral and temporal domains are detected. [50]

The Use

Using this method it is possible to study very fast dynamics such as short-lived exciton formation seen in solid-state semiconductors[51] or organic semiconductors [52], carrier dynamics and studies on single-wall nanotubes[53], ultrafast spectroscopic studies of photo induced processes such as electron transfer in semicondcuting polymers to C_{60}[53]and ultrafast (transient) absorption processes in general[54]. Recently, femtosecond studies of spin-state photo switching of molecular SCO iron nanocrystals were reported. [55] Relaxation dynamics in electronically excited C_{60}^{-} were also reported. [56]

1.7 Thesis Overview

This work presents fundamental research with a view towards possible applications.

In total more than 100 compounds were prepared and characterised. Some were studied in considerable depth using a range of characterisation methods to gain understanding about the electronic structures of them. Others systems were developed with a view to gaining insights into self-assembly processes and how they may be controlled. Furthermore, starting materials and several reference compounds were also prepared.

Chapter 2 presents a comparative study of a Fe_2Dy_2 family of Coordination Clusters (CCs). These compounds show Single Molecule Magnet (SMM) behaviour, including Quantum Tunnelling of Magnetisation (QTM), have a robust structure and contain Fe^{III} allowing for investigation using the Mössbauer method, and the Ln centre can be varied across the lanthanides. Thus this family presents a relatively simple Fe/4f cluster core motif and was selected in order to provide a “test bed” for monitoring the effect of changing details of the core’s electronic structure through variation in the 4f ion and within the ligand shell. In particular, it was of interest to gauge the effect of varying the substituent (its electronic nature) on the benzoate ligands in these CCs on the magnetic anisotropy of the system. The structure also contains two triethanolamine ligands which can be replaced by related amino alcohol ligands. Chapter 2 reports results on the full series of 13 $\{Fe_2Ln_2\}$ which were prepared and structurally characterized and subjected to intensive study using bulk magnetic susceptibility, Mössbauer and EPR methods. Moreover, 28 $\{Fe_2Dy_2\}$ (as well as for some cases Gd and Y as well) compounds could be prepared with different benzoates and ligand combinations. Theoretical calculations were also done for the series and for some $\{Fe_2Dy_2\}$ compounds in order to investigate the role of the substituent from a different angle. In this way it was possible to elucidate the effect on the electronic structure by the use of these complementary techniques.

Chapter 3 provides a bridge between chapter 2 and chapter 4. The fact that triethanolamine can form cyclic iron-containing CCs was used in order to prepare Fe/4f CCCs using an adaptation of the synthetic strategy for the non-cyclic compounds presented in chapter 2. Furthermore, several subtle synthetic changes were used in order to control the self-assembly of CCCs. In other words, the changes in the synthesis of $\{Fe_2Ln_2\}$ system will be “ringed”.

In total 19 CCCs with different ion arrangements and properties were prepared and studied using Mössbauer and bulk magnetic susceptibility methods. This chapter underlines the importance of the Mössbauer method in explaining the behaviour of these systems in more detail than is possible from bulk magnetic susceptibility measurements alone. Furthermore, two $\{Dy_6\}$ CCCs were prepared for comparative purposes.

In chapter 4 a series of 11 $\{Fe_{10}Ln_{10}\}$ CCCs is presented. The magnetic behaviour, the optical properties, the Mössbauer spectra and the behaviour in water were all studied. The compounds are magnetically interesting and the Dy analogue is a good SMM. Furthermore, all compounds are predicted to be useful systems utilising the Magnetocaloric Effect (MCE) on a molecular level for magnetic cooling. The Dy and Gd systems were investigated in more detail to this end, and do indeed show promising parameters as well as achieving very high spin ground states.

The optical behaviour was studied by steady-state absorption spectroscopy as well as using femtosecond spectroscopy (Pump-Probe technique). This system has remarkable characteristics which might be generally representative for Fe/4f CCCs and perhaps for 3d/4f in general. The observation that the characteristic charge-transfer band expected for Fe^{III} ions in the coordination environments found here seems to be missing prompted an in-depth investigation of the properties of these materials. The femtosecond spectroscopy results made it possible to propose that exciton formation is responsible for the “stolen” CT band and that the materials can be thought of lanthanide-doped ferric oxide systems. Thus the chosen as lanthanide can be used to modulate the overall behaviour of the system.

Furthermore, these systems appear to be photosensitive and show fascinating behaviour in aqueous solution involving gas evolution. A series of qualitative experiments was devised to gain insights into the processes of the system. These form the basis for future work on the compounds which seem to have very promising potential as multifunctional materials.

Chapter 5 gives a summary for all results and more importantly an outlook/ perspective for future work. In chapter 6 the experimental details are given and chapter 7 lists the literature sources. Chapter 8 contains an appendix with details of some of the work presented in the thesis for further reference.

Chapter 2

A Comparative Study of a Tetranuclear $\{Fe_2Ln_2\}$ Family

2.1 Introduction

In this chapter a study on the effects of introducing different substituents on the magnetic anisotropy of lanthanides (mainly Dy^{III}) within an $\{Fe_2Ln_2\}$ system is presented. It seems reasonable to propose that the electronic characteristics of ligands can directly influence the Single Molecule Magnet (SMM) behavior without changing the ground spin state. For these purposes a 3d/4f cluster system was selected, in which the influence of the ligand on the anisotropy of the lanthanide ion can be gauged by using the 3d centre (here Fe^{III}) as a sensor through a combination of bulk magnetic susceptibility and Mössbauer measurements.

A suitable $\{Fe_2Dy_2\}$ coordination cluster was selected for use as "test-bed". This cluster type is obtained by reacting triangular oxo-bridged trinuclear iron carboxylate complexes of general formula $[Fe_3O(O_2CR)_6(L)_3](X)$, with X= anion and L= H_2O, py, solvent such as methanol or ethanol and/or carboxylic acid with the ligand triethanolamine (H_3tea) and lanthanide salts. [58]

Oxo-bridged iron complexes play important roles in many areas of science and especially in understanding the biochemistry of iron.[58] The octahedral coordinated iron centres in dinuclear units of such systems can be connected through corner-sharing (singly bridged), edge sharing (doubly bridged) or face-sharing (triply bridged) oxygen atoms. The first two groups are far more common than the latter and in both cases tend to lead to mostly antiferromagnetic coupling of the two high-spin d^5-ions with J-values between small values such 0 and -15 cm^{-1} up to 100 cm^{-1}.

In addition, some of these complexes can be used as homogenous-catalysts for oxidation-reactions.[59a)] In case of intramolecular electron transfer processes, the trinuclear mixed-valence compounds had been intensively investigated. The redox properties[59b)] as well as kinetic studies via NMR-spectroscopy of 3d heterometallic and mixed valence oxo trinuclear clusters have been reported.[59c)] Mössbauer studies of many triangular clusters are also known.[59d)] In addition, magnetic studies in conjunction with HFEPR studies on some of the $\{Fe_3O(O_2CPh)(py)_3\}^+$ systems show that such a spin-frustrated compounds can have out-of-phase *ac* signals, which is a signature for slow relaxation of magnetization[59e)] . Other studies on such coordination clusters include Inelastic Neutron Scattering (INS)[59f)] and electrochemistry.[59b)] They are known with L-amino acids[59g)].

The trinuclear starting materials with different *para*-substituted, *meta*-substituted benzoates or *ortho*-substituted and other carboxylates were prepared using adaptations of methods in the literature [58, 59] (experimental chapter, starting materials with code **2.sm**).

The {Fe_2Ln_2} compounds have the general formula [$Fe_2Ln_2(\mu_3\text{-}OH)_2(O_2CPh)_6(teaH)_2$] (where $teaH_3$ is triethanolamine).

The published synthesis and crystal structure of [$Fe_2Ho_2(\mu_3\text{-}OH)_2(teaH)_2(O_2CPh)_4(NO_3)_2$]·6MeCN by Murugesu *et al.* [20a)] used the reaction of [$Fe_3O(O_2CPh)_6(H_2O)_3$](O_2CPh) with triethanolamine ($teaH_3$) and $Ho(NO_3)_3\cdot5H_2O$ in MeCN/MeOH solution. From the corresponding reactions with $Dy(NO_3)_3\cdot6H_2O$ or $Tb(NO_3)_3\cdot6H_2O$ they obtained complexes formulated as [$Fe_2Ln_2(\mu_3\text{-}OH)_2(teaH)_2(O_2CPh)_6$]·4MeCN·$3H_2O$ (Ln = Dy, Tb) from microanalytical data, which were assumed to have an isostructural core to that of the Fe_2Ho_2 complex although no crystallographic structural data were published. In my "Diplomarbeit" [60] the Dy^{III} analogue assumed by Murugesu *et. al.* could be isolated as well as those with some other lanthanides. In this work the series was completed and fully studied using a variety of different methods.

It was also found that by using the trinuclear complex [$Fe_3O(O_2CPh)_6(H_2O)_3$](O_2CPh) **(2.sm1)** [60] as starting material, and making small modifications to the published reaction conditions, a series of isostructural compounds [$Fe^{III}_2Ln^{III}_2(\mu_3\text{-}OH)_2(teaH)_2(O_2CPh)_6$]·3MeCN {Ce (**2.1**), Pr (**2.2**), Nd (**2.3**), Sm (**2.4**), Eu (**2.5**), Gd (**2.6**), Tb (**2.7**), Dy (**2.8**), Ho (**2.9**), Er (**2.10**), Tm (**2.11**), Yb (**2.12**)} can be obtained in high yield for all Ln^{III} ions (apart from radioactive Pm^{III}). Attempts to obtain analogues with the diamagnetic La^{III} and Lu^{III} ions were, however, unsuccessful. With La^{III} salts, a tetradecanuclear cluster [$Fe_8La_6(\mu_4\text{-}O)_4(\mu_3\text{-}OH)_8(tea)_4(O_2CPh)_{14}(OH_2)_4$]·$H_2O$·4MeCN (**2.15**) was obtained, which was discussed in the Diplomarbeit and will not be included here because, since it is not a part of the tetranuclear family, it is not important for the comparative study discussed in this chapter. Reactions with Lu^{III}, on the other hand, resulted in an [$Fe_4Lu_2(\mu_4\text{-}O)_2(\mu_3\text{-}OH)_2(teaH)_2(O_2CPh)_7(MeO)_2$] complex (**2.14**) and the previously reported octanuclear [$Fe_8O_3(O_2CPh)_9(tea)(teaH)_3$]·MeCN ({$Fe_8$}, **2.16**) [61]. The synthetic modification in this work avoids formation of the homometallic complex (**2.16**), which has been reported to form from reactions of the trinuclear benzoate starting material with triethanolamine in the absence of lanthanide salts. It is assumed that the compounds **2.7** and **2.8** are identical to Murugesu's Fe_2Tb_2 and Fe_2Dy_2 [20a] Despite the fact that there are slight differences between the lattice solvent content found in the crystal structures reported here and that estimated from their microanalytical data, we find that these complexes are moderately hygroscopic and these differences are not significant. Furthermore, the corresponding complex with the diamagnetic rare earth cation Y^{III}, $[Fe_2Y_2(\mu_3\text{-}OH)_2(teaH)_2(O_2CPh)_6]\cdot 3MeCN$ (**2.13**), could be obtained.

The $[Fe_2Ln_2]$ compounds with differently substituted benzoates have the general formula $[Fe^{III}{}_2Ln^{III}{}_2(\mu_3\text{-}OH)_2(L)_2(p,m\text{-}R\text{-}C_6H_4COO)_X]$, where X can be either 4 or 6, L= $teaH_3$ or Me-$teaH_3$ ligands and Ln= **8= Dy** (see scheme 2.2). In order to simplify the discussion about all these similar compounds a special code-numbering system will be also used which is $\mathbf{2.Ln}^{\mathbf{L\text{-}X}\boldsymbol{p,m,o}\mathbf{R}}$. For example, the $[Fe_2Dy_2]$ compound in the reference series has the number **2.8** and this compound contains six *p*-H- benzoates and it was prepared with triethanolamine as ligand, so the code can be **2.8 or** $\mathbf{2.8}^{\mathbf{teaH\text{-}6}\boldsymbol{p}\mathbf{H}}$ for compound $[Fe^{III}{}_2Dy^{III}{}_2(\mu_3\text{-}OH)_2(teaH)_2(O_2C_6H_4C\text{-}p\text{-}H)_6]$. The code $\mathbf{2.8}^{\mathbf{Me\text{-}tea\text{-}6pH}}$ implies the similar compound but with Me-$teaH_3$ as ligand $[Fe^{III}{}_2Dy^{III}{}_2(\mu_3\text{-}OH)_2(Me\text{-}teaH)_2(O_2C_6H_4C\text{-}p\text{-}H)_6]$. Similarly, the code $\mathbf{2.8}^{\mathbf{Me\text{-}tea\text{-}4}\boldsymbol{pH}}$ describes the compound $[Fe^{III}{}_2Dy^{III}{}_2(\mu_3\text{-}OH)_2(Me\text{-}teaH)_2(O_2C_6H_4C\text{-}p\text{-}H)_4(NO_3)_2]$. Another example is the compound $\mathbf{2.8}^{\mathbf{tea\text{-}6mCN}}$ which is $[Fe^{III}{}_2Dy^{III}{}_2(\mu_3\text{-}OH)_2(teaH)_2(m\text{-}CN\text{-}C_6H_4COO)_6]$. The $[Fe_2Tb_2]$ compound in the series (**2.1-2.13**) has the number **2.7**, so the $[Fe^{III}{}_2Tb^{III}{}_2(\mu_3\text{-}OH)_2(teaH)_2(O_2CC_6H_4\text{-}pCN)_6]$ has the code number $\mathbf{2.7}^{\mathbf{tea\text{-}6}\boldsymbol{p}\mathbf{CN}}$ and so on. For the $[Fe_2Dy_2]$ compounds with other carboxylates, for example, with six 9-anthracenecarboxylate we can continue using this code but as $\mathbf{2.8}^{\mathbf{teaH\text{-}6(9\text{-}anthr)}}$ and for the non-aromatic one with cyclopropanecarboxylate we can use the code $\mathbf{2.8}^{\mathbf{teaH\text{-}6cp}}$. The other compounds discussed in this chapter will have usual numbers continued up to **2.16**. In total 50 Fe/4f compounds will be mentioned, presented or/and discussed in this chapter from which 48 compounds have tetranuclear $\{Fe_2Ln_2\}$ cores. From these compounds are 31 with Fe_2Dy_2 core. In total 28 tetranuclear $[Fe_2Dy_2]$ compounds with benzoates and with $teaH_3$ or Me-$teaH_3$ were prepared and they can be categorized as follow.

i) In total, eleven $[Fe_2Dy_2]$ compounds were prepared by using triethanolamine and which have in their structures six *para*-substituted benzoates, including the unsubtituted one: -H ($\mathbf{2.8}^{\mathbf{teaH\text{-}6}\boldsymbol{p}\mathbf{H}}$), $\text{-}CH_3$ ($\mathbf{2.8}^{\mathbf{teaH\text{-}6}\boldsymbol{p}\mathbf{Me}}$), **-**^{t}Bu ($\mathbf{2.8}^{\mathbf{teaH\text{-}6}\boldsymbol{pt}\mathbf{Bu}}$), $\text{-}NO_2$ ($\mathbf{2.8}^{\mathbf{teaH\text{-}6}\boldsymbol{p}\mathbf{NO2}}$), -CN ($2.8^{\text{teaH-6}p\text{CN}}$), $\text{-}N_3$ ($2.8^{\text{teaH-6}p\text{N3}}$), $\text{-}N(CH_3)_2$ ($2.8^{\text{teaH-6}p\text{NMe2}}$), -Ph ($\mathbf{2.8}^{\mathbf{teaH\text{-}6}\boldsymbol{p}\mathbf{Ph}}$), -OMe ($\mathbf{2.8}^{\mathbf{teaH\text{-}6}\boldsymbol{p}\mathbf{OMe}}$), -Br ($\mathbf{2.8}^{\mathbf{teaH\text{-}6}\boldsymbol{p}\mathbf{Br}}$), and –F ($\mathbf{2.8}^{\mathbf{teaH\text{-}6}\boldsymbol{p}\mathbf{F}}$)}.

ii) Four compounds were isolated by using triethanolamine but which contain only four *para*-substituted benzoates: {-H ($\mathbf{2.8}^{\textbf{teaH-4\textit{p}H}}$),-CN ($\mathbf{2.8}^{\textbf{teaH-4\textit{p}CN}}$),-Ph ($\mathbf{2.8}^{\textbf{teaH-4\textit{p}Ph}}$),-MeSO$_2$ ($\mathbf{2.8}^{\textbf{teaH-4\textit{p}MeSO2}}$). The other two carboxylates in the structure were replaced by nitrates.

iii) With Me-teaH$_3$ ligand instead of teaH$_3$ and six *para*-substituted benzoates (see scheme 2.1): two [Fe$_2$Dy$_2$] compounds {-H ($\mathbf{2.8}^{\textbf{Me-teaH-6\textit{p}H}}$), -^{t}Bu ($\mathbf{2.8}^{\textbf{Me-teaH-6\textit{p}tBu}}$)}, one [Fe$_2Dy_2$] with only four 4H-benzoates {-H ($\mathbf{2.8}^{\textbf{Me-teaH-4\textit{p}H}}$)}, were prepared.

iv) Two compounds with six *meta*-substituted benzoates: {-Me ($\mathbf{2.8}^{\textbf{teaH-6\textit{m}Me}}$), -CN ($\mathbf{2.8}^{\textbf{teaH-6\textit{m}CN}}$)} and other two with only four *meta*-substituted benzoates and two nitrates: {-Me ($\mathbf{2.8}^{\textbf{teaH-4\textit{m}Me}}$), -CN ($\mathbf{2.8}^{\textbf{teaH-4\textit{m}CN}}$)}.

v) Attempts to isolate an [Fe$_2$Dy$_2$] with 3,5-dinitrobenzoate examples were made with the aim of isolating the 3,5-dimethoxybenzoate, 3,5-dinitrobenzoate, 3,5-ditertbutylbenzoate complexes. The use of the trinuclear Fe^{III} triangle of the two latter carboxylates yield indeed crystals which, however, were not suitable for X-ray full measurements. Cell measurements and CHN analyses as well as IR data confirm that they are indeed the desired [Fe$_2$Dy$_2$] compounds. Only the 3, 5-dinitrobenzoate compound ($\mathbf{2.8}^{\textbf{teaH-6(3,5diNO2)}}$) will be briefly discussed in line with the Mössbauer study.

vi) In addition, efforts were made to isolate an *ortho*-substituted example. The steric effect of the substituents might hinder isolating such an example with groups such as methyl. However, only one example with the smallest F group could be indeed isolated $\mathbf{2.8}^{\textbf{teaH-6\textit{o}F}}$.

vii) Furthermore, three examples with carboxylates other than benzoate could be isolated in order to help understand the role of aromaticity: {with 2-naphthoate (2-naphth) ($\mathbf{2.8}^{\textbf{teaH-6(2-naphth)}}$), 9-anththracenecarboxylate (9-anthr) ($\mathbf{2.8}^{\textbf{teaH-6(9-anthr)}}$) and with cyclopropanecarboxylate (cp) ($\mathbf{2.8}^{\textbf{teaH-6cp}}$)}.

From all these examples, certain cases were selected for magnetic (in total over 13 Fe$_2$Dy$_2$ examples), Mössbauer (in total over 16 Fe$_2$Dy$_2$ examples) or other measurements such as EPR, as being representative for probing the electronic effect of various substituents. In addition, samples were chosen which can be prepared in high yields, for example, for Mössbauer measurements, and which were also available early on in the work presented here in order to allow enough time to study the scope of the test bed in depth. In some cases, the same system was prepared using other lanthanides in order to clarify the behavior or/and for EPR measurements (in total over 5 Fe$_2$Ln$_2$ examples are present in this work). The results of the studies on the compounds reported in this work were sufficient in order to draw conclusions regarding the effect of substituents on the benzoate on modulating the anisotropy or/and SMM behaviour.

The next step was to perturb the stability of the core of the "test-bed" system, in order to have further reference systems for better understanding of the collective magnetism in the Fe_2Dy_2 cluster systems.

One aim, for example, was to remove one of the Fe^{III} centres and to replace it by a diamagnetic one such Al^{III}. This target was not fully achieved. Indeed, one Fe^{III} centre was removed but the Al^{III} did not occupy its place in the structure. Furthermore, the $[Fe_2Dy_2]$ compound (with some changes) is still present in the same crystals. In other words, a co-crystallization also of trinuclear $[Dy_2Fe]$ and tetranuclear $[Fe_2Dy_2]$ was the result. The Gd^{III} and Y^{III} in these syntheses show different percentages of the trinuclear and tetranuclear species. The compounds in this series have the formulas:

$\{[FeGd_2(\mu\text{-}OH)_2(teaH_2)_2(O_2CPh)_3(HO_2CPh)(NO_3)_2]\}_{0.74}$:$\{[Fe_2Gd_2(\mu_3\text{-}OH)_2(teaH)_2(O_2CPh)_4(NO_3)_2]\}_{0.26}\cdot 0.8$ THF 1MeCN.1H_2O **(2.17)**, $\{[FeDy_2(\mu\text{-}OH)_2(teaH_2)_2(O_2CPh)_3(HO_2CPh)(NO_3)_2]\}_{0.82}$:$\{[Fe_2Dy_2(\mu_3\text{-}OH)_2(teaH)_2(O_2CPh)_4(NO_3)_2]\}_{0.18}$0.8THF.1MeCN.1$H_2O$ **(2.18)**, and $\{[FeY_2(\mu\text{-}OH)_2(teaH_2)_2(O_2CPh)_3(HO_2CPh)(NO_3)_2]\}_{0.88}$:$\{[Fe_2Y_2(\mu_3\text{-}OH)_2(teaH)_2(O_2CPh)_4(NO_3)_2]\}_{0.12}\cdot$ 1.2THF.0.8MeCN 0.5 H_2O **(2.19)**.

Another target was to remove the two Fe^{III} centres in order to have a pure Ln^{III} reference compound with a similar ligand environment for future studies. Indeed, the $[Dy_2(Htea)_2(O_2CPh)_4]\cdot MeOH$ **(2.20)** could be isolated. Attempts to isolate a mononuclear Dy^{III} complex containing triethanolamine and benzoate ligands, in order to use it as reference for theoretical calculations, were not successful. A mononuclear complex could instead be prepared by using tris-(2-pyridylmethyl)amine (tpma) as ligand $[Dy(tpma)(O_2CPh)(NO_3)_2]$ **(2.21)**. This compound was used to support the theoretical results (see theoretical section).

A further target in this work was, to prepare other "test-bed" systems (for example tetranuclear $[Fe_2Ln_2]$ complexes) with a similar core-topology by using the 4H-benzoate trinuclear starting material but probing other ligands such as 1,1,1-tris(hydroxyethyl)ethane ($thmeH_3$) or 2-amino-2-methyl-1,3-propandiol ($ampdH_4$) and 3-diethylamino-1,2-propandiol ($deapdH_2$) (scheme 2.1). With $thmeH_3$ and benzoate starting materials a tetranuclear $[Fe_2Dy_2(thme)_2(O_2CPh)_4(thmeH_3)_2]^{2+}[Fe_2Dy_2(thme)_2(O_2CPh)_4(NO_3)_4]^{2-}\cdot 2MeCN\cdot 2Py$ chain compound (**2.22**) could indeed be prepared. Using $ampdH_4$ as ligand tetranuclear $[Fe_2Ln_2(ampdH_3)_2(ampdH_2)_2(O_2CPh)_6]$ compounds ((Gd) **2.23** and (Y) **2.24**) could be isolated. However, the Dy analogue could not be isolated and instead an $[Fe_{18}Dy_6]$ (**3.21**) wheel was the result (see chapter 3). The use of tropic acid (3-hydroxy-2-phenylpropanoic acid, $C_9H_{10}O_3$) and deapdH_2, yields [Fe_2Dy_2] compound (**2.25**) and using benzoic acid and deapH_2 yields an octanuclear [Fe_6Dy_2] (**2.26**) complex. (Scheme 2.1 shows the ligands used in this chapter).

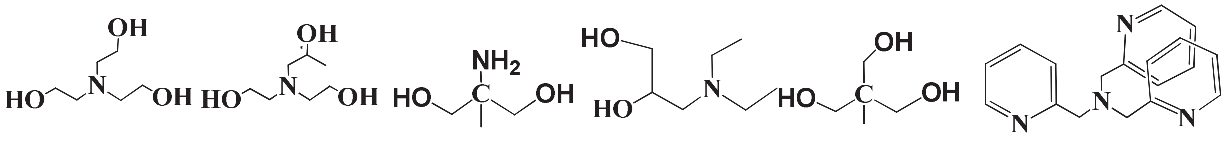

Scheme 2.1. (from left to right) triethanolamine (teaH_3), 1-[N, N-Bis(2-hydroxyethyl)amino]-2-propanol (bheapH_3 or Me-teaH_3), 2-amnio-2-methyl-1,3-propandiol (ampdH_4), 3-(diethylamino)-1,2-propandiol (deapdH_2), 1,1,1-tris(hydroxymethyl)ethane (thmeH_3) and tris-(2-pyridylmethyl)amine (tpyma).

The synthesis of the trinuclear starting materials, the tetranuclear compounds as well as of the other related systems and their structures will be discussed in this chapter. The magnetic behaviour of selected tetranuclear [Fe_2Dy_2] compounds will be compared. Furthermore, Mössbauer studies of several selected systems will be presented in parallel with the magnetic studies. X-band EPR measurements (in collaboration with V. Voronkova, Physical Institut Kazan, Russian federation) were done for the majority of the [Fe_2Dy_2] compounds but only selected examples which have been analyzed to date will be discussed as adjuncts to the magnetic and Mössbauer studies here. The data in the case of Fe_6Dy_2 will be discussed in more detail because this presents an interesting and unusual system which could be useful for furthering the fundamental understanding of SMM behaviour.

Theoretical calculations for the Dy, Gd and Y compounds from the reference series will also be discussed as well as the results of theoretical calculations for *para*-examples compared with *meta*-examples in order to understand the role that the ligand can play in terms of concepts such as “local” electronegativity with the aim to give a quantitative conclusion in addition to the qualitative results.

2. 2 Synthesis and Crystal Structures

The Trinuclear Starting Materials

The trinuclear starting materials are well known and their importance and properties as well as possible applications were discussed in chapter 1.

The Fig. 2.1 shows three examples of the trinuclear starting materials which were used in this work: the benzoate [$Fe_3O(O_2CPh)_6(MeOH)_3$] **(2.sm1)** , the trinuclear compound with *meta*-

tolyate and cyclopropanecarboxyalte $[Fe_3O(O_2CC_3H_5)_3(HO_2CC_3H_5)(H_2O)_2]Cl$ (**2.sm2**) complexes. These structures are presented as a demonstration that it is possible to crystallize any of the trinuclear starting material used in this work (crystallographic data in Tab. 2.17, appendix).

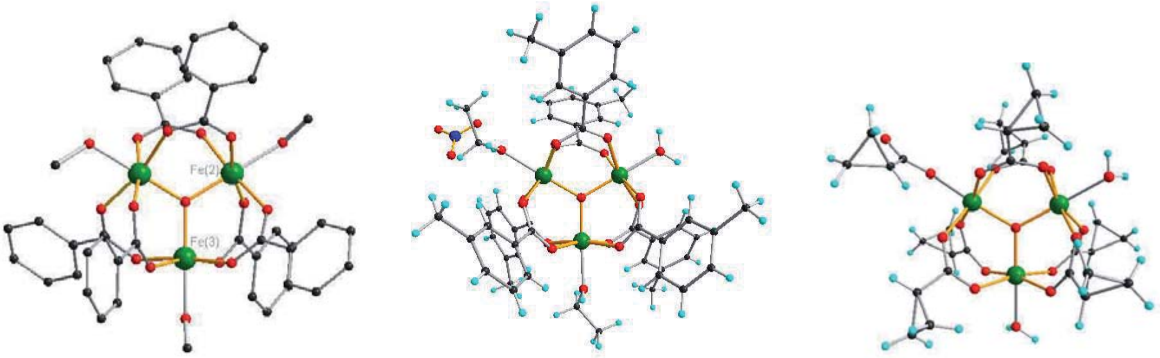

Figure 2.1. Structures of $[Fe_3O(O_2CPh)_6(MeOH)_3](O_2CPh)$ (**2.sm1**), $[Fe_3O(_2CC_6H_4\text{-}m\text{CH}_3)_6(H_2O)(EtOH)_2]NO_3\cdot 2EtOH$ (**2.sm3**) and $[Fe_3O(O_2CC_3H_5)_3(HO_2CC_3H_5)(H_2O)_2]Cl$ (**2.sm2**). Crystallographic data are summarized in Tab. 2.17 in appendix.

The starting materials were first prepared using a method similar to that of the syntheses of triangular iron carboxylates in the literature.[58, 59] Either the acid was reacted with iron salt (mostly nitrate) or a mixture of the sodium salt of the acid and the acid. The starting material with cyclopropanecarboxylate was prepared similar to the method used for preparing the acetate one also only in water. [62] In all cases either a mixture of water/ethanol or only water was used. All have to be washed after preparing with water, ethanol and ether in order to remove the excess of the used acid. In order to obtain high yields from the starting materials it is important to tune the quantity of water to ethanol because some of these acids are more soluble in ethanol rather than in water or vice versa (see chapter 5 for experimental details). If a mixture of ethanol and water was used, the product was microcrystalline and its identity was confirmed by CHN and IR. The use of water always led to coordinating of three water molecules on the Fe^{III} centres. Further characterization methods are not necessary since these compounds are well known and stable. These compounds can be also obtained as crystals and their structures can be confirmed by simply removing water from the reaction and refluxing in ethanol for longer time. In this case, ethanol molecules can replace either the three water molecules or only two (Fig. 2.1). If the three water molecules were replaced by solvent molecules or by mono coordinating acids, this does not affect the synthesis of the tetranuclear compounds in any way.

The reaction of the trinuclear iron starting material with triethanolamine or similar ligands and the lanthanide salts (mostly $Dy(NO_3)_3\cdot 6H_2O$) have been done first for all in a similar way as the benzoate one (for example compound **2.8**). Then based on the result the reaction conditions and solvent-mixture as well as quantities were modified, so that suitable crystals for crystallographic investigations as well as better yield and less crystallisation time could be achieved. In some cases no crystals were obtained and thus the reaction conditions were completely changed and other solvents than acetonitrile or methanol was used.

The Mechanism

It is also important to mention the fact that several synthetic attempts were made to isolate the tetranuclear compounds without using the trinuclear starting material, i.e. by reacting, the free acid, an iron salt, dysprosium salt with triethanolamine ligand. Applying this strategy it was never possible to isolate the tetranuclear compounds. Instead, a triethanolammonium nitrate salt (well formed colorless crystals) was the product (Fig. 2.2). This indicates that the use of the trinuclear, triangular starting material is very important in the mechanism and hence in controlling the self-assembled synthesis. Cyrstallographic data of the salt are summarized in Tab. 2.19 (see appendix).

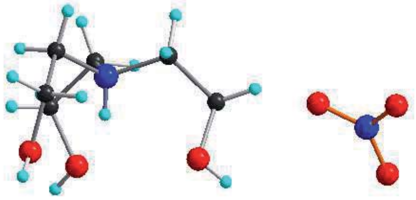

Figure 2.2. The structure of the triethanolammonium nitrate salt. Crystallographic data are in **Tab. 2.19**, see appendix.

In the literature species such as $[Ln(teaH_3)_2](OTf\ or\ NO_3)_3$ are known. Furthermore, the trinuclear starting material of benzoate is widely used in different syntheses, for example, in the synthesis of tetranuclear $[Fe_4(OHO)(OH)_2(O_2CR)_4(phen)_4](ClO_4)$ or $[Fe_2O(O_2CR)_4(phen\ or\ pyridine)_2]$ and $[Fe_2(\mu\text{-}OH)(O_2CR)_2(phen)]^{2+}$ (phen= 1, 10-phenanthroline).[63] A possible explanation for formation of the stable $[Fe_2Dy_2]$ compounds from $[Fe_4(OH)_2(O_2CR)_4]$ and two $[Ln(teaH)(O_2CR)]$ is given in scheme 2.2.

The {Fe_8} Problem

If the trinuclear starting material does not follow the pathway via Fe_4 and then Fe_2Ln_2, it might aggregate to the {Fe_8} compound as mentioned in the introduction, according to the following formulation. [63]

$$8[Fe_3O(O_2CC_6H_4\text{-}R)_6(H_2O)_3] + 12\ teaH_3 \rightarrow 3[Fe_8O_3(O_2CC_6H_4\text{-}R)_9(tea)(teaH)_3] + 21HO_2CC_6H_4\text{-}R + 23\ H_2O + 8H^+$$

In Fig .2.3 are selected structures of $\{Fe_8\}$ compounds presented.

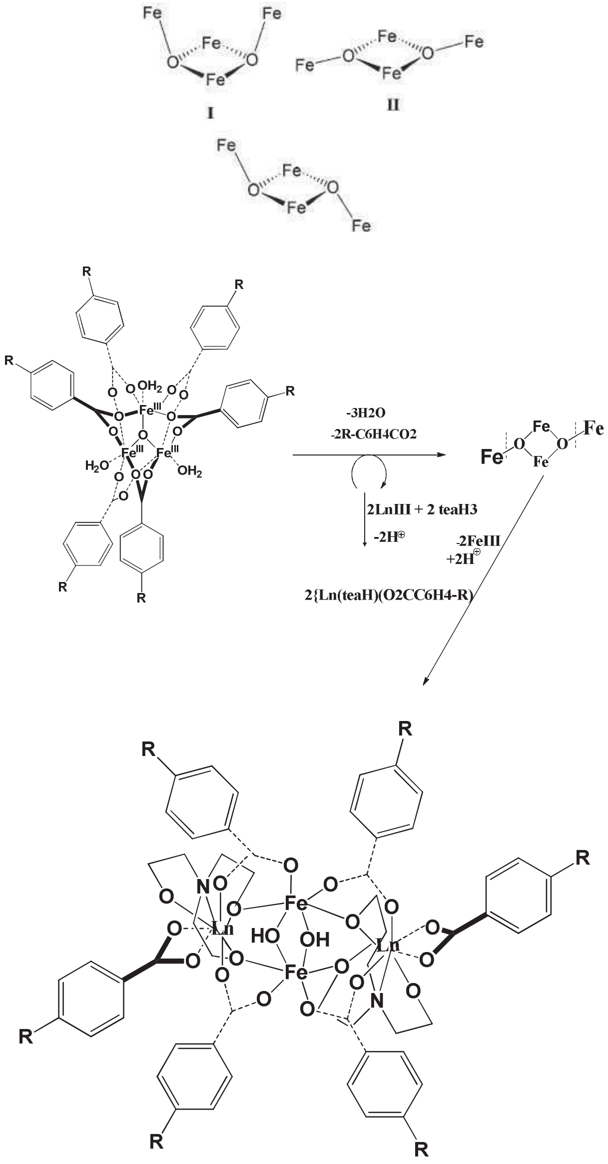

Scheme 2.2. (Upper) The possible tetranuclear Fe^{III} arrangements.[63] Mechanistic representation of formation of the tetranuclear Fe_2Ln_2 compounds from the trinuclear starting material through one of the Fe_4 arrangments. The scheme is also representative for meta-substituents as well.

From the synthetic experience in this work it became clear that the octanuclear $\{Fe_8\}$ compounds and the tetranuclear Fe_2Ln_2 compounds are in competition. In most cases the formation of the $\{Fe_8\}$ species, such as **2.16** but with cyclopropanecarboxylate (cp) or *para*-fluorobenzaote (pf) (Fig. 2.3), could be surpressed.

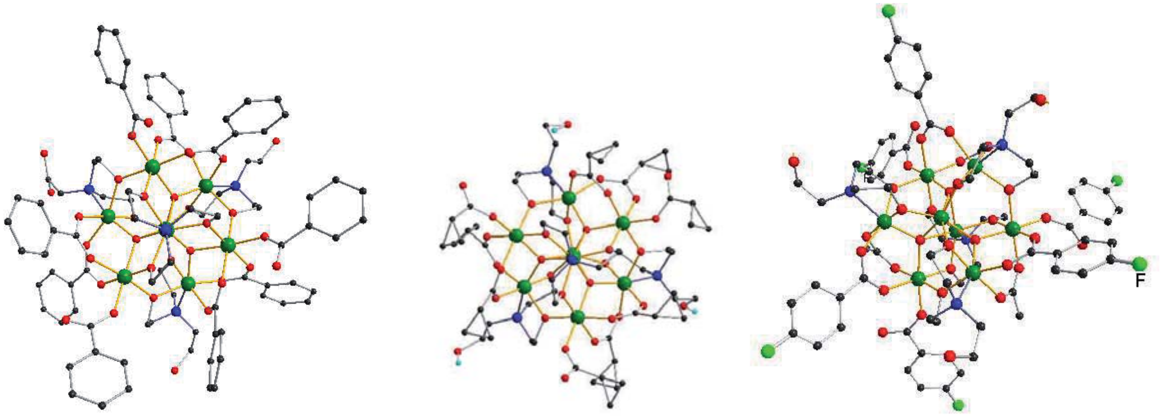

Figure 2.3. The Structures of $[Fe_8O_3(O_2CPh)_9(tea)(teaH)_3]$ (**2.16**) (left), $[Fe_8O_3(O_2CC_3H_5)_9(tea)(teaH)_3]$ (**2.16** with cp) (middle) and $[Fe_8O_3(O_2CC_6H_4F)_9(tea)(teaH)_3]$ (**2.16** with pf) (right). Some benzoates were omitted for clearity. (Crystallographic data are summarized in Tab. 2.18, see appendix). H atoms are omitted for clearity.

The "Test-Bed" Series

The isostructural complexes $[Fe_2Ln_2(\mu_3\text{-}OH)_2(teaH)_2(O_2CPh)_6]\cdot 3MeCN$ (**2.1-2.13**) form two isomorphous series, **2.1-2.6** and **2.7-2.13**. In both series the molecules crystallise in the space group $C2/c$ with $Z = 4$, however the unit cells are different for the two sets of compounds. Full structural determinations were carried out for **2.1** and **2.6**, the first and last members of the first series. The intervening Fe_2Pr_2, Fe_2Nd_2, Fe_2Sm_2 and Fe_2Eu_2 congeners (**2.2-2.5**) were shown to be isomorphous to **2.1** and **2.6** by powder diffraction (Fig. 2.4 and Fig. 2.5, appendix). For the second series, all compounds except for the Fe_2Tm_2 complex **2.11** were structurally characterised; **2.11** was shown to be isomorphous to the others by powder diffraction. All the compounds reported here thus have molecules with crystallographically-imposed inversion symmetry. (See Tab. 2.1, summary of crystallographic data of the compounds (**2.1-2.15**) in appendix). The structures of **2.14** and **2.15** are presented in Fig. 2.6 in appendix.

The molecular structures of the centrosymmetric $[Fe_2Gd_2(\mu_3\text{-}OH)_2(teaH)_2(O_2CPh)_6]$ and $[Fe_2Dy_2(\mu_3\text{-}OH)_2(teaH)_2(O_2CPh)_6]$ complexes in compounds **2.6** and **2.8**, as representatives of the two isomorphous series of the hexabenzoate complexes, are compared in Fig. 2.7. These three isostructural complexes have a planar rhomboidal Fe_2Ln_2 core, in which the two Fe_2Ln triangles are each bridged by a $(\mu_3\text{-}OH)^-$ ligand, one above and one below the Fe_2Ln_2 plane.

Each Ln^{III} cation is chelated by a doubly-deprotonated $(teaH)^{2-}$ ligand, with the two deprotonated oxygens forming alkoxo bridges along the Ln···Fe edges, while the still-protonated oxygen simply coordinates to the Ln^{III} ion. Each Ln··Fe edge is additionally bridged by a *syn,syn*-bridging benzoate, resulting in the familiar “defect-dicubane” or “butterfly” Fe_2Ln_2 motif. The coordination shell of each cluster is completed by two further benzoates which each chelate a lanthanide ion. The iron centers have octahedral environments, while the lanthanide O_8N coordination shells are best described as a distorted capped square antiprism, with the nitrogen atom capping a square O_4 face of the antiprism. Each Fe_2Dy trinuclear sub-unit is bridged by a μ_3-OH ion above and below the plane. Each of the two $teaH_2$ ligands binds in a tetradentate chelate fashion to Dy(1) or Dy(1’), with their protonated alcohol arms binding terminally to the Dy, and their two deprotonated alkoxide arms each bridging to an adjacent Fe atom. There is also a chelating benzoate group on each Dy atom, and ligation is completed by a *syn*, *syn*, bridging benzoate group across each of the four Dy-Fe edges of the rhombus. The Fe and Dy atoms are as in case of the first series six- and nine-coordinate, respectively.

From Fig. 2.7 it is clear that the structures of Fe_2Gd_2 **2.6** and Fe_2Dy_2 **2.8** are very similar, with only very slight differences in the orientation of some of the phenyl groups. In Fig. 2.7, a general representation of the *para*-examples is also shown.

The Para-Examples

Other Fe_2Ln_2 compounds with different substitutions have been prepared in a similar way. The difficulty of the synthesis of these compounds varies from simple with large crystals and high yield for *para*-tolyate (**2.8**$^{\textbf{teaH, 6}\boldsymbol{p}\textbf{Me}}$) to more difficult for other examples such as the *meta*-examples and the non-aromatic one (**2.8**$^{\textbf{teaH-6cp}}$).

All these compounds have the general formula $[Fe_2Dy_2(OH)_2(teaH)_2(p\text{-R-}C_6H_4COO)_6]$, where $teaH_3$ – triethanolamine, *p*-R = H , CH_3 , *t*-But , NO_2 , CN , Ph , Br , F, N_3 , OMe and $N(Me)_2$ (Figs. 2.8-2.13; appendix). These compounds have a similar motif to the Fe_2Ln_2 coordination clusters series discussed in this section. Complexes **2.8**$^{\textbf{teaH, 6}\boldsymbol{pt}\textbf{Bu}}$ and **2.8**$^{\textbf{teaH-4}\boldsymbol{m}\textbf{Me}}$ crystallize in the monoclinic space group C2/c as in case of **2.8**$^{\textbf{teaH, 6}\boldsymbol{p}\textbf{H}}$.

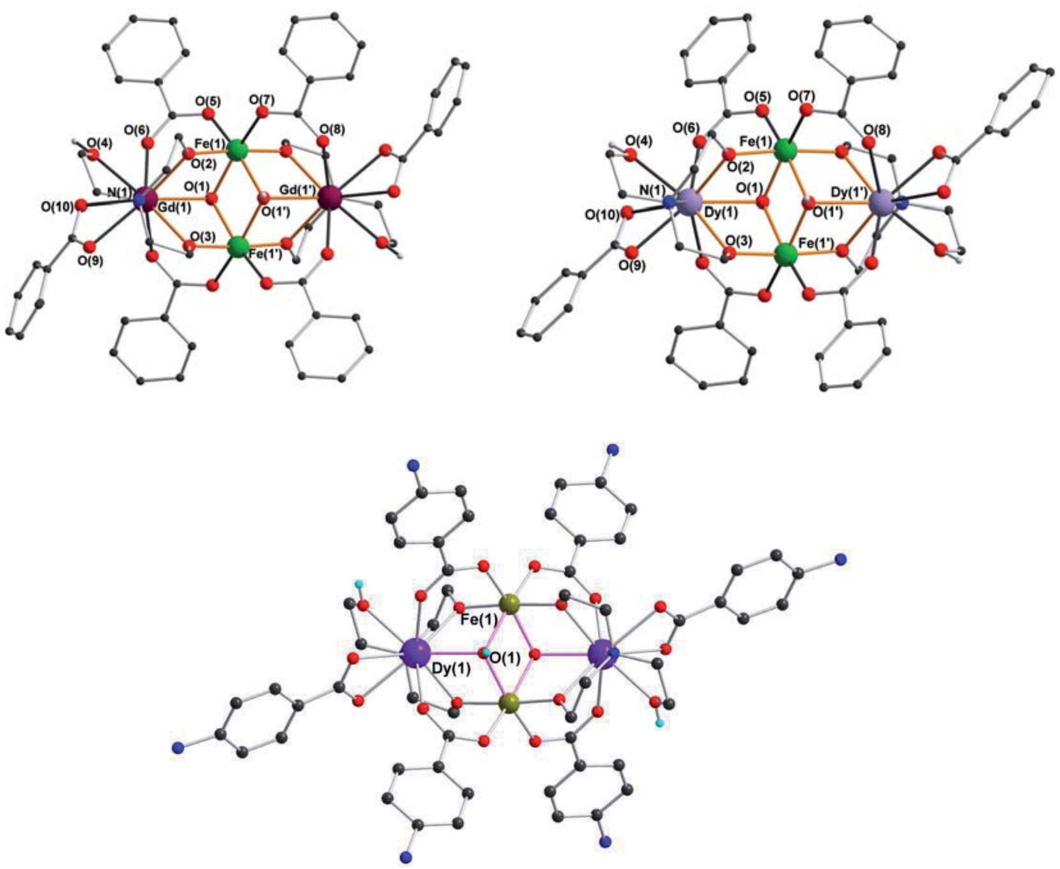

Figure 2.7. (Upper) Molecular Structures of $[Fe_2Ln_2(\mu_3\text{-}OH)_2(teaH)_2(O_2CPh)_6]$ (Ln = Gd **2.6**, above; Dy **2.8**, center); organic H-atoms and lattice solvent molecules omitted for clarity. The structures of **2.14** and **2.15** are in appendix. (Lower) General representation for the *para*-examples: $[Fe_2Ln_2(\mu_3\text{-}OH)_2(Htea)_2(O_2CC_6H_4\text{-}p\text{-}R)_6]$ (*p*-R in blue= -H (**2.8**$^{teaH,\ 6pH}$) , $-CH_3$ (**2.8**$^{teaH,\ 6pMe}$) , $-C(CH_3)_3$ (**2.8**$^{teaH,\ 6ptBu}$) , $-NO_2$ (**2.8**$^{teaH,\ 6pNO2}$) , -CN (**2.8**$^{teaH,\ 6pCN}$), -Ph (**2.8**$^{teaH,\ 6pPh}$), -Br (**2.8**$^{teaH,\ 6pBr}$) , $-N_3$ (**2.8**$^{teaH,\ 6pN3}$) , -OMe (**2.8**$^{teaH,\ 6pOMe}$), $-N(Me)_2$ (**2.8**$^{teaH,\ 6pNMe2}$) and –F (**2.8**$^{teaH,\ 6pF}$). All tetranuclear structures from this family with different substituents are presented in Fig's 2.8-2.13) in appendix.

Apart from these three and the *ortho* example, all others crystallize in the triclinic space group P-1, with the central cores consisting of a planar Fe_2Dy_2 rhombus (Fig. 2.7). The crystallographic data of the Fe_2Ln_2 series are given in Tab. 2.1 (chapter 6). The crystallographic data of all Fe_2Dy_2 compounds discussed in this chapter can be found in Tab. 2.2-2.11 (sorted according to the position of the substituents). In addition, some of these compounds were prepared for other lanthanides such as Gd and Y to show that it is possible to isolate a series from each system, see some examples in Tab. 2.3-2.5 (appendix).

The meta- and ortho-examples

Additionally, some examples with *meta*-substituted benzoates with the general formula $[Fe_2Dy_2(OH)_2(teaH)_2(O_2CC_6H_4\text{-}m\text{-}R)_6]$ (with *m*-R= CH_3 (**2.8**$^{teaH,\ 6mMe}$), CN (**2.8**$^{teaH,\ 6mCN}$))

(Fig. 2.9 and Tab. 2.6, Appendix) could be isolated in order to test the influence of the electronic effect from this aspect.

The synthesis and crystallization of these compounds were more difficult than for the *para*-examples and the steric effect of these groups within the tetranuclear core could be the reason for this. Indeed, this became more pronounced when the crystallization of the *meta*-nitro compound was attempetd. Furthermore, the isolation of an example with a group in *ortho*-position (even for Me) need more synthetical efforts. Finally, crystals could be obtained with *ortho*-fluoro benzoate (pale-yellow) which is the wished complex **2.8**$^{\textbf{teaH-6}\boldsymbol{o}\textbf{F}}$ (structure in appendix) toward the end of this work. An example with F in the *para*-position could be isolated towards the end of this work, but the octanuclear $\{Fe_8\}$ (Fig. 2.3, right) Fe_2Dy_2 compound crystallises simultaneously with compound (**2.8**$^{\textbf{teaH-6}\boldsymbol{p}\textbf{F}}$, see Fig. 2.8, appendix). An analogue with fluoro at *meta*- position was not probed because of limited time. However, the fact that the ortho-example could be isolated means that with flouro all will be possible and will be an excellent comperative system in future work.The *para* Fe_2Dy_2 complex could be obtained for the bromo analogue after many synthetic variations. This again has the same problem as fluoro analogue because $\{Fe_8\}$ crystals appear together with **2.8**$^{\textbf{teaH, 6}\boldsymbol{p}\textbf{Br}}$. In general the halo-substituted analogues are very difficult to obtain.

Exampels with Only four Carboxylates

Consistent with the results of Murugesu *et al.*, it was found that with Tb^{III}, Dy^{III} and Ho^{III} the reaction is somewhat flexible, yielding either the complexes with six benzoates (**7**-**9**) or complexes $[Fe_2Ln_2(\mu_3\text{-}OH)_2(teaH)_2(O_2CPh)_4(NO_3)_2]$ (for Tb; **2.7**$^{\textbf{teaH,4}\boldsymbol{p}\textbf{H}}$, for Dy; **2.8**$^{\textbf{teaH, 4}\boldsymbol{p}\textbf{H}}$**,** and for Ho; **2.9**$^{\textbf{teaH,4}\boldsymbol{p}\textbf{H}}$, see structures (Fig. 2.10, appendix) and crystallographic data in Tab. 2.8, appendix), including Murugesu's Fe_2Ho_2, in which the two chelating benzoates have been replaced by two nitrate ligands. However, it was also found that it is possible to direct the reaction to produce cleanly either one compound or the other. In particular, replacement of these lanthanide nitrates with the corresponding trifluoromethanesulfonate (triflate) salts reliably yields compounds 2.**7**-2.**9**. However, to avoid both compounds rystallising in the same reaction a new synthetic strategy was made to guarantee that only the analogue with six or with four carboxylates is isolated.

By changing the concentrations and reaction conditions and by adding $Fe(NO_3)_3{\cdot}9H_2O$ to the reaction, the compounds with chelating nitrates for different benzoate ligands could be cleanly isolated. The two structural types are of course readily distinguishable from microanalytical data, the presence or absence of the nitrate band at 1384 cm^{-1} in the infrared spectrum, and by X-ray powder diffraction. Indeed, {Fe_2Dy_2} compounds with only four carboxylates are very important for the comparative study (Fig. 2.9, appendix).

A tetranucelar {Fe_2Dy_2} compound with the six sulfonyl-groups -SO_3H in the *para*-position is desirable in order to explore the strong electron withdrawing effect of this group. However, this target could not be achieved because of bad solubility of such acids and further by heating polymerization seems to increase the difficulty in obtaining the starting material. Instead of this the use of *para*-methylsulfonylbenzoic acid (4-$CH_3SO_2H_4C_6CO_2H$) would be helpful in dissolving the acid in water/ethanol in order to form the trinuclear starting material. The use of the latter acid indeed helped in getting the trinuclear species and the tetranuclear {Fe_2Dy_2} compound with very low yield but with only four carboxylates **2.8**$^{\mathbf{teaH,\ 4\mathit{p}MeSO2}}$. This indicates that the analogous complex with six benzoates should be obtainable, but requires further synthetic efforts. In Fig. 2.10 the structures containing only four carboxylate *para* or *meta* are shown. All other structures s well as are shown in the appendix.

Examples with disubstituents

The particular problem of the synthesis of the Fe_2Dy_2 compound with 3,5-dinitrobenzoate was formation of the salt 3,5-dintrobenzoate triethanolammonium, (Fig. 2.14, crystallographic data in appendix, Tab. 2.19). However, by tuning the reaction conditions the Fe_2Dy_2 compound with 3,5-dinitrobenzoate could be obtained but the crystals always went off after short irradiation time. This nevertheless made it possible to determine the unit cell, which are in line those of the other Fe_2Dy_2 compounds. This compound will be briefly discussed in the Mössbauer section.

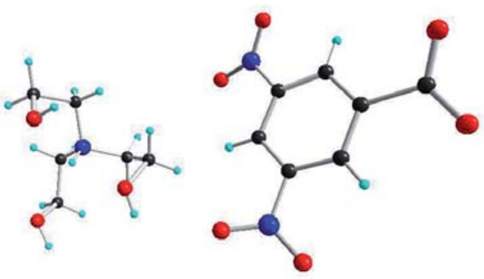

Figure 2.14. The structure of the 3,5-dinitrobenzoate triethanolammonium salt.

Rich aromatic and non-aromatic {Fe_2Dy_2}

In order to explore this systematic study from “different angles” further examples with other aromatic carboxylates such as 9-antharcencarboxylate (9-anth) and 2-naphthoate (2-napthth) could be isolated as the compounds [$Fe_2Dy_2(\mu_3\text{-}OH)_2(Htea)_2(2\text{-}naphth)_6$] (**2.8**$^{\mathbf{teaH,\ 6(2\text{-}naphth)}}$) and [$Fe_2Ln_2(\mu_3\text{-}OH)_2(Htea)_2(9\text{-}anth)_6$] (**2.8**$^{\mathbf{teaH,\ 6(9\text{-}anthr)}}$) (Fig 2.11, appendix).

The fact that the trinuclear, as well as the {Fe_2Dy_2} complexes, using the 9-anthracene carboxylic acid 2-naphthoate acid are the easiest to obtain in relatively high yields and with very good quality crystals indicates that bulky groups further stabilize the core of the tetranuclear species. This became even clearer when starting materials of aliphatic carboxylates were used.

An example without aromatic carboxylate was required in order to understand the role of aromaticity in this cluster-family; this was by far the most difficult target. While the use of a formate or propionate triangle did not lead to any product, the use of acetate trinuclear [$Fe^{III}_3O(OAc)_6(H_2O)_3$]Cl $6H_2O$ **[62]** as starting material yield a series of high nuclearity cyclic {$Fe_{16}Ln_4$}aggregates (**3.15-3.20**) (see chapter 3.).

Theoretically, the “best” non-aromatic example is that of cyclohexanecarboxylate. The trinuclear compound can be synthesized as in case of acetate. At the same time the non-polar nature of the cyclohexane groups makes it very hard to crystallize the desired product; intensive synthetic efforts did not help. Furthermore, the triangle with cyclopentane carboxylate as well as with cyclobutane carboxylate could not be synthesized. Finally, a trinuclear compound using cyclopropane carboxylic acid could be prepared according to the synthetic procedure used for acetate. Dark red and large crystals of [$Fe_3O(O_2CC_3H_5)_6(HO_2CC_3H_5)(H_2O)_2$]Cl (Fig. 2.1) could be obtained in high yield. In general it is possible to crystallize all mentioned trinuclear compounds by reaction of iron(III) nitrate nonahydrate (15 mmol) with an excess of the corresponding acid (90 mmol) in ethanol and refluxing for a number of hours, except in the case of the azido compound which was reacted at r.t. for 24 h. After cooling, the crystals appear in high yield. Usually, in the synthesis of the trinuclear sm compounds either crystals or powder result. The microcrystalline products can be obtained by similar reaction but using carefully controlled amounts of water. Some of these trinuclear compounds have been synthesized for the first time such as the ones discussed here with the cyclopropane carboxylates. The purity of the products was confirmed using elemental analysis (see experimental part).

By using the $[Fe_3O(O_2CC_3H_5)_6(HO_2CC_3H_5)(H_2O)_2]Cl$ trinuclear compound in similar synthetic strategy as for the others the triethanolammonium nitrate salt (Fig. 2.3) was obtained. Replacing the Dy^{III} nitrate salt by triflate yields a similar salt but with triflate as counterion and then and subsequently the $\{Fe_8\}$ compound (Fig. 2.2, crystallographic data Tab. 2.18, appendix). The fact that under similar conditions and ratios the triethanolamine salts and $\{Fe_8\}$ were obtained forced to a rethink of the synthetic strategy. The concentrations of the starting materials were fundamentally changed. The amount of triethanolamine was increased in order to have more ligand than necessary for forming the salt and the $\{Fe_8\}$ fragment (see experimental part).

The solution, which was left sealed was diluted with MeCN after 3 months and then layered with ether. Six months later one crystal of the non-aromatic example could be obtained. In total 4 mg of this compound could be collected after something in excess of one year, but finally, the existence of this molecule could be demonstrated (Fig. 2.12, appendix).

Other ligands in place of triethanolamine were probed in order to obtain further tetranuclear $\{Fe_2Dy_2\}$ complexes with the same core structure. The triethanolamine ligand could be easily and successfully replaced by Me-teaH$_3$ ligand resulting in three new $\{Fe_2Dy_2\}$ compounds. The same concentrations for each component were used as in case of the most other $\{Fe_2Dy_2\}$ compounds discussed before. The three compounds are one with six unsubstituted benzoate $[Fe_2Dy_2(\mu_3\text{-}OH)_2(Me\text{-}teaH)_2(O_2CPh)_6]$ ($\mathbf{2.8}^{\textbf{Me-teaH, 6}\boldsymbol{p}\textbf{H}}$), one with four unsubstituted benzoates $[Fe_2Dy_2(\mu_3\text{-}OH)_2(Me\text{-}teaH)_2(O_2CPh)_4(NO_3)_2]$ ($\mathbf{2.8}^{\textbf{Me-teaH, 4}\boldsymbol{p}\textbf{H}}$) and the third is with six 4-tertbutylbenzoate ligands $[Fe_2Dy_2(\mu_3\text{-}OH)_2(Me\text{-}teaH)_2(O_2CC_6H_4\text{-}p^tBu)_6]$ ($\mathbf{2.8}^{\textbf{Me-teaH, 6}\boldsymbol{pt}\textbf{Bu}}$). These compounds were made to show that it is possible to obtain all the previously discussed compounds made using teaH$_3$ using the similar ligand Me-teaH$_3$. The aim was firstly to understand the role of the small inductive effect of the methyl group, but also the possible roles of steric and chirality effects, in particular in other systems which are discussed in chapters 3 and 4. The structures obtained with this ligand and discussed in this chapter are presented in Fig. 2.13 in the appendix.

Crystallographic Data Comparison

In addition to the fact that the majority of these Fe_2Dy_2 compounds crystallize in the P-1 space group, all these compounds have very similar bond distances and angles (Tab. 2.20). Note, that these compounds were not all measured at the same temperature and that there are deviations in the quality of their data sets; this means that the distances and angles might be even closer than presented here. Furthermore, a comparison of the distances between molecules in addition to their packing of these compounds indicates that there cannot be any communication between the individual molecules (see magnetic and Mössbauer discussions). The packing will therefore not be considered further.

Table 2.20. Space groups, selected geometry data of some Fe_2Dy_2 examples.

Compound	Space group	Fe1···Fe2	Dy···Dy	Fe··O··Fe*
$\mathbf{2.8}^{\text{teaH-6}p\text{H}}$	C2/c	3.2294(9)	6.0742(9)	103.363(140)
$\mathbf{2.8}^{\text{teaH-6}p\text{Me}}$	P-1	3.2502(8)	6.0283(6)	104.261(133)
$\mathbf{2.8}^{\text{teaH-6}pt\text{Bu}}$	P21/c	3.2359(8)	6.0678(3)	103.794(112)
$\mathbf{2.8}^{\text{teaH-6}p\text{NO}_2}$	P-1	3.2025(8)	6.0875(6)	103.011(116)
$\mathbf{2.8}^{\text{teaH-6}p\text{CN}}$	P-1	3.2008(4)	6.1078(3)	102.465(68)
$\mathbf{2.8}^{\text{Me-teaH-6}p\text{H}}$	P-1	3.2277(11)	6.0494(8)	103.824(109)
$\mathbf{2.8}^{\text{teaH-4}p\text{H}}$	P-1	3.2467(7)	5.9932(6)	104.551(103)
$\mathbf{2.8}^{\text{teaH-6}}m^{\text{CN}}$	P-1	3.2467(7)	6.0653(19)	103.420(303)
$\mathbf{2.8}^{\text{teaH-4}}m^{\text{CN}}$	P-1	3.2544(22)	5.9930(13)	104.551(103)
$\mathbf{2.8}^{\text{teaH-6anthr}}$	P-1	3.2046(20)	6.0868(10)	102.206(243)
$\mathbf{2.8}^{\text{teaH6cp}}$	P-1	3.2399(7)	6.0844(6)	103.721(97)
$\mathbf{2.8}^{\text{teaH-6}p\text{N3}}$	P-1	3.2233(9)	6.0790(5)	103.286(107)

- The Fe··O··Dy angles are in all cases very similar about ~100°.

Table 2.20. (continued).

Compound	Fe1···$N^{\text{teaH*}}$	Dy···$O9^{**}$
$\mathbf{2.8}^{\text{teaH-6}p\text{H}}$	2.6264(40)	2.3911(32)
$\mathbf{2.8}^{\text{teaH-6}p\text{Me}}$	2.6191(35)	2.4291(32)
$\mathbf{2.8}^{\text{teaH-6}pt\text{Bu}}$		
$\mathbf{2.8}^{\text{teaH-6}p\text{NO}_2}$		
$\mathbf{2.8}^{\text{teaH-6}p\text{CN}}$	2.6085(22)	2.4408(17)
$\mathbf{2.8}^{\text{Me-teaH-6}p\text{H}}$	2.5968(27)	

2.8$^{\text{teaH-4}p\text{H}}$		
2.8$^{\text{teaH-6}m\text{CN}}$		2.4479(71)
2.8$^{\text{teaH-4}m\text{CN}}$	2.5727(87)	2.4798(60)
2.8$^{\text{teaH-6anthr}}$	2.6000(72)	2.4816(71)
2.8$^{\text{teaH6cp}}$		
2.8$^{\text{teaH-6}p\text{N3}}$		

* All others in same range,

** Very similar values for the distances between Dy and O9 or O10 of nitrates or carboxylates.

Two other synthetic strategies were tested, which were designed to remove one of the two iron ions in the tetranuclear core (to remove the antiferromagnetic interaction) or even to remove both irons.

The Solid Solutions

The first strategy was based on replacement of one of the irons by a diamagnetic metal ion such as Al^{III}. It was found that by reacting a tetranuclear aluminium(III)-triethanolamine complex with the benzoate starting materials and with Ln nitrate, indeed one iron could removed but not replaced by aluminium. A co-crystallization of a trinuclear and tetranuclear $\{[FeLn_2(\mu_3\text{-}OH)_2(teaH_2)_2(O_2CPh)_3(HO_2CPh)(NO_3)_2]\}_x\{[Fe_2Ln_2(\mu_3\text{-}OH)_2(teaH)_2(O_2CPh)_4(NO_3)_2]\}_y$ complex was the result. The x and y vary for different lanthanides probed: for Gd **2.17** (x= 0.74, y= 0.26), for Dy **2.18** (x= 0.82, y= 0.18) and for Y **2.19** (x= 0.88, y= 0.12). The tetranuclear motif (right, Fig. 2.15) is that of **2.8**$^{\mathbf{teaH,\ 4pH}}$ and the trinuclear motif is also similar. These compounds are very stable and can be obtained in high yields, maybe as a result of the hydrogen bonds within the trinuclear species (left, Fig. 2.15). They crystallise in the triclinic space group P-1. By moving right in the lanthanide series, the percentage of the trinuclear species increases. This justifies calling these compounds “solid solutions”. Further lanthanides were not probed; however, it would be interesting to see if only the trinuclear species can be isolated for heavier (smaller) lanthanides. The crystallographic data of compounds **2.17-2.19** are summarized in Tab. 2.12 in appendix).

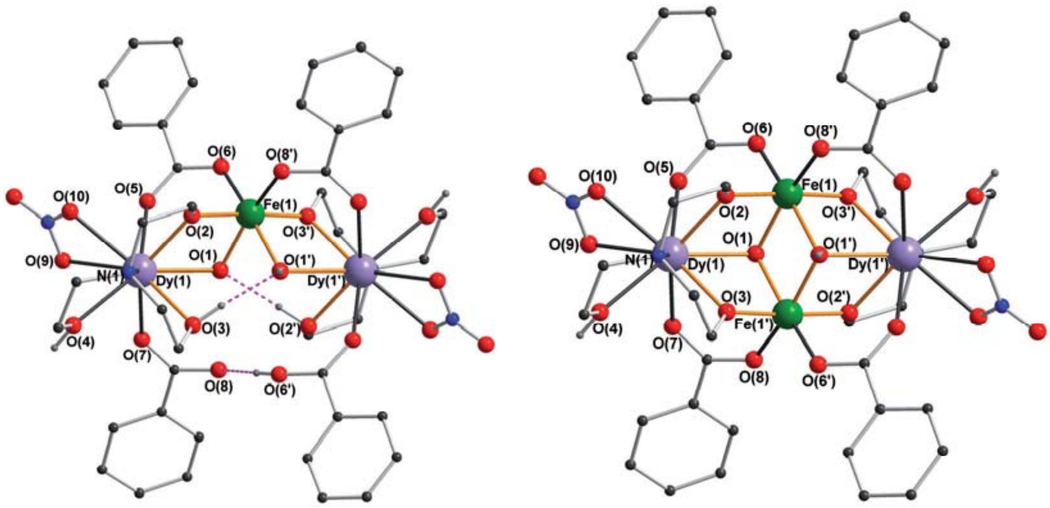

Figure 2.15. (Left) the trinuclear species in **2.17** and (right) the tetranuclear one. They are comparable similar with even similar bond lengths and coordination environments. The triethanolamine ligands chelate as in other tetranuclear species with one alcohol (O(4)) arm on Ln centres.

The Dinuclear and Mono-nuclear Dy Refence Compounds

The second strategy was indeed successful. Reacting the compound [Dy(O_2CPh)$_3$(DMF] (synthesized as in the literature)**[64]** with triethanolamine in presence of triethylamine as base yields the [Dy_2(teaH)$_2$(O_2CPh)$_4$] (**2.20**). It crystallizes in the triclinic space group P-1. The structure is shown in Fig. 2.16 and the crystallographic data in Tab. 2.13 in appendix. The triethanolamine coordination is the same as in the Fe_2Dy_2 compounds. In addition, the benzoate chelates as in case the Dy^{III} centres of Fe_2Dy_2. The main difference here is that one alkoxy arm bridges between the Dy^{III} centres. As a result of this bridging, the Dy··Dy distances are with 3.7854(7) Å shorter than the distances of Dy^{III} centres in Fe_2Dy_2 compounds.

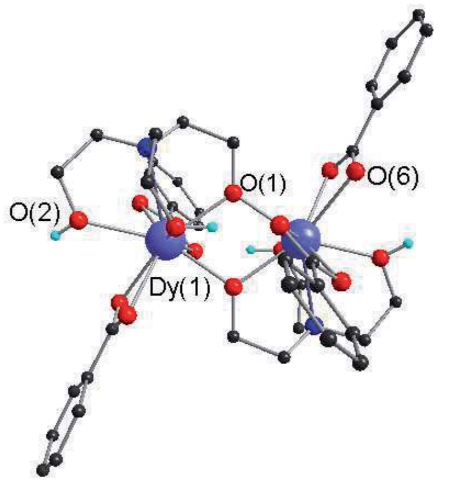

Figure 2.16. The structure of [Dy_2] compound **2.20**.

A mononuclear Dy^{III} complex (**2.21**) could be isolated by using benzoic acid and tris-(2-pyridylmethyl)amine instead of triethanolamine. Compound **2.21** crystallizes in the triclinic space group P-1, as well. Two perspective views of the structure of **2.21** are given in Fig. 2.17 and the crystallographic data in Tab. 2.13, appendix.

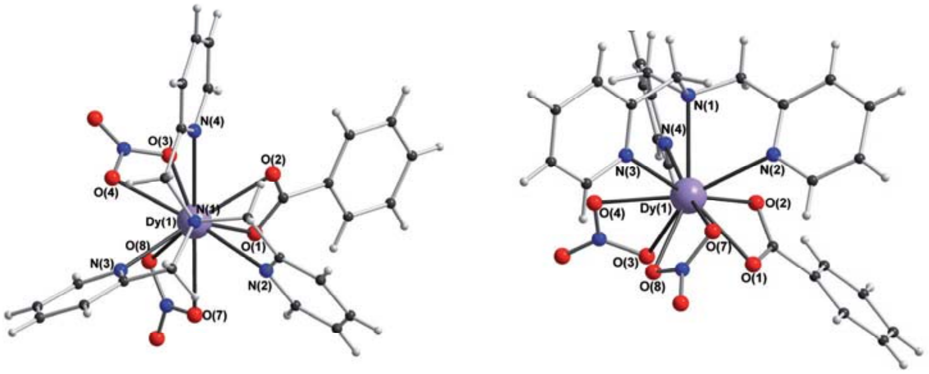

Figure 2.17. The structure of **2.21**. If we neglect the difference between benzoate and nitrate, then the structure has threefold symmetry. The oxygen-Dy^{III} (O(1) and O(2)) distances are similar to those in **2.20** or **2.8** systems.

New Test-Bed Systems

The ligand 2-amino-2-methyl-1,3-propandiol ($ampdH_4$) has only two alcohol groups. Nevertheless, it was assumed that it is possible to obtain a tetranuclear $[Fe_2Ln_2]$ system with it. The fact that the alcohol arms are shorter means that they can be expected to chelate the Ln^{III} centres and by the extra two arms can bridge Fe^{III} centres with two Ln^{III} neighbours via their extra alcohol functions and a similar synthesis to **2.6** and **2.13** using the same molarities (0.25 mmol benzoate starting material, 0.25 mmol $Ln(NO_3)_3$ and 2 mmol of $ampdH_4$) was used. The distances and angles in these compounds are similar to those in **2.6** and **2.13**. An important difference to the other Fe_2Ln_2 compounds is that the alcohol arms of the ligands are all completely deprotonated, thus bridging the metal ions in place of water-derived hydroxyl-groups. This system is actually an excellent comparative reference system for the other Fe_2Ln_2 compounds because the benzoate arrangement is also different from that in the Fe_2Ln_2 compounds. Furthermore, the amino-functions coordinate both the Fe^{III} and Ln^{III} centres. The same reaction but using $Dy(NO_3)_3$ yields yellow microcrystalline material. This material does not have the same PXRD as the Gd and Y compounds. After filtering this yellow material, the clear yellow filtrate gave after several weeks' one large yellow crystal and many other small yellow crystals. The large yellow crystals are a $Fe_{18}Dy_6$ wheel (chapter 3). The new small yellow crystals are once again not the desired Fe_2Dy_2 compound or the $Fe_{18}Dy_6$ compound and have not yet been fully characterised. This indicates that several other products form in this reaction. An explanation for this can be taken from the difference between **2.22** and **2.23**. The Y^{III} are seven and Gd^{III} ions are eight coordinated. The reason is that benzoate group in **2.23** is mono-coordinating and in **2.22** chelating the Ln^{III}. This indicates that this structure might be less stable for larger Ln^{III}. The Y structure is foremost stabilized by hydrogen bonds (pale pink, Fig. 2.18). Compounds 2.22 and 2.23 crystallize in the monoclinic space group $P2_1/n$ and the crystallographic data are given in Tab. 2.14 (appendix).

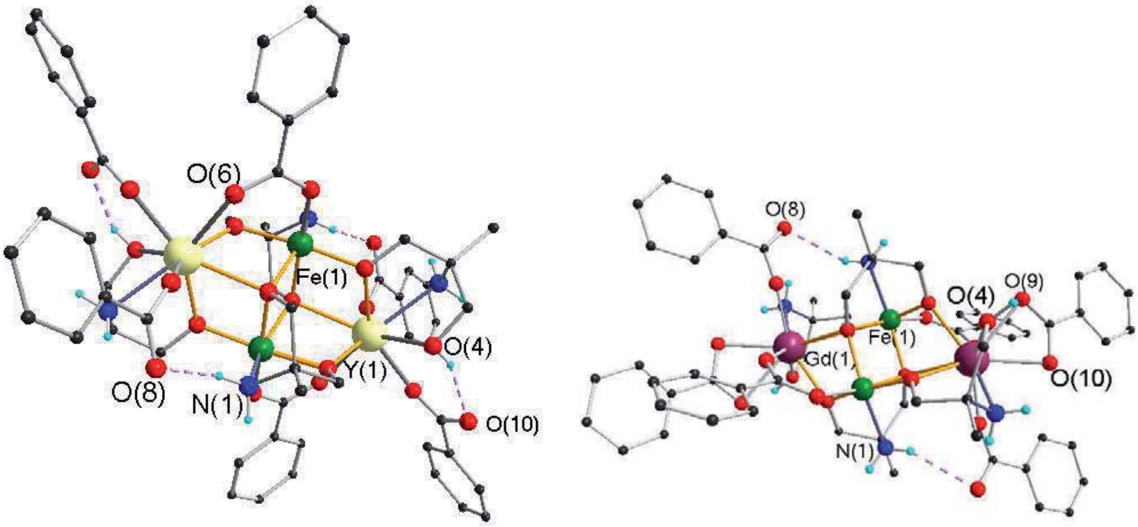

Figure 2.18. The structures of **2.23** (left) and of **2.22** (right). The amino functions coordinate either the Fe^{III} or the Ln^{III} ions. The ligand which chelates Fe^{III} has its two alcohol arms deprotonated. The ligand which chelates the Ln^{III} has only one arm.

The result of **2.22** and **2.23** shows that it is necessary to continue searching for another and more stable tetranuclear Fe/Ln compound which can be also obtained for the anisotropic ions such as Dy^{III}.

Using the benzoate starting material seems to stabilize the tetranuclear species, this why it will be used further. The reaction of the benzoate starting material with 1,1,1-tris(hydrxymethyl)ethane ($thmeH_3$) and $Dy(NO_3)_3$ in presence of pyridine as base yield indeed a tetranuclear complex **2.24** (Fig. 2.19).

Compound **2.24** is a chain-salt complex. It contains two tetranuclear Fe_2Dy_2 fragments, one is cationic and the other is an anion. While in the cationic $[Fe_2Dy_2]^{2+}$, the two Dy^{III} ions are chelated each by a $tmheH_3$ (all arms remain protonated) and further two bridging with their alkoxy arms the metal ions, the anionic $[Fe_2Dy_2]^{2-}$ has nitrate groups chelating on the Dy^{III} centres and two ligands bridge between the metal ions. In both, the benzoates bridge the Fe^{III} and Dy^{III} centres. Compound **2.24** crystallizes in the monoclinic space group $P2_1/n$ and the crystallographic data are summarized in Tab. 2.15, Appendix.

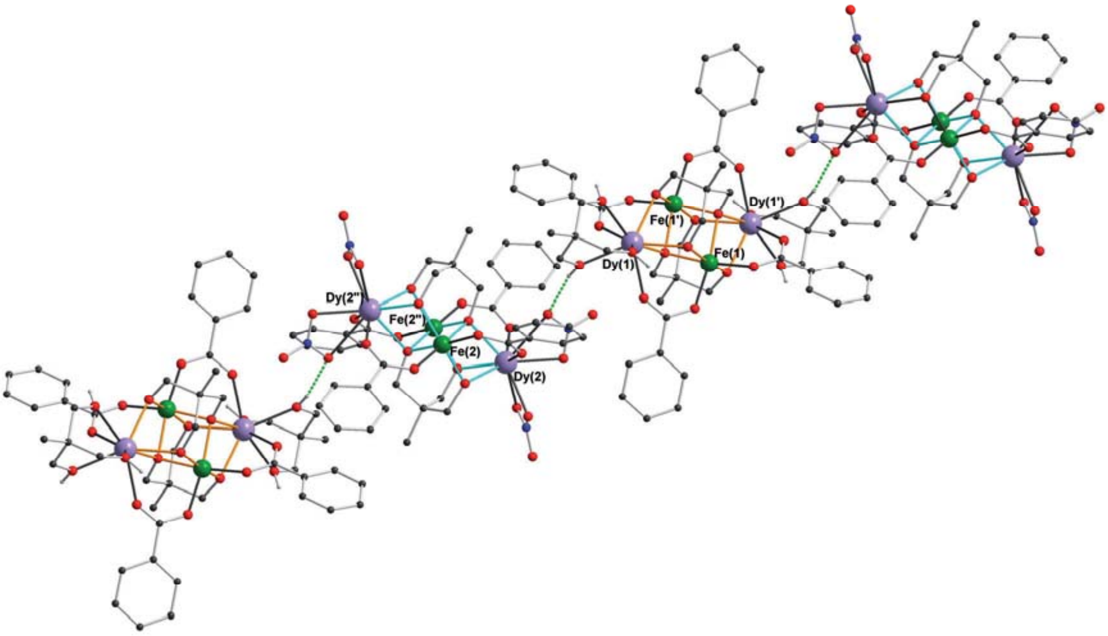

Figure 2.19. The structure if the salt-chain-like **[{Fe_2Dy_2}$^{2+}${Fe_2Dy_2}$^{2-}$]** complex **2.24**.

Complex **2.25** crystallises in the R-3 space group (Fig. 2.20). The compound has the formula [$Fe_2Dy_2(\mu_3\text{-}OH)_2(trop)_2(tropH)_2(deapdH)_2(NO_3)_4$] **2.25**. The crystallographic data are summarised in the appendix. It has the same core-structure as the Fe_2Dy_2 family discussed above and the tetranuclear planar rhombus has two bridging hydroxy-groups. The tropic acid and the 3-(diethylamino)-1,2-propandiol both have chiral carbons. In the structure four tropic acids are present, two as completely deprotonated (the alcohol and the acid groups) while for the other two only the acid function is deprotonated. Furthermore, two amino alcohol ligands are in the structure. Both are mono-deprotonated. The other alcohol arms remain protonated and coordinate to the Dy^{III} centres. This situation is often encountered in this work and seen in various structures in which the protonated alcohol arms prefer to coordinate the lanthanide ions. The nitrogen (tert-amine functions) of the ligands is, however, also protonated. The same situation is manifested in the structure of **2.26**. Two nitrates chelate each Dy^{III}, respectively. This compound represents a useful example of how it is possible to control the self-assembly process in order to isolate compounds with desired cores. The distances and angles of the metal ions to the bridging oxygens are smaller but very similar to those in the Fe_2Dy_2 family of clusters. This compound is actually an excellent reference compound for our Fe_2Dy_2 family systems and an interesting new “test-bed” system. However, the fact that, the tropic acids need to be functionalized with different substituents makes it more difficult. The fact that, the alcohol arms of the tropic carboxylates are not sharing in the structure, motivated us to try a similar strategy but using benzoic acid. This, however, yielded compound **2.26**.

Compound **2.26** was obtained by reacting benzoic acid with the basic (pH= 12) ligand 3-(diethylamino)-1,2-propandiol and the nitrates of Fe^{III} and Dy^{III} (2: 4: 1: 1) in THF/MeCN (2:1) yielding the compound $[Fe^{III}_6Dy_2(\mu_3\text{-}O)_2(\mu_2\text{-}OH)_2(H_2O)_2(O_2CPh)_8(HL)_4(NO_3)_6]\cdot THF$ **(2.26).** The strategy was based on deprotonating the acid by the amine function of the ligand. At the same time the amino function of the ligand is so basic that it accepts a proton from an alcohol group to give zwitterionic form. Furthermore, the two forms of the racemate ligand (R and S) are present in the structure (see Fig. 2.20 lower and right).

Attempts, to isolate the same structure for other lanthanides were rather surprisingly not successful, which indicates that this compound is selective for only Dy^{III}. For all other lanthanides, instead of isolating the analogous octanuclear compound, the known $[Fe_{11}O_6(OH)_6(O_2CPh)_{15}]$ **[65]** cluster was always obtained.

Compound **Fe_6Dy_2** (**2.26**) crystallizes in the monoclinic space group $P2_1/c$ with Z = 2. The structure can be described as an Fe4-butterfly resulting from two-shared triangles with Fe(2) and Fe(3) in the body (hinge) of the motif. The butterfly is augmented by two five-coordinated (square-pyramidal) Fe^{III} ions on both sides bridged through one alkoxy arm of the ligand resulting in a hexanuclear core. The second alcohol arm bridges to these two Fe^{III} with two Dy^{III} from each side, respectively.

The complex contains four N-protonated ligands with ammonium functions +HN(Et), which bridge with their deprotonated alkoxy arms between the butterfly, Fe(3) through (O(4), O(6)) and the Dy-ions through (O(3), O(5)). Eight benzoate ligands are involved in the structure. Two of them are bidentate chelating the Dy-ions and the other two are monodentate coordinatred to the Fe(2) ions. The last four benzoate are bridging between Fe(1) and Fe(2) ions. Six nitrate groups are involved in the structure. Two complete the ligation of each dysprosium ion, the other two nitrates are mono-coordinated to Dy^{III} ions. Leaving Fe(3)-ions square-pyramidal. Two Hydroxy ions (O(2)) bridge between Fe(2) and Fe(3) and two H_2O molecules (O(24)) complete the ligation of Fe(2).

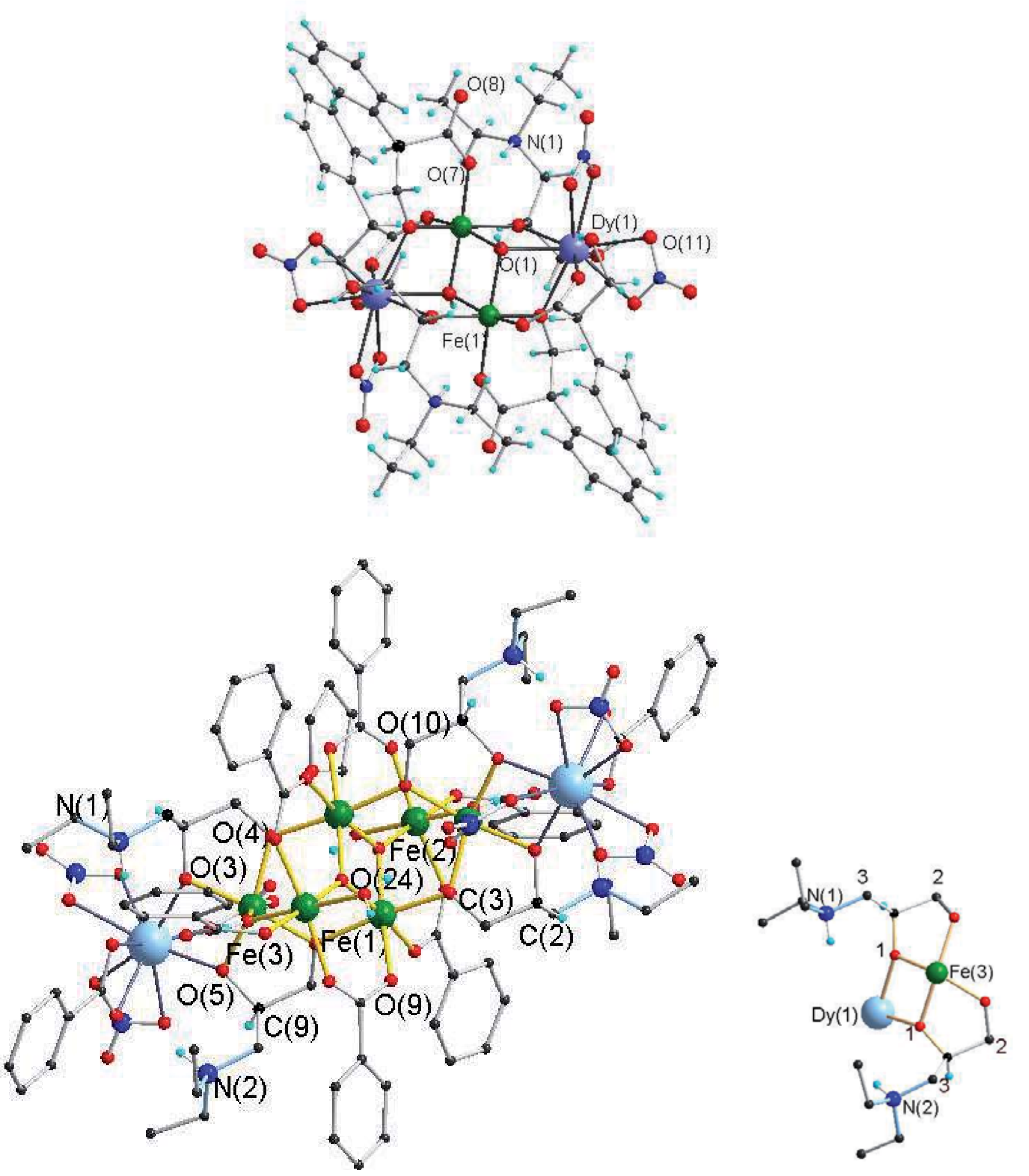

Figure 2.20. (Upper) The structure of **2.25**. (Lower, left) the structure of **2.26** and (right) the two forms or enantimers (R and S) of the ligand.

Compound **2.26** represents a unique example of $\mathrm{Fe^{III}/Ln^{III}}$ clusters which contains a square pyramidal $\mathrm{Fe^{III}}$ and at the same time the neighbours of it are $\mathrm{Dy^{III}}$ ions, which gives the chance for better understanding the interaction of these two ions and the their magnetic anisotropies, the main concern of this chapter. However, the fact that Y analogue cannot be obtained makes understanding its properties challenging (see magnetic and Mössbauer parts and theoretical considerations). Moreover, this system is selective for Dy and cannot be obtained with any other lanthanide. Note, this is the first coordination compound obtained by using the 3-diethylamino-1,2-propandiol ligand. The crystallographic data of **2.26** are summarized in Tab. 2. 16, in the appendix.

2.2 Magnetism

The Fe_2Ln_2 series

The magnetic susceptibilities of polycrystalline samples of **1–13** were measured over the 1.8–300 K temperature range under an applied dc field of 0.1 T. The dc magnetic data for all compounds are summarized in Tab. 2.21 and shown as χT vs T plots in Fig.2.21. All compounds show a more or less steady decrease of their χT products on decreasing the temperature from 300 to 1.8 K as a result of the thermal depopulation of the Ln^{III} excited states (in particular with Ln = Tb, Dy and Er), although antiferromagnetic interactions between paramagnetic centers might also contribute partially to the χT decrease. For all the compounds, the χT products at 300 K are lower than the values expected for non-interacting metal ions, i.e. the sum of the respective Curie constants for the ions; another indication that antiferromagnetic interactions may be present. This is particularly the case for **13** with diamagnetic Y^{III} ions, for which the room temperature χT products is much smaller than the expected value for two non-interacting Fe^{III} ions ($^6A_{1g}$, $S = 5/2$, $g = 2$), suggesting that the Fe^{III} ions are strongly antiferromagnetically coupled and χT for **13** is approaches zero (0.09 cm^3Kmol^{-1}) at 1.8 K indicating a spin ground state with $S = 0$. However, for the other Fe_2Ln_2 complexes the χT products at 300 K are generally in reasonable agreement with the sum of the experimental value for the $Fe^{III}{}_2Y_2$ complex **13** and the Curie constants for two respective Ln^{III} metal ions (Tab. 2.21), indicating at most weak Fe-Ln interactions.

Magnetization measurements at low temperatures were carried out on all compounds. The field dependence of the magnetization curves are shown in Fig.2.22 and the magnitudes of magnetization are summarized in Tab. 2.21. The general behavior is that the magnetization increases steadily with the application of external field with no true saturation of magnetization even at 7 T. The Fe_2Gd_2 compound **6** comes close to saturation, reaching M = 13.9 μB at 7 T, a value consistent with parallel alignment of the spins on the two Gd^{III} ions but with the two Fe^{III} spins remaining essentially antiparallel. For the other Fe_2Ln_2 compounds this indicates the likely presence of both magnetic anisotropy (from the Ln^{III} cations) and the presence of low-lying excited states (resulting from the weak Fe-Ln coupling). The reduced magnetisation plots at low temperatures are not superposed, supporting this conclusion.

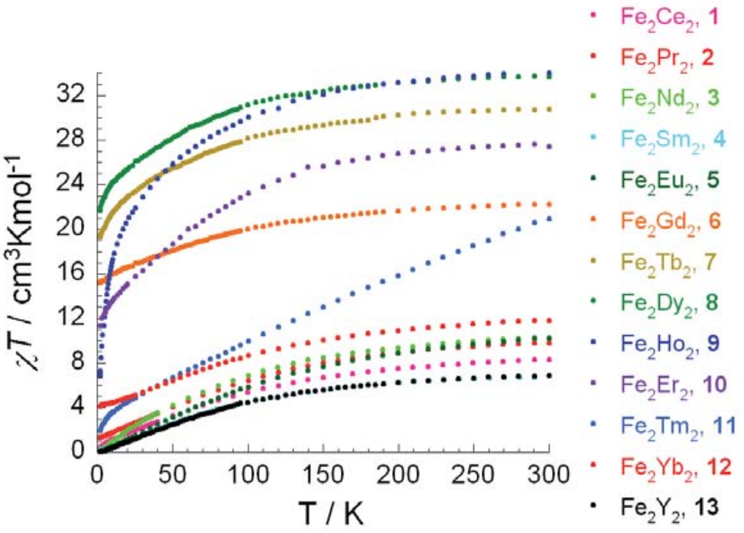

Figure 2.21. Temperature-dependence of the χT product under 0.1 T (with χ defined as the dc magnetic susceptibility equal to *M/H* and normalized per molecular unit). Compound codes are indicated in the inset of figures.

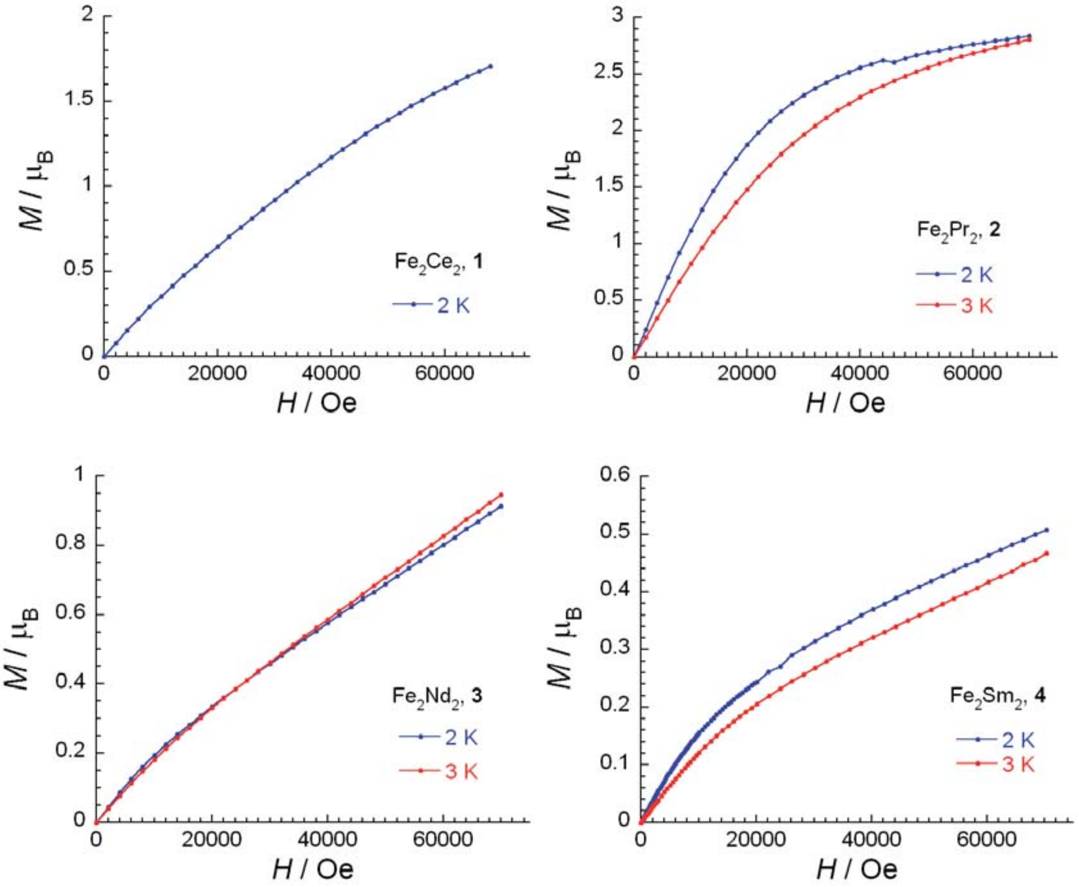

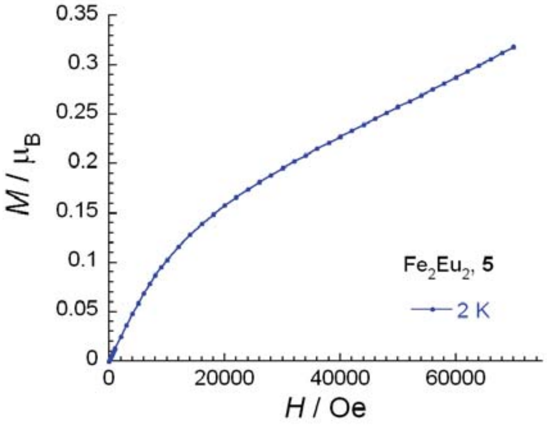
M / μB
H / Oe
0
0.05
0.1
0.15
0.2
0.25
0.3
0.35
0
20000
40000
60000
Fe2Eu2, 5
2 K

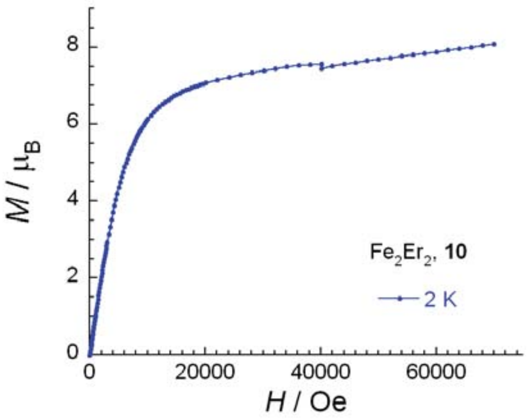
M / μB
H / Oe
0
2
4
6
8
0
20000
40000
60000
Fe2Er2, 10
2 K

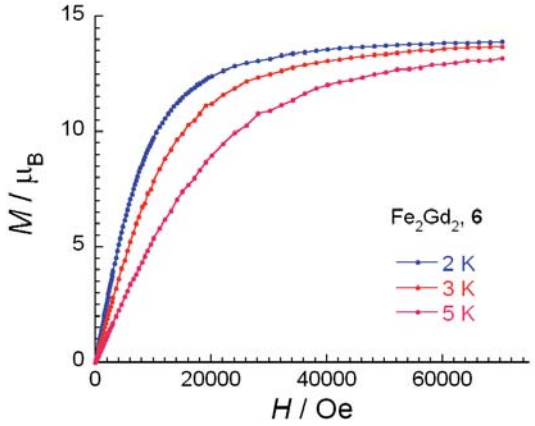
M / μB
H / Oe
0
5
10
15
0
20000
40000
60000
Fe2Gd2, 6
2 K
3 K
5 K

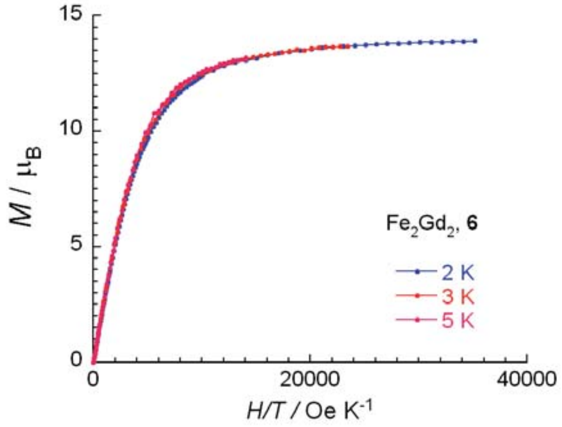
M / μB
H/T / Oe K-1
0
5
10
15
0
20000
40000
Fe2Gd2, 6
2 K
3 K
5 K

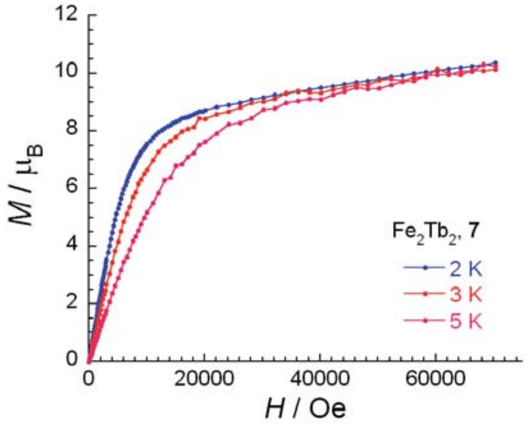
M / μB
H / Oe
0
2
4
6
8
10
12
0
20000
40000
60000
Fe2Tb2, 7
2 K
3 K
5 K

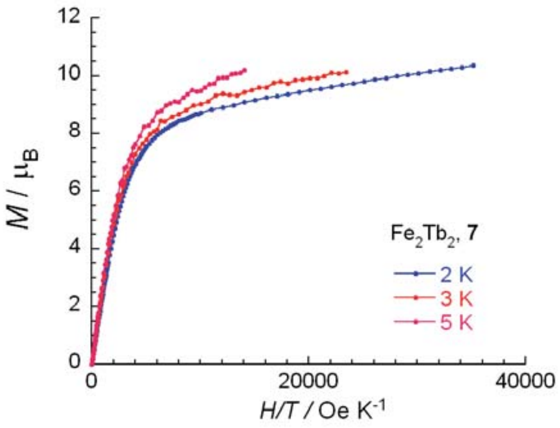
M / μB
H/T / Oe K-1
0
2
4
6
8
10
12
0
20000
40000
Fe2Tb2, 7
2 K
3 K
5 K

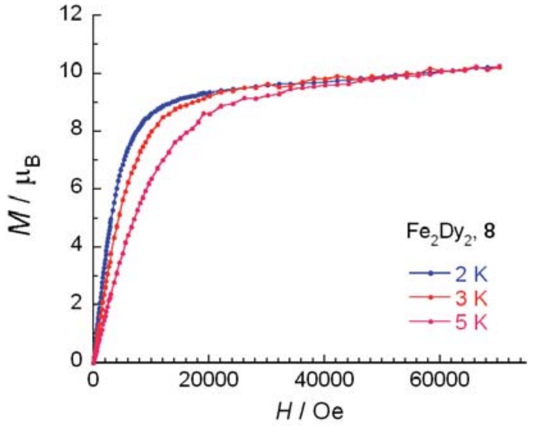
M / μB
H / Oe
0
2
4
6
8
10
12
0
20000
40000
60000
Fe2Dy2, 8
2 K
3 K
5 K

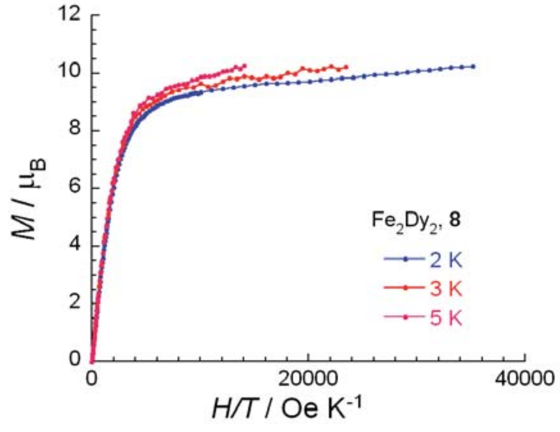
M / μB
H/T / Oe K-1
0
2
4
6
8
10
12
0
20000
40000
Fe2Dy2, 8
2 K
3 K
5 K

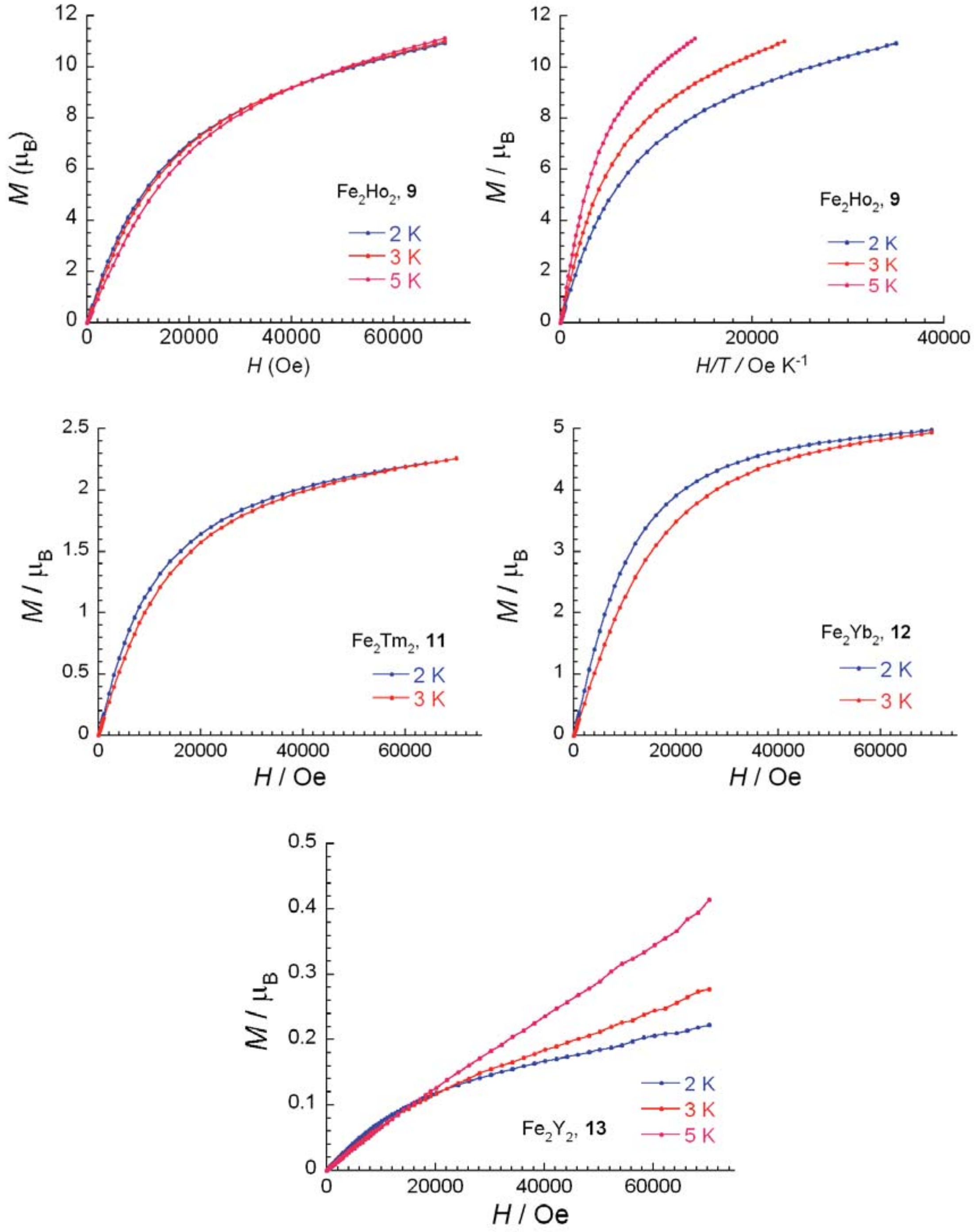

Figure 2.22. Field dependence of magnetization at low temperatures for all compounds. Compound codes are indicated in the inset of figures.

Table 2.21. Magnetic data summarized from the dc measurements.

Compounds	Ground state of Ln	Curie constant for each Ln^{III} (cm^{3}Kmol^{-1})	χT calc. for four non-interacting ions per complex.[a] (cm^3 K mol^{-1})	χT calc. for Fe$_2$ unit with two non-interacting Ln^{III} ions per complex.[b] (cm^3 K mol^{-1})	χT at 300 K per complex (cm^3 K mol^{-1})	χT at 1.8 K per complex (cm^3 K mol^{-1})	Magnetization at 2 K and 7 T (μB)
Fe_2Ce_2 (**2.1**)	$^2F_{5/2}$	0.80	10.35	8.51	8.29	0.41	1.7
Fe_2Pr_2 (**2.2**)	$^3H_4$	1.60	11.95	10.11	9.79	1.36	2.8
Fe_2Nd_2 (**2.3**)	$^4I_{9/2}$	1.64	12.03	10.19	10.24	0.24	0.9
Fe_2Sm_2(**2.4**)	$^6H_{5/2}$	0.09	8.93	7.09	6.73	0.21	0.5
Fe_2Eu_2 (**2.5**)	$^7F_0$	0	8.75[c]	6.91[c]	10.22	0.13	0.3
Fe_2Gd_2 (**2.6**)	$^8S_{7/2}$	7.875	24.50	22.66	22.26	15.33	13.9
Fe_2Tb_2 (**2.7**)	$^7F_6$	11.82	32.39	30.55	30.81	19.55	10.8
Fe_2Dy_2 (**2.8**)	$^6H_{15/2}$	14.17	37.09	35.25	33.70	21.77	10.2
Fe_2Ho_2 (**2.9**)	$^5I_8$	14.07	36.89	35.05	34.03	6.87	10.9
Fe_2Er(**2.10**)	$^4I_{15/2}$	11.5	31.75	29.91	27.66	11.39	8.1
Fe_2Tm_2 (**2.11**)	$^3H_6$	7.15	23.05	21.21	20.96	1.93	2.3
Fe_2Yb_2(**2.12**	$^2F_{7/2}$	2.57	13.89	12.05	11.86	4.11	5.0
Fe_2Y_2 (**2.13**)	diamagnetic	0	8.75	-	6.91	0.09	0.2

[a] taking g = 2.00 for Fe^{III} ions; [b] the sum of the RT χT product for the Fe_2Y_2 analogue **2.13** and the Curie constants for the two Ln^{III} ions. [c] assuming diamagnetic low-spin Eu^{III}

Assessing the Fe^{III}-Fe^{III} magnetic interactions in the Fe_2Ln_2 tetranuclear unit can best be done by analysing the data for the Fe_2Y_2 analogue (**2.13**). This can be magnetically viewed as dimer of two S = 5/2 spins and the van Vleck equation used to give an analytical expression for the magnetic susceptibility from the spin Hamiltonian: $H_d = -2JS_1S_2$ with $S_1 = S_2 = 5/2$. The best set of parameters obtained using this model (with g fixed at 2.00) is J = -6.53(5) cm^{-1} and a residual mononuclear S = 5/2 paramagnetic impurity amounting to 2.29(1) %, corresponding to a $S_T = 0$ spin ground state (Fig.2.23). Given the similar core structure of all the Fe_2Ln_2 complexes, it is reasonable to assume that in the other compounds of this family the Fe^{III}-Fe^{III} interactions are all antiferromagnetically coupled to a similar extent.

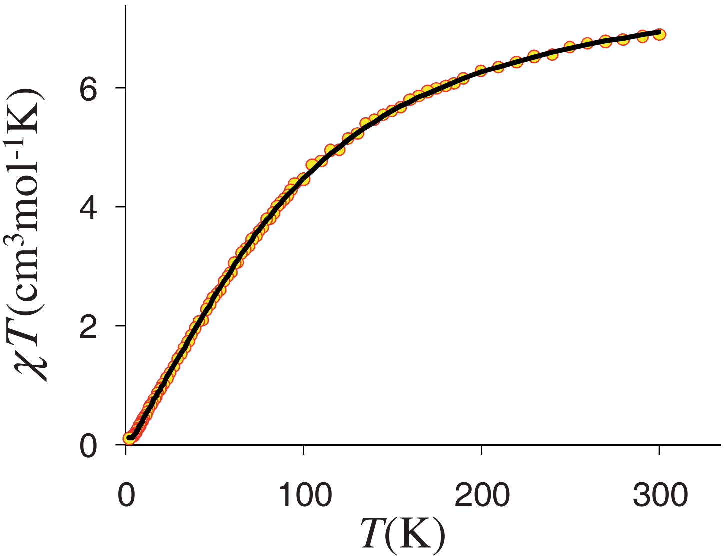

Figure 2.23. The χT versus T plot for Fe_2Y_2 (**2.13**). The black solid line corresponds to the best fit with parameters discussed in text.

Since the Gd^{III} ion ($^8S_{7/2}$, $S = 7/2$, $L = 0$, $g = 2$) has no orbital contribution, a similar fitting of the χT versus T plot for the Fe_2Gd_2 compound **2.6** is also possible. Based on the structure, the two independent Fe-Gd interactions are likely to be very similar, the complex can be magnetically viewed as a tetramer with $S_1 = S_3 = 5/2$ and $S_2 = S_4 = 7/2$; (Fig.v2.24, inset). Application of the van Vleck equation to the Kambe vector coupling scheme,**[66]** allows an analytical expression of the magnetic susceptibility to be determined from the following spin Hamiltonian: $H_t = -2J_1\left(S_1S_2 + S_2S_3 + S_3S_4 + S_4S_1\right) - 2J_2S_1S_3$, where J_1 and J_2 represent the average of the Fe^{III}-Gd^{III} interactions and the Fe^{III}-Fe^{III} interaction, respectively. The best-fit parameters obtained are $J_1 = 0.18(1)$ cm^{-1}, $J_2 = -6.71(4)$ cm^{-1} and $g = 1.99(2)$, with a good agreement factor ($R = 1.2 \times 10^{-4}$) (the solid line in Figure 2.20). The Fe^{III}-Fe^{III} interaction obtained here is very similar to that for the Fe_2Yb_2 compound **2.12**, but the Fe^{III}-Gd^{III} interaction, although non-zero and ferromagnetic, is very weak. Indeed, the experimental magnetization curves of **2.6** at 2.0, 3.0 and 5.0 K can also be fitted using the sum of the Brillouin functions corresponding to two non-coupled Gd^{III} ions with $S = 7/2$ and $g = 2.01$ (Fig.2.20) giving further evidence for the weakness of the Fe^{III}-Gd^{III} interactions.

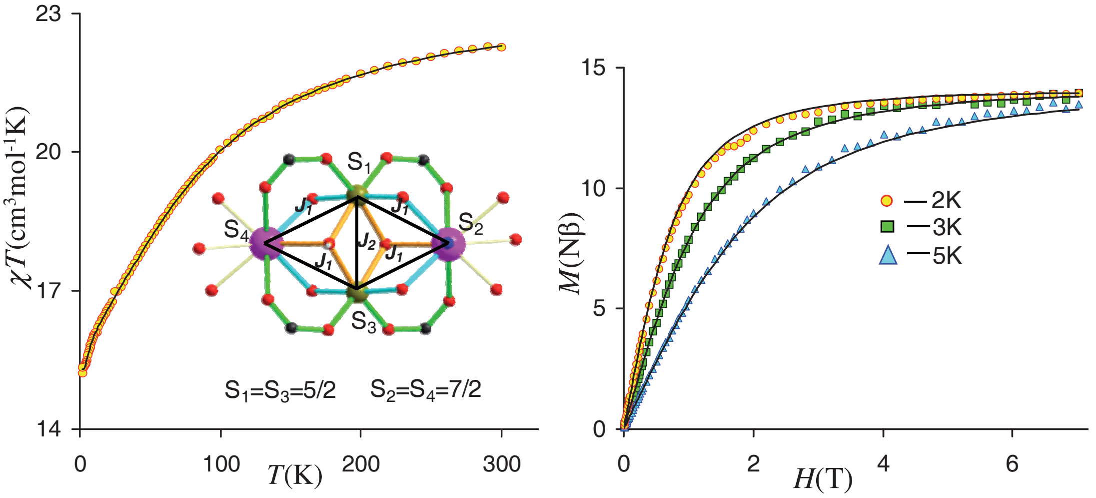

Figure 2.24. (Left) The χT versus T plot for Fe_2Gd_2 (**2.6**). The black solid line corresponds to the best fit with the spin Hamiltonian and parameters indicated in text. (Inset, left) Scheme of spin topology of **2.6**; (Right) Magnetisation M vs applied field H at 2, 3, 5K for Fe_2Gd_2 (**2.6**). The black solid lines represent the Brillouin functions of two isolated Gd^{III} ions with $S = 7/2$ and $g = 2.01(1)$.

To probe magnetic anisotropy, ac magnetic susceptibility measurements were performed for all compounds. For the Fe_2Ln_2 series, a non-zero out-of-phase component was detected only for Fe_2Dy_2 (**2.8**$^{\textbf{teaH-6}\boldsymbol{p}\textbf{H}}$). In the absence of an external dc field, the intensity of the out-of-phase signal observed is very weak in comparison to that of the in-phase one with a ratio χ’’/χ’ (1:40) (Fig. 2.25), and no maximum is observable above 1.8 K. Very similar data were observed in the Fe_2Dy_2 compound of Murugesu et al., who found evidence for fast zero-field Quantum Tunnelling of Magnetization in the microSQUID hysteresis loops, which prevented them from quantifying the height of the barrier to relaxation of magnetisation.[20a)]

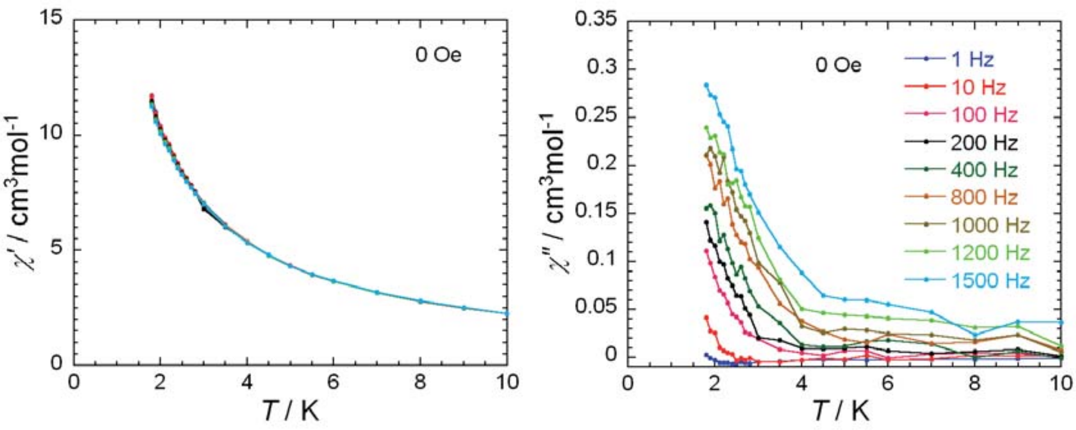

Figure 2.25. Plots of in-phase (left) and out-of-phase (right) ac susceptibility signals vs. temperature for **2.8**$^{\textbf{teaH-6}\boldsymbol{p}\textbf{H}}$ at the indicated oscillation frequencies.

However, QTM can be suppressed by applying a small dc field, which removes the degeneracy of corresponding energy levels on the positive and negative spin sides of the barrier, often greatly reducing the probability of such tunnelling processes. [67] In this way useful information on the dynamics of the magnetization in the thermally activated regime can be extracted. Therefore, ac measurements at several applied static fields (0, 0.5, 1.0, 1.5, 2.0 kOe) (Fig.2.26) were recorded.

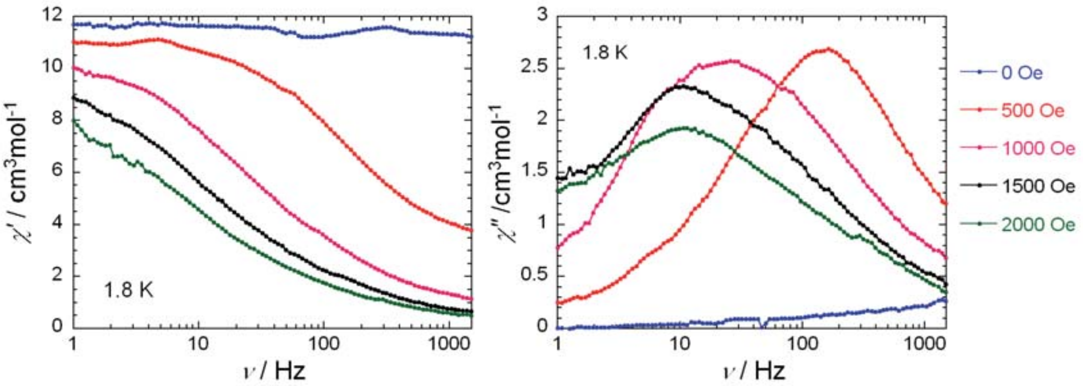

Figure 2.26. Plots of in-phase (left) and out-of-phase (right) ac susceptibility signals vs. frequency for Fe_2Dy_2 $\mathbf{2.8}^{\mathbf{teaH\text{-}6}\boldsymbol{p}\mathbf{H}}$ at 1.8 K under the indicated external dc fields.

A strong field dependence of χ’’ is observed at 1.8 K, with an applied field of ca. 1.5 kOe shifting the maximum in a plot of χ’’ against frequency to lowest frequency. This dc field was then applied to investigate the dynamic susceptibility. Well-defined maxima are now observed in plots of χ’’ against temperature, and the intensities of χ’ and χ’’ have become more comparable in magnitude, with the ratio of χ’’/χ’ now 0.58 at 2.8 K and 200 Hz (Fig.2.27). Both the temperature and frequency dependence of the in-phase and out-of-phase susceptibilities are now strongly frequency dependent below 10 K; this observation is characteristic of SMMs presenting a narrow distribution of the relaxation times. [67a)]

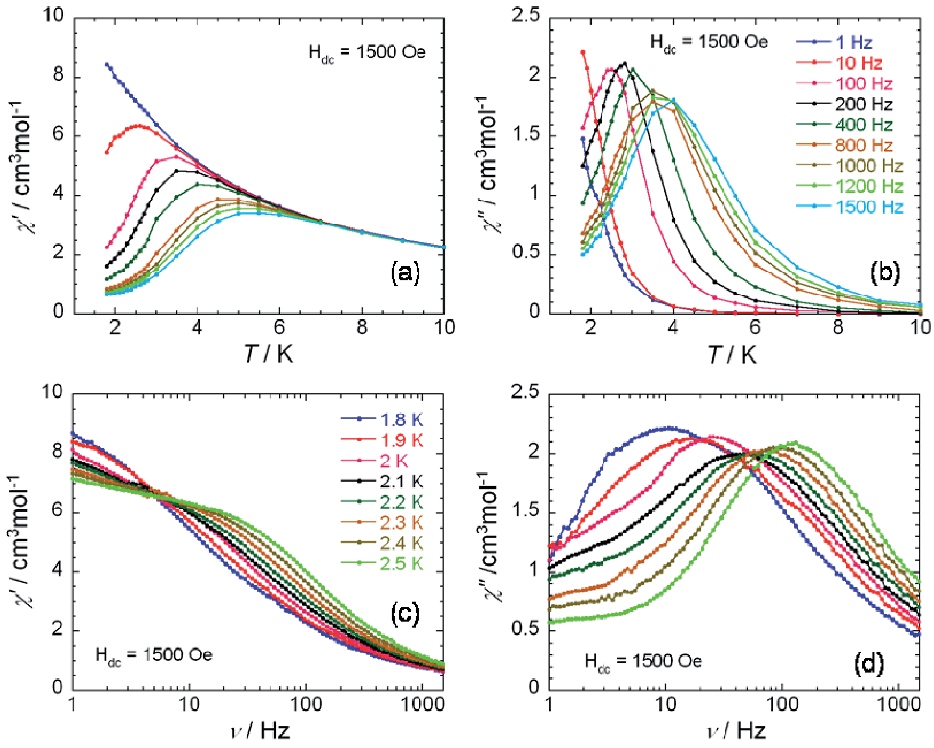

Figure 2.27. Temperature dependence of the in-phase (a) and out-of-phase (b) components of the ac magnetic susceptibility, for Fe$_2$Dy$_2$ ($\mathbf{2.8}^{\mathbf{teaH\text{-}6}\boldsymbol{p}\mathbf{H}}$) under 1500 Oe applied dc field. Frequency dependence of the in-phase (c) and the out-of-phase (d) components of the ac susceptibility at different temperatures for Fe$_2$Dy$_2$ ($\mathbf{2.8}^{\mathbf{teaH\text{-}6}\boldsymbol{p}\mathbf{H}}$) under 1500 Oe applied dc field.

Since both datasets demonstrate the nature of the slow relaxation of the magnetisation which is directly responsible for its SMM behaviour, the parameters of the relaxation process from both datasets can be extracted. The thermal variation of τ is described by the best fit of the data to an Arrhenius expression $\tau = \tau_0 \exp(U_{\text{eff}}/k_BT)$ which gives an effective energy barrier U_{eff} = 16.21 K and a relaxation time $\tau_0 = 1.9\text{x}10^{-6}$ s (Fig. 2.28). In order to study the relaxation process further, Cole-Cole plots of the in-phase versus out-of-phase susceptibilities at low temperatures were constructed. Fitting the data using a generalized Debye model [67] gives a range of α value of 0.27-0.48. The best fit for the Cole-Cole plot at 1.9 K gave the following parameters: α = 0.454(3), χ_0 = 9.72(3) cm^3/mol, χ_∞=0.14(2) cm^3/mol and τ = 0.0094(1) s (0.0093896 std dev 9.14E-05) (Fig.2.24 inset). The values of τ and α are consistent with the characteristic parameters for classic SMMs. [68]

$$\chi'(\nu_{ac}) = \chi_\infty + \frac{(\chi_0 - \chi_\infty)\left[1 + (2\pi\nu_{ac}\tau)^{1-\alpha}\sin(\alpha\pi/2)\right]}{1 + 2(2\pi\nu_{ac}\tau)^{1-\alpha}\sin(\alpha\pi/2) + (2\pi\nu_{ac}\tau)^{2(1-\alpha)}}$$

The relatively large value of α indicates that more than one relaxation process might be operating at this temperature.

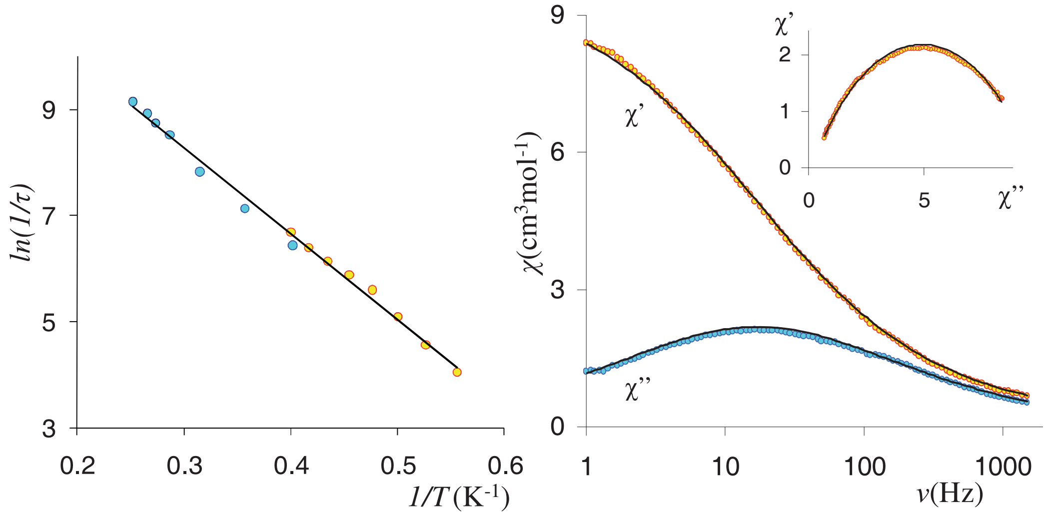

Figure 2.28. Arrhenius plot for Fe_2Dy_2 (**2.8$^{teaH\text{-}6pH}$ 8**). The blue points are extracted from frequency-scan and the yellow points from temperature-scan. The solid line is the best fit of the both data sets. Inset: Cole-Cole plot at 1.9 K. The solid line is a least-squares fitting of the data to a generalized Debye model. See the parameters discussed in the text.

The magnetism of Fe_8La_6 (**2.14**) was studied in the Diplomarbeit and will not be discussed here since we want to give our attention in this work for the Fe_2Dy_2 (**2.8 systems**) compounds. The Fe_4Lu_2 (**2.15**) compound was not studied magnetically and it was mentioned just for synthetic discussion. Furthermore, these two compounds are not tetranuclear and their magnetic data might not add any important information to this comparative study.

Para-Fe_2Dy_2 examples

It should be noted that not all the possible *para*-examples will be discussed here because some of these examples have not yet been isolated. Nevertheless, we could study the most important examples which cover all kinds of substituents according their electronic nature (see chapter 1). Note further, that such a study can produce a large amount of magnetic data and figures. In this work, the comparative study will be simplified as much as possible to avoid confusing the reader. Most figures and tables can be found in the appendix (chapter 6).

It is known, in particular from organic chemistry where substituents on carbon frameworks play important roles in terms of electronically-directed effects, that groups such as $-CH_3$, -tBu are sigma donating groups with a strong +I effect. In addition, groups such as $-NO_2$ and –CN are known to be strong electron-withdrawing groups showing both –I and –M effects. Our strategy was to investigate these molecules first and then proceed to further examples if trends were perceived.

The temperature-dependence of the χT curves under 0.1 T, with χ defined as the dc magnetic susceptibility equal to *M/H* and normalized per molecular unit, and the magnetization for these compounds are very similar. The ac magnetism, however, is significantly different. That is where the magnetic anisotropy becomes more important.

In Fig. 2.29 are the χT product versus T plots presented for Fe_2Dy_2 compounds with six *p*-R-benz. (H (benz.), pt (*para*tolyate), (tb) tertbuylbenzoate, (nb) nitrobenzoate and (cb) cyanobenzoate}, as well as the magnetizations.

All compounds (with substituents pt, tb, nb, nitrobenzoate and cb, cyanobenzoate) show a more or less steady decrease of their χT products on decreasing the temperature from 300 to 1.8 K as in case of the unsubstituted benzoate (4H, benz.), suggesting that antiferromagnetic interactions between paramagnetic centers are dominant in these Fe_2Dy_2 molecules. For all the compounds, the χT products at 300 K are lower than the values expected for non-interacting metal ions, i.e. the sum of the respective Curie constants for the ions, also indicating antiferromagnetic interactions. This is particularly the case for pt, tb, nb and cb compounds. However, in case of **2.8**$^{\mathbf{teaH\text{-}6pMe}}$ (for pt substituent) the χT product at lower temperature deviates from antiferromagnetism to ferrimagnetism.

Magnetization measurements at low temperatures were carried out on all these compounds. The field dependence of the magnetization curves are shown in Fig.2.29 as well. The general behavior is that the magnetization increases steadily with the application of external field of magnetization up to 7 T. The magnetization curves are similar to the reference compound-system with unsubstituted benzoate **2.8**$^{\mathbf{teaH\text{-}6}\boldsymbol{p}\mathbf{H}}$ (Fig. 2.29 (upper)). In addition, the plots of in-phase and out-of-phase *ac* susceptibilities and their signals vs. temperature at different oscillation frequencies as well as signals vs. frequency at 1.8 K and under different dc fields are in Fig. 3.30 for compounds **2.8teaH**$^{\mathbf{\text{-}6}\boldsymbol{p}\mathbf{Me}}$ and **2.8**$^{\mathbf{teaH\text{-}6}\boldsymbol{p}\mathbf{tBu}}$ and the Arrhenius plots for these two compounds are in Fig. 3.31. The plots of in-phase and out-of-phase *ac* susceptibilities and their signals vs. temperature at different oscillation frequencies as well as signals vs. frequency at 1.8 K and under different dc fields for and the Arrhenius plots for **2.8**$^{\mathbf{teaH\text{-}6}\boldsymbol{p}\mathbf{NO2}}$ are in Fig. 3.33 and for compound **2.8**$^{\mathbf{teaH\text{-}6}\boldsymbol{p}\mathbf{CN}}$ in Fig. 3.34.

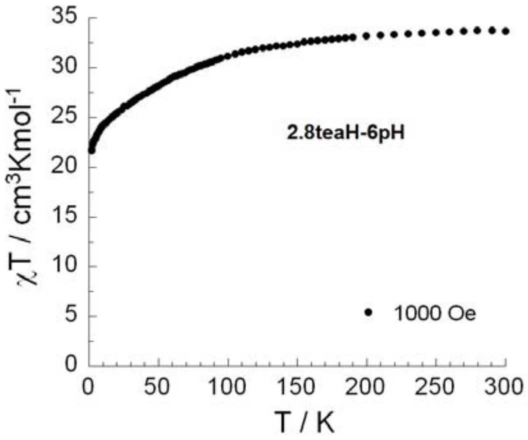
χT / cm^{3}Kmol^{-1}
T / K
2.8teaH-6pH
1000 Oe
0
5
10
15
20
25
30
35
0
50
100
150
200
250
300

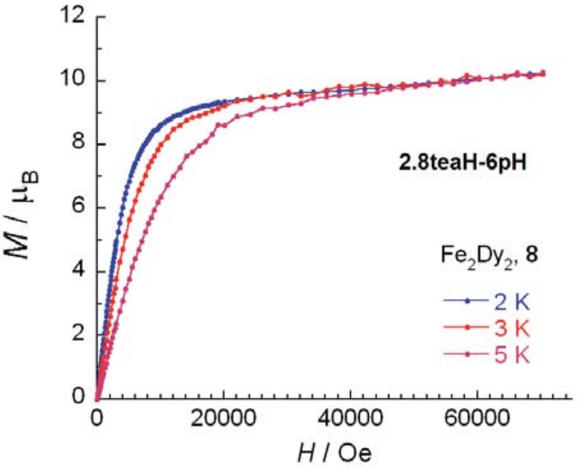
M / μ$_B$
H / Oe
2.8teaH-6pH
Fe$_2$Dy$_2$, 8
2 K
3 K
5 K
0
2
4
6
8
10
12
0
20000
40000
60000

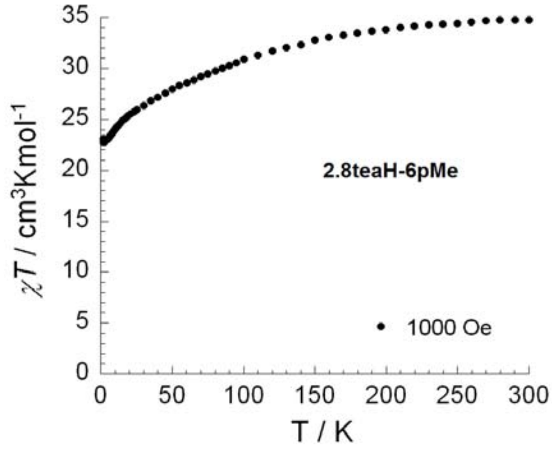
χT / cm^{3}Kmol^{-1}
T / K
2.8teaH-6pMe
1000 Oe
0
5
10
15
20
25
30
35
0
50
100
150
200
250
300

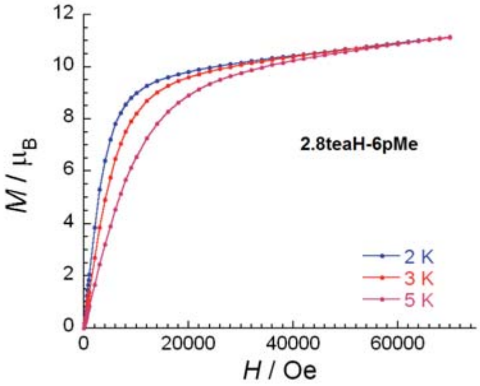
M / μ$_B$
H / Oe
2.8teaH-6pMe
2 K
3 K
5 K
0
2
4
6
8
10
12
0
20000
40000
60000

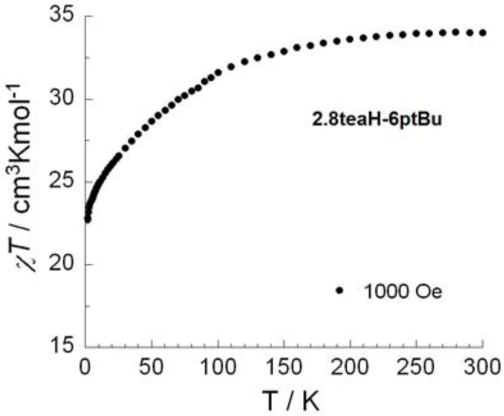
χT / cm^{3}Kmol^{-1}
T / K
2.8teaH-6ptBu
1000 Oe
15
20
25
30
35
0
50
100
150
200
250
300

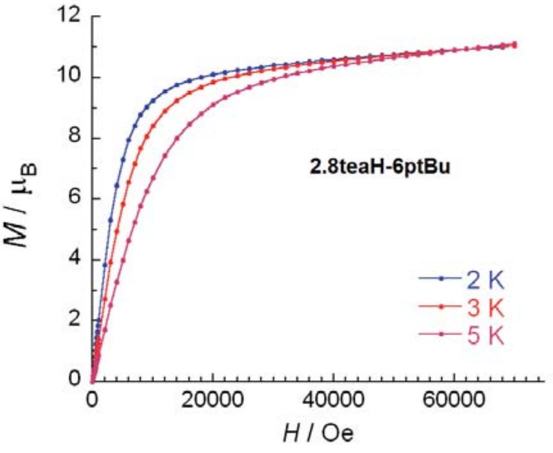
M / μ$_B$
H / Oe
2.8teaH-6ptBu
2 K
3 K
5 K
0
2
4
6
8
10
12
0
20000
40000
60000

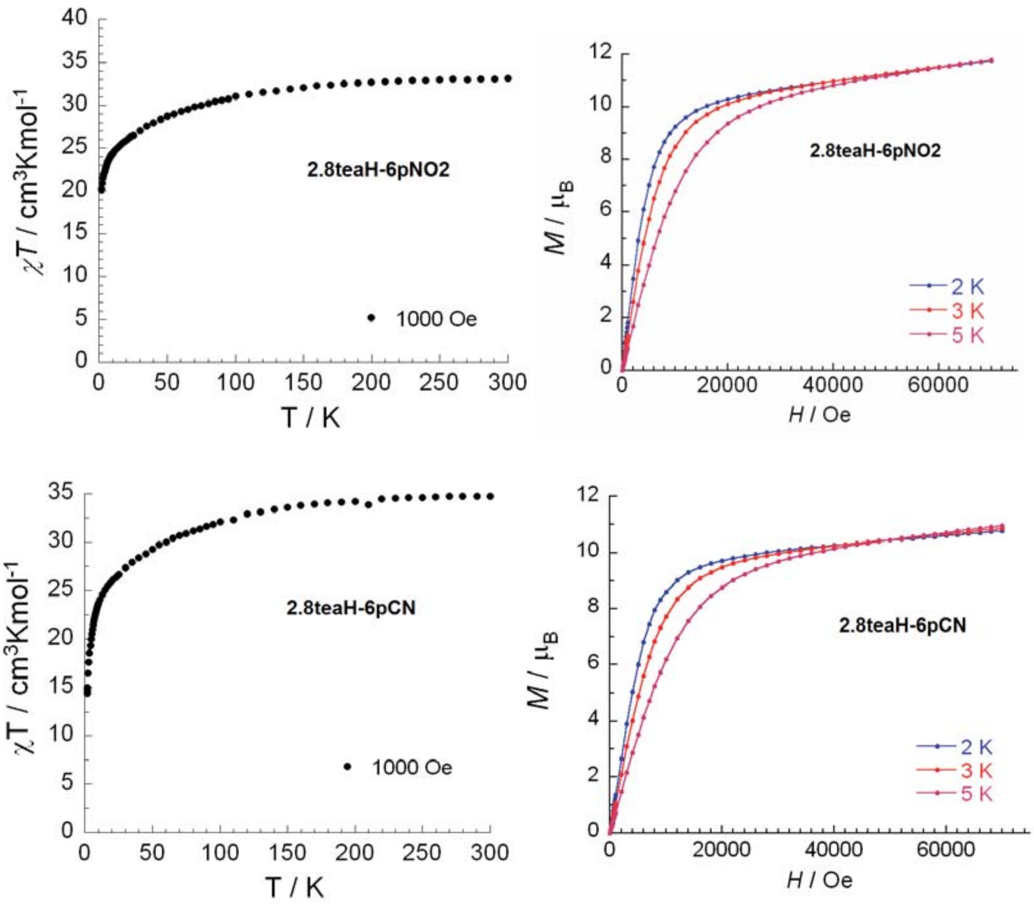

Figure 2.29. The temperature-dependence of the χT product under 0.1 T and the magnetization plots of **Fe$_2$Dy$_2$** compounds with *para*-substituents {**H (2.8**$^{\text{teaH-6}p\text{H}}$**), Me (2.8**$^{\text{teaH-6}p\text{Me}}$**), ^{t}Bu (2.8**$^{\text{teaH-6}p\text{Bu}}$**), NO$_2$ (2.8**$^{\text{teaH-6}p\text{NO2}}$**) and CN (2.8**$^{\text{teaH-6}p\text{CN}}$).

The fact that *dc* magnetism is similar in these five compounds is indeed useful for a comparative study. This indicates that the coupling (and the resulting spin ground state) remains fairly constant. This clearly shows that this system was the correct choice in order to investigate the substituent effect on the anisotropy. To probe magnetic anisotropy, *ac* magnetic susceptibility measurements were also performed for all these four compounds. For the Fe$_2$Dy$_2$ compound with **2.8**$^{\text{teaH-6}pt\text{Bu}}$ a non-zero out-of-phase component was detected (Fig. 2.30) as in case of the reference Fe$_2$Dy$_2$ (**2.8**$^{\text{teaH-6}p\text{H}}$) compound (Fig.2.25). In contrast, the Fe$_2$Dy$_2$ (**2.8**$^{\text{teaH-6}p\text{Me}}$) does not have a non-zero out-of-phase component. In the absence of an external dc field, the intensity of the out-of-phase signal observed is not weak in comparison to that of the in-phase one and no maximum is observable above 1.8 K for **2.8**$^{\text{teaH-6}pt\text{Bu}}$. However, in case of Fe$_2Dy_2$ (**2.8**$^{\text{teaH-6}p\text{H}}$) the intensity of the out-of-phase signal is very weak in comparison with the in-phase one. In compounds Fe$_2$Dy$_2$ (**2.8**$^{\text{teaH-6}p\text{H}}$) and Fe$_2Dy_2$ (**2.8**$^{\text{teaH-6}pt\text{Bu}}$) we also find evidence for fast zero-field Quantum Tunnelling of Magnetization, which prevents quantification of the height of the barrier to relaxation of magnetisation (Fig. 3.31). The fact that Fe$_2$Dy$_2$ (**2.8**$^{\text{teaH-6}p\text{Me}}$) shows out-of-phase *ac*-signals on application of a dc field also indicates that slow relaxation of magnetization occurs in this compound. The differences in the in-phase and out-of-phase *ac* susceptibilities between these three compounds are indeed remarkable and they show first indications for a possible influence on the magnetic anisotropy, the magnetic relaxation and the SMM behaviour in this system. The in-phase and out-of-phase *ac* susceptibilities signals vs. temperature at the indicated oscillation frequencies as well as signals vs. frequency at 1.8 K and under the indicated *dc* fields for compounds are shown in Fig. 3.31 for **2.8**$^{\mathbf{teaH\text{-}6}\boldsymbol{p}\mathbf{Me}}$ and **2.8**$^{\mathbf{teaH\text{-}6}\boldsymbol{pt}\mathbf{Bu}}$. These indicate that QT regimes for **2.8**$^{\mathbf{teaH\text{-}6}\boldsymbol{p}\mathbf{Me}}$ and **2.8**$^{\mathbf{teaH\text{-}6}\boldsymbol{pt}\mathbf{Bu}}$ can be suppressed by applying 1000 Oe and 2000 Oe, respectively. With the help of these data and using the Arrhenius equation, the energy barriers resulting from the relaxation process, which is suppressed by QT, could be calculated as 24 K for **2.8**$^{\mathbf{teaH\text{-}6}\boldsymbol{p}\mathbf{Me}}$ and 19.4 K for **2.8**$^{\mathbf{teaH\text{-}6}\boldsymbol{pt}\mathbf{Bu}}$. Two substituents with two different +I-effect lead to significant differences in the energy barriers and QT processes as well as in the relaxation process in total. It is now interesting to investigate how this effect will operate for a substituent such as nitro with one of the strongest known electron displacement properties (–I and –M effects). The dc susceptibility of the nitro compound **2.8**$^{\mathbf{teaH\text{-}6}\boldsymbol{p}\mathbf{NO2}}$ is much closer to that of the reference compound **2.8**$^{\mathbf{teaH\text{-}6}\boldsymbol{p}\mathbf{H}}$ than of **2.8**$^{\mathbf{teaH\text{-}6}\boldsymbol{p}\mathbf{Me,}}$ for example. Should we expect the same SMM behavior?

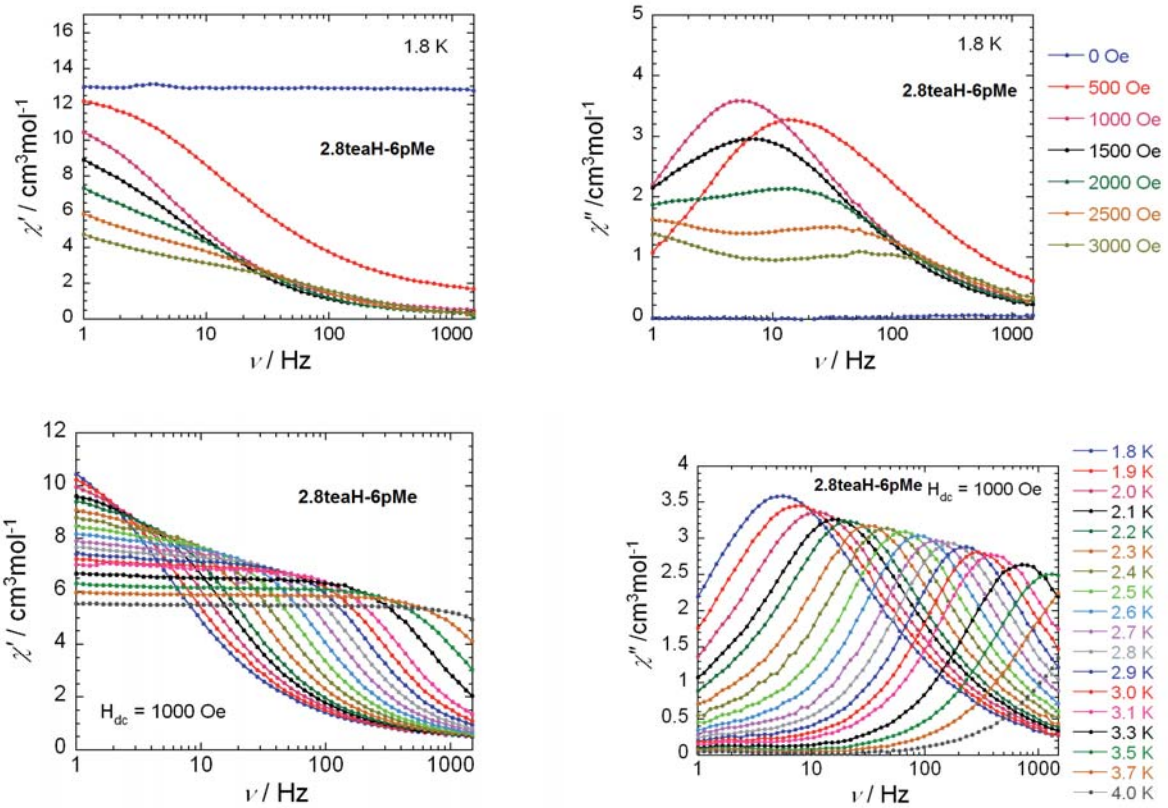

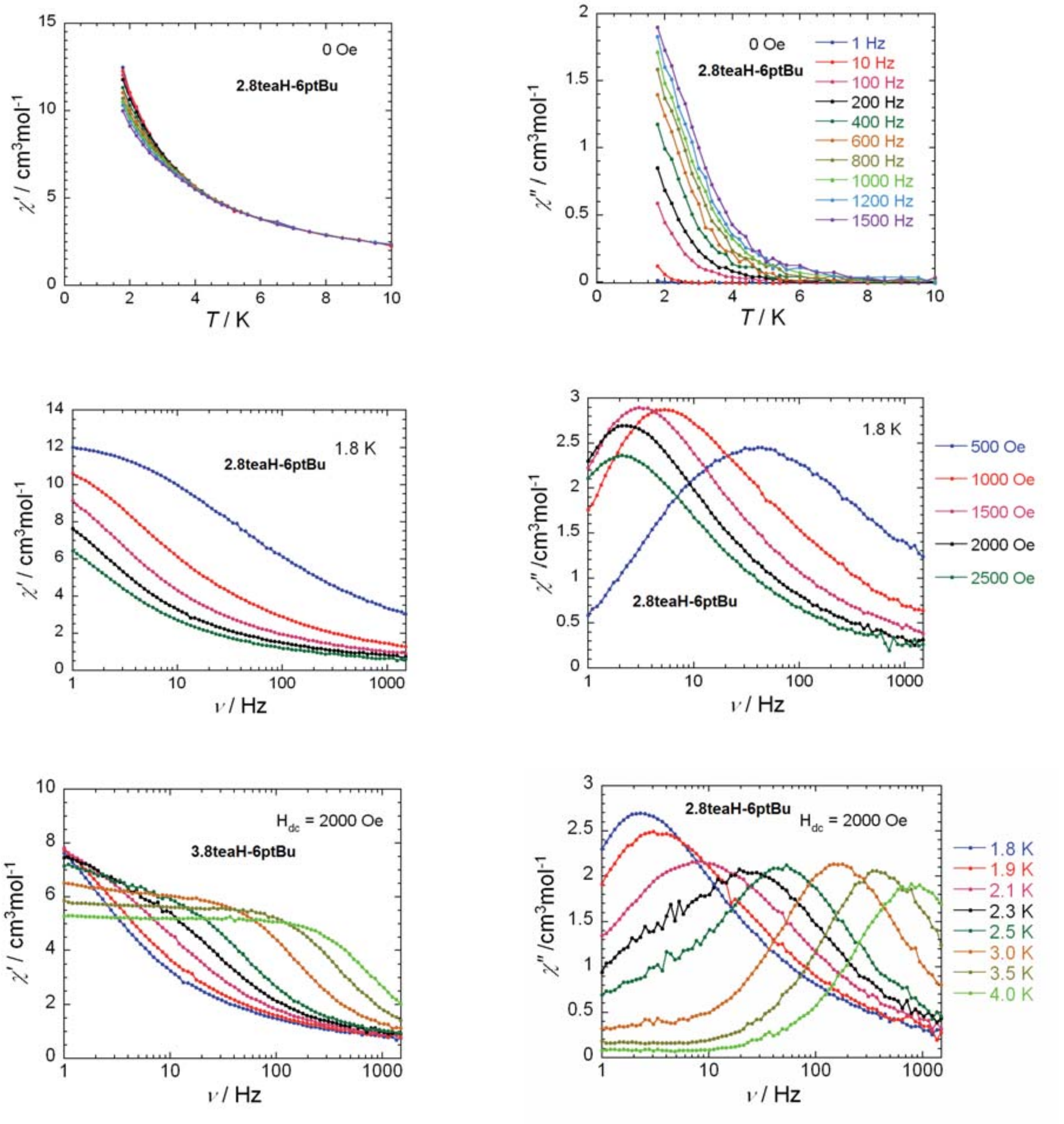

Figure 3. 30. Plots of in-phase and out-of-phase ac susceptibilities signals vs. temperature at indicates oscillation frequencies as well as signals vs. frequency at 1.8 K and under the indicated dc fields for compounds $\mathbf{2.8}^{\textbf{teaH-6pMe}}$ and $\mathbf{2.8}^{\textbf{teaH-6ptBu}}$.

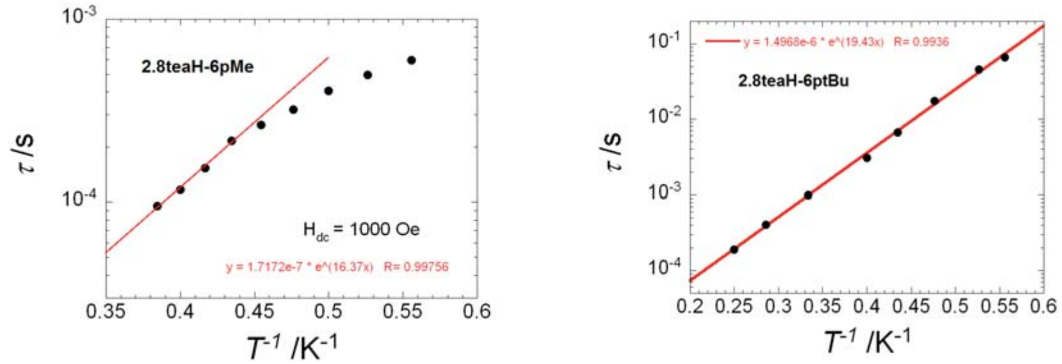

Figure 3. 31. Arrhenius plots for $\mathbf{2.8}^{\textbf{teaH-6}\boldsymbol{p}\textbf{Me}}$ and $\mathbf{2.8}^{\textbf{teaH-6}\boldsymbol{p}\textbf{tBu}}$.

For the Fe_2Dy_2 compound with $\mathbf{2.8}^{\mathbf{teaH\text{-}6}\boldsymbol{p}\mathbf{NO2}}$ a non-zero out-of-phase component was detected (Fig. 2.32) and very strong *ac*-signals observed with maxima at 3.1 K (Fig. 2.33). Furthermore, two different relaxation regimes were observed in applied dc field, one at 500 Oe and another at 2000 Oe. Under zero dc fields, the thermally activated regime is above 2.4 K, and the quantum regime below 2.4 K. With the increase of the external dc field, the thermally activated regime is extended to a lower temperature: 2.1 K with a dc field of 500 Oe. Under a dc field of 2000 Oe, the relaxation process follows a thermally activated behaviour in the whole accessible temperature range down to 1.8 K. From the analysis of the in-phase and out-of-phase ac susceptibilities curves as a function of temperature measured at different oscillation frequencies (as well as signals vs. frequency at 1.8 K) and under different applied dc fields, the parameters of the thermally activated relaxation process were extracted as follows: 0 Oe: $\Delta = 8.1$ K, $\tau = 1.4\ 10^{-5}$ s, 500 Oe: $\Delta = 14.7$ K, $\tau = 4.0\ 10^{-6}$ s and at 2000 Oe: $\Delta = 15.6$ K, $\tau = 1.5\ 10^{-6}$ s (Fig. 2.33, with $\Delta = U_{eff}$ = energy barrier). The relaxation regime at 2000 Oe for $\mathbf{2.8}^{\mathbf{teaH\text{-}6}\boldsymbol{p}\mathbf{NO2}}$ is also observed for $\mathbf{2.8}^{\mathbf{teaH\text{-}6}\boldsymbol{p}\mathbf{tBu}}$ with relaxation time $\tau = \sim 1.5\ 10^{-6}$ s, but with a lower energy barrier.

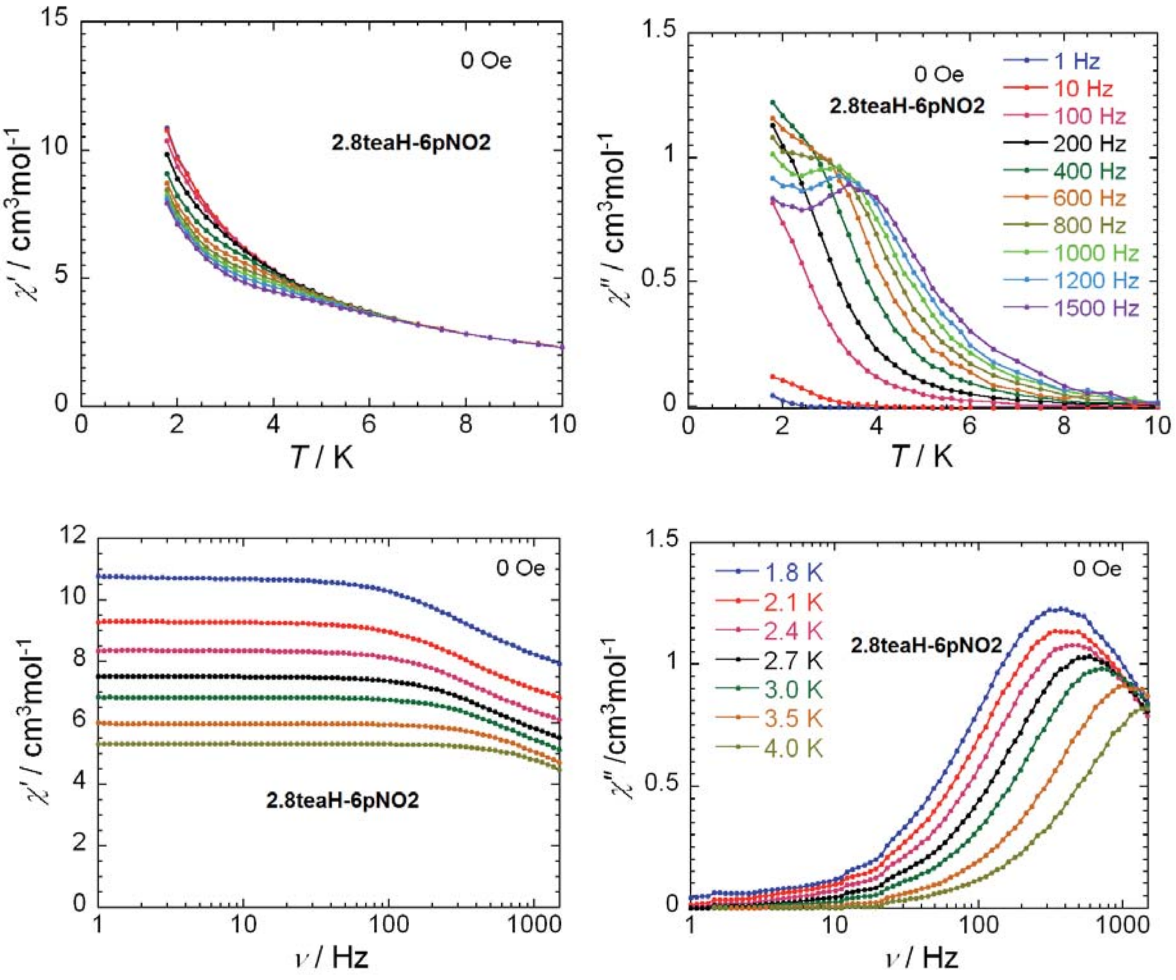

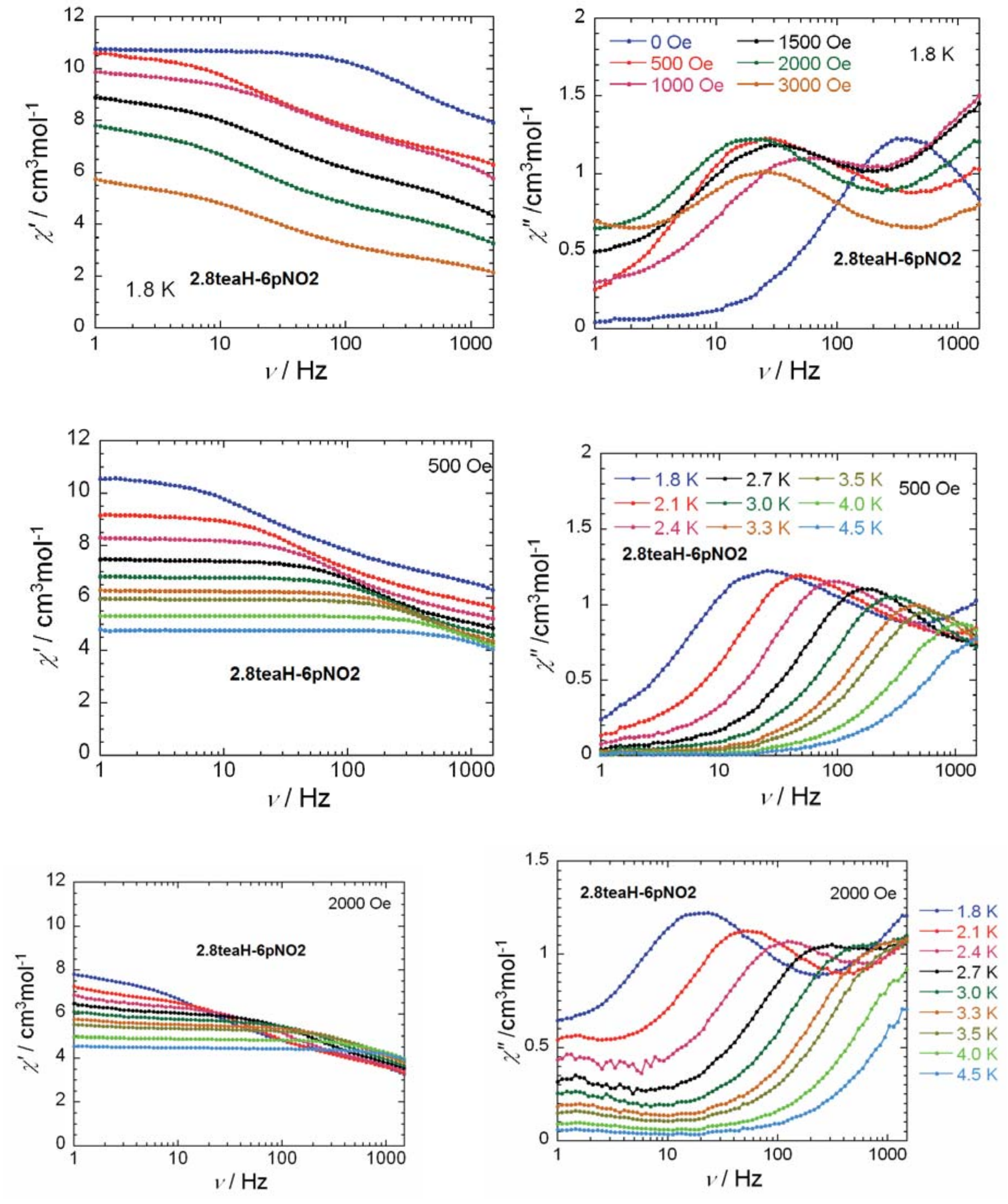

χ' / cm^{3}mol^{-1}
ν / Hz
1.8 K
2.8teaH-6pNO2
χ'' /cm^{3}mol^{-1}
0 Oe
500 Oe
1000 Oe
1500 Oe
2000 Oe
3000 Oe
1.8 K
2.8teaH-6pNO2
500 Oe
2.8teaH-6pNO2
1.8 K
2.1 K
2.4 K
2.7 K
3.0 K
3.3 K
3.5 K
4.0 K
4.5 K
500 Oe
2.8teaH-6pNO2
2000 Oe
2.8teaH-6pNO2
2.8teaH-6pNO2
2000 Oe
1.8 K
2.1 K
2.4 K
2.7 K
3.0 K
3.3 K
3.5 K
4.0 K
4.5 K

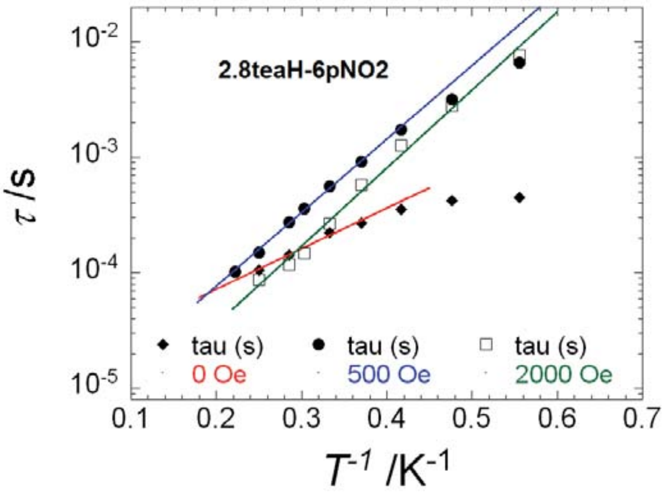

Figure 2.32. Plots of in-phase and out-of-phase ac susceptibilities signals vs. temperature at indicates oscillation frequencies as well as signals vs. frequency at 1.8 K and under the indicated dc fields (O, 500 and 2000 Oe) for compounds **2.8**$^{\mathbf{teaH\text{-}6pNO2.}}$ The lowest are the Arrhenius plots for the three relaxation processes.

The influence of the substituent seems to affect the QT in a remarkable way. In particular, in case of the nitrobenzoate three relaxation processes are observed together with QT processes. Quantum Tunnelling (QT) is a result of mixing the sub-states in a metal ion, which leads to faster relaxation processes. The reference Fe_2Dy_2 compound shows slow relaxation of magnetization (SMM), and additionally QT was observed. Although several well known 3d SMMs show QT (such as the Mn_{12} system), QT actually disturbs the slow relaxation process in a magnet, and it is a phenomenon which is less understood than the relaxation process itself. Removing the QT and at the same time controlling the relaxation process from the lowest –Ms to the highest +Ms (in 3d SMMs, for example) should therefore enhance the SMM behaviour. The Fe_2Dy_2 family could be an excellent study case to understand more about the QT in 3d/4f systems. The influence on the QT (and on magnetic properties in general) through substituent exchange is also evident from the relaxation time constants. The relaxation time of **2.8**$^{\mathbf{teaH\text{-}6}\boldsymbol{p}\mathbf{Me}}$ (~1.172 x10^{-7}s) is the fastest in comparison with all compounds discussed until now; this could explain, at least in part, why no non-zero-field *ac*-signal was observed. The relaxation times for compounds **2.8**$^{\mathbf{teaH\text{-}6}\boldsymbol{p}\mathbf{H}}$, **2.8**$^{\mathbf{teaH\text{-}6}\boldsymbol{pt}\mathbf{Bu}}$ and **2.8**$^{\mathbf{teaH\text{-}6}\boldsymbol{p}\mathbf{NO2}}$ are in a similar time-scale (10^{-6}s) for fields (1500-2000 Oe) where QT is suppressed. It is also remarkable that the energy barrier in case of nitro is lower than for the substituents with positive inductive effect (electron drawing effect).

The cyano group is known in organic chemistry as less strongly electron-withdrawing than nitro, as seen in particular with the inductive effect in alkyl compounds.

The in-phase and out-of-phase ac susceptibilities signals vs. temperature at the indicated oscillation frequencies, as well as signals vs. frequency at 1.8 K and under the indicated dc fields for compounds $\mathbf{2.8}^{\textbf{teaH-6}\boldsymbol{p}\textbf{CN}}$ are shown in Fig. 2.33**.** The lowest Figures in 2.33 show the Arrhenius equation from which the energy barrier and the relaxation time were calculated.

A strong non-zero-field *ac*-signal (SMM) was observed for compound Fe_2Dy_2 $\mathbf{2.8}^{\textbf{teaH-6}\boldsymbol{p}\textbf{CN}}$ with maxima at 2.5 K. In addition, different relaxation regimes were observed under 1000 Oe. The energy barrier was estimated as 8 K at 0 Oe and 13 K at 1000 Oe.

This trend is similar to the behaviour observed for compound $\mathbf{2.8}^{\textbf{teaH-6}\boldsymbol{p}\textbf{NO2}}$. However, interesting differences are obvious, in particular in the QT processes since similar time scales are observed for the relaxation process. More importantly, both compounds lead to lower energy barriers in contrast to the compounds with electron drawing substituents. Furthermore, they show more than one relaxation process and QT windows in contrast to the compounds with electron drawing substituents. Finally, they show stronger *ac* for both in-phase and out-of-phase components.

Further attractive examples, which could be magnetically investigated within the scope of this work were those with azido groups, since $–N_3$ is also an electron withdrawing group, for compounds Fe_2Dy_2 $\mathbf{2.8}^{\textbf{teaH-6}\boldsymbol{p}\textbf{N3}}$, the compounds with meta-substituents $\mathbf{2.8}^{\textbf{teaH-6m}\boldsymbol{p}\textbf{Me}}$ and $\mathbf{2.8}^{\textbf{teaH-6}\boldsymbol{m}\textbf{CN}}$, most compounds with only four carboxylates $\mathbf{2.8}^{\textbf{teaH-4}\boldsymbol{p}\textbf{H}}$ (the reference compound for those with four carboxylates), $\mathbf{2.8}^{\textbf{teaH-4}\boldsymbol{p}\textbf{Ph}}$, $\mathbf{2.8}^{\textbf{teaH-4}\boldsymbol{m}\textbf{Me}}$ and $\mathbf{2.8}^{\textbf{teaH-4}\boldsymbol{m}\textbf{CN}}$, and compound $\mathbf{2.8}^{\textbf{teaH-6(9-anthr)}}$. All the magnetic data for these compounds can be found in Figs. 2.34-2.41 in appendix.

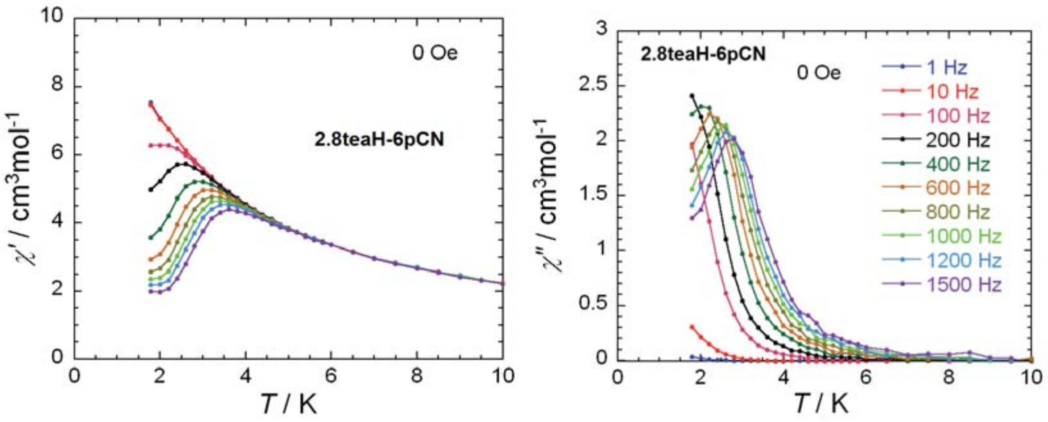

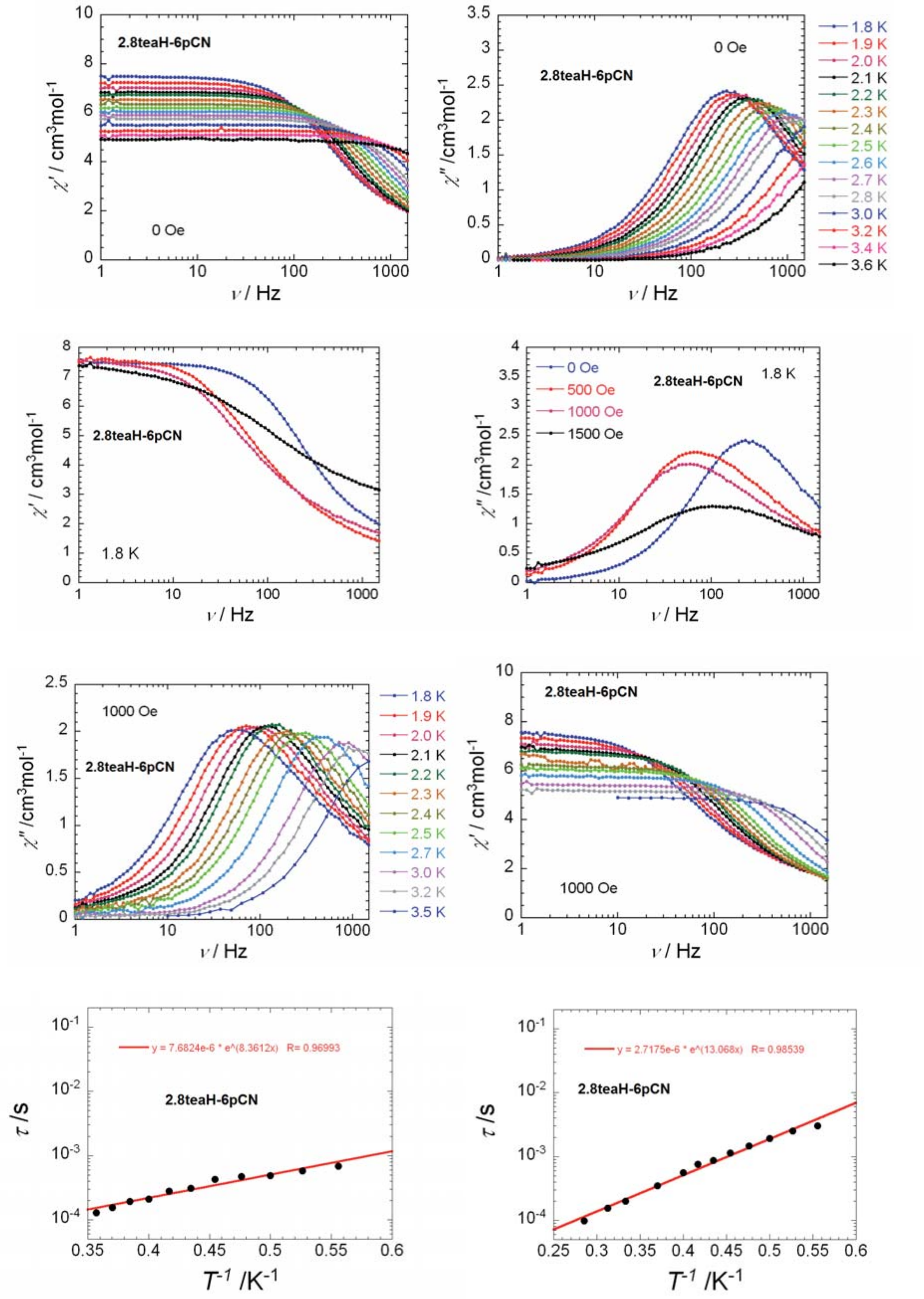

Figure 2.33. Plots of in-phase and out-of-phase ac susceptibilities signals vs. temperature at indicates oscillation frequencies as well as signals vs. frequency at 1.8 K and under the indicated dc fields (O, 500 and 2000 Oe) for compounds **2.8**$^{\textbf{teaH-6}\boldsymbol{p}\textbf{CN.}}$ The lowest are the Arrhenius plots for the two relaxation processes.

The temperature-dependence of the χT products and the magnetization plots of all **Fe_2Dy_2** compounds (the first two figures left and right in Figs 2.34-2.41 in appendix) are very similar to the reference compound and are indicative of antiferromagnetic interaction between the magnetic centres of these molecules.

However, the ac-magnetism for all these compounds is different in comparison both with the reference compound and with each other (the significant values and behaviour of all Fe_2Dy_2 compounds discussed in this chapter are summarized in Tab. 2.22).

An ac-signal was observed for **2.8**$^{\text{teaH-6}p\text{N3}}$ compound but without maxima in contrast to cyano and nitro compounds (Fig. 2.34, appendix). The in-phase signal is however strong in comparison with the out-of-phase signal and the QT is suppressed at 2000 Oe for a wide range of frequencies which indicates that, even in absence of maxima in the *ac*-signal (for out-of-phase), slow relaxation of magnetization is detected in the time scale of the reference compound and that the energy barrier might be even higher. Indeed, the analysis of the in-phase and out-of-phase signals vs. different T and frequencies (υ) and with help of Arrhenius equation, the time scale could be determined as 1.9 x 10^{-6} s and the energy barrier was 18.3 K (Fig. 2.34, lowest).

The azido group also did not lead to a lower energy barrier and at same time to maxima as observed for the compounds with nitro and cyano but still lower than for the compounds with methyl and tertbutyl substituents.

Comparison with Meta-Examples

In contrast to the Fe_2Dy_2 compound with six *para*-methylbenzoate (*para*-tolyate) **2.8**$^{\text{teaH-6}p\text{Me}}$ a zero-field *ac*-signal was observed for Fe_2Dy_2 compound with six *meta*-methylbenzoate **2.8**$^{\text{teaH-6}m\text{Me.}}$ In addition, the ac-signal observed has no maxima in the out-of-phase component. The plots of in-phase and out-of-phase vs. different T and υ indicate QT suppression at higher H_{dc} (1500 Oe) than **2.8**$^{\text{teaH-6}p\text{Me}}$ (1000 Oe). One relaxation process also appears which indicates that the QT is strongly suppressed in this regime and that the slow relaxation of magnetization is more evident than in case of **2.8**$^{\text{teaH-6}p\text{Me}}$. Nevertheless, the relaxation time in both cases is faster than all other examples (10^{-7} s) (Fig. 2.35, appendix).

On the other side, the Fe_2Dy_2 compound with six *meta*-benzoate ligands **2.8**$^{\text{teaH-6}m\text{CN}}$ (Fig. 2.36, appendix) shows remarkable and very interesting differences to the Fe_2Dy_2 compound with six para-cyanobenzoate ligands **2.8**$^{\text{teaH-6}p\text{CN}}$ and to all other compounds. While, the *meta*-

methyl compound shows *ac*-signals in contrast to the *para*-methyl compound, the *meta*-cyano compound does show *ac*-signals as in the case of *para*-cyano but without maxima. Furthermore, the *meta*-cyano compound has two QT (at 1000 Oe and 2000 Oe) regimes and these are well separated (see Fig. 2.36, in-phase vs. indicates frequencies). Such QT regimes were not seen for any of the other compounds. These two QT regimes as well as two relaxation processes are "cleanly" separated because of the two relaxation time scales (10^{-6} s and 10^{-5} s). The latter, is indeed the slowest in comparison with the other compounds, and may indicate that the slow relaxation of magnetization in this compound is much less perturbed than in case of *para*-cyano Fe_2Dy_2 compound. At the same time the effective energy barriers are more separated than in the case of *para*-cyano with 22.84 K and 6.3 K (Fig. 2.36, Arrhenius plots). This example shows also the lowest observed energy barrier and at the same time for the first relaxation process a higher one in comparison with the reference compound. This compound can be indeed described as a "hard" Single Molecule Magnet.

The "small" movement of the methyl and cyano groups from *para* to *meta*-positions yield also significant and important differences, strengthening the assumption that substituent exchange is indeed influencing the magnetic anisotropy. The fact that QT is always connected with significant changes in the relaxation process (energy barrier and time) indicates that, the 16 m_J ($2J_{Dy}$+ 1) states are involved in a complicated way in the mixing and in the resulting tunnelling processes; tunnelling may also occur between different m_J's for different substituents. The SQUID method is an average method and thus cannot always help in finding a clear explanation for such behaviour. A method with faster life time is needed, a more sensitive technique, a technique with time scale closet to the time scale of the slow relaxation time scale, such as the Mössbauer method. Indeed, a Mössbauer study was performed for most of the compounds presented in this work (see Mössbauer section).

In order to support the assumption that the substituent change is influencing directly the magnetic anisotropy of Dy^{III}, Fe_2Dy_2 compounds were prepared which contain only four carboxylates and two nitrates chelating the Dy^{III} centres. These examples demonstrate that whilst the Fe^{III}_2 unit is antiferromagnetically coupled, weak ferromagnetic Fe-Dy interactions are expected in all cases as seen in the reference compound.[20b)] In other words, the spin density for the Fe_2 unit is expected to be zero but not for the Dy^{III} centres, which means that a strong change could be observed by removing the two chelating benzoates and replacing them by more "innocent" ligands such as nitrates.

For the Fe_2Dy_2 compound $\mathbf{2.8}^{\mathbf{teaH\text{-}4}\boldsymbol{m}\mathbf{CN}}$ and the reference $\mathbf{2.8}^{\mathbf{teaH\text{-}4}\boldsymbol{p}\mathbf{H}}$ a non-zero out-of-phase component was not detected. (Fig. 2.37 in appendix).

However, a “non-localized” QTM can usually be suppressed by applying a small dc field, which removes the degeneracy of corresponding energy levels on the positive and negative spin sides of the barrier, often greatly reducing the probability of such tunnelling processes (see section 1.2). In this way useful information on the dynamics of the magnetization in the thermally activated regime can be extracted. Therefore, ac measurements at several applied static fields (0, 0.5, 1.0, 1.5, 2.0 kOe) (Fig.2.37) were recorded. The relaxation time is too fast (10^{-5} s scale), now in the range of Fe_2Dy_2 compounds with *methyl*-substituents. The energy barrier obtained from the Arrhenius plot is 9.25 K. However, this is a “soft” SMM behaviour in comparison with the *para* one where ac with maxima at 0 Oe can be detected.

The difference to the compounds $\mathbf{2.8}^{\mathbf{teaH\text{-}6}\boldsymbol{p}\mathbf{CN}}$ and $\mathbf{2.8}^{\mathbf{teaH\text{-}6}\boldsymbol{m}\mathbf{CN}}$ is remarkable and indicates that the absence of the two carboxylates chelating the Dy^{III} centres has an important effect on the magnetic properties. A possible explanation is that the absence of the two carboxylates changes the electron density around the *f*-orbitals of the Dy^{III} ions and thus the anisotropy tensor is moved which can lead to faster relaxation of magnetization (see Mössbauer and theoretical sections). At this stage, two further examples are necessary; one like the reference compound but with only four benzoates and one with only four *meta*-methylbenzoate ligands.

In addition, the magnetism of the compound with only four phenylbenzoate ligands was studied, and here no *ac*-signal was observed as in case of the reference compound $\mathbf{2.8}^{\mathbf{teaH\text{-}4}\boldsymbol{p}\mathbf{H}}$ and also $\mathbf{2.8}^{\mathbf{teaH\text{-}4}\boldsymbol{p}\mathbf{CN}}$.

The Fe_2Dy_2 compound with 9-antharcenecarboxylate (six ligands) shows ac signals without maxima and QT suppression at 1500 Oe, while its energy barrier is about 16.3 K (Fig. 2.41, chapter 6, appendix). Actually, the behaviour of this compound is the same as for the reference compound. Whether the π- π stacking in the structure has suppressed the relaxation process as known in SMM chemistry [69], is an open question. In order to understand this further, the magnetic data for the 2-naphthoate example could help and further examples are probably required to explore this further. The magnetic data of the 2-naphthoate examples are not presented here and still need to be analyzed. Furthermore, the non-aromatic example should be a very important example to clarify this point. From the behaviours observed until now, however, it can be inferred that substituents with strong withdrawing effects, which actually decrease the electron density in the aromatic rings, lead to "harder" SMM behaviour in comparison with those which increase it.

Summary

Table. 2.22. Summary of the most important magnetic data/behaviour of the discussed Fe_2Dy_2 compounds.

Compounds	**Magnetic properties***
$2.8^{\text{teaH-6}p\text{H}}$	**AF, ac signal without maxima, QT at 1500 Oe, U_{eff}=16.2 K**
$2.8^{\text{teaH-6}p\text{Me}}$	**Ferri-, no ac, QT at 1000 Oe, U_{eff} =24.0 K**
$2.8^{\text{teaH-6}pt\text{Bu}}$	**AF, ac signal without maxima, QT at 2000 Oe, U_{eff}=19.4 K**
$2.8^{\text{teaH-6}p\text{NO2}}$	**AF, ac with maxima at 3.1 K, energy barrier of 8.1 K, QT at 500 (14.7 K), 2000 Oe (15.6 K)**
$2.8^{\text{teaH-6}p\text{CN}}$	**AF, ac with maxima 2.5 K, QT under 1000 Oe, 8 K (0 Oe), 13 K (1000 Oe)**
$2.8^{\text{teaH-6}p\text{N3}}$	**AF, ac, no maxima, QT=2000 Oe, U_{eff} =18.3 K**
$2.8^{\text{teaH-6(9-anthr)}}$	**AF, ac, no maxima, QT=1500 Oe, U_{eff} =16.3 K**
$2.8^{\text{teaH-6}m\text{CN}}$	**AF, ac, no maxima, QT=1000 & 2000 Oe**

$\mathbf{2.8}^{\mathrm{teaH\text{-}4}p\mathrm{H}}$	**AF, No ac**
$\mathbf{2.8}^{\mathrm{teaH\text{-}4}m\mathrm{CN}}$	**AF, No ac**
$\mathbf{2.8}^{\mathrm{teaH\text{-}4}p\mathrm{Ph}}$	**AF, No ac**

- AF: antiferromagnetic, QT: quantum tunneling, Oe: Oestred, U_{eff}: effective energy barrier, ac: ac-signal.

The magnetic behaviour of some new "test-bed" system candidates will be discussed here briefly, and might support our results of the Fe_2Ln_2 family. Furthermore, new magnetic properties which can help in understanding SMM behaviour will be studied further. The compounds **2.17-2.19** and **2.26** will be briefly discussed here.

Since compound **2.22** contains two Fe_2Dy_2 units (one cationic and one anionic), it is not a useful system for a systematic study because its magnetic interpretation will be harder. In addition, the compound is antiferromagnetic and does not show ac signal, therefore it will not be discussed further.

The series of $[FeLn_2]_x[Fe_2Ln_2]_y$ *compounds* ***(2.17-2.19)***

An interesting new "test-bed" system would be the series of compounds **2.17-2.19.** In addition to their interesting composition (trinuclear and tetranuclear), the trinuclear composition is in higher percentage. The tetranuclear component has the same structure as compound $\mathbf{2.8}^{\mathrm{teaH\text{-}4}p\mathrm{H}}$. The study of the Fe_2Dy_2 family might make it easier to understand this system, and the "dilution" of the AF coupling through the higher presence of the trinuclear species might be an interesting feature as well. In addition, SMM behaviour is still present in the Dy analogue (Fig. 2.42). The change of composition also seems to influence the susceptibility as expected.

The susceptibility curve, the magnetization as well as the reduced magnetization plots confirm the ferromagnetic coupling expected from two Gd^{III} ions (in trinuclear component) and ferromagnetic coupling of Fe···Gd (in the tetranculear component as observed in the reference Fe_2Gd_2 compound, see also Mössbauer and EPR sections) for compound **2.17** show dominant ferromagnetic behaviour (Fig. 2.43).

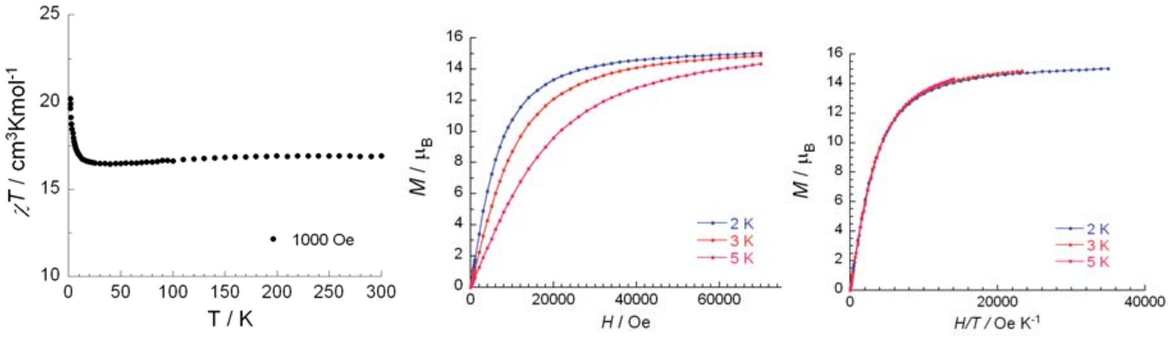

Figure 2.42. The χT versus T plot, the magnetization and the reduced magnetization for the gadolinium compound **2.17**.

The Dy compound **2.18** shows ferromagnetic behaviour (mainly arising from the tetranuclear component) at low temperatures. A weak ac-signal is observed but no QTM. This system is clearly different from the reference compound **2.8**$^{\mathbf{teaH\text{-}6}\boldsymbol{p}\mathbf{H}}$. In addition both Gd and Dy compounds **2.17** and **2.18** compounds are ferromagnetic which inidicates that indeed the trinuclear component is dominant, consistently with the structural studies.

We expect from the Y compound **2.19** an antiferromagnetic behaviour not only because of the absence of the ferromagnetic coupling between Fe and Gd or Dy, but also because of the increase of the tetranuclear component. In case of the Y compound **2.19** indeed antiferromagnetic behaviour is present (Fig. 2.44). However, the curve is not as expected for a paramagnetic centre since the antiferromagnetic interaction is very strong and since the SQUID technique is an average method and cannot differentiate between two species in one sample.

In the EPR and Mössabuer measurements for the Y compound the presence of the two units becomes more clear since both these methods are more sensitive to impurities/dopants than the magnetic bulk susceptibility method. The magnetic data of these compounds are summarized in Tab. 2.23.

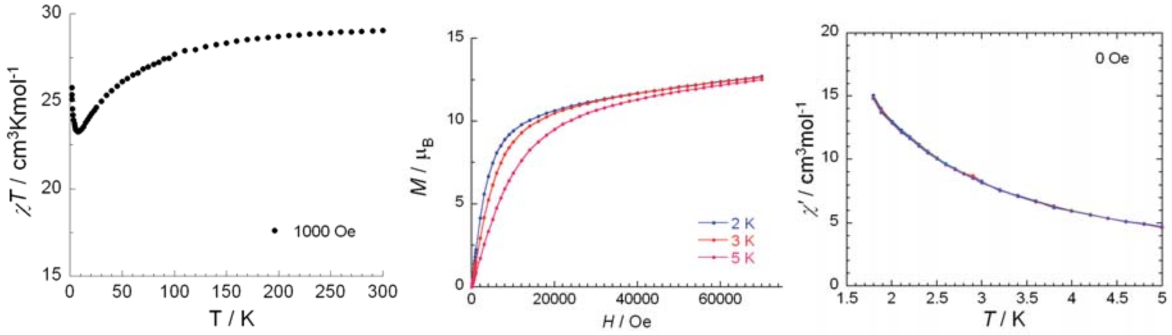

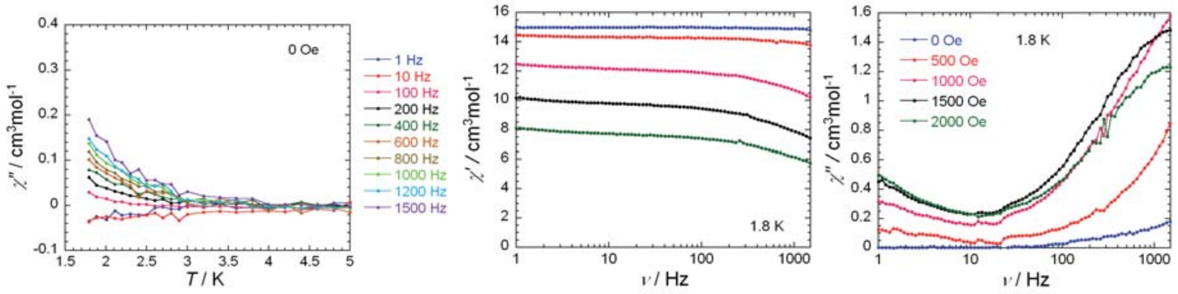

Figure 2.43. The χT versus T plot, the magnetization and in-phase and out-of-phase vs. indicated T and υ for compound **2.18**.

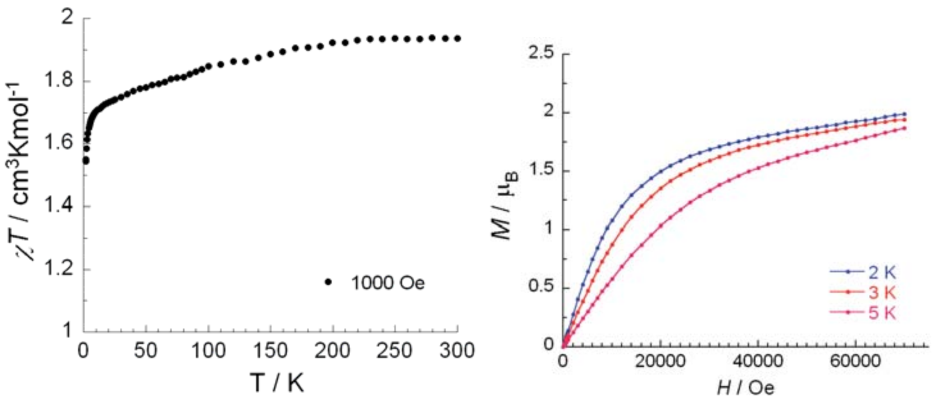

Figure 2.44. The χT versus T plot and the magnetization for **2.19**.

Table 2.23. Summary of the magnetic data for compounds **2.17-2.19.**

Compounds	χT at 300 K (cm^{3}K/mol)	χT at 1.8 K (cm^{3}K/mol)	M at 1.8 K, 70 kOe (μB)	Dominant interactions	ac out-of-phase signal
2.17	16.91	20.21	15.0	ferromagnetic	No
2.18	29.05	25.78	12.7	Ferromagnetic plus orbital contribution from Dy ions	yes, weak ac, no obvious QT
2.19	1.94	1.54	2.0	antiferromagnetic	No

Fe$_6$Dy$_2$ compound

Simple calculations using the equ's. 1.5 and 1.6 (from chapter 1) suggest that the central Fe^{III} ions might be weaker antieferromagnetic coupeld to may be even ferromagnetically coupled since the angle is smaller than 98°. However, using these equations suggests further that the other Fe^{III} ions are very strong antiefrromagnetically coupled. Antiferromagnetic (AF) interactions are present above 10 K (Fig. 2.45 (Upper, left). The dominant AF interactions might be present within the central 'butterfly' unit of Fe^{III} ions in octahedral environment even The magnetic behavior then becomes ferromagnetic below 10 K, which we attribute to a ferromagnetic interaction between the outer Fe$^{III}\cdots$Dy^{III} pairs. Noteworthy, is the sharp decreasing of χT vs. T in the region between 10 K and 3K. The curve does show a remarkable form which does not correspond to what is usually expected for ferromagnetic behavior; it has a minimum at ~ 6K and a maximum at 3.4 K. A sharp decrease is further detected at 3 K. Such magnetic behaviour was investigated by spin-Hamiltonian calculations (see the theoretical section). Additionally, Fe/Dy compounds containing Fe^{III} in a square pyramidal geometry are indeed very rare. This example could also help in understanding the interaction between Fe^{III} ion (square pyramidal) and Dy^{III}. The magnetization might correspond to a diamagnetic Fe$_4$-butterfly and ferromagnetic interaction between the square-pyramidal Fe^{III} and the Dy^{III} ions. It is, however, challenging to understand this system without having the Y analogue. No out of phase signal was observed and by applying small *dc* field no shifting for the signal was possible, indicating that no QTM and also no slow relaxation of magnetization are observable (Fig. 2.45, middle and lower).

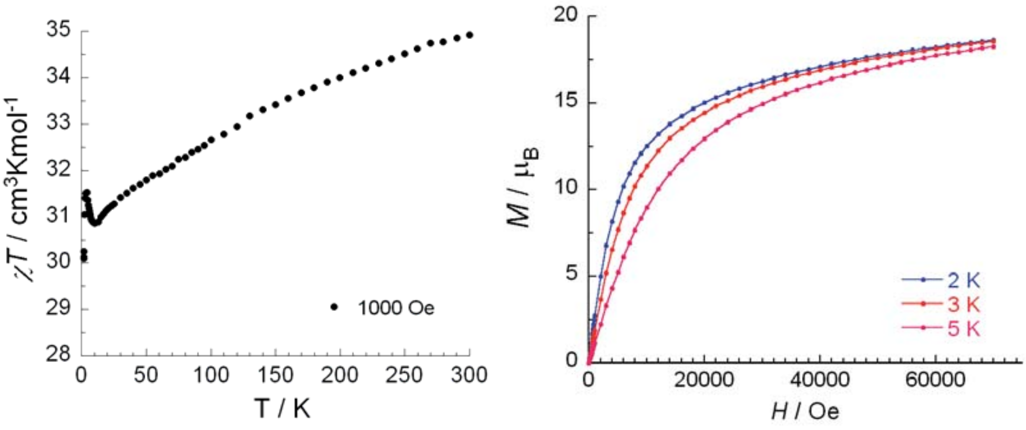

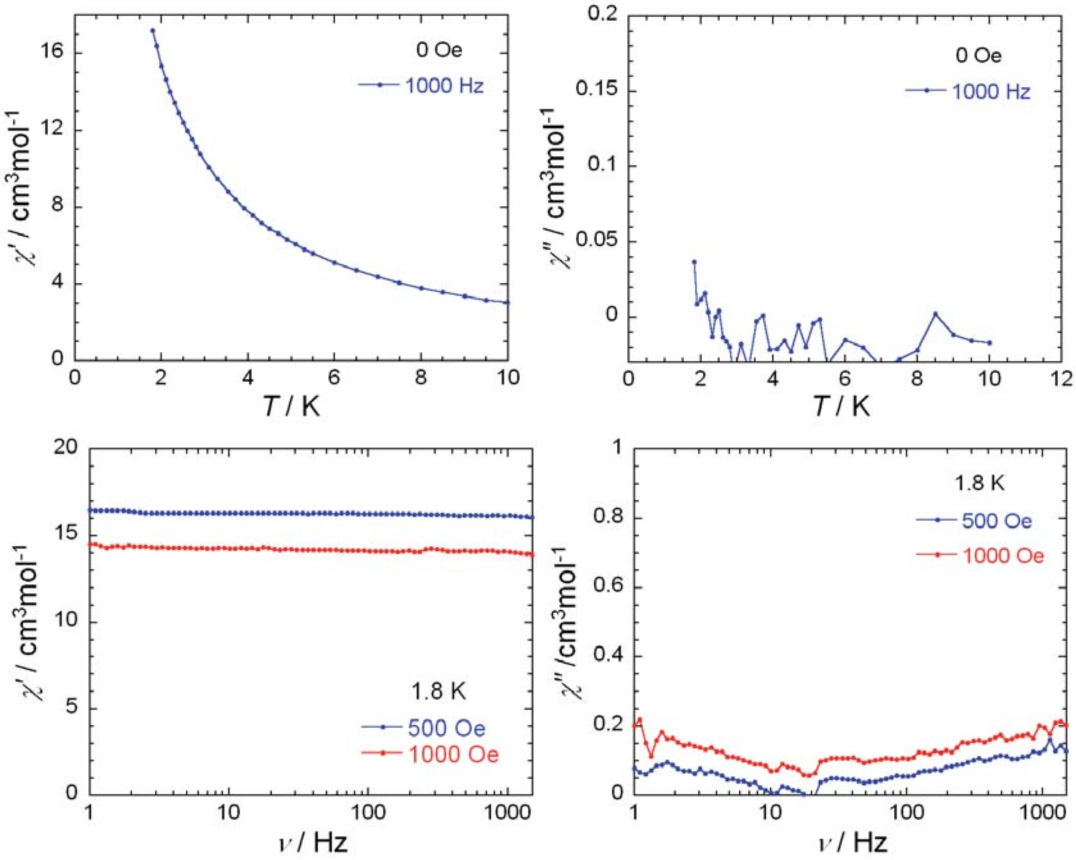

Figure 2.45. (Upper) The χT vs. T (left) and magnetization (right) plots for **2.26**. (Middle) The plots of in-phase (left) and out-pf-phase vs. indicated temperatures (right) for 2.26. (Lower) The in-phase (left) and out-of-phase (right) vs. indicated frequencies and at 1.8 K.

2.3 Mössbauer Spectroscopy Study

The Reference Series

The Mössbauer study of the "reference" series of compounds will be discussed first, followed by the other compounds from the Fe_2Dy_2 family. From the reference series, we focused on the compounds **2.13** (with diamagnetic Y), **2.6** (with isotropic Gd), **2.7, 2.8** and **2.9** (with anisotropic lanthanides).

At temperatures higher than 3 K the Mössbauer measurements for all five (Fe_2Y_2 (**2.13**), Fe_2Gd_2 (**2.6**), Fe_2Tb_2 (**2.7**), Fe_2Dy_2 (**2.8**) and Fe_2Ho_2 (**2.9**)) clusters yielded equivalent spectra (Fig. 2.46, Tab.2.24).

The doublets observed, are characterized by similar values of quadrupole splitting (ΔE_Q), which implies that two Fe sites with similar coordination spheres are present, in agreement with the molecular structure (Fig. 2.6). At 3K the Mössbauer spectra (MS) of Fe_2Y_2, Fe_2Gd_2, Fe_2Tb_2 and Fe_2Ho_2 still have paramagnetic spectra (or, more clearly, they are non-magnetic;

Fig. 2.46) as seen for other reported compounds containing the $[Fe_2(O)_2]^{2+}$ core.[70,71] This confirms the presence of a diamagnetic ground state, S = 0, for Fe_2Y_2 in agreement with the magnetic susceptibility measurements.

Table 2.24. Summary of Mössbauer parameters for compounds **2.6-2.9** and **2.13**.

Compound	T, K	δ[a], mm/s	ΔE_Q or ε, mm/s	Γ, mm/s	B_{eff}, T
Fe_2Y_2	50	0.499(1)	0.999(1)	0.418(1)	-
	3	0.497(1)	0.982(2)	0.382(4)	-
Fe_2Gd_2	77	0.492(2)	0.919(2)	0.467(4)	-
	3	0.501(1)	0.911(2)	0.412(3)	-
Fe_2Dy_2	25	0.502(1)	0.947(6)	0.583(7)	-
	3	0.497(2) [b] 0.497(2) [b]	0.938(4) 0.014(1)	0.607(7) 0.58(2)	- 11.94
Fe_2Tb_2	3	0.500(1)	0.922(2)	0.362(3)	-
Fe_2Ho_2	3	0.482(1)	0.96(2)	0.384(3)	-

[a] Relative to α-Fe at room temperature. The statistical errors are given in parentheses. [b] Constrained to the same value for both spectra.

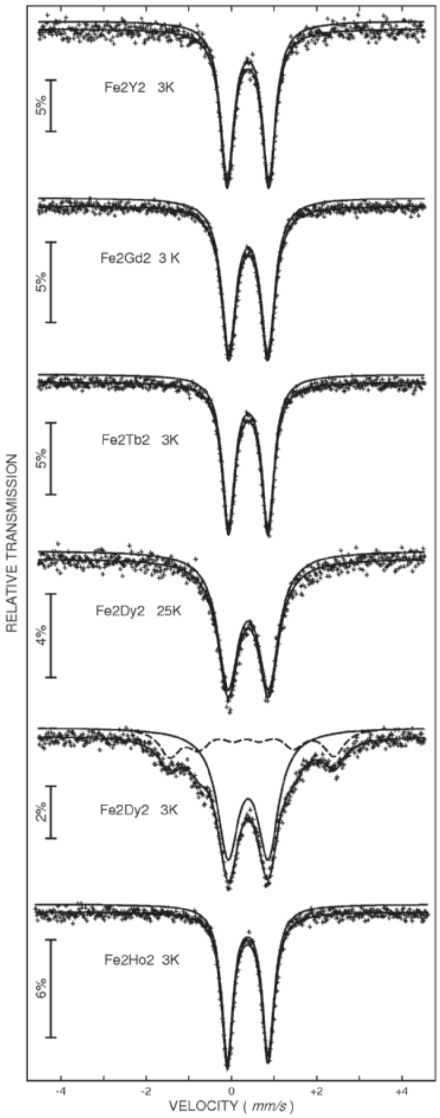

Figure 2.46. The ^{57}Fe Mössbauer spectra for compounds Fe_2Y_2 (**2.13**), Fe_2Gd_2 (**2.6**), Fe_2Tb_2 (**2.7**), and Fe_2Ho_2 (**2.9**) at 3K, as well as, for Fe_2Dy_2 (**2.8**) at 3K and 25K.

The isomer shift (δ) of 0.49-0.50 mm/s and quadrupole splitting ΔE_Q of 0.91-0.99 mm/s are of the expected magnitude for high-spin Fe^{III}. In contrast to Fe_2Y_2, Fe_2Gd_2, Fe_2Tb_2 and Fe_2Ho_2 the 3K MS for Fe_2Dy_2 exhibits relaxation at intermediate rate in the absence of an applied field (Fig. 2.46, bottom). It is significantly broadened, with wings that extend from about –1.5 to + 2.5 mm/s. The broadening of the MS indicates that the relaxation time is of (or covered by) the magnitude of the Mössbauer time scale. The final result is an overlapping of a doublet and a six-line pattern with the effective hyperfine field of 11.9 T at the iron nuclei. Applying an external magnetic field of 4 – 5 T, the magnetic inset vanish with the increasing field and the Mössbauer spectra at high fields exhibit patterns typical of a diamagnetic complex. This remarkable observation is difficult to explain at this stage of the study. At 4 or 5 T, the spectra of Fe_2Dy_2 (**2.8**), Fe_2Tb_2 (**2.7**) and Fe_2Ho_2 (**2.9**) derivatives are similar and the very close values of simulation parameters obtained show that experimental data fit very well the $H_{eff} = H_{appl}$ condition (Fig. 2.47).

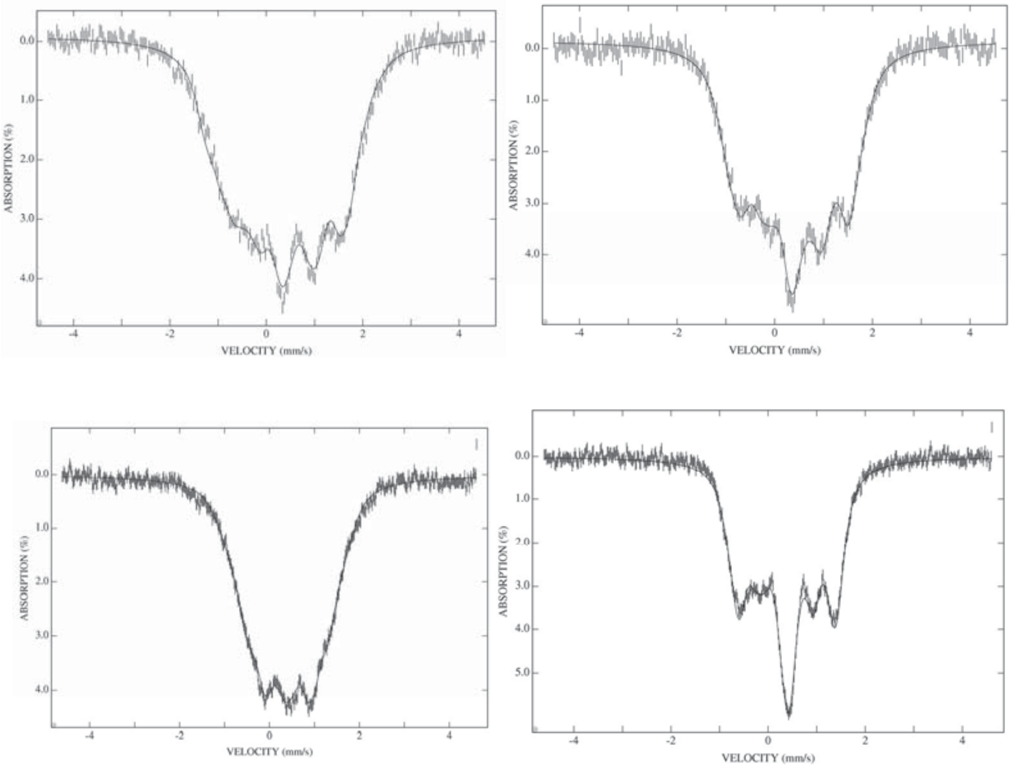

Figure 2.47. The ^{57}Fe Mössbauer spectra for Fe_2Dy_2 (top, left) and Fe_2Tb_2 (top, right) at 3K, applied field of 5 T and Fe_2Gd_2 (bottom, left) and Fe_2Ho_2 (bottom, right) at 3K, applied field of 4 T. The solid lines are the spectral simulations for $\Delta E_Q = 0.94$ mm/s, $\delta = 0.49$ mm/s, $H_{eff} = 5.0$ T and $\eta = 1.0$ for Fe_2Dy_2, $\Delta E_Q = 0.92$ mm/s, $\delta = 0.50$ mm/s, $H_{eff} = 5.0$ T and $\eta = 0.9$ for Fe_2Tb_2, $\Delta E_Q = 0.91$ mm/s, $\delta = 0.50$ mm/s, $H_{eff} = 3.3$ T and $\eta = 0.7$ for Fe_2Gd_2, and $\Delta E_Q = 0.96$ mm/s, $\delta = 0.48$ mm/s, $H_{eff} = 4.0$ T and $\eta = 1.0$ for Fe_2Ho_2, assuming an isolated ground state with $S = 0$.

This implies that in all three compounds there is no contribution from the magnetic hyperfine interaction other than the applied field and the central $Fe_2(OH)_2$ unit is antiferromagnetically coupled. But why does the magnetic inset vanish under external field, and why is the magnetic inset missing in case of Fe_2Tb_2 or Fe_2Ho_2 compounds with anisotropic Ln’s (as in case of Dy)? The answer to these questions might become clearer after studying the other $\{Fe_2Dy_2\}$ compounds with different substituents on the benzoate ligands. What can be said at this stage is that the ground-state anisotropy depends on the crystal field acting on the orbital moment. Probably, the type of crystal field around lanthanide ions (see magnetic properties of Ln^{III}, section 1.2) in this series of compounds leads to an anisotropic ground state for Dy ion, but which is not appropriate for Tb or Ho ions. Although Tb and Ho ions are also strongly anisotropic, being non-Kramers ions the bi-stable ground state requires that a more exact axial symmetry be preserved, which is not the case in present series of compounds. A peculiar behavior was observed in case of Fe_2Gd_2 in applied magnetic field of 4T.

Although in the case of compounds **2.8, 2.7, 2.9**, Fe_2Dy_2, Fe_2Tb_2 and Fe_2Ho_2, under applied field the resulting H_{eff} is equal to applied field, for Fe_2Gd_2 the H_{eff} is ~19 % smaller than H_{appl}. This may be due to weak ferromagnetic interaction between Fe and Gd that leads to an induced magnetic field on the iron nucleus that is opposite to the external 4 T applied field. Therefore, the effective magnetic field experienced by the iron nuclei is 4 T in the diamagnetic ground state but lower when a ferromagnetic communication is mixed in.

The Mössbauer spectra of polycrystalline samples of compounds **2.8**$^{\mathbf{teaH\text{-}6}\boldsymbol{p}\mathbf{H}}$, **2.8**$^{\mathbf{teaH\text{-}6}\boldsymbol{p}\mathbf{Me}}$, **2.8**$^{\mathbf{teaH\text{-}6}\boldsymbol{pt}\mathbf{Bu}}$, **2.8**$^{\mathbf{teaH\text{-}6}\boldsymbol{p}\mathbf{NO2}}$ and **2.8**$^{\mathbf{teaH\text{-}6}\boldsymbol{p}\mathbf{CN}}$ at 3 K are typical of the crossover from intermediate to slow relaxation with magnetic hyperfine lines developing below 5 K superimposed on a broad absorption doublet at the centre of the spectrum (Fig. 2.48) with ΔE_Q = 0.95 - 1.06 mm/s, δ = 0.46 - 0.48 mm/s (relative to Fe metal at 298 K). The parameters for the central doublet are very similar to those obtained for spectra at higher temperatures, 25 or 50 K (Fig. 2.49) and to those observed for the antiferromagnetically coupled Fe^{III}_2 sites of iron-oxo proteins and relevant model compounds.[72] Along the series we observe that the hyperfine field determined from the magnetic inset is not constant, but varies from compound to compound from 5.9 to 19.9 T (Fig. 2.48, see also Modell). As already discussed (section 2.1) the bond lengths and angles around the iron and dysprosium ions have very similar values for all compounds (Tab. 2.20). Moreover, the polyhedral environments of the dysprosium ions, which play an important role in controlling the direction of the magnetic anisotropy, are similar for all compounds.

Mössbauer spectroscopy senses in these compounds also the hyperfine interactions present at the nucleus of the Mössbauer isotope. The internal hyperfine field H_{int} is determined by four contributions: H_{fc} (Fermi contact), H_{ls} (orbital moment), H_{dd} (dipole field) and H_{latt} (lattice). In the case of **2.8**$^{\mathbf{teaH\text{-}6}\boldsymbol{p}\mathbf{H}}$ (**2.8**), **2.8**$^{\mathbf{teaH\text{-}6}\boldsymbol{p}\mathbf{Me}}$, **2.8**$^{\mathbf{teaH\text{-}6}\boldsymbol{pt}\mathbf{Bu}}$, **2.8**$^{\mathbf{teaH\text{-}6}\boldsymbol{p}\mathbf{NO2}}$, **2.8**$^{\mathbf{teaH\text{-}6}\boldsymbol{p}\mathbf{CN}}$ the first three contributions are zero because of zero electronic spin density on the nuclei. H_{latt} is very small even in paramagnetic systems. Therefore, the only contribution to the internal hyperfine field at iron nuclei in these compounds results from the magnetic interaction with the anisotropic Dy^{III} ions. Since the exchange interaction between Dy^{III} and Fe^{III} is expected to be negligible due to the fact that the 4f electrons of dysprosium ions are well shielded by their 5s and 5p electrons, any observed interaction is essentially magnetic dipolar in nature or else due to polarization of Fe^{III} electronic clouds by the magnetic Dy ions.[73]

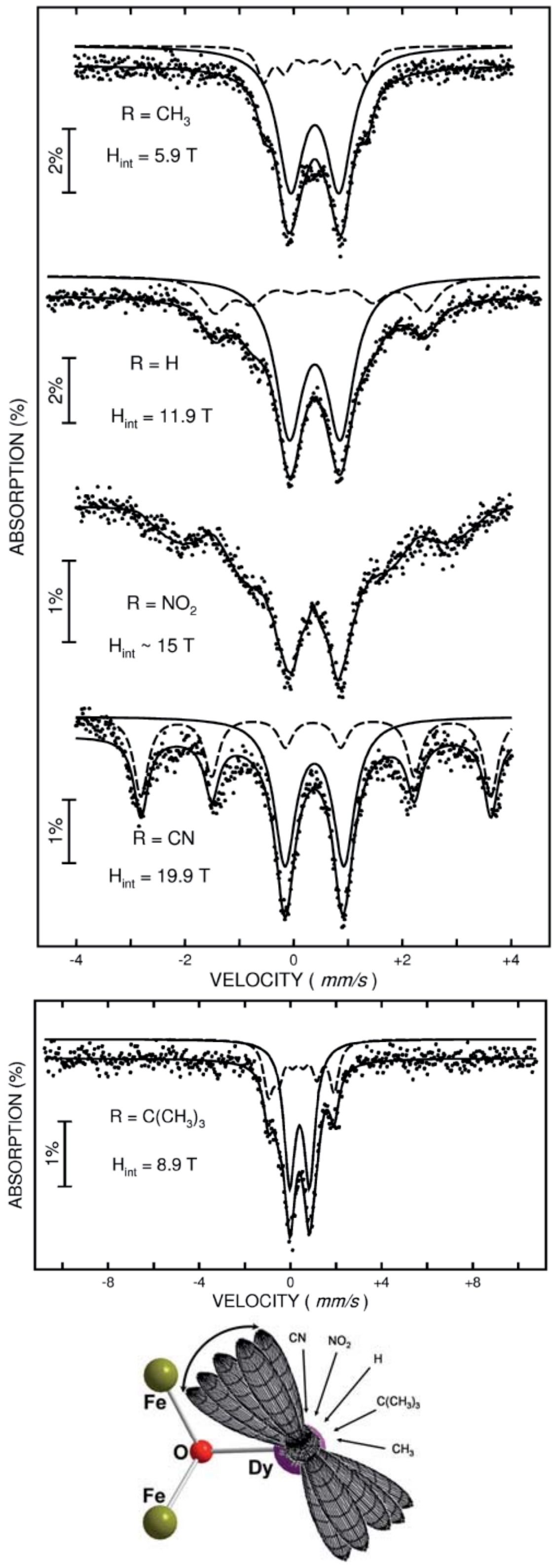

Figure 2.48. (Upper) ^{57}Fe Mössbauer spectra of $2.8^{\text{teaH-6}p\text{H}}$, (R = H), $2.8^{\text{teaH-6pMe}}$, (R = CH$_3$), $2.8^{\text{teaH-6}pt\text{Bu}}$, (R = C(CH$_3$)$_3$), $2.8^{\text{teaH-6}p\text{NO2}}$, (R = NO$_2$) and $2.8^{\text{teaH-6}p\text{CN}}$, (R = CN) in zero-applied field at 3.0 K. On left-hand side of every spectrum, the values for the internal hyperfine field H_{int} determined from the sextets are given. The MS of $2.8^{\text{teaH-6}pt\text{Bu}}$ is splitted because at different velocity. (Lower, modell) possible arrangements of the local magnetic moments (anisotropic axes) on Dy ions relative to the Fe$_2$ unit. [20b]

One possible explanation is that the orientations of the easy axes of magnetization (or magnetic flux density) of dysprosium ions is different in the different compounds presented here. If we imagine that every Dy ion corresponds to a dipole, the orientation of this will be dictated by the local crystal field and ground state of Dy ion. This observation using the Mössbauer effect is indeed a phenomenological observation and no such observation was ever obtained using this method.

The central $\{Fe_2(OH)_2\}$ unit is antiferromagnetically coupled and thus has an $S = 0$ ground state, as determined on the Y^{III} analogue of $\mathbf{2.13}^{\mathbf{teaH\text{-}6\mathit{p}H}}$ or others such as $\mathbf{2.13}^{\mathbf{teaH\text{-}6\mathit{p}CN}}$ (Fig. 2.50). Furthermore, the susceptibilities and magnetizations confirm clearly that in all strong antiferromagnetic coupling is dominant (see also EPR and theoretical sections). In addition, the magnetic study shows significant differences in the slow relaxation of magnetization. This allows us to establish the dependence on the orientation of the magnetic dipolar anisotropy with respect to the central non-magnetic Fe_2 unit and shows that the magnetic interactions are of different strengths between Fe and Dy ions for the five compounds. The five clusters are very closely isostructutral, differing only in the *para*-substituent on the phenyl rings of the benzoate ligands.

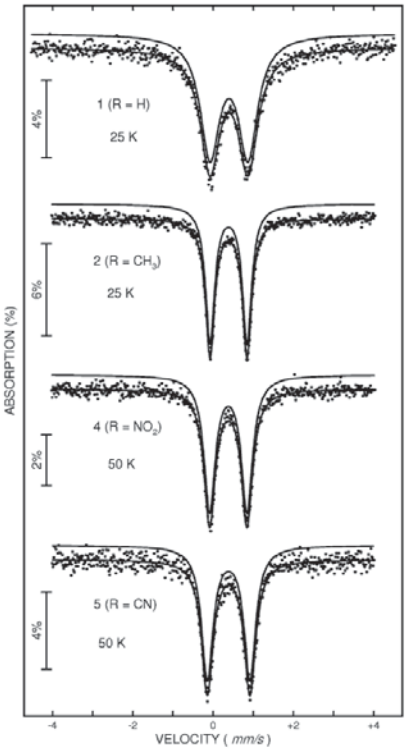

Figure 2.49. Mössbauer data for $\mathbf{2.8}^{\mathbf{teaH\text{-}6\mathit{p}H}}$, $\mathbf{2.8}^{\mathbf{teaH\text{-}6\mathit{p}Me}}$, $\mathbf{2.8}^{\mathbf{teaH\text{-}6\mathit{p}NO2}}$ and $\mathbf{2.8}^{\mathbf{teaH\text{-}6\mathit{p}CN}}$ at different temperatures.

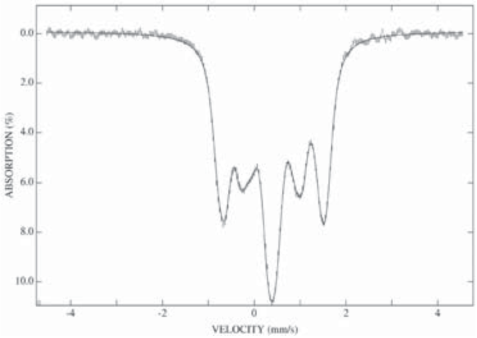

Figure 2.50. Experimental and simulated Mössbauer spectra of solid $[Fe_2Y_2(OH)_2(teaH)_2(C_6H_5COO)_6]$ ($\mathbf{2.13}^{\text{teaH-6}p\text{H}}$) recorded at 3.0 K in applied magnetic field of 5 T perpendicular to the γ-beam. The solid lines are the spectral simulations for $\Delta E_Q = 0.98$ mm/s, $\delta = 0.49$ mm/s, and $\eta = 1.0$, assuming an isolated ground state with $S = 0$.

If we apply an external magnetic field, the magnetic insets in spectra of all compounds $\mathbf{2.8}^{\text{teaH-6}p\text{Me}}$, $\mathbf{2.8}^{\text{teaH-6}p\text{NO2}}$ and $\mathbf{2.8}^{\text{teaH-6}p\text{CN}}$ vanish with increasing field as in case of the reference compound $\mathbf{2.8}^{\text{teaH-6}p\text{H}}$ (as an example, the spectra for $\mathbf{2.8}^{\text{teaH-6}p\text{CN}}$ are shown in Fig. 2.51, upper and left) and the Mössbauer spectra at high fields exhibit patterns typical of a diamagnetic complex. The experimental spectrum for $\mathbf{2.8}^{\text{teaH-6}p\text{CN}}$ obtained at $H_{appl} = 4.0$ T is shown in Fig. 2.51. In the same figure (upper, right) the spectra for the reference compound are also presented. In order, to investigate if this process is reversible we repeated the measurement at 3K and 3T and then reduced the field by 0.5 T steps until zero; the process, as it was found, is indeed reversible.

The Tb^{III} analogue compounds exhibit diamagnetic spectra for all cases (Fig. 2.51, lower and right). The reason why only Dy^{III} compounds behave as magnets around the Fe nuclei will be given later in more details.

While only the two compounds with substituents of nitro and cyano $\mathbf{2.8}^{\text{teaH-6}p\text{NO2}}$ and $\mathbf{2.8}^{\text{teaH-6}p\text{CN}}$ have *ac* maxima in the out-of-phase component in contrast to the other Fe_2Dy_2 compounds (Tab. 2.22), they have in the Mössbauer the highest H_{int} from the five compounds discussed until now. On the other hand, the Fe_2Dy_2 compound $\mathbf{2.8}^{\text{teaH-6}p\text{Me}}$ with the very strong donating inductive group $-CH_3$ which does not show an ac signal at 0 field, has the smallest H_{int} in Mössbauer scale. In addition, the two compounds with unsubstituted benzoate and tertbutylbenzoate, both show *ac* signals without maxima; however, their H_{int} lies between the methyl and the cyano examples.

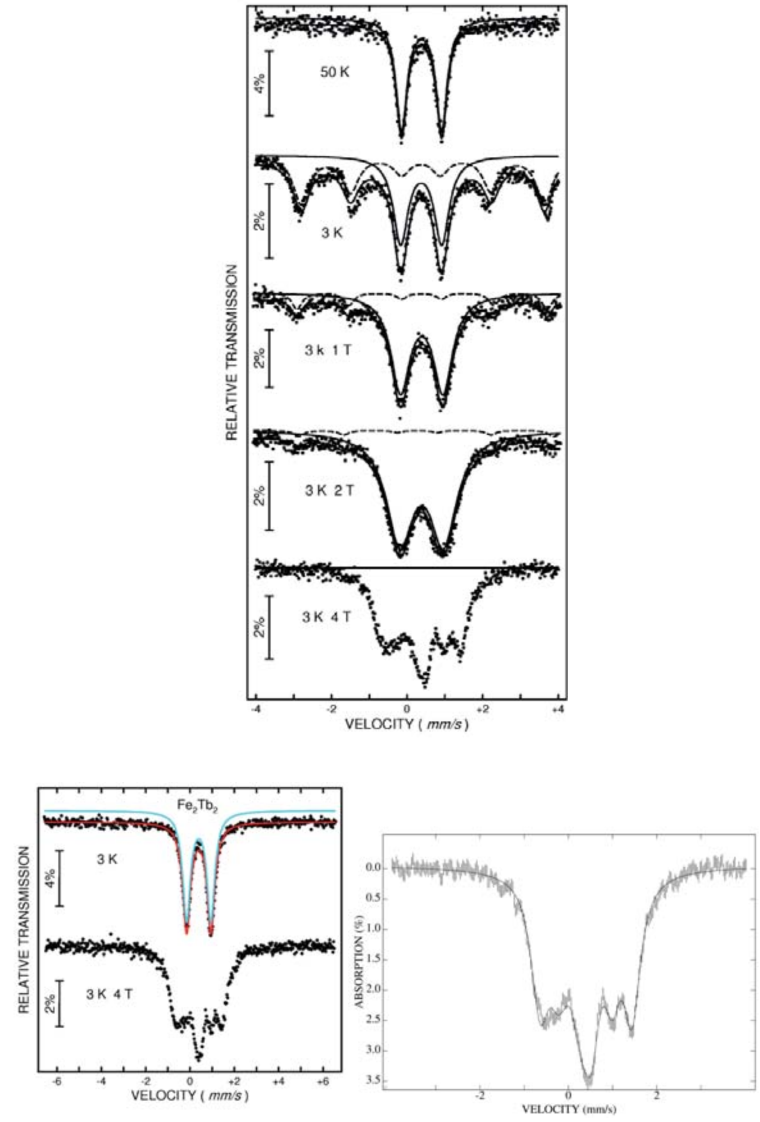

Figure 2. 51. (Upper) 50 K, 3 K and 3 T in different applied external fields Mössbauer spectra of polycrystalline $[Fe_2Dy_2(OH)_2(teaH)_2(NC\text{-}C_6H_4COO)_6]$ ($\mathbf{2.8}^{\mathbf{teaH\text{-}6}\boldsymbol{p}\mathbf{CN}}$). (Lower, left) MS at 3K and 3K and 4T for Fe_2Tb_2 $\mathbf{2.7}^{\mathbf{teaH\text{-}6}\boldsymbol{p}\mathbf{CN}}$. (Lower, right) 3 K Mössbauer spectrum of polycrystalline (R = CN, $2.8^{teaH\text{-}6pCN}$) recorded in a perpendicular applied field of 4.0 T. The solid line is a spectral simulation for $\Delta E_Q = 1.09$ mm/s, $\delta = 0.50$ mm/s, and $\eta = 1.0$, assuming an isolated ground state with S = 0.

Furthermore, both compounds with –Me and –^{t}Bu groups which have higher energy barriers, show lower H_{int} than the reference compound in the Mössbauer data and the opposite case is for the nitro and cyano compounds. Keeping in mind the differences between the SQUID technique (slow time scale) and Mössbauer (fast time scale) methods the results seem to correlate qualitatively for all five compounds. In addition, for the investigation of the magnetism of the compounds, in order to gain a better understanding of the slow relaxation of the magnetization, H_{dc} should be applied. In all these compounds on applying a *dc* field in the SQUID measurements with an oscillating *ac* field, QT disappears. Applying a *dc* field in the

Mössbauer technique leads to different insights although there are no Mössbauer studies, which discuss the QT of molecular nano magnets.

Comparison with meta-Examples

All these results speak clearly for a role of the substituent in both the magnetic and Mössbauer studies. The fact that, the inductive and mesomeric effect (strength) vary from *para* and *meta* positions for the same substituent and that we indeed observed significant differences in the magnetic study, increases our curiosity to study the MS of the *meta* examples for the two extremes (Me and CN) and to investigate similar compounds but with only four *meta*-carboxylates. In Fig. 2.52 the MS spectra at 3K for the four compounds $\mathbf{2.8}^{\mathbf{teaH\text{-}6}\boldsymbol{m}\mathbf{CN}}$, $\mathbf{2.8}^{\mathbf{teaH\text{-}6}\boldsymbol{m}\mathbf{Me}}$, $\mathbf{2.8}^{\mathbf{teaH\text{-}4}\boldsymbol{m}\mathbf{CN}}$ and $\mathbf{2.8}^{\mathbf{teaH\text{-}4}\boldsymbol{m}\mathbf{Me}}$ are shown and compared with *para* methyl and cyano compounds (see also MS at 3K for $\mathbf{2.8}^{\mathbf{teaH\text{-}4}\boldsymbol{p}\mathbf{Ph}}$ and the MS for $\mathbf{2.8}^{\mathbf{teaH\text{-}6}\boldsymbol{m}\mathbf{CN}}$ at different T in chapter 6, Fig. 53, right and left). The MS at 3K for compound $\mathbf{2.8}^{\mathbf{teaH\text{-}4}\boldsymbol{p}\mathbf{H}}$ is shown in Fig. 2.54, right in appendix.

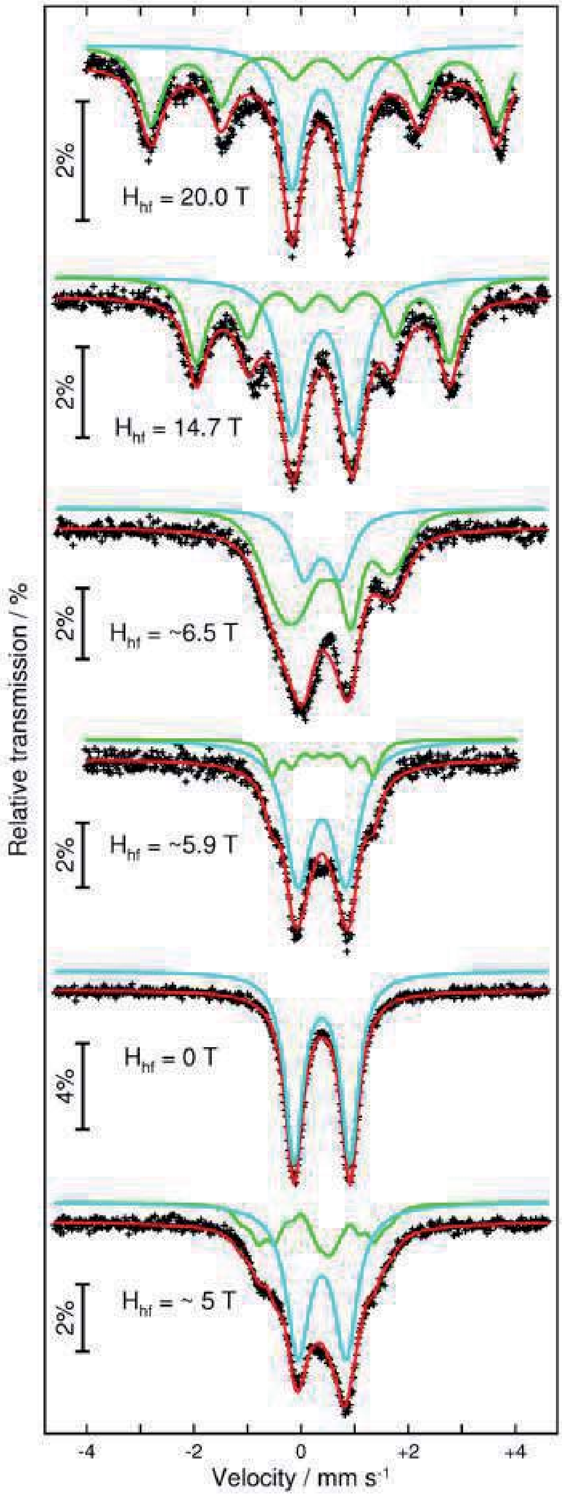

Figure 2.52. (Left) The MS at 3K for compounds (upper to lower) **2.8**$^{\text{teaH-6}p\text{CN}}$, **2.8**$^{\text{teaH-6}m\text{CN}}$, **2.8**$^{\text{teaH-6}m\text{Me}}$, **2.8**$^{\text{teaH-6}p\text{Me}}$, **2.8**$^{\text{teaH-4}m\text{CN}}$, **2.8**$^{\text{teaH-4}m\text{Me}}$.

While no *ac* signal was observed for the compounds with six and four *meta*-cyano benzoates, the MS spectra differ significantly; the compound **2.8**$^{\text{teaH-6}m\text{CN}}$ shows a clear and broadened sextet, as in case of *para*-cyano but with smaller H_{int}. It is remarkable, however, that in the MS of the Fe_2Dy_2 compound with only four *meta*-cyano ligands and two nitrates the sextet disappears and the spectrum can be fitted with one doublet. This is even more surprising in light of the fact that the compounds with six and four *meta*-tolyate ligands show no *ac* signal in the magnetic study, in contrast to the *para*-tolyate one. The MS of **2.8**$^{\text{teaH-4}m\text{Me}}$ still shows slow relaxation, in contrast to the case for **2.8**$^{\text{teaH-6}p\text{Me}}$.

According to the strength of the electron-withdrawing effect of substituents, we now expect the compounds **2.8**$^{\text{teaH-6}p\text{N3}}$ (see Fig. 2.52 (above) and Fig. 2.53 (left) in Appendix) and **2.8**$^{\text{teaH-6(3,5-diNO2)}}$ to show sextets in the MS with large H_{int}, and they indeed do (Fig. 2.52) with values for H_{int} of 14-15 T for azido and 17-18 T for dinitro (see also vanishing of the sextet by applying field for dinitro compound in Fig. 2.53, appendix). Furthermore, we expect for the dimethylaminobenzoate one **2.8**$^{\text{teaH-6}p\text{N(Me)2}}$ as an example with six *para*-substituents to have the smallest H_{int}, and it indeed does with H_{int}= 5-5.5 T (Fig. 2.54, appendix).

Fig. 2. 51 shows the MS of Fe_2Tb_2 **2.7**$^{\text{teaH-6}p\text{CN}}$, which does not show relaxation as in the case of the Dy^{III} analogue. The same observation was made in the reference system where **2.7**$^{\text{teaH-6}p\text{H}}$ also shows only a doublet at 3K. Moreover, also the Ho^{III} **2.9**$^{\text{teaH-6}p\text{CN}}$ analogue compound shows a doublet as observed in the reference series. The explanation given for the Tb and Ho in the reference series should be true for all other Tb and Ho compounds in this family.

Effects: Inductive, Hammet Constants, Dipole Moment

Whether an organic substituent is an electron donor or acceptor is mainly determined by the electronegativity of the atoms which form this substitutent. Moreover, there are different concepts which can be considered when talking about organic groups attached to an aromatic or non-aromatic system. In aromatic systems the effect of substituent is particularly different than in aliphatic or systems with double bonds where the mesomeric effect (electron displacement over pi-bonds) is much more effective. The concepts and factors which can be considered are the bond-dissociation energy, the Hammet constants and the dipole moments (see chapter 1 and Tab. 2.24). See further Fig. 2.56 which shows the trend for H_{int} of the Fe_2Dy_2 compounds compared with the Hammet constants of the substituents. The role of the substituent is known in organic chemistry in the derigation of nucleophilic aromatic substitution reactions. For example, the reaction of 2,4-dinitrochlorobenzene with basic aqueous would lead to the substitution of the chloro function by O- (and H_2O) because of the dirigation effect of the nitro groups. If we consider this from the perspective of the dipole moment of the free acids, now in general, so the effect is justified.

In Tab. 2.25 are simple calculations for the dipole moments of some acids presented. They can be calculated by taking the phenyl ring as zero and COOH group dipole moment which is

-2.96 D on a phenyl ring. It depends now which substituent is on the other side and if it is in *para* or other position. It depends also on the angle (cos0=1 and cos180=-1). If we leave the angle as α, then follow formulas can be used from which the values in Tab. 2.25 were calculated.

For *para*-substituent on benzoic acid: (as vector): $\mu_{p,\ tot}^2 = \mu^2_{sCOOH} + \mu^2_{s2} - 2\ \mu_{SCOOH}\ \mu_{S2}$

For m*eta*- substituent on benzoic acid: $\mu_{m,\ tot}^2 = \mu^2_{sCOOH} + \mu^2_{s2} -\ \mu_{SCOOH}\ \mu_{S2}$

For *ortho*- substituent on benzoic acid: $\mu_{o,\ tot}^2 = \mu^2_{sCOOH} + \mu^2_{s2} +\ \mu_{SCOOH}\ \mu_{S2}$

Plus means the direction of the vector is toward the metal ion core, which is consistent with the electronic force of the substituents.

The MS at 3K of the Fe_2Dy_2 **2.8**$^{\mathbf{teaH\text{-}6}\boldsymbol{p}\mathbf{tBu}}$ and the azido **2.8**$^{\mathbf{teaH\text{-}6}\boldsymbol{p}\mathbf{N3}}$ compounds follow further the expected trend according to the nature and strength of the substituents.

However, the fact that they also show similar magnetic properties is confusing. They both display *a*c signal without maxima, and they possess similar energy barriers at 2000 Oe. The fact that both show slow relaxation of magnetization in the same time scale (10^{-6} s) which is covered by the Mössbauer method (hence it is assumed that QTM is “filtered” by the Mössbauer method but not by SQUID) gives the Mössbauer method more credibility as a means for investigating the slow relaxation properties alone. On the other hand, this would mean that the Mössbauer method is not necessarily able to explain the whole behaviour in terms of QTM and slow relaxation and, hence, is not useful to identify the energy barrier or the QTM.

The case may therefore be even more complicated. Further investigations are necessary to consider the anisotropic D and E parameters as well as the coupling strength between Fe^{III} and Dy^{III} centres (see EPR section).

We selected two examples of the Me-teaH_3 compounds, which are analogues to the reference compounds with six and four benzoate ligands, in order to see if the methyl-group on one of the alkyl arms with its small +I effect can exert any influence on the interaction between the anisotropic Dy^{III} and the Fe nuclei (Fig. 2.55, Appendix). The MS is very similar to that of the reference compound with six benzoate ligands and hence if there is such an effect, it must be very small. Moreover, a doublet was observed for **2.8**$^{\mathbf{Me\text{-}teaH\text{-}4}\boldsymbol{p}\mathbf{H}}$ (Fig. 2.55, right in Appendix) as in case of **2.8**$^{\mathbf{teaH\text{-}4}\boldsymbol{p}\mathbf{H}}$ or **2.8**$^{\mathbf{teaH\text{-}4}\boldsymbol{p}\mathbf{H}}$.

Table 2.25. Selected Hammet constants from literature and calculated dipole moments of free acids as an approximation.

Substituent	I/ M Effect	Hammet Constants[74]	Dipolmomnet* [D][75]	Dipolmomnet of the free carboxylic acid [D][75]
H	No effect	0.00	0	-2.96 cosα
Me	+I	σ_p (-0.17) σ_m (-0.07)	+0.35	+3.1 cosα
^{t}Bu	+I	σ_p (-)	-	+4.25 cosα
N(Me)$_2$	+I/+M	σ_p (0.23) σ_m (0.39)	1.23-1.56	+4.35 cosα
OMe	+M	σ_p (-0.27)	-	-
Ph	+I/-M	σ_p (-)		
Br	-I/+M	σ_p (0.23)	-1.52	-1.513 cosα
F	-I/M	σ_p (0.06), σ_m (0.34)	-1.43	
N$_3$	-I/-M	σ_p (0.37)	Not found	Not found
CN	-I/-M	σ_p (0.66), σ_m (0.56)	-3.92**	-1.17 cosα
NO$_2$	-I/-M	σ_p (0.78) σ_m (0.71)	-3.95**	-1.20 cosα

*Substituents on benzene (free acid not benzoate). Zero menas the benzene ring. D= Debye. COOH Dipolmoment on benzene= -2.96 D. ** On alkyl chains, the different between CN and NO$_2$ is larger.

All these observations are however qualitative, even if the trend follows the electronic displacement nature of the susbtituents (and the Hammet constant) in a remarkable way. In order to achieve a quantitative explanation we have to consider further factors/concepts and to use theoretical models. A good example is the dipole moment, which differs significantly for a substituent on an aromatic ring compared with on an alkyl arm. Furthermore, the dipole moment of the whole benzoate ligand can be calculated (theoretical section). The larger the

Hammet constant, the larger is the H_{int} and vice versa. The larger and more negative the dipole moment of the substituent is, the smaller is that of the whole benzoate and the larger the H_{int}. It is also true to say that when there is less electron density in the aromatic ring, H_{int} becomes larger and the magnetic relaxation slower.

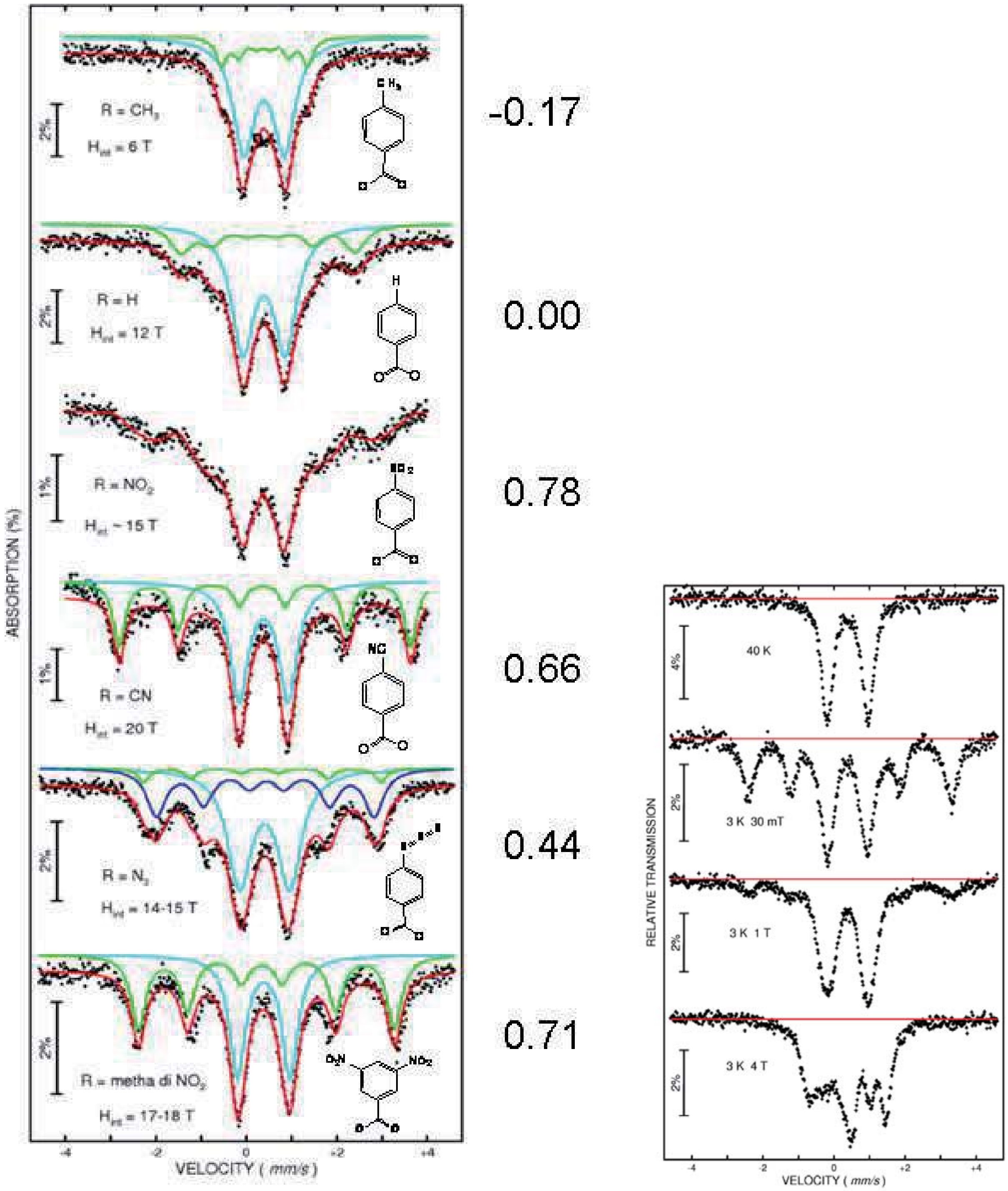

Figure 2.56. (Left) MS at 3K for compounds **2.8**$^{\mathbf{teaH\text{-}6\mathit{p}N3}}$ and **2.8**$^{\mathbf{teaH\text{-}6(3,5\text{-}diNO2)}}$ compared with the others discussed before and with Hammet the constants. (Right) shows the vanishing of the sextet MS of the dinitro compound by stepwise applying the magnetic fields, 30 mT, 1 T and 4T.

Other Exampels

In Fig. 2.57 (Appendix) are the MS of the Fe_2Dy_2 with six 9-anthracenecarboxylate $\mathbf{2.8}^{\mathbf{teaH\text{-}6(9\text{-}anthr)}}$ and Fe_2Dy_2 with six 2-naphthoates $\mathbf{2.8}^{\mathbf{teaH\text{-}6(2\text{-}naphth)}}$. The MS (and Hint) for the anthracene compound is very similar to the reference compound as observed from the magnetic measurement as well. More interesting is, however, the MS at 3K for the naphthoate compound, where it is similar to that of the reference compound and additionally to the anthracene one, but is asymmetric. One explanation might involve the asymmetric naphthoate rings ("trans" chelating the Dy, structure Fig. 2.9, Appendix). Such behaviour needs more investigations, i. e., synthesizing the 1-naphthoate example for comparison. More aromatic rings also do not influence the slow relaxation or energy barrier. In fact, the substituents on the ring seem to play decisive role. They can draw electron density out of the rings or push it into the ring. Furthermore and from our results in this study, as long as the aromatic rings are not influenced by a substituent, no siginificant change can be expected. The change in the aromatic (electron density in the aromate) might then cause spin density fluctuations, which influences the density on the f-orbitals of the anisotropic Dy^{III} (and only Dy). At the same time, the antiferromagntism is robust (because of strong Fe···Fe antiefrromagnetic coupling). If however, the weak ferromagnetic coupling of Fe ··Dy is influenced in the different cases cannot be clearly said. Lying on the magnetic results the change in the dc behaviour is in most cases very similar except few examples and to confirm that this change comes mainly from Fe···Dy and not Fe···Fe interactions, EPR measurements and theoretical calculations for the density of the f-orbitals are needed. Furthermore, theoretical calculations for determination of the anisotropy axes are current work. In order to make a useful EPR study, the Y and Gd analogue of each system are needed (see EPR and Theoretical sections). The EPR study of few of them is presented here and the other are under investigation and analyses.

The Mössbauer of some new candidates being "test-bed" systems have done. The Mössbauer of the series **2.17-2.19** and Fe_6Dy_2 (**2.26**) will be briefly discussed here in order to tied up our results in the Fe_2Dy_2 family system.

Solid Solution Compounds ***2.17-2.19***

The Mössbauer of the Y trinuclear-tetranuclear compound **2.19** was measured in order to confirm the presence of both the trinuclear and the tetranuclear fragments. In addition the MS of the Dy compound **2.8** was measured for comparison. The spectra of this system are “noisy” because of the smaller content of iron in comparison with lanthanides (which can also absorb gamma radiation) and organic constituents. (Fig. 2.58)

All spectra from 155 to 30 K for **2.19** show composite quadrupole-split doublets appearing as two broad absorptions. No dipolar splitting due to internal magnetic field was observed until 3 K. As could be expected from these partly split absorptions it was not possible to fit the Mössbauer spectra of **2.19** by considering a unique quadrupole-split doublet.

In order to satisfactorily fit the spectra, it was necessary to consider two quadrupole-split doublets with very close isomer shift (δ), but different quadrupole splittings (ΔE_Q) corresponding to single ions from the trinuclear molecules $\{FeY_2\}$ and to dinuclear Fe_2 units from $\{Fe_2Y_2\}$ molecules. The isomer shift values for all sites are close to each other and are as expected for high-spin Fe^{III} ($S = 5/2$).

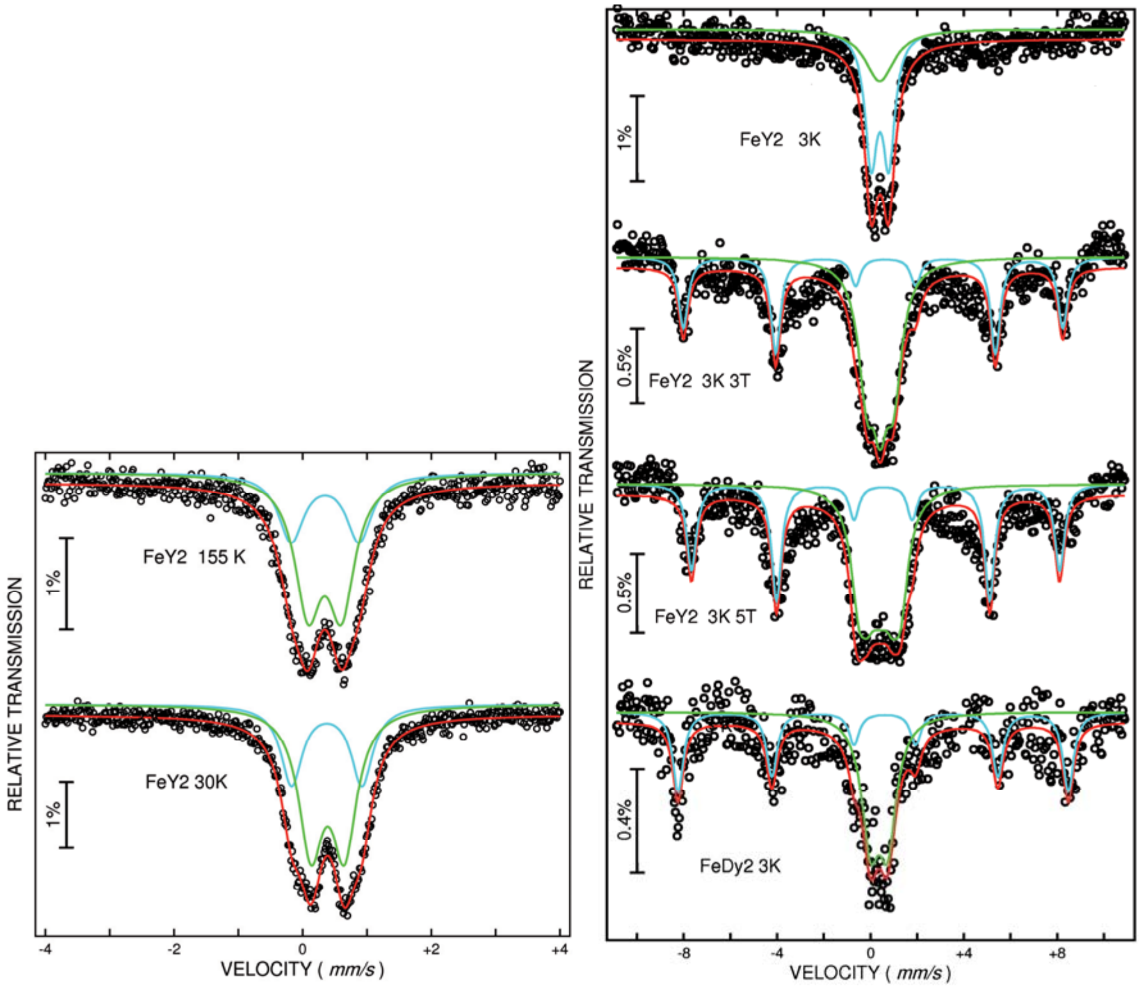

Figure 2.58. The MS of **2.19** at 155 K, 30 K, 3 K, 3K and 3 T, 3K and 5 T. (Right, lowest) the MS of **2.18** at 3K.

The quadrupole splitting values are, however, different, an indication of small differences in the local distortions at the three Fe^{III} sites.

In contrast to high temperature MS, the low temperature (3 K) MS for **2.19** (Fig. 2. 58, right) exhibits a superposition of a broad doublet and a broad inset corresponding to intermediate relaxation times between 10^{-8} and 10^{-9} s.

Applying external magnetic fields the obtained spectra exhibit a superposition of a sextet and a broad doublet. The sextet was assigned to the single Fe^{III} in the trinuclear component. The doublet was attributed to two irons from Fe_2Y_2 molecules as in the reference compound **$2.13^{teaH\text{-}6pH}$**.

These results indicate that the Fe ions in {Fe_2Y_2} components (with 24%) are essentially equivalent and antiferromagnetically coupled as observed for other Fe_2Y_2 compounds in the Fe_2Ln_2 family.

With increasing external magnetic field, the total field at the single iron nucleus, H_{eff}, decreases with increasing H_{appl}. The field is reduced because the Fermi contact term is opposite in sign to the applied field. The same behaviour we have observed for **2.18** compounds.

Whereas at temperatures higher than 3 K, the MS for **2.19** are identical with the spectra of **2.18**, distinct behavior is observed at 3 K in zero applied magnetic field. (See Fig. 2.58, right and lowest).

The spectrum of **2.18** contains a central doublet (similar to **2.19**) and a sextet with effective magnetic field H_{eff} = 52 T, which is slightly lower than T= 55 T (with 11 T expected from each spin 5/2).

This different behaviour is due to interaction between Dy^{III} and Fe^{III} ions which slows down spin relaxation on single irons (and therefore allow the observation of magnetic spectra). The hyperfine parameters are comparable to those obtained for the **2.19** compound. The Fe_2Dy_2 component is also diamagnetic as observed for $\mathbf{2.8^{teaH\text{-}4pH}}$ and thus the similarity in MS between **2.18** and **2.19** demonstrate according to the structure that the trinuclear component is dominant.

Mössbauer study of Fe_6Dy_2 ***2.26***

The Mössbauer spectra indicate the absence of any magnetic sextet at 5 K and above, and have been analyzed with the superposition of three symmetric Lorentzian doublets assigned to the three crystalographically inequivalent Fe^{III} sites (Fig. 2. 59, left). If the three crystallographic sites have the same recoil free fraction at all temperatures, the expected relative areas of the five doublets are 1:1:1 for Fe(1), Fe(2), and Fe(3), respectively. The assignment was based on iron ions crystallographic environment and the percentage bond distortions. Although the Fe(1) and Fe(2) are both six coordinate and expected to have close quadrupole splittings (ΔE_Q), nevertheless the ΔE_Q for Fe(2) is bigger. These features are regarded as due to the regular octahedron for the Fe(1) and the slightly distorted one for the latter.

The doublet with biggest quadrupole splitting, ΔE_Q, can be assigned to Fe(3) site which is five coordinate. The hyperfine parameters for all three doublets are given in Tab. 2.26 The quadrupole splittings show little temperature-dependence between 30 and 300 K, as expected for high-spin Fe^{III} ions for which the quadrupolar interaction arises only from a lattice contribution to the electric field gradient at the iron. An increase in the isomer shift upon cooling is attributed to a second-order Doppler Effect.

At 6 and 3K, the zero-field spectra are significantly broadened (Fig. 2.61,) with wings that extend from about -2 to +2 mm/s. The broadening of the Mössbauer spectrum implies that the relaxation time is of the order of the nuclear Larmor precession time, or about 10^{-7} s. Although all doublets assigned to iron ions are getting broader from 30 to 3 K, the most essential broadening is only in case of doublet assigned to Fe(3) (blue) (from ~ 0.30 to 1.15 mm/s). The reason may lie in the position of this iron center and its neighborhood with the magnetic dysprosium ions which makes it relaxing slower than other iron centers.

The applied magnetic fields at low temperature will magnetize the net spin of the cluster along the field direction, decrease the relaxation time and magnetic hyperfine lines should appear as a superposition of three magnetic sextets (Fig. 2.60).

As in case of spectra in paramagnetic region, the fit of the magnetic spectra (Fig. 2.60) was made by a superposition of three components. Fits with one common line-width for the five sextets were not as good, therefore the line-width values were left free.

For a magnetic sextet the six component areas in the thin absorber limit are 3:2:1:1:2:3 only if there is no texture in the sample and there is a random distribution of the angles between the magnetic easy axis and the propagation direction of the gamma-ray. In general the ratio is 3:x:1:1:x:3, where x = 0 if the easy magnetic axis and the gamma-ray direction are parallel and x = 4 if the easy magnetic axis and the gamma-ray direction are perpendicular.

Since a perfect thin-limit absorber is unachievable in practice, the ratio is actually 3:x:y:y:x:3, where y is usually larger than 1 because of thickness effects. In addition to these effects in case of compound **2.26** we still have strong magnetic relaxation present.

The variation in B_{eff} vs B_{appl} intrinsically contains information about both the orientation of the spin with respect to the applied field as well as about spin relaxation mechanisms. In the static case conditions (at low enough temperature so that no relaxation exists), the effect of the applied field is to reorient the molecule's spin with respect to its direction. Depending on the coupling inside the molecule, some spins will orient along the field, the others, opposite to the field. Any further increment of B_{appl} will provide either an increasing or a decreasing trend of B_{eff}, due to the addition/subtraction of B_{appl} to/from B_{int}, depending on their relative orientation. Therefore, the dependence of B_{eff} vs B_{appl} is considered in terms of a vectorial model, since more knowledge about the magnetic coupling inside the cluster is retrieved. In the dynamical case (activated magnetic relaxation in the absence of the applied field), the first effect of the field is to freeze the cluster spin by field-induced anisotropy and then to reorient it. In the beginning the effective field increases under the applied field mainly due to the increment of the time averaged internal field and subsequently by spin reorientation and addition/subtraction of the applied field. In the dynamical case a deduction of the real B_{int} from B_{eff} and B_{appl} is unachievable. The only unitary treatment for all considered Fe positions concerns the variation in B_{eff} versus B_{appl}, which show that lines of two sextets are moving outwards and of the third sextet – inwards (Fig. 2.61). This shows unambiguously that the interaction between iron ions inside the Fe_6 core is ferrimagnetic. Due to strong magnetic relaxation, the lines are still very broad and a correct assignment of sextets to iron sites to get magnetic structure of the central Fe_6 cluster is challenging. The decreasing of the line widths with increasing external magnetic field indicates that spins are getting frozen, but to freeze them completely we need much higher fields. The presence of an anisotropic center close to the $\{Fe_6\}$ unit might facilitate to slow down the relaxation [76]. Although previously it was found that this is possible, in compound **2.26** seems that crystal field around Dy ions leads to a non-anisotropic ground state, weaker interaction with the central ferric unit and faster relaxation of the iron spins giving rise to paramagnetic (doublets) Mössbauer spectra at 3 K.

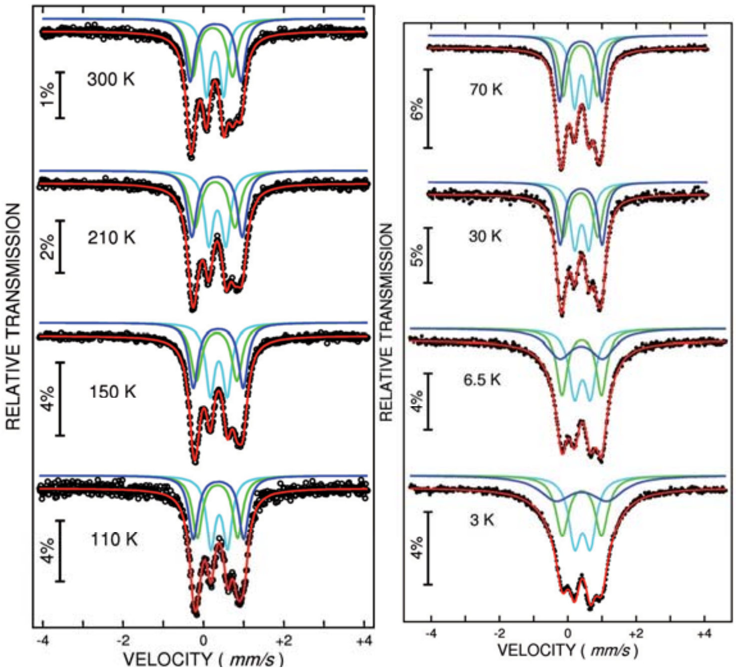

Figure 2. 59. The ^{57}Fe Mössbauer spectra of **2.26** obtained at the indicated temperatures.

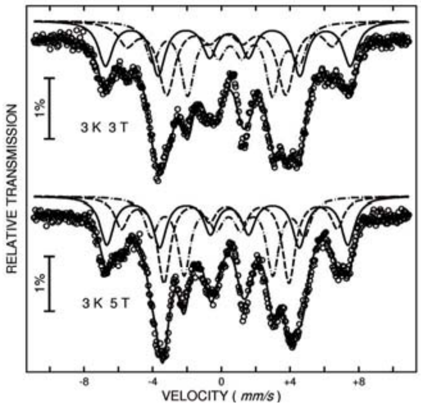

Figure 2.60. The ^{57}Fe Mössbauer spectra of **2.26** obtained at 3 K and indicated external magnetic fields.

Table 2.26. Mössbauer data for **Fe_6Dy_2** (**2.26**) at 300 – 30K in zero-field and at 3 K in applied magnetic fields of 3 T and 5T.

T, K	Fe sites	δ[a], mm/s	ΔE_Q or ε[c], mm/s	Γ, mm/s	B_{eff}, T
300	Fe(1)	0.387(1)	0.428(2)	0.232(5)	-
	Fe(2)	0.32(1)	0.99(1)	0.30(1)	-
	Fe(3)	0.398(8)	1.26(1)	0.274(4)	-
210	Fe(1)	0.444(1)	0.42(1)	0.267(2)	
	Fe(2)	0.384(2)	0.993(6)	0.335(1)	
	Fe(3)	0.437(1)	1.254(4)	0.286(4)	
150	Fe(1)	0.479(1)	0.41(1)	0.261(2)	
	Fe(2)	0.426(1)	1.011(5)	0.319(4)	
	Fe(3)	0.466(1)	1.239(4)	0.282(4)	
110	Fe(1)	0.490(2)	0.415(5)	0.263(5)	
	Fe(2)	0.448(3)	1.00(1)	0.29(1)	
	Fe(3)	0.473(2)	1.25(1)	0.28(1)	
70	Fe(1)	0.502(1)	0.417(1)	0.273(2)	
	Fe(2)	0.464(1)	0.996(3)	0.308(3)	
	Fe(3)	0.481(1)	1.243(2)	0.281(2)	
30	Fe(1)	0.506(2)	0.415(4)	0.299(8)	
	Fe(2)	0.469(2)	1.01(1)	0.34(1)	
	Fe(3)	0.49(2)	1.229(7)	0.298(7)	
6.5	Fe(1)	0.527(1)	0.462(3)	0.384(4)	
	Fe(2)	0.490(1)	1.150(2)	0.370(4)	
	Fe(3)	0.491(2)	1.26(1)	0.88(2)	
3	Fe(1)	0.529(1)	0.454(4)	0.413(4)	
	Fe(2)	0.491(2)	1.15(1)	0.45(3)	
	Fe(3)	0.50(1)	1.50(3)	1.15(4)	
3 K,	I	0.52[b]	0.28(1)	1.01(1)	37.1(1)

3 T	II	0.49[b]	-0.07(1)	0.99(1)	44.19(6)
	III	0.50[b]	-0.22(1)	0.97(1)	26.55(6)
3 K, 5 T	I	0.52[b]	0.20(1)	0.89(1)	38.75(7)
	II	0.49[b]	-0.08(1)	0.90(1)	43.57(6)
	III	0.50[b]	-0.05(1)	0.89(1)	27.58(6)

[a] Relative to α-Fe at room temperature. [b] Fixed values. [c] For magnetically-split spectra the quadrupole shifts, $\varepsilon = \frac{1}{2}\Delta E_Q(3\cos^2\varphi - 1)$. φ - angle between the B_{int} and the main electrical field gradient (EFG) principal axis (V_{zz}). The quadrupole shifts are easy to observe from the magnetic spectra as a difference in the splitting of 1 and 2 and 5 and 6 iron(III) lines. $B_{\mathrm{eff}} = B_{\mathrm{int}} + B_{\mathrm{appl}}$: B_{eff} - the effective magnetic field, B_{int} – internal (hyperfine) magnetic field and B_{appl} – applied magnetic field. δ is the isomer shift, ΔE_Q - quadrupolar splitting. The numbers obtained from fittings of magnetic spectra should be considered with caution because of very broad lines and too intensive central absorptions (lines 3 and 4). The statistical errors are given in parentheses. The relative areas for the doublets and sextets have been constrained to the 1:1:1 ratio.

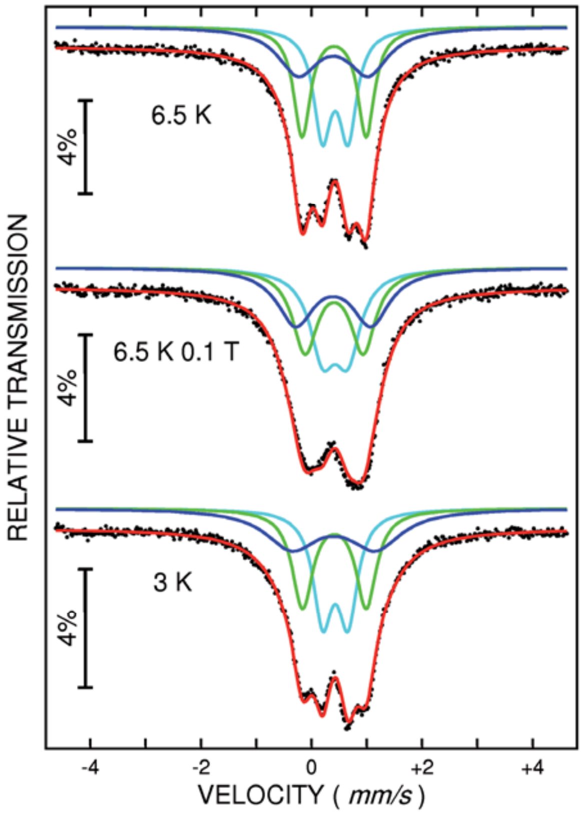

Figure 2.61. The ^{57}Fe Mössbauer spectra of **2.26** obtained at the indicated temperatures.

2.5 Theoretical calculations

The {Fe_2Ln_2} Reference Series

A complementary insight into the nature of the magnetic interactions of the Fe_2Ln_2 reference series could be achieved using *ab initio* calculations in collaboration with Marilena Ferbinteanu (University of Bucharest, Faculty of Chemistry Inorganic Chemistry, Bucharest, Romania).

CASSCF(14,12) calculations (including 10 singly occupied and 2 doubly occupied MOs) for the {Fe_2Lu_2} idealized model yielded a coupling parameter J_{FeFe}^{CAS}= -3.74 cm^{-1}. A Broken Symmetry **[77-79]** DFT calculation on the same system gave J_{FeFe}^{DFT}= -9.12 cm^{-1}. Both estimations are in the range of experimental fitting results (magnetic section 2.2), J_{FeFe}^{exp}= -6.2 to -6.9 cm^{-1}, verifying the semi-quantitative use of *ab initio* calculations as providing qualitatively reliable information on the nature of the magnetic effects. The *d-f* interaction in the Fe-Gd system yielded a J_{FeGd}^{CAS} = +0.64 cm^{-1} estimation. As an absolute value this is slightly overestimated compared with the experimental fit (J_{FeGd}^{exp} ~ +0.2 cm^{-1}) but the range is consistent to the fit magnitude. We note here that the inherent errors of computation vs. experiment are scaled with the expected range of the energy effects, having in all the discussed cases a good relative account of the competing parameters.

A very important computational advance has been achieved in terms of understanding the effect of the magnetic anisotropy of the Dy^{III} ion in Fe_2Dy_2, **2.8$^{teaH\text{-}6pH}$** from the reference series. The CASSCF(9,7) computation accounted well for the Ligand Field regime of the Dy^{III} in the complex, retrieving a full split of the ^{6}H term of about 580 cm^{-1}, in accordance with the expected range.**[68]** The Spin Orbit (SO) calculation on this wave function gives full information relating to the magnetic anisotropy. The first 16 states from CASSCF-SO calculations correspond to a combined Ligand Field and Spin Orbit splitting of the J=15/2 formal spin-orbit state (see Tab. 2.27). The computed relative energies of the 8 degenerate pairs are as follows: 0, 116.5, 204.3, 247.1, 267.1, 321.5, 396.9, and 533.1, in cm^{-1}. The double degeneracy's are formally assignable to the ± J_z components, even though the full relationship is more intricate since, rigorously speaking; the J_z projections are no longer good quantum numbers.

The *ab initio* simulation of the anisotropic magnetization tensors is based on the search of the variation of computed CASSCF-SO energy levels as function of magnetic field applied from different orientations around the lanthanide ion in the given coordination site. The polar diagram of the *-dE/dB* variations, taken for the lowest state of the spectrum, numerically estimated when the applied field *B* runs over the corresponding space orientations renders the ground state magnetization tensors represented in Fig. 2.62. The size, shape and orientation of the computed magnetization tensor are valuable nontrivial results, revealing how the ligand field determines the magnetic anisotropy of the system.

In order to probe the role of the two anisotropic lanthanide centers of the $\{Fe_2Dy_2\}$ compounds, the calculation the magnetization tensors was done in model systems where the paramagnetic ions are replaced by diamagnetic references, $\{Dy^ALu^B,Co^{III}_2\}$, and $\{Lu^ADy^B,Co^{III}_2\}$, respectively. The simplification is justified by the local nature of the lanthanide ion anisotropy and is necessary to identify in the correct spectrum of relevant states from the CASSCF-SO calculations. Thus, in our case we have chosen for a $\{DyLuCo^{III}_2\}$ model system a set of 11 orbital states in a state-averaged CASSCF calculation, obtaining a full 66 levels SO spectrum (i.e. $(2L+1)\cdot(2S+1)=11\cdot6=66$) after the CASSCF-SO treatment. The full treatment of the $\{Dy_2Fe_2\}$ system would imply $11^2\cdot6^2\cdot6^2$ =156816 explicitly accounted levels, a goal which is absolutely intractable with current computational technologies (the 11^2 factor results from orbital multiplicities of the Dy pair, and the 6^2 ones arise from the spin multiplicities of both Fe^{III} and Dy^{III} couples). In these cases, Lu^{III} was chosen as diamagnetic analogue for the 4f contribution as it has a full (i.e. not empty) shell of f-electrons. Similarly, L.S. Co^{III} with its one extra electron over Fe^{III} was chosen as a diamagnetic analogue with a full t_{2g} set of d-orbitals.

Table 2.27. The table containing the $H[S,M_{S,}\ S,M_S]|\equiv H[S,M_{S,}\ S,M_S]|\{J_z^A,\ J_z^B\ \}$ diagonal elements of the block Hamiltonian matrices, independently running as function of the four possible combinations of $J_z^A= \pm15/2$ and $J_z^B= \pm15/2$.[a]

$H[(0,0);(0,0)]=0$	$H[(4,-4);(4,-4)]=-20J_{dd}-2j_zJ_z^A-2j_zJ_z^B$ $H[(4,-3);(4,-3)]=-20J_{dd}-\frac{3j_zJ_z^A}{2}-\frac{3j_zJ_z^B}{2}$ $H[(4,-2);(4,-2)]=-20J_{dd}-j_zJ_z^A-j_zJ_z^B$

$$H\left[(1,-1);(1,-1)\right]=-2J_{dd}-\frac{j_zJ_z^A}{2}-\frac{j_zJ_z^B}{2}$$

$$H\left[(1,0);(1,0)\right]=-2J_{dd}$$

$$H\left[(1,1);(1,1)\right]=-2J_{dd}+\frac{j_zJ_z^A}{2}+\frac{j_zJ_z^B}{2}$$

$$H\left[(2,-2);(2,-2)\right]=-6J_{dd}-j_zJ_z^A-j_zJ_z^B$$

$$H\left[(2,-1);(2,-1)\right]=-6J_{dd}-\frac{j_zJ_z^A}{2}-\frac{j_zJ_z^B}{2}$$

$$H\left[(2,0);(2,0)\right]=-6J_{dd}$$

$$H\left[(2,1);(2,1)\right]=-6J_{dd}+\frac{j_zJ_z^A}{2}+\frac{j_zJ_z^B}{2}$$

$$H\left[(2,2);(2,2)\right]=-6J_{dd}+j_zJ_z^A+j_zJ_z^B$$

$$H\left[(3,-3);(3,-3)\right]=-12J_{dd}-\frac{3j_zJ_z^A}{2}-\frac{3j_zJ_z^B}{2}$$

$$H\left[(3,-2);(3,-2)\right]=-12J_{dd}-j_zJ_z^A-j_zJ_z^B$$

$$H\left[(3,-1);(3,-1)\right]=-12J_{dd}-\frac{j_zJ_z^A}{2}-\frac{j_zJ_z^B}{2}$$

$$H\left[(3,0);(3,0)\right]=-12J_{dd}$$

$$H\left[(3,1);(3,1)\right]=-12J_{dd}+\frac{j_zJ_z^A}{2}+\frac{j_zJ_z^B}{2}$$

$$H\left[(4,-1);(4,-1)\right]=-20J_{dd}-\frac{j_zJ_z^A}{2}-\frac{j_zJ_z^B}{2}$$

$$H\left[(4,0);(4,0)\right]=-20J_{dd}$$

$$H\left[(4,1);(4,1)\right]=-20J_{dd}+\frac{j_zJ_z^A}{2}+\frac{j_zJ_z^B}{2}$$

$$H\left[(4,2);(4,2)\right]=-20J_{dd}+j_zJ_z^A+j_zJ_z^B$$

$$H\left[(4,3);(4,3)\right]=-20J_{dd}+\frac{3j_zJ_z^A}{2}+\frac{3j_zJ_z^B}{2}$$

$$H\left[(4,4);(4,4)\right]=-20J_{dd}+2j_zJ_z^A+2j_zJ_z^B$$

$$H\left[(5,-5);(5,-5)\right]=-30J_{dd}-\frac{5j_zJ_z^A}{2}-\frac{5j_ZJ_z^B}{2}$$

$$H\left[(5,-4);(5,-4)\right]=-30J_{dd}-2j_zJ_z^A-2j_zJ_z^B$$

$$H\left[(5,-3);(5,-3)\right]=-30J_{dd}-\frac{3j_zJ_z^A}{2}-\frac{3j_zJ_z^B}{2}$$

$$H\left[(5,-2);(5,-2)\right]=-30J_{dd}-j_zJ_z^A-j_zJ_z^B$$

$$H\left[(5,-1);(5,-1)\right]=-30J_{dd}-\frac{j_zJ_z^A}{2}-\frac{j_zJ_z^B}{2}$$

$$H\left[(5,0);(5,0)\right]=-30J_{dd}$$

$$H\left[(5,1);(5,1)\right]=-30J_{dd}+\frac{j_zJ_z^A}{2}+\frac{j_zJ_z^B}{2}$$

$$H\left[(5,2);(5,2)\right]=-30J_{dd}+j_zJ_z^A+j_zJ_z^B$$

$$H\left[(5,3);(5,3)\right]=-30J_{dd}+\frac{3j_zJ_z^A}{2}+\frac{3j_zJ_z^B}{2}$$

$H[(3,2);(3,2)] = -12J_{dd} + j_z J_z^A + j_z J_z^B$	$H[(5,4);(5,4)] = -30J_{dd} + 2j_z J_z^A + 2j_z J_z^B$
$H[(3,3);(3,3)] = -12J_{dd} + \frac{3j_z J_z^A}{2} + \frac{3j_z J_z^B}{2}$	$H[(5,5);(5,5)] = -30J_{dd} + \frac{5j_z J_z^A}{2} + \frac{5j_z J_z^B}{2}$

[a] The phenomenological Hamiltonian for Fe_2Dy_2 system is based on Heisenberg interaction between Fe(III) ions (the $J_{d\delta}$ parameter) and Ising like Fe-Dy effects (the $j_z \equiv j_{df}$ parameter), involving the $J_z = \pm 15/2$ states on lanthanide and $|S,M\rangle|J,J_z^A\rangle|J,J_z^B\rangle$ product wavefunctions.

A slight anisotropy is also found on the Fe^{III} center, the corresponding CASSCF-SO calculation yielding the following sequence of doubly degenerate levels: 0, 1.254 and 2.191 cm^{-1}, which can be fitted with the following ZFS parameters: $D = 0.28$ cm^{-1} and $E = \pm 0.13$ cm^{-1}. However this small anisotropy does not play any significant role in the magnetism of the system as a result of the antiferromagnetic ground state of the Fe_2 fragment (as seen from the magnetic and Mössbauer studies) in the discussed systems and the fact that the relatively large exchange parameter supercedes any potential effects arising from the slight anisotropy of the Fe^{III}.

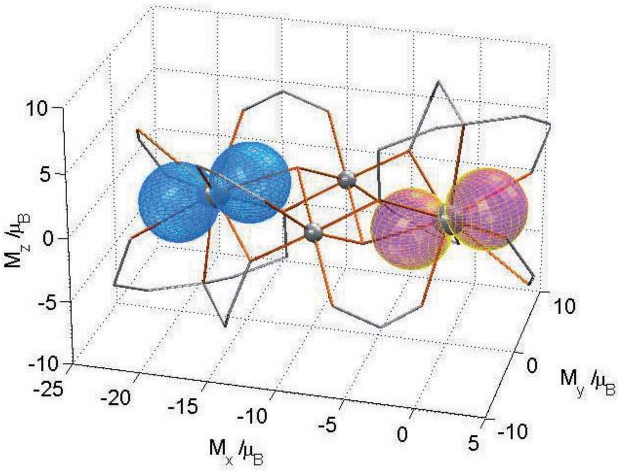

Figure 2.62. The ab initio computed magnetization tensors (in Bohr Magneton units, μB) on each of the Dy(III) sites in the $\{Fe_2Dy_2\}$ compound. The molecular skeleton is figured in arbitrary units, in order to visualize the orientation of the anisotropy with respect of the molecular frame. The second center is conventionally shifted, while the computation of its tensor is made with respect of its own atom as origin of the axes. The figure contains the representation of two calculations performed for each respective dysprosium site.

Calculations considering the substituents

Different calculations were done in collaboration with Dr. Jukliusz Wolny and Prof. Volker Scheunemann (Physik Institut, Universität Kaiserslautern) in order to understand the role of the substituents more qualitatively and at the same time aiming quantitative interpretation.

i) The electronic effect, the Hammet constants, the dipolmoments of substituents and the calculated dipolmoments of the free acids were considered for discussion (Tab. 2.28).

ii) The calculated average of the Mulliken charges of the oxygen's (O9 and 010) and the calculated dipolmoments of the substituted benzoate (not free acids) are in Tab. 2.29 (appendix).

The permanent dipole moments of the benzoate ligands were calculated at various theoretical levels, including Hartree–Fock, third-order Møller–Plesset perturbation (MP2), and hybrid density functional theory at B3LYP level. It is found that, the B3LYP method fails to provide correct results for the geometry and the permanent dipole moment for free acids. These results are significantly improved by MP3 calculations.

iii) Mulliken Charges of different oxygen's of the benzoate ligands were plotted vs. the dipolmomnets and Hammet constants (Fig. 2.63, left and right).

iv) The different electric dipolmoment components ($\mu_{x,y,z}$) were calculated as well as the polarisability tensor (Tab. 2.30, appendix)

v) The dissociation energies for different levels (MP2 and MP3) were calculated (Tab. 2.31, appendix).

vi) Influence of the different substituents (para and meta) on the density (and oreination) of the *d* and *f* orbitals of Fe^{III} and Dy^{III} ions (Fig.'s 2.65-2.67, appendix)

In the Mössbauer discussion, we discussed briefly a possible correlation to the Hammet constants of the substituents. A correlation indeed can be seen in particular for the trend observed for H_{int} in the Mössbauer study. Furthermore, the Fe_2Dy_2 compounds with only four carboxylates does not show *ac*-signal and have almost in all cases a diamagnetic MS (doubeltt) at 3K or/and under applied fields. This, however, shows clearly that the two carboxylates chealting the Dy^{III} ions are very important sources of electron density and thus electronic effect. To deepness this remarkable observation, calculations of the average Milliken charge of the carboxylates oxygen's (O9 and O10) were performed (see Tab. 2.26). These values were then put in relation to the Hammet constants (Fig. 2.64, left,).

In addition, calculations for the dipolmoments for selected carboxylates (anions) were done (Tab. 2.27). Usually, dipolmoments of free acids can be measured (in gas phase or in solutions such as in benzene) and also calculated. [80] However, it is much harder to measure anions of carboxylates, only if they are adducts of cations. Four benzoates with strong donating substituents larger Milliken charge average and at the same time larger dipolmoments (in Debye) are observed (Tab. 2.27).

Both Mulliken vs. Hammet constants and Mulliken vs. Dipolmoment show correlation to the observed results from magnetic and Mössbauer study as well as the EPR study (see later).

The Hammet constants give a sort of free relationship and therefore are related to the thermodynamic of the cluster systems discussed here (Fig. 2.64). [74]

Substituents, such as, nitro or cyano, which have strong withdrawing (-I and –M) effects, with smaller negative Mulliken Charges (Tab. 2.27, Appendix), have at the same time larger negative dipolmoments (Tab. 2.26, appendix). Their carboxylates have further smaller values of dipolmoments and their free acids smaller negative dipolmoment values. Exactly, Fe_2Dy_2 compounds with these substituents have strong ac-signal and maximum in the out-of-phase component and have sextets with the large H_{int}. All these values, however, correlate to the Hammet constants. The substituents with smaller Mulliken charges have larger Hammet constants (Fig. 2.64, left) and smaller dipolmonets (Fig. 2.64, right). The curves in Fig. 2.64 indicate indeed a correlation between these three different values.

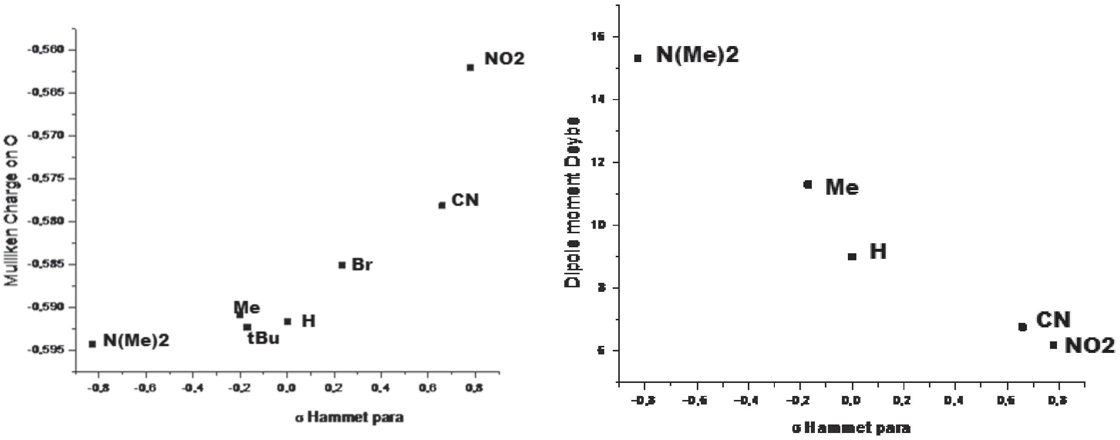

Figure. 2.63. (Left) the calculated Mulliken charges of the oxygen's of the benzoates for selected substitutes vs. Hammet constants. (Right) calculated dipolmoments for selected substituents vs. Hammet constants.

MP3 and B3LYP methods give similar trend for *p*-Me, *m*-Me substituents, i.e., μ_y (*p*-Me) < μ_y (*m*-Me) and μ_x (*p*-Me)> μ_x (*m*-Me) (Tab. 2.28, appenidx). With x is the dipole along the x axies of the benzoates and y is parallel to the plane. The different polarisability tensor values obtained for the cyano groups are the largest and for the methyl groups are the smallest.

If we assume that, the y-component has a strong influence on the Fe-Ln birding benzoates and thus on the charge (oxygen) between Fe^{III} and Dy^{III}, then this might even influence the magnetic exchange. The substituent *para*-methyl has the highest values for x axis and this is actually the example with the ferri magnetism. As discussed in the magnetic part, while all Fe_2Dy_2 compounds show similar *dc* magnetism, namely strong antiferromagnetism, the compound $\mathbf{2.8}^{\mathbf{teaH\text{-}6}\boldsymbol{p}\mathbf{Me}}$ shows at low temperature significant ferromagnetic behaviour. The y component of the dipole (Tab. 2.28, appendix) is almost zero and the z one is the largest.

The dipoles (in x axis) for the cyano groups are much lower than those for methyl groups. Furthermore, the MP3 and B3LYP calculations for the para-cyano group give closre values than for the meta-cyano one. The y components of the *meta*-benzoates are larger than for x dipoles. This is reasonable since the *meta* benzoates are asymmetric.

The cyano groups have lower values than methyl groups as from withdrawing groups expected and also seen in Tab. 2.26 and Tab. 2.27. At the same time the poalrisability tensors are larger.

The poalrisability results can be understood if we see the ligand interaction of the benzoates, in particular those chelating the Dy^{III} ions as negative or as electron density clouds (nephelauxetic effect), where by substituting with cyano groups those “pull” the clouds from the metal ion, so that the magnetic anisotropy becomes influenced.

The MP3 and MP2 calculations give also larger dissociation energies for the cyano substituents in comparison for a proton (Tab. 2.29, appendix).

Although, the energies for *para*- or *meta*-cyano groups are in general similar, they would dissociated differently charged from the phenyl ring (Tab. 2.29, appendix).

The proton would release neutral as well as the *meta*-cyano group but not the *para*-cyano group which would dissociate as an anion.

Again, in different studies the *para*-methyl substituent and the *para*-cyano substituent have always significant differences to the others.

Very recent studies (in 2012) on the electronic effect on atom tunnelling, -conformational E/Z isomerization of monomeric para-substituted benzoic acid derivatives-, show that the potential H/D tunnelling is stronger influenced by Me substituent rather than ^{t}Bu. They further, show with help of different measurements and computation that, Me groups is stronger σ-donating than ^{t}Bu. They, however, studied the nitro group but not the cyano one. The nitro group in their study has the strongest σ-acceptor character. [81]

DFT (PBE exchange correlation-exchange functional, CEP-31G basis set) calculations were done for the compounds with $\mathbf{2.8}^{\mathbf{teaH\text{-}6}\boldsymbol{p}\mathbf{CN}}$, $\mathbf{2.8}^{\mathbf{teaH\text{-}6}\boldsymbol{p}\mathbf{H}}$ and $\mathbf{2.8}^{\mathbf{teaH\text{-}6}\boldsymbol{p}\mathbf{Me}}$.

Fig's. 2.65-2.66 in appendix show the HOMO orbitals of the complexes in the *p*-CN (left), *p*-H (middle) and *p*-Me (right) substituents. From these calculations it seems that the d_z2 orbitals are independent from the substituent-change.

In contrast to the situation around Fe orbitals, the substituent change show strong influence on the f_{z3} (xy-plane) orbitals of Dy^{III}. Other perspectives for the whole molecule are given in Fig. 2.67 (appendix). In this figure, we see that the orientation of the *d*-orbitals to the *f*-orbitals is slightly different which might be a result of different dipoles as observed in the above discussed results. To proof this strategy of calculations the mononuclear compound with benzoate **2.21** was calculated theoretically for cyano and methyl groups. Indeed the substituent change influences even one Dy^{III} centre (Fig. 2.68, Appendix).

One can see that the change of the substituent to the more donating one (4-Me) results in change of the location of z –axis. It is no longer defined by the N of „top“ pyridine and (approx.) one of carboxylate oxygens, but N of another pyridine and the nitrate *trans* to it. I believe it is a purely electrostatic effect. Even in this rather symmetric charge distribution, the slight change of it (by means of substituent effect) may result in the change of localisation of the quantisation axis. There the small change of the dielectric constant was inducing a change of orientation of the elongation axis.

There are slightly different openions about the interpretation of all these results. The author of this work tends to the follow explanation.

A strong withdrawing group such as cyano in *para*-position leads to lower electron density in the aromatic ring. As result of that, the oxygen's of the carboxylic group, which have samller Mulliken charge as in case of *para*-methylbenzoate (as discussed before), would interact with Dy^{III} in a different way than the methylbenzoates or even *meta*-cyanobenzoate, say stronger. For lanthanides the force which is caused on the valence electrons can be ordered (in comparison with that on the nuclea) as follow: $H_{ee} > H_{so} > H_{lf.}$ (ee: electron-electron-interaction, so: spin-orbit coupling and lf: ligand field).

According this series we expect for a chemical bonded Ln-ion similar behaviour such as for free-ions. That was at least longer time the assumption. Often, is the ground state of Ln^{III} (Dy: $4f^9$, $^6H_{15/2}$) enough for magnetic interpretation. In our system we exchanged the *para*-cyanobenzoate wit *meta*-cyanobenzoate (both have different Mulliken charges, electric dipoles, Hammet constants…etc).

All these values are actually related to each other and related finally to electron negativity which defines the inductive and mesomeric effects. The change in the electron nature of the ligand will influence $H_{lf.}$. However, the change of the dipole moment is may be the most dramatic in comparison with the other factors.

The change of substituent to *meta*-position means also significant change in the dipole moment. The vector of the dipole moment tells if the electron density is moving in the direction of the carboxyalate oxygens or out from them. If this vector can reorient, when a magnetic field is presence? is an open question. The change then could be understood as follow: smaller dipole moment means stronger withdrawing effect (*para cyano*) and as result the vector of dipolmoment is oriented straightforward out of the aromatic ring. Crystal field rotates some how and the H_{lf} becomes more effective against H_{ee}. If H_{ee} is weaker, this will change the electron density distribution of the 4f-orbitals as we saw from the theoretical aclculations. Fe-Nuclea can feel that (because of dipolar interaction) and this lead to different grades of zeeman-splitting. This interpretation is in line with all observed results.

Another interpretation which might be also in line with first one is suggested by my collabortor Dr. Valeriu Merecare as follows.

General Interpretations

From the analyses of the *ac* magnetic data of *para* and *meta* cyano compounds its seems that, one can give a straightforward explanation for these different effective magnetic fields on iron nuclei. *ac* susceptibility measurements show that if in case if *p*-CN complex the blocking temperature for the relaxation of magnetisation is ~ 3 K (at 1500 Hz), then in case of *m*-CN complex - no maxima in *ac* measurements. Only applying a *dc*-field one could shift the blocking temperature to higher values. Analysing these results one can conclude that in dependence on the position of CN groups in benzoic ring there is different relaxation of the dysprosium moments and, respectively, stronger or weaker magnetic interaction with the iron nuclei. Because of their different time windows, ^{57}Fe Mössbauer spectroscopy and *ac* magnetic susceptibility measurements provide an apparently different view of the relaxation dynamic. Specifically, the characteristic measuring time for Mössbauer spectroscopy is ~10^{-8} s, whereas that for *ac* magnetic susceptibility measurements is often ~1 s., but here emerges a question: - Why when a *dc* field is applied in *ac* measurements the slowing down of the relaxation is observed, but in Mössbauer spectra the sextets are vanishing? A reasonable reason may lye in the super exchange mechanism: in the ground state the two *p* electrons of O^{2-} (of three oxygen ions between dysprosium and iron (all three oxygen ions are lying on the opposite side to the benzoates)) remain in the 2*p* shell of oxygen. Changing the position of CN group from *meta*- to *para*-position there is stronger electron-withdrawing effect, the electron flux density on Dy (see also Fig. 2.67 from theoretical calculations) ions is shifted in direction of CN-benzoates which results in a stronger asymmetric anisotropy on Dy ions and a poorer electron density on opposite side of the dysprosium nucleus. Given that the low energy state of the oxygen ion is a superposition of the ground state O^{2-} and of a small portion of excited state O^{-}, the excited state O^{-} (which is long-lived in comparison to Mössbauer time scale) may be achieved by the jump of one 2*p* electron to the empty 6*s* orbital of dysprosium ion. The remained *p* electron will polarize the electronic cloud of the antiferromagnetically coupled iron ions. The polarization effect will depend strongly on amount of spin of 6*s* electron on dysprosium: stronger withdrawing effect, more 6s electron spin on dysprosium, more remained free spin on 2*p* orbitals, and, respectively, bigger polarization of electronic cloud of iron nuclei. We can assign the field produced by this polarization as H_F (so called Fermi contact interaction). When we apply an external magnetic field (although in ac measurements an increase of the blocking temperature is observed), the magnetic onsets in spectra of both compounds vanish with increasing field and the Mössbauer spectra at high fields exhibit patterns typical of a diamagnetic complex. If the explanation by a superexchange mechanism is correct, then the vanishing of the magnetic spectra is because the hyperfine field due to the Fermi-contact term is opposite in sign to the applied field and H_{eff} decreases with increasing H_{appl}.

In the other families studied before [14, 16-18] the change in the magnetic properties was always connected with a change in the structure or/ and clear change in the *dc* susceptibility. This is the first compeartive study of a 3d/4f system. Morover, this srudy presents the highest number of family members.

Spin-Hamiltonian calculations on Fe_6Dy_2 Compound **2.26**

These calculations were done in collaboration with Dr. Nicola Magnani.

Fig. 2.69 shows an attempt to reproduce the low-temperature susceptibility curve of **2.26**. We model the cluster as a diamagnetic Fe_4 core bridging two non-interacting ferromagnetically coupled Fe-Dy dimers; our assumption is that the S = 0 ground state generated by the dominant antiferromagnetic wing-body interaction of this “butterfly” core is well isolated and is the only populated state at low temperature, where the “peak” behaviour is observed. For this reason our investigation is limited to the temperature range below 10 K. Both the Dy and the Fe ions are treated as ½ pseudospins; the best results are obtained assuming a ferromagnetic Ising coupling, with an effective Hamiltonian including the exchange and Zeeman contributions:

$$H = -2J\left(S_{\mathrm{Dy}}^{(z)} S_{\mathrm{Fe}}^{(z)}\right) - \mu_B B_z \left(g_{//}^{\mathrm{Dy}} S_{\mathrm{Dy}}^{(z)} + g_{//}^{\mathrm{Fe}} S_{\mathrm{Fe}}^{(z)}\right)$$

The best fit is obtained with $g_{//}^{\mathrm{Dy}} = 20.5$, $g_{//}^{\mathrm{Fe}} = 2.0$ and J = -12 cm^{-1}. It is interesting to notice that a significant anisotropy is present on both ions but is markedly easy-axis for Dy and easy-plane for Fe, since the g factor for Dy is very close to that of a pure ±15/2 doublet and that of Fe indicates that the ±1/2 doublet is the ground state. Remarkably, this simple model does not only reproduce the increase of χT with decreasing temperature typical of ferromagnetically-coupled centres, but also the subsequent sharp decrease, which is attributed to a depopulation effect of the coupled-system first excited level.

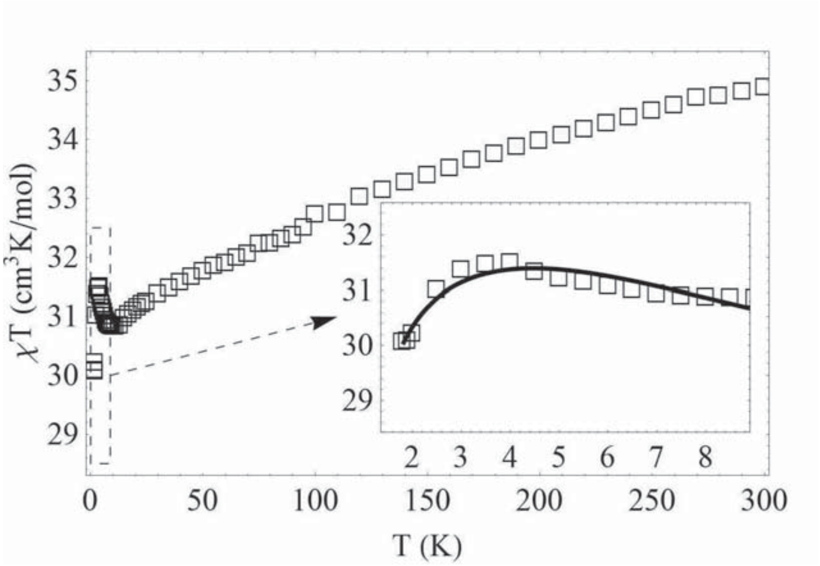

Fig. 2.69 Temperature dependence of the susceptibility of **2.26** (in terms of χT vs T). The inset shows the experimental data (squares) compard with the spin-Hamiltonian calculations discussed in the text (line).

2.6 EPR Spectroscopy

*The reference system (**2.6, 2.8 and 2.13**)*

The EPR studies were done in collaboration with Dr. Andrey Sukhanov and Prof. Violeta Voronkova (Institution of the Russian Academy of Sciences Kazan Russian Federation).

Analysis of the EPR spectra of Fe_2Y_2 (**2.13**) indicated that the major contribution to the signals arises from the transition in the excited multiplet with S=2 (Fig. 2.70).

The change in the simulated spectrum for J=-6.5cm^{-1} at decrease of the temperature conforms to the experimentally observed temperature dependence of EPR spectra. Simulated spectrum of Fe_2Y_2 for parallel –mode with same parameters D_{Fe} = -0.266 cm^{-1}, E_{Fe}= 0.044 cm^{-1}, g=1.98 also it satisfactorily conformed to experimentally spectrum, that certified accuracy selected parameters. Using obtained values of D_{Fe}, one can estimates $D_{S=1}$=1.33cm^{-1} for Fe_2 dimer fragment.

Fig. 2.71 shows the EPR spectra of compound Fe_2Gd_2 **2.6** at several temperatures. The low temperature spectrum corresponds to the spectrum expected for Gd^{III} in agreement with the results of magnetic and Mössbauer (isotropic) measurements as well as the theoretical calculations, according to which the ground state of Fe_2Gd_2 cluster corresponds to a state with two isolated S=7/2 contributions and/or also ferromagnetic interaction with Fe^{III} centres.

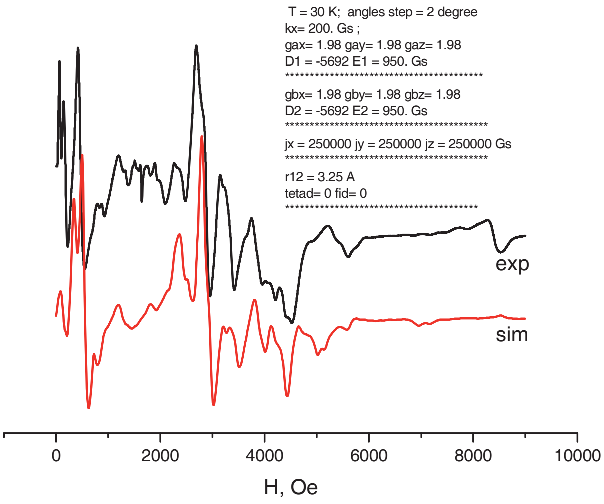

Figure 2.70. Experimental (black) spectrum of compound Fe_2Y_2 in X-band at T=30K and simulated spectrum (red) of Fe(III)-Fe(III) dimer with $S_1=S_2=5/2$, J = -6.5 cm^{-1}, D_{Fe} = -0.266 cm^{-1}, E_{Fe}= 0.044 cm^{-1}, g=1.98. Dipole-dipole contribution was taken into account using the model of point dipoles for R=3.25 A.

Some changes in the spectrum on increasing temperature cannot be explained as a simple overlay of spectra arising from excited multiplets of dimer fragment, but rather indicate the presence of weak exchange and dipole-dipole interactions between the Fe^{III} and Gd^{III} ions.

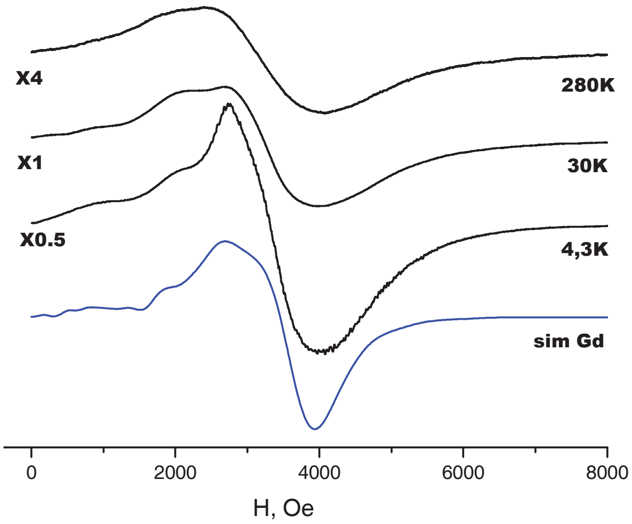

Figure 2.71. EPR spectra of Fe_2Gd_2 cluster **2.6** at X-band at various temperatures. Spectra are shown with different relative gain values given on the left. The simulated spectrum (blue trace) for a single Gd^{III} ion with S=7/2, D=0.037 cm-1, E=0.0033 cm^{-1} gives a satisfactory fit to the low temperature spectrum of compound **2.6.**

The interaction of the Ln ions with the excited states of the dimeric fragment was manifested more clearly in the EPR spectrum of the reference compound Fe_2Dy_2 **2.8**$^{\textbf{teaH-}\textit{\textbf{6pH}}}$.

The temperature dependence of the EPR spectrum (Fig. 2.72) allowed us to attribute these signals to the transitions between the excited states for the Fe_2Dy_2 system. In the absence of the interaction between Dy^{3+} and Fe^{3+} ions the excited states correspond to the multiplet with the spin S=1 of the dimeric fragment Fe_2: the $\psi_{1,\pm1},\psi_{1,0}$ states, the splitting between which is about 1.33 cm^{-1} (for simplicity, the term *E* is neglected).

The exchange and dipole-dipole Fe-Dy interactions in the Fe_2Dy_2 cluster can be described as:

$$\mathrm{H} = -j_0(\mathbf{S}^{\mathbf{Fe1}}\mathbf{S}^{\mathbf{Dy1}} + \mathbf{S}^{\mathbf{Fe1}}\mathbf{S}^{\mathbf{Dy2}} + \mathbf{S}^{\mathbf{Fe2}}\mathbf{S}^{\mathbf{Dy1}} + \mathbf{S}^{\mathbf{Fe2}}\mathbf{S}^{\mathbf{Dy2}}) + (\mathbf{S}^{\mathbf{Fe1}}\mathbf{D}_{\mathbf{dip}}^{\mathbf{Fe\text{-}Dy}}\mathbf{J}^{\mathbf{Dy1}} + \mathbf{S}^{\mathbf{Fe1}}\mathbf{D}_{\mathbf{dip}}^{\mathbf{Fe\text{-}Dy}}\mathbf{J}^{\mathbf{Dy2}} + \\ + \mathbf{S}^{\mathbf{Fe2}}\mathbf{D}_{\mathbf{dip}}^{\mathbf{Fe\text{-}Dy}}\mathbf{J}^{\mathbf{Dy1}} + \mathbf{S}^{\mathbf{Fe2}}\mathbf{D}_{\mathbf{dip}}^{\mathbf{Fe\text{-}Dy}}\mathbf{J}^{\mathbf{Dy2}})$$

Where S^{Dyi} is the operator of the spin moment of the Dy ions, the dipole-dipole Fe-Dy interactions are presented in the local coordinate systems.

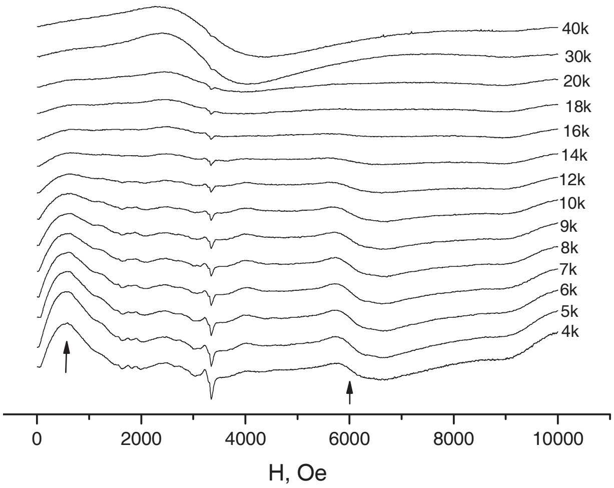

Figure 2.72. Temperature dependence of EPR spectra of compound Fe_2Dy_2 **2.8** in X-band.

The Hamiltonian (above) can be expressed in terms of the effective S_{Dy}^{eff} spins which describe the ground doublet $|J,\pm J_z>$ of the Dy ions, thus only the terms with S_{ZDy}^{eff} are taken into account. The interactions in are weaker than the Fe-Fe interaction in the Fe_2 fragment and after the transition to the effective spin was calculated in the basis of the $\psi_{1,\pm1}^{\pm\pm},\psi_{1,0}^{\pm\pm}$ and

$\psi_{1,\mp1}^{\pm\pm},\psi_{1,0}^{\pm\pm}$ states which are presented as a direct product of the $|S,M>$ states in the Fe$_2$ fragment and the spin projections of S_{ZDy}^{eff}.

In this notation the subscripts are the spin S and its M projection for the *d-d* moiety, while the superscripts denote the sign of the projections related to the $\pm J_z$ doublets on the individual Dy ions of the *f-f* fragment. Such a function corresponds to the product of the Heisenberg Hamiltonian states on the Fe$_2$ fragment and the two individual Dy components: $\Psi_{S,M}^{Jz1,Jz2} = \left|S,M\right\rangle \cdot \left|J,J_{z1}\right\rangle \cdot \left|J,J_{z2}\right\rangle$

For the convenience of calculation of the dipole interaction, the $\psi_{1,\pm1},\psi_{1,0}$ states were expressed as a products of the spin projections of S_Z^{Fe1} and S_Z^{Fe2}. The calculations show that the energies of the $\psi_{1,\pm1}^{\pm\pm}$ and $\psi_{1,\mp1}^{\pm\pm}$ states differ by ±10 ($-j_0(g_J-1)+D_{dip}^{'Fe-Dy}$) with respect to $\psi_{1,\pm1}$. The signal at H~500Oe indicates that the splitting between the $\psi_{1,\pm1}^{\pm\pm}$ and $\psi_{1,0}^{\pm\pm}$ or $\psi_{1,\mp1}^{\pm\pm}$ and $\psi_{1,0}^{\pm\pm}$ states is approximately equal to the r.f. quantum, i.e., 0.33 cm^{-1}. The calculation of the dipole-dipole contribution $D_{dip}^{'Fe-Dy}$ allows us to estimate j_0~-0.03 cm^{-1}.

EPR of para-cyano Fe$_2$Dy$_2$ and meta-cyano Fe$_2$Dy$_2$

Since we now have an EPR reference study for **2.8$^{\mathbf{teaH\text{-}6pH}}$**, so the spectra can be compared with other Fe$_2$Dy$_2$ compounds in order to confirm the differences obtained from the magnetic and Mössbauer studies. Interesting would be (as an example) to see the EPR spectra of the compounds **2.8$^{\mathbf{teaH\text{-}6\mathit{p}CN}}$** and **2.8$^{\mathbf{teaH\text{-}6\mathit{m}CN}}$**. On one hand, these two are great examples according to the sensitivity of substituent effects. Both have the same substituent but one is in *para* and the other in *meta* positions. On the other hand, they show significant differences of magnetic and Mössbauer data. In addition, the theoretical calculations show significant differences between the *para-* and *meta*-cyano benzoates.

The EPR spectra of **2.8$^{\mathbf{teaH\text{-}6\mathit{p}CN}}$** and **2.8$^{\mathbf{teaH\text{-}6\mathit{m}CN}}$** show indeed significant differences (Fig. 2.73, both perpendicular B1and Bo and parallel (B1//Bo) polarization).

We calculated the EPR spectra at low temperature (4 K) as spectra of two Dy-ions taking into account dipole-dipole interactions. The calculated spectra depend on value of the g-tensor and the angle Q between Dy-Dy direction and axis of anisotropy (g_z). The analysis showed that angle Θ is important, but there is some uncertainty in the choice of parameters. For the simulation the same agreement can be obtained with two different values of the angle. For the simulation of the experimental spectra of **2.8**$^{\mathbf{teaH\text{-}6pCN}}$, the parameters $g_x=g_y=0.1$, $g_z=19.8$, r (Dy···Dy distance)= 6Å and Θ= 62(48)° were chosen. For compound **2.8**$^{\mathbf{teaH\text{-}6mCN}}$ different parameters were taken; $g_{□}$= 19.5, g_{per}= 0.1, r (Dy···Dy distance)= 6Å and Θ= 40(73).

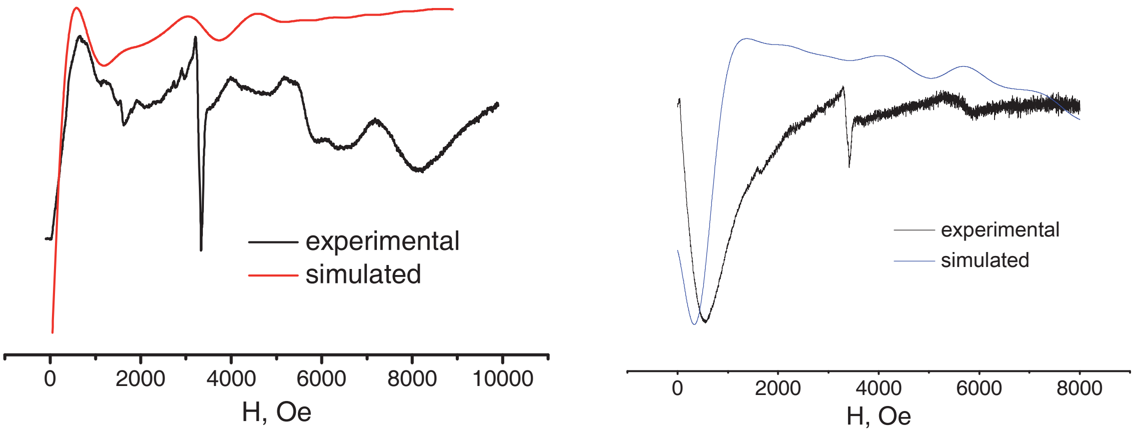

Fig. 2.73. X-band EPR spectra, per-mod (experimental and simulated) of *para* cyano Fe_2Dy_2 compound **2.8**$^{\mathbf{teaH\text{-}6}\boldsymbol{p}\mathbf{CN}}$ (left) and meta cyano one **2.8**$^{\mathrm{teaH\text{-}6}m\mathrm{CN}}$ (right).

*EPR study on compounds **2.17-2.19***

The temperature dependence of EPR of **2.19** is presented in Fig. 2.74 (Upper, left). The observed spectrum corresponds to a Fe^{III} monomer with S=5/2, D=0.33, E=0.074, and can therefore be attributed to the trinuclear fragment. Only very small signals in the low field which can be detected at 30-60K at high gain correspond to the Fe^{III} in the tetranuclear $\{Fe_2Y_2\}$ fragment.

The temperature dependece of **2.17** is presented in Fig. 2.74 (Upper, right). These spectra correspond to Gd spectra which are split by its fine structure and by the dipole-dipole interaction. This range covers the spectrum of the iron ions as more intense. The temperature dependence of intensity of **2.17** is well described by the Curie law.

The temperature dependence of **2.18** is presented in Fig. 2.74 (Lower, left). The experimental temperature dependence of intensity has a maximum at 8-9K and decreases around 10K. The simulated temperature dependence of the spectrum of Dy_2Fe fragment with exchange interaction between Dy and Fe (J = 2 cm^{-1}) is presented in Fig. 2.74 (lower, right). The simulated spectra are similar to experimental spectra but there are some differences. The intensity of simulated spectrum has maximum at 10K and decreases at 15K. These data indicate the presence of exchange interaction between Fe^{III} and Dy^{III} ions.

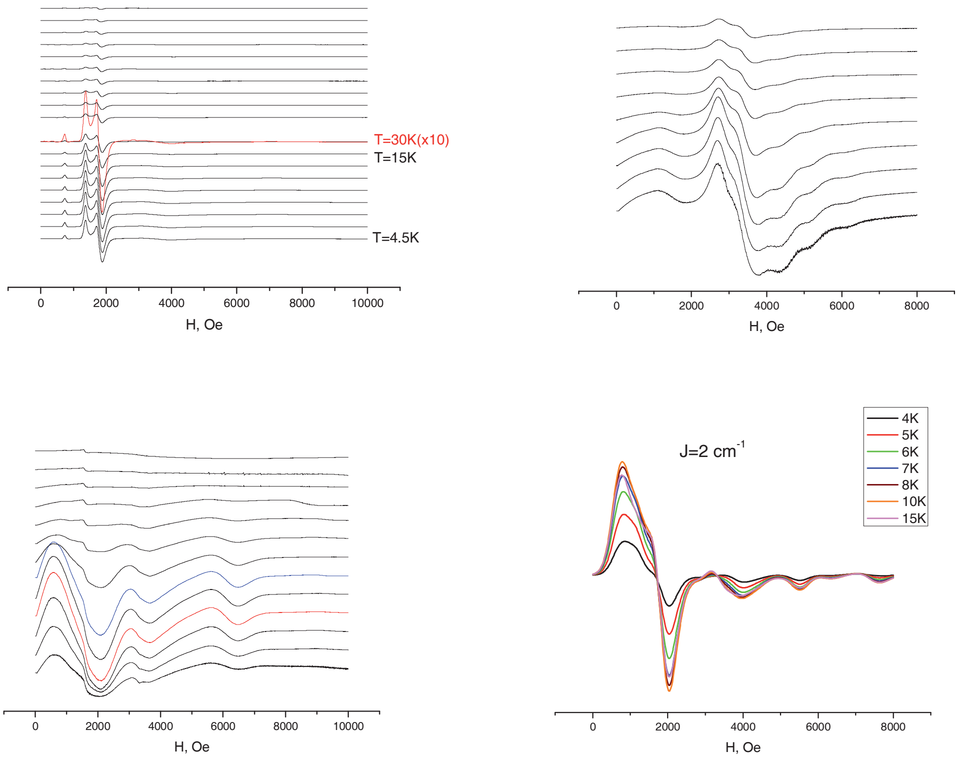

Figure 2. 74. (Upper) Temperature dependence spectra of **2.19** (left) and **2.17** (right). (Lower) Temperature dependence EPR spectra for **2.18** (left) and simulated for Dy_2Fe fragment (right).

2.7 Conclusion

An assumption was made that the electronic nature of substituent could influence the magnetic anisotropy. In order to prove this, a Fe_2Ln_2 cluster system was chosen as reference coordination cluster system, for two basic reasons: on one hand, this cluster type with its defect double cubane core is stable; on the other hand, it was possible to prepare it with the whole lanathanide series. In addition, the unsubstitued benzoate ligand could be replaced; furthermore, most Fe_2Dy_2 compounds crystallize in same space group P-1 and the distances and angles are very similar.

The trinuclear starting materials were prepared first, and then reacted with ligand and dysprosium (III) salts (mainly nitrate). Forming of other products was mostly controlled. In total, more than 25 Fe_2Dy_2 compounds with triethanolamine or Me-triethanolamine could be prepared and structurally characterized. Magnetic and Mössbauer measurements were carried on most of the compounds in this cluster family; EPR measurements were done for some of these compounds in order to improve the understanding of observed results. In addition, theoretical calculations were done for compounds in the reference series and others in order to understand the role of substituents on the behaviour.

The *dc* and magnetization data confirm that antiferromagnetic coupling is dominant and the data are very similar. However, the SMM behaviour is remarkably different and follows a trend, which in general indicates that, substituents with electron donating nature influence the SMM behaviour in a different way than those with withdrawing effect.

The Mössbauer measurements yield a phenomenological effect, where the slow relaxation can be observed as sextets as a result of the interaction of the anisotropic Dy^{III} and the ^{57}Fe nuclei. A clearer trend is observed here, in that substituents with withdrawing effect lead to higher internal field and those with electron donating to lower than the reference compound with six unsubstituted benzoate ligands.

Generally, a correlation between magnetic study and Mössbauer study is observed; however, the different natures of both methods and in particular their different time scales leave many incongruences which require further investigations. The EPR measurements, on the other hand, support and confirm the results obtained from magnetic and Mössbauer studies.

Attempts to isolate new “test-bed” systems were successful, but at the same time they have serious limitations with respect to the Fe_2Ln_2 system studied in this work. This confirms our assumptions that, indeed, this system is an excellent one for a systematic study.

Finally, this extensive systematic study was done with the aim to put the attention of researcher in this field on the importance of ligand field even for lanthanides in order to make a step forward towards obtaining SMMs with realistic applicative potential.

Chapter 3

Fe^{III}-Ln^{III} Cyclic Coordination Clusters

3.1 Introduction

In chapter 2 the use of triethanolamine and related amino alcohol ligands to capture a tetranuclear and previously reported **$\{Fe_2Ln_2\}$** coordination cluster core motif was described. The aim there was to use this core motif as a stable building-block element within the reaction system and to vary the ligand shell characteristics in order to judge whether there really is any subtle influence from electronic effects of substituents on the organic peripehery of the encapsulating ligands in the shell surrounding the coordination cluster. Indeed, this proved to be the case, as gauged by using Dy^{III} ions as sensors for transmitted electronic effects delivered to the Fe^{III} ions and which could be "read" using Mössbauer spectroscopy. For example, the electronic effect of changing substituents on the benzoate ligand coordinated to Ln^{III} centre was found to correlate with the blocking temperature of the magnetisation, as determined from Mössbauer spectroscopy, as well as the degree and sign of coupling between the Fe-Ln centres.

On the other hand, these types of ligands also have the ability to stabilize cyclic coordination clusters as is known from the literature and discussed before in **chapter 1**. This ability comes mainly from their flexible arms which, in addition to chelating to a central metal ion, can bridge between any two metal ions and can help to complete the coordination spheres of these ions.

There are several reasons why it was assumed that it is possible to control the self-assmebly process and to form cyclic complexes based on the synthetic strategy to form **$\{Fe_2Ln_2\}$** clusters as outlined below.

The fact that the syntheses of $\{Fe_2Ln_2\}$ (**2.1-2.13**) compounds using triethanolamine (which are excellent to form cyclic clusters) can also lead to a second product which is $[Fe_8O_3(O_2CR)_9(tea)(teaH)_3]$ (**2.16**) (With Fe_2 pair in the middle of non-flat Fe_6 disk-like) cluster (Fig. 2.2), and which cannot necessarily be obtained for all systems if the lanthanide salts are omitted. This suggests that other mixed iron-lanthanide products might form in the series between the metastable tetranuclear **{Fe_2Ln_2}** and the octanuclear homometallic {Fe_8} systems.

The fact that triethanolammonium nitrate salt can be formed might be an indication for the role of the lanthanide salt. Evidence for this is provided by the compounds with central triethanolammonium ions in the **{Fe_5Ln_3}** rings described in this chapter.

The fact that an {Fe_8La_6} (**2.14**) and a {Fe_4Lu_2}(**2.15**) clusters are obtained using the synthetic procedure for the **{Fe_2Ln_2}** series indicates that the lanthanide size and even the stability of the tetranuclear core can be important structure-directing factors.

Seven synthetic factors can perturb the system and make it possible, mostly for the last three of the lanthanides, to counter the stability of the tetranuclear and octanuclear systems and make it possible to access a number of new cyclic Fe-Ln complexes. These synthetic strategies can be sumarized as follows.

> i) Exchanging the lanthanide nitrate salts in the **{Fe_2Ln_2}** synthesis strategy with others such trifluoromethanesulfonates and at the same time testing the sensitivity of different lanthanides on this exchange. This yields three octanuclear cyclic **{Fe_5Ln_3}** **(Ln= Tm (3.1), Yb (3.2) and Lu (3.3)**) supramolecular complexes.
>
> ii) Replacing the ligand triethanolamine in the **{Fe_2Ln_2}** synthesis strategy with related ligands such 1-[*N*,*N*-(2-hydroxyethyl)amino]-2-propanol (Me-teaH_3) which yields four cyclic hexanuclear **{Fe_4Ln_2} (Ln= Er (3.4) ,Tm (3.5), Yb (3.6), Lu (3.7))** or else with trisisopropanolamine to give three dinuclear **{Ln_2} (Ln= Tm (3.12), Yb (3.13) and Lu (3.14}** compounds.
>
> iii) A combination of both of these yield four pentanuclear **{Fe_3Ln_2}(Ln= Er (3.8), Tm (3.9), Yb (3.10) and Lu (3.11)**) cyclic compounds.
>
> iv) Furthermore, the replacement of the benzoate trinuclear starting material with acetate in order to obtain a non-aromatic **{Fe_2Ln_2}** yielded however six 20-membered cyclic **{$Fe_{16}Ln_4$} (Ln= Sm (3.15), Eu (3.16), Gd (3.17), Tb (3.18), Dy (3.19) and Ho (3.20)**) aggregates.
>
> v) The replacement of triethanolamine with 2-methyl-2-amino-1,3-propandiol in the {Fe_2Ln_2} synthesis can yield a **{$Fe_{18}Dy_6$}** cyclic complex (**3.21**).

vi) The use of 2`-hydroxy-4`-methoxy-acetophenone instead of benzoate as co-ligand yields an octanuclear **{Fe_4Dy_4}** cyclic cluster (**3.22**). In this context, the strategy of exchanging triethanolamine with Me-triethanolamine yields **{$Fe_{10}Ln_{10}$}** cyclic cluster systems which will be discussed separately in chapter 4.

vii) Removing Fe salts and benzoate ligands from the reaction mixture gives three cyclic hexanuclear **{Ln_6}** (compounds **Dy_6-teaH 3.23, Dy_6-Me-teaH, Tm_6-Me-teaH and Ho_6 (3.24-3.26) and Dy_6-amine 3.27**) complexes.

These compounds will be discussed in this chapter, but they are also relevant to the synthesis and properties of the compounds described in chapter 4. In this chapter and in chapter 4 we will see the importance of both steric effects and of chirality in controlling the self-assembly process. The main target of the synthesis these compounds is to check for cooperative effects and compare results from magentic and Mössbauer methods in order to strengthe basic knowlegede about SMM behavior.

3.2 Syntheses and Structures

Fe_5Ln_3, Fe_4Ln_2, Fe_3Ln_2 and Ln_2 ***3.1-3.15***

All crystallographic data of the compounds which will be discussed in this chapter can be found in the appendix.

The first strategy to avoid the metastable traps of both the tetranuclear and the octanuclear cores was indeed successful and the octanuclear {Fe_5Ln_3} cluster system could be isolated. This was achieved by replacing the lanthanide nitrate salts in the {Fe_2Ln_2} synthesis strategy with triflate salts. The strategy was successful for the last three lanthanides. The other lanthanides yielded only the tetranuclear species. All other salts such as acetate, chloride, acetylacetonate and tosylate [82] also yielded the tetranuclear compounds (**1-13**). In addition, an exchange of the ligand from triethanolamine to 1-[*N*,*N*-(2-hydroxyethyl)amino]-2-propanol (Me-triethanolamine) was the second choice yielding {Fe_4Ln_2} rings. Subsequently, a combination of both (using triflate salts of the last four lanthanides and Me-triethanolamine) was also successful in the formation of pentanuclear pentanuclear {Fe_3Ln_2} compounds.

However, replacing the triethanolamine (teaH_3) ligand, with trisisopropanolamine (tipaH_3) in the same synthetic strategy but using triflates, yielded dinuclear compounds $\{Ln_2\}$ and only for the three heaviest and smallest lanthanides (**3.12-3.14**).

A schematic representation is given in scheme. 3.1 in order to simplify the different synthetic strategies. Sometimes, the concentration was slightly varied in order to improve the yield of the product. However, the role of the solvent is limited only for improving crystal quality except in the case of the hexanuclear compounds where methanol as solvent becomes deprotonated and is incorporated into the molecular strcuture.

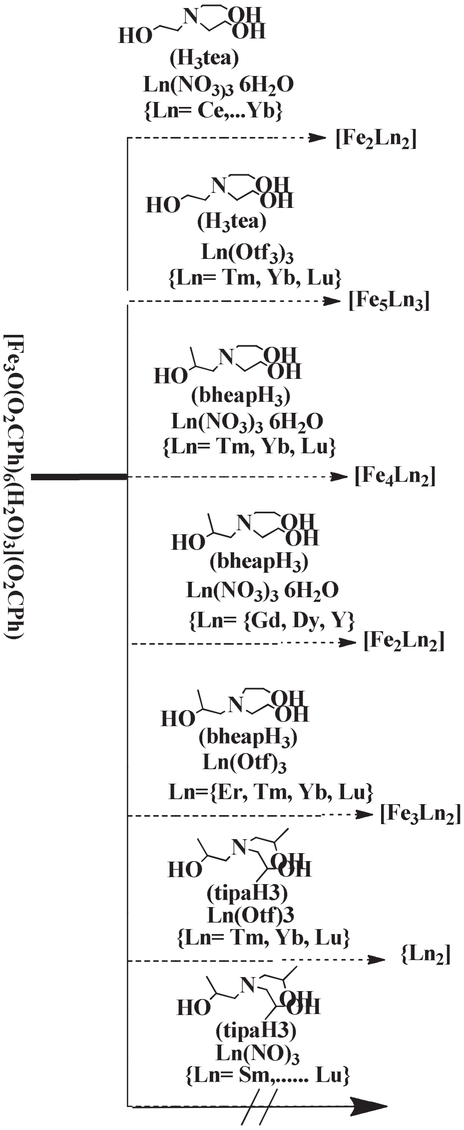

Scheme 3.1. Rrepresentation to the synthetic relation between the tetranuclear cluster systems and the cyclic clusters influenced by choice of either lanthanide salts or the type of triethanolamine ligands or both.

In addition to the known common lanthanide salts, two lanthanide compounds were prepared as in literature and used in place of nitrate salts as starting materials. One is $[Ln(O_2CPh)_3(DMF)]n$ [83] and the other is $[Ln(teaH_3)_2(OTf)_3]\cdot$ 3THF [84].

Only when trifalte salts of the three latest lanthanides (Tm, Yb and Lu) or the trifalte containing $[Ln(teaH_3)_3(OTf)_3]\cdot 3THF$ (method B experimental part) compound were used did the octanuclear compounds **$[Fe_5Ln_3(\mu_3\text{-}OH)(Htea)_7(O_2CPh)_8](CF_3SO_3)\cdot x\ MeCN\ yH_2O$ {Ln= Tm (3.1), Yb (3.2), Lu (3.3)}** form. This shows how it is possible to control the self-assembly reaction by simply using the triflate salts of the smallest lanthanides.

Using triethylamine as base in place of cesium carbonate yields the tetranuclear system. This indicates that possibly the deprotonation of the amine fucntion of the triethanolamine ligand templates the cyclic structure of the $\{Fe_5Ln_3\}$ complexes (**3.1-3.3**).

The influence of triflate salts in these syntheses might arise from two factors:

i) The size of only the last three lanthanides fits with a cyclic cluster such as **Fe_5Ln_3 (3.1-3.3)** and ii) the Lewis acid-base (Ln / OTf) pair in comparison with other Ln-OTf pairs might adjust the pH in this reaction so that only the octanuclear **$\{Fe_5Ln_3\}$** compounds aggregate and not the tetranuclear $\{Fe_2Ln_2\}$ (**2.1-2.13**) or octanuclear $\{Fe_8\}$ **(2.16)**.

The reaction between $[Fe_3O(O_2CPh)_6(H_2O)_3](O_2CPh)$ **(2.sm1)**, triethanolamine or 1-[*N*,*N*-(2-hydroxyethyl)amino]-2-propanol (Me-triethanolamine) and lanthanide nitrate yields a tetranuclear $[Fe_2Ln_2(\mu_3OH)_2$(teaH or Me-teaH$_3)_2(O_2CPh)_6]$ {Ln=early and middle lanthanides}.

The tetranuclear $[Fe_4O_2(O_2CPh)_7(bpy)_2](ClO_4)$ [25] was prepared according to the literature and used as starting material in place of the trinuclear benzoate one [85] However, this yields the tetranuclear $\{Fe_2Ln_2\}$ system without any change.

By replacing teaH$_3$ by Me-teaH$_3$ in the synthesis of the $\{Fe_2Ln_2\}$ (see chapter 2) for the latest four lanthanides the hexanucelar system $[Fe_4Ln_2O(\mu_3\text{-}OH)_2(Me\text{-}teaH)_4(O_2CPh)_7]$ {Ln=Er, Tm, Yb and Lu} **(3.4-3.7)** could be isolated.

The ring structure systems can be obtained in high yield and again the sensitivity is for the three latest lanthanides only. The syntheses is the same like for $[Fe_2Ln_2(\mu_3\text{-}OH)_2(Me\text{-}teaH)_2(O_2CPh)_6]$ {Ln= Nd, Gd, Dy, Y} (see chapter 2) without any change in solvent or conditions and also using the lanthanide nitrates. In this case the difference in ionic radius suffices to stabilise the new cluster types.

Again replacing the lanthanide nitrates by triflate results in a series of $[Fe_3Ln_2(\mu\text{-}OH)(Me\text{-}teaH)_4(O_2CPh)_6]$ {Ln= Er, Tm, Yb, Lu} **(3.8-3.11)** compounds. It was found that small changes in the ratio of reactants (for example, increasing the molarity of the used lanthanide salts, see experimental part) leads to higher yields.

Within each series the compounds crystallize isotypically thus $\{Fe_5Ln_3\}$ **(3.1-3.3)** in the triclinic space group P-1; compounds $\{Fe_4Ln_2\}$ **(3.4-3.7)** in the triclinic space group P-1; compounds $\{Fe_3Ln_2\}$ **(3.8-3.11)** in $P2_1/c$ and the dinuclear compounds $\{Ln_2\}$ (**3.12-3.14)** $P2_1/c$ as well.

The structures of $[Fe_3Yb_2]$ (**3.9**), $[Fe_4Tm_2]$ (**3.4**), and $[Fe_5Lu_3]$ (**3.3**) as well as of $[Yb_2]$ (**3.12**) are shown in Fig.3.1.

Crystallographic data of $\{Fe_5Ln_3\}$ (**3.1-3.3**) are summarized in Tab. 3.1, the data of $\{Fe_4Ln_2\}$ (**3.4-3.7**) in Tab. 3.2, data of $\{\mathbf{Fe_3Ln_2}\}$ (**3.8-3.11**) in Tab. 3.3 and those of $\{Ln_2\}$ (**3.12-3.14**) compounds in Tab. 3.4. All these tables can be found in the appendix.

These four series are obtained using related synthesis as well as being related in several structural aspects. All of them can be described as cyclic coordination clusters. They all contain benzoate as well as triethanolamine or the singly substituted Me-teaH_3 ligand. The fact that using trisisopropanolamine did not form cyclic Fe-Ln cluster can be understood by looking at the brdiging and chelating properties of the triethanolamine and Me-triethanolamine ligands (scheme. 3.1). It is hard for three hydrogens of the alcohol arms of trisisopropanolamine (tipH_3) to be deprotonated, since (and additionally to their steric effect) the +I effect of the methyl groups increases the basicity of the the alcohol groups. This might be the reason why the alcohol-oxygen arm with the methyl group in Me-teaH_3 is mostly chelating and remains protonated.

The pentanuclear $\{Fe_3Ln_2\}$ clusters contain six, the hexanuclear $\{Fe_4Ln_2\}$ seven and the octanuclear $\{Fe_5Ln_3\}$ eight benzoate ligands. In the pentanuclear rings as well as in the hexanuclear rings there are additionally four doubly-deprotonated Me-teaH^{2-} ligands involved in the structure. However, in the octanuclear rings seven doubly-deprotonated teaH^{2-} ligands are involved.

The pentanuclear compounds contain the same number of benzoates as present in the trinuclear starting material. Even if the pentanuclear or hexanuclear ring-clusters are a result of a self-assembly process we can discuss some points which could give a possible mechanistic explanation of how they form (scheme 3.2).

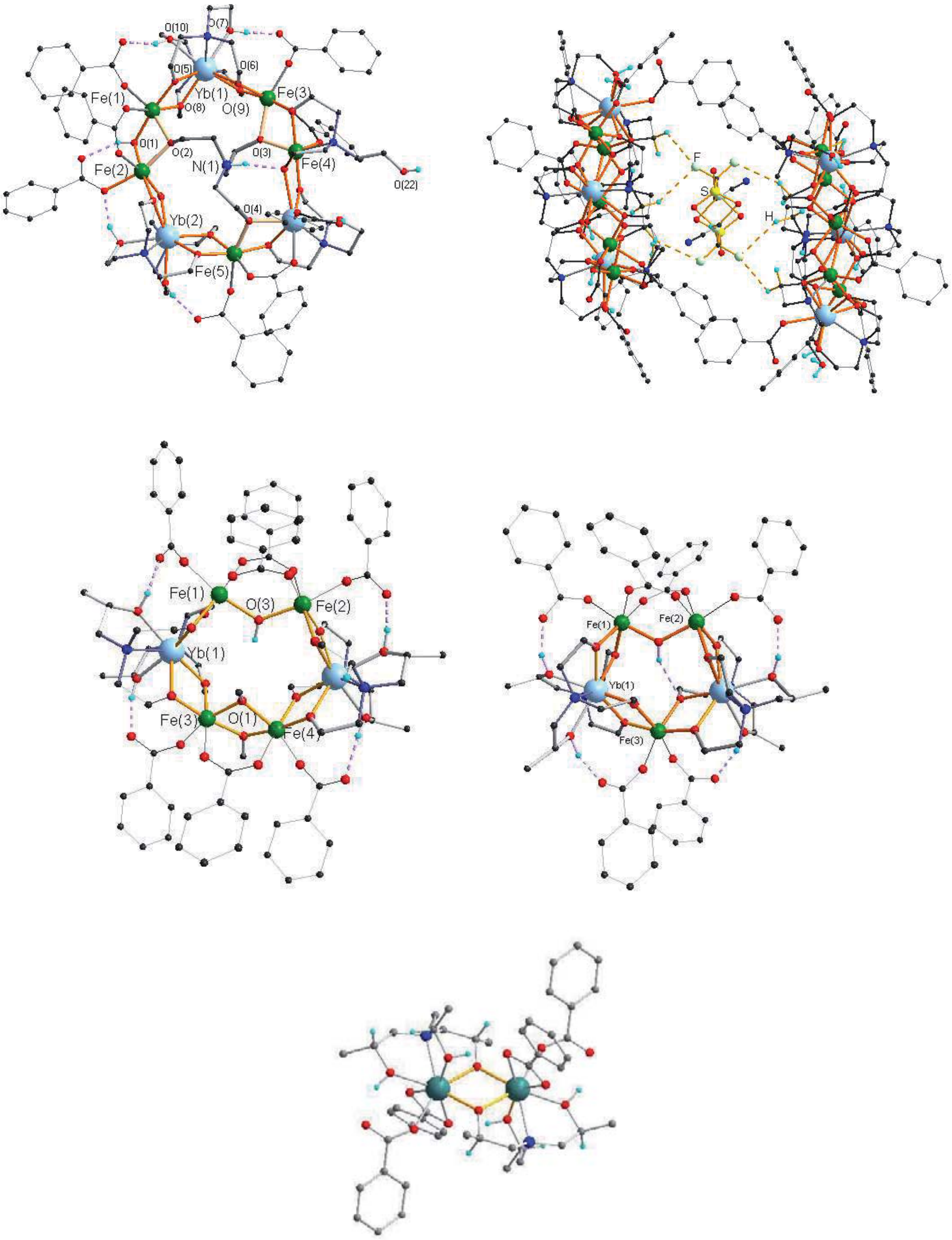

Fig.3.1. (Upper) structures of Fe_5Yb_3 **3.2** and their interaction through triflate ions. (Middle, left) Fe_4Yb_2 **3.6** and Fe_3Yb_2 **3.10** (right). (Lower) Yb_2 **3.12**.

The trinuclear $[Fe_3O(O_2CPh)_6(H_2O)_3]^+$ cation separates into two fragments, the neutral $\{Fe_2O(O_2CPh)_4(H_2O)_2\}$ and cationic $\{Fe(O_2CPh)_2(H_2O)\}^+$. After loss of water molecules two,

$\{(Yb(bheapH))_2\}^{2+}$ units bridge with their alkoxy arms to Fe^{III} ions and complete their coordination spheres. The positions which the $\{Yb(bheapH)_2\}^+$ fill seem to be size-limited, and only fit for the last four lanthanides. The role of the triflate ions could be in balancing the charge which leads in some way to protonation of the oxo-group in the dimer iron fragment leading to a second cationic fragment $\{Fe_2O(O_2CPh)_4(H_2O)_2\}$. This neutralises the charge of the cluster resulting in the neutral pentanuclear ring-compounds (scheme. 3.2).

The hexanuclear $\{Fe_4Ln_2\}$ compounds can be formed from two neutral $\{Fe_2O(O_2CPh)_4(H_2O)_2\}$ units. One of these undergoes the following change. One water ligand becomes a briding hydroxy-group, the other gives a proton to the oxo-group, which becomes the second hydroxyl group. Both hydroxyl groups bridge two irons and one benzoate is ejected resulting in an $\{Fe_2(OH)_2(O_2CPh)_3\}^{+1}$. Again two $(\{Tm(bheapH)_2\})_2{}^{2-}$ units fit between iron fragments forming the hexanuclear clusters. The bridging methoxy results from deprotonation of methanol which is used as solvent in this synthesis.

Both the pentanuclear and hexanuclear systems contain the ligand Me-teaH_3. This ligand is a racemate (50:50 R and S). The above explanation might help in understanding how these compounds could be formed in relation to the starting material. Furthermore, there is possible role of the in situ formed acids corrosponidng to their pKa: super acid triflic acid with pKa -14, strong acid nitric acid with pKa -1.3 and weak benzoic acid with pKa 4.2.[86]

The same reasoning could explain why in case of the teaH_3 and $Ln(NO_3)_3$ tetranuclear clusters for $Ln(OTf)_3$ octanuclear clusters form as well as bearing in mind the relative size of Ln^{III}.

The reason why for Me-teaH_3 different compounds are obtained compared with for teaH_3 may originate from the nature of ligand itself. The fact that Me-teaH_3 is chiral and used as a racemate and that the methyl group increases the basicity of the hydrogen on the chiral alcohol arm seems to be decisive. By carefully looking at the structures of the pentanuclear and hexanuclear systems we can see indeed that the R and S enantiomers of the ligand are present in both structures in equal amounts (scheme. 3.2, lower). This influnces the structural stability because in these two systems the ligand is only doubly (not triply) deprotonated. The orientation of the methyl groups influences the hydrogen bonding resulting from the interactions of the protonated alcohol groups with neighbouring alkoxy oxygens. The influence of the chirality of this ligand becomes more important in the discussion of the structure of the larger $\{Fe_{10}Ln_{10}\}$ system in chapter 4.

It is much harder to follow the mechanistic process in the case of the octanuclear rings because their structures are asymmetric and much more complicated. It is, however, assumed that they are formed in a similar way to the other cyclic ring systems and with similar pH effects arising from the use of different salts. They not only contain a single-Fe^{III} centre as in the case of the pentanuclear complexes, they also contain Fe^{III}_2 units as in case of the hexanuclear complexes.

The overall structure of the $\{Fe_5Ln_3\}$ (**3.1-3.3**) compounds can be described as a ring-aggregate built from two Fe^{III}_2 dimer-units, where one Yb^{III} ion bridges with the iron dimers from one side. Two other Yb- ions bridge with the Fe^{III}_2 units from the other side and with the fifth Fe^{III} ion in the other part of cluster (Fig. 3. 1). In Tab. 3.5a-e the distances and angles between the different metal ions are listed for the octanuclear compounds, in Tab. 3.6 those of the hexanuclear and in Tab.3.7 those of the pentanuclear complexes.

Two triethanolamine ligands chelate to Yb(1) with the amine functions and alcohol arms (O7, O10), respectively. The other alkoxy arms bridge the "isolated" Yb(1) to the iron dimer pairs (Fe(1)-Fe(2) and Fe(3)-Fe(4)) through (O5, O8) and (O6, O9), respectively. The benzoates are all monodentate. ´

The ligation of Fe(1) and Fe(3) is completed by one oxygen (O29, O33) of the benzoate ligands, respectively. The Fe-ions in the Fe_2-units do not have equivalent environments, whereas Fe(2) is not coordianted by triethanolamine at all; Fe(4) alone is chelated by the teaH ligand.

In addition unlike Yb(1) and Yb(2), the Yb(3) alone is coordinated to one triethanolamine as well as benzoate ligands. The Fe(4) metal ion in this structure which does not interact with benzoate ligands.

The sixth coordination position of the irons in the dimer units is completed (through μ_3-O2 and μ_3-O3) and by the oxygen of a bridge between Yb(3) and Fe(5) (μ_3-O4) from the three alkoxy arms of the seventh and the only (N^+(1))-protonated triethanolamine in this structure. However the third alcohol arm of triethanolamine ligand, which coordinates Fe(4) with two alkoxy arms where the third, is not involved in the bridging or chelating. In the molecule there is also intramolecular interaction of the hydrogens with the non-coordinated oxygens of the benzoate ligands. One benzoate and one triflate ion are the ccounter-ions balancing the charge and resulting is a neutral molecule.

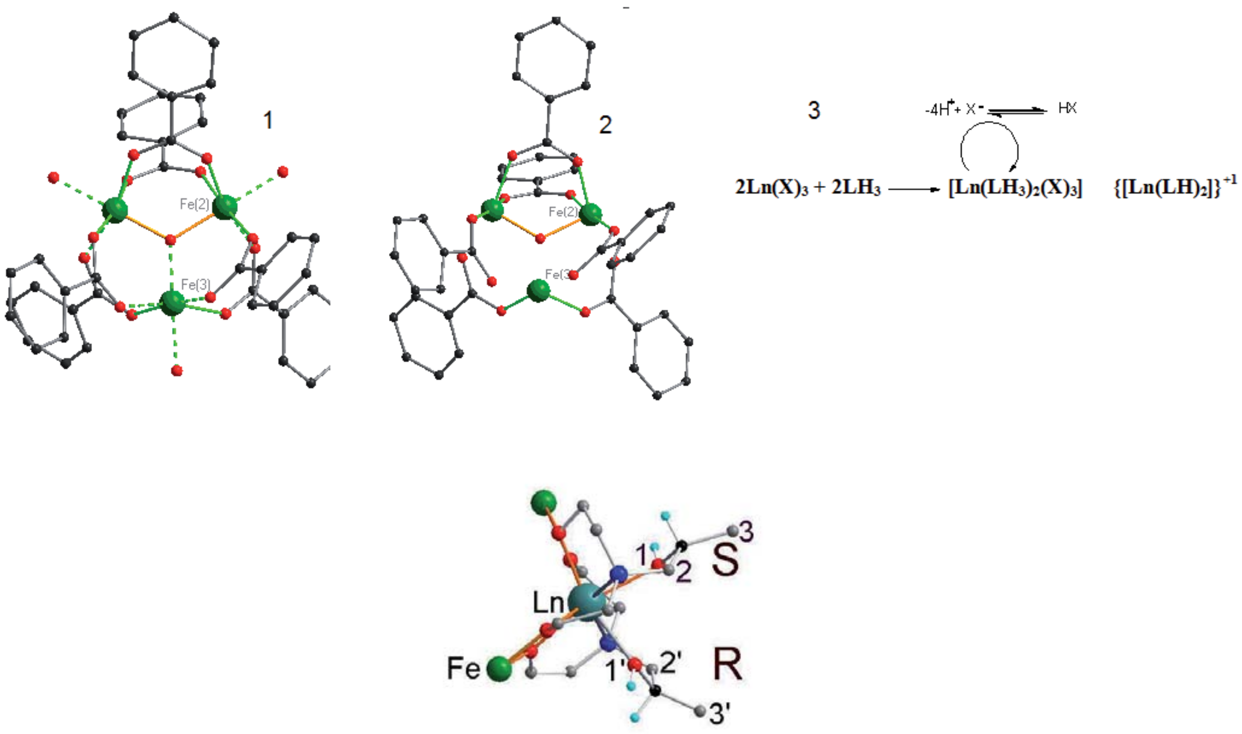

Scheme 3. 2. (Upper) Simple schematic representation of the trinuclear reaction with the ytterbium (III) trilfate and Me-teaH_3 ligand. Step 1 the triangular, splits into two fragments after loss of water. Step 2 a mono unit fragment and a dinuclear fragment as often seen in all ring structures. Step 3 lanthanide salts reacts at same time with the ligands to build the known compounds $[Ln(LH_3)_2(X)_3]$ with X= nitrate or triflate and HL teaH_3 or Me-teaH_3. The “formally” building of the acid HX in solution affects the pH in different ways and this might influence the reaction process. (Lower) the Me-teaH_3 Ligand in the pentanuclear and hexanuclear compounds is one time R and other time S. On the other sides is the opposite.

The larger size of the octanuclear complexes compared with the hexanuclear and pentanuclear ones leads to greater distances between the lanthanide metal ions. The distance between Yb(2) and Yb(3) in **3.2** is ~8.5 Å. and between Yb(1) and Yb(2) in **3.5** is 7.17 Å. However, in the smallest ring is the Yb(1) –Yb(2) distnace ~5.8 Å. The differences in the Fe-Fe distances in particular in the Fe-Fe-Fe triangules of the octanuclear and pentanuclear systems prove to be important for the magnetic and Mössbauer interpretation.

$Fe_{16}Ln_4$ ***3.15-3.20***[36f]

Reaction of $[Fe^{III}_3O(O_2CCH_3)_6(H_2O)_3]Cl·6H_2O$ and $Ln(NO_3)_3·6H_2O$ (Ln = Sm, Eu, Gd, Tb, Dy, Ho) with $teaH_3$ in acetonitrile at ambient temperature yields the heterometallic metallo-ring complexes, $\mathbf{[Fe_{16}Ln_4(tea)_8(teaH)_{12}(\mu\text{-}OAc)_8](NO_3)_4·16H_2O·10MeCN}$ (Ln = Sm **3.15**; Eu **3.16**; Gd **3.17**; Tb **3.18**; Dy **3.19**; Ho **3.20**). Care should be taken not to heat the reaction mixture, as in this case a yellow-orange oil deposits together with the crystals.

Compounds **3.15 – 3.20** are isomorphous, crystallising in the orthorhombic space group *Ccca* with Z = 4 (Table 3.8) such that the asymmetric unit constitutes a quarter of the molecule. Full structure determinations were carried out for **3.16**, **3.17** and **3.19** and the remaining three compounds were shown to be isomorphous from their unit cells and powder X-ray diffraction patterns (data in appendix). The structure of the heterometallic $Fe_{16}Dy_4$ ring cation in **3.19** is described in detail here (Fig. 3.4).

The $Fe_{16}Dy_4$ complex is centred on a Wyckoff *b* site with 222 (D_{2d}) site symmetry (Fig. 3.5). All the metal ions in the complex are chelated by either a $(tea)^{3-}$ or a $(teaH)^{2-}$ ligand. For all of these, two deprotonated oxygens form μ_2-bridges to the two adjacent metal ions, resulting in an $Fe_{16}Dy_4$ ring in which adjacent metal centres are linked by pairs of μ_2-alkoxo bridges. Within the ring, the four Dy centres are situated between two Fe_2 units and two Fe_6 chains, which can be designated as sub-chains.

The Dy centres are also linked pairwise by two *anti,anti*-acetate bridges lying lie on a twofold axis and with Dy(1)···Dy(1˝) 6.8909(4) Å. These two bridges pinch the 20-membered ring into a twisted conformation, giving rigidity to an otherwise floppy system.

Fe(1) and Fe(2) are each chelated by a $teaH^{2-}$ ligand *via* the two deprotonated oxygens and nitrogen. The protonated ethanolic arms of these ligands, O(3) or O(9), do not coordinate, but are involved in hydrogen bonding. The hydrogen bond from O(3) to O(12), shown dotted in Fig. 3.2, is involved in stabilising the ring structure. In contrast, Fe(3) and Fe(4) are both chelated by tea^{3-} ligands. For these ligands, all three deprotonated oxygens coordinate to the iron centres, two forming bridges and the third terminally bonded.

Dy(1) is chelated by a $teaH^{2-}$ ligand, but in contrast to those about Fe(1) and Fe(2) the protonated ethanolic arm is terminally coordinated with O(6) forming a hydrogen bond to a nitrate counterion. Additional peripheral coordination is provided by six *syn,syn*-bridging acetate ligands linking either Fe(2) and Dy(1) or Fe(1) and Fe(1”) with the latter two lying on a twofold axis. The iron centres all have a *quasi*-octahedral NO_5 coordination sphere, while the NO_7 environment of Dy(1) is close to dodecahedral.

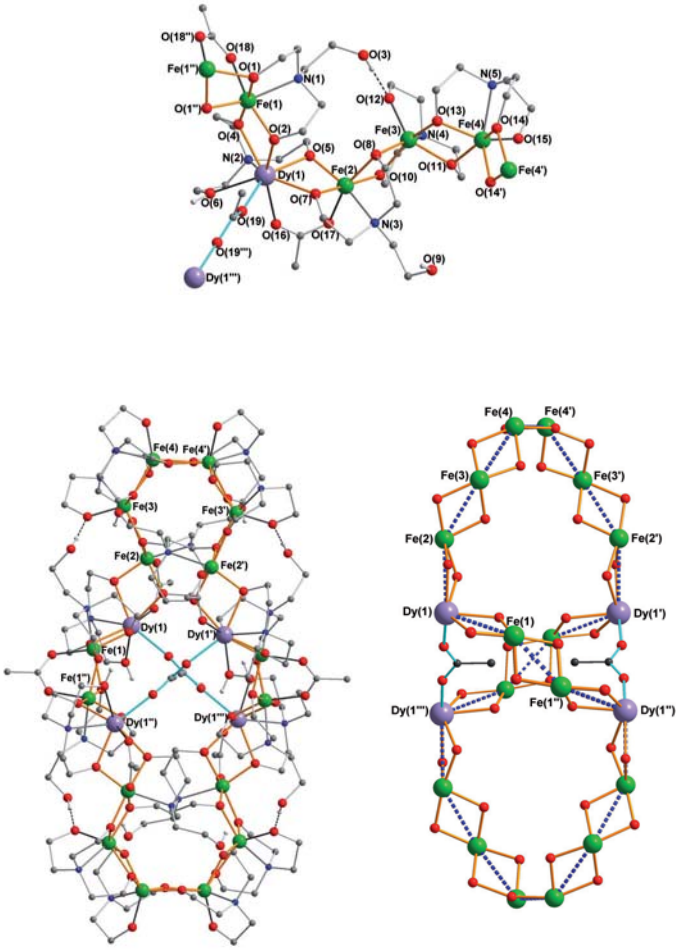

Figure 3.2. Top: The asymmetric unit of the molecule $[Fe_{16}Dy_4(tea)_8(teaH)_{12}(OAc)_8]^{4+}$ in **3.19** (Symmetry codes: ′ 1-x, ½-y, z; ″ 1-x, y, 1½-z; ‴ x, ½-y, 1½-z). Lower left: The complete $Fe_{16}Dy_4$ molecule viewed approximately down the *a*-axis (organic H atoms omitted for clarity). Lower right: The $\{Fe_{16}Dy_4\}$ ring viewed approximately along the *b*-axis with the ring connectivity shown by the dark blue dotted lines. All μ_2-OR bridges highlighted in orange with *anti,anti*-acetate bridges between Dy centres highlighted in pale blue.

As is to be expected from the high site symmetry of the complexes, in the crystal lattice the metallorings are aligned with their principal axes coparallel. The long axes of the molecules are oriented parallel to the crystal *c*-axis (Fig. 3.3). When viewed along the *a*-axis, the Fe_6 sub-chains of adjacent molecules appear to be well aligned, although the molecules themselves are in fact well-separated.

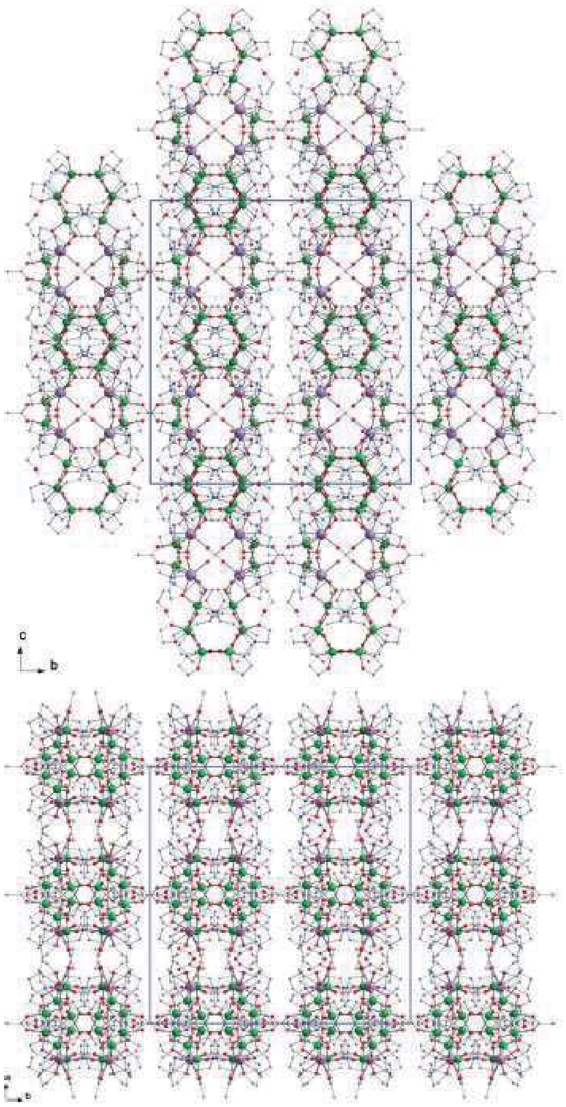

Fig. 3.3. Packing of $Fe_{16}Dy_4$ **3.19** viewed down the a-axis (above) and the c-axis (below).

$Fe_{18}Dy_6$ ***3.21***

The aim from reacting $[Fe_3O(O_2CPh)_6(H_2O)_3](O_2CPh)$ with 2-amino-2-methly-1,3-propandiol ($ampdH_4$) and $Ln(NO_3)_3$ was to isolate a new tetranuclear cluster complex which can be used as a test-bed system and in order to compare with the $\{Fe_2Ln_2\}$ cluster family discussed in chapter 2. This strategy yields indeed in the case of Gd and Y the desired tetranuclear $\{Fe_2Ln_2\}$ (compounds **2.23** and **2.24**) cluster system. However, for Dy the same product could not be isolated. Several synthetic efforts were tried to control the self assembly reaction in order to isolate the Dy analogue. By increasing the molarity of the $Dy(NO_3)_3\cdot 6H_2O$ slightly, one of the options which one can do, from 0.25 mmol to 0.35 mmol, the giant cyclic cluster with the formula $[Fe_{18}Dy_6(\mu\text{-}OH)_6(ampdH)_{12}(ampd)_{12}(O_2CPh)_{24}](NO_3)_6\cdot$ ˜49 MeCN (**3.21**)

(Fig. 3.4) was obtained. This compound was not magnetically investigated or by any other analytic method because of too low yields. Its structure will be, however, discussed in this chapter because of its relation to compounds in chapter 2 and at the same time because it is a large metallacyclic compound. Such a compound should be in future studied in detail as it might have very interesting properties in different areas in chemistry. Furthermore, this compound is presented here, to show that also other related amino alcohol ligands can from cyclic clusters.

The discussion about the slight different between the Gd and Y compounds in chapter 2, might help in understanding that the tetranuclear cluster with 2-amino-2-methyl-1,3-propandiol seems to be by far less table than those with triethanolamine ligands. (See discussion in chapter 2).

Compound **3.21** crystallizes in the orthorhombic space group Pccn. Crystallographic data are summarized in Tab. 3.9 (appendix).

The C···C distances of the benzoates which form the organic shell are ~30.4682 Å. The distances between the Fe---Fe in the molecule from different sides are in the range of 17-19 Å. The benzoate bridge the irons and making a large ligand sphere around the metallic core (see Fig. 3.4, space filling from the top). In addition, they alternate around the core up and down and six of them are oriented perpendicular to the metallic core to form a further cyclic organic shell (see space filling, top). The outer 2-amino-2-methly-1,3-propandiols chelate with their amino function the Dy^{III} centres and the inner ones act as alkoxy ligands, where they bridge between the irons. Through the hydrogen bonds of the inner ligands with the nitrate groups, the Dy centres from a non-planar cyclic fragment. The diameter of the cyclic $\{Dy_6\}$ ring is ~16 Å. The centremost nitrate ring correspond to a hexanuclear cyclic frgament with a diameter taken the N atoms of the nitrates across the motif ~10-10.5 Å.

The amino functions of the inner 12 ligands are protonated and cannot coordinate. Nevertheless, their role is very important in stabilizing the structure as they form hydrogen bonds to the non-chelating nitrate groups. The nitrate groups are also important for two reasons. One is that they balance the charge of the molecule and the other that they further stabilize it through hydrogen bonds to the ligands. The structure can be viewed as a non-planar composition made-up of concentric rings. (Fig. 3.5).

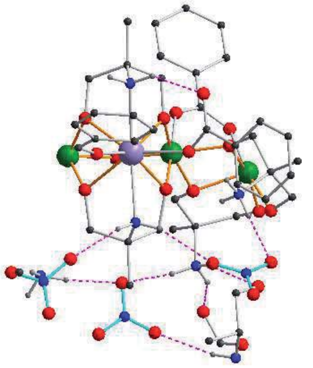

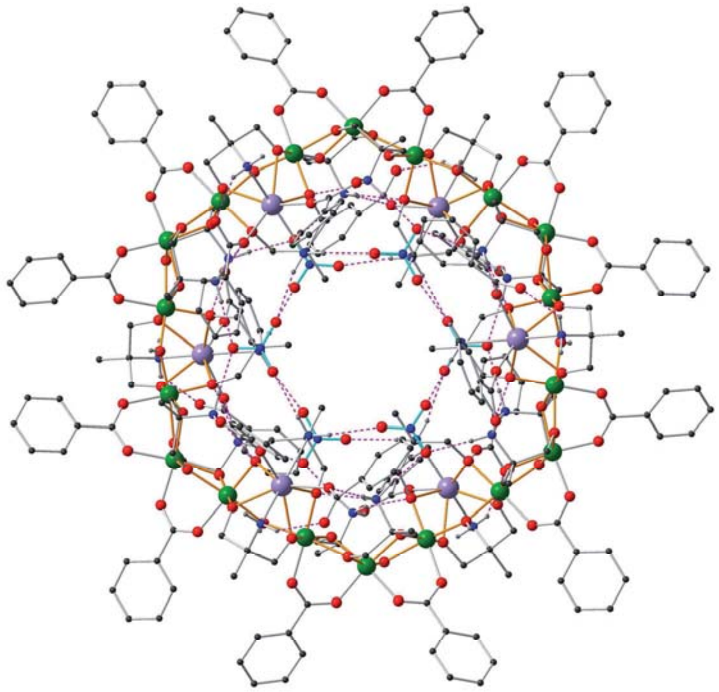

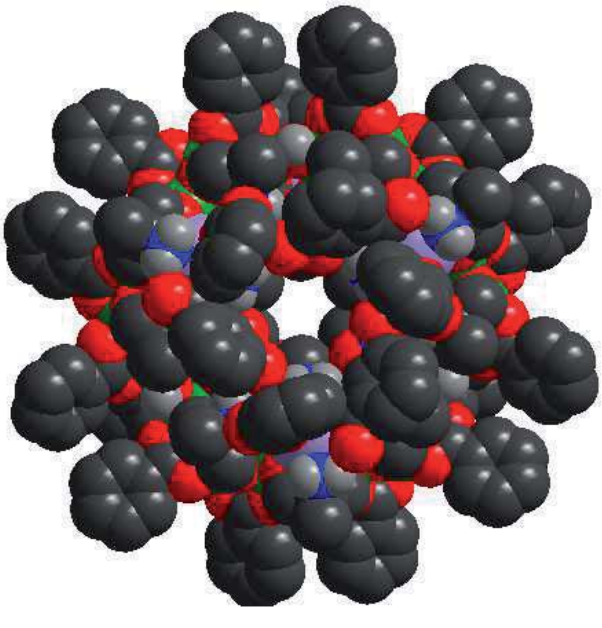

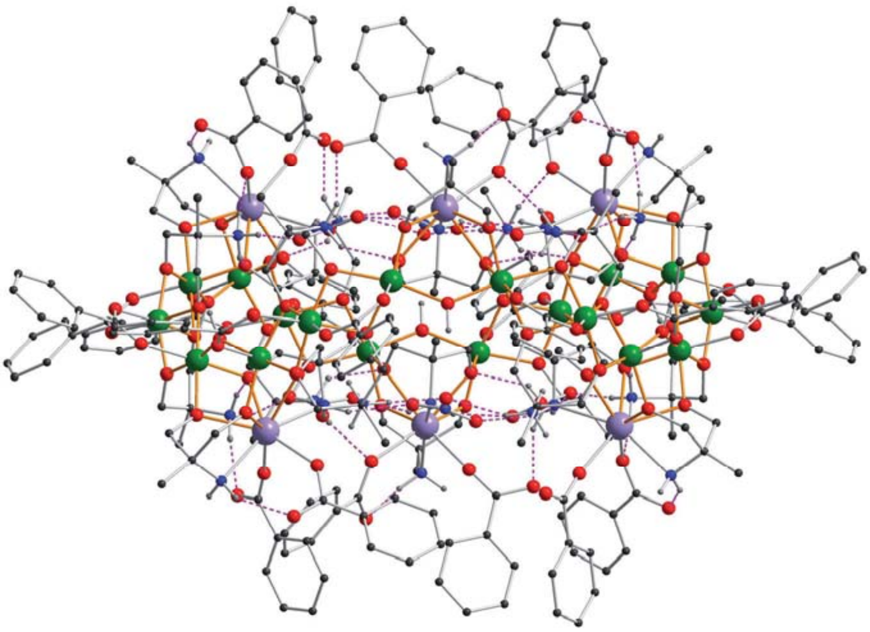

Figure 3.5. (Upper) highlighting the hydrogen bonding and top view $Fe_{18}Dy_6$ (**3.21**) as well as space filling representation**.** (Lower) side view of **3.21**.

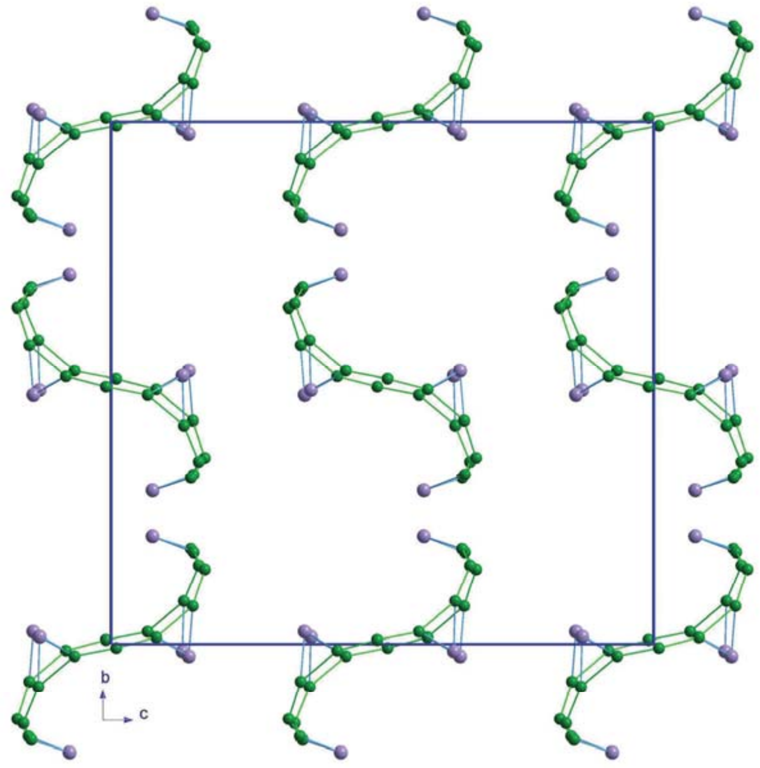

Figure 3.6. Simple presentation of the packing of **3.21**. Here it is clear seen that the ring molecules are not planar. Organic shells and nitrates omitted for clearity.

Fe_4Dy_4 ***3.22***

The reaction of 2`-hydroxy-4`-methoxy-acetophenone (hmacphH) with iron(III) nitrate nonahydrate, dysprosium(III) nitrate hexahydrate and triethanolamine in presence of triethylamine yields a $[Fe_4Dy_4(teaH)_8(O_2CH_3C_6H_3OCH_3)_4(H_2O)](NO_3)_4$ **(3.22)** cyclic aggregate. Recently, our group published the first ferromagnetically coupled Fe-Ln-SMM $[Fe_4Dy_4(teaH)_8(N_3)_8(H_2O)]$ (**3.23**) using triethanolamine, iron(III) chloride and dysprosium chloride, where additionally azido groups monocoordinate on Fe^{III} centers. Each Fe^{III} is coordinated by two azido ligands.[36g)] (see Fig. 3.7)

While **3.23** crystallizes in $P2_1/n$, the **3.22** does in the triclinic space group P-1. The crystallographic data are in Tab.3.9 in the appendix. In compound **3.22** the Fe^{III} centers are instead chelated by one hmacph ligand. The phenol was also deprotonated and the phenoxy-group with the ketone oxygen chelates the Fe^{III} centers.

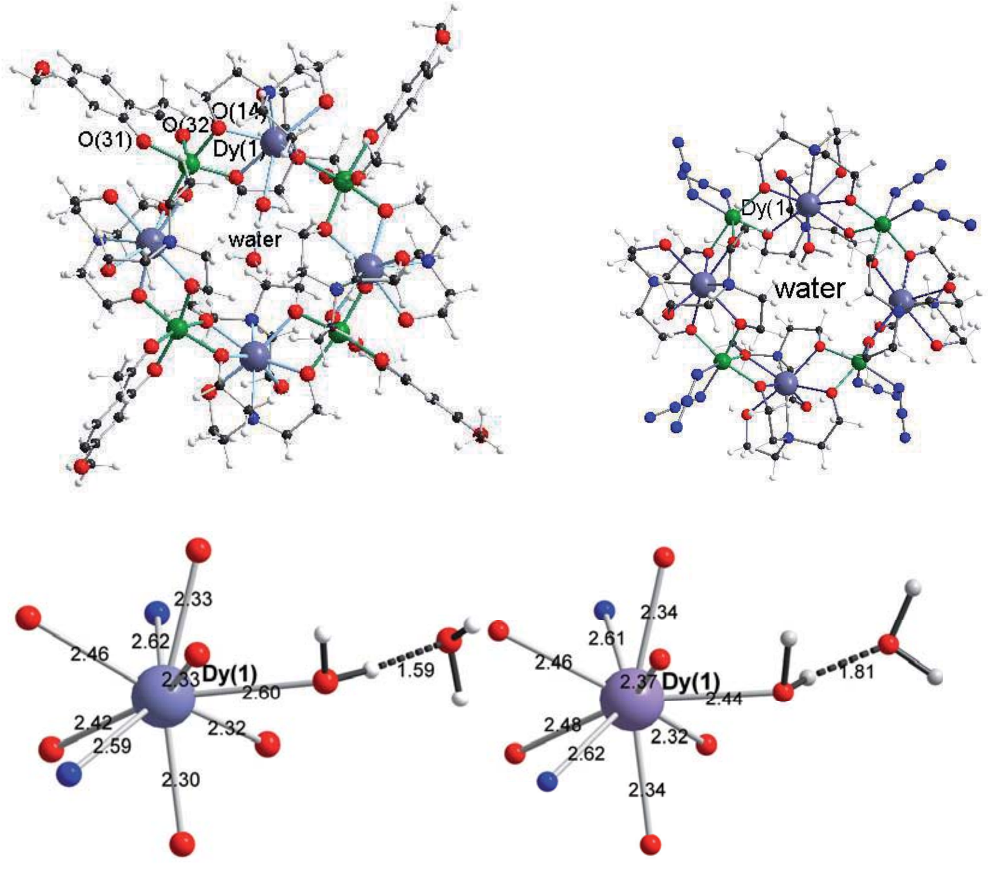

Figure 3.7: (Upper) the structures of **3.22** and **3.23**, (Lower) Capped square-antiprismatic N_2O_7 environment for Dy(1) of compound **3.22** (left) and reported Fe_4Dy_4 (**3.23**) (right) with average bond lengths.

In both compounds there are eight doubly deprotonated $teaH^{2-}$ and moreover the geometry is very similar in both compounds. However, some important differences in the bond lengths seem to be decisive in terms of the magnetic behaviour and Mössbauer spectra and are discussed further in the correpsonding sections below.

The fact that four phenoxy groups chelate means the charge needs to be balanced by four nitrates in contrast to compound **3.23** where the molecule is neutral. A further and more interesting difference is that in both compounds water molecules form intramolecular hydrogen bonds (Fig. 3.7, lower).

*Ln₆ **3.24-3.28***

Cyclic lanthanide complexes are rare. In addition, there is no comparative study on SMM behaviour on lanthanide compounds in order to understand the role of the electronic nature of ligands. Murray's group reported the possibility of synthesizing {Ln_6} wheels from reacting triethanolamine with lanthanide nitrates in methanol and in presence of triethylamine as base.[87]

This compound seems to be rather stable and was obtained at different stages in this work and it has the formula $[Dy_6(teaH)_6(NO_3)_6]\cdot 8MeOH$ **(3.24)** [87]. It is an excellent purly homometallic 4f "test-bed" for a comparative study to understand the effect of ligand-exchange on SMM behaviour in new cyclic 4f compounds. Indeed, the exchange of $teaH_3$ with Me-$teaH_3$ yields a new isotypic $[Dy_6(Me\text{-}teaH)_6(NO_3)_6]$ (**3.25**) compound as well as the Tm and the Ho analogues (**3.26 and 3.27**).

In addition, compounds **3.25** and **3.28** provide reference compounds for better understanding the properties of the system investigated in chapter 4. In order to have a third example and at the same time to investigate the effect of having an amino function instead of alcohol function on the ligand, 2,2'-(3-aminopropylazanediyl)diethanol ($apadH_4$) was used and yields indeed a new $[Dy_6(apadH_2)_6(NO_3)_6)]$ cyclic complex (**3.28**) (Fig. 3.8, right). Since this ligand is more basic than the other two, the amount of the added base was reduced. The two protons of the ethanol arms were indeed deprotonated. The amine function was not protonated allowing the nitrogen to coordinate the Dy^{III} centres. This is a further example in this work of control the serendipity of reactions. The use of similar ligand with shorter alkoxy-chain (ethylene), colourless crystals were obtained but were, however, usuitable for single crystal structure X-ray study (scheme, chapter 1).

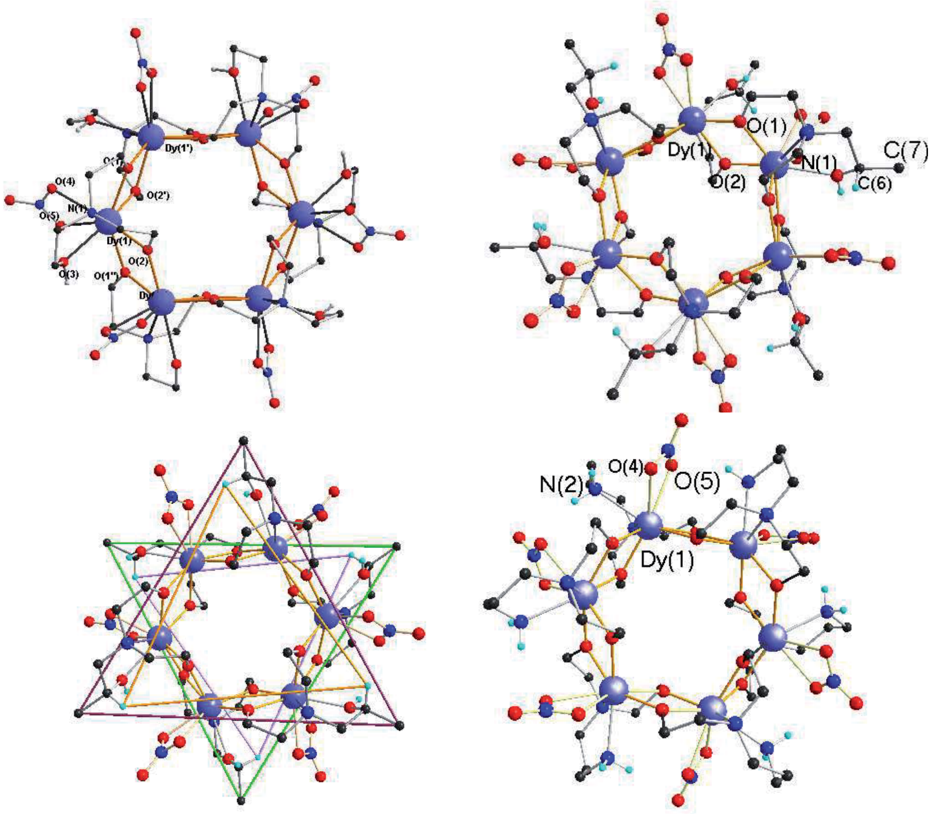

Figure 3.8. (Upper, left) Structures of Dy_6 with teaH (**3.24**), (upper, right) Dy_6 (**3.25**) with Me-teaH. (Lower, left) Violett represents the connection of the methyl groups attached to chiral C, they build a triangle. On the other side the triangle shows in opposite direction (green). The yellow triangle represents the H sitting on the chiral C, and on the other side with pink. (Lower, right) Dy_6 with $apadH_2$ (**3.27**).

All these compounds crystallize in the trigonal space group R-3 also with inversion centre. (cyrstallographic data of all three summarized in appendix Tabl. 3.10).

The fact that cluster **3.25** aggregates from Me-teaH ligand with chiral C, is indeed seen in in the structure. Both R and S enantiomers of the ligand are presence, froming triangles (Fig. 3.8, lower).

Each Dy^{III} is coordinated by the central N from the ligand. Two alkoxy arms bridge with the next Dy centre. The third alkoxy arm in case of **3.24** and **3.25** chelates the Dy centre and in case of **3.27** it is the amine fucntion which does this. Compounds **3.24** and **3.25** have similar Dy-O bond distances and angles fore example Dy-O distances in the range 2.2478-2.2849 Å, $Dy-N^{tert}$ 2.580 Å, Dy-Dy 3.7271 Å, Dy-O-Dy 108.37 and 111.78 °. However, compound **3.27** has slightley but not significant different Dy-O distances in the range 2.26 to 2.30 Å. Longer distance between the Dy^{III} centres and the N atoms of triethanolamine $Dy-N^{tert}$ ~2.69215 Å for **3.27**. Furthermore, the and $Dy-N^{prim}$ with 2.5062

Å, is longer than Dy-OH (chelating alcohol group) with 2.4721(26) which might be a result of longer alkyl-chain (propylene instead ethylene). The Dy-Dy distances for **3.27** are slightely longer with 3.7606 Å and the Dy-O-Dy are similar to the others with 109.723 and 111.90 °.

3.3 Magnetic properties

Fe_5Ln_3 (**3.1-3.3**)

Solid state *dc* magnetic susceptibility (χ) data for compounds Fe_5Tm_3-Fe_5Lu_3 **(3.1-3.3)** were collected in the 1.8-300 K temperature range under a field of 1000 Oe. On lowering the temperature the χT product continuously decreases down to 1.8 K for compounds **Fe_5Tm_3** and **Fe_5Lu_3**, while **Fe_5Yb_3** compound first exhibits a continuous decrease and then reaches a plateau of 9.0 cm^3K/mol between 6 and 3.5 K before slightly decreasing again to 8.8 cm^3K/mol at 1.8 K (Fig. 3.9, left). Such behaviour suggests the presence of antiferromagnetic (AF) interactions dominating between spin carriers for all compounds. This does not preclude the presence of ferromagnetic interactions, but does suggest that AF interactions are dominant. For complex Fe_5Lu_3 **(3.3)** containing diamagnetic Lu^{III} ions ($S = 0$, $^1S_0$), the room temperature experimental χT product of 14.5 cm^3 K mol^{-1} is much lower than the expected value (21.875 cm^3 K mol^{-1}) for five Fe^{III} ($^6A_{1g}$, $S = 5/2$, $g = 2$)

ions indicating the presence of strong antiferromagnetic interactions. However, for complex Fe_5Yb_3 **(3.2)**, the clear saturation observed between 3.5 and 6 K is suggestive of a presence of well-defined ground state. Based on the plateau of 9.0 cm^3K/mol in χT, a $S = \sim 4$ ground state might be correct. In order to assess the nature of magnetic interactions between Fe^{III} and Ln^{III}, we subtracted the magnetic contribution of Fe_5Lu_3 from the total RT susceptibility product in each case to give suitably adjusted plots. As shown in Fig. 3.9 (right), the continuous decrease of its adjusted χT vs T curve in Fe_5Tm_3 **(3.1)** suggests antiferromagnetic Fe^{III}-Tm^{III} coupling, while the slight increase of the adjusted χT below 10 K observed in **Fe_5Yb_3** may result from the ferrimagnetic arrangement of Fe^{III} and Yb^{III} ions.

The only compound that can be satisfactorily modeled is **Fe_5Lu_3** which contains diamagnetic Lu^{III} ions. In line with the structure, the coupling scheme is shown in Fig.3.1 1. To avoid over-parameterization problem, we had different attempts to reproduce the magnetic susceptibility with two coupling constants, i.e. a) $J_1 = J_2$ and $J_3 = J_4 = J_5$; b) J_1, J_2 and $J_3 = J_4 = J_5 = 0$, none of which however was successful. Furthermore, according to the magneto-structural correlation, two pairs of adjacent Fe^{III} ions are likely to be strongly antiferromagnetically coupled. In that case, the spins on the odd Fe^{III} ion of $S = 5/2$ is then uncompensated. However, the field dependence of the magnetisation at low temperature for compounds **Fe$_5$Tm$_3$** could not be fitted with a Brillouin function of $S = 5/2$ and $g = 2.0$

Fig. 3.11, and the experimental data lie below the calculated curve indicating that the spin on the fifth odd Fe^{III} ion is not independent but that it is involved in antiferromagnetic interactions. With the above modelling attempts, we have conclude that there are at least more than two magnetic pathways within this system.

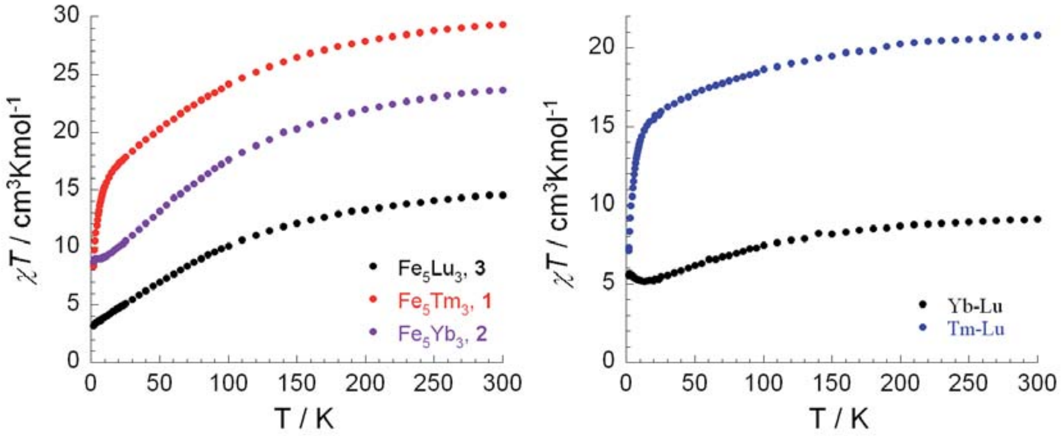

Fig. 3.9. (Left) χT versus T plots at 1000 Oe for **Fe$_5$Tm$_3$ – Fe$_5$Lu$_3$**; sample codes are indicated in the inset of the Figure. (Right) The χT vs T plots for **Fe$_5$Tm$_3$** and **Fe$_5$Yb$_3$** with the data for **Fe$_5$Lu$_3$** subtracted, i.e. without the magnetic contribution of the Fe$_5$ unit.

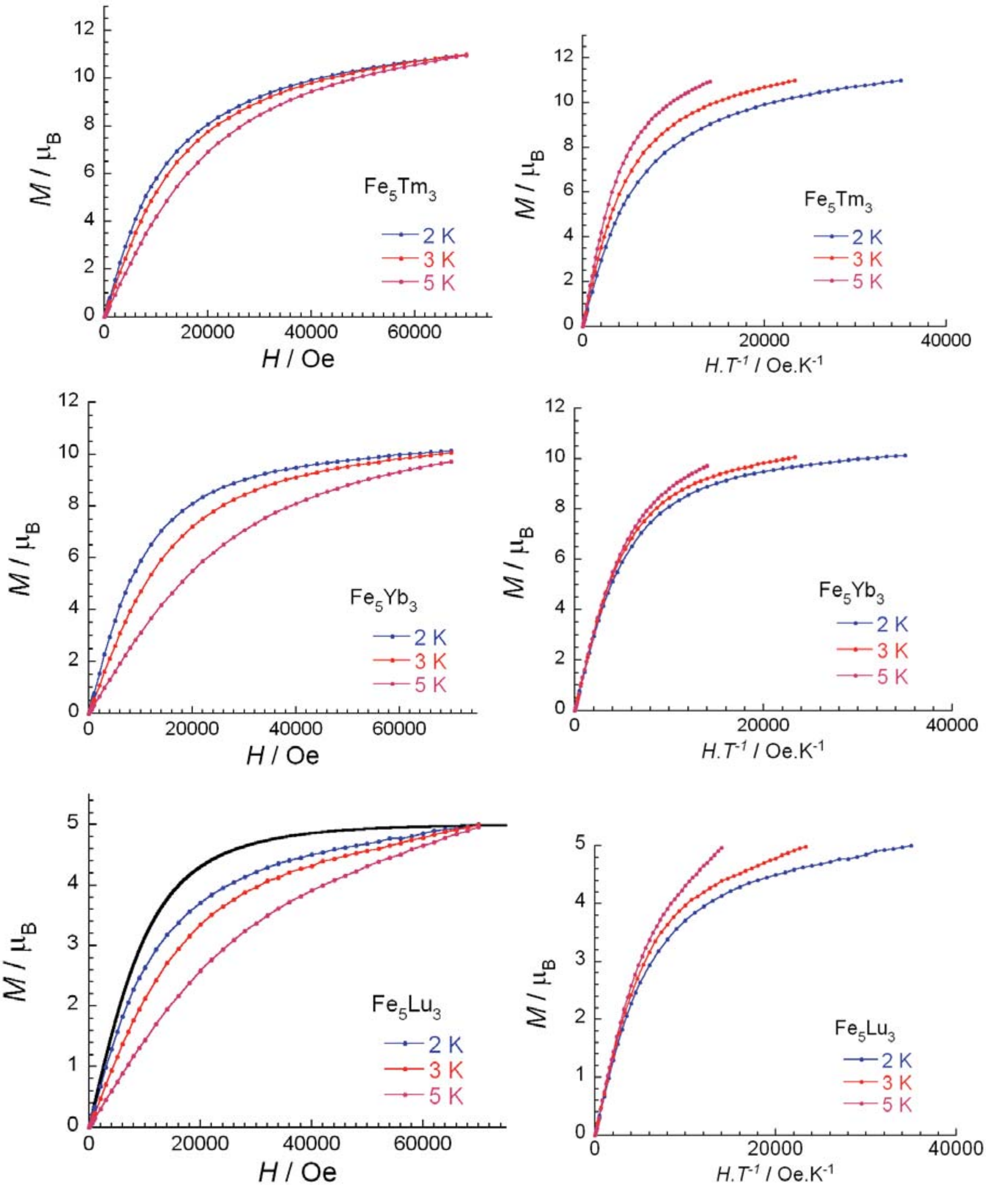

Figure 3.10. Field-dependence of magnetization of compounds **Fe_5Tm_3-Fe_5Lu_3**. In the case of **Fe_5Lu_3**, the black line corresponds to the calculated curve of one Brillouin function with $S = 5/2$ and $g = 2.0$.

Considering the number of magnetic pathways and the difficulty in modelling such a big system, we have done DFT calculation in calloboration with Dr. Eliseo Ruiz, Inorganic Chemistry, University of Barcelona (Spian). In Fig. 3.12 and Tab. 3.11 to estimate the coupling constants between the spin carriers.[88]

The *ac* susceptibility was checked for all compounds. No out-of phase signal was observed for all cases suggesting that the slow relaxation of the magnetization cannot be detected in the time scale of this measuring method.

To calculate the exchange coupling constants (*J*) we have used the following Heisenberg Hamiltonian:

$$\hat{H} = -J_1\hat{S}_1\hat{S}_2 - J_2\hat{S}_3\hat{S}_4 - J_3\hat{S}_1\hat{S}_3 - J_4\hat{S}_4\hat{S}_5 - J_5\hat{S}_2\hat{S}_5$$

where J_1-J_2 are the nearest Fe^{III}-Fe^{III} interactions, meanwhile J_3-J_5 are next second neighbourhood interactions through the diamagnetic Lu^{III}.

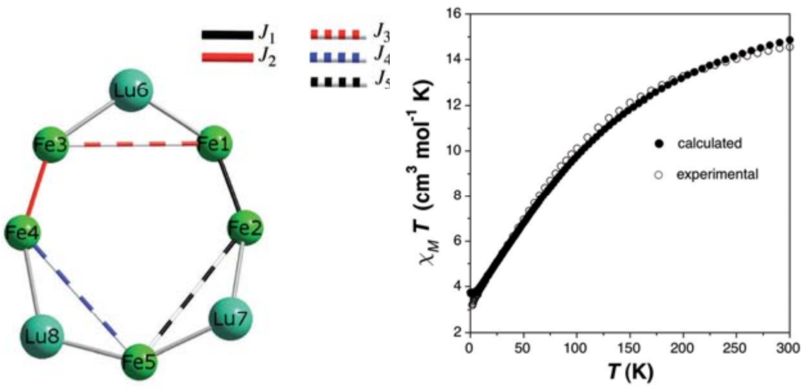

Figure 3.11. (Left) Topology of the exchange coupling constants for complex Fe_5Lu_3 **(3.3)**. (Right) Representation of the magnetic susceptibility curves for complex $\mathbf{Fe_5Lu_3}$. For the reproduced curve from the calculated *J* values a g = 1.95 has been used.

Both are antiferromagnetic, however the latter are very weak been reported for the only two such experimentally adjusted magnetic compounds $Cu^{II}_2Lu^{III}$ (-0.4 cm^{-1})^1 and $Ni^{II}_2Lu^{III}$ (-1.3 cm^{-1}).[89]Although weak antiferromagnetic coupling is calculated between Fe(5) and Fe(2) the system is still too complex to be understood from the magnetic measurements.

Table 3.11. Exchange Coupling Constants (J in cm^{-1}) together with metal-metal and metal-ligand distances (in Å) and metal-ligand-metal angle (in degrees).

	Bridging Ligands	Fe···Fe	Fe-X^a	Fe-X-Fe	J
J_1	μ_2-OH, μ_2-OR μ-O_2CMe	3.063	1.970, 1.963, 2.056, 2.028 2.089, 2.059	102.3, 97.2	-13.3
J_2	2(μ_2-OR) μ-O_2CMe	3.127	2.064, 1.996, 2.042, 1.995 2.098, 2.027	101.5, 100.7,	-23.7
J_3	-	5.718	-	-	-0.4
J_4	-	5.881	-	-	-0.3
J_5	-	6.090	-	-	-0.4

A method with a faster time scale, such as Mössbauer spectroscopy, is needed to be able to understand this system and the others below better. Indeed bulk sussceptibility studies give only an average of the magnetic moment (1s time scale) and this is not always enough to understand such complex magnetic clusters (see Mössbauer section). The details about the calculations and the programm used will be given in the experimental part.

Fe_4Ln_2 (**3.4-3.7**)

Strong antiferromagnetic interactions (AF) are present in compound **Fe_4Lu_2**. The antiferromagnetic interaction is between the pairs of Fe^{III} ions leading to a total spin ground state of zero. The shape of the magnetization at 2 K confirms the strong nature of interactions. Based on the model with two pairs of dinuclear Fe^{III} ions ($S_1 = S_2 = 5/2$) using Hamiltonian of $H = -4JS_1 \cdot S_2$, the magnetic data could be reproduced well by the following parameters: $g = 1.92(1)$, $J/k_B = -8.15(8)$ K. The fit is shown as the red solid line (Fig. 3.12). In compounds Fe_4Er_2 (**3.4**) and Fe_4Yb_2 (**3.5**) dominant AF interactions are also present. The susceptibility measurement (Fig. 3.13, left) as well as the magnetization (Fig. 3.13, right) confirm that the interactions between the Yb^{III} and Fe^{III} ions are also antiferromagnetic in nature, which can be manifested from the 'subtracted' plot. (see Fig. 3.15)

The magnetic behaviour in the compound Fe_4Tm_2 (**3.5**) is similar to that of the Yb-compound (**3.6**). In other words, the coupling between Tm^{III} and Fe^{III} is additional to the strong antiferromagnetic coupling of the Fe^{III} ions, antiferromagnetic. (Fig. 3.14)

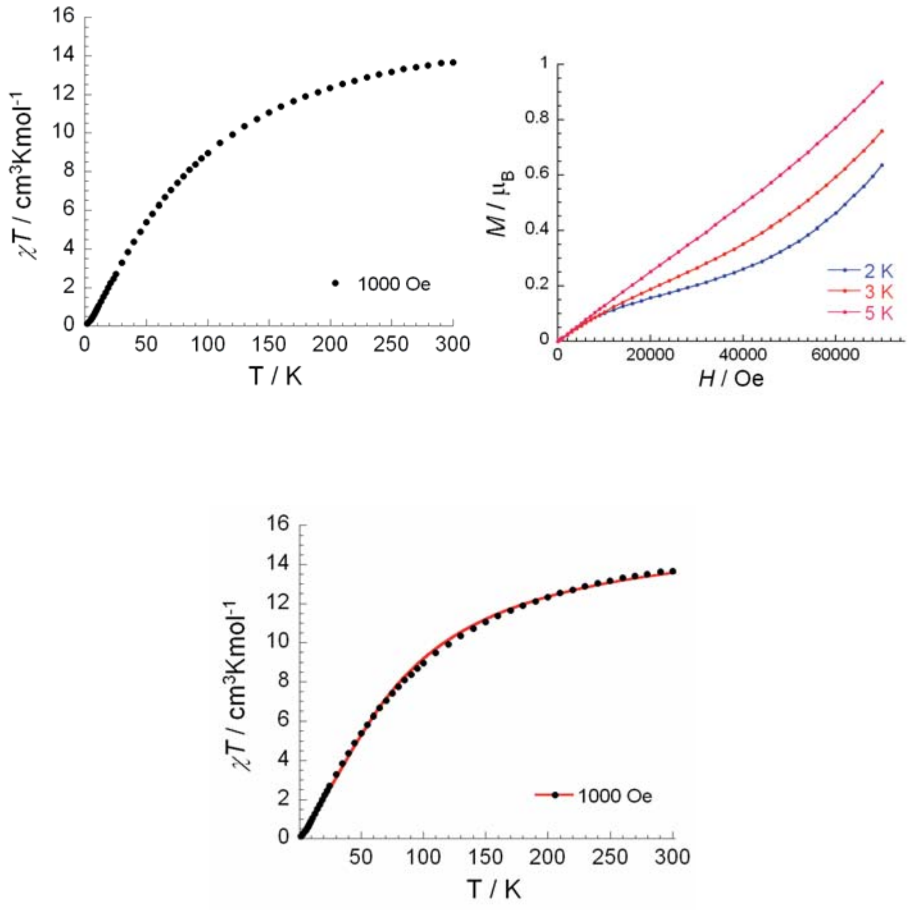

Figure 3.12. (Left, above) χT versus T plots at 1000 Oe for Fe_4Lu_2 (**3.7**);. (right, above) Field-dependence of magnetization of compound . (Lower) the fit of χT versus T as dinuclear Fe(III) ions ($S_1 = S_2 = 5/2$) using Hamiltonian of $H = -4JS_1{\cdot}S_2$, $g = 1.92(1)$ and $J/k_B = -8.15(8)$ K.

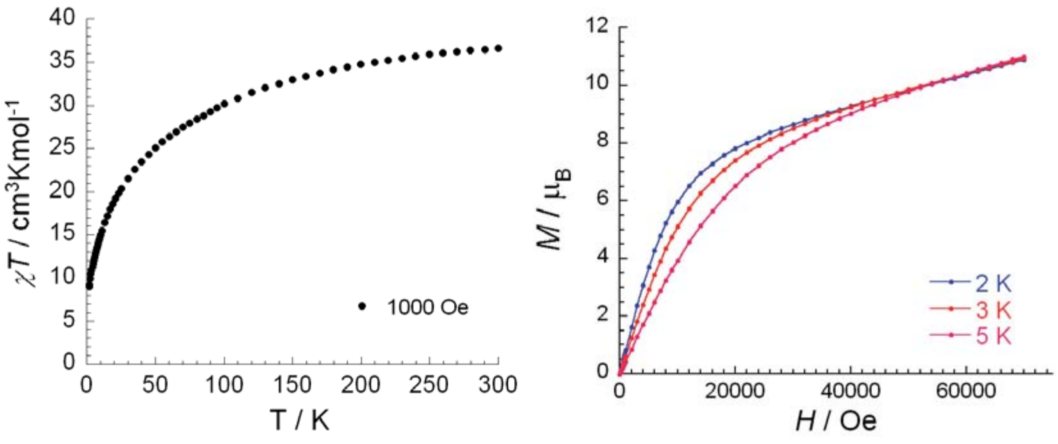

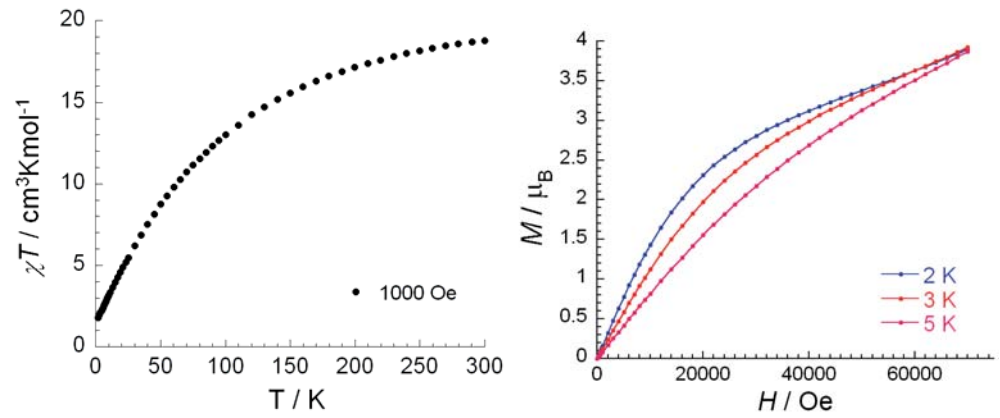

Figure 3.13. (Upper) (Left) χT versus T plots at 1000 Oe for Fe_4Er_2 (**3.4**);. (right) the field-dependence of magnetization of compound **3.4**. (Lower, left) χT versus T plots at 1000 Oe for Fe_4Yb_2 (**3.6**); (right) Field-dependence of magnetization of compound **3.6**.

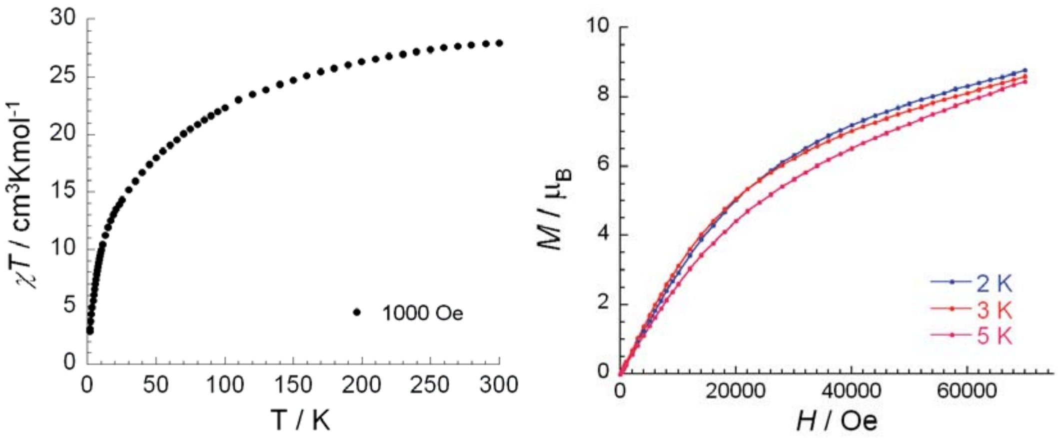

Figure 3.14. (Left) χT versus T plots at 1000 Oe for Fe_4Tm_2 (**3.5**); (right) field-dependence of magnetization of compound.

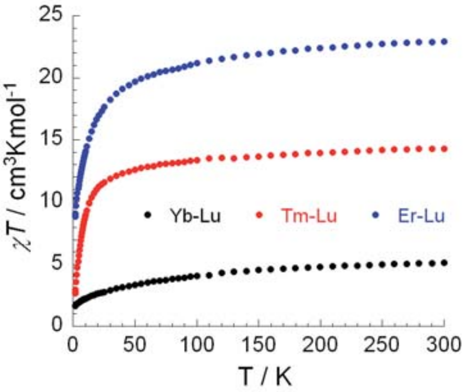

Figure 3.15. The χT vs T plot at 1000 Oe without the magnetic contribution of the $[Fe_4Lu_2]$ unit for **3.4**, **3.5** and **3.6** compounds.

No out-of-phase signal is detected under zero dc fields in all cases. Even with the application of dc field, no obvious slow relaxation of magnetization could be observed, indicating there is no appreciable quantum tunneling effect in this series of compounds.

Fe_3Ln_2 (**3.8-3.11**)

Overall antiferromagnetic interactions are present in compound Fe_3Lu_2 (**3.10**). Strong antiferromagnetic interactions are likely to be present between the pair of Fe^{III} ions bridged by double oxo-groups as expected and seen in the previously discussed ring systems. This is confirmed by both the χT vs T and M vs H measurements (Fig. 3.16). The χT reaches a plateau of 4.14 cm^3K/mol between 8.0 and 3.5 K and the magnetization at 2 K almost reaches a saturation of 4.6 µB, which both indicate the pair of Fe^{III} ions are non-magnetic at low temperatures and the system almost behaves as an isolated Fe^{III} ion at these low temperatures. However, the spin on the Fe^{III} ion located between the Lu^{III} ions is not independent because the magnetization curve at 2 K could not be reproduced by one Brillouin function of $S = 5/2$. This was also the case in the Fe_5Lu_3 compound, where the spin structure could not be satisfactorily modelled. This is general for these cyclic compounds, even those containing diamagnetic Lu^{III} ions and shows the necessity of using more sensitive methods to understand wthe origin of such behaviour (see Mössbauer section).

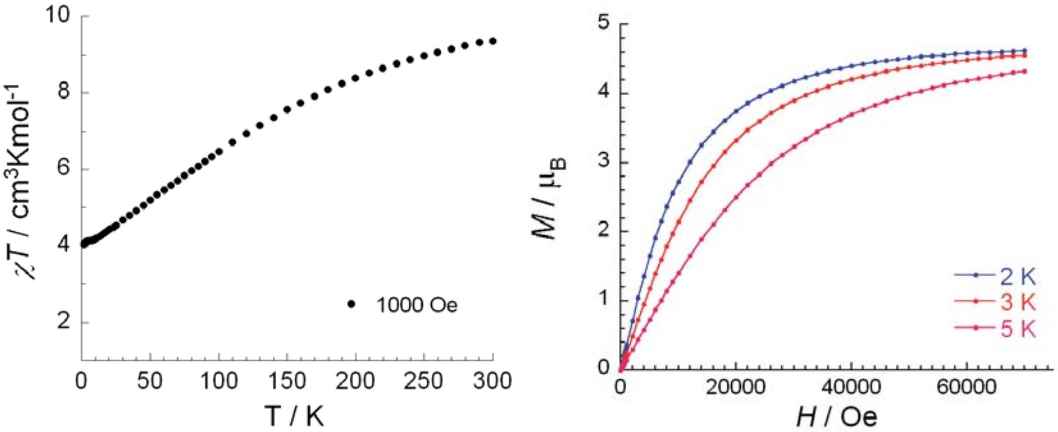

Figure 3.16. (Left) χT versus T plots at 1000 Oe for Fe_3Lu_2 (**3.10**); (right) field-dependence of magnetization of compound **3.10**.

Dominant AF interactions are present in the ytterbium analogue compound (**3.9**) as well. However, the interactions between the Yb^{III} and Fe^{III} ions are weak ferromagnetic (see the 'subtracted' plot in Fig. 3.20) and not as in case of the ytterbium compound Fe_4Yb_2 (**3.7**) (discussed later). The slightly decreasing slope above 18 K in the 'subtracted' χT plot is the result of the thermal depopulation of the Stark sublevels of the Yb^{III} ions. (see Fig. 3.17)

Dominant AF interactions are present in the Fe_3Tm_2 compound (**3.8**). The interactions between the Tm^{III} and Fe^{III} ions are very weak antiferromagnetic and not as in case of **3.9**. (see Fig. 3.18)

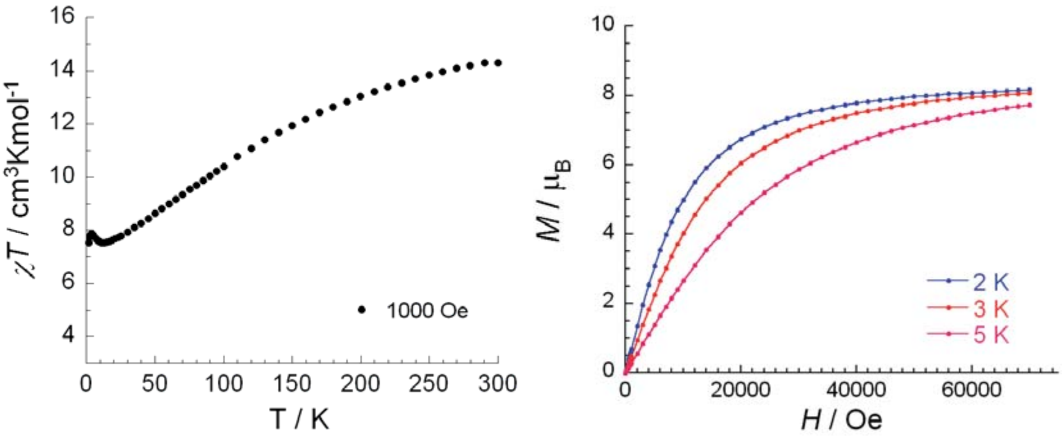

Figure 3.17. (Left) χT versus T plots at 1000 Oe for Fe_3Yb_2 (**3.9**); (Right) field-dependence of magnetization of compound **3.9**.

Dominant AF interactions are present in the erbium analogue compound Fe_3Er_2 (**3.7**). The interactions between the Er^{III} and Fe^{III} ions are ferromagnetic (see the 'subtracted' plot Fig. 3.19). The decrease above 11 K in the 'subtracted' χT plot could be contributed to by the thermal depopulation of the Stark sublevels of the Er^{III} ions. (see Fig. 3.20)

No out-of-phase signal is detected under zero dc field in all cases. Even with the application of dc field, no obvious slow relaxation of magnetization could be observed, indicating there is no appreciable quantum tunnelling effect in this series of compounds.

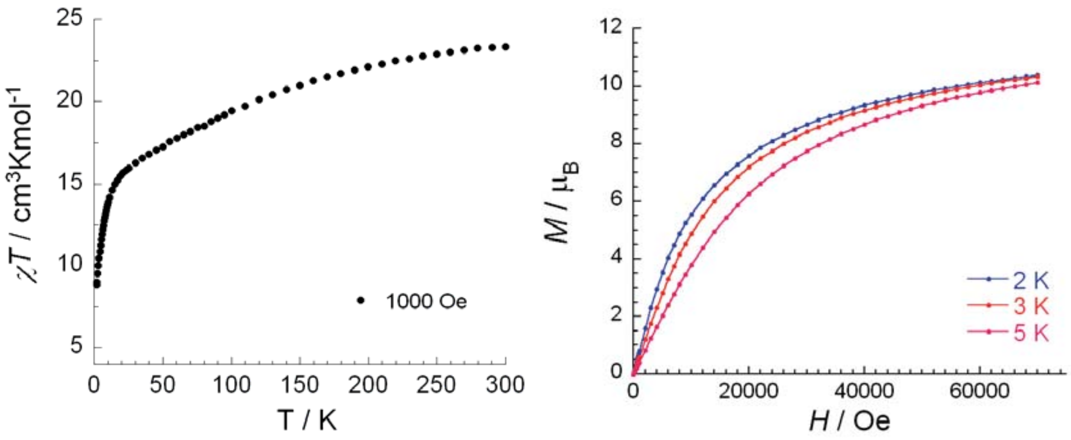

Figure 3.18. (Left) χT versus T plots at 1000 Oe for Fe_3Tm_2 (**3.8**); (right) field-dependence of magnetization of compound **3.8**.

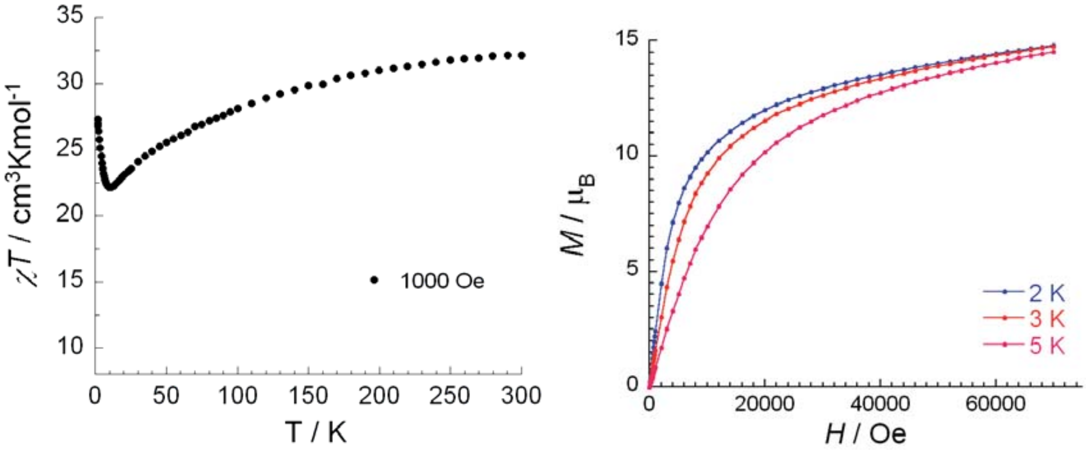

Figure 3.19. (Left) χT versus T plots at 1000 Oe for Fe_3Er_2 (**3.7**); (right) field-dependence of magnetization of compound **3.7**.

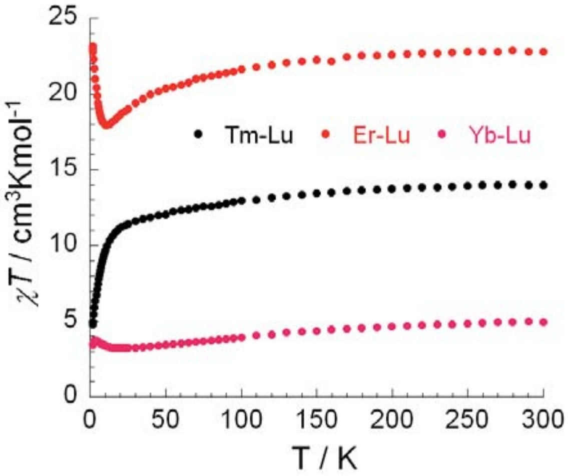

Figure. 3.20. The χT vs T plot at 1000 Oe without the magnetic contribution of the [Fe_3Lu_2] unit for **3.7**, **3.8** and **3.9** compounds.

$Fe_{16}Ln_4$ (**3.15-3.20**) [36f]

The variation with temperature of the *dc* magnetic susceptibility shows similar behaviour for all the compounds **3.14** – **3.19** (Fig. 3.21). The magnetic data are summarised in Tab. 3.12. The monotonic decrease of the χT product (at H = 0.1 T) from room temperature to 1.8 K is indicative of the presence of antiferromagnetic interactions in all cases. For complex **3.15** containing Eu^{III} ions which are diamagnetic (S = 0, $^7F_0$, at least at low temperature), the experimental χT value clearly tends to zero, reaching 0.52 cm^3 K mol^{-1} at 1.8 K, indicating that the Fe_2 and Fe_6 sub-chains within the ring have their component spins antiparallel and fully compensated resulting in zero spin ground states. Indeed, magnetostructural correlations for oxygen-bridged Fe^{III} complexes indicate that the geometries of the $Fe^{III}(\mu\text{-}OR)_2Fe^{III}$ bridges within these rings are consistent with significant antiferromagnetic interactions between the Fe^{III} ions. Similar behaviour is observed for the analogue **3.14** containing very weakly paramagnetic Sm^{III} ions, where the χT product also tends to zero at low temperatures, reaching 0.57 cm^3 K mol^{-1} at 1.8 K.

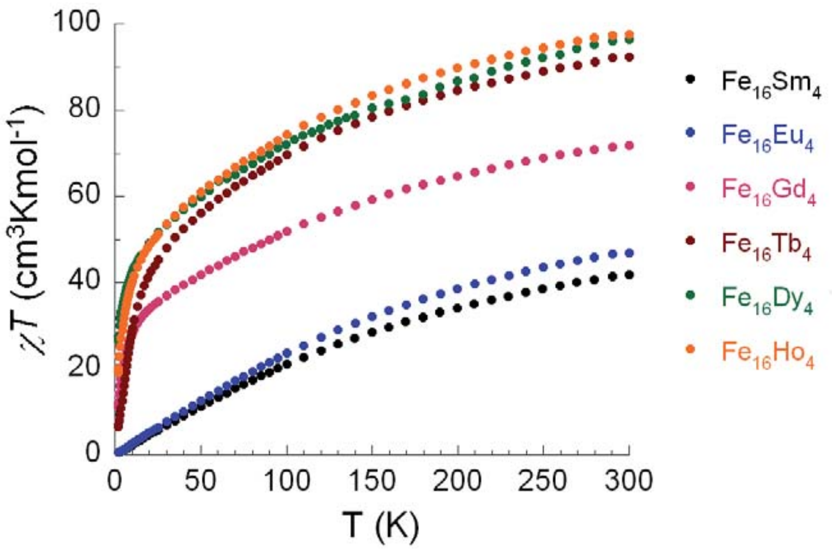

Figure 3.21. The χT versus T plots at 0.1 T for **3.15** – **3.20**.

If we subtract the magnetic contribution of four respective Ln^{III} ions from the observed value of χT at 300 K for each compound, the remainder of the χT product then corresponds to the magnetic susceptibilities of the 16 Fe^{III} ions. The resulting susceptibility and temperature products (Table 3.12) are all significantly smaller than the expected value of 70.0 cm^3 mol^{-1} K for 16 independent Fe^{III} ($^6A_{1g}$ S = 5/2, g = 2) ions, confirming that the Fe^{III} ions are strongly antiferromagnetically coupled. Furthermore, the adjusted susceptibilities are fairly similar, lying in the range 40.3 - 41.4 cm^3 K mol^{-1} for **3.15**, **3.17**, **3.19** and **3.20**, indicating that the Fe-Fe interactions are both of similar magnitudes in each compound and dominate over the substantially weaker Fe-Ln inteactions. Compounds, **3.18** and **3.20,** show slightly higher adjusted values. For **3.16**, the higher value might arise from thermal population of magnetically active excited states of the Eu^{III} ion. However, for the Tb compound **3.18**, the higher value might result from trace amounts of the oil which always forms alongside this compound, and which might be paramagnetic. For this reason, caution should be exercised in reading anything into these magnetic values for **3.18** and the results will not be described in detail.

Figure 3.22 shows the field-dependence of the magnetisation at low temperatures for all compounds. The magnitude of the magnetisation at 7 T and 2 K for each compound is also listed in Table 3.18. Given that the iron centres are strongly antiferrmagnetically coupled, the contribution to the magnetisation at 2K will arise solely from the 4 lanthanide ions.

Table 3.12. DC magnetic data for compounds **3.16-3.21**.

	Ground state of Ln^{III}	Curie constant **[91]** for Ln^{III}	Predicted χT (cm^{3}mol^{-1}K) at 300 K	Observed χT (cm^{3}mol^{-1}K) at 300 K	Observed χT (cm^{3}mol^{-1}K) at 1.8 K	Adjusted χT for Fe$_{16}$ contribution at 300 K (cm^{3}mol^{-1}K)	Magnetisation at 2 K and 7 T (μB)
3.15	Sm^{III}: $^6H_{5/2}$	0.09	70.36	41.80	0.57	41.44	2.8
3.16	Eu^{III}: $^7F_0$	0	70.0	46.92	0.52	46.92	2.7
3.17	Gd^{III}: $^8S_{7/2}$	7.875	101.50	71.86	11.33	40.36	28.0
3.18	Tb^{III}: $^7F_6$	11.82	117.28	92.29	6.61	45.01	22.5
3.19	Dy^{III}: $^6H_{15/2}$	14.17	126.68	97.13	26.49	40.45	21.0
3.20	Ho^{III}: $^5I_8$	14.07	126.28	97.67	19.10	41.39	27.2

For compounds **3.15** and **3.16**, the slow and *quasi*-linear increase of the magnetisation with field, not reaching 3 μB in either case is further evidence for the strength of the antiferromagnetic Fe-Fe interactions.

The magnetisation of compound **3.17** at 2 K reaches 28.0 μB with an applied field of 7 T, in good agreement with the value expected for four non-coupled Gd^{III} ions. This further substantiates that in **3.17**, as for **3.15** and **3.16**, at low temperature the spins within the Fe$_2$ and

Fe_6 units are completely compensated with $S_{\text{subchain}} = 0$ for both the dinuclear and hexanuclear sub-chains.

The absence of true saturation (even at 7 T), together with the non-superposition of the reduced magnetisation curves, indicates the presence low-lying excited spin states, as for **3.16**, with essentially isotropic Fe^{III} and Gd^{III} ions, significant anisotropy is unlikely.

Interestingly, the magnetisation of **3.17** could not be fitted with the sum of four Brillouin functions for $S = 7/2$ and $g = 2.0$ (Fig. 3.23).

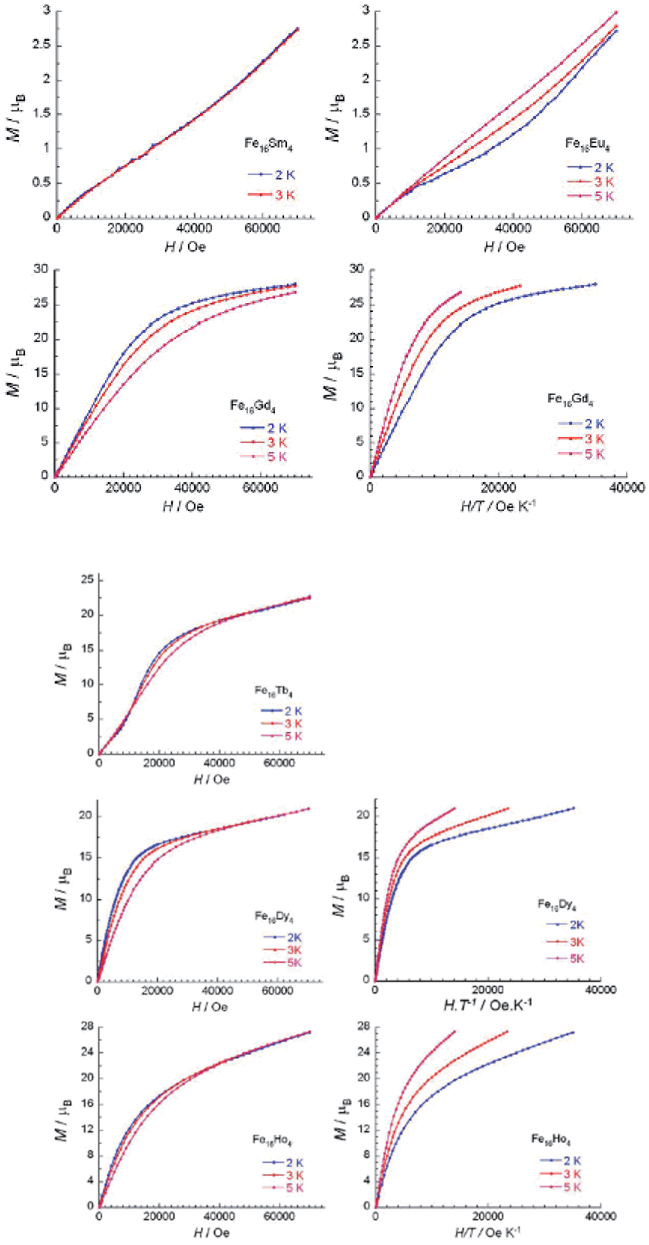

Figure 3.22. The field dependence of magnetization for all compounds (**3.15-3.20**) at indicated T.

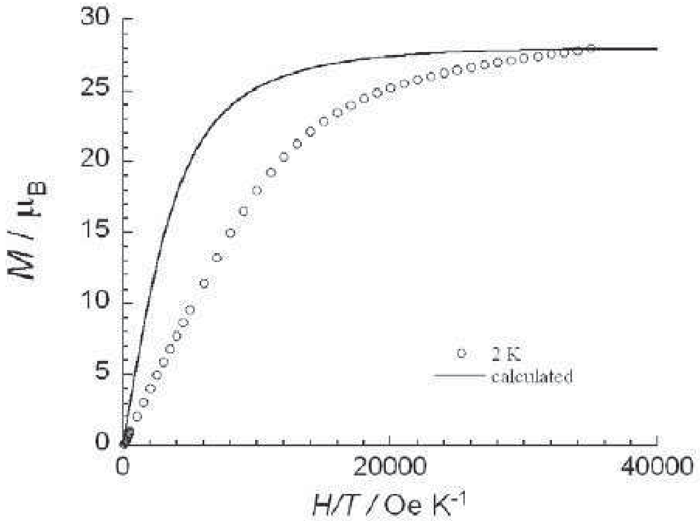

Figure 3.23. Field dependence of experimental magnetization of $Fe_{16}Gd_4$ (**3.17**) (open circels) together with the calculated magnetization for the sum of four uncoupled S= 7/2 spins (g = 2.0).

The experimental data lie well below the calculated curve, indicating that the spins on the Gd^{III} ions are not independent. Any direct Gd^{III}-Gd^{III} interaction through the very long *anti,anti*-acetate bridges can safely be expected to be extremely small and can be neglected in favour of the Fe^{III}-Gd^{III} interactions. Since at low temperature the spins on the two Fe^{III} centres in each Fe_2 sub-chain are antiparallel, as are those on the Fe^{III} centres at each end of an Fe_6 sub-chain, then on going around the ring the Gd^{III} spins will alternate “up” and “down” regardless of the sign of the Fe-Gd interaction. But the directions of the four spins should be related by the D_{2d} site symmetry of the molecule (as long as the magnetic and structural unit cells are the same). The Gd^{III} spins can therefore be regarded as pinned by their positions between the Fe_2 and Fe_6 sub-chains in the ring. The observation that this pinning can be overcome by an applied field of up to 7 T confirms that the Fe-Gd interactions are much weaker than the Fe-Fe antiferromagnetic interactions. The likely presence of low-lying spin states, as shown by the lack of saturation of the magnetisation, is also consistent with weak Fe-Gd interactions.

Any evaluation of the Fe^{III}-Gd^{III} (and any Gd^{III}-Gd^{III}) interactions is, however, not feasible, since the Fe^{III}-Fe^{III} interactions are very likely to be much larger and so overwhelm the contribution from the Fe^{III}-Gd^{III} (and any Gd^{III}-Gd^{III}) interactions. In any case neither *ab initio* calculations nor fitting of the magnetic data is likely to be practicable because of the large number of unpaired electrons in the system.

The magnetisations for compounds **3.18-3.20** at 2 K under 7 T applied field (Tab. 3.12) are also consistent with the expected values for the respective four Ln^{III} ions and the lanthanide spins are likely to be pinned in the same way as for Gd^{III}. However, the anisotropy of the lanthanide ions will now be contributed to the lack of saturation of their magnetisations.

The *ac* susceptibility was measured for all six compounds with no out-of phase signal observed for compounds **3.15-3.18** and **3.20**. The Dy compound **3.19** does show a very weak χ" signal, the intensity of which was unchanged on application of a small d.c. field and which shows a rather low χ''/χ' ratio of 1:50 (Fig's. 3.24 and 3.25).

The origin of this is difficult to judge. The Ising easy axes of the four Dy^{III} ions in **3.19** will be related by the D_{2d} site symmetry of the molecule, such that these single-ion anisotropies might be expected to cancel each other out within the molecular overall tensor sum, and Single-Molecule Magnet behaviour is thus highly unlikely.

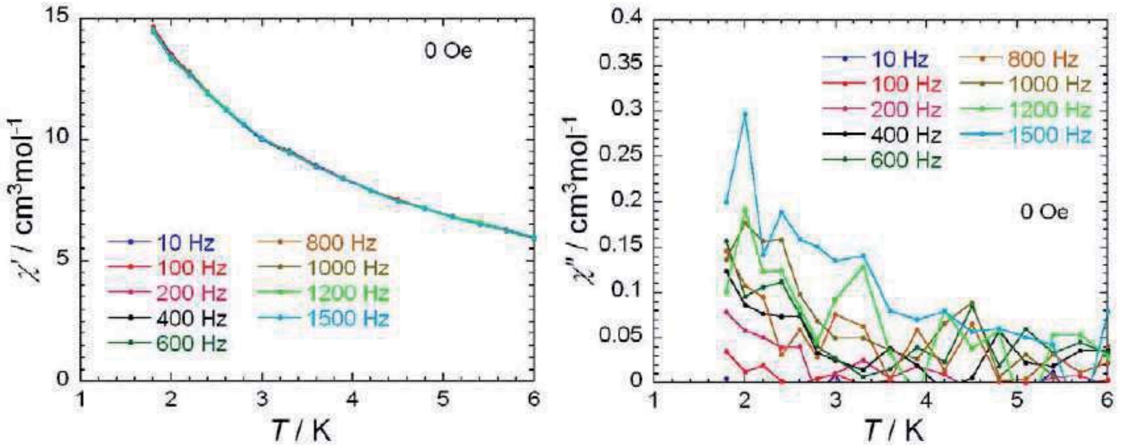

Figure 3.24. Temperature dependence of the in-phase and out-of-phase ac susceptibility components at different frequencies under zero dc field for $Fe_{16}Dy_4$ **(3.19).**

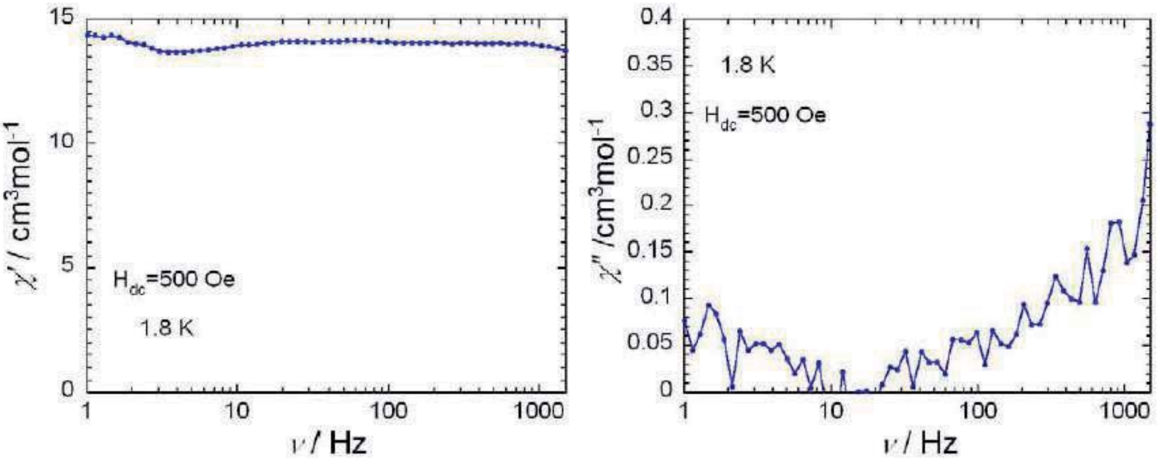

Figure 3.25. Frequency dependence of in-phase and out-of-phase ac susceptibility components at 1.8 K under a dc field of 500 Oe for $Fe_{16}Dy_4$ **(3.19).**

Fe_4Dy_4 ***3.22***

Direct Current *dc* magnetic susceptibility were collected under a field 0.1 T (Fig. 3.26 (upper, left)) for compound **3.22** as for compound **3.23** [36g)]. The value for the product χT at 300 K is about the expected value of 74.18 cm^3 K mol^{-1} for four high spin Fe^{III} with g= 4/3, S= 5/2, L= 5, J= 15/2, C= 14.17 cm^3 K mol^{-1}. On lowering the temperature, the χT product stays almost constant until around 60 K for both compounds, then increases coninuously to reach a maximum value of 161.2 cm^3 K mol^{-1} at 3K for compound **3.23** and ~120 cm^3 K mol^{-1} for compound **3.22**, then rapidly falls at 1.8 K to ~146 cm^3 K mol^{-1} for **3.22**, to a much lower value < 90 cm^3 K mol^{-1} for **3.23**. This type of magnetic behavior indicates in both cases dominant ferromagnetic behaviour. The strong ferromagnetic behavior in **3.23** seems to be enough to not be overwhelmed by any thermal depopulation of the Dy^{III} excieted states. However, in the case of **3.22** the ferromagnetic behviour is affcted by the antiferromagnetic behaviour as seen from the values of susceptibility at low temperatures. A possible reason is the much shorter Fe---Fe distances in **3.22** compared with **3.23**. The distances between Fe(1)---Fe(2) (6.3668(4) Å for **3.22** and 6.6541(11) Å for **3.23**) and Fe(3)---Fe(4) (6.1966(5) Å for **3.22** and 6.2848(12) Å for **3.23**) , which are shorter than than in case of **3.23**. The field dependence of magnetization curves at low temperature shows for both compounds **3.22** and **3.23** a rapid increase at low fields, which then increases with only a slight slope and thus without clear saturation. In case of **3.22** the magnetization is a bit more separated by different temperatures (Fig. 3.26 (upper, right)) and even no clear saturation is observed.

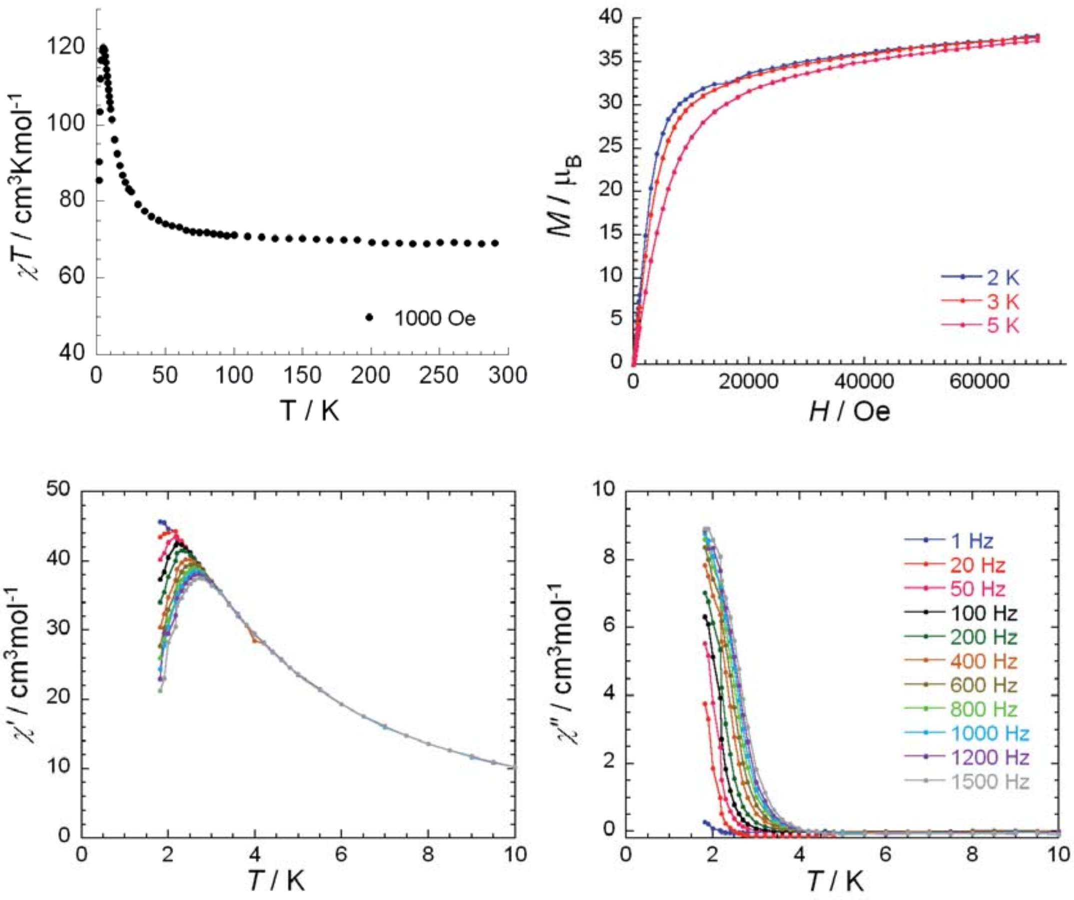

Figure 3.26. (Upper, left) χT versus T plots at 0.1 T for **3.22** compaired in text with **3.23** from. (Upper, right) Magnetaization cuvers at different temperatures. (Lower) temperature dependence of the in-phase (left) and out-of-phase (right) *ac* susceptibility components at different frequencies under zero dc field for **3.22**.

The alternating current *ac* magnetic susceptibilities were studied as a function of temperature and frequency. The data reveal that both compounds possess strong frequency-dependent in-phase and out-of-phase signals, however below 4K for **3.23** and below 3K for **3.22**, indicating slow relaxation of magnetization for both compounds and this why both can be described as SMMs. The maximum of the out-of-phase signal was obserevd at 2.8 K for **3.23** but at ~2.0 K for **3.22**. This difference in ac behaviour is supported somewhat by the dc behaviour, where at very low temperature the sudden decrease of susceptbility is actually an indication for magnetic anisotropy. Furthermore, this is in both cases slightly different. This difference is seen more clearly in the ac behaviour and Mössbauer spectrum of **3.22**. The reasons therefore, are as discussed before and in the Mössbauer section and can be understood in terms of the electronic nature of the ligand and from the differences in bonds distances and angles.

Dy_6 (**3.24**, **3.25** and **3.28**)

In Fig. 3.27 the susceptibility and magnetization curves of the three compounds are shown comparatively.

All three compounds show similar *dc* magnetic behaviour (Fig.3.27). The overall interactions in all compounds are antiferromagnetic. Moreover, all three compounds show slow relaxation of the magnetization, indicating that they are all SMMs. In addition, compounds **3.24** and **3.25** (with teaH$_3$ and Me-teaH$_3$ ligands) have even similar *ac* magnetic behaviour.

However, significant differences to these two are observed in compound **3.27** which has the amine function coordinating on the Dy^{III} ions. While compounds **3.24** and **3.25** have *ac*-signals below 1.8 K, compound **3.28** has a maximum (at 1500 Hz) at 4 K. A higher blocking temperature is observed in case of compound **3.28**. (See Fig. 3.28)

Furthermore, quantum tunnelling is observed in all cases, but, for compound **3.25**, the relaxation process is too fast to be observed in the apparatus window even under an external dc field, so the tunnelling regime for compound **3.25** is located at very low temperatures.

For compound **3.28**, the thermal activated relaxation regime is 2.3 - 4.0 K (under 0 Oe); 7.0 - 11.0 K (under 2000 Oe). For compound **3.28**, the energy barrier of the relaxation process is 8.1 K (under 0 Oe) and 70.0 K (under 2000 Oe); and the relaxation time is 1.3 10^{-5} s (under 0 Oe) and 1.5 10^{-7} s (under 2000 Oe). In other words compounds **3.24** and **3.25** show one relaxation process while compound **3.27** two relaxation processes (Fig. 3.28, lower).

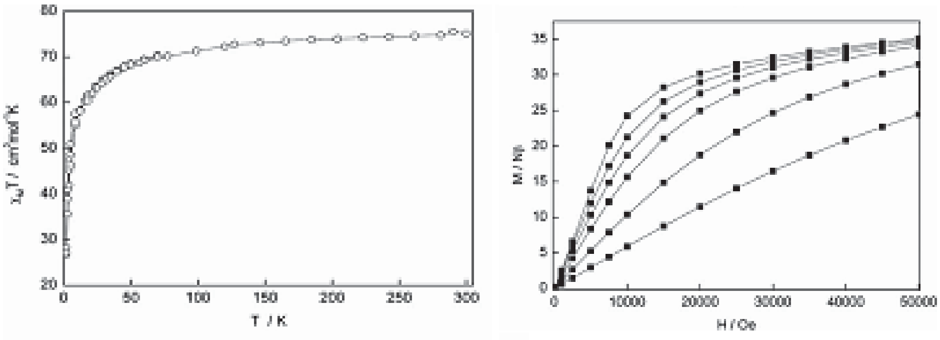

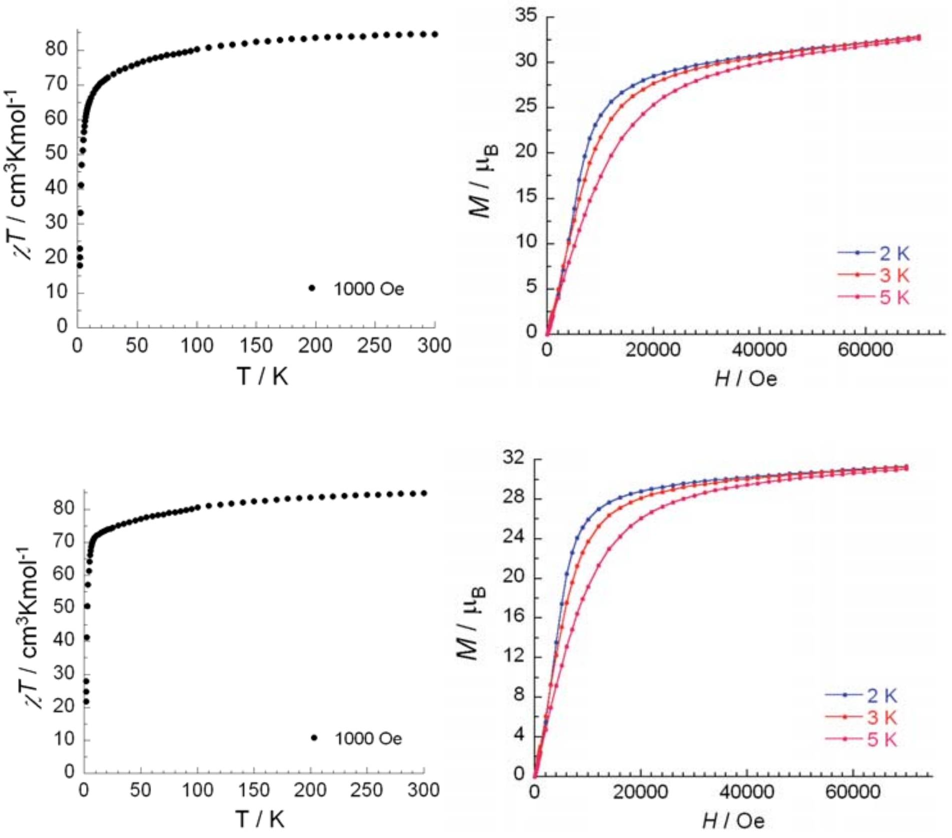

Figure 3.27. χT versus T plots at 1000 Oe for all three compounds; and field-dependence of magnetization of all three compounds.

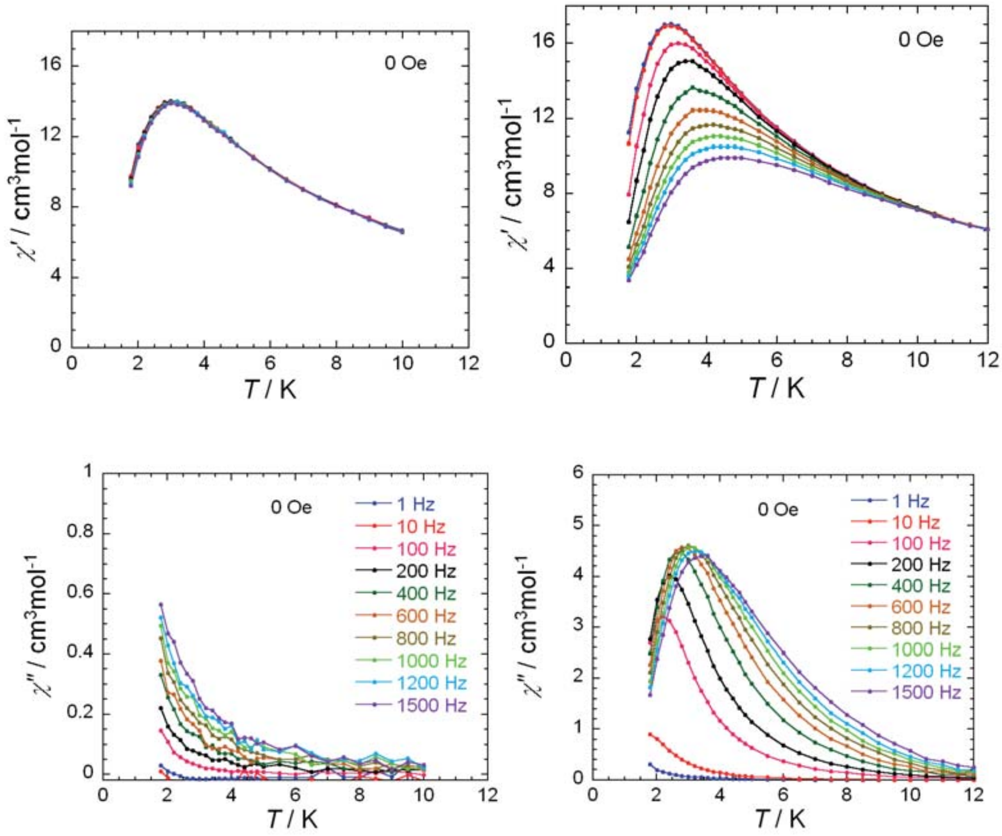

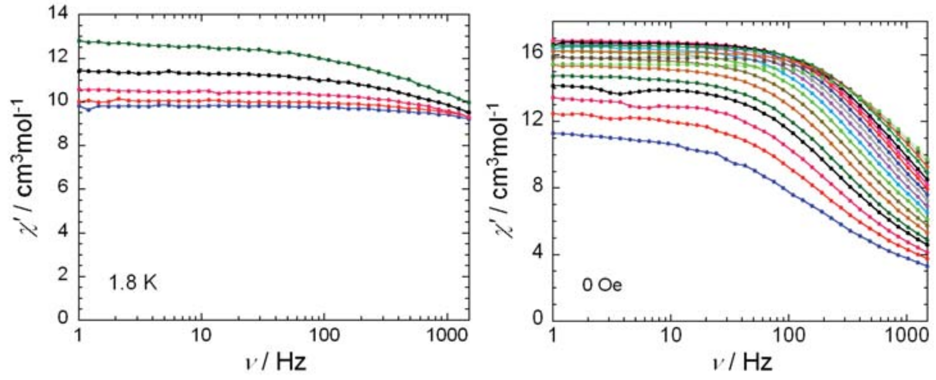
χ′ / cm³mol⁻¹
1.8 K
ν / Hz
χ′ / cm³mol⁻¹
0 Oe
ν / Hz

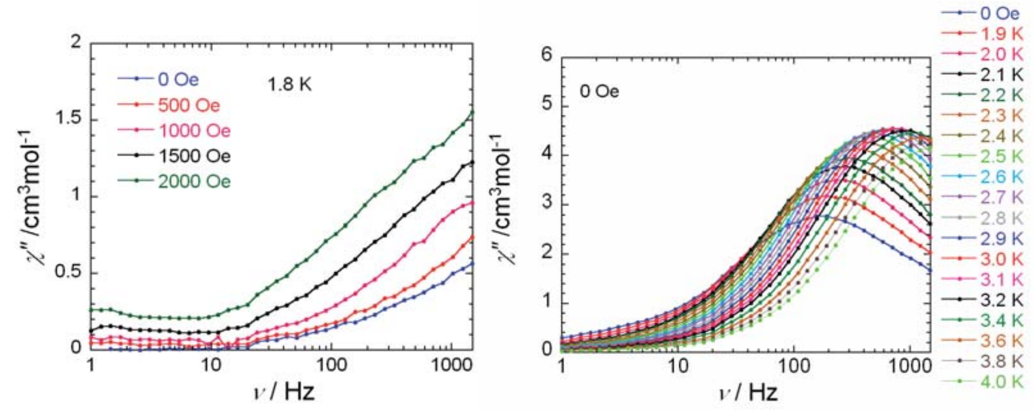
χ″ /cm³mol⁻¹
1.8 K
0 Oe
500 Oe
1000 Oe
1500 Oe
2000 Oe
ν / Hz
χ″ /cm³mol⁻¹
0 Oe
ν / Hz
0 Oe
1.9 K
2.0 K
2.1 K
2.2 K
2.3 K
2.4 K
2.5 K
2.6 K
2.7 K
2.8 K
2.9 K
3.0 K
3.1 K
3.2 K
3.4 K
3.6 K
3.8 K
4.0 K

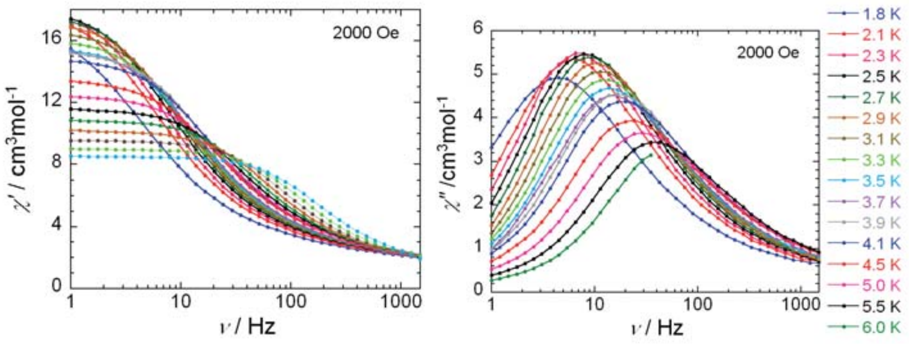
χ′ / cm³mol⁻¹
2000 Oe
ν / Hz
χ″ / cm³mol⁻¹
2000 Oe
ν / Hz
1.8 K
2.1 K
2.3 K
2.5 K
2.7 K
2.9 K
3.1 K
3.3 K
3.5 K
3.7 K
3.9 K
4.1 K
4.5 K
5.0 K
5.5 K
6.0 K

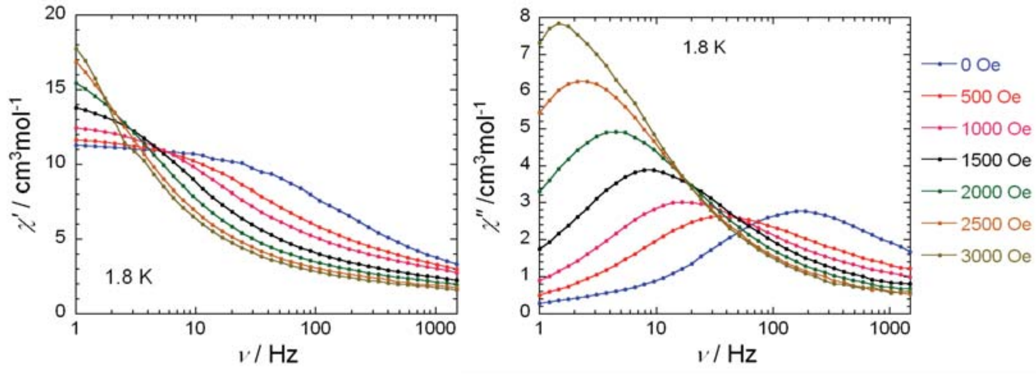
χ′ / cm³mol⁻¹
1.8 K
ν / Hz
χ″ / cm³mol⁻¹
1.8 K
ν / Hz
0 Oe
500 Oe
1000 Oe
1500 Oe
2000 Oe
2500 Oe
3000 Oe

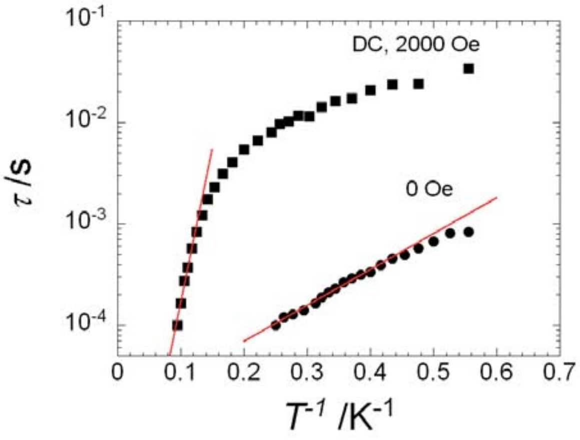

Figure 3.28. The *ac* magnetism of compounds **3.24** and **3.26** (this work). (Left, compound **3.24**) the in-phase signals (real part of *ac* susceptibility) by zero field, the out-of-phase (imaginary part of *ac* susceptibility) by zero field showing the maxima at 1.8 K, and the other following plots represent the in-phase and out-of-phase by different frequencies and fields showing the frequency and field dependency of them which confirm that 3.25 is a SMM. (Right, compound **3.26**) the in-phase and out-of-phase signals at zero field for **3.26** and the following plots represent the frequency and field dependency of *ac* susceptibility of both parts (real and imaginary). The maxima observed from out-of-phase is higher (~4K) for **3.26**. The out-of-phase frequency dependency signals show that **3.26** posses two relaxation processes at 2000 Oe. These data were used to plot the Arrhenius function in order to calculate the energy barriers at zero and 2000 Oe *dc* fields.

To be able to explain this large different in the SMM behaviour between these three compounds and in partciular for compound **3.28** which has two relaxation processes with relatively high energy barriers other experimental techniques are needed. ^{161}Dy-Mössbauer spectroscopy and other physical methods as well as theoretical calculations will be done in near future which might help in explaining the significant and remarkable differences between compounds **3.25** and **3.28**.

Furthermore, the synthesis using other Ln's will be neccesary, in particular the anisotropic ones such as Ho^{III} or Tb^{III}, in order to correlate to the ligand field influence, since these split with different m$_j$- levels compared with Dy^{III} (see chapter 1). If we, however, consider the observations in the tertanuclear system, where the substituent influence on the anisotropy of Dy^{III} centres was clear, then in case of Dy$_6$ systems the effect is expected to be even stronger, since the ligand here coordinates directly to the Dy^{III} centres.

For the hexanuclear 4f complexes with no ligands containing aromatic groups it is not possible to argue on the basis of Hammet constants. What we can do is to consider the dipole moment of a substituent on an alkyl-chain. Usually, as an approximation the alkyl-chains do not have a dipole moment although this is a rather arbitrary point-of-view.

At the same time, it might be useful to consider the electrostatic induction (inductive effect) of the groups –OH and -NH_2 as an approximation. Both are connected to an alkyl-chain. In case of –NH_2 is it a propylene chain and in case of –OH it is attached on the second position of a propyl. The calculated bond energies of C-N and C-O are both about ~280 kJ/mol. However, the experimental data are different with 353 kJ/mol for C-N and 463 kJ/mol for C-O. In addion, the covalence moment for N-H is 0.85 D slightly higher than for for O-H with 0.65 D. **[75]** As a first approximation we can say that the electron denisty is more shifted to N than to O. This can be easily understood when we take NH_3 as an example where the total dipole moment is shifted to N because of the difference in the electronegativity.

However, the group dipolmoment of –NH_2 group attached to an alkyl-chain in organic compounds is +1.23 Debye (D) (electron giver) and –OH is +1.70 D. This means that in a free Me-teaH_3 ligand the group dipolmoment with +1,70 -if we ignore the effect of the tert-amine because distance of three bonds the inductive effect decreases strongly makes the –OH group more positiv than the –NH_2 group with +1.23 D. In other words the –NH_2 group is indeed more basic and this could shift electron denisty in the direction of Dy^{III} and this ligand field could have a stronger influence on the f_z^{3} oribitals with lowest magnitude (prolate shape, see chapter 1) as seen in the DFT calculations done for Fe_2Ln_2 system. If we assume that, the anisotropy is concentrated in the volume-direction of f_z^{3}, then this might have the effect in case of –NH_2 group in increasing the zero fields splitting paramter D. The simple definition as $4f^9$ Kramers' Dy^{III} is in this case not enough. However, the term symbol for spin-orbit coupled ground state $^5H_{15/2}$ (S=5/2, L= 5/2, L=5 and J=15/2) still too complicated to be helpful in explaining this situation. A possible solution to this problem is to describe these ring structures as six repeating mono-nuclear Dy^{III} units and to modle the compound as a cyclic chain. Usually it is thought that for the lanthanides spin-orbit coupeld, J, is of more importance, since the spin-orbit coupling is larger than the effect of the cyrstal field for f-elements. Furthermore, a possible interpretation is that –NH_2 group or the cyrstal field cuased by is in interaction with spin-orbit coupeld J state so that a separation of spin ground state in the direction of the cyrstal field bigger than in case of –OH. The interaction of J with the cyrstal field not the field alone since this is much smaller than the effect of spin-orbit in lanthanides. Dy^{III} with $2J_{Dy}+1$ gives also 16 m_J (±15/2, ….., ±1/2) or (+J, J-1, J-2, …..-J). A small ligand field effect would be also enough to interact with J in a way causing larger zero field splitting and thus different relaxation process and sometimes mixing of the sub-states which then induce quantum tunelling. The observation of two relaxation processes in **3.26** could be explained through intercation of the cyrstals field with different m_J states by applying different magnetic fields.

3.4 Mössbauer Spectroscopy

{Fe_5Ln_3} Series

Mössbauer spectra (MS) of powdered sample of Fe_5Lu_3 **(3.3)** have been recorded at temperatures from 220 to 3K (Fig.3.29).

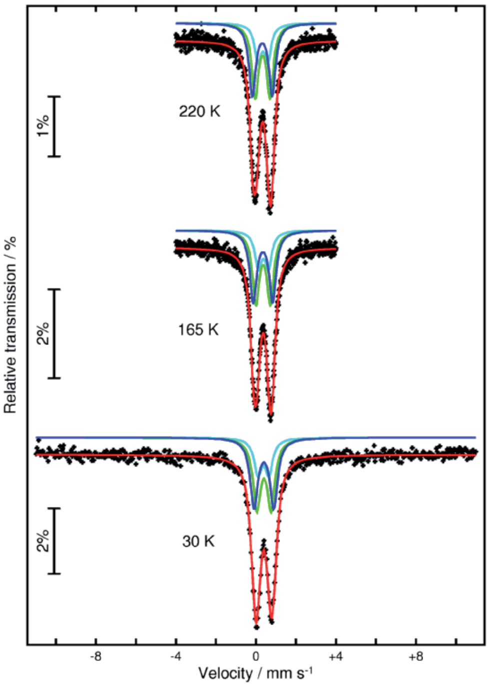

Figure 3.29. The ^{57}Fe Mössbauer spectra for Fe_5Lu_3 **(3.34)** at indicated temperatures.

The spectra from 220 to 30 K show composite quadrupole-split doublets appearing as two broad and asymmetric absorptions. No dipolar splitting due to an internal magnetic field was observed until 3 K. As could be expected from these partly split absorptions it was not possible to fit the Mössbauer spectra of Fe_5Yb_3 **(3.2)** by considering a unique quadrupole-split doublet. In order to satisfactorily fit the spectra, it was necessary to consider three nested quadrupole-split doublets, i.e. of very close isomer shift (δ), but different quadrupole splittings (ΔE_Q). The calculated values of bond-length distortions **[90]** around every iron ion are: Fe(1) = 2.04, Fe(2) = 2.20, Fe(3) = 2.11, Fe(4) = 3.47 and Fe(5) = 1.49. Although, according to these values all five iron sites have different distortion of the coordination sphere, the fit of the Mössbauer spectra at temperature of 30 K and above was done using three doublets corresponding to Fe(1) and Fe(3), Fe(2) and Fe(4), and Fe(5), respectively. Consequently, we constrained the area ratio of doublets to 2:2:1. The data corresponding to these fits are collated in Tab. 3.13.

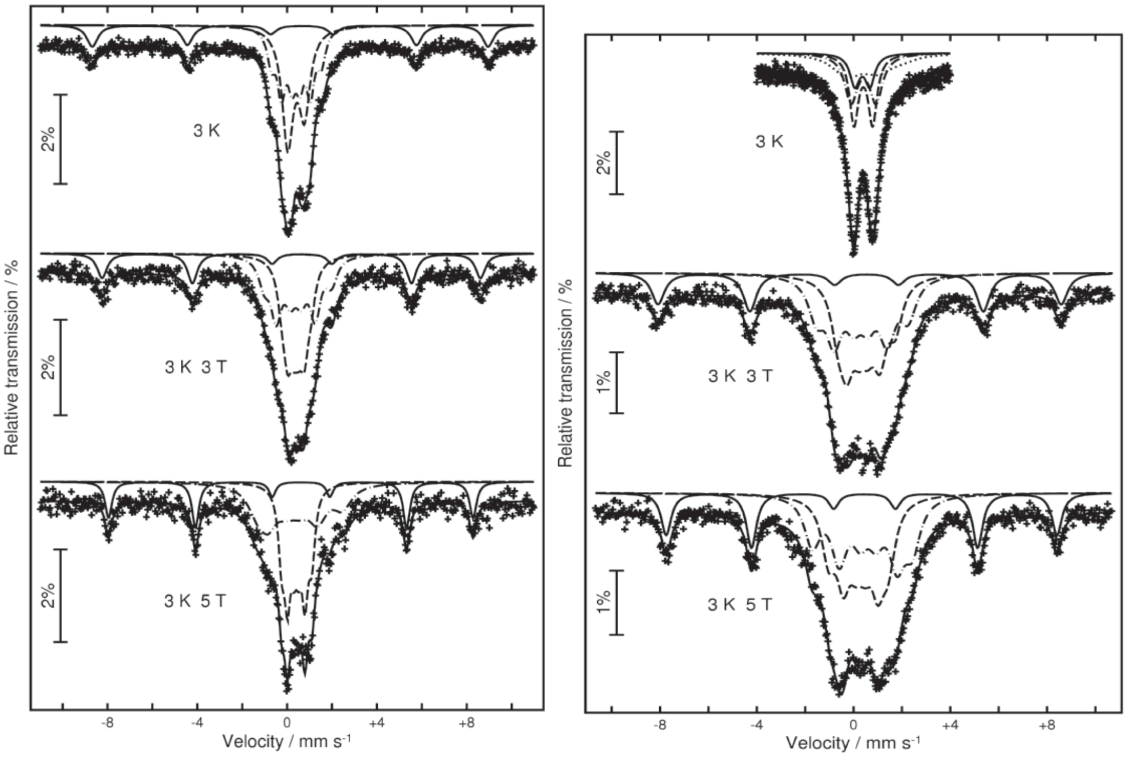

Figure 3.30. The ^{57}Fe Mössbauer spectra of $\{Fe_5Lu_3\}$ **(3.3)** (above) and $\{Fe_5Yb_3\}$ **(3.2)** (down) obtained at 3 K and at 3 K in an applied field of 3 and 5 T.

The isomer shift values for all sites are close to each other and are as expected for high-spin Fe^{III} (S = 5/2). The quadrupole splitting values are, however, different, clearly indicating small difference in the local symmetries at five Fe^{III} sites. The δ values decrease with increasing temperature because of the second-order Doppler Effect. There is no significant thermal variation of the ΔE_Q values, which is unexpected for high spin Fe^{III} with S = 5/2, $^6A_1$. For $^6A_1$, each orbital is occupied by a single electron, and there is no electric field gradient created by the electron cloud of the Fe atom.

The electric field gradient at the Fe nucleus is only due to the lattice charge distribution and if there is no crystal structure transition in the measured temperature, changes in ΔE_Q are negligible.

It is thus clear that there are different Fe^{III} (S = 5/2) sites in $\{Fe_5Lu_3\}$: the difference in local symmetry of the ligand environments is enough for allowing Mössbauer spectroscopy to easily distinguish these Fe sites.

Table 3.13. Mössbauer data for **Fe_5Lu_3** at the indicated temperatures and external magnetic fields.

T, K; H_{appl}, T	Fe sites	δ[a], mm/s	ΔE_Q or ε, mm/s	Γ, mm/s	H_{eff}, T
220 K	Fe(1,3)	0.442(6)	0.740(8)	0.406(7)[b]	-
	Fe(2,4)	0.425(6)	0.99(1)	0.406(7)[b]	-
	Fe(5)	0.45(1)	0.49(2)	0.406(7)[b]	
165 K	Fe(1,3)	0.468(9)	0.722(9)	0.417(7)[b]	-
	Fe(2,4)	0.457(4)	0.96(1)	0.417(7)[b]	-
	Fe(5)	0.481(9)	0.50(3)	0.417(7)[b]	
30 K	Fe(1,3)	0.51(1)	0.71(1)	0.46(1)[b]	-
	Fe(2,4)	0.505(6)	0.98(1)	0.46(1)[b]	-
	Fe(5)	0.49(2)	0.55(2)	0.46(1)[b]	
3 K	Fe(1,3)	0.50(1)[b]	0.74(1)	0.60(1)	-
	Fe(2,4)	0.50(1)[b]	0.022(7)	0.44(8)	6.9
	Fe(5)	0.50(1)[b]	-0.52(2)	0.59(2)	54.7
3K, 3T	Fe(1,3)	0.50[c]	0.02(1)	0.47(6)	4.0
	Fe(2,4)	0.50[c]	0.09(1)	0.60(2)	9.3
	Fe(5)	0.50[c]	-0.48(2)	0.53(2)	52.3
3K, 5T	Fe(1,3)	0.50[c]	0.024(8)	0.36(1)	4.2
	Fe(2,4)	0.50[c]	0.30(1)	0.98(2)	11.8
	Fe(5)	0.50[c]	-0.45(1)	0.36(1)	50.3

[a] Relative to α-Fe at room temperature; [b] constrained to the same value for all sites;

[c] Fixed values; For magnetically-split spectra $\varepsilon = ½\Delta E_Q(3\cos^2\theta\text{-}1)$.

On the basis of the crystal structure and magnetic susceptibility measurements, we can propose the magnetic structure which consists of two dinuclear antiferromagnetically coupled Fe units and a free Fe^{III} ion separated by three diamagnetic Lu ions. (Note, that, at low temperatures, in the case of mononuclear Fe^{III} containing units, the iron ions are far apart from each other and this results in a weak spin–spin interaction, a slow paramagnetic spin relaxation and consequently, magnetic splitting. In the super-paramagnetic particles of high-spin ferric ions we have an opposite situation; Fe^{III} ions will be close to each other, the spin–spin interaction will be stronger, the paramagnetic spin relaxation will be faster and the magnetic structure disappears.) In contrast to the MS at high temperatures, those at low temperatures (for example at 3 K) for compound **3.3** (Fig. 3.30 left) exhibit a superposition of a sextet and a broad and asymmetric doublet. The sextet was assigned to Fe(5) because of above mentioned explanations. The hyperfine field H_{hf} is the sum of several contributions: $H_{hf} = H_F + H_L + H_d$, where H_F is the field produced by the polarization of the core s electrons by the d electrons (so called Fermi contact interaction), H_L is the field produced by the orbital moment, and H_d is the dipolar field. In iron ions the dominant contribution to H_{hf} comes from H_F and is negative. Since high-spin Fe^{III} has no orbital moment, H_L is zero. H_d is also zero, because the ion has spherical symmetry, although a small dipolar field can be produced by covalent mixing of electrons from the ligands if the symmetry is lower than cubic. Hence for high-spin Fe^{III} H_{hf} is essentially equal to H_F.

The hyperfine interaction for a $3d^5$ electron configuration expected from Fermi contribution is of 55 T [91] The experimental value of H_{hf} for Fe(5) in compound Fe_5Lu_3 is 54.7 T. This fits very well with the expected one (55 T) and with values obtained for oxides (~11 T per S=1/2)[21]. It is imperative to mention here, that the H_{hf} contribution strongly depends on the strength of ionic bond and dimensionality, [92]. Indeed the largest H_F was found for FeF_3 (H_{hf} = 62.2 T), a 3D compound, while a reduction of 13% occurs for the two-dimensional one, $RbFeF_4$, and further decrease to 34% for the one-dimensional structure, in K_2FeF_5. Taking the reported value of 62.2 T for the five *d* electrons, in the most ionic configuration, one obtains 12.44 T per S=1/2 value. However, for Fe^{III} oxides [91] and $\{Fe(5)O_6\}^{9-}$ in compound **3.3**, a lower value of ~ 11 T per S=1/2 is obtained. Therefore, the value obtained for Fe(5) could be use as an additional reference for the assessment of the H_F contribution in measured systems and extrapolate it to cases of polynuclear coordination compounds where it cannot be directly measured. The decreased value of H_F term for the Fe^{III} oxides and Fe(5) in comparison with the value in FeF_3 is due to increased covalency in the ligand bonds.[93]

Applying external magnetic fields, the total field at the Fe(5) nucleus, H_{eff}, which is the sum of the applied and magnetic hyperfine fields, decreases with increasing H_{appl}. The field is reduced because the Fermi contact term is opposite in sign to the applied field.[94]

The central part of the spectrum at 3K represents a doublet which is broader than one registered at 30 K and has shoulders at about –1, +1.8 and +2 mm/s, but no obvious magnetic hyperfine lines are resolved. Attempts to fit this doublet with two overlapping doublets assigned to Fe(1) - Fe(3) and Fe(2) - Fe(4) dimers was not possible – the fits always gave very high χ^2 values. A reasonable fit was only possible introducing an additional sextet with a small internal field. This sextet was attributed to Fe(2) and Fe(4) ions which are closer to the Fe(5) ion. The much smaller field observed for the Fe(2) and Fe(4) ions may result from a transferred field arising from the Fe(5) ion (intra-ion Fe···Fe distances, Fe(2)···Fe(5) and Fe(4)···Fe(5) are 6.117 and 5.895 Å, respectively. Under applied magnetic field the H_{eff} on Fe(2) and Fe(4) increases, which now is the sum of applied and transferred fields.

The high-spin (d^5) Fe^{III} ions are isotropic, therefore the local spins tend to align along the direction of the applied field. The relative intensity of the $\Delta m=0$ lines of the sextet (number 2 and 5) with respect to the $\Delta m=1$ lines yields information on the angle φ between H_{eff} and γ-rays. In the case when the quadrupole interaction is treated as a small perturbation and the absorber thickness tends to zero, for ^{57}Fe, the relative intensities of the sextet lines, the outer, middle, and inner pairs of the sextet pattern, are given by $3(1+\cos^2\varphi):4\sin^2\varphi:(1+\cos^2\varphi)$. We have observed that the second and fifth lines of the sextet corresponding to Fe(5) are increasing in intensity and, respectively, the angle φ increases from 50.8° at 3 T to 54.7° at 5 T. This indicates that applying external fields it is possible to align the local moment of the Fe(5) ion along the direction of the applied field. The same tendency was observed for the Fe(1) - Fe(3) and Fe(2) - Fe(4) dimmers. In many cases of measurements on polycrystalline samples or powders, due to a far from vanishing absorber thickness, texture, and competitive electronic mechanisms, the ratios between the relative intensities of the sextet lines show smaller values than the theoretical ones. Therefore, it is not possible to establish very reliably the value of the angle between the H_{eff} and the incident gamma ray in the present case. However, from the clearly increasing trend of relative ratio between middle and inner line area for the external sextet, one may conclude that the effective fields tend, as physically expected, to orient themselves perpendicular to the incident ray direction, i.e., parallel to the direction of the applied field. This feature, in a parallel way, is also suggested by the variation of the angle θ between the main electrical field gradient (EFG) principal axis (V_{zz}) and the H_{hf}. This angle can be obtained from the quadrupole shift values (Tab. 3.13) observed in the magnetically ordered, ε, and quadrupole splitting observed in the disordered (paramagnetic) spectra ΔE_Q, according to the formula: $\varepsilon = ½\Delta E_Q(3\cos^2\theta\ -1)$. The quadrupole shifts are easy to observe from the spectra as a difference in the splitting of 1 and 2 and 5 and 6 iron(III) lines at 3 K in zero field and external fields of 3 and 5 T. Although for the two central sextets the quadrupole shift values are not so consistent, a clear variation of the ε values for the external sextet is observed from – 0.52 mm/s at 3 K to – 0.45 mm/s at 3K, 5T. It is obvious that the angle θ also changes under applied field.

Whereas at T>25 K the MS of compound **3.2** (Fig. 3.31) are almost identical with the spectra of complex **3.3**, distinct behavior is observed at 3 K (Fig. 3.30, right). The MS of **3.2** obtained at 3 K shows only an asymmetric doublet with significantly larger linewidth than in higher temperature range. No obvious sextet of slow paramagnetic relaxation, as in case of compound **3.1,** was observed. Only based on severe absorption line broadening and loss of intensity one can admit the domination of 3 K spectrum by intermediate spin relaxation phenomena.

Although the interaction between Yb^{III} and Fe^{III} ions is very weak and mostly of a dipole nature, the paramagnetic spin relaxation on Fe(1) - Fe(5) ions in compound **3.2** is faster than in case of Fe(1) - Fe(5) ions in compound **3.3** and magnetic structure (spectrum) at 3 K disappears. For this nonmagnetic form H_{hf} for, e.g. Fe(5), was determined by applying an external field, and the value of H_{hf} measured in this way was identical with that found in **3.3**. Since the largest contribution to H_{hf} (H_F) is negative, H_{appl} must be added to H_{eff} to obtain H_{hf}.

As in case of compound **3.3**, with application of external magnetic field we have observed changes of the values of quadrupole shifts and in the intensities of the second and fifth absorption lines. The ε values for Fe(5) in compound **3.2** are different from those found in compound **3.3** (Tab. 3.14).

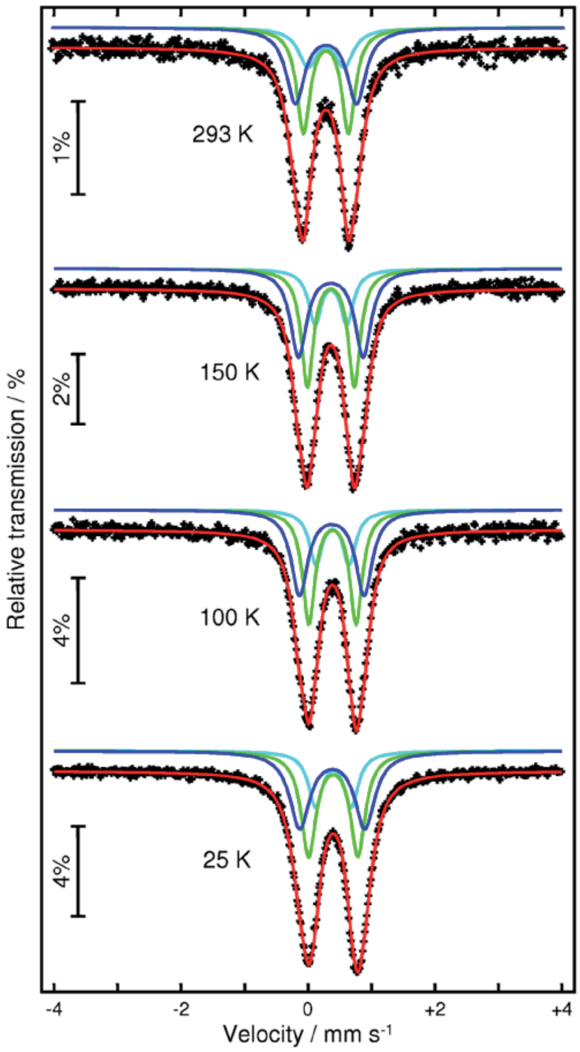

Figure 3.31. Mössbauer spectra of Fe_5Yb_3 (**3.2**) at different T.

Tab. 3.14. Mössbauer data for $\mathbf{Fe_5Yb_3}$ at the indicated temperatures and external magnetic fields.

T, K; H_{appl}, T	Fe sites	δ[a], mm/s	ΔE_Q or ε, mm/s	Γ, mm/s	H_{eff}, T
293 K	Fe(1,3)	0.390(1)	0.70(4)	0.25(6)	-
	Fe(2,4)	0.390(1)	0.96(2)	0.35(2)	-
	Fe(5)	0.390(1)	0.56(2)	0.35(1)	
150 K	Fe(1,3)	0.466(9)	0.74(1)	0.231(9)	-
	Fe(2,4)	0.466(2)	1.018(7)	0.309(8)	-
	Fe(5)	0.47(1)	0.50(3)	0.25(1)	
100 K	Fe(1,3)	0.492(4)	0.745(9)	0.23(1)	-
	Fe(2,4)	0.481(1)	1.017(8)	0.315(9)	-
	Fe(5)	0.492(2)	0.52(2)	0.25(1)	
25 K	Fe(1,3)	0.504(1)	0.777(6)	0.283(9)	-
	Fe(2,4)	0.489(1)	1.026(8)	0.384(9)	-
	Fe(5)	0.505(1)	0.564(9)	0.270(6)	
3 K	Fe(1,3)	0.50(1)[b]	0.75(5)	0.51(8)[b]	-

	Fe(2,4)	0.50(1)[b]	0.93(5)	0.51(8)[b]	-
	Fe(5)	0.50(1)[b]	0.56(9)	0.51(8)[b]	-
3K, 3T	Fe(1,3)	0.50[c]	0.14(1)	0.70(6)	7.3
	Fe(2,4)	0.50[c]	0.06(1)	0.80(2)	11.8
	Fe(5)	0.50[c]	-0.28(1)	0.65(2)	51.7
3K, 5T	Fe(1,3)	0.50[c]	0.15(1)	0.70(6)	7.9
	Fe(2,4)	0.50[c]	0.12(1)	0.80(2)	12.2
	Fe(5)	0.50[c]	-0.11(1)	0.51(1)	50.1

[a] Relative to α-Fe at room temperature; [b] constrained to the same value for all sites;

[c] Fixed values; for magnetically-split spectra $\varepsilon = \frac{1}{2}\Delta E_Q(3\cos^2\theta\text{-}1)$.

Although the orbital moment for Yb^{III} ion is very small, nevertheless different values for ε suggests that the observed changes originate from the interaction of Fe^{III} with Yb^{III} ions in the molecule. Given that the high-spin Fe^{III} is a relatively isotropic ion and Yb^{III} has a single *f* unpaired electron which is shielded by 5*s* and 5*p* orbitals, this suggests that the major contribution to the interaction is induced by the small anisotropy of Yb^{III} ions which could be considered as small dipoles which interact with iron ions or nuclei.

Although the H_{eff} on Fe(5) is very similar to the H_{eff} found in compound **3.3**, the values of H_{eff} for the Fe(1) - Fe(3) and Fe(2) - Fe(4) dimers are a bit bigger which shows that in the last case there is transfer of field not only from paramagnetic Fe(5), but also from Yb^{III} ions.

From the beginning (to avoid overparameterization) the MS was fitted using three doublets, one being assigned to Fe(2) and Fe(4) ions which have the biggest bond length distortions. Fe(4) has a $\{O_5N\}$ and Fe(2) a $\{O_6\}$ coordinations, respectively. As discussed before, the covalent transfer of the outer electrons of an atom affects both the charge and spin density at the nucleus, and results in measurable changes in the isomer shift and hyperfine field, which are directly related to these two quantities. Although the small difference between Fe-O and Fe-N covalencies should not affect much the isomer shifts, it might affect the hyperfine fields. Therefore, we assume that the best fit of central envelope at 3 K would have been with a sextet for Fe(2) and one for Fe(4) ions, which is not an easy task for such a narrow region.

Whereas at T>25 K and at 3 K in applied magnetic field, the MS for compound **3.1** are identical with the spectra of **3.2**, distinct behavior is observed at 3 K (Fig. 3.32 and Tab. 3.15).

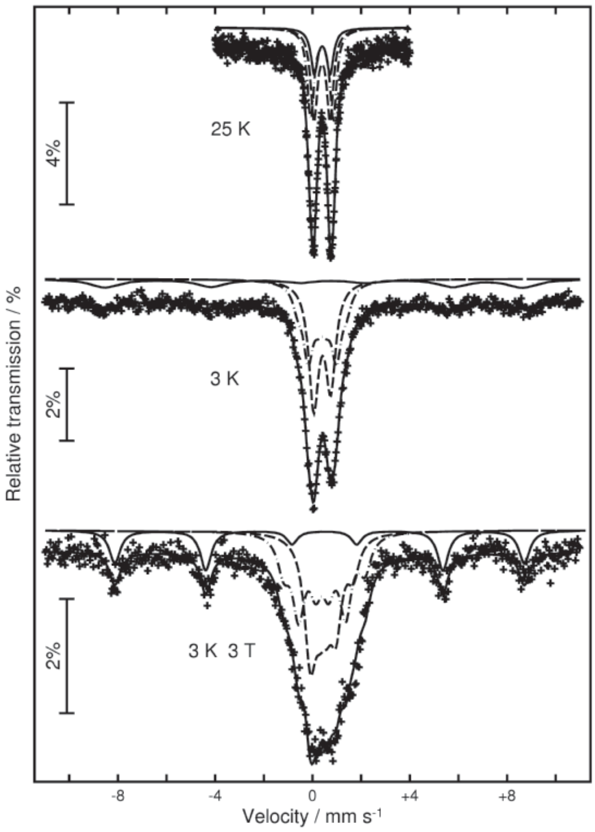

Figure 3.32. The ^{57}Fe Mössbauer spectra for Fe_5Tm_3 **3.1** at indicated temperatures and field.

Tab. 3.15.Mössbauer data for Fe_5Tm_3 **3.1** at the indicated temperatures and external magnetic fields.

T, K; H_{appl}, T	Fe sites	δ[a], mm/s	ΔE_Q or ε, mm/s	Γ, mm/s	H_{eff}, T
25 K	Fe(1,3)	0.50(4)	0.66(9)	0.33(1)[b]	-
	Fe(2,4)	0.49(1)	0.93(1)	0.33(1)[b]	-
	Fe(5)	0.506(2)	0.65(2)	0.33(1)[b]	
3 K	Fe(1,3)	0.50[c]	0.69(1)	0.50(1)	-
	Fe(2,4)	0.50[c]	-0.01(1)	0.49(2)	6.2
	Fe(5)	0.52(5)	-0.75(9)	1.45(9)	53.2
3 K, 3 T	Fe(1,3)	0.50[c]	0.32(2)	0.57(2)	5.6
	Fe(2,4)	0.50[c]	0.09(5)	0.61[c]	10.3
	Fe(5)	0.52(5)	-0.19(1)	0.53(2)	52.2

[a] Relative to α-Fe at room temperature; [b] constrained to the same value for all sites;

[c] Fixed values; for magnetically-split spectra $\varepsilon = ½\Delta E_Q(3\cos^2\theta\text{-}1)$.

The spectrum contains a central asymmetric doublet with significantly larger linewidth than in higher temperature range (similar to **3.2**) and a broadened inset with wings that extend from about -9 to +9 mm/s. The hyperfine parameters are comparable to those obtained for the **3.2** compound.

The broadened magnetic inset could appear because of Fe^{III} – Tm^{III} interaction, which is weaker in comparison to Fe^{III} – Yb^{III}, and as a result, slow spin relaxation corresponding to intermediate relaxation times.

Fe_4Ln_2 (**3.4-3.7**)

At 3 K and higher temperatures the Mössbauer measurements for all Fe_4Ln_2 complexes **3.5-3.7** yielded equivalent spectra – doublets, which are characterized by similar values of quadrupole splitting (ΔE_Q), implying four Fe sites with similar coordination spheres, in agreement with the molecular structure. The Fe(1)-Fe(2) and Fe(3)-Fe(4) units are antiferromagnetically coupled and thus have an S = 0 ground state, as determined from MS at 3K in applied magnetic field on the Fe_4Lu_2 **3.7** analogue (Fig. 3.33) for which $H_{eff} = H_{appl}$. Remarkable difference were observed at 3 K in an external applied magnetic field of 4 T: the Mössbauer spectra for Fe_4Tm_2 **3.5** (Fig. 3.34) and Fe_4Yb_2 **3.6** (Fig. 3.35) are dominated by intermediate relaxation phenomena. They are significantly broadened, with wings that extend from about – 1.5 to + 2 mm/s and – 3 to + 3 mm/s for the Fe_4Tm_2 and Fe_4Yb_2, respectively. The MS of Fe_4Er_2 (**3.4**) is very similar to the others an dit is not introduced in this work because it was measured nearby the end of this work.

Although the magnetic moment for the Tm^{III} ion is bigger than for Yb^{III}, nevertheless the interaction or transferred field from Yb^{III} to Fe^{III} is bigger, giving rise to a much broader Mössbauer spectrum. The reason may lie in the anisotropy of individual m_J states, and zero-field splitting of the Ln^{III} ion *J* ground states. Probably the crystal field created by the ligand environment generates stronger single-ion anisotropy for the Yb ion than for Tm^{III}. The most favorable coordination environment for the Yb^{III} ion having noticeable separation between the $m_J = 7/2$ ground state and first excited state is equatorial. This was shown recently by Brooker and co-workers [95], how for such ligand-field symmetry, stabilization of sublevels with a large m_J value can be attained, thus achieving an easy-axis of the magnetization for Yb^{III} ion. Although absence of out-of-phase *ac* signals was observed at low temperature, slow relaxation was achieved by applying a small *dc* field. The same situation we have in Mössbauer spectra in external magnetic field: the effective magnetic fields on iron nuclei are bigger than external ones, which might be due to slower relaxation of magnetization on Yb ions and stronger magnetic interaction with Fe ions of the antiferromagnetically coupled binuclear units. Similar, though smaller effects were seen for the Fe_4Tm_2 (**3.5**) compound. An alternative reason may be that on applying an external magnetic field there is an increase in the difference between the energy of the ground and first exited states of Yb^{III} or Tm^{III} ions, thus enabling the system to increase its energy and, respectively, its anisotropy. This is opposite to the effect observed for the {Fe_2Dy_2} series (chapter 2), for which it was proposed that the applied magnetic field affected the ground state of Dy^{III} ions lowering its energy and, as a result, Mössbauer spectra typical for antiferromagnetic coupled dinuclear iron compounds were obtained.

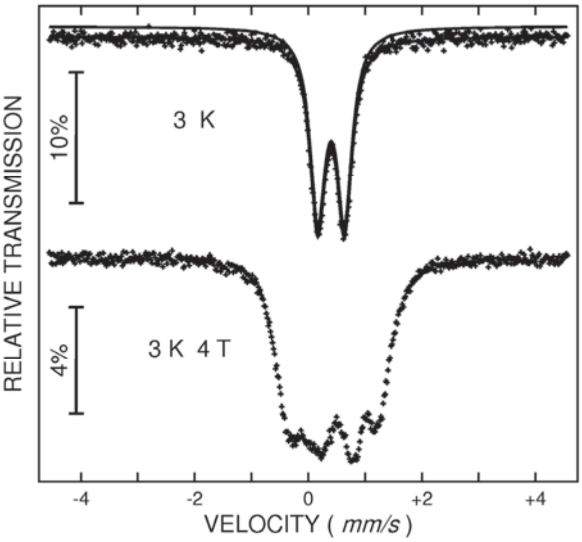

Figure 3.33. Mössbauer spectra of Fe_4Lu_2 (**3.6**) at 3 K and 3 K and 4 T.

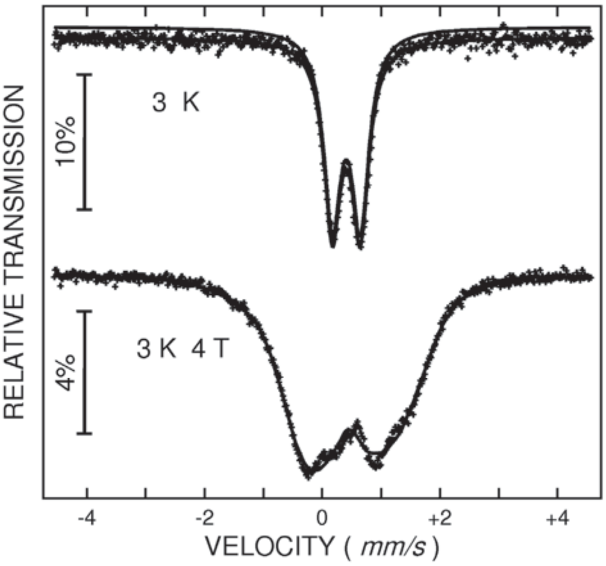

Figure 3.34. Mössbauer spectra of Fe_4Tm_2 (**3.4**) at 3 K, 3 K and 4 T.

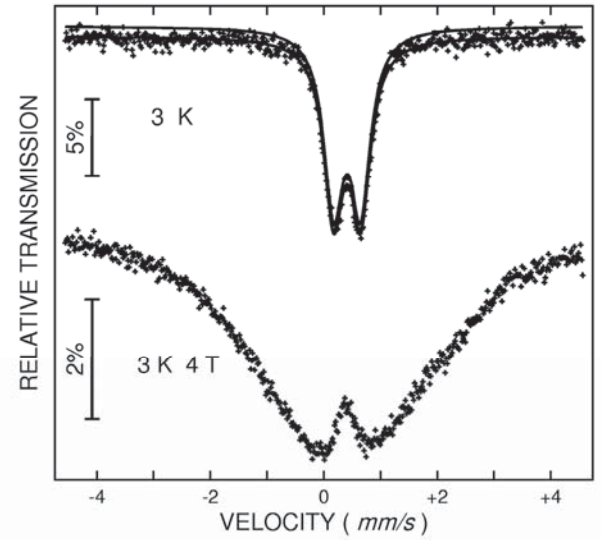

Figure 3.35. Mössbauer spectra of Fe_4Yb_2 (**3.5**) at 3 K, 3K and 4 T.

Fe_3Ln_2 (**3.8-3.11**)

The Mössbauer spectra of compounds (**3.8-3.11**) at different T and fields are shown Fig.'s 3.36-3.38.

According to the crystal structure of Fe_3Ln_2 (**3.8-3.11**), which consists of a dinuclear antiferromagnetically coupled Fe unit and an Fe^{III} ion separated by two Ln ions, the Mössbauer spectra at 3 K were fitted correspondingly as a superposition of a sextet and a doublet. The sextet was assigned to Fe(3) and doublet – to Fe(1) and Fe(2). As in case of Fe_4Ln_2 (**3.4-3.7**) series, under applying external magnetic field, the central inset shows distinct behaviour dependent on the nature of the neighbouring lanthanide: for Ln = Lu^{III}, $H_{eff} = H_{appl}$, for Ln = Tm^{III} or Yb^{III}, $H_{eff} > H_{appl}$. As stated above, this is due to different properties of the Ln^{III} ions: diamagnetic or paramagnetic. Different behaviour is also observed at 3 K: the sextets assigned for the single Fe(3) ion in Fe_3Lu_2 and Fe_3Tm_2 (**3.9**) show well defined absorption lines indicating slower than Mössbauer time scale ($\sim10^{-8}$ s) relaxation of the spins on those Fe ions. For the Fe_3Yb_2 (**3.10**) also a magnetic sextet could be defined, but with significantly larger linewidths indicating a relaxation at the intermediate rate. The reason may well be the same as in case of Fe_4Ln_2 series: the Fe^{III} – Yb^{III} interaction is stronger than the Fe^{III} – Tm^{III} or Fe^{III} – Lu^{III}, and as a result, slow spin relaxation corresponding to intermediate relaxation times.

The Er analouge (**3.8**) was not measured because of time limitations and the fact that since no Er compounds were obtained in the other series there would be no insight in terms of this comperative study aimed at understanding the influnce of the last three lanthanides.

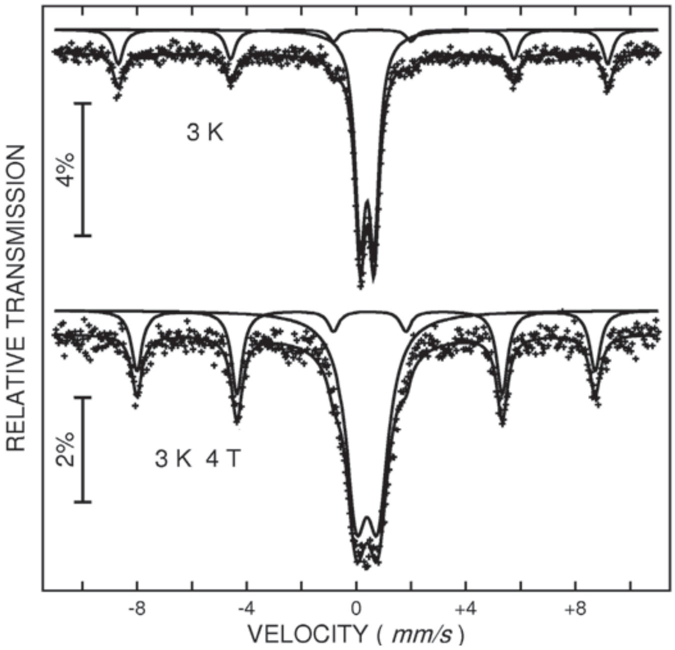

Figure 3.36. Mössbauer Spectra of Fe_3Lu_2 (**3.11**) at 3K, 3 K, 4T.

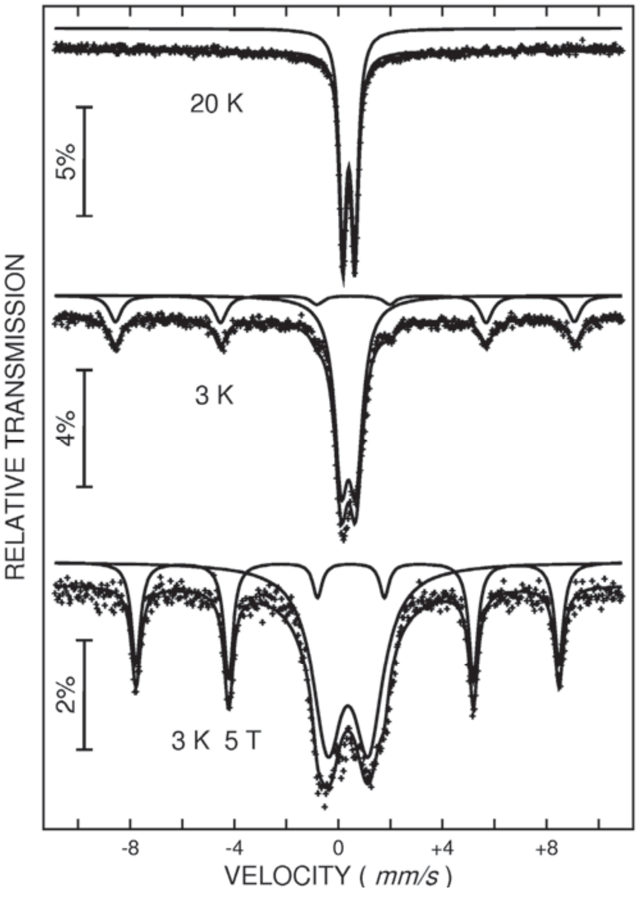

Figure 3.37. Mössbauer spectra of Fe_3Tm_2 **(3.9)** at 20 K, 3K, 3K and 5 T.

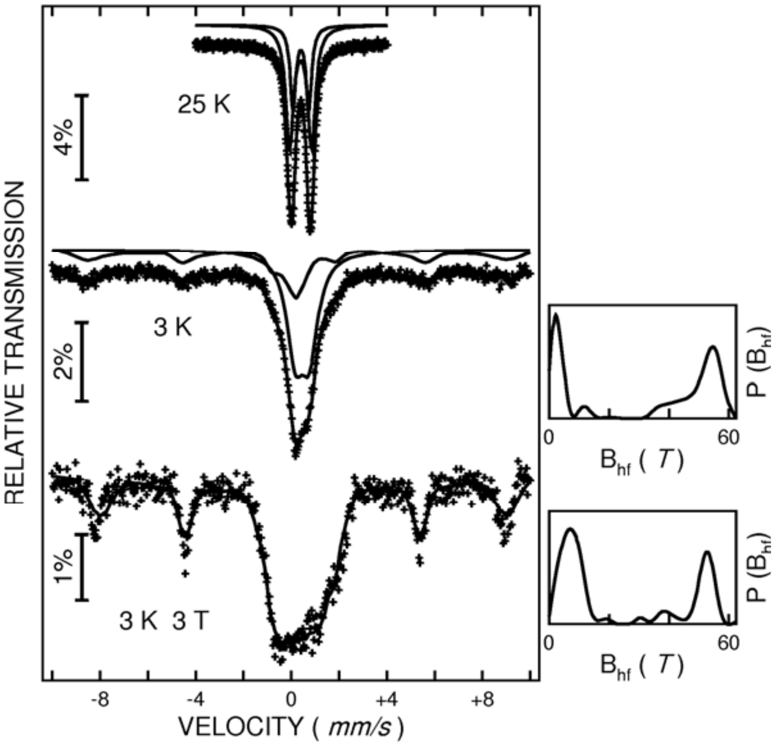

Figure 3.38. Mössbauer spectra of Fe_3Yb_2 (**3.10**) at 25 K, 3 K, and 3 K and 3 T.

$Fe_{16}Ln_4$ (**3.15-3.20**) [36f)]

^{57}Fe Mössbauer spectra for **3.17** were obtained at 3 K both in zero fields and in an external field of 5 T (Fig. 3.39).

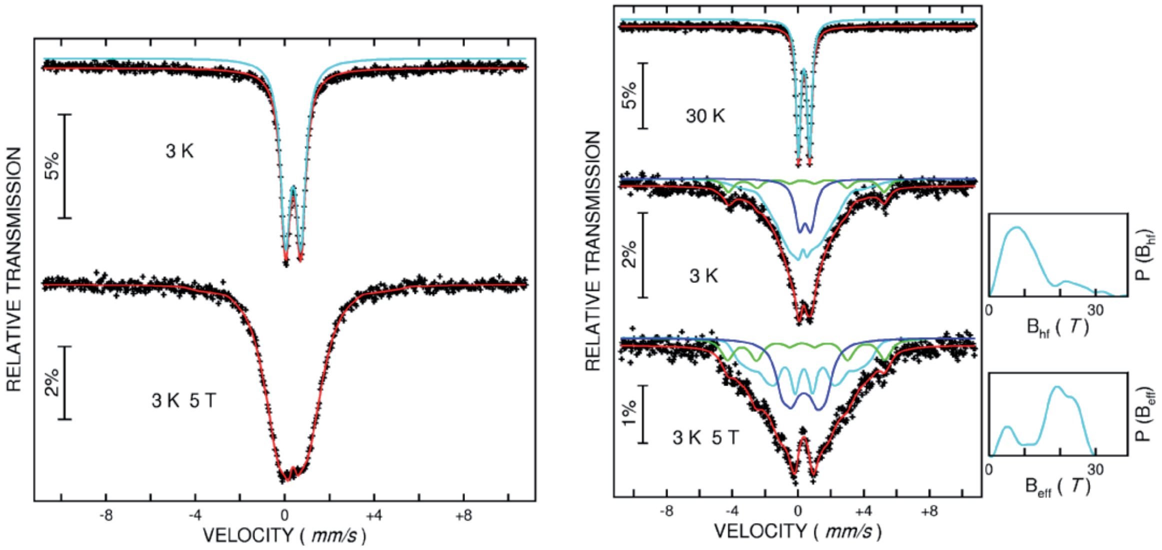

Fig. 3.39. (left) Mössbauer spectra of $Fe_{16}Gd_4$, **3.17** at 3 K in zero field and a transverse magnetic field of 5 T. (right) Mössbauer spectra of **3.19** at 30, 3 K in zero field and a transversal magnetic field of 5 T. The probability distribution of the magnetic hyperfine field is shown on the right side.

The zero field spectrum consists of a single symmetric quadrupole doublet with identical isomer shift (0.47 mm/s) and quadrupole splitting (0.68 mm/s) values as found for the Dy analogue, **3.19**, at 30 K. The spectrum in external magnetic field is readily interpreted in terms of a single iron site with the magnetic field at the nucleus equal to the applied field. These results indicate that the iron atoms in **3.17** are essentially equivalent and strongly antiferromagnetically coupled. At 3 K no magnetic hyperfine interaction apart from that of the nucleus with the applied field is observed. The distance of ~ 6.9 Å between Gd ions in every {Gd-OCO-Gd} unit suggests there will be an almost negligible interaction between them. In line with this, in both the zero and applied field spectra there is no indication of any transferred field effects which can occur via contact delocalisation. This would be caused by delocalisation of electronic spin density in the cluster from Gd ions to the antiferromagnetically coupled iron ions.

In contrast, the zero-field 3 K spectrum (Fig. 3.39) is exceedingly complex, better reflecting the complexity of the structure. Although such spectra are usually fitted with a distribution of hyperfine fields, this is not appropriate here although we can try to rationalise what we observe. If we assume that, as in the case for the Gd compound **3.17**, the Dy^{III} ions in every $\{Dy_2\}$ dimer unit are essentially non-coupled, then the local magnetic field induced by the anisotropic Dy^{III} ions might polarise the *s*-electronic density of the Fe nuclei, as a result of which magnetic lines are seen in Mössbauer spectra. The absorption peaks at ca. –4.15 and 5.30 mm/s could correspond to the first and sixth lines, respectively, of a magnetic sextet (H_{hf} = 29.4 T). The central two absorption peaks fit very well a doublet with similar parameters to 30 K spectrum. The remaining part of the spectrum can only be fitted using a distribution of hyperfine fields. Consequently, the obtained spectrum is a superposition of three distinct spectra, attributed to different iron ions in the structure.

The 5 T spectrum of $Fe_{16}Dy_4$ (**3.19**) s also very complicated. Since the interactions between f-d electronic systems are essentially of magnetic dipolar nature, it will be the dipole interactions of Dy^{III} with Fe nuclei, which in essence determine the ^{57}Fe magnetic hyperfine interactions. These are different for all irons in applied magnetic field and this might also be dependent on the relative position of Fe^{III} and Dy^{III} ions and the directions of their easy axes of magnetisation. The peripheral iron nuclei, in comparison to central ones, experience different hyperfine fields, and consequently, the resultant Mössbauer spectrum at 3K in applied field of 5 T, as in the case of the zero-field one, has contributions from each of the peripheral iron sites as well as from the central iron ions and is a superposition of three spectra. The applied magnetic field does not have much influence on the interaction between Dy ions and iron nuclei. The main difference is seen in the shape of the central sextet (blue line), which was initially a doublet and now is a sextet with the magnetic field at the nuclei roughly equal to the applied field.

Fe_4Dy_4 ***3.22***

Mössbauer spectrum of powdered sample of **3.22** at 40 K shows an asymmetric quadrupole-split doublet (Fig. 3.40, Table 3. 16). The isomer shift (δ) of 0.50 mm/s and quadrupole splitting ΔE_Q of 0.61 mm/s are as expected for high-spin Fe^{III}. At 3 K, a well defined magnetic spectrum with the characteristic six absorption lines is observed (Fig. 3.44), which indicates that the spin-relaxation has crossed from fast to slow with respect to the Mössbauer timescale. The lines are asymmetric and weakly broadened, most likely due to slight differences in the local symmetries and hyperfine internal magnetic fields on the four Fe^{III} ions. Therefore, the spectrum was fitted with two sextets with parameters listed in Table 3.16.

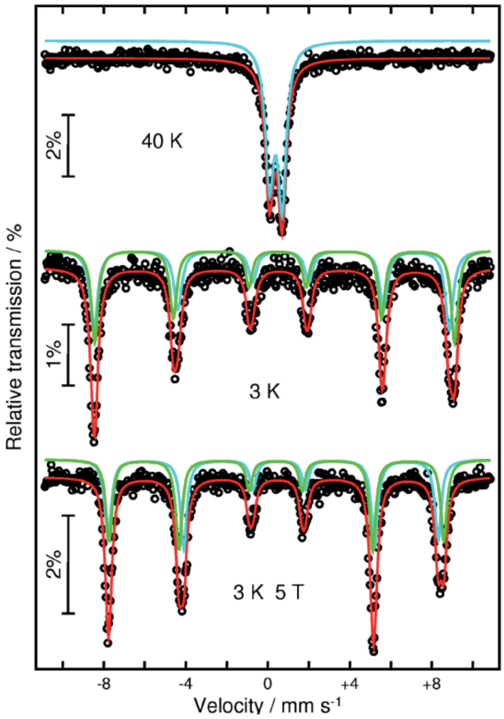

Figure 3.40. The ^{57}Fe Mössbauer spectra for **3.22** at 40 K and 3 K in zero and applied magnetic field of 5 T oriented perpendicular to the γ- ray.

Table 3.16. Mössbauer data for **3.22** at 40 and 3 K in zero-applied magnetic field and at 3K in applied magnetic fields of 5T.

T, K	δ[a], mm/s	ΔE_Q or ε[c], mm/s	Γ, mm/s	θ[d], °	B_{eff}, T
40	0.506(3)	0.612(4)	0.51(1)	-	-
3	0.52[b]	-0.45(2)	0.46(2)	52.6	53.80(7)
	0.52[b]	-0.14(2)	0.40(1)	52.6	54.41(6)
3K, 5T	0.52[b]	-0.30(1)	0.38(1)	66.8	49.92(5)
	0.52[b]	0.03(1)	0.37(1)	66.8	50.63(5)

δ is the isomer shift, ΔE_Q - quadrupolar splitting, θ - angle between B_{eff} and direction of γ-rays, B_{eff} - the effective magnetic field. [a] Relative to α-Fe at room temperature. [b] Fixed values. [c] For magnetically-split spectra $\varepsilon = ½\Delta E_Q(3\cos^2\varphi-1)$. φ - angle between the B_{int} and the main electrical field gradient (EFG) principal axis (V_{zz}). The quadrupole shifts are easy to observe from the spectra as a difference in the splitting of 1 and 2 and 5 and 6 iron(III) lines at 3 K. [d] Constrained to the same value for all sites.

A polycrystalline sample is to be measured in an external magnetic field in order to determine the type of magnetic ordering. If the material is ferromagnetic, one would expect the rotation of the internal field directions to reduce the internal hyperfine field. The field is reduced because the Fermi contact term will be opposite in sign to the applied field and as result we see the decrease in the magnetic splitting. In addition, if the direction of the external field is perpendicular to that of the Mössbauer γ-rays, the $\Delta m = 0$ transitions (represented by the second and fifth peaks of a sextet) will increase in intensity for ferromagnetic materials. As is seen from the MS at 3 K in external magnetic field of 5 T, there is no additional magnetic splitting in the Mössbauer spectra and the applied magnetic field reduce the internal hyperfine field. In addition, the intensities of the middle lines increases, which corresponds to an increase of angle θ from 52.6 to 66.8°, i.e., the effective field tends to orient perpendicular to the incident ray or parallel to the applied field, respectively. This should not be missinterpreted, because four weakly coupled or uncoupled spins of S_{Fe} = 5/2 exhibit similar behaviour. But in present case we have evidence of ferromagnetic interaction from susceptibility data which support Mössbauer results. In conclusion, this compound, like the compound **3.23**, is a ferromagnet.[36g)] This obeservation form Mössbauer measuerements indeed supports the bulk magnetic measurements. However, it remains the question if we could see the difference observed in magnetism also in Mössbauer spectra and refere it to the nature of the ligand used in **3.22**.

Although both compounds show very similar behaviour, there is a very peculiar difference between Mössbauer spectra of **3.22** compared with **3.23**. The unusual influence on the iron ions generated by the magnetic Dy ions in compound **3.22** is revealed by the spectra measured at 3 K at $B_{\mathrm{appl}} = 0$ and also acquired with applied field. Though, the spectra for $\{Fe_4Dy_4\}$ **3.23** have been fitted with one sextet, while the fit for **3.23** was only possible with two sextets having the same value for δ, but different quadrupolar shifts, ε, and effective magnetic fields, B_{eff}. The reason may lie in different interaction between iron and dysprosium ions. The difference in quadropole parameters is understandable resulted from different Fe^{III} ligand enviroment. According to the structure of **3.22**, three lanthanides are eight-coordinate with distorted square-antiprismatic N_2O_6 coordination environments and one lanthanide are additionally coordinated by an aqua ligand, resulting in a capped square-antiprismatic N_2O_7 environment. The coordination fashion around Dy ions in **3.23** is the same, except the coordination shells of the four iron ions are distorted octahedral with O_6 environment. However, the Fe---Fe distances are significantley different in **3.22** compared with **3.23**.

The Ln's anisotropy of the ground state depends on the crystal field acting on the orbital moment. Having the same environment, but small differences in bond lengths (Fig. 3.8, lower) and angles, it is expected to see a different direction of the easy axes of magnetization on Dy^{III}, which respectively will influence the ^{57}Fe Mössbauer hyperfine parameters (especially the quadrupole splittings, which depend on the orientation of the electric field gradient, dictated by the lattice, relative to the magnetization direction) of the adjacent iron ions.

This results in two overlapped magnetic sextets with slightly different hyperfine parameters. Although this is a very small observation, nevertheless it shows how very small changes in the crystal field environment of lanthanide can have dramatic influence on the anisotropy of their ground state and this is enough for allowing Mössbauer spectroscopy to easily distinguish Fe sites interacting with those lanthanides.

3.5 Conclusions

In contrast to the synthetic strategy used to obatin the tetranuclear systems discussed in chapter 2 the synthesis of cyclic compounds was targeted. Through fine-tuning of several parameters such as nature of lanthanides, ligand and starting materials several new cyclic complexes could be indeed isolated. Through exchanging the $Ln(NO_3)_3$ salts of the last lanthanides with $Ln(OTf)_3$ rare and asymmetric cyclic Fe_5Ln_3 compounds could be prepared in high yield. These compounds were studied using a combination of Mössbauer and bulk magnetic studies but the description of their electronic structures remains challanging. It seems that the lanthanides Tm, Yb and even Lu can influence the magnetic enviroment of Fe nucleus. It is also clear from this study that such kind of magnetic hyperfine transfer cannot be expalined easily by using the bulk susceptibility sudies and that the more sensitive and faster time-scale (10^{-7}-10^{-8}s) method of Mössbauer is needed to understand the system.

For the hexanuclear $\{Fe_4Ln_2\}$ it is easier to correlate the SQUID data with Mössbauer measuerements at 3K and without field, since their non-magnetic nature is confirmed by both methods. However, Mössbauer method can detect relaxation which is not seen in SQUID measuerements even by applying a dc field, but which is best described as intermediate in nature. This is propably a result of slow time scale of the SQUID technique (~1s) for which only an average of the contributions can be analysed.

The case of the pentanuclear compounds is also very challenging. Again the magnetic method does not confirm the theoretical expected ground spin state even of the $\{Fe_3Lu_2\}$ compound. Mössbauer spectra of the Yb copound within this series indicate at 3K very fast spin relaxation. The spin relaxation cannot be “frozen” even at 4T. Here a very high field is needed, which is experimentally not possible with the instruments available.

The role of the ligand in these syntheses is very important. This we can see clearly in the case of the trisisopropanolamine ligand where no cyclic compound could be formed.

Six isostructural twisted 20-membered $Fe_{16}Ln_4$ metallo-rings have been synthesised. These rings are each braced into rigid structures by two *anit, anti*-bridging acetate groups. These are the largest such single-stranded oxygen-bridged metallo-rings so far reported. Magnetic and Mössbauer studies show that the magnetic behaviour for all results from the presence of the four Ln^{III} ions, the spins of which are pinned into a D_{2d} symmetry by coupling to the ends of the spin-compensated Fe_2 and Fe_6 moieties within the ring. Furthermore, the Mössbauer experimental data indicate that the interactions between the f and d electronic systems in the $Fe_{16}Dy_4$ complex are essentially of a magnetic dipolar nature. The contribution of the exchange interaction term, on the other hand, appears to be very small.

Two new Dy_6 systems could be prepared and were magnetically compared in order to deepnen the understanding of the ligand effect on the SMM behaviour.

A very high nuclearity $Fe_{18}Dy_6$ cyclic compound could be isolated. The interplay between the different cyclic situations in the strcuture is promissing, in order to have ususual magnetic properties.

Furthermore, a Fe_4Dy_4 cyclic complex was obtained by using an acetophenone and the triethanolamine ligands. Here was demonstrated that the exchange with carboxylates can favour ferromagnetic coupling between the Fe and Dy ions because the acetophenone is chealting and not bridging.

Chapter 4

$Fe_{10}Ln_{10}$ Cooperative Coordination Clusters

4.1 Introduction

In chapter 3 several cyclic coordination clusters with different nuclearities, metal ion arrangements and magnetic properties were discussed. One of these systems is the ring cluster $[Fe^{III}_4Dy^{III}_4(teaH)_8(hmacph)_4(H_2O)](NO_3)_4$ (**3.22**) with hmacph= $O_2CH_3C_6H_3OCH_3$= 2\`-hydroxy-4\`-methoxy-acetophenone (Fig. 3.7, left). In an equivalent synthesis to **3.22** but using Me-teaH_3 (methyl-triethanolamine) instead of teaH_3 (triethanolamine), a larger alternating Cyclic Coordination Cluster System (CCCS) $[Fe^{III}_{10}Ln^{III}_{10}(Me\text{-}tea)_{10}(Me\text{-}teaH)_{10}(NO_3)_{10}]$ ·XMeCN **{Nd (4.1), Eu (4.2), Gd (4.3), Tb (4.4), Dy (4.5), Ho (4.6), Er (4.7), Tm (4.8), Yb (4.9), Lu (4.10) and Y (4.11)}** was isolated. The hmacph ligand does not coordinate in the $\{Fe_{10}Ln_{10}\}$ CCCS system and these compounds (**4.1-4.11**) can be obtained without using it. The same system cannot be obtained by using triethanolamine which reflects the role of the methyl-groups and in particular the chirality in the Me-teaH_3 ligand on determining the final product. It seems likely that this system cannot be isolated by using an enantiopure Me-teaH_3 ligand because of the special hydrogen-bonding arrangement present in the system which leads to the structure being stabilised by a hydrogen pattern reminiscent of standing waves circualteing the ring. The result of this is that the molecule shows two “faces”; one all S and the other all R isomers of the ligand.

The magnetic measurements show that this system is dominated by ferromagnetic coupling, and very high ground spin states are expected. At low temperatures it is possible to achieve saturation on applying a field to give the maximum ground spin state of S=120/2 for $Fe_{10}Gd_{10}$. However, with the anisotropic lanthanides it is more challenging to understand the differences in the magnetic behaviour for each and especially so for $Fe_{10}Tm_{10}$. In this case the ferromagnetism becomes overwhelmed by antiferromagnetic coupling which cannot derive from the weak antiferromagnetic Fe···Fe interaction observed for all compounds at higher temperatures. Furthermore, the $Fe_{10}Tb_{10}$ and $Fe_{10}Dy_{10}$ compounds show similar SMM behaviour.

Moreover, high values for the magnetic entropy change (ΔSm) were calculated from the study of the Magneto Caloric Effect (MCE) [39] in the $Fe_{10}Gd_{10}$ and $Fe_{10}Dy_{10}$ compounds. MCE was discussed in more detail in chapter 1 (section 1.3) where it was pointed out that only recently has this effect, long known in solid-state physics, been explored in molecular systems. The ΔSm values for both compounds compare well with those for representative 3d and 3d/4f systems. Whilst the entropy change for $Fe_{10}Dy_{10}$ (**4.5**) is smaller than that of $Fe_{10}Gd_{10}$ (**4.3**), it is worth noting that the maximum change of ΔSm occurs at 6 K for $Fe_{10}Gd_{10}$ **4.3** and 5 K for $Fe_{10}Dy_{10}$ **4.5**, which are the highest temperatures observed for a coordination cluster to date. The theoretical entropy values are 48.0 J/kgK for $Fe_{10}Gd_{10}$ **4.3**, 45.4 J/kgK for $Fe_{10}Dy_{10}$ **4.5** and 36.14 J/KgK for $Fe_{10}Tm_{10}$ **4.8**, respectively. This system shows that it is not necessary to have a completely isotropic system and maximum spin states to achieve good molecular-based MCE parameters. However, at least in terms of the Dy^{III} $Fe_{10}Ln_{10}$ systems, it would seem that it is, indeed, possible to have a molecular system which can show both SMM behaviour and be an effective magnetic cooler. This might give the perspective of developing systems which act as self-cooling magnets and such putative systems represent an intriguing prospect in terms of energy efficiency and recycling.

The magnetic and MCE properties of the [$Fe_{10}Gd_{10}$] **(4.3),** [$Fe_{10}Dy_{10}$] **(4.5)** and [$Fe_{10}Y_{10}$] **(4.11)** will be discussed first in this chapter as representative compounds for isotropic Gd^{III}, anisotropic Dy^{III} lanthanides and for diamagnetic Y^{III} (with similar radius).

The fact that, the magnetic and MCE behaviour deviates at lower temperature arises from the onset of the importance of the antiferromagnetice Fe···Fe interaction. The Mössbauer study of the $Fe_{10}Dy_{10}$ **4.5,** $Fe_{10}Y_{10}$ **4.11,** $Fe_{10}Tm_{10}$ **4.8** and $Fe_{10}Er_{10}$ **4.7** compounds show that this effect is present in all compounds.

Moreover, the interesting optical appearance of these materials promoted a deeper study of their optical, and therefore electronic, properties. In solution compounds **4.1-4.11** are extremely pale in colour, in fact essentially colourless to the eye. In general, the crystals and the solutions have the same colours as the lanthanide (III) nitrates used in the synthesis, albeit the colour of isolated solid material is slightly stronger. When dried in vacuum, the loss of solvent molecules results in very pale, or essentially colourless for the Gd^{III} and Eu^{III} analogues, materials. Moreover, on exposure to sunlight or X-ray radiation some of the compounds, such as the Y^{III} and Er^{III} analogues, become brown.

Under UV-irradiation the materials do not emit light, which suggests that either there is no photoluminescence (fluorescence/phosphorescence) or this is very weak. The $Fe_{10}Ho_{10}$ solution is at the actually orange (as all) after reaction, while after that the compound undergoes a colour change from pale yellow to pale red as a result of internal *f-f* transitions on the Ho^{III} ions. The main question of this work is why is it that we do not see any evidence for the dark colours characteristic for Fe^{III} complexes of this and similar ligands arising from LMCT transitions? In general, unless the ligands complexing a high spin Fe^{III} are very hard and produce a very small crystal field splitting of the 3d levels, the electronic spectra of this ion are dominated by effects arising from charge transfer transitions (LMCT, MLCT and MMCT are all possible) and are expected to be highly coloured, especially in comparison with the Mn^{II} high spin ion which is famously virtually colourless. In fact, in contrast to the d-d electronic spectra of Mn^{II}, the spectra of Fe^{III} complexes are essentially swamped by dominating LMCT of MLCT bands tailing into the visible region from the UV region (this is an effect of the higher positive charge on hs Fe^{III} compared with hs Mn^{II}). In terms of MMCT bands the situation is more complicated since the position of such a band is determined by the nature of the bridging ligand mediating the electron transfer.

In order to explain the absence or quenching of Ligand to Metal Charge Transfer (LMCT) in this cluster system or better to understand what is behind such behaviour, femtosecond-spectroscopy studies as well as photolysis experiments were performed in addition to the structural, magnetic, Mössbauer and UV-VIS-NIR absorption measurements.

These experiments along with some qualitative experiments can indicate promising directions for future characterisation of what appears to be a very complicated system in terms of the huge variety of properties shown within a single system. Experiments performed so far have given deeper understanding concerning the observable colours, electron dynamics and aspects of other physical properties observed in this system. The comparative discussion of all of these results forms a central theme of this chapter. The ultimate goal of the investigations is to discover whether any unifying theme can be found to correlate these properties. This, in turn, would lead to the possibility of producing multitasking systems which are able to function in specific ways under different sets of conditions. To put this differently, although a current goal of "Green Chemistry" is to find systems which can perform many functions, too often the goal is to make these "Jack-of-all-trades" systems, implying that they perform reasonably well at many things but do not out-perform existing systems in any category. A more difficult goal is to find a system which can perform well at many tasks and to use a control over this, such as temperature or irradiation or mixed stimuli, to select the desired function of the material. In terms of green chemistry and element conservation this would represent an important step forward in making chemical systems act more like many organisms do. Put differently, organisms utilise their energy resources in an optimised fashion and select tasks according to the prevailing possibilities in terms of available energy and resources in general. Although this is a far cry from what we might expect a synthetically produced chmical system to achieve, it is still conceivable that a chemical system can be produced which can perform tasks well at different levels and that we only need to provide the right input to direct the system towards a specific task.

As an example concerning the discussion above, an even more intriguing aspect of these compounds is that they show remarkable behaviour in water with gas evolution observed and the formation of a new material on exposure to sunlight or by adding potassium ferricyanide to the aqueous solutions. When, however, mixed with potassium hexacyanoferrate $K_4[Fe^{II}(CN)_6]$ no gas evolution was observed (see results discussion).

They additionally, do interesting but for understanding a challenging behaviour, when they were mixed with potassium ferricyanide (for example in acteonitrile) and were left in the sunlight. The solid resulting form the experiment in acetonitrile was a blue-material. However, the blue material observed from this system could not be identified as isolated Prussian Blue but rather more Prussian Blue-like $Fe_{10}Ln_{10}$. In this chapter, attempts, to understand the nature of this material will also be discussed. The reduction of Fe^{III} to Fe^{II} by UV radiation for certain (usually carboxylato) iron(III)-complexes is well-known and was utilised, for example, in the original cyanotype or blue-print process. This uses ammonium iron(III) citrate or, more successfully, trisoxalato ferrate(III) salts, which are photoreduced to iron(II) and can be “developed” using potassium ferricyanide to give Prussian Blue deposits in the exposed areas.

In order to gain further understanding of the myriad of properties provided by this system, it was necessary to find ways to synthesize compounds which could serve as comparative systems with certain aspects of the compounds of interest “deleted”. There is analogy here with molecular biology were certain important amino acid side-chains suspected to be important for the specific biological function are deleted and then the system is tested to see whether it can still perform its function.

To this end, all possible variations on this theme were synthesised (and this is by no means trivial) in order to be discover by a process of elimination, which features of the system allow it to function as it does. For example, reference solutions were used to calibrate the basic response for the system thus solutions of $Fe(NO_3)_3 \cdot 9H_2O$ or $Ln(NO_3)_3 \cdot 6H_2O$ and solutions of the two similar ligands, differing only in having an additional methyl group on one of the arms of the parent teaH$_3$ ligand, were studied. In addition pure Fe-clusters were prepared using methods or improvements on these from the literature and include the successful preparation and reproduction of the $[Fe_6(tea)_6]\cdot 6MeOH$ (**4.12**) ring, the $[Fe(OMe)_2(O_2CCH_3)]_{10}$ ring (**4.13**) (similar stcruture as in Fig. 1.5, right) [96], a non-cyclic $[Fe_7O_3(O_2CCMe_3)_9(Me\text{-}teaH_3)_3(H_2O)_3]$ [97] complex (**4.14**) and the mono-nuclear $[Fe(tea)_2]Cl_3$ (**4.15**) [98]. More importantly, the ligand coordination in the $\{Fe_6\}$ (**3.12**), $\{Ln_6\}$ (**3.25-3.27**} rings is the same as for Fe^{III} and Ln^{III} in the $\{Fe_{10}Ln_{10}\}$ structure.

In contrast to the mixed Fe/Ln cyclic systems, all the oxo-bridged Fe^{III} rings have intense solution colours and strongly coloured crystals as expected from interactions of hs Fe^{III} ions in this environment. The lanthanide rings **$\{Ln_6\}$** (**3.25 - 3.27**) discussed in chapter 3 were also used as reference compounds. The Ho$_6$ crystals have even stronger colour (pink to pale yellow) than that seen for Fe$_{10}$Ho$_{10}$. On the other hand, the $\{Fe_{10}Tm_{10}\}$ compound (out of the solution) has slightly stronger greenish colour than for $\{Tm_6\}$ or $Tm(NO_3)_3$.

The Fe/4*f* clusters with triethanolamine or related ligands have somewhat darker colours to those seen for the Fe$_{10}$Ln$_{10}$ system. In chapter 2, the colours of the Fe$_2$Dy$_2$ compounds are different from each other but in most cases, they are yellow, paler yellow, orange or orange-brown. More importantly, they show family persistent colours in that the colours are not really affected by changing the lanthanide in the system. Furthermore, the magnetic susceptibility behaviour remains essentially constant as demonstrated, for example, by replacing Dy^{III} with other Ln^{III} ions (see chapter 2, for example compounds **2.1-2.13**).[36h), 36f)]

The results will be discussed paying attention to the possible influence of the nephelauxetic effect induced by the presence of lanthanide ions on the vicinity of the ferric ions, i.e. an unusual type of “ligand perturbation” on the electronic environment of the 3d ion, and the possible consequences in terms of the Racah parameters in helping to explain the optical properties of these systems.

The cyclic Fe^{III}/Tm^{III} compounds discussed in chapter 3 $\{Fe_5Tm_3\}$ (**3.1**), $\{Fe_4Tm_2\}$ (**3.4**) and $\{Fe_3Tm_2\}$ (**3.8**) were studied using femtosecond spectroscopy in order to gain a better understanding of the electron dynamics in the compound $\{Fe_{10}Tm_{10}\}$ **(4.8)** as discussed above. In general, the cyclic materials obtained in this work have paler colours than the tetranuclear or the other compounds. More importantly, in chapter 3 the susceptibility behaviour observed for Fe$_5$Ln$_3$ and Fe$_3$Ln$_2$ was found to vary according to the nature of the Ln^{III}. This raises the question as to whether if, the observed properties have a fundamental relation to the structure being cyclic in nature. In addition, can this study help us to gain greater understanding of the electronic nature of Ln^{III} metal ions?

The femtosecond studies show that the Tm^{III} and Eu^{III} ions have the most influence on the oxygene-iron or/and on the Fe^{III} dynamics. In contrast, Er^{III} has the lowest impact and the Y^{III} ion does not follow the any trend observed for the lanthanides. This could well be an extremely important finding, since it challenges the view that Y^{III} is a useful and innocent diamagnetic analogue for the later Ln^{III} ions. In all fairness, a few number of studies show that Y^{III} could mediate coupling between 3d ions, [99] but this area is hardly explored and yet suggests some very interesting avenues for further exploration of the field of “non-innocent cations”.

The photolysis and other experiments as well as the behaviour of the material in water indicate that the $Fe_{10}Ln_{10}$ system is perhaps photoreductive. The time constants are similar to those known for nano iron oxide nanoparticles [100]. Photochemistry has become increasingly important in recent years as the quest to discover ways to harness the free energy of sunlight gains momentum. For example, photoelectrochemical water oxidization [101] or the field of photo-induced electrolysis of water using various semiconductors to provide impetus for water-splitting from their valence bands has seen several significant advances over the past 30 years [102] However, indeed iron oxide doped systems have shown enhancing in the photo oxidization of water to produce hydrogen by solar but there is still an overwhelming need to find ways to produce stable, low cost semiconductors with the correct bandgap to allow for efficient absorption of as large as possible amounts of solar spectrum wavelengths which reach the surface of the Earth. [103] So far tuning the bandgap in iron oxide has been tested using various dopants has been investigated but not by using lanthanides.[103]

Conductivity Hall measurements performed at room temperature for $Fe_{10}Tm_{10}$ (**4.8**) show that, the system is an n-type semiconductor with a carrier concentration of 10^{19} per cm^3. Currently, we are doing low temperature transport measurements (down to 200 mK) in conjunction with other studies on this system, in order to confirm this first result and to understand how a molecular coordination compound can show properties usually associated only with compounds described as solid state materials. Ferromagnetic semiconductors are extremely important for applications and they are called magnetic semiconductors. [104] Furthermore, ferromagnets which are semicondutors are very important in the field of spin-tronics in general. For example, ferromagnetic semiconductors are great candidates for optical refregiration. [105]

Attempts, to isolate further cyclic system were sucesseful, for example, by replacing the nitrate salts of iron and lanthanides with tosylates and using the same overall synthetic protocol an $[Fe_4Yb_2(Me\text{-}tea)_4(Me\text{-}teaH)_2(Tos)_2]$ (**4.16**) cyclic structure could be obtained. This compound will be very important for future studies since the crystals are indeed colourless.

An important aspect for helping to understand and explain this system is to isolate analogues with Cr^{III} as a truly isotropic ion (the synthetic challenges are difficult here – this ion is very inert – more so than high spin Co^{III} since there are no energetically favourable electronic alternatives); Mn^{III} (as high spin 3d and anisotropic); Co^{III} (as ls diamagnetic but with nearby 3d (eg orbitals) which might be accessible to 4f electrons, but is also of interest since it is often used in DFT calculations as an “innocent” diamagnetic 3d ion for comparative purposes); Ga^{III} (as full 3d shell and empty 4p system); In^{III} (full 4d, empty shell 5p lying energetically near to full 6s and empty 4f orbitals) in place of high spin Fe^{III} to see if this behaviour can be also obtained for other transition metal ions. In fact none of these yielded the targeted systems and further synthetic efforts are needed. However, with Mn^{III} a **$[Mn_4Dy_3]$** (**4.17**) CCC could be isolated and with In^{III} a $[Dy_4(Me\text{-}teaH)_2(Me\text{-}teaH_2)_2(NO_3)_6]$ (**4.18**) compound. The use of Ga^{III} resulted in the isolation of the Dy_6 ring. These compounds will be discussed briefly to highlight the synthetic and structural relations to the $Fe_{10}Ln_{10}$ system.

4.2 Syntheses and Structures

Although the syntheses of **4.1-4.12** were initially successful using reactions very similar to those for the synthesis of **3.21**, the acetophenone, 2`-hydroxy-4`-methoxy-acetophenone ligand, was not incorporated in the crysral structures of these compounds. Thus, in order to test whether it plays a role in the synthesis, the reaction was performed in the absence of this compound and, indeed, clusters **4.1-4.12** can be readily obtained. The steric effect of the methyl groups in $Me\text{-}teaH_3$ as well as in the acetophenone ligands might represent a barrier to forming $\{Fe_4Dy_4\}$ with $Me\text{-}teaH_3$ as illustrated in the case of **3.21** (see Fig. 4.1).

The smallest distance between the proton on the alcohol alkoxy arm of the $teaH_3$ which is directed to the hydrogen atom from the methyl group of the acteophenone in compound **3.21** is ~ 4.25 Å. The methyl group would cause a shorter distnace to the CH_3 group of acetophenone about ~ 2.5 Å. On one hand, the chiral C in $Me\text{-}teaH_3$ would even makes it more difficult since both R and S can be presence and a $\{Fe_4Dy_4\}$ with $Me\text{-}teaH_3$ would not be circular as in case of teaH$_3$. On the other hand, we don’t expect to have Fe$_{10}$Ln$_{10}$ easiely with teaH$_3$ ligand (Fig. 4.2)

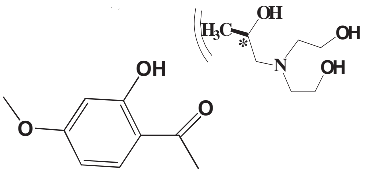

Figure 4.1 Schematic representation for hypothetic steric-situation between Me-teaH$_3$ and the acetophenone ligands.

While it is relatively easy to synthesize the Fe$_{10}$Ln$_{10}$ compounds with Dy-Lu in good to very good yields, it was very hard to isolate the Tb, Gd and Eu analogues. It seems that the larger the ionic radius of the lanthanide ions, the more difficult it is to isolate the cyclic coordination clusters and it was found necessary to use ether diffusion to favour crystallisation of the crystallize the Tb, Gd, Eu, Sm and Nd compounds (see experimental section).

Compounds **4.1-4.11** are isostructural and crystallise isotypically (although the cells of the Nd and Tb analogues have larger volumes, see later) in the triclinic space group P-1 with Z = 1. Here the Dy compound is described as an example. The compound is formed from ten {FeDy(Me-tea)(Me-teaH)(NO$_3$)} repeating units (Fig.4.2, upper and left) to give an Fe$_{10}$Dy$_{10}$ ring with alternating Fe and Dy ions (Fig.4.2, upper and middle). The crystallographic data of Fe$_{10}$Ln$_{10}$ compounds are listed in tab. 4.1 in the appendix.

Within each such unit, Fe(1) is chelated by the nitrogen and three oxygen atoms of a fully-deprotonated (Me-tea)$^{3-}$ ligand, and Dy(1) by a doubly-deprotonated (Me-teaH)$^{2-}$ ligand where the Me-substituted alcohol arm remains protonated.

The two deprotonated unsubstituted alcohol arms of each ligand form μ-alkoxo bridges to adjacent metal centres in the ring whilst the oxygens on the Me-substituted arms simply chelate their respective metal atoms. Within a unit these two non-bridging oxygens together form a strong hydrogen bond with O···O in the range 2.52-2.63 Å. The coordination sphere of each Dy ion is completed by a chelating nitrate ligand to give an overall a bicapped trigonal prismatic O$_7$N geometry (Fig. 4.3).

On going around the resulting elliptical ring the metals follow the path of a standing wave in that the FeDy units are displaced alternately above and below the mean plane of the ring with this wave pattern being constrained by the cyclic (chain) nature of the structure so that there are five peaks above and five below the plane on a circuit of the ring (see different perspectives of the molecule in Fig. 4.2, down left). Furthermore, within a FeDy unit the two Me-teaH ligands have the same chirality at the methyl-substituted quaternary carbon so that when both are R in one unit they must be S in the next (Fig. 4.3 (upper)).

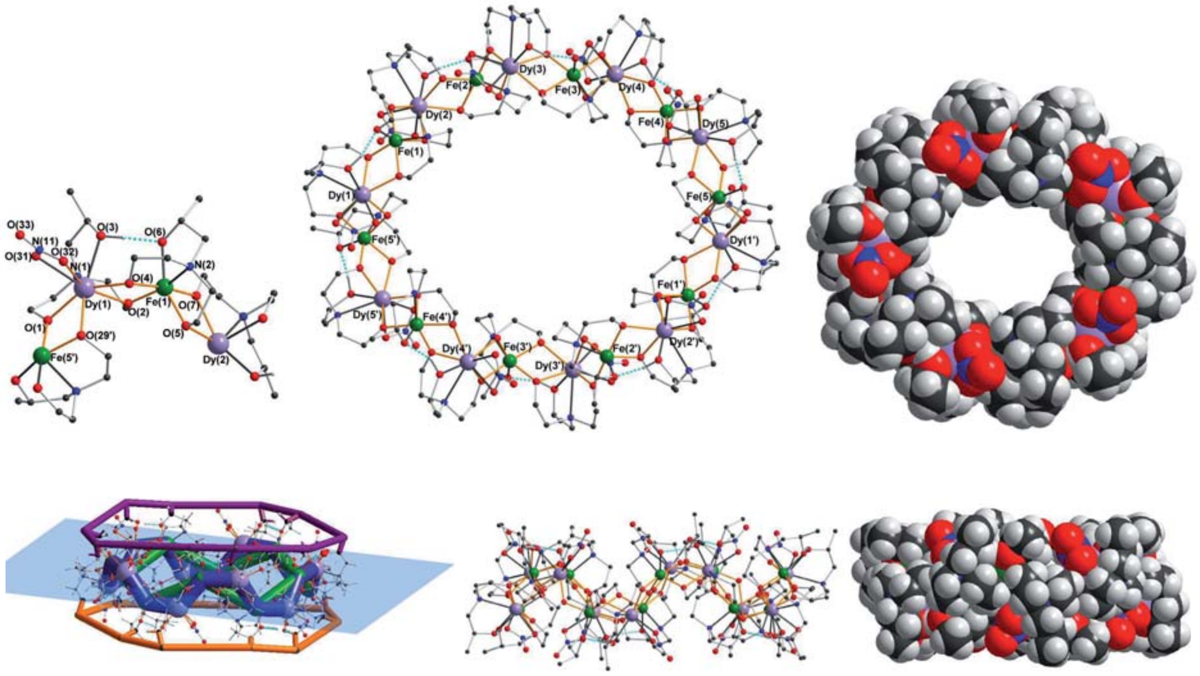

Figure 4. 2. Molecular structure of the $Fe_{10}Dy_{10}$ complex in **4.6**: Upper left: {FeDy(Me-tea)(Me-teaH)(NO_3)} repeating unit showing connections to adjacent units; middle: resulting $Fe_{10}Dy_{10}$ molecule projected on to the mean plane defined by the metal atoms; right: space filling depiction. Lower left: Schematic side-view of whole molecule emphasising the relative orientations of the important structural features. The violet and orange rings above and below the mean plane through the central metal atoms depict the clockwise and anticlockwise orientations of the methyl groups on the Me-tea ligands (see text). The thick blue line in the central portion follows the connectivity of the Fe-Dy cycle with the green line showing the connectivity of the Fe ions. Lower, middle and right, side and spacing filling view of the $Fe_{10}Dy_{10}$ ring. Dy violet, Fe green, O red, N blue, C black, organic H-atoms in (b) and (d) omitted for clarity. H-bonds are shown as light blue dashed lines.

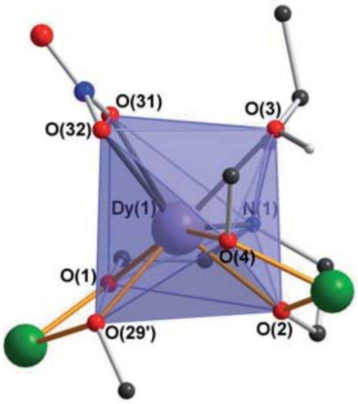

Figure 4.3. Coordination polyhedron of Dy(1) in $Fe_{10}Dy_{10}$.

This in turn means that the ten ligands on one side of the ring mean plane are all R with those on the other side of the plane all being S. With this arrangement of enantiomers, the methyl groups are tightly packed within the body of each subunit to give a rigid ligand shell. The chiral arms of the ligands are also involved in strong hydrogen-bonding between the units which seems to be an important feature in stabilizing the overall structure (Fig. 4.3 (down)). It can be conjectured that attempting to isolate an analogue using unsubstituted triethanolamine would prove difficult as a result of the lack of the rigidity arising from the combination of methyl substitution and H-bonding seen here. It also seems to be the case that the interplay of R and S stereochemistries in tandem with the resulting H-bonding interactions plays a decisive role in terms of the robustness and stability of the whole system. Indeed, it may be further conjectured that a different structural outcome would arise not only from using H_3tea, but also if enantiopure ligands were used. To test this, the triethanolamine ligand H_3tea used in place of the Me-teaH_3 ligand with the result that no product could be obtained.

Including the organic ligands the molecule has dimensions 28.4 × 26.3 Å across the ellipse and is 12.7 Å thick. The internal cavity has major and minor diameters of 12.2 and 8.3 Å, respectively. The packing is presented in Fig. 4.5.

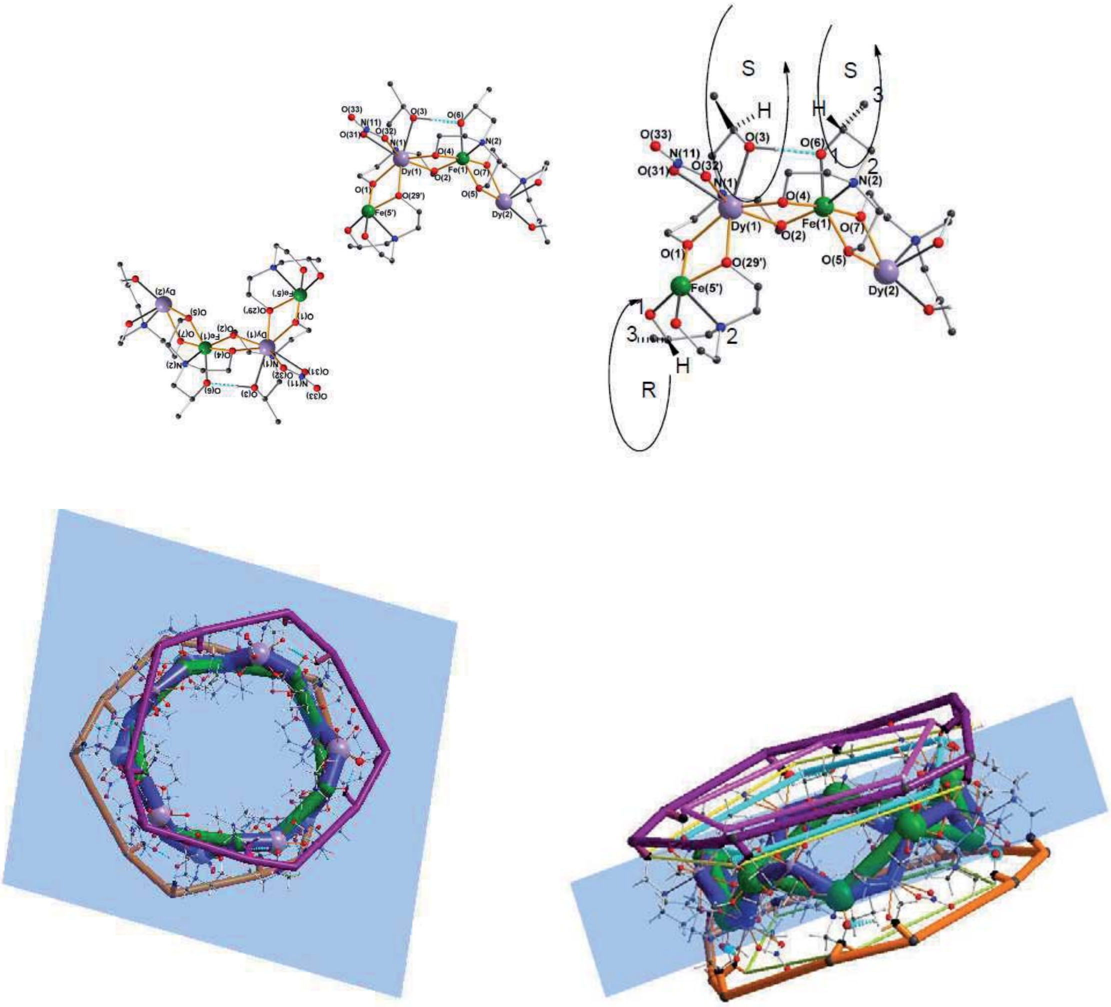

Figure 4.3. (Upper, left) flip 180° of the repeat unit and (right) S, S enantiomers on one side, the next will be then R, R on the other side. (Bottom) is the perpendicular insight through the structure and right side view. The large black balls connected by the decagon "pipework" above and below the central plane are the all R or all S methyl carbons on the Me-tea ligands (see main text). In Above the central plane of the metals the purple/pink pentagon represents the line of the H-atoms attached to the chiral C which point upwards, the yellow pentagon indicates the other 5 H-atoms pointing downwards. The turquiose line represents the 5H-atoms involved in the H-bonding. Below the plane of the metals, the lime-green pentagon joins the line of 5H-atoms attached to the chiral C pointing in the opposite direction to those joined by the purple-pink pentagon in the upper portion.

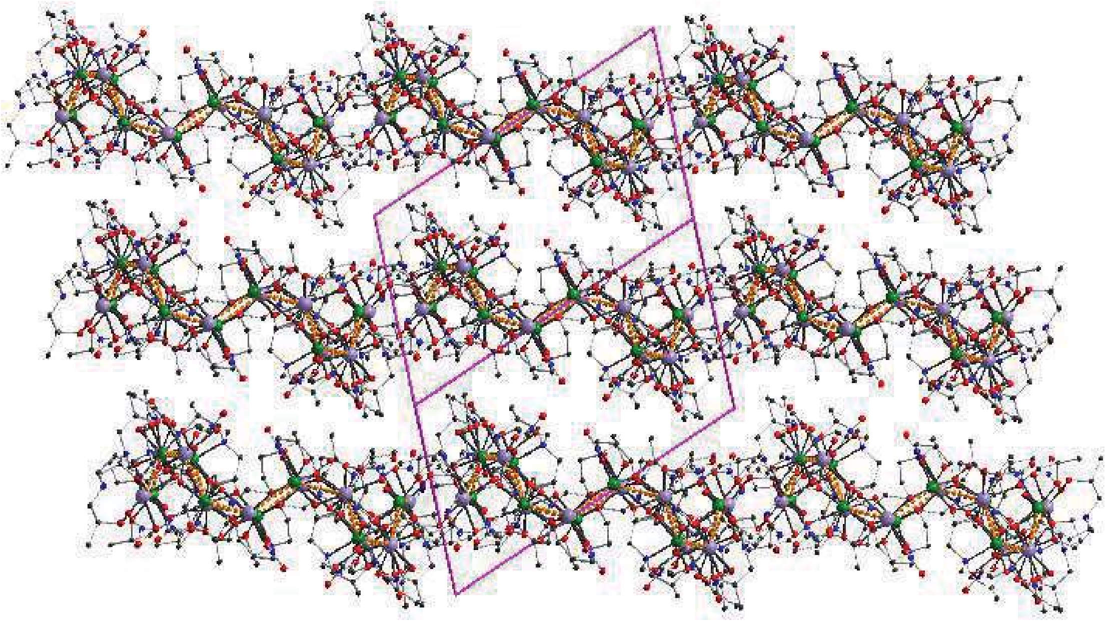

Figure 4.5. The Packing of the $Fe_{10}Dy_{10}$ Rings are presented. The bonds of the organic ligands are presented thin in order to highlight the ring-shape of the molecules in the packing.

The bond lengths and angles are similar-for example-for compounds $Fe_{10}Dy_{10}$ **4.5** and $Fe_{10}Tm_{10}$ **4.8**. Selected bond lengths and angles of $Fe_{10}Dy_{10}$ **4.5** are listed in tab. 4.2 in the appendix.

The Reference Compounds

Cyclic homometallic complexes, ideally $\{Fe_{20}\}$ and $\{Ln_{20}\}$, were needed as reference compounds in order to investigate the influence of Ln^{III} in $Fe_{10}Ln_{10}$ cluster system. At the same time these complexes should have similar coordination environments as in $Fe_{10}Ln_{10}$ cluster system.

Since the Ln^{III} ligand environment is similar in both $\{Fe_{10}Ln_{10}\}$ and $\{Ln_6\}$, they provide excellent reference systems. An "$\{Fe_{20}\}$" ring system with same ligand (Me-teaH$_3$) as Fe^{III} in $Fe_{10}Ln_{10}$ would be the most favourable. We keep here in mind that we are dealing with self-assembly synthesis.

However, an $[Fe_6]$ ring cluster could be indeed prepared, using teaH$_3$ instead of Me-teaH$_3$. This cluster contains six completely deprotonated $(tea)^{3-}$ ligands which coordinate in the same way as in the $Fe_{10}Ln_{10}$ complexes. The analogous compound with Me-teaH$_3$ could not be crystallized. This suggests that programmed hydrogen-bonding seen for the cyclic compounds formed with the protonated Me-teaH_3 ligand is the driving force for holding these compounds together. This is also why it was important to study relevant calibration solutions containing either Me-teaH_3 or teaH_3 to use as references in this study.

A physical study was reported on the $\{Fe_6\}$ (**4.12**) cluster (Fig 4.6) in the Diplom thesis of Andreas Geisselmann, who synthesized this compound and was subsequently contacted by the author of this work and kindly provided details of the synthesis to help in obtaining the desired wheel.

Compound **4.12** can be obtained by reacting $Fe(NO_3)_3 \cdot 9H_2O$ with triethanolamine in MeOH/EtO_2 and using triethylamine as base (see experimental part).

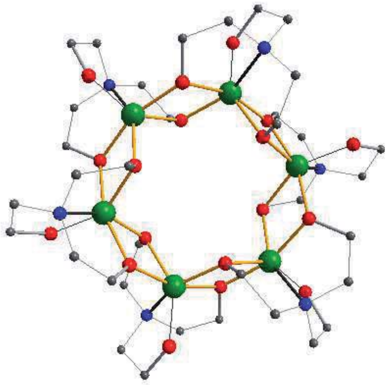

Figure 4.6. The structure of $[Fe_6(tea)_6] \cdot$ 6MeOH (**4.12**) (left) .

The $[Fe(OMe)_2(OAc)]_{10}$ (**4.14**) compound was reproduced according to the literature method. It has a wheel structure made famous by the designation of this motif as a “Ferric Wheel” (Fig. 4.6, right).

The mononuclear Fe compound $[Fe(tea)_2]Cl_3$ **4.15** was reproduced using a method from the literature. It was obtained by reacting $FeCl_3$ with triethanolamine in water. Such coordination compounds can be obtained for a wide range of elements. (See Fig. 4.7, left)

The only ferric CC reported in the literature using Me-teaH_3 is $[Fe_7O_3(O_2CCMe_3)_9$(Me-tea$H_3)_3(H_2O)_3]$ (**4.14**)[97] which was obtained by reacting the pivalate trinuclear $[Fe_3O]$ compound with Me-teaH_3 ligand in acetonitrile. Interestingly, exactly the same structural motif is reported in the same publication using teaH_3 as ligand (Fig. 4.7).

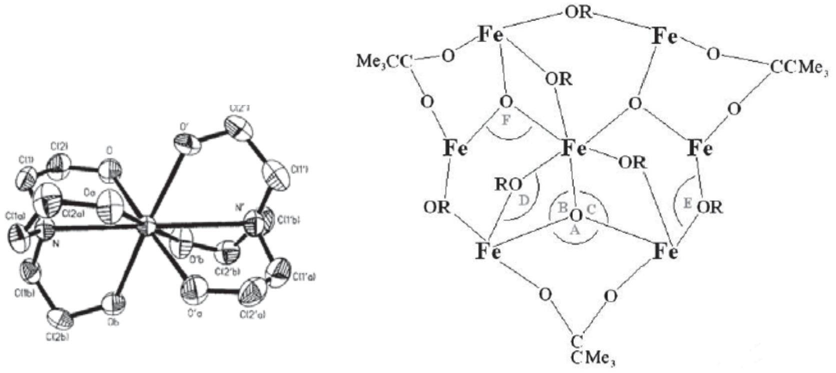

Figure 4.7. The stable monomeric structure type of [M(tea)$_2$] and the simplified structure of **[$Fe_7O_3(O_2CCMe_3)_9$(Me-teaH_3)$_3$(H_2O)$_3$] 4.14**. OR= one arm of Me-teaH_3 ligand.**[97, 98]**.

The chirality of the ligand was not considered in this article since both teaH_3 and Me-teaH_3 build the same structure which is not the case we have.**[97]** The structure is described in the literature as a dome-like cage.

Other Compounds

The fact that {Fe_6} compound only forms from Fe^{III} and tea ligands deserves further consideration. The question arises as to whether the anions present in the system might confer any structural stability. To test this, the lanthanide nitrate salt starting materials were replaced with the corresponding triflates, with triflate essentially counted as an innocent, non coordinating species expected only to form counteranions. However, this synthetic attempt did not result in any isolable compound. The next choice for supplying innocent counteranions was to use the tosylates of Fe^{III} and Ln^{III} (here Yb^{III}) which resulted in the [Fe_4Yb_2(Me-tea)$_4$(Me-teaH)$_2$(TOs)$_2$] (**4.16**) cyclic compound. The crystals are colourless and compound Fe_4Yb_2 crystallizes in the monoclinic space group P2$_1$/c (Fig. 4.8).

The unit Fe(Me-tea), which is also seen in $Fe_{10}Ln_{10}$ and Fe_6 structures is four times presence in this structure. In **4.16** two Fe(Me-tea) units are removed from the {Fe_6} (**4.12**) motif and replaced by two Yb(Me-teaH)(TOs) units to give the Fe_4Yb_2. The Yb^{III} ions are not in the plane of the irons and consequently the whole structure is not planar. A similar unit to the Yb(Me-teaH) motif can be found in the {$Fe_{10}Ln_{10}$} and {Ln_6} structures but with tosylate replaced by nitrate. Both the R and S forms of the ligand are present in this structure.

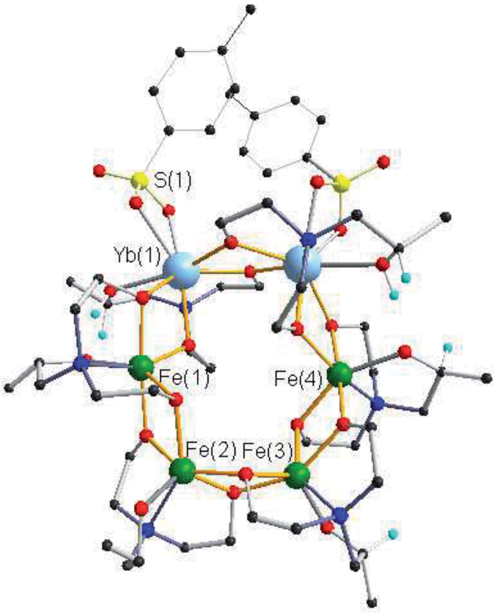

Figure 4.8. The structure of **[Fe_4Yb_2(Me-tea)$_4$(Me-teaH)$_2$(TOs)$_2$]** (**4.16**).

The use of $Mn(NO_3)_2$ in place of $Fe(NO_3)_3$ yielded the heptanuclear $Mn^{II}Mn^{III}{}_3Dy^{III}{}_3$ CCC cyclic coordination cluster (**4.17**) (Fig. 4.9). The alcohol arms of Me-teaH3 ligands coordinate the Dy^{III} centres. Similar coordination modes as for $\{Fe_{10}Ln_{10}\}$, however, the other alkoxy arms bridge to Mn^{II} additionally to the hydroxy groups. One can assume that Mn^{II} stopped grwoing the wanted $\{Mn_{10}Dy_{10}\}$ aggregate and that starting with Mn^{III} might yeild it.

Attempts were made to replace Fe^{III} by In^{III} or Ga^{III} ions in order to have a diamagnetic analogue of the 3d centre, but in all case this but were for Ga^{III} this gave the Dy_6 ring and for In^{III} a $\{Dy_4\}$ cluster. The Dy_4 crystallizes in the monoclinic space group P12/n. The structure is shown in Fig. 4.9 (right).

The coordination environment of the two central Dy^{III} centres is the same as that in Dy_6. However, the outer Dy^{III} centres have only mono-deprotonated ligands where two arms are chelating the Dy^{III} and have two additional nitrate groups as ligands.

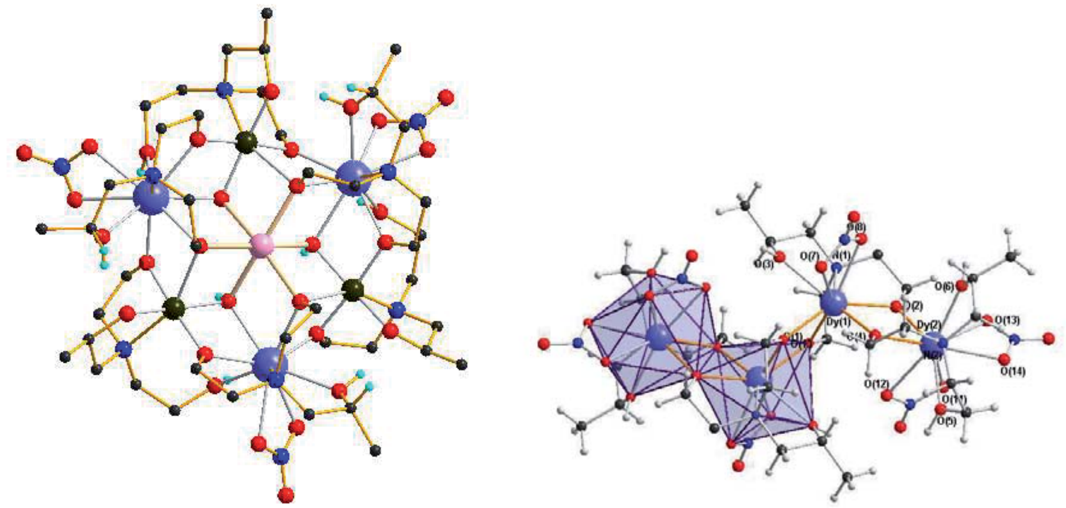

Figure 4.9. The structure of [Mn_4Dy_3] (**4.17**, left) and [Dy_4] (**4.18**, right)

If we imagine replacing the Dy centres with C the structure could be described as structurally similar to the arrangement in *trans*-butadiene. This might indicate that this motif would rearrange to the *cis*-version if In^{III} could be incorporated. One might need to adjust the pH, in order to obtain the $\{In_{10}Dy_{10}\}$ compound. The crystallographic data of all these compounds are summarized in the appendix (tab. 4.3).

4.3 Magnetic Properties

The χT versus T data for **$Fe_{10}Gd_{10}$ (4.3), $Fe_{10}Dy_{10}$ (4.5) and $Fe_{10}Y_{10}$ (4.11)** (Fig. 4.10) reveal that at 300 K all three compounds have values of χT in line with those expected for 10 non-interacting Fe^{III} and Gd^{III}/Dy^{III} (**4.3** and **4.5**) or 10 ioslated Fe^{III} ions (**4.11**). For compound **4.11** with diamagnetic Y^{III} ions on decreasing the temperature the χT rapidly decreases below 30 K reaching 22.9 $cm^3\,Kmol^{-1}$ at 1.8 K. Since the separation of the Fe^{III} ions is in the range 5.8 – 6.0 Å, any interactions between pairs of Fe^{III} ions are likely to be very weak. This is supported by the field dependence of the magnetization at low temperatures, in which the magnetization reaches at 48.5 μ_B at 70 kOe (Fig. 4.11) and slightly lower than the expected value ($10\times5.0\ \mu_B$) for 10 isolated Fe^{III} ions. The fact that the magnetization of **4.11** could not be fitted with the sum of ten Brillouin functions for $S = 5/2$ and $g = 1.95$ (Fig. 4.11) suggests that the spins on the Fe^{III} ions are not independent.

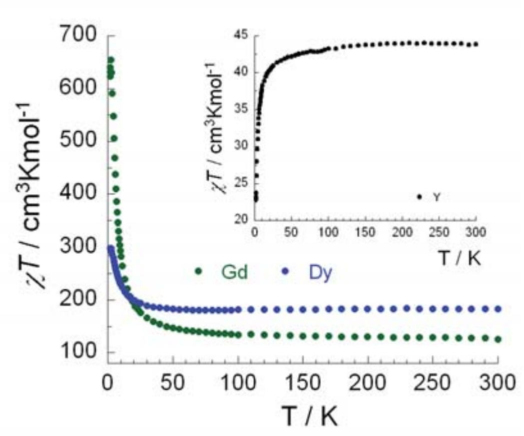

Figure 4.10. χT versus T plots at 1000 Oe for **4.3 –4.5**; **4.11** (inset) complexes.

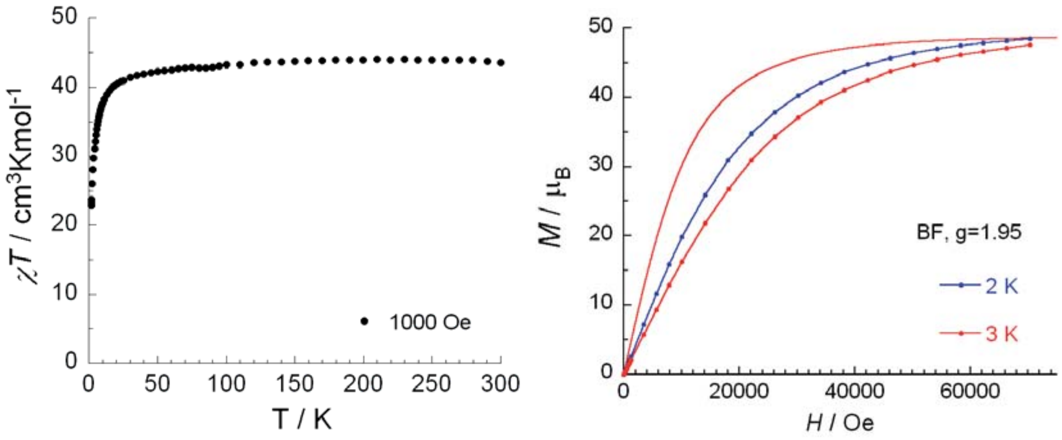

Figure 4.11. The χT vs T plot (left) and the M vs H plot (right) for compound **4.11**; the solid line without markers corresponds to the Brillouin function with ten $S = 5/2$ and $g = 1.95$.

Assuming that the underlying magnetic behaviour of the Fe^{III} centres remains constant we can subtract the molar susceptibility of **4.11** from **4.3** and **4.5** to give suitably adjusted plots (Fig. 4.12) to assess contributions from the Fe^{III}-Ln^{III} interactions as well as the intrinsic contribution from the Ln^{III} ions.

For the isotropic Gd case, the monotonic increase of the susceptibility in the Gd compound suggests the presence of ferromagnetic interactions between Fe^{III} and Gd^{III}, which is in a higher order of magnitude than of Fe^{III}-Fe^{III} interactions and implies that the Fe^{III}-Dy^{III} interaction is ferromagnetic as well. The field dependence of the magnetization at low temperatures for compounds **4.3** and **4.5** also suggests dominant ferromagnetic interactions. For **4.3** the magnetization increases rapidly at low fields up to 10 kOe, followed by a slope to reach at 118.3 μ_B at 70 kOe (Fig 4.13 and Fig. 4.14).

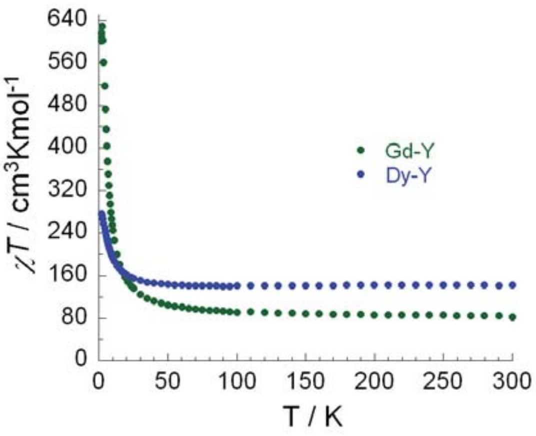

Figure 4.12. The χT vs T plots for **4.3** and **4.5** with the data of **4.11** subtracted, i.e. without the magnetic contribution of the Fe$_{10}$ unit.

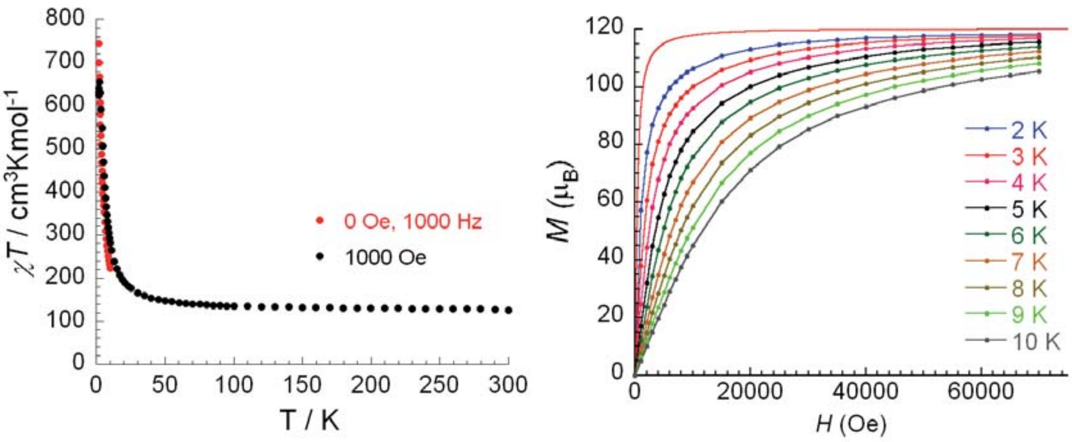

Figure 4.13. The χT vs. T plots (left) and the M vs. H plot (right) for compound **4.3**; the solid line without markers corresponds to the Brillouin function with S = 60 with g = 2.0.

The magnetization curve at a field lower than 20 kOe is offset to the calculated Brillouin function of S = 60 with g = 1.97, corresponding to a complete ferromagnetically-coupled system (Fig.4.13, right). This observation is consistent with that for the diamagnetic Y^{III} system, further suggesting that the spins on the Fe^{III} ions are not independent. Furthermore, the maximum of the temperature dependence of in-phase susceptibility ($\chi'T$) of 745 cm^{3}K/mol observed in **4.3** (Fig. 4.13, left) suggests that a spin ground state of S = 38 (assuming g =2) is defined below 3 K.

Variable-temperature ac susceptibility measurements were carried out under zero dc fields. No ac signals were observed for **4.3** and **4.11**, but frequency-dependent out-of-phase signals were detected for **4.5** below 10 K (Fig. 4.15), indicative of the slow relaxation of the magnetisation behaviour characteristic of SMMs.

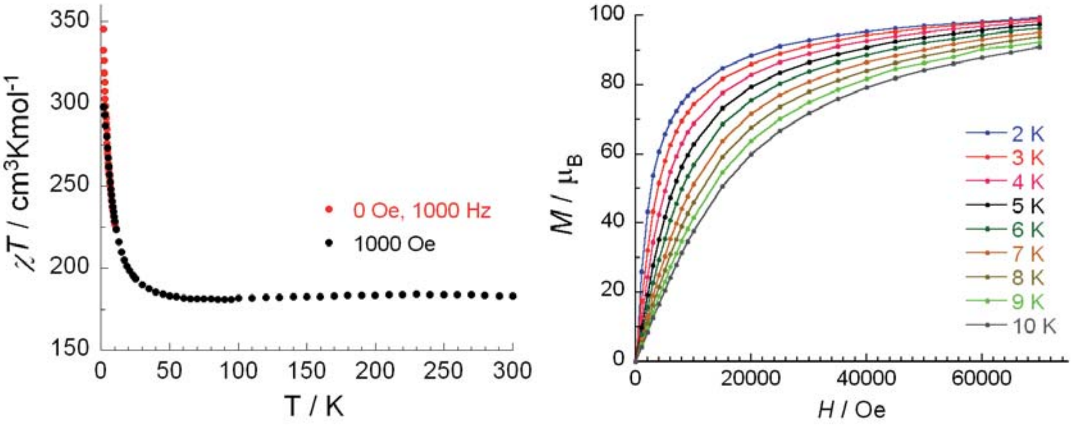

Figure 4.14. The χT vs T plots (left) and the M vs H plot (right) for compound **4.5**.

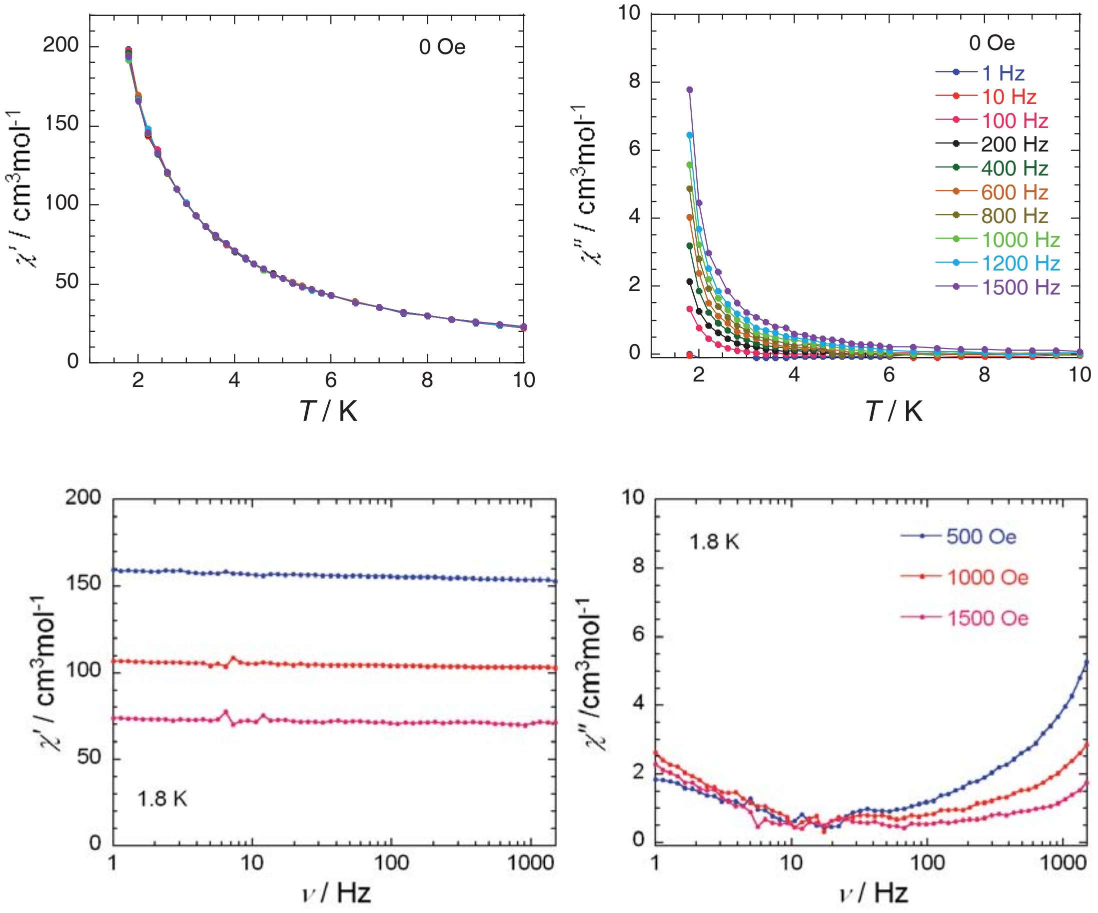

Figure 4.15. AC magnetic data for compound **4.5**

.

Even with the application of an external dc field, the relaxation of the magnetisation was still too fast to be observed in the window of the frequency limit of the SQUID indicating that any quantum tunnelling regime is either absent of else located at very low temperature. In order to investigate this further, single crystal magnetization measurements were performed in collaboration with Prof. Wolfgang Wernsdorfer using an array of micro-SQUIDs at temperatures down to 40 mK. Hysteresis loops collected for complex **4.5** at varying temperatures and sweep rates (Figs 4.16, 4.17 and the magnetization decay in Fig. 4.18) show superparamagnetic type behaviour with increasing coercivity with decreasing temperature confirming **4.5** to be a SMM. No steps due to quantum tunneling of magnetization (QTM) were observed. dc magnetization decay data were collected in the 0.04 - 1.0 K range. The effective energy barrier and the relaxation time are determined as 11.5 K and 8 x 10^{-13} s (Fig. 4.16 (left)).

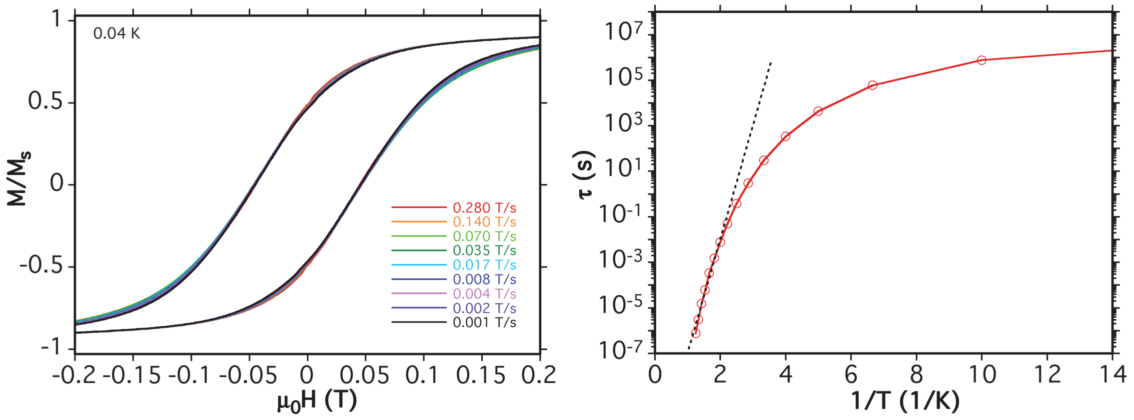

Figure 4.16. (left) Magnetization (*M*) *vs* applied field (*μ_oH*) at different field sweep rates at a fixed temperature of 0.04 K for **4.5**. (right) Arrhenius plot constructed using the dc data from the decay plots, see the parameters from the text.

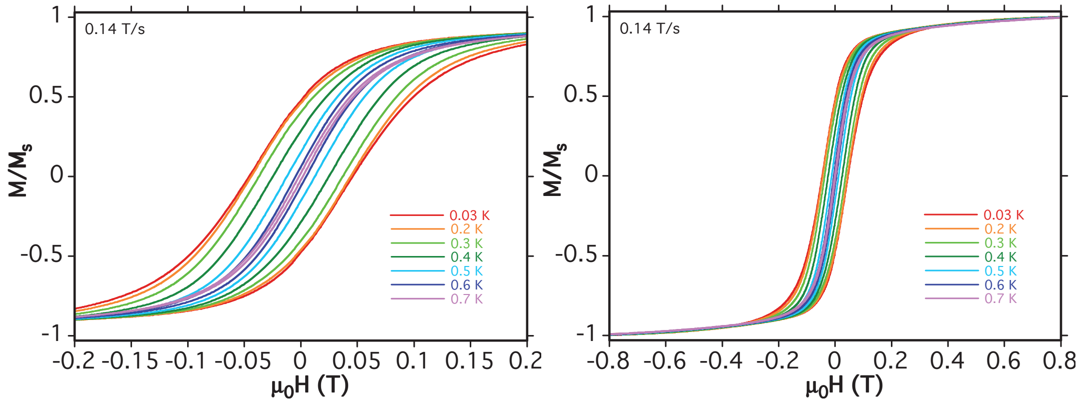

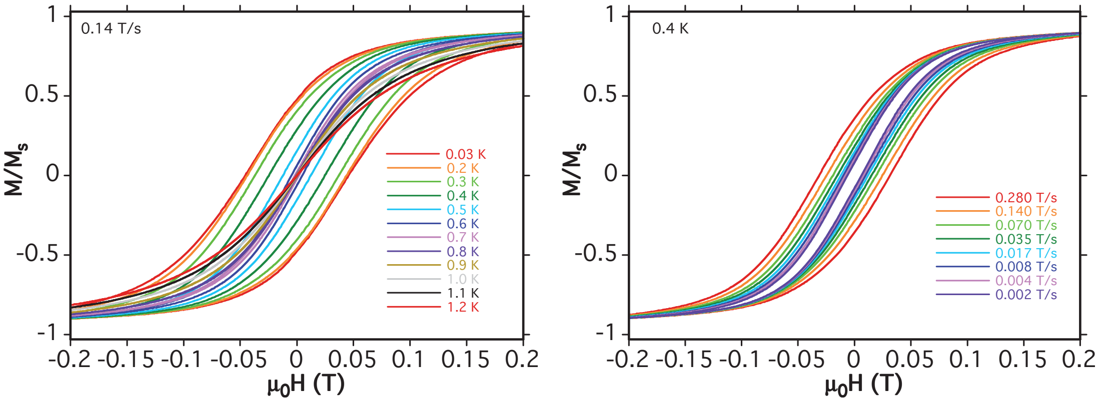

Figure. 4.17. Magnetization (*M*) *vs* applied field (*μ$_o$H*) at different temperatures and different field sweep rates for $Fe_{10}Dy_{10}$ **4.5**.

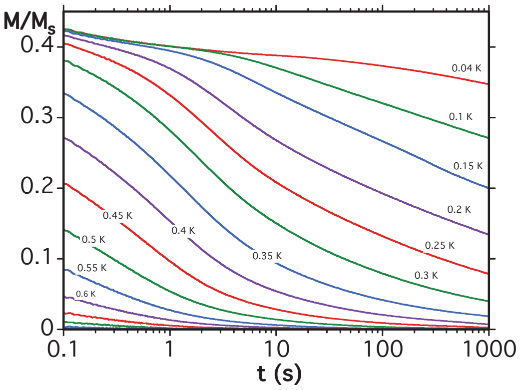

Figure 4.18. Magnetization decay data for compound **4.5**.

The magnetic behaviour of the $Fe_{10}Lu_{10}$ (**4.10**) compound is comparable with that of $Fe_{10}Y_{10}$ (**4.11**) in the sense that both are diamagnetic ions. In both cases the intra-anti ferromagnetic interaction of Fe--Fe becomes clearer than in case of $Fe_{10}Gd_{10}$ or $Fe_{10}Dy_{10}$ for example. (Fig. 4.19)

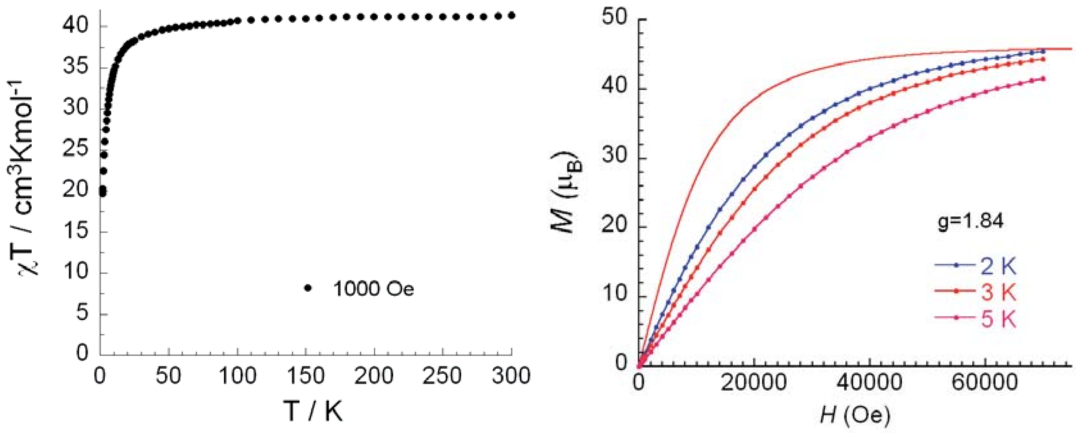

Figure 4.19. The χT vs T plots (left) and the M vs H plot (right) for compound **4.10.**

Antiferromagnetic interactions between the relatively distant Fe^{III} ions are still present in the $Fe_{10}Yb_{10}$ compound (**4.9**) but the presence of 10 Yb^{III} ions seems to weaken the overall antiferromagnetic interaction in this compound and at very low temperatures $Fe_{10}Yb_{10}$ compound is ferromagnetic. (Fig. 4. 20).

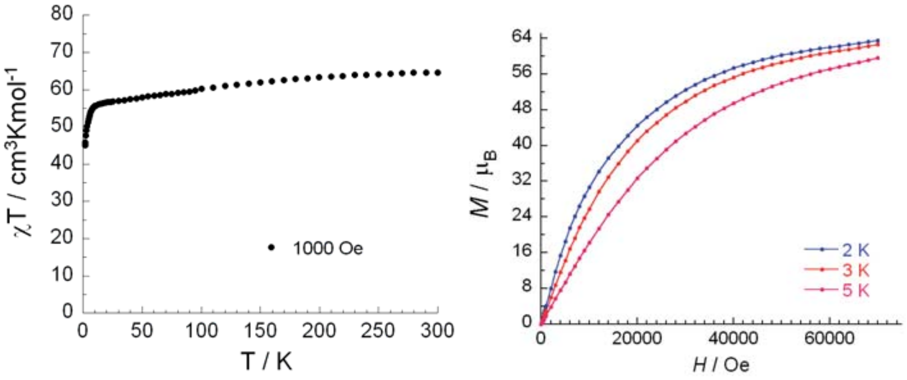

Figure 4.20. The χT vs T plots (left) and the M vs H plot (right) for compound **4.9.**

For $Fe_{10}Er_{10}$ (**4.7**) in Fig. 4.21, at temperatures above 12 K a weak antiferromagnetic interaction presumably from Fe···Fe interaction is seen. A remarkable behvaiour is observed below 12 K, where there is a rapid decrease. strong decreasing of the suscebtibility indiactes dominanat ferromagnetic behaviour. At very low temperatures then again sharp increasing and then decreasing till a minimum at 3 K. Such behaviour is similar to ferrimagnetic behaviour of purley iron(III) complexes. However, ferrimagnetic behaviour is when antiferromagnetism is observed for wide range of temperature then an increasing in the susceptbility happens. Such behaviour as in case of $Fe_{10}Er_{10}$ (**4.7**) is indeed complex and can have its origin in the interplay between Fe···Er interaction and/or from depopulation of the sub-levels for internal Er^{III} ions. Another reason might be fast spin relaxation or very fast magnetic relaxation which cant be detcetd in this short time intervall. The Er compound is the only one in this series which show such shape of magnetic susceptibility curve. (Fig. 4. 21)

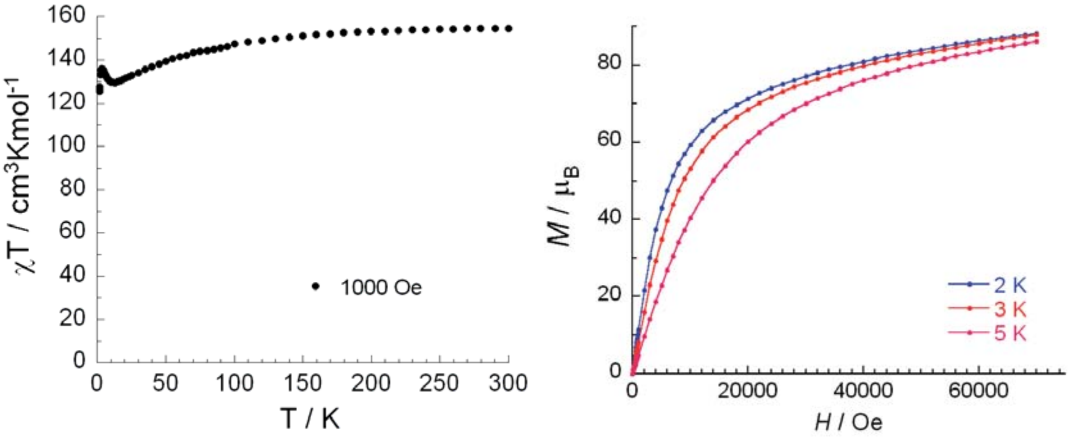

Figure 4.21. The χT vs T plots (left) and the M vs H plot (right) for compound **4.7**.

Remarkable magnetic behavior is observed for $Fe_{10}Tm_{10}$ (**4.8**). The magnetic behaviour here is clearly antieferromagnetic. Even at very low temperatures, antiferromagnetic behavior still dominant. Such behavior in this series is only seen for the Tm compound. The reason might be complex of nature the stong antiferrmagnetic Fe···Tm interaction. To be able to explain this bahviour in particular in case of $Fe_{10}Tm_{10}$ (**4.8**) and $Fe_{10}Er_{10}$ (**4.7**) compounds further methods are necessary (see later and see Fig. 4.22).

Overall ferromagnetic behaviour is observed for $Fe_{10}Ho_{10}$ (Fig. 4.23). The increase in the susceptibility at low temperatures might come from the antiferromagnetically Fe···Fe inetarction and the orbital contribution of Ho^{III} ions.

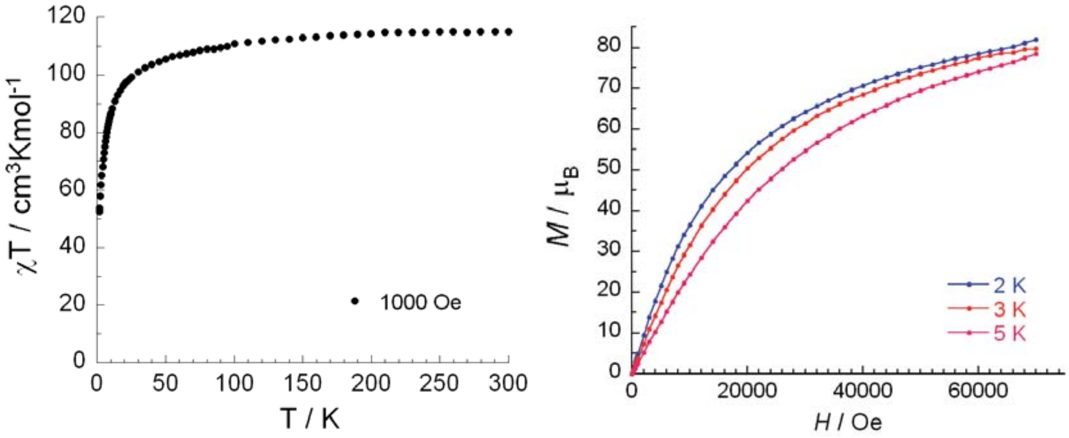

Figure 4.22. The *χT* vs T plots (left) and the M vs H plot (right) for compound **4.8**.

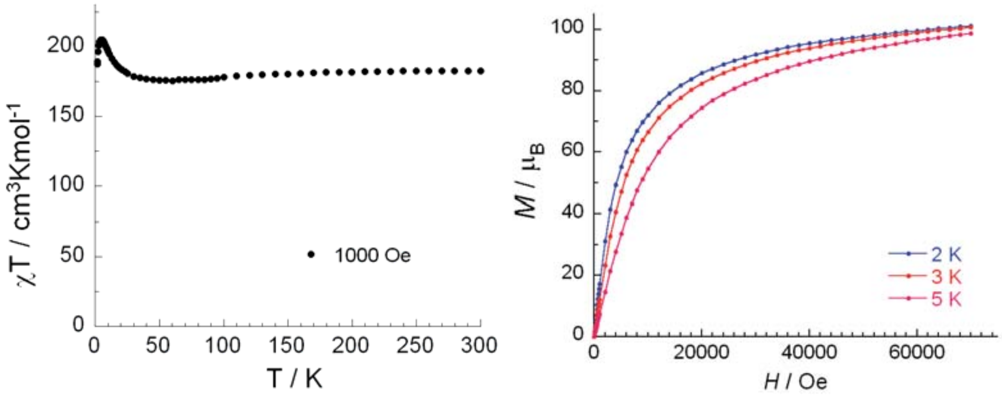

Figure 4.23. The *χT* vs T plots (left) and the M vs H plot (right) for compound **4.6.**

In Fig. 4.24 are the susceptibilities of all compounds compared and in Fig. 4.25 those shown without contribution of the $\{Fe_{10}\}$ unit. The susceptibilities of these compounds deviate from each other significantly which indicates that the nature of the Ln^{III} ion plays an important role in modulating the magnetic susceptibility. In comparison for the tetranuclear series discussed in chapter 2 (**2.1-2.13**), no such differences were observed by changing the lanthanide ions. At this stage such differences cannot be explained easily and might be a result of cooperative effects modulated by the electronic nature of the "doped" lanthanides within the weakly antiferromagnetically coupled Fe^{III}_{10} wheel. Note further, that all these magnetic measurements were done in darkness since the method allows this usually. All these compounds will be measured in future in presence of light (see later), in order to understand them and the relation to the magnetic behaviour much better.

The magnetic data for the $Fe_{10}Ln_{10}$ compounds are summarized in Tab. 4.3.

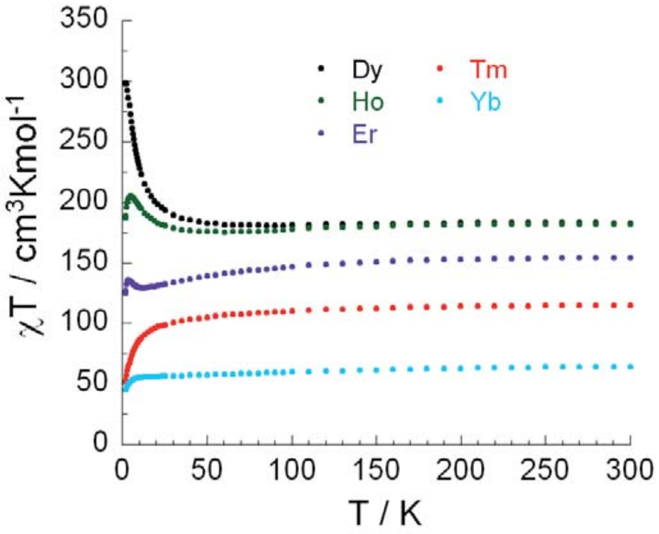

Figure 4.24. Magnetic data extracted from the plots of χT vs T (under 0.1 T).

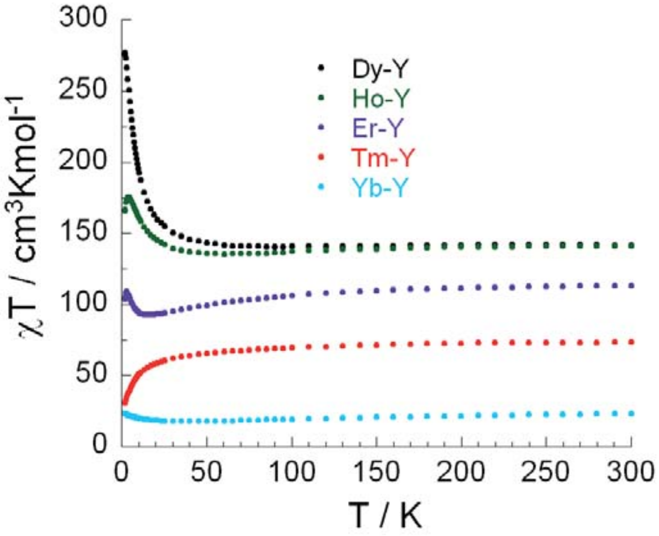

Figure 4.25. The χT vs T plot at 1000 Oe without the magnetic contribution of the $[Fe_{10}]$ unit for other analogues as indicated. Here referring to Y.

Tablen 4.3. Magnetic data extracted from the plots of χT vs T (under 0.1 T).

Compounds	*Curie Constant* for each Ln ion at 300 K (cm^3K/mol)	χT (cm^3K/mol) predicted for per complex at 300 K	χT (cm^3K/mol) measured for per complex at 300 K	χT (cm^3K/mol) measured for per complex at 1.8 K	Overall interactions	Out-of-phase ac signal
[$Fe_{10}Y_{10}$] (**4.11**)	0	43.75	41.1	21.6	weak AF	no
[$Fe_{10}Lu_{10}$] (**4.10**)	0	43.75	41.4	19.7	weak AF	no
[$Fe_{10}Yb_{10}$] (**4.9**)	2.57	66.8	64.6	45.1	weak AF and dominant	no
[$Fe_{10}Tm_{10}$] (**4.8**)	7.15	112.6	114.9	52.5	Clear AF	no
[$Fe_{10}Er_{10}$] (**4.7**)	11.5	156.1	154.7	125.4	Ferro with orbital contribution	no
[$Fe_{10}Ho_{10}$] (**4.6**)	14.07	181.8	182.4	187.5	Ferro with orbital contribution	no
[$Fe_{10}Dy_{10}$] (**4.5**)	14.17	182.8	183.0	298.5	Ferro	Weak ac
[$Fe_{10}Tb_{10}$] (**4.4**)	9.72	140.2	139.0		Ferro	Weak ac
[$Fe_{10}Gd_{10}$] (**4.3**)	7.94	124.0	120.0		Ferro	no

4.4 Magneto Caloric Effect

As this system produces high spin ground states in general and the Gd^{III} compound in particular exhibits a small anisotropy, [39c)] we studied the magnetocaloric effect for **4.3** and **4.5** and **4.8.** The magnetic entropy change ΔSm for several applied field changes ΔH from the M(H,T) data was calculated using the Maxwell relation as basis (Fig. 4.26).[38] The value of ΔSm increases gradually with increasing ΔH, reaching a value of 25.4 J/kgK at 6 K for Gd () and 18.1 J/kgK at 5 K for Dy (**4.5**) with the experimentally accessible maximum ΔH of 70 kOe . The ΔSm of both compounds are comparable to those for several 3d [39] systems reported so far. The MCE of **4.5** is determined smaller than that of **4.3**, which is a consequence of the magnetic anisotropy of the Dy^{III} ions. It is worth mentioning that the maximum change of ΔSm occurs at 6 K for **4.3** and 5 K for **4.5**, which represents the highest temperature reported to date, compared to the largest values of ΔSm observed in Ni_6Gd_6 (ΔH =70 kOe at 3 K) [106] and Cu_5Gd_4 (ΔH = 90 kOe at 3 K) [107] clusters. The maximum allowable entropy per mole given by $R\ln(2S+1)$ where the gas constant $R = N_Ak_B$ can be calculated from the sum of the individual contributions from each metal ion. The theoretical entropy value is then calculated as 48.0 J/kgK for **4.3** and 47.7 J/kgK for **4.5**, respectively. With comparison, the observed magnetic entropy change ΔSm is much smaller than the maximum allowable one, indicating that the presence of antiferromagnetic interactions and/or magnetic anisotropy within this system probably reduce the entropy changes.

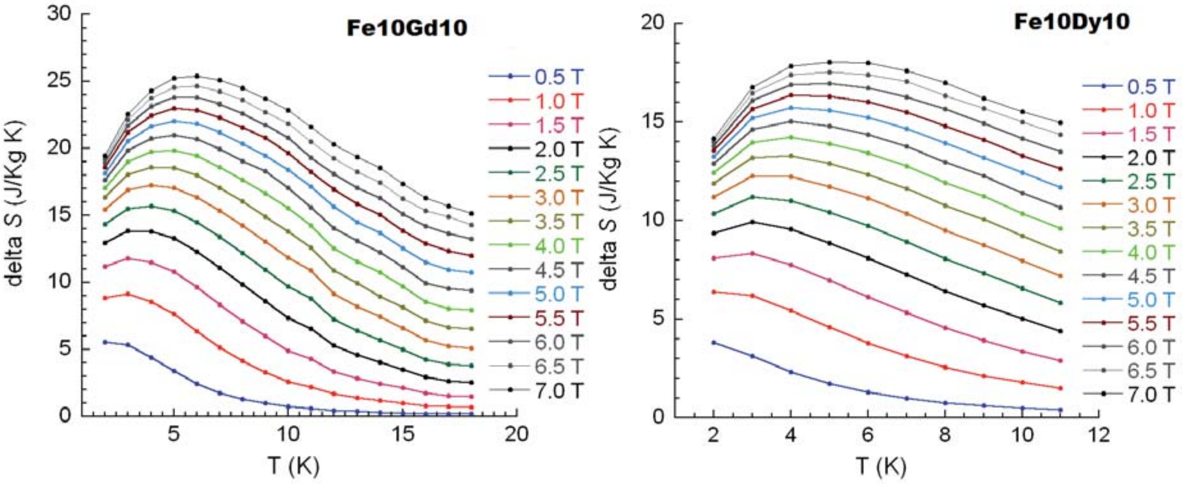

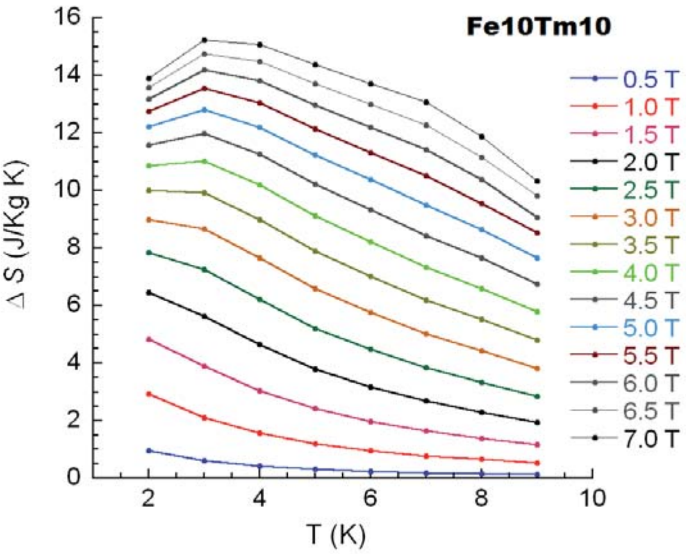

Figure 4.26. (Upper) Experimental ΔSm for compounds of **4.3** (left) and **4.5** (right) at various fields and temperatures. Lines are guides to the eye. (Lower) for **4.8**.

The Tm^{III} ($4f^{12}$) compound with two unpaired *f* electrons and with antiferromagnetic behaviour shows very high observed entropy change (15.25 J/KgK) and it shows in comparison with Gd (25.4 J/KgK) and Dy (18.1 J/KgK), the smallest different in the calculated and measured entropy change (20.89 J/KgK) but at lower temperature (3K). For Dy the difference is 27.4 J/KgK and for Gd 22.6 J/KgK.

MCE calculations and specific heat measurements of all other $Fe_{10}Ln_{10}$ compounds are in process.

4.5 Mössbauer Spectroscopy

The high temperature Mössbauer spectra for **4.11** show broad and asymmetric doublets. Such line-width asymmetry is typical for well-isolated ferric ions and is the result of relatively long paramagnetic relaxation times for these centres. At 3 K, the zero-field spectrum is significantly broadened (Fig. 4.27, left) with wings that extend from about - 8 to +8 mm/s. The 0.5 T spectrum and at 3 K is also similar to the zero-field spectrum except for slightly more definition in the wings of the spectrum and asymmetry at the centre. In the spectrum of **4.11** at 3 K and applied field of 3 T the outer peaks are inwardly broadened with shoulders, indicating that at this field there still exist iron species with different relaxation frequency and not all iron spins are aligned along the applied external magnetic field. Almost full alignment is achieved only at 5 T. Although at low enough temperatures small fields are enough to align the spins of well-isolated ferric ions, nevertheless in case of **4.11** higher fields than 3 T are needed. This is because of relatively small distances between the iron ions in the rings (5.8 –

6.0 Å) which cause a faster relaxation. The magnetization measurements suggest that the spins on the Fe^{III} ions are not independent. At low temperatures, given that the iron ions are far apart from each other (> 7.0 Å), there is only a very weak or negligible spin–spin interaction, a slow paramagnetic spin relaxation and consequently magnetic splitting appears. If the $iron^{III}$ ions are closer to each other (< 7.0 Å), the spin–spin interaction will be a bit stronger and the paramagnetic spin relaxation will be faster leading to the magnetic structure disappearing. The MS spectra of compounds **4.7** and **4.8** are similar to the others, which indicate that, the Fe···Fe interaction is present in the whole system.

The Mössbauer spectra of **4.5** (Fig. 4.28) at higher temperatures than 15 K have similar shapes to those seen for the **4.11** compound and dipolar splitting resulting from internal magnetic fields was not observed at these temperatures. At 3 K, the spectrum consists of a very broad absorption sextet, indicating that the relaxation of iron spins is slower than in **4.11**. It was discovered that compared with the case of **4.11** where the application of a magnetic field slows down the relaxation, it was not necessary to apply any field and the slower relaxation in **4.5** is the result of the interaction between iron and dysprosium ions. As seen from the Mössbauer spectra at 3 K in external fields of 2 and 4 T (Fig. 4.28) the positions of the peaks shift slightly inwards, that is, the hyperfine field is slightly reduced, which is typical for a ferromagnetic material in which an alignment of the magnetic moments along the external field B_{ext} with a concomitant rotation of the internal field is expected and thereby reduces the nuclear hyperfine field. Mössbauer measurements for compound **4.3** were not done because of the very small yield. The MS data for compounds **4.5** and **4.11** are summarized in tab. 4.4.

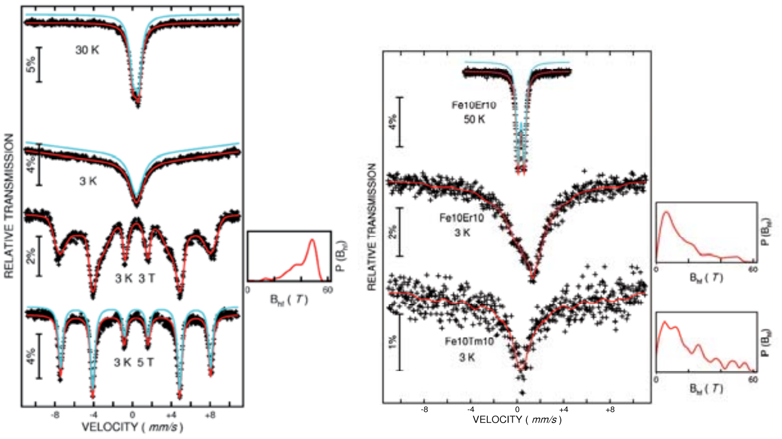

Figure 4.27. (Left) The Mössbauer spectra of **$Fe_{10}Y_{10}$** **(4.11)** obtained at 30, 3 K, and at 3 K in an applied field of 3 and 5 T. The distribution of probability for the magnetic hyperfine field for the spectrum at 3 K 3 T is presented on the right side. (Right) The MS of **4.7** and **4.8** at 3 K.

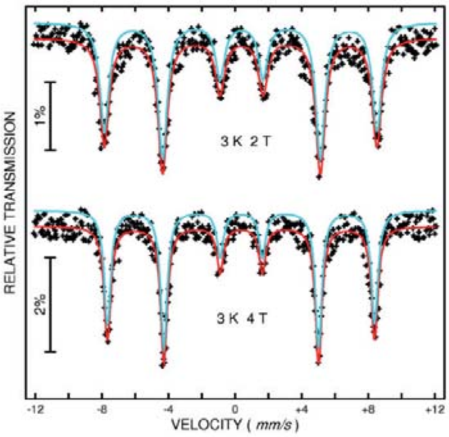

Figure 4. 28. The Mössbauer spectra of **4.5** obtained at 3 K in an applied field of 2 and 4 T.

Table 4.4. Mössbauer data for **4.11** and **4.5** at different temperatures and applied magnetic fields.

Complex	T, K and H_{appl}	$\delta^{[a]}$, mm/s	ΔE_Q or $\varepsilon^{[b]}$, mm/s	Γ, mm/s	H_{eff}, T
$Fe_{10}Y_{10}$ (4.11)	130K, 0T	0.45(1)	0.57(1)	0.89(1)	-
	3K, 5T	0.46(2)	-0.06(1)	0.55(1)	48.5(1)
$Fe_{10}Dy_{10}$ (4.5)	50K, 0T	0.46(1)	0.55(1)	0.43(2)	-
	3K, 2T	0.47(1)	-0.05(1)	0.67(2)	50.8(1)
	3K, 4T	0.47(1)	-0.02(1)	0.48(2)	49.8(1)

[a] Relative to α-Fe at room temperature. [b] For magnetically-split spectra the quadrupole shifts, $\varepsilon = \frac{1}{2}\Delta E_Q(3\cos^2\varphi\text{-}1)$. φ - angle between the H_{int} and the main electrical field gradient (EFG) principal axis (V_{zz}). The quadrupole shifts are easy to observe from the magnetic spectra as a difference in the splitting of 1 and 2 and 5 and 6 iron(III) lines. δ is the isomer shift; ΔE_Q - quadrupolar splitting; H_{eff} - the hyperfine field; H_{appl} – applied field; Γ - half-height-line width.

4.6 Optical studies

Steady-State Absorption Spectroscopy

The optical behaviour of these molecular compounds in solution and in the solid state is unprecedented. It is clear that the each system is worthy of detailed study on its own and this is beyond the scope of a single PhD thesis. This is clearly seen for the $Fe_{10}Ho_{10}$ and $Fe_{10}Er_{10}$

compounds, where dramatic colour changes are seen for both in sunlight. The almost colourless nature of most of the compounds leads to the question as to why the colour of expected for Fe^{III} is suppressed or, more precisely, what has happened to the O-Fe^{III} LMCT process?

According to the spectral chemical series H_2O and OH^- cause stronger ligand field than F^-. If the central metal ion is constant and the ligand field strength (*f*) deviates, becomes larger when the field is stronger, hence Fe^{III} in air or water environment has stronger colour than in $[FeF_6]^{3-}$. The MO theory, however, explains better why an anionic ligand such F- causes a weaker ligand field rather than one as water, since the ligand field theory is based on the electrostatic interaction model suggested by Bethe. When the metal ion is different but same ligand field, the Δ_O can also change and it depends further on the oxidation state of the metal ion.

For example, Mn^{II} and Fe^{III} ions have both d^5 (high spin) configurations and the d-d transitions are expected to contribute very little to the colour of the complex since in an octahedral environement they are spin and parity forbidden. The Mn^{II} is a softer ion as a result of its lower charge and larger ionic radius than the Fe^{III}, which is relatively hard. More importantly, Fe^{III} is more easily reduced than Mn^{II} since the LMCT process occurs at a lower energy for the Fe^{III} ion and thus the bands usually occur or tail into in the visible part of the spectrum. A similar change in colour relating to reduction potential of a metal ion can be observed for the d^0 systems of the permanganate ion MnO_4^-, which absorbs in the visible to give a violet colour, and chromate CrO_4^{2-} which absorbs in the uv/blue to give a yellow colour. For the permanganate ion this means lower energy LMCT and thus easier electron transfer to the metal ion (M) from the ligands (L), i.e, Mn^{7+} is a better oxidizing agent. For the chromate ion, the higher LMCT means that it is harder to transfer electrons from L to M permanently and so Cr^{6+} is a weaker oxidizing agent than Mn^{7+}.

For d^5 systems understanding ligand field effects requires covalency to be taken into account via the Racah parameters, which give an indication of the modification of the electronic structure of the metal ion on complexation compared with the situation for the free ion. The effect of this on the relative energies of the various accessible electronic states is summarisd in the form of a Tanabe-Sugano diagram. The Racah repulsion parameters are ligand-dependent and as the complex becomes more covalent the electrons are to some extent spread over the ligands so the electron-electron repulsion is reduced. This reduction in repulsion as covalency increases is called the nephelauxetic effect (literally "cloud expanding")

A nephelauxetic series can be set up based on the variation of the B Racah parameter. A large reduction in B (free ion) indicates a strong nephelauxetic effect with {B(free ion)- B'(Complex)} / B(free ion). This series has a completely different order from the one found in the spectrochemical series and a few ligands are listed below:

$$F^- < H_2O < \text{urea} < NH_3 < \text{en} \sim C_2O_4^{2-} < NCS^- < Cl^- \sim CN^- < Br^- < S^{2-} \sim I^-$$

This series is consistent with fluoride complexes being the most ionic and giving a small reduction in B while covalently bonded ligands such as I- give a large reduction of B. For Mn^{II} and other d^5 cases, the ground state is ^6S and higher states include, ^4G,^4D, ^4P ^4F etc. It is expected that since there are no spin-allowed transitions possible, the electronic spectrum should only contain very weak bands. For the other electronic configurations spin-forbidden bands are rarely observed since they are hidden by the more intense spin-allowed transitions.

The nephelauxetic effect does not only depend upon the ligand type, but also upon the central metal ion. These too can be arranged in order of increasing nephelauxetic effect as follows:

$$Mn^{II} < Ni^{II} \approx Co^{II} < Mo^{II} < Re^{IV} < Fe^{III} < Ir^{III} < Co^{III} < Mn^{IV}$$

The Tanabe-Sugano diagram can be used to interpret these bands by once again calculating the ratio of the energies of the peaks and finding that position on the diagram.

The main question of this work is also, how to explain the absence of the LMCT in the $Fe_{10}Ln_{10}$ system? Was it “stolen” by the doping lanthanide?

In Fig. 4.28 the steady-state spectra of $Ho(NO_3)_3$ and $Fe_{10}Ho_{10}$ are shown. A diluted solution of $Ho(NO_3)_3$ with the same solvent ratio was also prepared and measured as well (Fig. 4.28).

The spectra in Fig. 4.28 show a characteristic peak around 300 nm in the blue/ultraviolet region. The spectrum observed for $Fe_{10}Ho_{10}$ is rather different than that of $Ho(NO_3)_3$. In both the excepted weak peaks of the 4*f*-4*f* transitions are present (for example the transitions $^5S_2$ to $^5I_8$ (546 nm) and $^5F_5$ to $^5I_8$ (661 nm)). However, these are suppressed (Fig. 4.28, enlargement) in the case of $Fe_{10}Ho_{10}$ and the (blue/UV) absorption is actually the characteristic region for the $Fe_{10}Ho_{10}$.

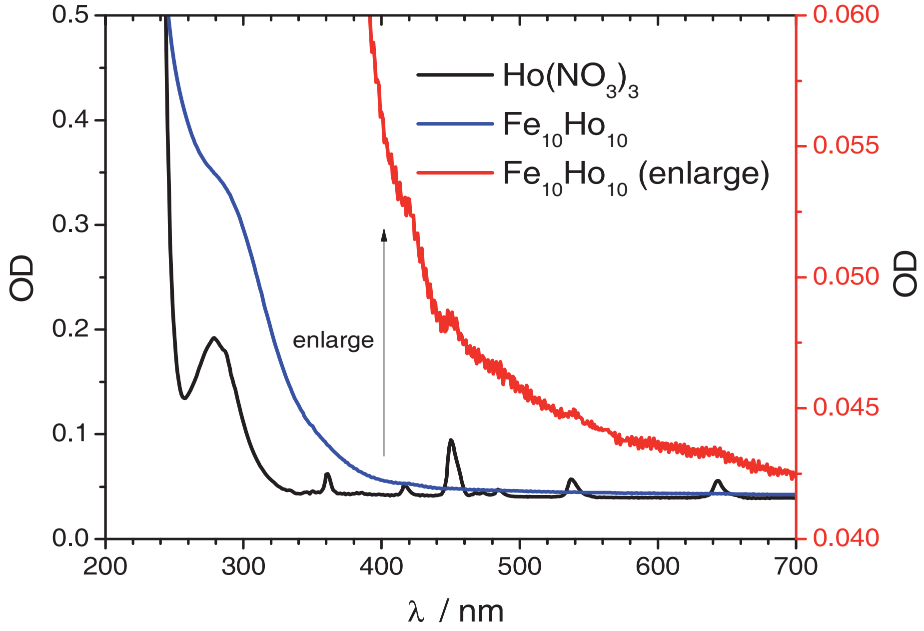

Figure 4.28. Steady-state spectra of $Fe_{10}Ho_{10}$ and $Ho(NO_3)_3\cdot$ $6H_2O$ solution.

In order to investigate this further, the steady-state spectra of compound $Fe_{10}Dy_{10}$ (**4.5**) and of the Dy_6 (**3.24**) were measured. In addition, the steady-state spectra of the ligands Me-teaH_3 and teaH_3 and diluted solutions from all lanthanide nitrates were taken. (See Fig. 4.29)

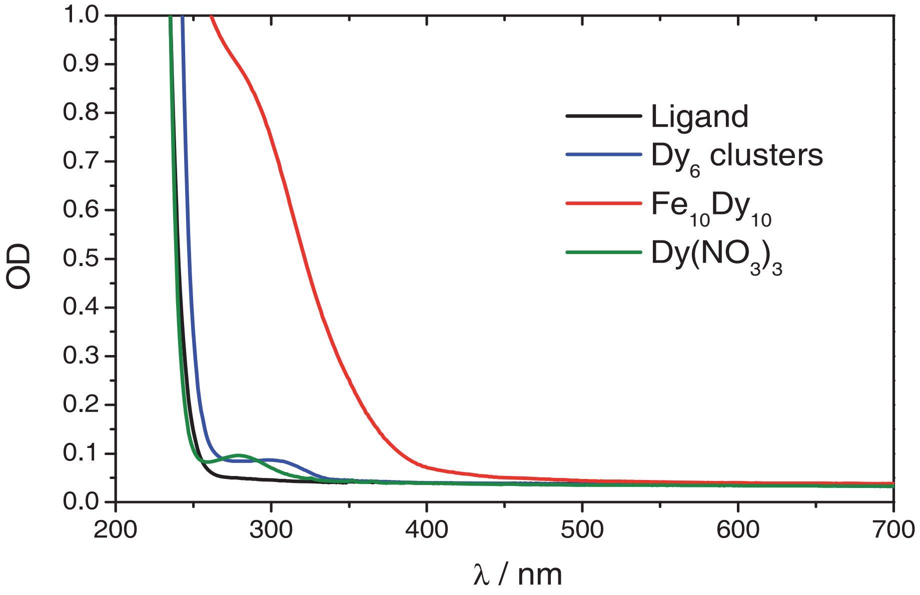

Figure 4.29. Steady-state spectra of $Fe_{10}Dy_{10}$ compared with the reference probes of Me-teaH_3 ligand, $Dy(NO_3)_3$ and Dy_6 ring cluster.

The absorption spectrum of $Fe_{10}Dy_{10}$ is similar to that of $Fe_{10}Ho_{10}$. While no peaks are observed for the free ligand in the spectral regions of interest, the spectra of Dy_6 and $Dy(NO_3)_3$ show shifted peaks in the blue region and Dy_6 an extremely weak peak around 300 nm. Although the Dy^{III} ions in the cluster are chelated by nitrate groups, the $Fe_{10}Dy_{10}$ compound shows a unique spectrum clearly independent from those of $Dy(NO_3)_3$ or/ and Dy_6. In other words, the spectra of $Fe_{10}Ho_{10}$ and $Fe_{10}Dy_{10}$ seem to be compound-characteristic and should be investigated further.

Fig. 4.30 shows the steady-state absorption spectra for all compounds, including the solutions of the Sm analogue which could not be crystallography measured due to poor crystal quality. It is likely that ithas a similar structure to the other examples as it was also possibleto isolate the Nd compound. Although no crystals for the Pr compound could be obtained the spectrum was taken from the solution in order to compare with the others (see discussion later in the next section). The steady-spectrum of the Fe_6 reference compound (**4.12**) was also measured (Fig. 4.30).

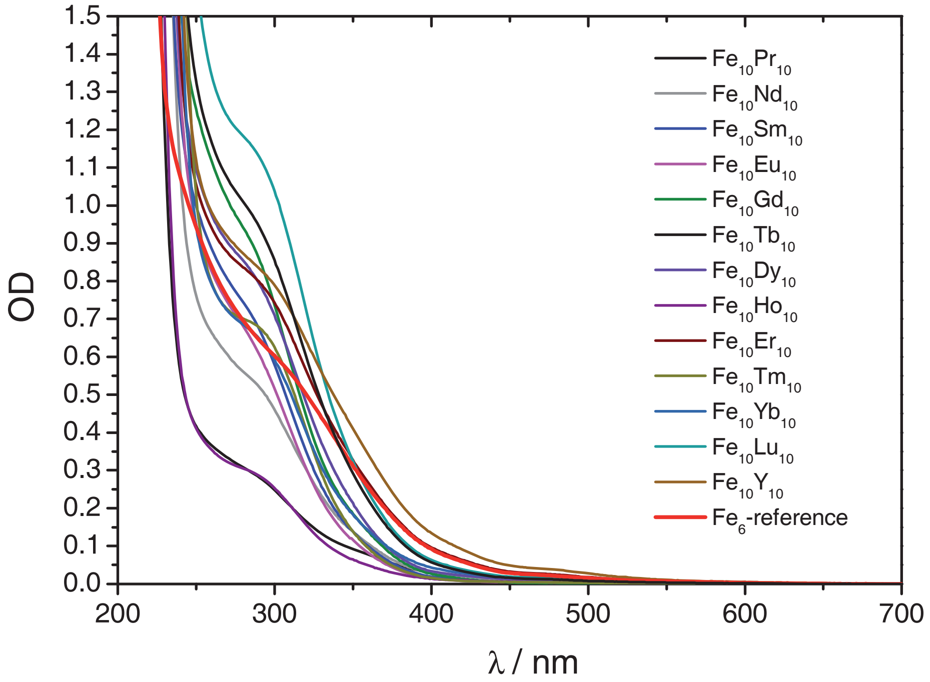

Figure 4.30. Steady-state absorption spectra of all diluted solutions of $Fe_{10}Ln_{10}$ (**4.1-4.10**) compounds, of $Fe_{10}Y_{10}$ (**4.11**), of Fe_6 (**4.12**) and the solutions resulted from the analogue reactions for Pr and Sm.

In order to gain” more qualitative, and may be -more than that- quantitative data, femtosecond study was performed on all of these compounds.

Femtosecond Spectroscopy (Pump-Probe Technique)

The transient spectra resulted from a Pump at 310 nm, with energy= 0.8 μJ and Probe at 550 nm of $Fe_{10}Ho_{10}$ (**4.6**) and $Fe_{10}Dy_{10}$ (**4.5**) as well as from the reference compound Fe_6 (**4.12**) are shown in Fig. 4.31. The reference materials $Ln(NO_3)_3$ solutions, Dy_6 and the ligand Me-teaH_3 as well as the simpler ligand teaH_3 and the solvents methanol and acetonitrile gave no signals in the femtosecond experiments, and thus they are not shown here.[for more details about the spectroscopic studies, (see Yu Liang, Dissertation, under supervising of Dr. Andreas N. Unterreiner, Karlsruhe (Germany))[49b)].

The absorption bands in the region 250-450 nm might be only –so our interpretation corresponds to the LMCT within the Fe^{III}-O^{-}_{Ligand} units in the cluster. In more clear words, that is the unit we excit and not the Lanthanides. The analysis of the spectra observed from the Pump-Probe experiments are summarized in Tab. 4.5 (appendix). While the data (time constants and amplitudes) observed for the electron dynamics in the Ho and Dy compounds are similar, the data for the {Fe_6} (**4.12**) reference compound remain different. Three dynamic processes are actually observed. The first occurs in the femtosecond time scale (~ 200 to 300 fs), the second and the third dynamics happen in the interval of a few picoseconds. More informative are the amplitudes, which might reflect the involvement and influence of the lanthanide ions. The fact that the dynamic of Fe_6 (**4.12**) is different may result from the compound having no lanthanide ions (doping effect) or be related to the size of the ring.

At this stage, it is hard to say whether these dynamics relate to the above mentioned two factors. A comparison with the dynamics observed using ultrafast studies might give useful and helpful information. This is, however, not so simple because most such studies are performed in the context of solid state science, e.g. on nanoparticles. The $Fe_{10}Ln_{10}$ are giant molecular materials with diameters larger than 2 nm. Nevertheless, this is much smaller than, for example, the widely studied iron oxide nanoparticles which are usually at least 10 nm in size.

A survey of the leiterature on ultrafast dynamic studies of iron-oxides shows that the data observed for Fe_2O_3-nanoparticles havel similar time constants and amplitudes as we observed for the {Fe_6} ring (4.12)[100]. The carrier dynamics we observed for **4.12** are in agreement with the literature data of Fe_2O_3-nano particles. They are not absolutely the same but similar and in particular the excitation region is actually the same. But which role and influence have the lanthanides and on which process from these three?

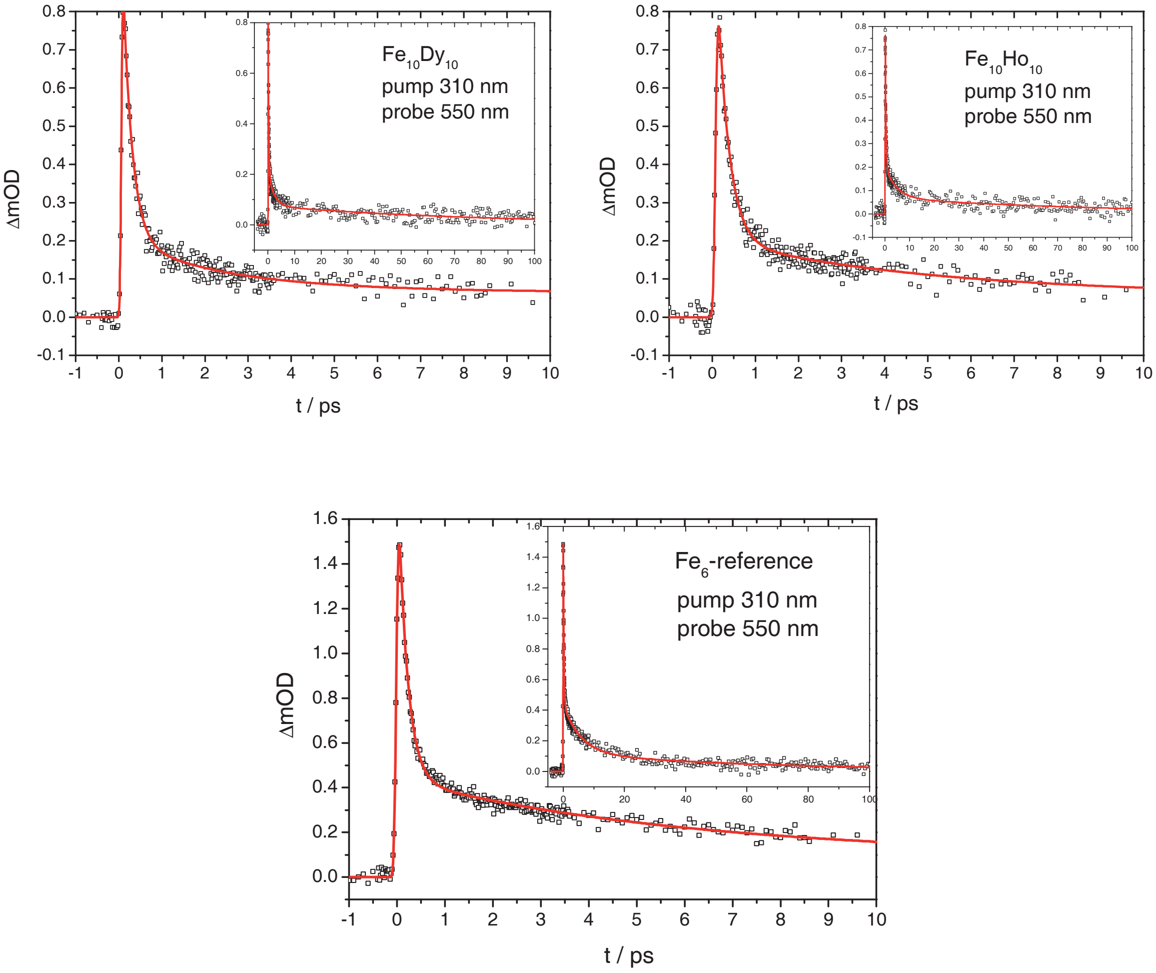

Figure 4.31. Transient spectra of Fe$_{10}$Ho$_{10}$, Fe$_{10}$Dy$_{10}$ and Fe$_6$ as labelled.

In order to understand this properly, three compounds were measured as next, firstly the Fe$_{10}$Tm$_{10}$ (**4.8**) and Fe$_{10}$Er$_{10}$ (**4.7**) compounds, which show significant differences in colour, in magnetism and in their absorption spectra, when compared with all other compounds. In addition to these two the Fe$_{10}$Y$_{10}$ compound (**4.11**) was measured, noting that Y^{III} is actually not a lanthanide ion and does not have any f electrons, but is of a very similar ionic radiues to the later lanthanide ions. This is important for comparative purposes and to help to understand if the effect on the iron dynamics is lanthanide specific. The Pump-Probe experiments for these three compounds were done and the spectra are shown in Fig. 4.32 and the time constants as well as the amplitudes are summarized and compared with Fe$_{10}$Ho$_{10}$ and Fe$_{10}$Dy$_{10}$ in Tab. 4.6.

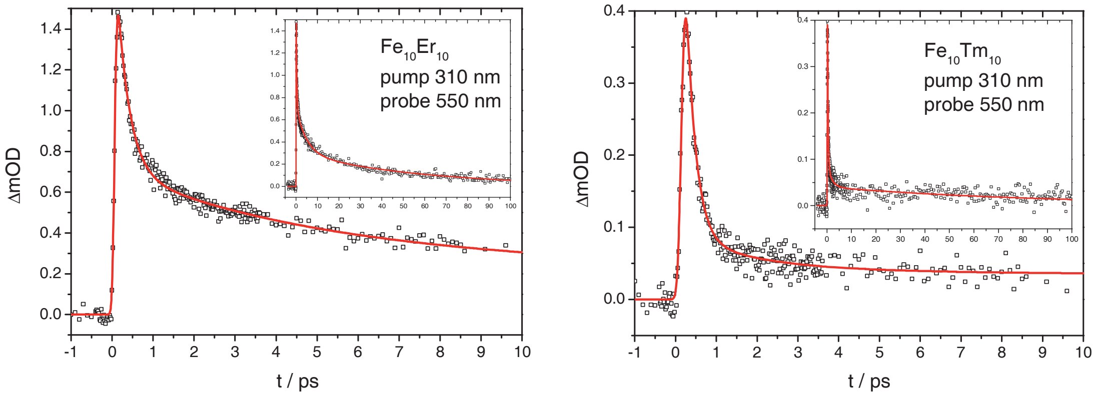

Figure 4.32. Transient Spectra of Fe$_{10}$Er$_{10}$, Fe$_{10}$Tm$_{10}$ and Fe$_{10}$Y$_{10}$.

The data for Fe$_{10}$Y$_{10}$, Fe$_{10}$Er$_{10}$ and Fe$_{10}$Tm$_{10}$ show remarkable differences to Fe$_{10}$Dy$_{10}$ and Fe$_{10}$Ho$_{10}$ as well as to each other and, of course, in comparison to the reference compound the {Fe$_6$} ring, where only the iron or more precisely the O-Fe^{III} unit contributes to the dynamics. From the time constants and amplitudes (see Tab.4.6) is it clear that the influence of the presence of Tm^{III} in Fe$_{10}$Tm$_{10}$ with τ_1 ~305 fs on the first relaxation process (τ_1) is more efficient ($\Sigma A_1 = 0.88$) in comparison to the other Fe$_{10}$Ln$_{10}$ clusters.

In contrast to Fe$_{10}$Tm$_{10}$ (**4.8**), Fe$_{10}$Er$_{10}$ (**4.7**) has the amplitude of the first relaxation process at $\Sigma A_1 = 0.64$ which is less efficient in terms of the electron dynamic and it is actually the same as for the Fe$_6$ (**4.12**). On the other hand, the time constant of the first relaxation process τ_1= ~196 fs is the shortest in comparison with all others and in particular to the Tm^{III} compound.

Table 4.6. The data observed from transient spectra for the compounds: **4.5, 4.6, 4.7, 4.8, 4.11** and **4.12.**

Property	**Time constants τ_i**			**Relative amplitudes ΣA_i**		
Factor	τ_1 (fs)	τ_2 (ps)	τ_3 (ps)	ΣA_1	ΣA_2	ΣA_3
Fe$_{10}$Dy$_{10}$	**201± 19**	**1.5±0.4**	**88 ± 21**	**0.77**	**0.14**	**0.09**
Fe$_{10}$Ho$_{10}$	**251± 26**	**2.8±0.4**	**79 ± 15**	**0.78**	**0.12**	**0.10**
Fe$_{10}$Er$_{10}$	**196± 18**	**3.2±0.6**	**55 ± 10**	**0.64**	**0.20**	**0.16**
Fe$_{10}$Tm$_{10}$	**305± 30**	**4.2±0.7**	**59 ± 16**	**0.88**	**0.05**	**0.07**
Fe$_{10}$Y$_{10}$	**382±27**	**6.7±1.2**	**37 ± 13**	**0.52**	**0.24**	**0.24**
Fe$_6$	**363± 75**	**5.2± 1.4**	**38 ± 11**	**0.64**	**0.23**	**0.13**

The time constants and amplitudes in the case of the two magnetically anisotropic Ho and Dy are comparable. Interestingly, the first time constant τ_1 for Y compound is even slower than Er and tends to be close to the reference compound Fe_6. However, the influence on the first relaxation dynamic process significantly smaller than in case of or any other Ln (ΣA_1=0.52). It is noteworthy that the “influence” of Y^{III} on the electron dynamic is completely opposite to that of the lanthanides.

All other $Fe_{10}Ln_{10}$ compounds were measured. In addition, in Fig. 4.33 all the transient spectra (pumped and probed) samples are given. In Tab.4.7 are the time constants and relative amplitudes of all compounds summarized.

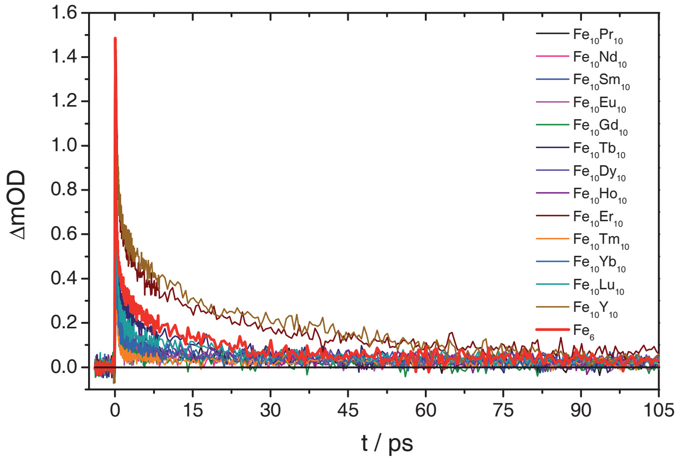

Figure 4.33. Transient absorption of all $Fe_{10}Ln_{10}$ probes.

The first relaxation processes in the $Fe_{10}Eu_{10}$ and $Fe_{10}Tm_{10}$ compounds seem to be the same (Table 4.7 (dark green)). The first time constant in both is about ~300 fs. In addition, the first amplitude is the same with ΣA_1= 0.88. Moreover, the second and third relaxation process parameters are similar. While the time constants, for example, τ_1 for compounds **4.3** and **4.9** are also in the region of **4.8**, the first amplitude maximum is, however, different. In tab. 4.7 the compounds given in black type are those with similar amplitudes. The compound **4.7** seems to be indeed the only one which shows similar dynamics to the reference compound **4.12**. Furthermore, the Y compound (**4.11**) does not show the typical dynamics for the lanthanides. Although, we didn not isolate the structure of the Pr and Sm analogues we assume that this is possible in particular for Sm. Their solutions were measured for comparison.

Table 4.7. Summary of the time constants and amplitudes (data from transient spectra) for all compounds discussed above.

Property	**Time constants τ_i**			**Relative amplitudes ΣA_i**		
Factor	τ_1 (fs)	τ_2 (ps)	τ_3 (ps)	ΣA_1	ΣA_2	ΣA_3
$\mathrm{Fe_{10}Pr_{10}}$	191± 20	2.1±0.1	45 ± 15	0.81	0.13	0.06
$\mathrm{Fe_{10}Nd_{10}}$	**272± 19**	**2.5±0.3**	**78 ± 20**	**0.75**	**0.21**	**0.04**
$\mathrm{Fe_{10}Sm_{10}}$	**272± 27**	**3.4±0.5**	**84 ± 26**	**0.82**	**0.11**	**0.07**
$\mathrm{Fe_{10}Eu_{10}}$	**298± 31**	**2.9±0.4**	**58 ± 11**	**0.88**	**0.05**	**0.07**
$\mathrm{Fe_{10}Gd_{10}}$	**197± 18**	**1.9±0.2**	**60 ± 14**	**0.79**	**0.15**	**0.06**
$\mathrm{Fe_{10}Tb_{10}}$	**258± 22**	**5.3±0.9**	**71 ± 19**	**0.75**	**0.17**	**0.08**
$\mathrm{Fe_{10}Dy_{10}}$	**201± 19**	**1.5±0.4**	**88 ± 21**	**0.77**	**0.14**	**0.09**
$\mathrm{Fe_{10}Ho_{10}}$	**251± 26**	**2.8±0.4**	**79 ± 15**	**0.78**	**0.12**	**0.10**
$\mathrm{Fe_{10}Er_{10}}$	**196± 18**	**3.2±0.6**	**55 ± 10**	**0.64**	**0.20**	**0.16**
$\mathrm{Fe_{10}Tm_{10}}$	**305± 30**	**4.2±0.7**	**59 ± 16**	**0.88**	**0.05**	**0.07**
$\mathrm{Fe_{10}Yb_{10}}$	**198± 21**	**2.5±0.2**	**65 ± 16**	**0.72**	**0.16**	**0.12**
$\mathrm{Fe_{10}Lu_{10}}$	**293± 24**	**2.6±0.3**	**45 ± 12**	**0.69**	**0.17**	**0.14**
$\mathrm{Fe_{10}Y_{10}}$	**382±27**	**6.7±1.2**	**37 ± 13**	**0.52**	**0.24**	**0.24**
$\mathrm{Fe_6}$	**363± 75**	**5.2± 1.4**	**38 ± 11**	**0.64**	**0.23**	**0.13**

Comparing the time constants with the literature values for $\mathrm{Fe_2O_3}$-nanopartciles[100] and considering the origin of the peak at 310 nm in the steady-state absorption spectrum, this might infer that the initial excitation energy is localized within a single O-Fe$^{\mathrm{III}}$ LMCT unit, because all the transient spectroscopic results in the samples show similar excited state dynamics. This localized excitation between LMCT units is reminiscent of the weak cooperative of other O-Fe^{III} LMCT unit in cluster. In addition to this, we performed the pump-intensity dependent transient absorption measurements in order to search for possible interactions between the LMCT units. As seen in Fig.4.34, for the sample $Fe_{10}Er_{10}$ as an example, no significant difference between high- and low-intensity excitation in decay profiles was observed. The corresponding maximum of the amplitudes at 5 ps of the transient absorption signals scale exhibits a linear dependence on excitation energy. This result suggests the possibility of localized excitation. It is also assumed that one exciton per unit is generated. After ecitation, a recombination process is possible or/ and trapping process (within 100 ps time scale). The lnathanides influence also the dynamic of the iron oxide unit.

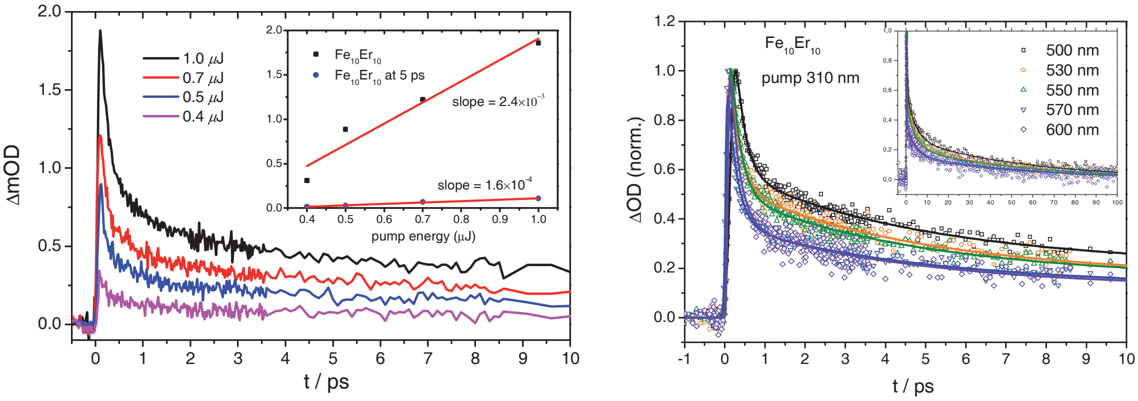

Figure 4.34. (Left) transient absorption responses of $Fe_{10}Er_{10}$ with different intensities of pump pulses (1.0, 0.7, 0.5 and 0.4 μJ) and probe at 550 nm. (Left, inset) shows the corresponding amplitudes of the transient absorption scale linearly with the pump intensity. (Right) the transient absorption responses of $Fe_{10}Er_{10}$ with excitation at 310 nm and probe wavelength between 500-600 nm. The difference of the transient absorption decay profiles may be is the result of the carrier dynamics being affected by thermalization with the laser pulse.

The fact that the time decay constants of the reference Fe_6-clusters are very similar to that in Fe_2O_3-nanoparticles, supports the assumption that $Fe_{10}Ln_{10}$ system can be understood in terms of an "Fe_{10}" nano-sized coordination cluster and that the presence of the lanthanides acts with a doping effect in the cluster, which is well-documented for doped iron oxides. Further evidence for this is the fact that the dynamics is dominated by the iron oxide domain as explained before. The decay dynamics also suggest that the excitation beam at 310 nm creates a hot electron population which rapidly relaxes to the band edge or to trapped states on a subpicosecond time scale via exciton trapping, as explained by Cherepy *et al.*, and the hot electron can also recombine with holes on the timescale of several picoseconds. [100] The trapped electrons have a different lifetime of hundreds of picoseconds.[49b)]

The time constants show a wide range of time scales. There is a weak interaction between the lanthanide ions and the exciton in excited O-Fe^{III} unit. In general, the influence of lanthanide ions on the dynamics leads to a slower depopulation relaxation process from the excited LMCT-state unit.

It is highly probable that the different dynamics observed for the various lanthanides depend on the details of the electronic structure of each one. In other words, after pumping, the upconvesrion to the ground state from the excited states happens in different ways and at different rates depending on the energy terms of either the Fe^{III} or, maybe more likely, on the O-Fe^{III} unit (see discussion later). Morover, one could say that the different colour behaviour observed for this system might depend on the time constants (τ_1 and τ_2) and their corrosponidng amplitudes.

In the search for other iron analogues to study, the cyclic compound $\{Fe_{10}\}$ (**4.13**) with acetate ligands was also measured and shows different electron dynamic processes from those seen for the $\{Fe_6\}$ or the $Fe_{10}Ln_{10}$ compounds. Therefore, this compound cannot be used as reference compound for this study. Likewise, the compound $\{Fe_7\}$ (**4.14**) which was obtained with the same ligand Me-teaH_3 and with pivalate also shows different dynamic processes and they are not helful for understanding the $Fe_{10}Ln_{10}$ (for more details, see [49b)].

Thus, all measurements which were done and discussed above indicate that this behaviour is characteristic for this cluster system and furthermore does not depend on the ring size.

The cyclic complexes obtained in chapter 3 $\{Fe_5Tm_3\}$ (**3.1**), $\{Fe_4Tm_2\}$(**3.5**) and $\{Fe_3Tm_2\}$ (**3.9**) are suitable refernce compounds for this study since they are all cyclic but with different ions arrangements and magnetic behaviour as well as they all contain Tm^{III} ions. Indeed, steady-state absorption spectra and femtosecond measurements were done for all these three compounds. The steady-state absorption spectroscopy and femtosecond study of these three systems will be discussed in more details in the phD thesis of Yu Liang [49b)]. What can be said here is that the time constants as well as the amplitudes are indeed similar to those of $Fe_{10}Tm_{10}$ comound. For example, the values for ΣA_1 from the relaxation process in range of 300 fs, also the trapped state whereafter the coupling between the hole (positive) and an electron (negative) or say after an exciton generates, are as follows.

The values are for $Fe_{10}Tm_{10}$, 0.88; Fe_4Tm_2, 0.85; Fe_5Tm_3, 0.78; and for Fe_3Tm_2, 0.74. All show strong influence on the iron dynamic and actually even on the exciton-recombination process. The fact that time constants and amplitudes are similar for all these TmIII containing compounds might be a result of being cyclic and having indeed a specific Inter System Crossing process (ISC) or/ and an energy transfer between the Tm^{III} and Fe^{III} levels. Remarakable is, however, that the two systems with the antiferromagnetic nature, Fe_4Tm_2 **3.5** and $Fe_{10}Tm_{10}$ **4.8** have almost same values allows us again to ask if we can one day discuss a magneto-opto correlation. On the other hand, the first time constant as said before could explain the colour differences. Here we note that compounds **3.5** and **4.8** have greenish colours (their solutions and crystals in dry form). Compound 3.8 solution is yellow-greenish and crystals are more yellow. Compound **3.1** solution is orange and the crystals are yellow-orange. A femtosecond study of a non-cylic Fe/4f such as the system in chapter 2 and in particular the $\{Fe_2Tm_2\}$ (2.11) compound would be helpful in order to understand wethher this behaviour is specific for cyclic 3d/4f systems or not. We are indeed doing such a measurement for the moment. The results from this study as well as more detailed results about the Fe/Tm rings will be discussed in the phD thesis of Yu Liang.[49]

Photolysis and other measurements and experiments

In order to investigate if the excitation pulses indeed create a hole on the nearby oxygen, causing the transfer of a hot electron to Fe^{III} within the O-Fe^{III} unit (oxide like) in a process like Ligand Metal Charge Transfer (LMCT) as well as whether this causes electron delocalization or hopping, a series of systematic qualitative tests and photolysis experiments were performed. The original idea was that a photo-reduction process whereby Fe^{III} becomes reduced to Fe^{II} can be activated in this cluster system. The pump or excitation at 310 nm might prevent electron delocalization via an upconversion to the ground state with a mechanism where Ln^{III} ions can transfer electron to the Fe^{III} ions. The fact that, we do not detect Fe^{II} in the magnetic and Mössbauer measurements may be due to the fact that these measurements were carried on in darkness. In all coming experiments we will focus on the $Fe_{10}Tm_{10}$ (**4.8**) compound since this one shows the highest efficiency in the electron dynamics of Fe^{III} or/and on the LMCT or/and on the exciton recombination process.

Fig. 4.35 shows the spectrum (200- 850 nm) of solid $Fe_{10}Tm_{10}$ (greenish). Most optical studies on Tm^{III} concern research in the area of doping lanthanides into different glasses.[108] However, Tm^{III} is the rarest rare earth and the most expensive one and is actually much less studied than any other lanthanide. [108]The Tm^{III} ion can have the following transitions to the ground state in UV-VIS-NIR spectral regions which are: $^3H_6 \leftarrow {}^1G_4$ (465 nm), $^3H_6 \leftarrow {}^3F_2$ (657 nm), $^3H_6 \leftarrow {}^3F_3$ (685 nm), $^3H_6 \leftarrow {}^3H_4$ (790 nm), $^3H_6 \leftarrow {}^3H_5$ (1209 nm) and $^3H_6 \leftarrow {}^3F_4$ (1665 nm). [108]

In our experiments we are not pumping (with 310 nm) any of these transitions in the femtosecond study. The fact that the 4f-4f transitions cannot be seen as their characteristic sharp peaks is a result of the dilution of the compounds. Indeed the first four transitions can be seen in the standard spectrum in Fig. 4.35. Moreover, a cut off about 450 nm is observed (after long absorbtipon in the UV region) which looks to correspond to the bandgap as known from solid-state science. The first two transitions are weak and the two about 700 and 800 nm are stronger. In all literature concerning Tm^{III} these four bands can be clearly seen, however, the last two which occur in the NIR region are not measured in our spectrum and they are usually broad. In general, most lanthanides have more transitions in the NIR region than in the visible.

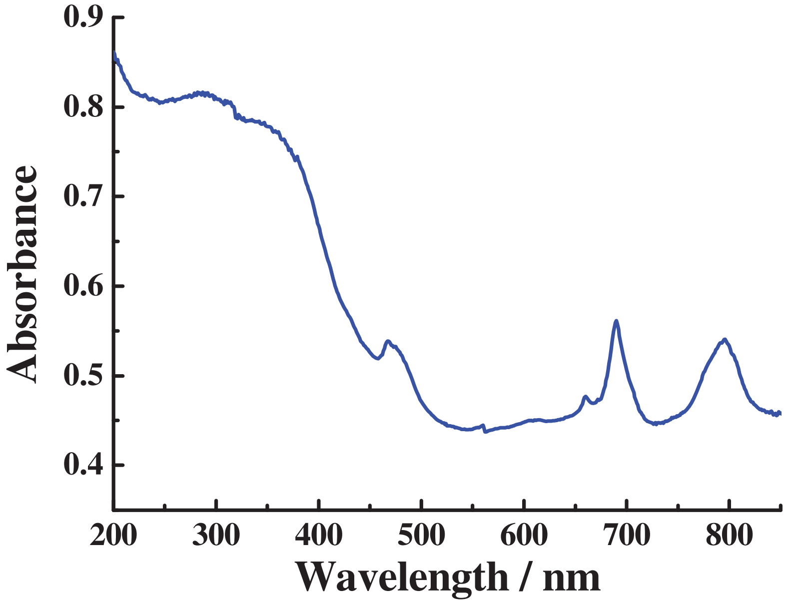

Figure 4. 35. The UV-VIS-NIR spectrum of solid $Fe_{10}Tm_{10}$.

It is of relevance that for Fe^{II} complexes the relative energies are for high spin systems (10Dq (h.s)) < 11000 cm^{-1} (909 nm), for a SCO complex (10Dq (h.s)) is ~ 11500- 12500 cm^{-1} (869.5- 800 nm) and (10Dq (l.s)) is~ 19000-21000 cm^{-1} (526.3 - 476.2 nm) and for 10Dq (l.s) is > 21500 cm^{-1} (465.11 nm) also for a low spin Fe^{II} complex. If this would explain that there is an electron hopping withing $Fe_{10}Tm_{10}$ system? Or that $Fe_{10}Tm_{10}$ behaves formally as Fe^{II} species? These are open questions and need more fundamental understanding as well as more investigations to be understood.

From the first relative amplitude (transient data), indeed trapping likely occurs in a large fraction of the carriers. The trapped electrons then might lead to a high electronic density around Fe^{III} ion and reduce it “formally” to Fe^{II}. More precisely, the whole cluster $Fe^{III}_{10}Ln^{III}_{10}$ might then show “formally” properties similar to the Fe^{II} ion. If this is indeed correct or nearly so, then adding potassium ferricyanide to $Fe^{III}_{10}Ln^{III}_{10}$ should yield Prussian blue if the compound decomposes. **[109]** In order to obtain evidence of Fe^{II} in cluster after light excitation, a photolysis experiment with a mixture of $Fe^{III}_{10}Ln^{III}_{10}$ and potassium ferricyanide (red $K_3[Fe(CN)_6]$) was carried using a UV lamp to irradiate, a blue colour presents within 1 second in the case of $Fe_{10}Tm_{10}$ but this is a much darker blue than that which can be obtained from the cyanotype process (Fig.4.36).

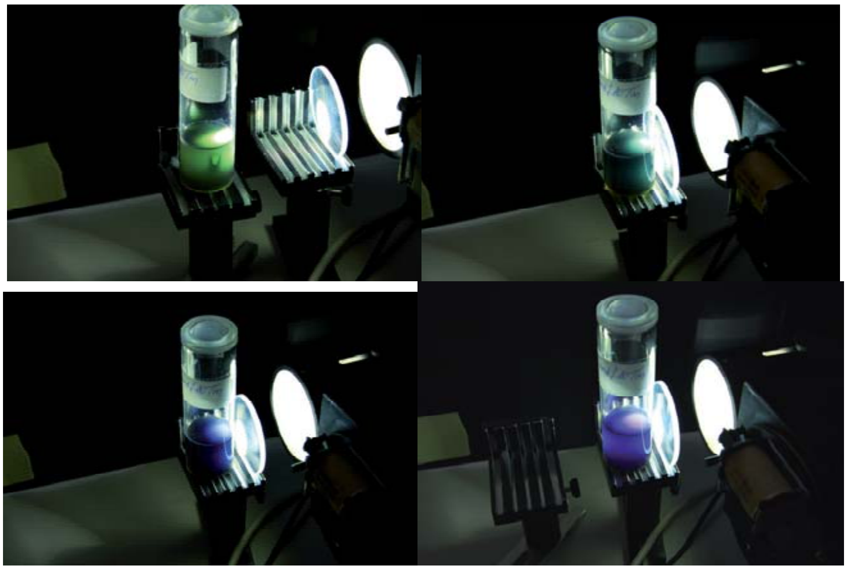

Figure 4.36. (Upper, left) Microscope-photo was taken from a crystal of $Fe_{10}Tm_{10}$ (with the mother solution) with black background. (Upper, right) Microscope-Photo but with pale background. (Middle, left) The crystals and solution of $Fe_{10}Tm_{10}$ 1 day after the reaction. (Middle, right) After adding few ferricyanide crystals and irradiating with UV-lamp. (Lower) The photolysis experiment with $Fe_{10}Tm_{10}$ clear solution plus a few crystals of $K_3[Fe(CN)_6]$ (not soluble in MeCN/MeOH) after 1 sec., 3 sec., 7 sec. and 32 sec.

The same experiment shows that all the $Fe_{10}Ln_{10}$ compounds behave in this way but at different rates and with different degrees of development of the blue colour. Thus, while for the $Fe_{10}Tm_{10}$ compound the onset of visible detection of the blue colour occurs after 1 second and is the fastest in this respect, the $Fe_{10}Er_{10}$ compound starts developing the blue colour after ~ 5 sec. and is the slowest. The same experiment for the Fe_6 ring (**4.12**) requires a much longer time for the solution to become blue (more than 40 min.) The same results are obtained if the crystals are tested in their mother solutions or if only the filtrates are used and also if the crystals are dissolved in other solvents apart from water (see discussion later). The photolysis experiment performed with potassium ferrocyanide rather than feericyanide does not produce blue material.

Absorption spectrum were measured for some reference systems such as irradiation with a solution of potassium ferricyanide or potassium ferrocyanide or else a mixture of potassium ferricyanide with lanthanide nitrates, and in all cases no blue colour was observed. Furthermore, taking the Fe_7 compound (**4.14**) or $Fe(NO_3)_3$ instead of the $Fe_{10}Ln_{10}$ system did not produce the blue material is likely to be Prussian blue (see further discussion). It is interesting to compare the steady-state absorption spectrum obtained for the blue solution resulting from the photolysis experiment performed on the clear filtrate of $Fe_{10}Tm_{10}$ plus potassium ferricyanide ("blue-$Fe_{10}Tm_{10}$") and, the steady-state absorption spectrum of Prussian blue and the original spectrum of the filtrate of $Fe_{10}Tm_{10}$ (Fig. 4.37). The Prussian blue shows a broad band centred on 690 nm, which is consistent with an intervalence interaction typically observed IVCT from Fe^{II} to Fe^{III} [110]. The spectrum of the product from the irradiation of $Fe_{10}Tm_{10}$ plus potassium ferricyanide has a charge transfer broad band centred on 590 nm which is common in cyanide bridged compounds. This position of this charge transfer band suggests intervalence charge transfer corresponding to transfer of an electron from Fe^{II} to Fe^{III} through the cyanide bridge.[111] In other words, compared with the band observed in Prussian blue, this band in the "blue-$Fe_{10}Tm_{10}$" is shifted to higher wavelength. Also noteworthy is the fact that the UV/VIS absorption spectra of $Fe_{10}Tm_{10}$ solution and "blue-$Fe_{10}Tm_{10}$" indicate that the ring structure is still intact. This suggests that the obtained "blue-$Fe_{10}Tm_{10}$" material, which can be indeed isolated, is not Prussian blue but rather a Prussian blue like material.

However, the $Fe^{III}{}_{10}Ln^{III}{}_{10}$ cluster system seems indeed to act as a "Fe^{II}-species" via light excitation and react quickly with potassium ferricyanide. Photolysis of the $Fe_{10}Tm_{10}$ cluster alone for longer times (over 30 min., Fig. 4.38) leads to formation of a brown precipitate and oily material in low yield, suggesting decomposition of the $Fe_{10}Tm_{10}$ cluster with the brown colour coming from some ferric oxyhydroxide or oxide materials such as Fe_2O_3 and/or $Fe(OH)_3$. This is also observed in the case of the $Fe_{10}Er_{10}$ compound but after much shorter times and this requires further investigation.

If the bottle is left closed for months, the solution of "blue-$Fe_{10}Tm_{10}$" stays clear, but as soon as it is opened, a colloidal blue material which seems to be Prussian blue starts forming. This material was collected and washed with acetonitrile/methanol several times. Remarkably, after washing and collecting the material it was violet rather than blue in colour and is designated "blue-violet-$Fe_{10}Tm_{10}$". This was found to be the case for all of the other systems.

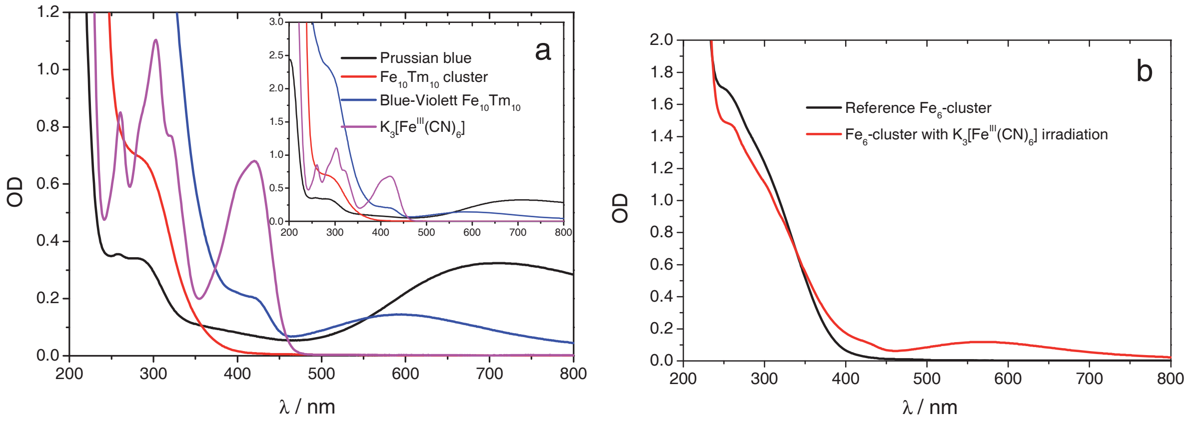

Figure 4.37. Steady-state absorption spectrum of Prussian blue (black), $Fe_{10}Tm_{10}$ (red) wheel and $Fe_{10}Tm_{10}$ with $K_3[Fe^{III}(CN)_6]$ after irradiation with UV-lamp (blue). b) Reference measurement with a mixture of $\{Fe_6\}$ clusters and potassium ferricyanide.The peak at 420 nm may arise from the rest potassium ferricyanide in solution. Another possibility may come from a diferent product of $Fe_{10}Tm_{10}$ cluster after long irradiation times.

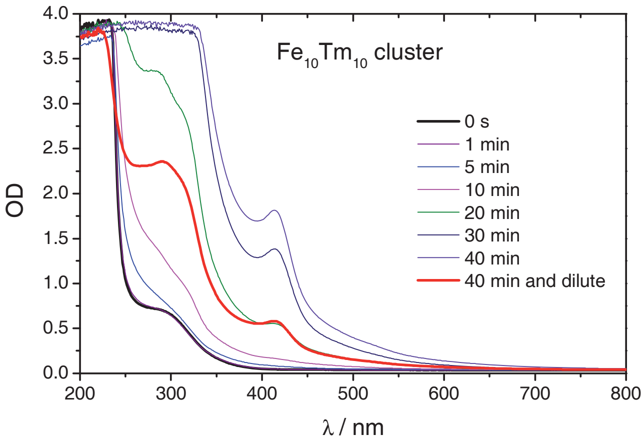

Figure 4.38. Steady-state absorption spectrum of $Fe_{10}Tm_{10}$ clusters after irradiation with UV-lamp.

The transient absorption measurements of the “blue-violet-$Fe_{10}Tm_{10}$” show typical decay curves for time resolved pump-probe measurements for Prussian blue, which were carried out by Arnett et al. and showed that Prussian blue exhibits a rapid initial decay and a relatively long-lived relaxation.[111] The same transient absorption studies of Prussian blue were also performed with a visible probe following IR (800 nm) excitation of the CN band.[112] The transient absorptions profiles we observe by excitation at 310 nm and probing at 550 nm and transient bleach by excitation at 310 nm and probing at 550 and 650 nm of Prussian blue are presented in Fig’s 4.39a and 4.39b, respectively. It important here is to consider the third time constant, which exhibits a long lifetime of the charge transfer state (CT-state) in the order of a few hundred picoseconds.

Transient bleach profiles of the irradiation product from the mixture of blue-Fe_6 and “blue-violett-$Fe_{10}Tm_{10}$” compounds (using the same experimental conditions) are shown in Fig. 4.40. The time constants observed for the “blue-Fe_6” could be determined as 922 ± 63 fs for the first relaxation process, 9 ± 2 ps for the second process and 266 ± 32 ps for the third process. In addition, the transient bleach of the irradiation product of “blue-$Fe_{10}Tm_{10}$” is similar to that of “blue-Fe_6” at least within a 50 ps time scale. With a tri-exponential fit-function up to 50 ps resulted in three time constants: 565 ± 60 fs, 5 ± 0.6 ps and 254 ± 78 ps. The measurement after 50 ps was disturbed by the newly produced blue coloured substance. Comparing the third time constant with that in $Fe_{10}Tm_{10}$ (< 100 ps) gives evidence that at least one new long lifetime state was created during the reaction, which might belong to a Fe^{II} species. Fig. 4.41 shows the measurements on the ferricyanide and ferrocynaide.

In order to gain deeper understanding of this, further lab-experiments and measurements are needed. For example, adding potassium ferrocyanide (yellow $K_4[Fe(CN)_6]$) to $Fe_{10}Tm_{10}$ and repeating the photolysis experiment or the experiment in the sun does not produce the blue colour or any new material, that is, $Fe_{10}Tm_{10}$ acts indeed like an Fe^{II}-sepcies. If it is really the case that photoreduction is occuring in this system, then repeating the same reaction with potassium ferrocyanide but in absence of light should produce blue colour, since there will be no photorecution to give an Fe^{II} species and “$Fe_{10}Ln_{10}$” should then show its “real face”, which is that of a compound containing ten Fe^{III} high spin centres. This experiment was done and in absence of light the solution indeed turned blue. This blue solution appears to contain Prussian blue, but it remains a clear solution without precipitation or any colloidal suspension being formed. This could not be studied further because of time limitations, but future work will involve trying to obtaion crystals from the solution n.

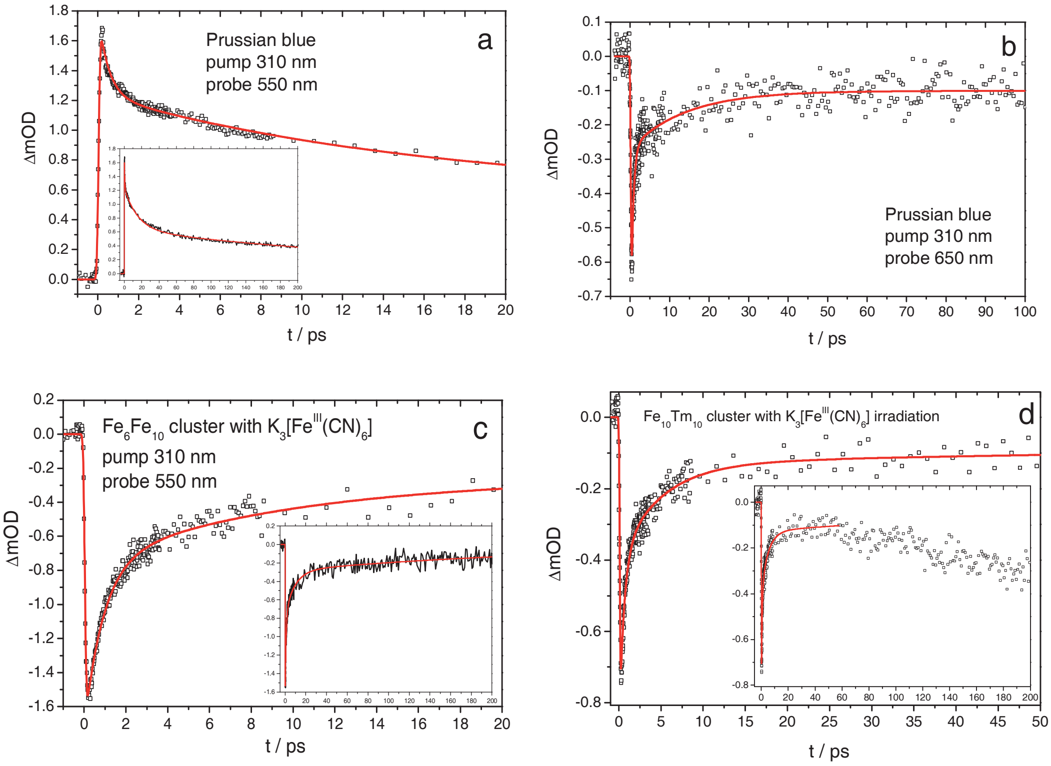

Figure 4.39. Transient absorption (a) and bleach (b) of Prussian blue, transient bleach of the irradiation product of mixture from reference Fe_6 clusters with potassium ferricyanide (c) and $Fe_{10}Tm_{10}$ cluster with potassium ferricyanide (d).

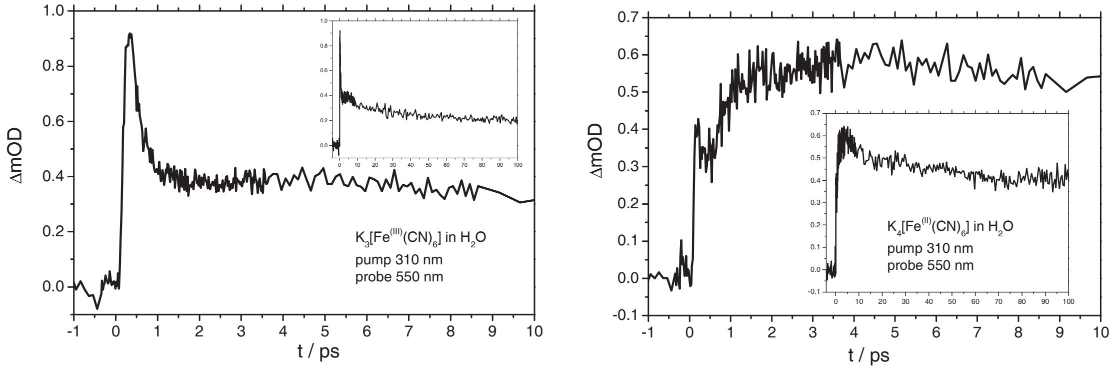

Figure 4.40: Transient absorption of $K_3[Fe^{III}(CN)_6]$ and $K_4[Fe^{II}(CN)_6]$ in water after excitation at 310 nm and probing at 550 nm.

The IR-spectra of the well washed “blue-violett-$Fe_{10}Tm_{10}$” show the cyanide band as at 2055 cm^{-1} as well as bands typically observed for $Fe_{10}Ln_{10}$ (see exp. Part, chapter 5 and Fig. 4.41).

PXRD of the “blue-violett-$Fe_{10}Tm_{10}$” is similar to that of “$Fe_{10}Tm_{10}$” (Fig. 4.42). The PXRD of the “blue-$Fe_{10}Tm_{10}$” does not show the reflection at 17.5° which correspond to Prussian blue (Fm3m cell). [113]However, the Mössbauer spectra (Fig. 4.43) were measured for the “blue-violet-$Fe_{10}Tm_{10}$” and it show spectra typical for Prussian blue. Furthermore, CHN-analysis was done for the same material in order to compare with those of $Fe_{10}Tm_{10}$ and the results were consistent with values for $Fe_{10}Tm_{10}$ rather than for Prussian blue.

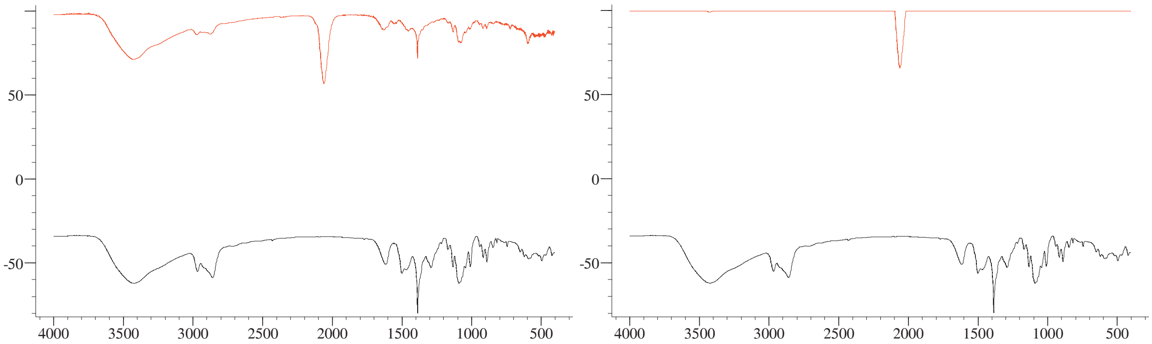

Figure 4.41. (Left) shows the IR spectra of the blue-violet-$Fe_{10}Tm_{10}$ (red) and $Fe_{10}Tm_{10}$ (**4.8**) (black). (Right) shows the Substraced IR frequencies of **4.8** from the blue one. It remains the strong oscilliation of the cyano group. The frequeincies from 400 to 4000 are given in cm^{-1} unit, so the x-axis.

The intensity of the other peaks is strongly suppressed because of the strong intensity of the cyano group. Better IR spectra could not be obtained.

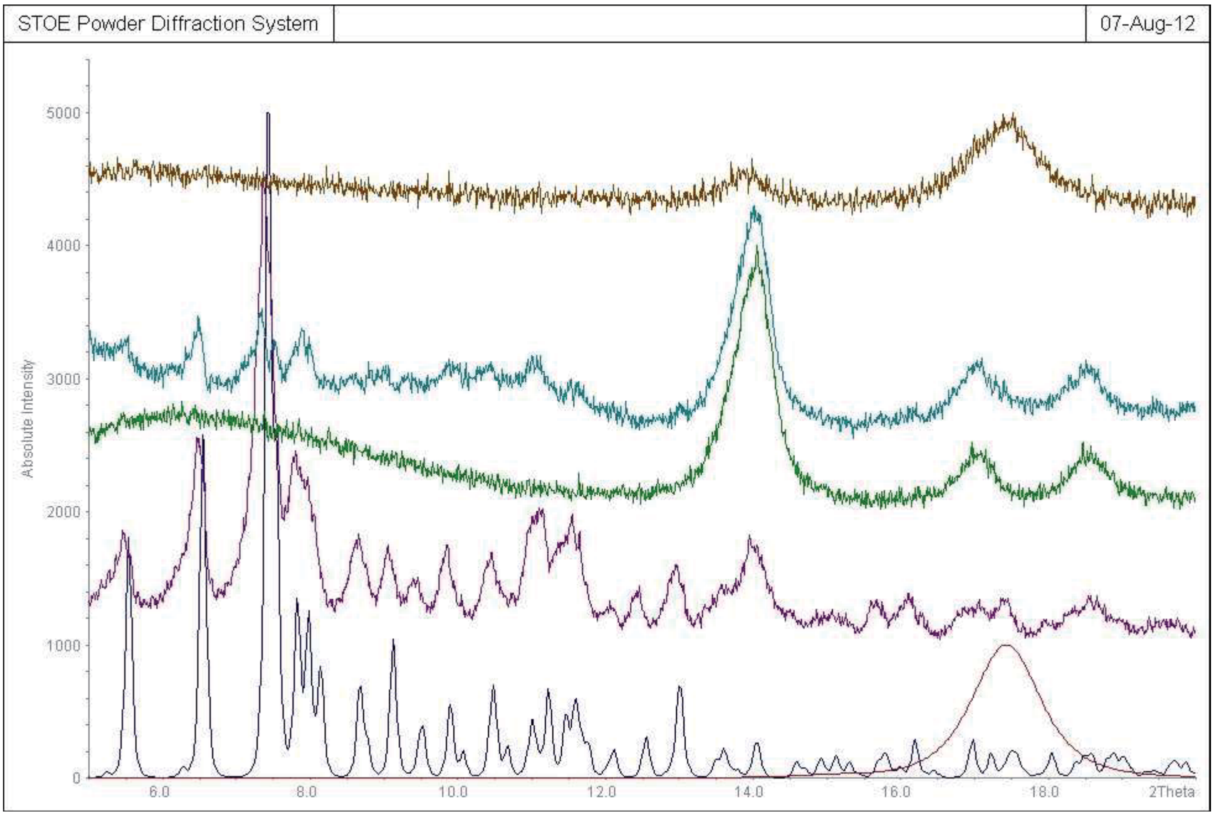

Figure 4.42. The simulated PXRD of $Fe_{10}Tm_{10}$ (**4.8**) (lowest, solid dark grey), the simulated PXRD of Prussian blue (cell Fm3m) (lowest, solid brwon), the experimental PXRD of $Fe_{10}Tm_{10}$ (**4.8**) (purple), in green the teaser used to stick the samples, the background, the PXRD of the "blue-$Fe_{10}Tm_{10}$" (torques) and the PXRD of the home-made Prussian blue according to the lit. [113] (upper, brown) which is consistent with the simulated one.

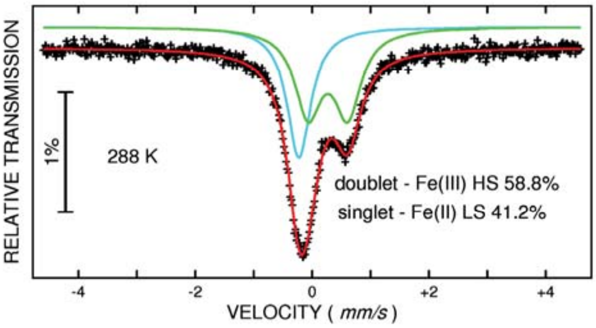

Figure 4.43. The Mössbauer spectrum of "blue-violet $Fe_{10}Tm_{10}$" at 288 K.

The solubility of the “blue-violet-$Fe_{10}Tm_{10}$” is better than that of Prussian blue. For example, the blue-material is moderately soluble in acetone and other solvents. It is, however, insoluble in several other solvents. Attempts were made to crystallize the “blue-$Fe_{10}Tm_{10}$”. The following experiment was indeed successful. A few crystals of $K_3[Fe(CN)_6]$ were collected at one end of an alumina-boat. From the other end 1 ml of a clear solution of $Fe_{10}Tm_{10}$ was dropped in the direction of the red crystals (note, not soluble in MeCN/MeOH). The alumina-boat was left in the sun for 2 hours. A blue material was formed between the two ends of the boat. This material was wetted with 2 ml acetone and 0.5 ml MeCN. After 1 day blue-crystals grew and some non-reacted red crystals of ferricyanide reamined (Fig. 4.44). These crystals were, however, not suitable for X-ray measurement and further efforts are needed in order to obtain better quality crystals.

Figure 4.44. The blue-violet crystals of $Fe_{10}Tm_{10}$ and some non-raected ferricyanide.

A further indicative result that the $Fe_{10}Ln_{10}$ system might be photoreductive is that it can undergo a colour change on exposure to the visible light or X-rays. In particular, the $Fe_{10}Y_{10}$ and $Fe_{10}Er_{10}$ when irradiated (X-ray) or left in the sun for several weeks, turn brown in colour.

In Fig. 4.45 the PXRD of the brown material is compared with the simulated one of $Fe_{10}Y_{10}$ (**4.11**). The PXRD of the brown material shows the presence of some of the $Fe_{10}Y_{10}$ and of another crystalline material which seems to have a larger unit cell. This material still needs to be investigated.

Earlier in this chapter, it was mentioned that, the $Fe_{10}Ln_{10}$ coordination cluster system shows remarkable behaviour in water. By mixing the $Fe_{10}Tm_{10}$ (or others) in water and leaving it in the sun or under UV-irradiation, gas evolution was observed with the colour of the solution colour remaining the same (Fig. 4.46, b). By mixing with potassium ferricyanide in water, gas evolution was seen and a purple material (precipitate) was formed after some days and the solution turned brown (Fig. 4.46, c). However, by mixing $Fe_{10}Tm_{10}$ (or other $Fe_{10}Ln_{10}$) with potassium ferrocyanide, no gas evolution was seen and the solution became purple (Fig. 4.46, e). Several months later, a little brown material was formed. Note, that c is opposite to e. In Fig. 4.46 d, the spectrum where a green solution was obtained when acetone was added is shown. The brwon materials were also soluble in acetone or even reacted in or with acetone. All these materials and behaviours will be investigated in future. This behaviour in water might have a relation to the photo-reduction process assumed in this system. In comparison with 4.46 e (purple), in Fig. 4.46 f, the spectrum where a blue solution was obtained when the compound was mixed with ferrocyanide in darkness is shown. The nature of th gas will e investigated soon in collaboration with the group of Prof. Christine McKenzie from Denmark using the Membrane Introduction Mass Spectrometric (MIMS) method which is usually also used for chlorine gas quantification. [114]

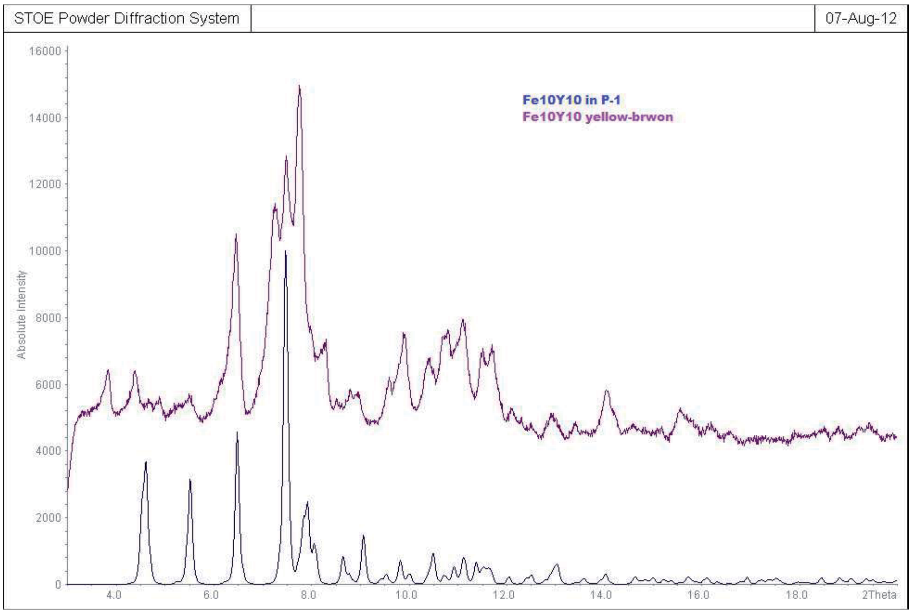

Figure 4.45. The PXRD of the brown $Fe_{10}Y_{10}$ (purple) and the simulated $Fe_{10}Y_{10}$.

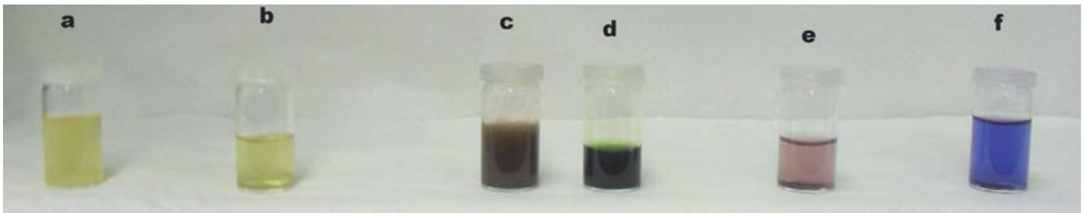

Figure 4.46. a) $Fe_{10}Tm_{10}$ crytals in mother solution (yellow greenish), b) $Fe_{10}Tm_{10}$ in water, c) $Fe_{10}Tm_{10}$ plus ferricyanide (brwon), d) after adding acetone to c, e) $Fe_{10}Tm_{10}$ plus ferrocyanide and f) $Fe_{10}Tm_{10}$ plus ferrocyanide after taking out from darkness room.

From the steady-state absorption spectrum of $Fe_{10}Tm_{10}$ in mother solution (clear without crystals) it was shown that, the $Fe_{10}Tm_{10}$ rings are intact. Furthermore, ESI mass spectra obtained on $Fe_{10}Tm_{10}$ in mother solution or in water are almost the same. In order to study the stability of complex $Fe_{10}Tm_{10}$ and to identify its species in solution, we used Electrospray Ionization Mass Spectrometry (ESI-MS, Fig. 4.47).

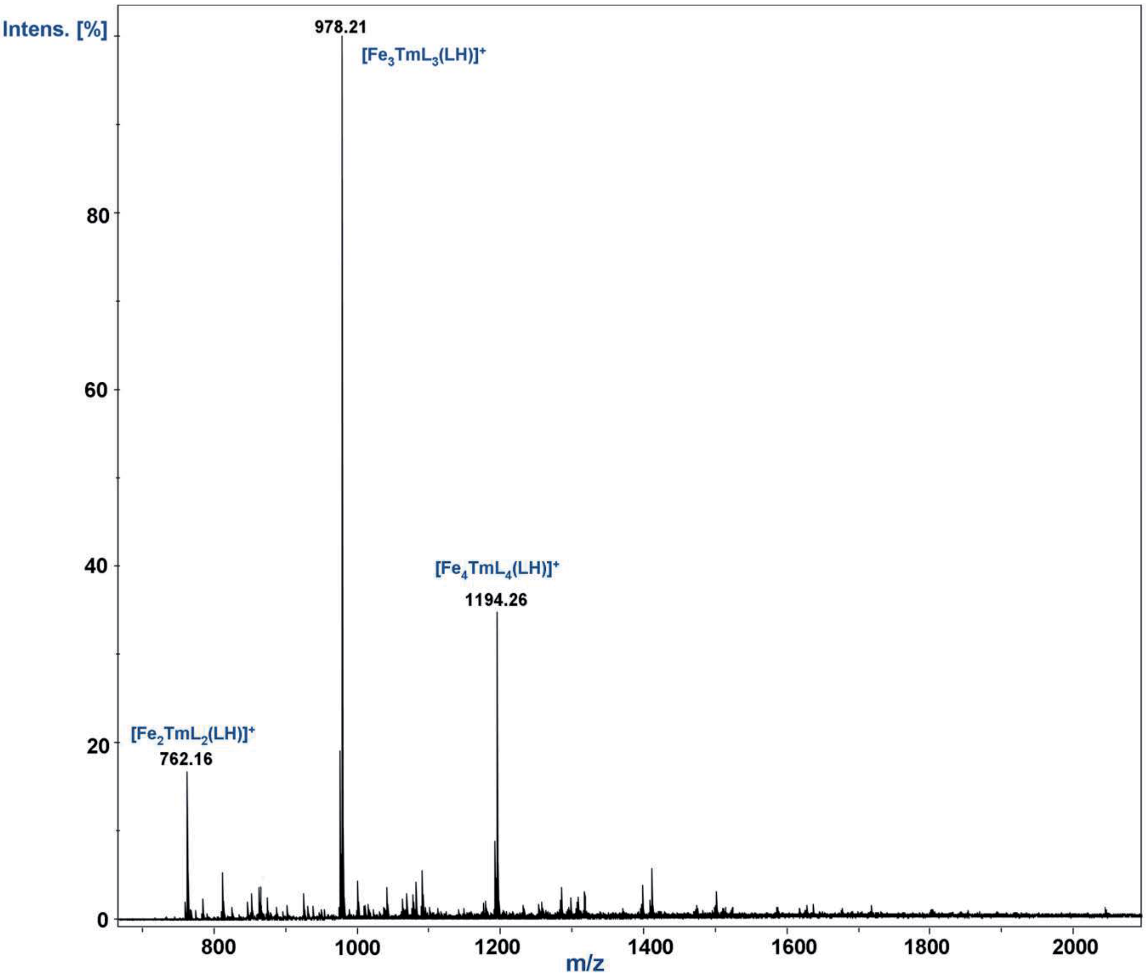

Figure 4.47. Positive ESI-MS spectrum of complex **4.8** in H_2O. The above fragment peaks correspond to the species $[Fe_2TmL_2(LH)]^+$ (*m/z* 762.16), $[Fe_3TmL_3(LH)]^+$ (*m/z*978.21) and $[Fe_4TmL_4(LH)]^+$ (*m/z* 1194.26). L and LH are the trianion (-3) and dianion (-2) of the Me-teaH_3 ligand, respectively.

A solution of it in H_2O (10^{-5} M) was measured in an instrument equipped with a Q-trap, time-of-flight MS (MicrOTOF-Q MS) detector and a source supplied by BrukerDaltonics Ltd. The data were analyzed with the BrukerDaltonics Data Analysis 4.0 software. The observed peaks indicated that the main species in solution are $[Fe_2TmL_2(LH)]^+$, $[Fe_3TmL_3(LH)]^+$ and $[Fe_4TmL_4(LH)]^+$ (see also Fig. 4.48).

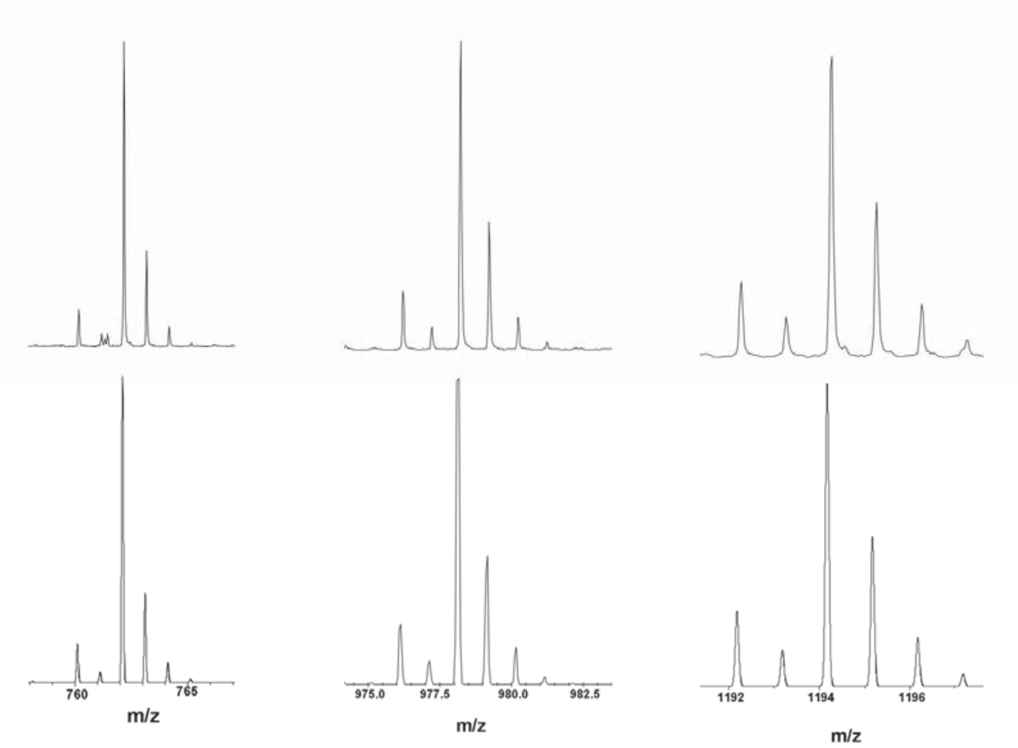

Figure 4.48. Comparison of the experimental (top) and theoretical (bottom) isotopic patterns for the $[Fe_2TmL_2(LH)]^+$, $[Fe_3TmL_3(LH)]^+$and $[Fe_4TmL_4(LH)]^+$species at 762.16, 978.21 and 1194.26*m/z*, respectively.

Further ESI experiments will be started soon in collaboration with the group of Prof. Dr. Manfred Kappes.

4.7 Conclusions

In conlusion, a giant cyclic coordination cluster system $\{Fe_{10}Ln_{10}\}$ was synthesized by reacting the nitrate salts of the metal ions with the ligand in presence of base and in abdication of a carboxylates or other co-ligands. The stability of the complexes can be referred to the nature of the ligand being having a chiral C atom. The cyclic motiv can be described as standing wave and thus of high aesthtetical pleasant. Additionally to the synthesis efforst which yield new cyclic and non-cyclic compounds in this chapter, crystallographic data of all these compounds were collected.

The magnetic behaviour, MCE study, Mössbauer study, optical behaviour study as well as other the stuzdy of the blue material were discussed in this chapter.

The bulk magnetic susceptibility measurements show that the system in general is ferromagnetic. The Mössbauer measuerements explain the origin of the weak antiferromagnetic interaction within thi system.

The MCE calculations show that this system show not only remarkable magnetic behaviour additionally for being SMM (for Dy and Tb) but also being a magnetic cooler.

The optical study as wel as other measurements and experiments show that this system can be unederstood as doped molecular iron nano cluster, where the lanthanides influence its magnetic, colour, electron dynamics and probably conductivity properties.

Several future works are planed for studying and better understanding this system. Currently, transport measurements are under process in collaboration with the group Prof. Lapo Bogani from physics department at the University Stuttgart.

Furthermore, X-ray measurements in presence of light in order to understand if the system is indeed photoreductive will be done in collaboration with the group Prof. Eric Collet from Institut de Physique de Rennes in France. See also Chapter 5.

Chapter 5

Summary and Outlook

The main goal of chapter 2 was to investigate whether the electronic nature of substituents can influence the magnetic anisotropy in Single Moelcule Magnets. A non-cyclic antiefrromagnetically coupled [$Fe_2Dy_2(\mu_3\text{-}OH)_2(teaH)_2(O_2CC_6H_4\text{-}R)_6$] cluster type was taken as a test-bed system from which a reference series (13 compounds) with the unsubstituted benzoate was prepared and intensively investigated using bulk magnetic susceptibility, Mössbauer and EPR measurements. Furthermore, theoretical calculations were done in order to have a further correlation to the other methods. This compound was synthesized from the reaction of benzoate-derivative of the trinuclear oxo-Fe^{III} complex with triethanolamine and dysprosium (III) nitrate. A further 31 {Fe_2Dy_2} compounds with different carboxylates (mainly with substituted benzoates) were prepared with different substituted benzoates and triethanolamine ligands. They were studied comparatively using magnetic and Mössbauer methods. Furthermore, theoretical calculations were done for the full series and for the substituents. Indeed, remarkable effects were observed from both magnetic and Mössbauer methods as well as EPR and the theoretical considerations. The slow relaxation of magnetization and the quantum tunneling of magnetization processes were influenced in remarkable way. Clear trends were observed; substituents with electron giving properties such as such as methyl or *tert*butyl groups lead to higher energy barriers and lower blocking temperatures as well being delendent on the time scale of the magnetic method. Substituents with electron withdrawing effects such as cyano and nitro lead to higher blocking temperatures. By using the Mössbauer technique we discovered a phenomenological effect. The substituent effect causes very strong tuning in the interaction between the anisotropic Dy^{III} and the ^{57}Fe-nuclei in the antiferromagnetically coupled Fe_2Dy_2 coordination clusters. This is reflected in the internal magnetic field H_{int} at 3K and without using external magnetic field. However, the internal field vanishes on applying a magnetic field. We observed also clear trends whereby substituents with +I and +M effects lead to smaller H_{int} and those with withdrawing effects -I, -M to larger H_{int}. EPR results and the results from the magnetic, Mössbauer studies as well as the theoretical calculations show remarkably good correlation in most cases even on changing the substituent position from *para* to *meta*.

The ability of triethanolamine to form Fe^{III} cyclic coordination clusters was utilized by adapting the synthetic strategy for obtaining the tetranuclear compounds in chapter 2. Thus, symmetric and asymmetric Fe^{III}/4f cyclic coordination clusters with novel properties were prepared. Interestingly, it is only possible to form these rings using last three lanthanides, presenting an opportunity to gain insights into the electronic and magnetic properties of the smallest lanthanide ions, which are less present in the literature on molecular magnets.

In chapter 3 an intensive study of an octanuclear asymmetric cyclic coordination clusters was was performed which makes this system the "heart" of this chapter. The reaction of triethanolamine (H_3tea) with [$Fe^{III}_3O(O_2CPh)_6(H_2O)_3$]($O_2CPh$) and trifluoromethanesulfonate (triflate) salts of the three latest lanthanide ions, $Ln(OTf)_3$, in acetonitrile yields [$Fe^{III}_5Ln^{III}_3(\mu_3\text{-}OH)(Htea)_7(O_2CPh)_8$]($CF_3SO_3$) ·xMeCN for the latest lanthanides Tm Yb, Lu. The structure is stabilized first and foremost by the protonated triethanolamine ligand, which connects Fe_2-dimers to a single lanthanide centre. These 8-memberd metallo-ring complexes are rare examples of such wheel-shaped aggregates with odd-number of Fe(III) and Ln(III) centres and diverse coordination. Moreover, they contain an Fe(III)-single ion and two $Fe(III)_2$ units separated from each other. The presence of Ln ions between these 3 units has a strong influence on the magnetic properties of the $Fe(III)_2$ dimers. Mössbauer measurements suggest that at low temperatures the isolated Fe(III) ion and, most importantly, the bound Ln ions manage to transfer hyperfine field in a localized manner to each of the ferric ions of the dimers. The antiferromagnetic coupling within each of the two $Fe(III)_2$-units is supported by theoretical calculations for the coupling constants which show a different perspective on the problem and indicate a weakening of Fe-O(R)-Fe superexchange within dimers plus the presence of weak antiferromagnetic couplings between one ferric ion of the $Fe(III)_2$-units and the single Fe(III) ion. The principal merit is, however, its theoretical tractability because it offers suitable and interesting molecular configurations that enable step-wise synthetic approaches to aid in clarification of such exceedingly complex interactions. This work might should be useful for future studies of SMM design and, by its striking similarity with the bias exchange interaction, perhaps also in real applications.

Chapter 4 discusses a unique example of cyclic ccordination clusters. The synthesis, the magnetic properties as well as the optical appearance of these materials were intensively investigated applying techniques with different time scales. Magnetic susceptibility measurements show that the system in general is ferromagnetic with high ground spin states. This system seems to be multitasking as, for example, in addition to be a ferromagnet and showing very interesting deviations in the susceptibility bevahiour, which could give a deeper insight to the electronic and magnetic individualism of the lanthanide(III) ions, this system seems to a magnetic self-cooler, as evidence by the entropy change on applying an external magnetic field. The Mössbauer study helped in understanding the Fe···Fe interaction within the single molecule which seems to affect all other properties observed from other measurements.

Steady-state absorption measurements and femtosecond spectroscopy study reveal that the system can be understood as a doped nano-sized iron molecular magnet, where the different lanthanides affect its behaviour (magnetically and electronically) in an amazing and complicated way. Attempts have been made to understand these multiple-properties of the system, including synthetic efforts and qualitative experiments. These led to the discovery of a blue material resulting from a photo-induced reaction between potassium ferricyanide and the $\{Fe_{10}Ln_{10}\}$ molecules, apparently without destroying the single molecules. This material could not be definiteively identified as Prussian Blue even if there are indications which suggest it might be. Gas evolution was seen on mixing the $\{Fe_{10}Ln_{10}\}$ in water (or under UV irradiation) and/or by mixing the material in water with iron ferricyanide. It was found that Tm^{III} and Er^{III} ions have an opposite influence on the electron dynamics of the Fe^{III} or O-Fe^{III} moieties. The system displays several fetures: exciton formation, a doping effect, it is molecular and nanoscale and shows semiconductivity. These are similar properties to those foun in (doped) semiconducting iron oxide nano particles. Thus it might be that these systems can be described in terms of molecular-based semi-conducting nanomagnets.

Overall, the work presented has indicated a number of promising directions for developing new systems utilising the many intriguing properties of 3d/4f CCs. In addition to shedding light on the influence of various lanthanide ions on the electronic properties of 3d/4f CCs, the subtle effects attainable be simple subtituent variation on the ligands encapsulating the CCs indicates that fine-tuning of systems is a very real possibility. Furthmore, the optical properties of such systems appear to extremely complicated but fascinating. Up to now, very little work has been done on correlating optical and magnetic properties for 3d/4f systems and the systems presented in chapter 4 provide a strong motivation to take this work further in terms of magneto-optical studies. A further point for consideration is whether the cyclic nature of some of the systems presented here is responsible for their unusual behaviour.

In summary, the systems and the investigation of them which has been presented here provides a strong motivation for expanding this research in many directions. Not least of these is the development of synthetic routes towards the desired compounds. Some of the work presented here shows that directing self-assembly is perhaps more easily “programmed” for 3d/4f systems, probably by virtue of the presence of the structurally more predictable 4f ions.

Chapter 6

Experimental

6.1 Characterization methods of compounds and properties

All reactions were carried out under aerobic ambient conditions, and reagents and solvents were used as received. The crystals obtained in this work were taken with a pipette into a filter paper. After that, they were washed with the main reaction solvent, mostly acteonitrile. If the material was hygroscopic, so it was washed with ether and dried under N_2-stream. Note, the final interpretation of all these results was done by the author of this work after discussions with the collaborators.

Next, FT-IR measurements were done in order to see if the stretching frequencies for the used ligands are presence. A small amount was ground with amount of KBr (usually 1:10 was used). This was pressed into KBr pellets. The correct amount of substance is important in order to avoid strong absorption which could yield a spectrum where some intensities are too strong which can suppress other weaker intensities and at same time important signals. The FT-IR spectra were collected using *Perkin-Elmer Spectrum One.*

Single X-ray measurements were done on different instruments and different temperatures (see Appendix, chapter 6). The Instruments used in the group of Prof. A. K. Powell are Bruker SMART APEX CCD, STOE IPDS (II). In addition, some of these data were collected at the ANKA Synchrotron, KIT. The Crystals were selected under a light microscope, with help of some perfluorether oil protected and amounted on the goniometer. The crystals were centred with help of a camera. Usually, 6 frames were measured each 6 minutes to determine the unit cell and to check the diffraction. The parameters collected were then taken for the full measurement. Structures solutions were done using direct methods, refined using full-matrix least-squares (against F_0^2 for the whole matrix) with the SHELXTL program suite.[115] The following factors are important while refining the structures. The residual factors, R_1 (detected data) and R_2 (for all data) and the goodness-of-fit S are defined as:[116]

$$R_1 = \frac{\sum \left\| F_0 \right| - \left| F_c \right\|}{\sum \left| F_0 \right|}$$

$$wR_2 = \sqrt{\frac{\sum \left[\omega (F_0{}^2 - F_c{}^2)^2 \right]}{\left[\omega (F_0{}^2) \right]}}$$

$$S = \sqrt{\frac{\sum \left[\omega (F_0{}^2 - F_c{}^2)^2 \right]}{(n-p)}}$$

The obtained raw data for the diffraction intensity (~ number of electrons) is expressed through $|F_0|$ and the corresponding calculated data (this why smaller) after structural analysis is $|F_c|$. $R_1 < 0.05$ means good structural analysis, and wR_2 should not be much more double. The numbers n (unique reflections) and p (parameters involved in refinement) should be so that S~1.0.

The value w is the weight of each diffraction point and depends on the accuracy with which F_0^2 was measured. This value w is defined as $1/\sigma^2$. In order to determine the temperature dependency of the atom factors f_0 , the temperature dependent factor B (Debye and Waller factor) can be used as follows.

$$f = f_0 \exp\left(-B \frac{\sin^2 \theta}{\lambda^2} \right) with$$
$$B = 8\pi^2 u^2 = 8\pi^2 U$$

With u is the displacement factor of the atom on the lattice plane. U is expected to be in ideal case isotropic. However, any deviation from that to ellipsoidal

The F_{000} is the number of electrons in the whole unit cell.

The visualization of the compound structure was done using the programm Diamond [117a)].

Often, by leaving the material drying in air a replacement of the solvent molecules in lattice with water molecules is the result. Since this material will be measured by bulk magnetic method (SQUID[118]), so the formula weight should be consistent with that used for analyzing the data. The crystals were mostly measured, the structures identified and primary refined by the author of this work for training reasons. However, in most cases they were remeasured and final refeint by the crystallographer in our group Dr. Christopher E. Anson. All cif files attached as CD to this work were refined by Dr. Anson.

In addition, powder measurements should be done in order to check if the material is phase-clean and were in all cases compared with the simulated one from single X-ray measurements. Here, it is important to choose those parameters from the experimental one such as angles and source…etc. PXRD reflexes were collected by using mainly STOE STADI P X-Ray Powder Diffractometer. The source is Cu-Kα1 radiation with λ= 1.5406 Å. The collected data were analyzed with the software WinX$^{\text{Pow}}$ [117b)]. The reflexes are given as a function of diffraction intensities against 2Θ. The CIF files and PXRD (diffractogramms) were submitted with this work on CD.

Is the compound clean? Elemental analyses (CHN) can be done, in order to have the exact weight to consider the loss of solvent molecules. Elemental analyses were performed using an Elementar Vario EL analyzer at the Institute of Inorganic Chemistry, Karlsruhe Institute of Technology.

If the theoretical calculated molecular weight accords with the experimental one (lying on CHN data), the two further measurements can be done, which are the magnetic measurements and the Mössbauer measurements. The molecular weight is not only important for magnetic, but also for Mössbauer measurement because an exact percentage of Fe is necessarily for Mössbauer measurement. In addition, the purity of the compounds is very important for EPR measurements. All these methods are complementary to each other and are mostly necessarily for compound characterization.

The magnetic measurements have been carried out with the use of a Quantum Design SQUID magnetometer MPMS-XL. [118] This magnetometer works between 1.8 and 400 K for dc applied fields up to 7 T. Measurements were performed on polycrystalline samples. ac susceptibility measurements have been measured with an oscillating ac field of 3 Oe and ac frequencies ranging from 1 to 1500 Hz. The magnetic data were corrected for the sample holder and the diamagnetic contribution. In some cases the measurement has been done by different fields and frequencies if it was necessarily for behaviour understanding (see results discussions and chapter 1 for basics about the theoretical background of the method). The Magnetic data analyses were carried out, being represented as χT *vs,* T and χ *vs.* T thermal dependences. The phenomenological interpretation by fit included temperature independent paramagnetism (*TIP*), impurity contribution (ρ) and intermolecular interaction (zj) (see chapter 1). Analysis of magnetisation data of M vs H was achieved by calculating the appropriate Brillouin function. Minimisation in case of the Fe_2Ln_2 series was carried out with an adapted version of *Visualiseur-Optimiseur* for Matlab® using built-in nonlinear least-squares algorithms.[119-121]The author of this work was taught by Dr. Yanhua Lan to prepare the sample for magnetic measurements, to use the SQUID. Dr. Yanhua Lan carried out the measurements and plotted the data. The magnetic interpretataion of the full series in chapter 2 (compounds **2.1-2-13**) was done in collaboration with Dr. Ghenadie Novitchi. The magnetic interpretations of several other systems were done by Dr. Lan. The magnetic interpreations in deep details of the most Fe_2Dy_2 compounds were done by the author of this work.

The magnetic entropy change ΔSm for several applied field changes ΔH from the M(H,T) data can be calculated using the Maxwell relation as basis.[38, 39]

$$\left(\frac{\partial Sm(T,H)}{\partial H}\right)_T = \left(\frac{\partial M(T,H)}{\partial T}\right)_H$$

Fore isothermal process; $\Delta S_m(T,\Delta H) = \int_{H_i}^{H^f} \left(\frac{\partial M(T,H)}{\partial T}\right)_H dH$

The relations to entropy, magnetization and temperature as well as specific heat are given in chapter 1. The calculations were done by Dr. Yanhua Lan.

The Mössbauer spectra were required using a conventional spectrometer in the constant – acceleration mode equipped with ^{57}Co source (3.7 GBq) in rhodium matrix. Isomer shifts are given relative to α-Fe at room temperature. The sample was inserted inside an Oxford Instruments Mössbauer-Spectromag 4000 Cryostat which has a split- pair superconducting magnet system for applied fields up to 5 T, with the field of the sample oriented perpendicular to the gamma-ray direction, while the sample temperature can be varied between 3.0 and 300 K. Furthermore, the measurement parameters (T, H and velocity) were changed/ adjusted for each system as necessarily for understanding the behaviour (see results discussion and chapter 1 for basics about the theoretical background of the method). The measuerements were done by Dr. Valeriu Mereacre. The results were in interperated in collaboration with him. He introduced the author of this work in the experimental measuring detilas and interpretating the spectra.

The EPR measurements were carried out on a Bruker EMXplus spectrometer in a X-band in the magnetic field range of 100 to 9000 Oe and the wide temperature range dwon to 3 K using the low temperature control system, ER 4112HV. Power parallel- and perpendicular –mode EPR spectra are presented in this work. In collaboration with Violeta Voronkova, physics institute, Kazan, Russian Federation, as mentioned in the results discussion.

The *ab initio* calculations for the Fe_2Ln_2 series were carried out with the GAMESS code[122], using SBKJC[123] effective core potential and basis set for lanthanide ions, 6-311G* basis set for the Fe, N and O atoms and 6-31G for the remaining skeleton of C and H atoms. In order to simplify the computational effort the clusters were taken using experimental geometry and idealized by replacing the terminal phenyl groups with hydrogen atoms. The computation aimed to address the exchange coupling effects in the $\{Fe_2Gd_2\}$ clusters and the magnetic anisotropy in the $\{Fe_2Dy_2\}$ SMM-type system. The CASSCF (Complete Active Space Self Consistent Field) calculations are rather prohibitive for the full tetranuclear system. For instance the minimal setting of the $\{Fe_2Gd_2\}$ system, CASSCF (24, 24), i.e. 24 electrons in 24 orbitals (2×5*d* +2×7*f*) imply for an antiferromagnetic ground state over 10^{12} configurations. However, reliable information can be obtained replacing certain *d* or *f* ions with diamagnetic congeners in order to investigate the magnetic effects on a selected moiety. Thus, the model complex $\{Fe_2Lu_2\}$ reveals the *d-d* exchange coupling between Fe^{III} centers, and the $\{Co^{III}_2Gd_2\}$ the *f-f* interaction. The system $\{FeGd\text{-}Co^{III}Lu^{III}\}$, where one half of the complex was replaced by diamagnetic ions, gives the *d-f* exchange states. Finally, a $\{DyCo^{III}_2Lu^{III}\}$, complex, containing only one magnetically active *f* center was used to investigate the Ligand Field (LF) and magnetic anisotropy effects on the Dy^{III} ion, using CASSCF(9,7) calculations (i.e. 9 electrons in 7 selected *f* orbitals) followed by Spin-Orbit (SO) treatment. All theoretical calculations were done in collaborations with different groups as mentioned in the results discussion.

Steady-state absorption spectrum was recorded by a Varian Cary5E spectrophotometer. By photolysis the samples were irradiated with a xenon arc lamp.

Femtosecond transient absorption measurements were done to investigate the excited-state dynamics of the samples at various excitations and probing wavelength. Briefly, the output of an amplified laser beam (CPA 2210, Clark-MXR) with a repetition rate of 1 kHz was split equally to pump two noncollinear optical parametric amplifiers (NOPAs, Clark-MXR). One of the two output pulses served for third harmonic generation (310 nm with pulse duration about 100 fs (FWHM)) via a sum frequency mixing process with the center wavelength of the CPA (775 nm). The probe pulses were set between 500-600 nm by another NOPA and pump pulses energy at the samples was varied between 0.4 and 1.0 μJ in order to check the excitation energy and probe wavelength dependence of the response. Otherwise, experiments were performed at pump energy of 0.8 μJ and probe wavelength at 550 nm. The probe energy was less than 0.1 μJ. The polarization of probe pulses was set at magic angle (54.7°) by means of a tunable λ/2 plate (Alphalas). The measurements were carried out at room temperature (more details see PhD Yu Liang). The steady-state measurements, the photolysis experiments and the femtosecond study were done in collaboration with Dr. Andreas N. Unterreiner and Yu Liang from Pyhsikalische Chemie Institut (KIT). UV-VIS-NIR measurement was done by Dr. Konstantis Konidaris and interpretated by the author of this work. ESI MASS spectrum-was done and interpretated by the author of this work and Dr. Konstantis Konidaris.

6.2 Compounds Preparations

Compounds belong to chapter 2

The trinuclear starting materials

The syntehtic proseducre of the trinuclear starting materials deviate in some cases from the literature as discussed in chapter 2. The reader should have the possibility to reproduce them. The synthesis of those also will be given here, where the deviation from the proseducre in the lierature was very important and which are relevant for the study.

$[Fe_3O(O_2CPh)_6(H_2O)_3](O_2CPh)$ (2.sm1)

A solution of $Fe(NO_3)_3{\cdot}9H_2O$ (6.06g, 15 mmol) in absolute ethanol (30 mL) was added to a second solution of sodium benzoate/ benzoic acid (7.2 g, 50 mmol)/ (4.6 g, 40 mmol) in dest. Water (50 mL). The resulting orange suspension was stirred at 60°C for 2 h and further 2 h at ambient temperature. The orange-brown product was washed with water/EtOH/Et_2O (5/5/5 mL). The product was then collected and dried under vacuum. Yield was 88% based on Fe. Crystals can be obtained by refluxing this material in MeCN/ MeOH (1:2). *Anal.* Calc. C, 52.50; H, 4.04; N, 0.00%. Found. C, 53.03; H, 4.4; N, 0.00%.

$[Fe_3O(O_2CC_3H_5)_6(HO_2CC_3H_5)(H_2O)_2]Cl\cdot 2H_2O$ (2.sm2)

A solution of $FeCl_2{\cdot}4H_2O$ (5 g, 0.025 mol) was added to a solution of (20.25 g, 0.366 mol)/ (2.33 g, 0.0583 mol) of cyclopropanecarboxylic acid/ sodium hydoxide in H_2O (70 mL). To this mixture was then added 20 mL of ethanol. The mixture was stirred for 20 minutes at room temperature. The dark red solution was left undisturbed (closed). After 2 days well formed red crystals were obtained in 69% yield. *Anal*. Calc. C, 37.88; H, 4.99; N, 0.00%. Found. C, 38.45; H, 4.89, N, 0.00%.

$[Fe_3O(O_2CC_6H_4\text{-}m CH_3)_6(H_2O)(EtOH)_2](NO_3)\cdot 2H_2O$ (2.sm3)

A solution of $Fe(NO_3)_3\cdot 9H_2O$ (6.06g, 15 mmol) and *meta*-tolyic acid (12.2 g, 90 mmol) in absolute ethanol (70 mL) was stirred at 80°. After 40 min. water (5 mL) was added. The mixture was further heated at 100°, till only 50 mL of solvent remained. At this point adding more water (20 mL) would give brown product microcrystalline or when it was left as is it to cool down, well formed red-brwon crystals were obtained in high yields over 70%. *Anal.* Calc. For the red-crystals from EtOH a little water: C, 51.93; H, 5.02; N, 1.16%. Found. C, 52.03; H, 5.04; N, 1.17%.

$[Fe_3O(O_2CC_6H_4\text{-}p CH_3)_6(H_2O)_3](NO_3)\cdot 2H_2O$ (2.sm4)

A solution of $Fe(NO_3)_3\cdot 9H_2O$ (6.06g, 15 mmol) and *para*-tolyic acid (12.2 g, 90 mmol) in absolute ethanol (50 mL) was stirred at 80° for 1h and at ambient temperature for 4h. To this mixture was added then water (20 mL). The resulting red-brown solid was washed in filter with EtOH/Et_2O (3/ 10 mL). The product was dried with N_2-spray. The yield was 59%. Large red Crystals can be obtained by refluxing the same quantities above in absolute ethanol for 2h. The clear dark red solution was left to cool down. Few minutes later high yield (over 90%) of the crystals were collected. *Anal.* Calc. for the microcrystalline product: C, 50.28; H, 4.60; N, 1.26%. Found. C, 49.03; H, 5.04; N, 1.57%.

$[Fe_3O(O_2CC_6H_4\text{-}p^tBu)_6(H_2O)_3](NO_3)\cdot 2H_2O$ (2.sm5)

(3.03 g, 15 mmol) of $Fe(NO_3)_3\cdot 9H_2O$ were dissolved in EtOH (15 ml). This solution was drooped to a solution of (8.02 g, 45 mmol) of 4-tertbutylbenzoic acid in H_2O (10 ml). The orange-mixture was stirred for 1h at 80°C. Then continued stirring without heating for 4 h. The orange product was then filtered off and washed with H_2O (3 ml), EtOH (5 ml) and Et_2O (5 ml). The product was then dried under vacuum. The yield was 23%. *Anal.* Calc. C, 56.66; H, 6.34; N, 1.00%. Found. C, 56.20; H, 6.75; N, 1.15%.

$[Fe_3O(O_2CC_6H_4\text{-}p NO_2)_6(H_2O)_3](O_2CC_6H_4\text{-}p NO_2)$ (2.sm6)

A solution of $Fe(NO_3)_3\cdot 9H_2O$ (6.06g, 15 mmol) and 4-nitrobenzoic acid (15.05 g, 90 mmol) in absolute ethanol/ H_2O (80/ 10 mL) was stirred at 60° for 3h and further at ambient temperature overnight. The pale-orange product was washed several times with EtOH and Et2O to remove the non-reacted acid. The product was dried under vacuum. The yield was 33%. Anal. Calc. C, 38.92; H, 2.33; N, 7.56 %. Found. C, 38.67; H, 2.54; N, 7.81 %.

[$Fe_3O(O_2CC_6H_4$-*p*CN$)_6(H_2O)_3](O_2CC_6H_4$-*p*CN) (2.sm7)

A solution of $Fe(NO_3)_3 \cdot 9H_2O$ (6.06 g, 15 mmol) and 4-cyanobenzoic acid (12.63 g, 11.65 mmol) in absolute ethanol/ Water (100/ 5 mL) was stirred at ambient temperature overnight. After, the brown product was precipitated the mixture was refluxed for 1h. The orange brwon product was washed with Et_2O. The yield was ~ 11%. FW = 1176.0 g/mol CHN: *Anal.* Calc. C, 48.98; H, 2.57; N, 8.33%. Found. C, 49.05; H, 3.07; N, 8.25%.

[$Fe_3O(O_2CC_6H_4$-*m*CN$)_6(H_2O)_3](O_2CC_6H_4$-*m*CN) (2.sm8)

A solution of $Fe(NO_3)_3 \cdot 9H_2O$ (6.06 g, 15 mmol) and 3-cyanobenzoic acid (12.63 g, 11.65 mmol) in absolute ethanol/ Water (100/ 5 mL) was stirred at ambient temperature overnight. After, the brown product was precipitated the mixture was refluxed for 1h. The orange brwon product was washed with Et_2O. The yield was ~ 11%. FW = 1176.0 g/mol CHN: Anal. Calc. C, 48.98; H, 2.57; N, 8.33%. Found. C, 49.05; H, 3.07; N, 8.25%.

[$Fe_3O(O_2CC_6H_4$-*p*$N_3)_6(H_2O)_3](O_2CC_6H_4$-*p*$N_3$) (2.sm9)

$Fe(NO_3)_3 \cdot 9H_2O$ (6.06 g, 15 mmol) and 4-azidobenzoic acid (14.68 g, 90 mmol) were dissolved in absolute ethanol (60 mL) and the suspension was stirred at ambient temperature for 30 min. After that water (20 mL) was added and the acid becames more soluble. The light yellow mixture was stirred in a closed beaker further at ambient temperature for 48 h. The resulted yellow product was filtered and washed with EtOH (10 mL) and Et_2O (20 mL). The product dries fast in air and then under vacuum. Note that water should not be added to the acid before reacting with Fe^{III} in ethanol. The yield was 73%. *Anal.* Calc. C, 42.88; H, 2.50; N, 21.43%. Found. C, 42.81; H, 2.57; N, 21.47.

[$Fe_3O(O_2CC_6H_4$-*p*Br$)_6(H_2O)_3](O_2CC_6H_4$-*p*Br)·2EtOH (2.sm10)

(6.06 g, 15 mmol) of $Fe(NO_3)_3 \cdot 9H_2O$ and (18.1 g, 90.0 mmol) of 4-bromobenzoic acid were reacted in EtOH/ H_2O (120/20 ml) for 1h at 80°C. The pale-orange slurry was stirred further for 24 h at ambient temperature. The very pale-orange product was filtered, and washed with EtOH/Et_2O (5/5 ml). The yield was 17%. *Anal.* Calc. C, 36.80; H, 2.68; N, 0.00%. Found. C, 36.77; H, 2.50; N, 0.00%.

[$Fe_3O(O_2CC_6H_4$-*p*Ph$)_6(H_2O)_3](NO_3) \cdot 2H_2O$ (2.sm11)

Was made in as similar way as for 4-bromobenzoic acid but with 4-phenylbenzoic acid. The yield was 21%. *Anal.* Calc. C, 61.68; H, 4.25; N, 0.00%. Found. C, 61.65; H, 4.53; N, 0.00%.

$[Fe_3O(O_2CC_6H_4\text{-}p\text{N}(CH_3)_2)_6(H_2O)_3](O_2CC_6H_4\text{-}p\text{N}(CH_3)_2)\cdot EtOH\ 2H_2O$ (2.sm12)

$Fe(NO_3)_3\cdot 9H_2O$ (6.06 g, 15 mmol) and 4-dimethylaminobenzoic acid (14.87 g, 90 mmol) were dissolved in absolute EtOH/ dest. H_2O (100/ 20 mL). The resulted dark blue solution was heated at 100° for 1h. The acid became after that more soluble. Dark red product started precipitating and the blue colour disappeared slowly. The product was left in air (fume hood) for dryness. It was then used without washing. The yield was over 60%. *Anal.* Calc. C, 53.14; H, 5.90; N, 6.67%. Found. C, 53.67; H, 5.76; N, 6.84%.

$[Fe_3O(O_2CC_6H_4\text{-}p\text{OMe})_6(H_2O)_3](O_2CC_6H_4\text{-}p\text{OMe})\cdot 2H_2O$ (2.sm13)

This compound was prepared in a similar way as but with 4-methoxybenzoic acid. The yield was 19%. *Anal.* Calc. C, 50.51; H, 4.46; N, 0.00%. Found. C, 51.01; H, 4.73; N, 0.00%.

$[Fe_3O(O_2CC_6H_4\text{-}p\text{MeSO}_2)_6(H_2O)_3](NO_3)$ (2.sm14)

A solution of $Fe(NO_3)_3\cdot 9H_2O$ (6.06 g, 15 mmol) and 4-(methylsulfonyl)benzoic acid (18.02 g, 90 mmol) were dissolved in EtOH/ H2O (40/ 40 mL). The mixture was stirred at ambient temperature (closed beaker) for 48h. The mixture was then heated at 60° for 2h. The pale-yellow product was washed with water. Although, the product was washed several times with (20 mL), EtOH (10 mL) and Et_2O (5 mL), the product still contains high amount of non-reacted acid even after several times washing. This seems to bee a particular problem with this acid. The reason might be the bad solubility of this acid.

$[Fe_3O(O_2CC_6H_4\text{-}p\text{F})_6(H_2O)_3](O_2CC_6H_4\text{-}p\text{F})$ (2.sm15)

The trinuclear compound with 4-fluorobenzoic acid was prepared by similar way as the bromo one. However, the yield was only 6%. The compound contained a lot of non-reacted acid, which could be removed after several times washing with EtOH and Et_2O. *Anal.* Calc. C, 48.58; H, 2.83; N, 0.00%. Found. C, 49.01; H, 2.91; N, 0.00%.

$[Fe_3O(O_2CC_6H_4\text{-}o\text{F})_6(H_2O)_3](O_2CC_6H_4\text{-}o\text{F})$ (2.sm16)

The same way as for *p*-F. CHN very similar.

$[Fe_3O(O_2CC_{14}H_9)_6(H_2O)_3](O_2CC_{14}H_9)$ (2.sm17)

$Fe(NO_3)_3\cdot 9H_2O$ (1.25 g, 3.1 mmol) and 9-anthracenecarboxylic acid (3.30 g, 15 mmol) were dissolved in absolute EtOH/ dest. H_2O (45/5 mL). The resulted dark unclear solution was heated at 120° till boiling. The solution was left cooling down. The solution is now dark green and it was left stirring at ambient temperature for 1h. The resulted suspension containing the green product was left in air (fume hood) for several days till dryness. The product was then washed with Et_2O (10 mL) and dried under vacuum. The yield was 53%. *Anal.* Calc. C, 70.60; H, 3.90; N, 0.00%. Found. C, 70.79; H, 3.90; N, 0.00%.

$[Fe_3O(O_2CC_{10}H_7)_6(H_2O)_3](O_2CC_{10}H_7)$ (2.sm18)

A solution of $Fe(NO_3)_3{\cdot}9H_2O$ (6.06 g, 15 mmol) and 2-naphthoic acid (15.5 g, 90 mmol) in absolute ethanol/ Water (60/ 10 mL) was stirred at 80° for 4h. The resulting orange brown product was filtered and washed with EtOH (10 mL) and Et_2O (10 mL). The yield was ~ 77%. *Anal.* Calc. C, 62.84; H, 4.04; N, 0.00%. Found. C, 63.05; H, 4.07; N, 0.00%.

$[Fe_3O(O_2CC_6H_3(NO_2)_2)_6(H_2O)_3](O_2CC_6H_3(NO_2)_2)$ (2.sm19)

Was made in a similar way as for of 4-nitrobenzoic acid but using 3,5-dinitrobenzoic acid. The yield was 59%. *Anal.* Calc. C, 33.46; H, 2.17; N, 11.15%. Found. C, 33.60; H, 2.17; N, 11.31%.

The tetranuclear compounds

$[Fe_2Ln_2(\mu_3\text{-}OH)_2(Htea)_2(O_2CPh)_6]{\cdot}3MeCN$ {Fe_2Ln_2-4H} compounds (2.1-2.13)

Method A (**2.1, 2.12, 2.13**): Solutions of $[Fe_3O(O_2CPh)_6(H_2O)_3](O_2CPh)$ (0.25 g, 0.242 mmol) in MeCN (5 ml) and $Ln(NO_3)_3{\cdot}6H_2O$ (0.3 mmol) and $teaH_3$ (0.22 g, 1.45 mmol) in MeCN/MeOH (10 mL/5 mL) were separately heated at 60°C for 2 minutes, and then mixed and stirred for 5 minutes at 80°C. The resulting yellow solution was allowed to cool to room temperature and left undisturbed. Pale yellow block-like crystals were collected after 1 day.

Method B (**2.2, 2.3, 2.4, 2.6**): To a solution of $[Fe_3O(O_2CPh)_6(H_2O)_3](O_2CPh)$ (0.25 g, 0.242 mmol) in MeCN (20 mL) was added dropwise a solution of $Ln(NO_3)_3{\cdot}6H_2O$ (0.25 mmol) and $teaH_3$ (0.30 g, 2 mmol) in MeCN/MeOH (30 mL/3 mL) over 5 mins, leading to a yellow solution. After 20 mins of stirring at room temperature, the resulting solution was left undisturbed. Pale yellow blocks crystallized after 1 hour.

Method C (**2.5, 2.8, 2.10 and 2.11):** As Method B, but using (0.30 g, 2 mmol) $teaH_3$.

The Fe_2Ln_2 complexes with six benzoate ligands are slightly hygroscopic on long exposure to the atmosphere.

Method D (2.**7** and **2.9**): $[Fe_3O(O_2CPh)_6(H_2O)_3](O_2CPh)$(0.27 g, 0.262 mmol), $teaH_3$ (0.30 g, 2 mmol) and $Ln(OTf)_3{\cdot}6H_20$, OTf= trifluoromethanesulfonate (0.22 mmol) were dissolved in

MeCN (40 mL) and stirred at room temperature for 40 min. The resulting clear yellow solution was left undisturbed closed. Pale-yellow blocks crystallized after 1 day for 2.**7** and 4 days for **2.9**.

$[Fe_2Nd_2(\mu_3\text{-}OH)_2(teaH)_2(O_2CPh)_6]\cdot 3MeCN$ (**2.3**): Yield 64%. Calc. for {**2.3** + $3H_2O$}: C 44.15, H 4.51, N 4.29%; found: C 44.23; H 4.40; N 4.40%. Selected IR data (cm^{-1}): 3358 (br), 2860 (m), 2250 (m), 1595 (m), 1543 (s), 1094 (s), 904 (s), 718 (s), 674 (s), 588 (s), 456 (s).

$[Fe_2Sm_2(\mu_3\text{-}OH)_2(teaH)_2(O_2CPh)_6]\cdot 3MeCN$ (**2.4**): Yield 64%. Calc. for {**2.4** + $4\frac{1}{2}H_2O$}: C 43.11, H 4.58, N 4.19%; found: C 43.09; H 4.39; N 4.21%. Selected IR data (cm^{-1}): 3510 (br), 2862 (m), 2251 (m), 1595 (s), 1544 (s), 1095 (s), 904 (s), 718 (s), 674 (s), 594 (s), 458 (m).

$[Fe_2Eu_2(\mu_3\text{-}OH)_2(teaH)_2(O_2CPh)_6]\cdot 3MeCN$ (**2.5**): Yield 80%. Calc. for {**2.5** + ½MeCN + $4H_2O$}: C 43.44, H 4.57, N 4.57%; found: C 43.63; H 4.38; N 4.60%. Selected IR data (cm^{-1}): 3424 (br), 2861 (m), 2250 (m), 1595 (s), 1544 (s), 1095 (s), 904 (s), 718 (s), 674 (s), 594 (s), 458 (m).

$[Fe_2Gd_2(\mu_3\text{-}OH)_2(teaH)_2(O_2CPh)_6]\cdot 3MeCN$ (**2.6**): Yield 64%. Calc. for {**2.6** + $3\frac{1}{2}H_2O$}: C 43.22, H 4.47, N 4.20%; found: C 43.15; H 4.21; N 4.25%. IR data (cm^{-1}): 3425 (br), 2862 (m), 1595 (s), 1544 (s), 1095 (s), 904 (s), 718 (s), 674 (s), 594 (s), 458 (m).

$[Fe_2Tb_2(\mu_3\text{-}OH)_2(teaH)_2(O_2CPh)_6]\cdot 3MeCN$ (**2.7**): Yield 64%. Calc. for {**2.7 + ~** 1½ H_2O}: C 43.95, H 4.37, N 4.48%; found: C 43.97; H 4.31; N 4.49%. Selected IR data (cm^{-1}): 3425 (br), 2860 (m), 2258 (m), 1596 (s), 1543 (s), 1095 (s), 907 (s), 720 (s), 674 (s), 594 (s), 460 (m).

$[Fe_2Dy_2(\mu_3\text{-}OH)_2(teaH)_2(O_2CPh)_6]\cdot 3MeCN$ (**2.8**): Yield 80%. Calc. for {**2.8** + $3H_2O$}: C 43.18, H 4.41, N 4.20%; found: C 43.06; H 4.06; N 4.19%. Selected IR data (cm^{-1}): 3385 (br), 2860 (m), 2250 (m), 1595 (s), 1543 (s), 1095 (s), 904 (s), 718 (s), 674 (s), 594 (s), 458 (m).

$[Fe_2Ho_2(\mu_3\text{-}OH)_2(teaH)_2(O_2CPh)_6]\cdot 2MeCN$ (**2.9**): Yield 73%. Calc. for {**2.9** + 2 H_2O}: C 43.08, H 4.27, N 3.54; found: C 42.97, H 4.30, N 3.54%. Selected IR data (cm^{-1}): 3385(br), 3066 (w), 2861 (w), 1597 (s), 1545 (s), 1493 (w), 1306 (w), 1095 (m), 1070 (m), 1026 (w), 907 (w), 719 (s), 674 (w), 600 (w), 462 (w).

$[Fe_2Er_2(\mu_3\text{-}OH)_2(teaH)_2(O_2CPh)_6]\cdot 3MeCN$ (**2.10**): Yield 40%. Calc. for {**2.10** + $3\frac{1}{2}H_2O$}: C 42.71, H 4.42, N 4.15%; found: C 42.60; H 4.18; N 4.28%. Selected IR data (cm^{-1}): 3385 (br), 2860 (m), 2250 (m), 1595 (s), 1543 (s), 1095 (s), 904 (s), 718 (s), 674 (s), 594 (s).

$[Fe_2Tm_2(\mu_3\text{-}OH)_2(teaH)_2(O_2CPh)_6]\cdot 3MeCN$ (**2.11**): Yield 61%. Calc. for {**2.11** + 2½H_2O }: C 43.08, H 4.33, N 4.18; found: C 43.09, H 4.30, N 4.29%. Selected IR data (cm^{-1}): 3342 (br), 3142 (w), 2892 (w), 1598 (s), 1537 (s), 1102 (s), 907 (s), 714 (s), 674 (s), 593 (s), 460 (m).

$[Fe_2Yb_2(\mu_3\text{-}OH)_2(teaH)_2(O_2CPh)_6]\cdot 3MeCN$ (**2.12**): Yield 68%. Calc. for {**2.12** + ½H_2O}: C 43.81, H 4.16, N 4.26%; found: C 43.71; H 4.30; N 4.05%. Selected IR data (cm^{-1}): 3509 (br), 3064(w), 2977 (w),2858 (m), 1596 (s), 1543 (s), 1095 (s), 907 (s), 719 (s), 673 (s), 592 (s).

$[Fe_2Y_2(\mu_3\text{-}OH)_2(teaH_3)_2(O_2CPh)_6]\cdot 3MeCN$ (**2.13**): Yield 84%. Anal. Calc. for {**2.13** + 1H_2O}: C 48.50; H 4.68; N 4.71%. Found: C 48.10; H, 4.64; N, 4.85%. IR data (cm^{-1}): 3385 (br), 2861 (s), 2257 (m), 1596 (s), 1545 (s), 1095 (s), 906 (s), 721 (s), 674 (s), 596 (s), 462 (m).

$[Fe_4Lu_2]$ (**2.14**) and $[Fe_8La_6]$ (**2.15**) were prepared in as similar way as **2.13**.

$[Fe_2Dy_2(\mu_3\text{-}OH)_2(teaH)_2(O_2CC_6H_4CH_3)_6]\cdot 2(HO_2CC_6H_4CH_3)\cdot 3CH_3CN\cdot 4H_2O$ ($2.8^{teaH\text{-}6pMe}$)

$[Fe_3O(O_2CC_6H_4CH_3)_6(H_2O)_3](O_2CC_6H_4CH_3)$ (0.273 g, 0.25 mmol), $teaH_3$ (0.298 g, 2 mmol) and $Dy(NO_3)_3\cdot 6H_2O$ (0.116 g, 0.25 mmol) were dissolved in MeCN (20 ml) and stirred at room temperature for 50 min. The clear yellow solution was left undisturbed in air. After one day large pale-yellow blocks were crystallized. Yield 88 %. *Anal*. Calc. C, 48.20; H, 5.08; N, 3.42; found C 48.25, H 5.16, N 3.18%. Selected IR data (cm^{-1}): 3365 (w), 3187 (br), 2873 (s), 1677(s), 1308 (m), 1292(m), 1178 (s), 905(m), 862(m), 768 (s), 758 (s), 693 (m), 622 (s), 602(s), 491(w), 444(w), 423(w).

$[Fe_2Dy_2(\mu_3\text{-}OH)_2(teaH)_2(O_2CC_6H_4\text{-}{}^tBu)_6]\cdot 2(HO_2CC_6H_4\text{-}{}^tBu)\cdot 1.5\ MeCN\cdot 0.5\ CH_2Cl_2$ ($2.8^{teaH\text{-}6ptBu}$)

To a warm solution (50°C) of $[Fe_3O(O_2CC_6H_4\text{-}{}^tBu)_6(H_2O)_3](O_2CC_6H_4\text{-}{}^tBu)$ (0.345 g, 0.242 mmol) in MeCN (5 ml) was dropwise added a solution of $teaH_3$ (0.31g, 2.08 mmol) and $Dy(NO_3)_3\cdot 6H_2O$ (0.119 g, 0.26 mmol) in MeCN (10 ml). The unclear yellow mixture was forward heated at 65°C for 15 minutes. After adding of CH_2Cl_2 (5 ml) becomes clear yellow solution was further stirred for one hour but at room temperature. The resulting solution was left undisturbed in air. Pale-yellow blocks were crystallized after 1 day. Yield 44%. *Anal.* Calc.: C, 53.7; H, 6.12; N, 2.92. Found: C, 53.7; H, 6.29; N, 2.40% . Selected IR data (cm^{-1}): 3357(br), 3152(w), 3069(w), 2964(s), 2903(m), 2868(m), 2254(w), 1937(br,w), 1810 (w), 1677(m), 1611(s), 1589(s), 1540(s), , 1459(m), 1386(s), 1315(w), 1269(m), 1189(m), 1102(m), 1067(m), 1067(w), 1016(m), 916(w), 902(w), 861(w), 788(s), 713(s), 594(m), 545(w), 460(w).

$[Fe_2Dy_2(\mu_3\text{-}OH)_2(teaH)_2(O_2CC_6H_4NO_2)_6]\cdot 3MeCN\cdot 3H_2O$ ($2.8^{teaH\text{-}6pNO2}$)

To a solution of $[Fe_3O(O_2CC_6H_4NO_2)_6(H_2O)_3](O_2CC_6H_4NO_2)$ (0.325 g, 0.242 mmol) and $teaH_3$ (0.298 g, 2 mmol) in MeCN/MeOH (10/3 ml) was added solid $Dy(NO_3)_3\cdot 6H_2O$ (0.116 g, 0.25 mmol). The bottle was closed and the mixture was stirred at room temperature for 90 min. The clear yellow solution was left undisturbed and closed. After three days large yellow blocks were crystallized. Yield 84%. *Anal*. Calc.: C, 37.10; H, 3.45; N, 7.93. Found: C, 37.70; H, 3.61 ; N, 7.41%. Selected IR data (cm^{-1}): 3356 (br), 3152 (w), 2869 (w), 1618 (m), 1565 (s), 1522 (m), 1410 (w), 1345 (m), 1163 (w), 1094 (s), 1080 (m), 1014 (w), 918 (m), 902 (m), 879 (m), 840 (m), 780 (m), 724 (s), 600 (w), 525 (w).

$[Fe_2Dy_2(\mu_3\text{-}OH)_2(Htea)_2(O_2CC_6H_4CN)_6]\cdot 2MeCN\cdot 3H_2O$ ($2.8^{teaH\text{-}6pCN}$)

To a solution of $[Fe^{III}_3O(O_2CC_6H_4CN)_6(H_2O)_3](O_2CC_6H_4CN)$ (0.291 g, 0.242 mmol) and $teaH_3$ (0.298 g, 2 mmol) in MeCN/MeOH (30 ml/ 10ml) was added solid $Dy(NO_3)_3\cdot 6H_2O$ (0.116 g, 0.25 mmol). The mixture was reacted for 40 min. at 50°C. The yellow solution was then left in air undisturbed. After 3 days well formed pale-yellow crystals were collected. Yield 23%. *Anal.* Calc.: C, 43.14; H, 3.60; N, 7.87. Found: C, 43.00; H, 3.37; N, 7.76%. Selected IR data (cm^{-1}): 3475 (br), 2863 (br), 2230 (s), 1603 (s), 1591 (s), 1545 (m), 1500 (w), 1460 (m), 1305 (w), 1177 (m), 1093 (s), 1019 (m), 780 (s), 644 (m), 436 (w).

$[Fe_2Gd_2(\mu_3\text{-}OH)(Htea)_2(O_2CC_6H_4p\text{-}CN)_6]$ ($2.6^{teaH\text{-}6pCN}$). Selected IR data (cm^{-1}): 3356 (br), 2856 (w), 2229 (m), 1594 (s), 1548 (s), 1408 (s), 1375 (s), 1292 (w), 1177 (w), 1092 (w), 1018 (w), 916 (w), 860 (w), 779 (s), 753 (w), 691 (m), 593 (m), 546 (w), 488 (w), 439 (w).

$[Fe_2Tb_2(\mu_3\text{-}OH)(Htea)_2(O_2CC_6H_4p\text{-}CN_2)_6]\cdot CH_3CN\cdot 6H_2O$ ($2.7^{teaH\text{-}6pCN}$)

Yield 25%. *Anal.* Calc.: C, 42.09; H, 3.69; N, 7.00. Found: C, 41.74; H, 3. 78; N, 6.57%. Selected IR data (cm^{-1}): 3476 (br), 2978 (w), 2864 (w), 2231 (s), 1591 (s), 1544 (s), 1459 (w), 1412 (s), 1304, 1176 (w), 1092 (s), 1019 (m), 904 (w), 780 (s), 753 (w), 694 (w), 592 (m), 547 (w), 487 (w), 435 (w).

$[Fe_2Ho_2(\mu_3\text{-}OH)(Htea)_2(O_2CC_6H_4p\text{-}CN_2)_6]\cdot CH_3CN\cdot 6H_2O$ ($2.9^{teaH\text{-}6pCN}$)

Yield 17.3%. *Anal.* Calc.: C, 41.79; H, 3.73; N, 7.00. Found: C, 41.47; H, 3. 76; N, 6.47%. The IR are similar to the others.

$[Fe_2Y_2(\mu_3\text{-}OH)(Htea)_2(O_2CC_6H_4p\text{-}CN_2)_6]\cdot CH_3CN\cdot 4H_2O$ ($2.13^{teaH\text{-}6pCN}$)

Yield 21.3%. *Anal.* Calc.: C, 46.31; H, 3.95; N, 7.84. Found: C, 46.46; H, 3. 93; N, 7.42%. Selected IR data (cm^{-1}): 3357 (br), 2863 (w), 2228 (m), 1595 (s), 1548 (s), 1464 (w), 1409 (s), 1375 (s), 1304, (w), 1177 (w), 1090 (w), 1018 (w), 906 (w), 779 (m), 692 (w), 597 (w), 546 (w), 489 (w), 445 (w).

$[Fe_2Dy_2(\mu_3\text{-}OH)_2(teaH)_2(O_2CC_6H_4m\text{-}CH_3)_6]$ ($2.8^{teaH\text{-}6mMe}$)

$[Fe_3O(O_2CC_6H_4m\text{-}CH_3)_6(H_2O)_3](O_2CC_6H_4m\text{-}CH_3)$ (0.273 g, 0.25 mmol), teaH$_3$ (0.298 g, 2 mmol) and $Dy(NO_3)_3\cdot 6H_2O$ (0.116 g, 0.25 mmol) were dissolved in MeCN (20 mL) and stirred at room temperature for 30 min then at 50°C for 5 min. The clear yellow-orange solution was left undisturbed in air. After 8 days large (twinned) pale-yellow blocks were collected in 22% yield. *Anal.* Calc.: C, 45.72; H, 4.47; N, 1.77. Found: C, 45.11; H, 5.03 ; N, 1.57 %.

$[Fe_2Dy_2(\mu_3\text{-}OH)_2(Htea)_2(O_2CC_6H_4m\text{-}CN)_6]$ ($2.8^{teaH\text{-}6mCN}$)

$[Fe_3O(O_2CC_6H_4m\text{-}CN)_6(H_2O)_3](O_2CC_6H_4m\text{-}CN)$ (0.288 g, 0.242 mmol), triethanolamine (0.298 g, 2 mmol) and $Dy(NO_3)_3\cdot 6H_2O$ (0.116 g, 0.25 mmol) were dissolved in MeCN/MeOH (10/10 mL). The mixture was reacted for 30 min. at 80°C. The yellow solution was then left in air undisturbed. After 3 days small block-like pale-yellow crystals were collected in 13% yield. *Anal.* Calc.: C, 43.78; H, 3.38; N, 7.74. Found: C, 43.95; H, 3. 40; N, 7.64%. Selected IR data (cm^{-1}): 3502 (br), 3077 (w), 2878 (m), 2231 (s), 1993 (w), 1773 (w), 1610 (s), 1556 (s), 1479 (w), 1459 (w), 1433 (s), 1377 (s), 1280 and 1267 (w), 1208 (m), 1165 (w), 1083 (s), 1067 (s), 1034 and 1018 (w), 921 (m), 904 (s), 831 (w), 790 (m), 789 (s), 682 and 670 (m), 599 (s), 564 (m), 490 (w), 462 (m), 410 (w).

$[Fe_2Dy_2(\mu_3\text{-}OH)_2(Htea)_2(O_2CC_6H_5)_4(NO)_3]$ ($2.8^{teaH\text{-}4pH}$)

$[Fe_3O(O_2CPh)_6(H_2O)_3](O_2CPh)$ (0.55 g, 0.54 mmol), $Fe(NO_3)_3\cdot 9H_2O$ (0.55 g, 1.36 mmol), triethanolamine (0.507 g, 3.4 mmol) and $Dy(NO_3)_3\cdot 6H_2O$ (0.55 g, 1.2 mmol) were dissolved (one pot) in MeCN (75 mL). This mixture was stirred at 100 °C for 25 min. The red solution was filiterd off (few white percipitate) and left undisturbed sealed. One day later yellow blokcs were formed. The yield was 16%.{1H$_2$O}. *Anal.* Calc.: C, 34.43; H, 3.61; N, 4.01. Found: C, 34.78; H, 3.61; N, 4.10 %. Selected IR data (cm^{-1}): 3652 (s), 3235 (br), 2873 (m), 1598 (s), 1558 (s), 1538 (m), 1493 (m), 1467 (w), 1543 (m), 1442 (m), 1384 (s), 1367 (s), 1307 (w), 1092 (s), 1070 (s), 1024 (m), 922 (s), 902 (s), 720 (s), 688 (m), 671 (s), 636 (w), 601 (s), 430 (w), 407 (w).

$[Fe_2Dy_2(\mu_3\text{-}OH)_2(teaH)_2(O_2CC_6H_4\ m\text{-}CH_3)_4(NO_3)_2]\cdot 3CH_3CN$ ($\mathbf{2.8}^{teaH\text{-}4mMe}$)

$[Fe_3O(O_2CC_6H_4m\text{-}CH_3)_6(H_2O)_3](O_2CC_6H_4m\text{-}CH_3)$ (0.136 g, 0.125 mmol), $teaH_3$ (0.298 g, 2 mmol) and $Dy(NO_3)_3\cdot 6H_2O$ (0.116 g, 0.25 mmol) were dissolved in MeCN (20 mL) and stirred at room temperature for 30 min then at 50°C for 5 min. The clear yellow solution was left undisturbed in air. After 4 weeks large pale-yellow blocks were crystallized. Yield was 8.3%. *Anal.* Calc.: C, 38.67; H, 4.22; N, 6.31. Found: C, 38.72; H, 4.18; N, 6.39%. Selected IR data (cm^{-1}): 3652 (m), 3272 (br), 3069 (w), 2952 (w), 2911 (w), 2873 (m), 2846 (w), 1785 (w), 1596 (m), 1557 and 1547 (s), 1467 (m), 1443 (s), 1391 and 1364 (s), 1342 and 1321 (m), 1227 and 1249 (m), 1162 (w), 1090 (s), 1069 (s), 919 (m), 901 (m), 817 (w), 782 (m), 759 (s), 710 (w), 667 (s), 602 (s), 525 (w), 486 (w), 495 (w), 455 (w), 430 (w), 407 (w).

$[Fe_2Dy_2(\mu_3\text{-}OH)_2(Htea)_2(O_2CC_6H_4m\text{-}CN)_4(NO_3)_2]$ ($\mathbf{2.8}^{teaH\text{-}4mCN}$)

Equivalent synthesis to $\mathbf{2.8}^{teaH\text{-}4pH}$ but using (0.54 mmol) of the *meta*-cyano trinuclear (**2.sm8**). The yield was 13%. %. {1 MeCN· $1H_2O$}. *Anal.* Calc.: C, 35.96; H, 3.21; N, 8.21. Found: C, 35.77; H, 3.17; N, 8.26%. Selected IR data (cm^{-1}): 3466 (s), 2868 (w), 2234 (s), 1556 (s), 1468 (w), 1434 (s), 1385 (vs), 1210 (w), 770 (m), 680 (w), 671 (w), 597 (w), 406 (w).

$[Fe_2Dy_2(\mu_3\text{-}OH)_2(teaH)_2(O_2CC_6H_4N(CH_3)_2)_6]\cdot 2(HO_2CC_6H_4N(CH_3)_2)\cdot 3H_2O\cdot 2MeCN$ ($\mathbf{2.8}^{teaH\text{-}6pNMe2}$)

$[Fe_3O(O_2CC_6H_4\text{-}N(CH_3)_2)_6(H_2O)_3](O_2CC_6H_4\text{-}N(CH_3)_2)$ (blue) (0.315 g, 0.242 mmol) of (0.305g, 2.044 mmol) triethanaolmine and $Dy(NO_3)_3\cdot 6H_2O$ (0.116 g, 0.25 mmol) were dissolved in MeCN/ MeOH (40/10 mL). The mixture was stirred at r.t. for 30 min and it became dark orange solution from which orange needles formed after 5 days. Yield is 9.11%. *Anal.* Calc.: C, 47.68; H, 5.54; N, 7.74. Found: C, 47.53; H, 5.45; N, 7.60% . Selected IR data (cm^{-1}): 3652 (w), 3357 (w), 3152 (w), 2863 (w), 1914 (w), 1655 (w), 1607 (s), 1572 (m), 1519 (s), 1486 (w), 1458 (w), 1362 (br, s), 1233 (w), 1195 (s), 1094 (w), 1069 (w), 1003 (w), 945 (w), 917 (w), 904 (w), 833 (w), 784 (m), 777 (w), 722 (w), 702 (w), 635 (w), 598 (m), 541 (w), 510 (w), 471 (w), 418 (w).

$[Fe_2Dy_2(\mu_3\text{-}OH)_2(teaH)_2(O_2CC_6H_4OCH_3)_6]\cdot 2(HO_2CC_6H_4OCH_3)$ ($\mathbf{2.8}^{teaH\text{-}6pOMe}$)

A solution of $[Fe_3O(O_2CC_6H_4\text{-}p\text{OMe})_6(H_2O)_3](O_2CC_6H_4\text{-}p\text{OMe})\cdot 2H_2O$ (**2.sm1**3) (0.3 g, 0.225 mmol), triethanolamine (0.3 g, 2 mmol) and Dy(NO3)3 6H2O (0.116 g, 0.25 mmol) were dissolved in MeCN (20 /10 mL) to give a pale yellow solution. The mixture was stirred at r.t. for 40 min. It was then left undisturbed sealed for 1 month. No crystals were formed in this period. To the same solution MeCN (30 mL) and CH_2Cl_2 (2 mL) were adedd. The solution was then heated at 60 °C for 30 min. Few greenish prodcut was obtained after solution removed under pressure. The prodcut was recrystalized in MeCN and MeOH (3/ 3 mL). Green cyrstals were obtained from the solution mixture after several weeks.The yield was less than 2%. {+ $2H_2O$}. *Anal.* Calc.: C, 45.27; H, 4.50; N, 1.39. Found: C, 45.29; H, 5.47; N, 1.19% .Selected IR data (cm^{-1}): 3652 (br), 3455 (br), 3211 (br), 2960 (w), 2899 (w), 2865 (w), 2841 (w), 1662 (m), 1606 (s), 1591 (m), 1588 (m), 1538 (s), 1510 (m), 1459 (m), 1444 (w), 1417 (m), 1312 (m), 1276 (s), 1170 (s), 1144 (m), 1131 (w), 1103 (w), 1093 (m), 1032 (m), 925 (w), 904 (m), 868 (m), 852 (m), 786 (m), 700 (w), 636 (w), 620 (w), 510 (w), 408 (w).

$[Fe_2Dy_2(\mu_3\text{-}OH)_2(teaH)_2(O_2CC_6H_4\text{-}Ph)_6]\cdot(HO_2CC_6H_4\text{-}Ph)_2\cdot 1CH_3OH\cdot 3\ H_2O$ ($2.8^{teaH\text{-}6pPh}$)

A Solution of $[Fe_3O(O_2CC_6H_4\text{-}Ph)_6(H_2O)_3](O_2CC_6H_4\text{-}Ph)\cdot 2H_2O$ (0.371 g, 0.224 mmol), $Dy(NO_3)_3\ \cdot 6H_2O$ (0.118g, zzmmol) and triethanolamine ($teaH_3$) (0.303 g, yy mmol) in 10 $MeCN/CH_2Cl_2$ (20/20 mL) was stirred at 60°C for 30 min. The resulting clear pale-yellow solution was then left undisturbed in air. Seven weeks later large block-like yellow crystals were collected in 8% yield. *Anal.* Calc.: C, 57.81; H, 4.64; N, 1.15. Found: C, 57.80; H, 4.65; N, 1.20%.

Preparation of $[Fe_2Dy_2(\mu_3\text{-}OH)_2(teaH)_2(O_2CC_6H_4\text{-}Ph)_4(NO_3)_2]\cdot 5MeCN\cdot 1CH_2Cl_2$ ($2.8^{teaH\text{-}4pPh}$)

Solutions of $[Fe_3O(O_2CC_6H_4\text{-}Ph)_6(H_2O)_3]\cdot O_2CC_6H_4\text{-}Ph\cdot 2H_2O$ (0.18 g, 0.125 mmol) in $MeCN/CH_2Cl_2$ (15/10 mL), $Ln(NO_3)_3\ \cdot 6H_2O$ (0.262 mmol) and triethanolamine ($teaH_3$) (0.12 g, 0.804 mmol) in 10 ml CH_3CN. Solutions were separated stirred for 10 minutes at room temperature, respectively. They after that mixed and stirred for 40 minutes at room temperature and then filtered off. After 1 day block- like pale-yellow crystals were collected.

Anal. Calc.: C, 45.27; H, 4.14; N, 6.40. Found: C, 42. 03; H, 3.77 ; N, 4.16% .Selected IR data (cm^{-1}): 3614 (m), 3360 (br), 2976 (w), 2949 (w), 2860 (m), 2262 (w), 1593 (s), 1576 (s), 1541 (s), 1476 (s), 1384 (vs), 1303 (m), 1199 (w), 1179 (m), 1090 (s), 1033 (m), 1007 (m), 902 (s), 864 (m), 752 (s), 699 (s), 608 (s), 499 (s). Yield was 44%.

$[Fe_2Dy_2(\mu_3\text{-}OH)_2(teaH)_2(O_2CC_6H_4\text{-}p\text{F})_6]\cdot 1\ H_2O$ ($2.8^{teaH\text{-}6pF}$)

$[Fe_3O(O_2CC_6H_4\text{-}p\text{F})_6(H_2O)_3](O_2CC_6H_4F)$ (0.303 g, 0.25 mmol), triethanolamine (0.26g, 1.45 mmol) and $Dy(NO_3)_3 \cdot 6H_2O$ (0.14 g, 0.218 mmol) were dissolved in MeCN/ MeOH (15/ 5 mL) and stirred at r.t. for 2h. The yellow-orange solution was filtered off and left selaed. Three weeks later yellow and brwon cyrstals of $\{Fe_8\}$ crystallized at same time. CHN and IR were not done yet because of prodcut mixture and limited time. The synthesis will be improved in future.

$[Fe_2Dy_2(\mu_3\text{-}OH)_2(teaH)_2(O_2CC_6H_4\text{-}o\text{F})_6]\cdot 1\ H_2O$ ($2.8^{teaH\text{-}6oF}$)

The same way as **$2.8^{teaH\text{-}6pF}$** but without $\{Fe_8\}$ yellow needles crystals were obtained after few days. CHN and IR were not done becasue of limited time.

$[Fe_2Dy_2(\mu_3\text{-}OH)_2(teaH)_2(O_2CC_6H_4\text{-}p\text{Br})_6]\cdot 1\ H_2O$ ($2.8^{teaH\text{-}6pBr}$)

$[Fe_3O(O_2CC_6H_4\text{-}p\text{Br})_6(H_2O)_3](O_2CC_6H_4\text{-}Br)$ (0.369g, 0.226 mmol) , (0.312 g, 2.1 mmol) of triethanolamine and (0.124 g, 0.272 mmol) of $Dy(NO_3)_3 \cdot 6H_2O$ were dissolved (one pot) in CH_3CN/CH_3OH (20/ 8 mL). The mixture was stirred at r.t. for 2 h. The few precipitate was filtered off. The clear pale-yellow solution was left undisturbed in air. White precipitate was formed after 2 days, which was filtered off and the bottle was closed. After 1 week pale-yellow blocks were obtained. Yield is13.4%. These compounds **are** bad soluble in several organic solvents. *Calc.*: C, 32.70; H, 2.74; N, 1.41. Found: C, 32. 64; H, 2.95; N, 1.17% Selected IR data (cm^{-1}): 3422 (br), 3075 (br), 2950 (w), 2904 (w), 2863 (w), 2837 (w), 1918 (w), 1701 (w), 1587 (s), 1543 and 1529 (s), 1482 (w), 1461 (w), 1397 and 1373 (s), 1301 (w), 1252 (w), 1169 (w), 1138 (w), 1098 (s), 1080 (m), 1071 (m), 1013 (m), 920 (w), 901 (m), 855 (m), 769 (s), 749 (w), 718 (w), 694 (w), 684 (w), 642 (w), 627 (w), 600 (m), 545 (w), 501 (w), 484 (w), 467 (w), 418 (w).

Preparation of $[Fe_2Dy_2(\mu_3\text{-}OH)_2(teaH)_2(O_2CC_6H_4\text{-}pSO_2Me)_4(NO_3)_2]$ ($2.8^{teaH\text{-}4pSO2Me}$)

$[Fe_3O(O_2CC_6H_4CH_3SO_2)_6(H_2O)_3](O_2CC_6H_4CH_3SO_2)$ (0.489 g, 0. 3 mmol), triethanolamine (0.4 g, 2.68 mmol) and $Dy(NO_3)_3\ 6H_2O$ (0.116 g, 0.25 mmol) in MeCN/ MeOH (20/ 20 mL) were reacted at 60°C for 35 min. Was filtered several times off. After 4 weeks, the orange-brwon solution (10 ml) was diluted with 40 ml MeCN. One week later pale-yellow needles were obtained. Yield was 4 %. The percipitate was identified as not reacted acid. This synthesis will be improved also in order to isolate the analouge with six carboxylates.

$[\mathrm{Fe_2Dy_2(\mu_3\text{-}OH)_2(Htea)_2(O_2CC_6H_4N_3)_6}]\cdot\mathrm{1.5H_2O\cdot 0.5CH_3CN}$ (2.8$^{\text{teaH-}6\text{pN3}}$)

$[\mathrm{Fe_3O(O_2CC_6H_4\text{-}N_3)_6(H_2O)_3}](\mathrm{O_2CC_6H_4\text{-}N_3})$ (0.3 g, mmol), triethanolamine (0.31 g, mmol) and $\mathrm{Dy(NO_3)_3\cdot 6H_2O}$ (0.116 g, 0.25 mmol) were dissolved in MeCN (50 mL) and stirred for 1h and 25 min. at r.t. (bottle closed). Pale-yellow solution was the result. Three days later well formed yellow crystals formed. Yield 11.7%. *Anal.* This compound is soluble in EtOH, THF and DMF (r.t.). *Anal.* Calc.: C, 37.21; H, 3.02; N, 16.12. Found: C, 37.41; H, 3.12; N, 15.60% .Selected IR data (cm^{-1}): 3357 (w), 3066 (w), 2941 (w), 2866 (w), 2843 (w), 2408 (w), 2250 (w), 2123 (s), 1685 (w), 1604 (s), 1591 (s), 1544 (s), 1502 (m), 1459 (m), 1415 (s), 1374 (s), 1300 (m), 1286 (s), 1176 (m), 1146 (w), 1125 (w), 1015 (w), 1099 (s), 1078 (m), 970 (w), 922 (w), 901 (w), 856 (w), 779 (s), 750 (w), 720 (w), 688 (w), 600 (m), 563 (m), 487 (w), 432 (w), 417 (w).

$[\mathrm{Fe_2Dy_2(\mu_3\text{-}OH)(Htea)_2(O_2CC_6H_3(NO_2)_2]_6]}$ $\mathrm{1H_2O}$ (2.8$^{\text{teaH-3,5-diNO2}}$)

$[\mathrm{Fe_3O(O_2CC_6H_3(NO_2)_2)_6(H_2O)_3}](\mathrm{NO_3})$ (0.285 g), triethanolamine (0.298 g, 2 mmol) and $\mathrm{Dy(NO_3)_3\cdot 6H_2O}$ (0.116 g, 0.25 mmol) were dissolved in MeCN/ MeOH (30/10 mL) and reacted for 1h and 40 min. at r.t. and clear yellow solution was the result. It was left undisturbed in air. Small yellow pale-yellow blocks were obtained in 7.3 %. This compound is bad soluble in different solvents. *Anal.* Calc.: C, 31.60; H, 2.36; N, 9.84. Found: C, 31.60; H, 2.36; N, 9.80%. Selected IR data (cm^{-1}): 3462 (br), 30865 (w), 2971 (w), 2880 (w), 2854 (w), 1700 (w), 1620 (s), 1571 (m), 1584 (w), 1544 (s), 1465 (m), 1394 (m), 1346 (s), 1269 (w), 1195 (w), 1101 (w), 1091 (m), 1071 (m), 1026 (w), 920 (w), 904 (w), 795 (w), 788 (w), 730 (s), 724 (s), 713 (m), 598 (w), 568 (w), 492 (w), 444 (w), 426 (w).

$[\mathrm{Fe_2Dy_2(\mu_3\text{-}OH)_2(Htea)_2(O_2CC_6H_3(^{\mathit{t}}Bu)_2)_6}]\cdot\mathrm{2MeCN\cdot 2H_2O}$ (2.$^{\text{8teaH-3,5-di}t\text{Bu}}$)

$[\mathrm{Fe_3O(O_2CC6H_3(^{\mathit{t}}Bu)_2)_6(H_2O)_3}](\mathrm{NO_3})$ (0.43 g, 0.242 mmol), triethanolamine (0.3 g, 2 mmol) and $\mathrm{Dy(NO_3)_3\cdot 6H_2O}$ (0.116 g, 0.25 mmol) were dissolved in MeCN (50 mL). The yellow-orange solution was stirred at 80°C for 1h. After filtration, the solution was left undisturbed (sealed). Three weeks later, high amount of yellow microcrystalline material was onbtaind. The product was filtered off. The remained clear yellow solution gave small yellow crystals several weeks later from which the unit cell could be determined. The CHN analysis of both, the microcrystalline material and the crystals is the same. *Anal.* Calc.: C, 55.76; H, 7.24; N, 2.45. Found: C, 55.77; H, 7.15; N, 2.67% .Selected IR data (cm^{-1}): 3375 (br), 2964 (s), 2905 (m), 2867 (m), 1550 (s), 1479 (m), 1461 (m), 1440 (m), 1396 (s), 1378 (s), 1289 (m), 1248 (m), 1202 (w), 1163 (w), 1108 (m), 1040 (w), 923 (w), 898 (m), 818 (w), 792 (m), 729 (m), 705 (m), 624 (w), 550 (w), 523 (w), 509 (w), 474 (w), 435 (w).

$[Fe_2Dy_2(\mu_3\text{-}OH)_2(C_6H_{13}NO_3)_2(O_2CC_{14}H_9)_6]\cdot(CH_3CN)_2\cdot5(H_2O)$ ($2.8^{teaH\text{-}6(9\text{-}anthr)}$)

$[Fe_3O(O_2C_{15}H_9)_6(H_2O)_3](O_2C_{15}H_9)$ (green) (0.398 g, 0.222 mmol), triethanolamine (0.298 g, 2 mmol) and $Dy(NO_3)_3\cdot6H_2O$ (0.123 g, 0.267 mmol) were dissolved in MeCN/ MeOH (20/ 10 mL) and recated at 50°C for 15 min. After that refluxed till everything was soluble and reacted (solution became orange). Left undisturbed in air and after 1 day orange-crystals formed. Yield 11.3 %. *Anal.* Calc.: C, 56.04; H, 4.36; N, 2.57. Found: C, 56.21; H, 4.40; N, 2.47%. Selected IR data (cm^{-1}): 2963 and 2851 (br), 1495 (s), 1361 (w), 1341 (w), 1340 (w), 1280 (s), 1166(w), 1129 (w), 1086 (s), 1059 (s), 1011 (m), 1004 (s), 913 (s), 884 (m), 844 (s), 816 (m).

$\{Fe_2Dy_2\text{-}2naph\}$ ($2.8^{teaH\text{-}6(2\text{-}naphth)}$)

$[Fe_3O(O_2C_{11}H_7)_6(H_2O)_3](O_2C_{11}H_7)$ (0.324 g, 0.25 mmol), triethanolamine (0.298 g, 2 mmol) and $Dy(NO_3)_3\cdot6H_2O$ (0.119 g, 0.26mmol) were dissolved in MeCN/ MeOH (20/ 10 ml) and reacted at 50°C for 20 min. then refluxed for 5 min. Yellow crystals have been collected form the yellow-orange solution after 5 days. Yield was 12 %. This compound is soluble in THF. Selected IR data (cm^{-1}): 3478 (w), 3202 (br), 3061 (m!), 2873 (s), 2850 (s), 1830 (w), 1668 (s), 1629 (m), 1586 (s), 1601 (s), 1546 (vs), 1504 (s), 1466 (s), 1382 (vs, br!), 1255 (w), 1269 (w), 1240 (m), 1200 (m), 1164 (w), 1150 (w), 1106 and 1094 (s), 953 (w), 917 and 905 (m), 865 (w), 808 (m), 792 and 785 (vs), 637 (w), 597 (s), 536 (w), 498 and 472 (m), 419 (w).

$[Fe_2Dy_2(\mu_3\text{-}OH)(Htea)_2(O_2CC_3H_5)_6]\cdot2MeCN\cdot2H_2O$ ($2.8^{teaH\text{-}6cp}$)

A solution of $[Fe_3O(O_2CC_3H_5)_6(HO_2CC_3H_5)_3]Cl\cdot2H_2O$ (0.308 g, 0.301 mmol), triethanolamine (0.415 g, 2.785 mmol) and $Dy(OTf)_3$ (0.345 g, 0.57 mmol) in CH_3CN (25 mL) was refluxed for 30 min. The resulting brown solution was cooled down and closed for 1 week. After 1 week in air few colourless crystals has been formed (H_3tea^+ OTf^-). These were filtered off and washed with CH_3CN (10 mL) which was drooped in the mother solution. After 1 week later the solution turned orange and pale-yellow crystals appeared. Yield was 26%.

$[Fe_2Gd_2(\mu_3\text{-}OH)(Htea)_2(O_2CC_3H_5)_6]\cdot2MeCN\cdot2H_2O$ ($2.6^{teaH\text{-}6cp}$)

Anal. Calc.: C, 35.11; H, 4.90; N, 4.09%. Found: C, 35.00; H, 4.74; N, 4.00%. Selected IR data (cm^{-1}): 3653 (w), 3523, 3085 and 3012 (br), 2843 (m), 2256 (w), 1561 and 1545 (s), 1460 (m), 1409 and 1427 (s), 1309 (s), 1102(s), 1023 (w), 947 (m), 904 (m), 820 (w), 663 (w), 593 (w), 482 (w), 431 (w).

$[Fe_2Dy_2(\mu_3\text{-}OH)(Me\text{-}teaH)_2(O_2CPh)_6](HO_2CPh) \cdot 3MeCN$ ($2.8^{\text{Me-teaH, 6}p\text{H}}$)

$[Fe_3O(O_2CPh)_6(H_2O)_3](O_2CPh)$ (0.25 g, 0.242 mmol), Me-teaH$_3$ (0.326 g, 2 mmol) and $Ln(NO_3)_3$ $6H_2O$ or $Ln(Otf)_3$ {Ln= Dy, Gd or Y} (0.25 mmol) were dissolved in MeCN/ MeOH (25/ 10 mL) and reacted for 35 min. at 50°C. The orange-brown solution was left to cool own and closed for one week. After one week pale-yellow roads formed. Yield was over 66%. *Anal.* Calc.: C, 47.26; H, 4.45; N, 3.99%. Found: C, 47.80; H, 4.46; N, 3.70%. Selected IR data (cm^{-1}): 3361 (br), 3064 (w), 2970 (w), 2853 (br), 2502 (w), 2251 (w), 1687 (m), 1596 (s), 1549 (s), 1491 (w), 1450 (m), 1389 (s), 1315 (m), 1267 (m), 1175 (m), 1123 (m), 1090 (m), 1037 (w), 1024 (w), 897 (m), 864 (w), 790 (w), 718 (s), 687 (m), 674 (m), 588 (m), 521 (w), 452 (w), 431 (w).

$[Fe_2Dy_2(\mu_3\text{-}OH)_2(bheapH)_2(Me\text{-}teaH)_6](HO_2CC_6H_4{}^tBu)_2 \cdot 2MeCN\ 1H_2O$ ($2.8^{\text{Me-teaH, 6}pt\text{Bu}}$)

$[Fe_3O(O_2CC_6H_4{}^tBu)_6(H_2O)_3](O_2CC_6H_4{}^tBu)$ (0.342 g, 0.242 mmol), bheapH$_3$ (0.326 g, 2 mmol) and $Dy(NO_3)_3\cdot$ $6H_2O$ (0.116 g, 0.25 mmol) were dissolved in MeCN/ MeOH (30/ 10 mL) and reacted for 35 min. at 50°C. The precipitate was filtered off and the pale-yellow solution was left closed for 1 day. After 1 day pale-yellow crystals (roads) appeared. Yield was 12.7%. The solubility not checked. *Anal. Calc.*: C, 55.47; H,6.36; N, 2.42. Found: C, 55. 04; H, 6.33 ; N, 2.46 .Selected IR data (cm^{-1}): 3299 (br), 3071 (w), 2967 (s), 2905 and 2870 (w), 2500 (w), 1934 (w), 1679 (m), 1612 (w), 1591 (s), 1540 (s), 1460 (w), 1410 (w), 1386 (s), 1362 (w), 1297 (w), 1269 (m), 1190 (m), 1103 (m), 1016 (w), 860 (m), 788 (s), 713 (m), 586 (m), 586 (m), 545 (w), 474 (w), 418 (w).

$[Fe_2Dy_2(\mu_3\text{-}OH)(C_7H_{16}NO_3)_2(O_2CPh)_4(NO_3)_2]MeCN$ ($2.8^{\text{Me-teaH, 4}p\text{H}}$)

This compound was made in same way as $\mathbf{2.8}^{\text{teaH-4}p\text{H}}$ but using (0.55 g, 0.304 mmol) of Me-teaH$_3$ ligand. *Anal.* Calc.: C, 35.94; H, 3.60; N, 3.90. Found: C, 35.92; H, 3.69; N, 3.71%. Selected IR data (cm^{-1}): 3652 (s), 3235 (br), 2873 (m), 1598 (s), 1558 (s), 1538 (m), 1493 (m), 1467 (w), 1543 (m), 1442 (m), 1384 (s), 1367 (s), 1307 (w), 1092 (s), 1070 (s), 1024 (m), 922 (s), 902 (s), 720 (s), 688 (m), 671 (s), 636 (w), 601 (s), 430 (w), 407 (w).

Preparation of $[FeLn_2][Fe_2Ln_2]$ (Ln=Gd, Dy, Y)

(0.7 g, 1.01 mmol,) of alumatrane tetramer $C_{24}H_{48}Al_4N_4O_{12}$ and (1g, 1mmol) of $[Fe_3O(O_2CPh)_6(H_2O)_3]\cdot(O_2CPh)$ were dissolved in of CH_3CN/ THF (40/45 mL). While stirring at r.t. was adedd (0.691 g, 1.5 mmol) of $Dy(NO_3)_3$ $6H_2O$. The pale-orange solution leaved stirring at r.t. for 30 min and was filtered off. The solution was then leaved undisturbed in air. Pale-orange crystals were obtained after 1 day in 33 % yield.

$\{[FeGd_2(\mu\text{-}OH)_2(teaH_2)_2(O_2CPh)_3(HO_2CPh)(NO_3)_2]\}_{0.74}\{[Fe_2Gd_2(\mu_3\text{-}OH)_2(teaH)_2(O_2CPh)_4(NO_3)_2]\}_{0.26}\cdot$0.8 THF 1MeCN $1H_2O$ (2.17)

Anal. Calc.: C, 37.72; H, 4.21; N, 4.86%. Found: C, 37.50; H, 4.22; N, 4.88%.: Selected IR-data (cm-1): 3686 (w), 3414 (br), 2954 (w), 2880 (w), 1602 (s), 1563 (s), 1467 (m), 1404 (s), 1384 (s), 1350 (w), 1109 (m), 1070 (s), 1024 (m), 921 (m), 832 (w), 818 (w), 721 (s), 678 (w), 614 (m), 476 (m). Yield was 67%.

$\{[FeDy_2(\mu\text{-}OH)_2(teaH_2)_2(O_2CPh)_3(HO_2CPh)(NO_3)_2]\}_{0.82}$ $\{[Fe_2Dy_2(\mu_3\text{-}OH)_2(teaH)_2(O_2CPh)_4(NO_3)_2]\}_{0.18}\cdot$1 THF 1MeCN $1H_2O$ (2.18)

Anal. Calc. : C, 37.40; H, 4.35; N, 4.74%. Found: C, 37.30; H, 4.00; N, 4.45%. Selected IR-data (cm-1): 3687 (m), 2954 (br), 3068 (m), 2881 (s), 2738 (w), 2254 (w), 1973 (w), 1918 (w), 1825 (w), 1787 (w), 1602 (s), 1577 (s), 1455 (br), 1384 (s), 1176 (m), 1163 (m), 1110 (s), 1070 (s), 1024 (m), 922 (m), 832 (m), 818 (m), 722 (m), 680 (w), 614 (w), 477 (w). Yield was 57.3 %.

$\{[FeY_2(\mu\text{-}OH)_2(teaH_2)_2(O_2CPh)_3(HO_2CPh)(NO_3)_2]\}_{0.88}$ $\{[Fe_2Y_2(\mu_3\text{-}OH)_2(teaH)_2(O_2CPh)_4(NO_3)_2]\}_{0.12}\cdot$1.2 THF 0.8MeCN 0.5 H_2O (2.19)

Anal. Calc.: C, 42.48; H, 4.80; N, 5.12%. Found: C, 42.55; H, 5.30; N, 5.00%.: Selected IR-data (cm-1): 3688 (w), 3415 (br), 2955 (w), 2882(w), 1603 (s), 1564 (s), 1550 (s), 1469(m), 1404 (s), 1384 (s), 1352 (w), 1110 (m), 1071 (m), 1024 (w), 923 (w), 832 (w), 722 (s), 680 (m), 615 (w), 480 (w).

$[Dy_2(Htea)_2(O_2CPh)_4]\cdot$MeOH (2.20)

A solution of $[Dy(O_2CPh)_3(DMF)]$ (0.599 g, 1 mmol) and triethanolamine (0.3 g, 2 mmol) in MeOH (25 mL) was prepared. To the colorless solution was triethylamine (0.3 mL) added. The mixture was stirred at ambient temperature for 30 min. The cyrstalization was achieved by ether diffucion. Colourless crystals were obtained after six weeks. The yield was 3%. *Anal.* Calc. CHN ($1H_2O$): C, 42.82; H, 4.31; N, 2.49. Found. C, 43.23; H, 4.30; N, 2.17%.

$[Dy(tpma)(O_2CPh)(NO_3)_2]$ (2.21)

$[Fe_3O(O_2CPh)_6(H_2O)_3](O_2CPh)$ (0.25 g, 0.242 mmol), tpma (0.197 g,) and $Dy(NO_3)_3 \cdot 6H_2O$ (0.12 g,) were dissolved in MeCN/MeOH (20/10 mL) and the solution was refluxed for 20 min. The pale orange solution gave crystals after 1 day. They were not characterized by IR and CHN becaue of limited time and because no magnetic measurements were done for it. Note, this compound could not be obtained without using **2.sm1**.

$[Fe_2Ln_2(ampdH_3)_2(ampdH_2)_2(O_2CPh)_6]$ (2.22 and 2.23)

Solutions of $[Fe_3O(O_2CPh)_6(H_2O)_3]\cdot O_2CPh$ (0.25 g, 0.23 mmol) in MeCN (10 mL), $Ln(NO_3)_3 \cdot 6H_2O$ (0.25 mmol) and 2-amino-2-methyl-1,3-propandiol (0.21g, 2.00 mmol) in CH_3CN/CH_3OH (20 mL) were stirred at room temperature for 30 minutes. The yellow solution was then warmed at 60°C for 10 minutes and little white precipitate filtered off. After 2 days the yellow solution turned to orange and yellow block like crystals were collected in a yield of 69%.

$[Fe_2Gd_2]\cdot 3H_2O$: *Anal. Calc.*: C, 42.80; H, 4.88; N, 3.40. Found: C, 42. 79; H, 4.77 ; N, 3.81 .Selected IR data (cm^{-1}): 3339(s), 3258 (s), 2965 (m), 2930 (m), 1968 (w), 1914 (w), 1816 (w), 1600 (s), 1567 (s), 1537 (s), 1491 (m), 1447 (m), 1379 (s), 1174 (w), 1155(w), 1073(s), 1025(s), 1009(m), 971 (w), 841 (m), 719 (s), 622 (s), 568 (m), 534 (m), 460 (m), 412 (w).

$[Fe_2Y_2]\cdot 3H_2O$: *Anal. Calc.*: C, 46.07; H, 5.03; N, 3.58. Found: C, 45. 72; H, 5.18 ; N, 3.60 3410 (s), 3328 (s), 3289 (s), 2960 (m), 2928(m), 2871 (m), 2839(w), 1913(w), 1598 (s), 1568 (s), 1533 (s), 1491 (m), 1445 (m), 1396 (s), 1375 (s), 1174 (w), 1155 (w), 1142 (w), 1074 (S), 1026 (s), 1005 (w), 980 (w), 860 (w), 840 (w), 798 (w), 720 (s), 688 (m), 675 (m), 623 (m), 584 (w), 464 (m), 415 (w).

$[Fe_2Dy_2(tripod)_2(O_2CPh)_4(tripodH_3)_2]^{2+}[Fe_2Dy_2(tripod)_2(O_2CPh)_4(NO_3)_4]^{2-} \cdot 2MeCN \cdot 2Py$ (2.24)

Solutions of $[Fe_3O(O_2CPh)_6(H_2O)_3](O_2CPh)$ (0.125 g, 0.125 mmol) in MeCN (5 mL), of 1,1,1-tris(hydroxymethyl)-ethane (0.24 g, 2.0 mmol) and (0.16 g, 0.25 mmol) of $Dy(NO_3)_3$ $6H_2O$ in MeCN (5 mL). To this mixture were 10/ 3 ml (EtOH/ pyridine) added. This was stirred for 30 minutes at room temperature. After 3 weeks dark green precipitate and orange oil were obtained. These were dissolved in MeCN (10 mL) without stirring. After 1 day big yellow-orange crystals were obtained in 19 % yield. *Anal. Calc.:* C, 40.16; H, 3. 86; N, 3.64. Found: C, 42.70; H, 5.58; N, 2. 58 .Selected IR data (cm^{-1}): 3352 (br), 3068 (w), 2952 (w), 2929 (w), 2872 (w), 2692 (w), 1596 (s), 1556 (s), 1496 (s), 1385(s), 1300 (s), 1175 (m), 1128 (s), 1056 (m), 1025 (m), 914 (m), 815 (m), 719 (s), 676 (s), 607 (s), 579 (m), 460 (s).

$[Fe_2Dy_2(\mu_3\text{-}OH)_2(trop)_2(tropH)_2(deapdH)_2(NO_3)_4]$ (2.25)

To a solution of 3-(dimethylamino)-1,2-propandiol (0.294 g, 2 mmol) and tropic acid (0.166 g, 1 mmol) in MeCN (20 mL) was added solid $Fe(NO_3)_3\cdot 9H_2O$ (0.23 g, 0.569 mmol). To the resulting orange solution was then added -while stirring at r.t.- $Dy(NO_3)_3\cdot 6H_2O$ (0.2 g, 0.313 mmol) in MeOH (5mL). The color became lighter and the reaction mixture was reacted at 60°C for 1h . Large pale-yellow crystals were obtained after 1 week. Yield was 7.3 %. Selected IR data (cm^{-1}): 3386 (br), 1629 (w), 1589 (s), 1497 (s), 1385 (vs), 1297 (s), 1139 (w), 1088 (m), 1034 (m), 938 (w), 893 (w), 869 (w), 816 (w), 747 (m), 702 (m), 649 (w), 607 (w), 484 (w).

$[Fe^{III}_6Dy_2(\mu_3\text{-}O)_2(\mu_2\text{-}OH)_2(H_2O)_2(O_2CPh)_8(HL)_4(NO_3)_6]\cdot THF$ (2.26)

A solution of $Fe(NO_3)_3\cdot 9H_2O$ (0.404 g, 1 mmol) and benzoic acid (0.245 g, 2 mmol) in THF/MeCN (50/ 25 mL) was stirred for 10 min at room temperature, followed by slowly dropped 3-(diethyamino)-1,2-propandiol (0.588 g, 4 mmol) and $Ln(NO_3)_3\cdot 6H_2O$ (1 mmol). The red-brown solution continued stirring at room temperature for 1h. No precipitate was obtained. Well formed block-like and pale red-brown crystals collected after 1 week. A high Yield of 92.42 % (based on Fe) for was obtained. *Anal. Calc*. C, 38.95; H, 4.48; N, 4.94%. Found: C, 38.25; H, 4.79; N, 5.58%. Selected IR data (cm^{-1}): 3369 (br), 3065 (m), 2982 (w), 2932 (w), 2881 (w), 2361 (w), 2342 (w), 1596 (s), 1546 (s), 1491(s), 1406 (s), 1384 (s), 1315(s), 1288(s), 1101(w), 1073(w), 1032(m), 948(w), 816(w), 722(s), 686(w), 643(w), 601(w), 445(w).

Compounds belong to chapter 3

$[Fe_5Ln_3(\mu_3\text{-}OH)(teaH)_7(O_2CPh)_8](CF_3SO_3)\cdot nMeCN$ (3.1-3.3)

Method A (Tm, Yb and Lu)

To a solution of $[Fe_3O(O_2CPh)_6(H_2O)_3]\cdot O_2CPh$ (0.25 g, 0.23 mmol) and triethanolamine ($teaH_3$) (0.298 g, 2.00 mmol) in CH_3CN (10 mL) was given as solid $Ln(OTf)_3$ (0.25 mmol).

The resulting orange solution was stirred 50 minutes at ambient temperature. The reaction mixture was then warmed for 5 min. at 50°. The clear yellow-orange solution was left undisturbed in air. Four, five and seven days later well formed pale-yellow crystals of **3.1, 3.2,** and **3.3** were collected in (77, 69, 61%), respectively. These compounds are very good soluble in MeOH.

Method B (example Yb)

To a solution of $[Fe_3O(O_2CPh)_6(H_2O)_3]\cdot O_2CPh$ (0.582g, 0.536 mmol) and $[Yb(H_3tea)_2(OTf)_3]\cdot 3THF$ (1.17 g, 0.70 mmol) in CH_3CN (50 mL) was given while stirring at room temperature as solid Cs_2CO_3 (0.464 g, 1.423 mmol). Then continued stirring at room temperature for 70 min. The clear yellow-orange solution was left undisturbed in air. After 1 week very good quality of **3.2** in high yield (82.3 %) were collected.

$[Fe_5Tm_3]$, 3.1 ·1.5 MeCN *Anal.* Calc. C, 40.91; H, 4.68; N, 3.54%. Found: C, 41.58; H, 4.58; N, 3.58%. IR data (cm^{-1}): 3342 (s, br), 3142 (s), 2892 (w), 2722 (w), 2617 (m), 2430 (m), 2361 (m), 1800-2100 (w, benzol finger), 1729 (s), 1598 (s), 1536 (s), 1468 and 1380 (double s, br), 1327 (s), 1304 (m), 1255 (m), 1166 (s), 1102. (s), 997 (s), 973 (s), (s), 899 (m), 840 (s), 714 (s), 689 (w), 670 (m), 639 (s), 562 (s), 460 (w), 424 (m).

$[Fe_5Yb_3]$, 3.2 ·1MeCN·3H_2O *Anal.* Calc. C, 39.60; H, 4.60; N, 3.66%. Found: C, 39.67; H, 4.82; N, 3.52%. IR data (cm^{-1}): 3356 (s, br), 3151 (s), 3062 (w), 2970 (w), 2932 (w), 2878 (m, br), 2349 (m), 2305 (m), 1800-2100 (w, benzol finger), 1713 (w), 1594 (s), 1540 (s), 1491 (m), 1407 (s, br), 1326 (w), 1266 (s, br), 1164 (s), 1091 (s), 1030 (m), 1003 (w), 916 (s), 899 (s), 830 (w), 718 (s), 689 (w), 670 (m), 639 (s), 562 (s), 460 (w), 424 (m).

$[Fe_5Lu_3]$, 3.3 ·1MeCN *Anal.* Calc. C, 40.28; H, 4.47; N, 3.72%. Found: C, 40.51; H, 4.70; N, 3.66%. IR data (cm^{-1}): 3434 (br), 3062 (w), 2874 (m, br), 2349 (m), 2305 (m), 1800-2100 (w, benzol finger), 1710 (w), 1630 (m), 1621 (w), 1594 (m), 1539 (s), 1491 (m), 1412 (s, br), 1257 (w), 1175 (w), 1090 (s), 1029 (m), 899 (m), 830 (w), 719 (s), 688 (w), 676 (m), 638 (m), 561 (m), 460 (w), 426 (m).

$[Fe_4Ln_2(OH)(OMe)_2(Me\text{-}teaH)_4(O_2CPh)_7]\cdot 3CH_3CN$ (Ln= Er, Tm, Yb and Lu) (3.4-3.7)

Same synthesis procedure as (numer from chapter 2) was used but for nitrate salts of Er, Tm, Yb and Lu.

[Fe_4Er_2], 3.4 ·1MeCN ·2H_2O *Anal.* Calc. C, 44.24; H, 4.63; N, 3.18. Found: C, 44.04; H, 4.62; N, 2.99. Selected IR data (cm^{-1}): 3065 (w), 2973 (w), 2861 (br), 2694 (w), 1721 (w), 1593 (s), 1538 (s), 1491 (vw), 1403 (s), 1305(w), 1175(m), 1133 (w), 1102 (s), 913 (m), 889(w) , 840 and 819 (w), 718 (s), 669 (m), 590 (w), 469 (m), 425 (w).

[Fe_4Tm_2], 3.5 1MeCN ·2H_2O *Anal.* Calc. C, 44.02; H, 4.97; N, 3.16. Found: C, 44.28; H, 4.92; N, 2.79. Selected IR data (cm^{-1}): 3578 (w), 3066 (w), 3027 (w), 2973 (w), 2861 (m), 2695 (w), 2547 (w), 1910 (w), 1622 (w), 1593 (s), 1538 (s), 1491 (m), 1403 (s), 1314 and 1204 (w), 1231 (w), 1173 (m), 1133 (m), 1103 (s), 1079 (m), 1068 (w), 913 (w), 889 (m), 840 and 819 (w), 717 (s), 669 (m), 689 (m), 591 (w), 467 (w), 429 (w).

[Fe_4Yb_2], 3.6·1MeCN ·2H_2O *Anal.* Calc. C, 44.02; H, 4.97; N, 3.16. Found: C, 44.28; H, 4.92; N, 2.79. Selected IR data (cm^{-1}): 3578 (w), 3066 (w), 3027 (w), 2973 (w), 2861 (m), 2695 (w), 2547 (w), 1910 (w), 1622 (w), 1593 (s), 1538 (s), 1491 (m), 1403 (s), 1314 and 1204 (w), 1231 (w), 1173 (m), 1133 (m), 1103 (s), 1079 (m), 1068 (w), 913 (w), 889 (m), 840 and 819 (w), 717 (s), 669 (m), 689 (m), 591 (w), 467 (w), 429 (w). (update)

[Fe_4Lu_2], 3.7 ·1MeCN ·2H_2O *Anal.* Calc. C, 43.78; H, 4.94; N, 3.15. Found: C, 43.67; H, 4.82; N, 2.99. IR data are very similar to **3.4** to **3.6**.

[$Fe_3Ln_2(\mu\text{-}OH)(Me\text{-}teaH)_4(O_2CPh)_6$]·nMeCN (3.8-3.11)

A solution of 1-[N,N-Bis(2-hydroxyethyl)amino]-2-propanol (Me-teaH_3) (0.326 g, 2 mmol) and [$Fe_3O(O_2CPh)_6(H_2O)_3$]·(O_2CPh) (0.25 g, 0.23 mmol) in CH_3CN (25 mL). To this solution was added while stirring at r.t. solid lanthanide (III) trifluoromethanesulfonate (0.274 mmol). The reaction mixture was stirred at r.t. for 40 min. after that for 15 min. at 50°C. The orange solution has been filtered warm off and leaved undisturbed in air. Pale-yellow plates were collected after 1 day in high yield.

[Fe_3Er_2], 3.8 ·2H_2O *Anal.* Calc. C, 43.64; H, 4.97; N, 2.90. Found: C, 43. 67; H, 4.97; N, 2.75. Selected IR data (cm^{-1}): 3420 (br), 3059 (w), 2854 (w), 1688 (w), 1596 (s), 1551 (s), 1491 (w), 1449 (w), 1390 (s), 1315 (br), 1269 (br), 1174 (w), 1125 (w), 1105 (m), 1039 (w), 1025 (w), 907 (w), 898 (w), 719 (s), 688 (w), 674 (w), 592 (w), 461 (w). Yield was 81%.

[Fe_3Tm_2], 3.9 ·1MeCN *Anal.* Calc. C, 43.57; H, 4.96; N, 2.90. Found: C, 43.77; H, 4.88; N, 2.55. Selected IR data (cm^{-1}): 3448 (br), 3064 (w), 2972 (w), 2855 (m), 1830 (w), 1595 (s), 1552 (s), 1490-1446 (w), 1396 (s), 1277 (w), 1174 (m), 1131 (m), 1106 (s), 1025 (w), 1011 (w), 908 (w), 890 (w), 765 (w), 718 (s), 669 (m), 594 (w), 543 (w), 472 (w). Yield was 83 %.

[Fe_3Yb_2], 3.10 ·2H_2O *Anal*. Calc. C, 43.40; H, 4.94; N, 2.90. Found: C, 43. 50; H, 5.02; N, 2.90. Selected IR data (cm^{-1}): 3449 (br), 3064 (w), 2973 (w), 2857 (m), 1830 (w), 1596 (s), 1552 (s), 1491-1447 (w), 1397 (s), 1278 (m), 1174 (m), 1133 (m), 1106 (s), 1026 (w), 1006 (w), 907 (w), 891 (w), 776 (w), 719 (s), 668 (m), 641 (w), 594 (w), 544 (w), 472 (w). Yield was 85 %.

[Fe_3Lu_2], 3.11 1MeCN *Anal.* Calc. C, 43.30; H, 4.93; N, 2.88. Found: C, 43.55; H, 5.02; N, 2.70. Selected IR data (cm^{-1}): 3446 (br.), 3064 (w), 2970 (w), 2928 (w), 2855 (w), 1569 (s), 1551 (s), 1396 and 1375 (ds), 1173 (w), 1106 (s), 890 (w), 719 (s), 669 (w), 596 (w), 474 (w). Yield was 91%.

[$Ln_2(tipH_2)_2(O_2CPh)_4$]·nMeCN (3.12-3.14)

(0.383 g, 2 mmol) of trisisopropanolamine, (0.216 g, 0.348 mmol) of $Yb(OTf)_3$ and (0.203 g, 0.2 mmol) of $[Fe_3O(O_2CPh)_6(H_2O)_3]\cdot(O_2CPh)$ in CH_3CN (20 mL). This mixture was stirred at r.t for 30 min. The clear orange solution was left undisturbed in air. Colorless crystals were obtained after 1 day.

[Tm_2], 3.12 ·1H_2O *Anal.* Calc. C, 45.25; H, 5.11; N, 2.29. Found: C, 45. 28; H, 5.15; N, 2.00. Selected IR data (cm^{-1}): Similar to **3.13**.

[Yb_2], 3.13 ·1/2 H_2O *Anal.* Calc. C, 45.28; H, 5.04; N, 2.20. Found: C, 45. 24; H, 5.04; N, 1.90. Selected IR data (cm^{-1}):3189 (br), 3064 (w), 2999 (w), 2967 (w), 2866 (w), 1599 (s), 1538 (s), 1494 (s), 1466 (m), 1318 (s), 1298 (m), 1174 (m), 1140 (m), 1047 (m), 980 (s), 939 (w), 868 (m), 673 (m), 638 (m), 533 (w), 404 (m), 424 (w).

[Lu_2], 3.14 ·1H_2O *Anal.* Calc. C, 44.81; H, 5.06; N, 2.27. Found: C, 45. 23; H, 4.93; N, 1.82. Selected IR data (cm^{-1}): Similar to **3.13**.

[$Fe_{16}Ln_4(tea)_8(teaH)_{12}(OAc)_8$]($NO_3$)$_4$·16$H_2O$·nMeCN (3.15-3.20)

A solution of $Dy(NO_3)_3\cdot 6H_2O$ (0.116 g, 0.25 mmol) in MeCN (5 mL) was added to $[Fe^{III}{}_3O(O_2CCH_3)_6(H_2O)_3]Cl\cdot 6H_2O$ (0.2 g, 0.272 mmol) and $teaH_3$ (0.3 g, 2.00 mmol) in MeCN (25 ml). The mixture was stirred at ambient temperature for 1 hour until a yellow solution was obtained which was filtered. The solution slowly turns yellow-orange and large yellow block-like crystals were obtained after up 1 week.

Note that the reaction should not be heated either oily material stick on the crystal-surface and in some cases the product cannot be isolated.

Note that all the compounds, on exposure to air, show a variable replacement of the lattice MeCN by water. $Fe_{16}Ln_4$ compounds are very good water soluble. The other compounds were synthesized in a similar manner using the corresponding lanthanide nitrate and were obtained in follow yields. (Sm 62% , Eu 39%, Gd 26% Tb 26%, Dy 26%, Ho 19%).

[$Fe_{16}Sm_4$], 3.15 ·$16H_2O$·11MeCN *Anal.* Calc. for $C_{138}H_{303}Sm_4Fe_{16}N_{25}O_{100}$ (corresponding to 1 MeCN and 12 H_2O of solvation): C 30.38, H 5.60, N 6.41%; found: C 30.38, H 6.12, N 6.47%. Selected IR data (cm^{-1}): 3414(br), 2874(w), 1739(w), 1635(s), 1550(s), 1384(s), 1256(w), 1163(w), 1072(vs), 903(m), 750(w), 600(w), 559(w), 461(w).

[$Fe_{16}Eu_4$], 3.16 ·$16H_2O$·11MeCN *Anal.* Calc. for $C_{144}H_{336}Eu_4Fe_{16}N_{28}O_{112}$ (corresponding to 4 MeCN and 24 H_2O of solvation): C 30.06, H 5.89, N 6.82%; found: C 30.05, H 5.69, N 7.06%. Selected IR data (cm^{-1}): 3434 (br), 2873 (m), 1634 (s), 1549 (s), 1384 (s), 1256 (m), 1072 (s), 903 (s), 749 (w), 661 (m), 585 (w), 460 (m).

[$Fe_{16}Gd_4$], 3.17 ·$16H_2O$·11MeCN *Anal.* Calc. for $C_{146}H_{337}Gd_4Fe_{16}N_{29}O_{111}$ (corresponding to 5 MeCN and 23 H_2O of solvation): C 30.24, H 5.83, N 6.83; found: C 30.16, H 6.03, N 6.90%. Selected IR data (cm^{-1}): 3413 (br), 2871 (m), 1616 (m), 1549 (s), 1384 (s), 1071 (s), 902 (s), 750 (m), 659 (m), 601 (s), 461(m).

[$Fe_{16}Tb_4$], 3.18 ·$16H_2O$·10MeCN *Anal.* Calc. for $C_{144}H_{336}Tb_4Fe_{16}N_{28}O_{112}$ (corresponding to 2 MeCN and 21 H_2O of solvation): C 29.79, H 5.78, N 6.45 %; found: C 29.83, H 5.65, N 6.43 %. Selected IR data (cm^{-1}): 3435 (br), 2872 (m), 1634 (s), 1549 (s), 1384 (s), 1255 (m), 1072 (s), 904 (s), 828 (w), 661 (m), 585 (w), 460 (m).

[$Fe_{16}Dy_4$], 3.19 ·$16H_2O$·10MeCN *Anal.* Calc. for $C_{136}H_{316}Dy_4Fe_{16}N_{24}O_{108}$ (corresponds to replacement of all lattice MeCN by 4 H_2O): C 29.38, H 5.73, N 6.05%; found: C 29.40, H 6.06, N 6.04%. Selected IR data (cm^{-1}): 3385 (br), 2860 (m), 2250 (m), 1595 (s), 1543 (s), 1383 (s), 1095 (s), 904 (s), 718 (s), 674 (s), 594 (s), 458 (m).

[$Fe_{16}Ho_4$], 3.20 ·$16H_2O$·10MeCN *Anal.* Calc. for $C_{144}H_{336}Ho_4Fe_{16}N_{28}O_{112}$ (corresponding to 5 MeCN and 24 H_2O of solvation): C 29.99, H 5.84, N 6.95 %; found: C 30.00, H 6.77, N 6.88 %. Selected IR data (cm^{-1}): 3435(br), 2872(w), 1738(w), 1634(m), 1549(s), 1385(s), 1255(w), 1072(vs), 904(m), 751(w), 661(w), 599(w), 558(w), 460(w).

[$Fe_{18}Dy_6(\mu\text{-}OH)_6(ampdH)_{12}(ampd)_{12}(O_2CPh)_{24}](NO_3)_6$· ~36 MeCN (3.21)

A solution of $Dy(NO_3)_3{\cdot}6H_2O$ (0.161 g, 0.35 mmol) and 2-amino-2-methyl-1,3-propandiol ($ampdH_4$) (0.210 g, 2.00 mmol) in MeCN (40 mL) was added to

$[Fe^{III}_3O(O_2CPh)_6(H_2O)_3](O_2CPh)·6H_2O$ (0.25 g, 0.242 mmol) in MeCN (5 ml). The mixture (closed) was stirred at ambient temperature for 1 hour until a yellow solution was obtained which was filtered. The solution slowly turns yellow-orange and high quantity of microcrystalline yellow product was collected (still unkown). From the remaining clear yellow solution (several weeks later) one large yellow block crystals of **3.21** was obtained. *Anal. Calc.*: C, 41.82; H,5.13; N, 3.22. Found: C, 42. 05; H, 4.80 ; N, 3.53 .Selected IR data of the mixture (cm^{-1}): Selected IR data: 3336 (s), 3278 (br), 2930 (m), 2962 (w), 2871 (m), 2837 (w), 2254 (w), 1967 (w), 1913 (w), 1599 (s), 1567 (m), 1491 (m), 1447 (m), 1394 (s), 1375 (s), 1305 (w), 1141 (w), 1173(w), 1155(w), 1073 (s), 1025 (s) , 1008(m), 977 (w), 841 (m), 798 (m), 719(s), 687(m), 675 (m), 624(s), 582 (m), 536 (m), 462(m), 414(w).

$[Fe_4Dy_4(teaH)_8(hmap)_4(H_2O)](NO_3)_4·4MeCN·H_2O$ (3.22)

A solution of triethanolamine (0.298 g, 2.00 mmol) and $Dy(NO_3)_3·6H_2O$ (0.228 g, 0.5 mmol) in MeCN (10 mL) was added drop wise over 5 minutes to red solution of $Fe(NO_3)_3·9H_2O$ (0.202 g, 0.5 mmol) and 2`-hydroxy-4`-methoxy-acetophenone (0.333 g, 2.00 mmol) in MeCN/ MeOH (15/10 mL). To the dark orange mixture was then added triethylamine (0.3 mL). The solution mixture became lighter and was heated strong till boiling, cooled down and left undisturbed in air. Orange crystals were obtained after 2 days in 13% yield. *Anal.* Calc. for zero solvents in lattice (%). C, 33.88; H, 4.81; N, 5.64. Found: C, 33.79; H, 4.893; N, 5.54. IR data (cm^{-1}) 2969 (w), 2840 (m), 1595 (v, s), 1579 (v, s), 1517 (s), 1460 (w), 1369 (w), 1330(s), 1274 (m), 1205(v, s), 1155(m), 1135(m), 1111(m), 1095(m), 1064(w), 1022(s), 880(m), 744 (m), 712 (m).

$[Ln_6(Me\text{-}teaH)_6(NO_3)_6]·6MeOH$ (3.24-3.26)

A solution of (0.228 g, 0.5 mmol) $Ln(NO_3)_3·6H_2O$ and (0.326 g, 2 mmol) 1-[N,N-Bis(2-hydroxyethyl)amino]-2-propanol ($Me\text{-}teaH_3$) in MeCN/ MeOH (18/14 mL) was stirred at 60°C for 10 min. To the clear colorless solution was then added triethylamine (0.3 mL). Then reaction mixture was refluxed for further 20 min. The clear solution was left undisturbed in air. After 1 day, well formed colorless block-like crystals were collected.

$[Dy_6(Me\text{-}teaH)_6(NO_3)_6]·6H_2O$ (3.24) *Anal.* Calc. (%): C, 20.90; H, 4.17; N, 6.96; found: C, 20.96; H, 4.00; N, 6.91.Selected IR (cm^{-1}): 3371(br), 2970(m), 2934 (w), 2863(s), 1637(w), 1474(m), 1385 (s), 1288(m), 1166(w), 1090(s), 1011(m), 817(m), 646(w), 561(m), 453(m), 400(w). Yield was 77%.

[Tm_6(Me-teaH)$_6$(NO_3)$_6$], 3.25·6H_2O and **[Ho_6(Me-teaH)$_6$(NO_3)$_6$], 3.26· 6H_2O** were synthesised in the same way as **3.24**. CHN and IR data are very similar. Yield was 41%, 91%, respectively.

[Dy_6(apdeaH_2)$_6$(NO_3)$_6$]·2THF·1MeCN (3.27)

A solution of (0.46 g, 1mmol) $Dy(NO_3)_3·6H_2O$ and (0.336 g, 2 mmol) of 3-(n)-amniopropyldiethanolamine (apdeaH_4) in CH_3CN/ THF (40/10 mL) was stirred at r.t. for 10 min. To it was added triethylamine (0.2 mL). Later reaction mixture was heated at 80°C for 10 min. White precipitate was filtered off (identified as **3.26**). The clear colorless solution was left undisturbed in air. After 1 day, well formed colorless crystals were collected. Yield was 83%. *Anal*. Calc. C, 24.89; H, 4.86; N, 10.61; found: C, 25.00; H, 4.66; N, 10.57. IR (KBr, cm^{-1}): (3344-3285) (br, w), 2947 (w), 2914 (w), 2886 (w), 2852 (m), 2712 (w), 2491 (w), 2319 (w), 1768 (w), 1740 (w), 1600 (w), 1487 (vs), 1385 (s), 1367 (s), 1304 (s), 1288 (s), 1243 (w), 1125 (w), 1092 (s), 1057 (m), 1036 (m), 1010 (m), 911 (m), 928 (m), 886 (m), 820 (w), 742 and 734 (w), 583 (m) and 568 (w), 494 (w), 386 (m), 386 (m).

Compounds belong to chapter 4

[$Fe_{10}Ln_{10}$(Me-tea)$_{10}$(Me-teaH)$_{10}$(NO_3)$_{10}$]·20MeCN (4.1-4.12)

$Fe(NO_3)_3·9H_2O$ (0.202 g, 0.5 mmol), $Ln(NO_3)_3·6H_2O$ (0.5 mmol) and 1-[N,N-Bis(2-hydroxyethyl)amino]-2-propanol (Me-teaH_3) (0.326 g, 2.0 mmol) were dissolved in MeCN/ MeOH (25/10 ml) and stirred at 50°C for 10 min. Then triethylamine (0.3 ml) was added dropwise to the brown solution and the thereafter the colour became yellow-orange. The mixture was heated further until the onset of boiling. The clear solution was then left in air undisturbed without filtration. In the case of compounds **4.6-4.12** well-formed extremely pale crystals in 26% yield (after 1 day, colourless in solution to very pale yellow as solid) for **4.6**, 35% (after 1 day, very pale pink to very pale yellow changing) for **4.7**, 41% (after few hours, very pale rosa in solution to rosa-yellow as solid) for **4.8**, 49% (after 1h, extremely pale or colourless in solution to greenish as solid) for **4.9**, 57% (after 1 h, extremely pale in solution to pale yellow-greenish as solid) for **4.10**, 33% (after 1 day, very pale yellow in solution to pale yellow as solid) for **4.12**. However, compounds **4.1- 4.7** can be obtained only by diffusion of ether to the mother solution. Ether diffusion (10 mL) to the mother solution of **4.5** gave after 3 days 17% yield. Mother solution of **4.4** was separated in three parts, where to each one double amount of ether was diffused. From the three parts was 2-3% (colourless in solution and dried form) was collected after several weeks.

Mother solution of compound **4.3** was separated to five small fractions. To each fraction triple amount of ether was diffused. From all these fractions few crystals (colourless in solution and after loss of solvent molecules) were collected after more than three months. Mother solution of **4.1** was separated to more than ten fractions (less than 3.5 mL). To each fraction was ether diffused more than 10 mL each. The half of these fractions each gave one crystals) (in total ~ 5 colourless crystals). Compound **4.2** was obtained as yellow microcrystalline material (same colour as $Sm(NO_3)_3$ by adding ether (100 mL bath) to the mother solution. The Pr solution gave after ether bath a product which is not clean.

[$Fe_{10}Nd_{10}$], 4.1 34MeCN could be not characterized by CHN and IR because too little.

[$Fe_{10}Eu_{10}$], 4.2·21MeCN could not be characteruzed by CHN and IR.

[$Fe_{10}Gd_{10}$], 4.3 16MeCN·4H_2O *Anal.* Calc. C, 30.86 (30.53); H, 5.21 (5.22); N, 9.62 (9.42). IR (KBr): ν (cm^{-1}) =2963 (w), 2861 (m), 1611 (w), 1495 (s), 1388 (m), 1280 (s), 1166 (w), 1129 (w), 1086 (m), 1059 (s), 1004 (s), 913 (m), 884 (m), 844 (w), 816 (w), 744 (w), 587 (w), 494 (w), 419 (w).

[$Fe_{10}Tb_{10}$], 4.4· 5H_2O (similar to Nd with 34 MeCN in lattice (N_2-spray). *Anal.* Calc. C, 27.78; H, 4.66; N, 6.94. Found: C, 27.80; H, 4.60; N, 7.08%. Selected IR (KBr): ν (cm^{-1})= 3043 (br), 2966(m), 2857 (m), 1497(m), 1385(s), 1288(m), 1169(w), 1131(m), 1076(s), 1004(m), 816(w), 740(w), 588(w), 493(w), 418(w).

[$Fe_{10}Dy_{10}$], 4.5 8MeCN·12H_2O *Anal.* Calc. C, 28.55 (28.66); H, 5.19 (4.91); N, 8.11 (8.00). IR (KBr): ν (cm^{-1}) =3424 (br), 2966 (w), 2858 (m), 1612 (m), 1498 (s), 1385 (s), 1289 (m), 1168 (w), 1131 (w), 1088 (m), 1006 (m), 914 (w), 887 (w), 844 (w), 816 (w), 742 (w), 588 (w), 493 (w), 419 (w)**.**

[$Fe_{10}Ho_{10}$], 4.6 20 MeCN *Anal.* Calc. **S**elected IR data (cm^{-1}): 3399 (br), 2966 (m), 2856 (s), 1653 (w), 1507 (m), 1385 (s), 1289 (m), 1132 8 (w), 1088 (m), 1005 (m), 913 (w), 887 (w), 845 (w), 816 (w), 743 (w), 585 (w), 495 (w).

[$Fe_{10}Er_{10}$], 4.7·3.5 MeCN·16.5 H_2O *Anal*. Calc. C, H, N analysis (%): C, 27.13; H, 5.16; N, 7.21; found: C, 26.67; H, 4.70; N, 7.55. IR (KBr): 3386 (br), 2967 (s), 2857 (s), 2716 (w), 2525 (w), 1772 (w), 1654 (w), 1505 (vs), 1385 (s), 1289 (w), 1169(w), {1132 (w), 1088 (m), 1041 (m), 1008 (m)}, 915 (m), 915 (w), 887 (m), 816 (w), 744 (w), 585 (w), 495 (w), 422 (w).

[$Fe_{10}Tm_{10}$], 4.8 9 MeCN·11 H_2O *Anal.* Calc. C, H, N analysis (%): C, 28.54; H, 5.13; N, 8.21; found: C, 29.00; H, 5.03; N, 8.20. IR (KBr): 3400 (br), 2967 (w), 2859 (m), 1654 (w), 1507 (s), 1385 (vs), 1291 (m), 1169 (w), 1132 (w), 1088 (s), 1007 (m), 914 (w), 888 (w), 846 (w), 816 (w), 745 (w), 585 (w), 495 (w), 420 (w).

[$Fe_{10}Yb_{10}$], 4.9 7.5 MeCN·12.5 H_2O *Anal.* Calc. C, H, N analysis (%): C, 27.93; H, 4.80; N, 7.70; found: C, 27.97; H, 5.10; N, 7.89. IR (KBr): 3424 (br), 2966 (m), 2858 (m), 1612 (m), 1498 (s), 1385 (vs), 1289 (m), 1168 (w), 1131 (w), 1088 (m), 1006 (m), 914 (w), 887 (w), 844 (w), 816 (w), 742 (w), 588 (w), 493 (w), 419 (w).

[$Fe_{10}Lu_{10}$], 4.11·20 MeCN 1H_2O *Anal*. Calc. C, H, N analysis (%). C, 31.05; H, 4.80; N, 10.06; found: C, 31.00; H, 4.81; N, 9.99%. IR (KBr): 3401 (br), 2968 (m), 2858 (m), 1653 (m), 1499 (s), 1385 (vs), 1290 (m), 1168 (w), 1131 (w), 1088 (m), 1006 (m), 914 (w), 887 (w), 844 (w), 816 (w), 742 (w), 588 (w), 495 (w), 419 (w).

[$Fe_{10}Y_{10}$], 4.11 8MeCN·12 H_2O *Anal.* Calc. C, H, N analysis (%): C, 32.20; H, 5.85; N, 8.63; found: C, 32.22; H, 5.85; N, 9.13. IR (KBr): 3399 (br), 2967 (m), 2858 (s), 2123 (w), 1769 (w), 1653 (w), 1605 (w), 1612 (m), 1504 (s), 1385 (vs), 1289 (m), 1169 (w), 1132 (w), 1088 (m), 1007 (m), 915 (w), 887 (w), 845 (w), 816 (w), 744 (w), 587 (w), 494 (w), 418 (w).

[$Fe_6(tea)_6$]·6 MeOH, 4.13

To a solution of (0.242 g, 0.6 mmol) $Fe(NO_3)_3$· $9H_2O$ and (0.09 g, 0.6 mmol) of $teaH_3$ in $MeOH/Et_2O$ (15/ 5 mL) was added triethylamine (0.4 mL). The orange solution was then stirred at ambient temperature for 5 min. The clear slution was left closed and undisturbed. After 3 weeks large yellow-green crystals were obtained in 27% yield. Please note that this is a modified version of the synthesis known in the literature mentioned in chapter 4. The CHN and IR data are the same as in the literature.

[Fe_4Yb_2(Me-tea)$_4$(Me-teaH)$_2$(TOs)$_2$], 4.17

Similar synthesis as $Fe_{10}Yb_{10}$ but replacing $Fe(NO_3)_3$·$9H_2O$ by $Fe(OTs)_3$ ·$6H_2O$ (0.339g, 0.5 mmol) and $Yb(NO_3)_3$ ·$6H_2O$ by $Yb(OTs)_3$. $6H_2O$ (0.397 g, 0.5 mmol). Few colorless crystals (in solution and a solid) were obtained after 1 day. OTs= tosylate= $SO_3C_6H_4CH_3$. The yield of this compound was too little.

[Mn_4Dy_3], 4.18

A solution of $Mn(NO_3)_2\cdot 4H_2O$ (0.115, 0.458 mmol), Me-teaH_3 (0.326g, 2.00 mmol) $Dy(NO_3)_3\cdot 6H_2O$ (0.228 g, 0.5 mmol) in MeCN/MeOH (25/ 10 mL). After heating at 50°C for 10 min., it was added to the solution (0.3 mL) tea, from which the solution became brown. The solution was then refluxed for few min. and filtered. The filtrate is green. After 7 weeks, green crystals of 4.18 were collected in 11% yield. Note that, the use of 0.5 or 1 mmol of $Mn(NO_3)_2\cdot 4H_2O$ yields the same product but in higher yield. The crystallization time in this case is even longer and ether diffusion is needed. CHN and IR were not done because of limited time.

[Dy_4(Me-teaH)$_2$(Me-teaH_2)$_2$(NO_3)$_6$]·MeCN, 4.19

Similar synthesis as $Fe_{10}Dy_{10}$ **4.6** but replacing $Fe(NO_3)_3\cdot 9H_2O$ with $In(NO_3)_3\cdot xH_2O$ (0.15 g, 0.5 mmol). To the the colorless mother solution was ether diffused (triple amount) and was left sealed undisturbed. Six weeks later colorless block like crystals. The yield of this compound was too little for further characterization. CHN and IR were not done because of limited time.

Chapter 7

Literature Sources

[1] a) A. Powell, *Angew. Chem. Int. Ed.* **2011**, 50(4), 800; b) http://ak-powell.chemie.uni-karlsruhe.de/index.php/research.html.

[2] H. Kopp, Geschichte der Chemie, Bd. I, Braunschweig, **1843**.

[3] L. H. Gade, Koordinationschemie, Wiley-VCH, **1998**.

[4] a) J. Huheey, E. Keiter, R. Reiter, Anorganische Chemie, 3. Auflage, de Gruyter, Berlin **2003**; b) E. Riedel, C. Janiak, T. M. Klöptke, H.-J. Meyer, Moderne Anorganische Chemie, 2. Auflage, de Gruyter, Berlin, **2003**.

[5] J.-M. Lehn, Supramolecular Chemistry-Concepts and Perspectives, VCH, Weinheim, **1995**.

[6] a) K. N. Power, T. L. Henningar, M. J. Zaworotko, *Chem. Commun*. **1998**, 595; b) G. R. Desiraju, *Acc. Chem. Res.* **1996**, *29*, 441; c) S. S. Kuduva, D. C. Craig, A. Nangia, G. R. Desiraju, *J. Am. Chem. Soc.* **1999**, *121*, 1936.

[7] Y.-B. Dong, M. D. Smith, R. C. Layland, H.-C. Loye, *Inorg. Chem*. **1999**, *38*, 5027.

[8] I. Vnamuno, J. M. Guttiérez-Zorilla, A. Luque, P. Román, L. Lezamq, R. Calvo, T. Rojo, *Inorg. Chem.* **1988**, *37*, 6452.

[9] a) P. M. Harrison, P. Arosio, *Biochem. Biophys. Acta.* **1996**, *3*, 161; b) S. C. Andrews, P. Arriso, W. Bottke, J. F. Briat, M. Darl, P. M. Harrison, J. P. Laulhere, S. Levi, S. Labreaux, S. J. Yewdall, *J. Inorg. Biochem.* **1992**, *47*, 161.

[10] C. J. Pederson, *J. Am. Chem. Soc.* **1967**, *89*, 7017.

[11] a) C. J. Pederson, Nobel-Vortrag, *Angew. Chem.* **1988**, *100*, 1051; *Angew. Chem. Int. Ed. Engl.* **1988**, *27*, 1021; b) D. J. Cram, Nobel-Vortrag, *Angew. Chem.* **1988**, *100*, 1041; **Angew. Chem. Int. Ed.** *1988*, *27*, 1009; c) J.-M. Lehn, Nobel-Vortrag, *Angew. Chem.* **1988**, *100*, 91; *Angew. Chem. Int. Ed.* **1988**, *27*, 89.

[12] a) A. Kloss, Geschichte des Magnetismus, Ofenbach, vde-Verlag, Berlin, **1994**; b) G. L. Verschuur, Hidden attraction, The Mustery and History of Magnetsim. Oxford university Press, Oxford, **1993**; c) A. H. Murrisch, In the physical and principles of Magnetism, Jhon Wiley and Sons, New York **1980**; d) R. L. Carlin, Magnetochemistry, Springer Verlag, Berlin, **1996**; e) J. B. Goodenough, Magnetsim and the chemical bond, Wiley-Interscience, New York, **1963**.

[13] a) W. Plass, Design magnetischer Materialien: Chemie der Magnete, Chemie in unserer Zeit, 32. Jahrg. **1998**, 6; Wiley-VCH Verlag GmbH, 69469, **1998**; b) H. A. Lowenstam, S. Weiner, On Biomineralization **1989**, Oxford University Express. ISBN 0195049772.

[14] For example: a) M. Soler, S. K. Charda, D. Ruiz, E. R. Davidson, D. N. Hendrickson, G. Christou, *Chem. Commun.* **2000**, 2417-2418; b) C. Boskovic, E. K. Brechin, W. E. Streib, K. Folting, J. C. Bollinger, D. N. Hendrickson, G. Christou, *J. Am. Chem. Soc.* **2002**, *124*, 3725-3736; c) H. L. Tsai, C.-I. Yang, T-Y. Jwo, C.-S. Wur, G.-H. Lee, Y. Wang, *Chem. Commun.* **2001**, *4*, 511-514; d) M. Soler, P. Artus, K. Folting, J. C. Huffman, D. N. Hendrickson, G. Christou, *Inorg. Chem.* **2001**, *40*, 4902-4912; e) D. W. Boukhanov, V. V. Dobrovitski, P. Kögerler, M. Al-Saqer, M. I. Katsnelson, A. I. Lichtenstein, B. N. Harmon, Inorg. Chem. 2010, DOI: 10.1021/ic101229p; and others therein.

[15] T. Lis, *Acta Crystallogr., Sect B: Struct. Crystallogr. Cryst. Chem*. **1980**, *36*, 2042.

[16] E. Kampert, F. F. B. J. Janssen, D. W. Boukhanov, J. C. Russcher, J. M. M. Smits, R. de Gelder, B. de Bruin, P. C. M. Christianen, U. Zeitler, M. I. Katsnelson, J. C. Maan, A. E. Rowan, *Inorg. Chem.* **2009**, *48*, 11903-11908; and others therein.

[17] a) C. J. Millios, R. Inglis, A. Vinslava, R. Bagai, W. Wernsdorfer, S. Parsons, S. Perlepes, G. Christou, E. K. Brechin, *J. Am. Chem. Soc.* **2007**, *129*, 12505-12511; and others therien; b) A.-R. Tomsa, J. Lillio, Y. Li, L. Chamoreau, K. Boubekeur, F. Farias, M. A. Novak, E. Cremades, E. Ruiz, A. Prast, M. Verdaguer, P. Gouzerh, *Chem. Commun*. **2009**, *46*, 5106-5108; and others therein.

[18] a) N. T. Madhu, J.-K. Tang, I. J. Hewitt, R. Clérac, W. Wernsdorfer, J. van Slageren, C. E. Anson, A. K. Powell, *Polyhedron* **2005**, *24*, 2864-2869; and others therein; b) Y.-Y. Zhu, X. Guo, C. Cui, B.-W. Wang, Z.-M. Wang, S. Gao, *Chem. Commun***. 2011**, *47*, 8049-8051.

[19] J. D. Rinehart, J. R. Long, *Chem. Sci.* **2011**, DOI: 10.1039/c1sc00513h.

[20] a) M. Murugesu, A. Mishra, W. Wernsdorfer, K. A. Abboud, G. Christou, *Polyhedron* **2006**, *25*, 613-625; b) V. Mereacre, A. Baniodeh, C. E. Anson, A. K. Powell, *J. Am. Chem. Soc.* **2011**, *133(39)*, 15335-15337.

[21] a) J. D. Jackson, Klassische Elektrodynamik, **2006**, 4. Auflage, De Gruyter **2006** ISBN 978-3110189 704; b) C. D. Cullity, Introduction to magnetic materials, **2008**, 2nd ed. New York, Wiley-IEEE, ISBN 0471477419; c) H. Lueken, Magentochemie, Teubner Studienbücher, **1999**; d) J. H. Van Vleck, The Theory of Electric and Magnetic Susceptibilities, Oxford University Press, Oxford 1932; e) P. W. Atkins, R. S. Friedmann, Molecular Quantum Mechanics, 3rd Oxford University Press, Oxford 1997.

[22] Cohen-Tannoudji, Claude; Diu, Bernard; Laloë, Franck **2006**. Quantum Mechanics (2 volume set ed.). John Wiley & Sons. ISBN 978-0471569527.

[23] O. Kahn, Molecular Magnetism, Wiley VCH **1993**, ISBN 0471188387.

[24] M. I. Donahue, D. G. Porter, *Transaction on Magnetics* **2002**, *38 (5)*, 2468–2470.

[25] W. H. Meiklejohn, C. P. Bean, *Phys. Rev. B.***1957**, *105 (3)*, 904–913.

[26] D. Gatteschi, R. Sessoli, *Angew. Chem.* **2003**, *115* (3), 278-309.

[27] a) J. Long, P. Yang, In Chemistry of Nanostructured Materials, **2003**, World Scientific Publishing, Hong Kong; b) L. Thomas, F. Lionti, R. Ballou, D. Gatteschi, R. Sessoli, B. Barbara, *Nature* **1996**, *383*, 145-147; c) J. R. Friedman, M. P. Sarachick, J. Tejada, J. Maciejewski, R. Ziolo, J. *Appl. Phys.* **1996**, *79*, 6031-6033; d) J. R. Friedman, M. P. Sarachick, J. Tejada, R. Ziolo, *Phys. Rev. Lett.* **1996**, *76*, 3830-3833.

[28] a) B. Seeber, T. Fredrich, SQUID- Superconducting Quantum Interference Device, **2009**, http://www.physik.uni-freiburg.de/~holyg/fp/squid.pdf; b) C. M Thiele, *Angew. Chem.. Int. Ed.* **2007**, *46*, 4820-4824.

[29] a) J. A. Mydosh, *J. Magn. Magn. Mater.* **1996**, *157/158*, 606; b) C. A. M. Mulder, A. J. Van Duyneveldt, J. A. Mydosh, *Phys. Rev. B.* **1981**, *32* , 1384; c) T. Jonsson, K. Jonason, P. Jönsson, P. Nordblad, *Phys. Rev. B.* **1999**, *59*, 8770; d) R. Singh, et. al., *Phys. Rev. B.* **1997**, *55*, 1216.

[30] a) R. E. Winpenny, Single-Molecule Magnets and related phenomena, Springer, Berling **2006**; b) G. Christou, D. Gatteschi, D. N. Hendrickson, R. Sessoli, MRS Bulltein, **2000**, 25(11), 66-71; c) W. Wernsdorfer, N. Alaiga-Alcalde, D. N. Hendrickson, G. Christou, *Nature* **2002**, *416*, 406-409.

[31] a) D. Gatteschi, R. Sessoli, A. Cornia, *Chem. Commun.* **2000**, 725-732; b) S. L. Heath, A. K. Powell, *Angew. Chem. Int. Ed.* **1992**, *31*, 91; c) A. K. Powell, S. L. Heath, D. Gatteschi, L. Pardi, R. Sessoli, G. Spina, F. Del Giallo, F. Pieralli, *J. Am. Chem. Soc.* **1995**, *117*, 249; d) J. C. Goodwin, R. Sessoli, D. Gatteschi, W. Wernsdorfer, A. K. Powell, S. L. Heath, *J. Chem. Soc. Dalton Trans.* **2000**, 1835-1840; e) E. M. Rumberger, G. Christou, D. N. Hendrickson, *Polyhedron* **2003**, *22*, 1865-1870; f) A. M. Ayuk, V. Mereacre, Y. Lan, W. Wernsdorfer, R. Clérac, C. E. Anson, A. K. Powell, *Inorg. Chem*. **2010**, *49(1)*, 1-3; g) W. Schmitt, J. P. Hill, M. P. Juanico, A. Caneschi, F. Constantino, C. E. Anson, A. K. Powell, *Angew. Chem. Int. Ed.* **2005**, *117(27)*, 4173; h) M. Murugesu, R. Clérac, W. Wernsdorfer, C. E. Anson, A. K. Powell, *Angew. Chem. Int. Ed.* **2005**, *117*, 2-7; l) D. Gatteschi, M. Fittipaldi, C. Sangregori, L. Sorace, *Angew. Chem. Int. Ed*. **2012,** *51*, 2-11.

[32] G. Christou, *Polyhedron* **2005**, *24*, 2065-2075.

[33] D. E. Freedmann, W. Hill Harman, T. David Harris, G. J. Long, C. J. Chang, J. R. Long, *J. Am. Chem. Soc.* **2010**, *132*, 1224-1225.

[34] C. Vilalta, T. A. O'Brien, E. K. Brechin, M. Pink, E. R. Davidson, G. Christou, *Inorg. Chem.* **2004**, *43*, 5505-5521.

[35] a) L. Sorace, C. Benelli, D. Gatteschi, *Chem. Soc. Rev.* **2011**, DOI: 10.1039/c0s00185f; b) N. Ishikawa, M. Sugita, T. Ishikawa, S. Koshihara, Y. Kaizu, *J. Am. Chem. Soc*. **2003**, *125*, 8694 – 8695; c) J. K. Tang, I. Hewitt, N. T. Madhu, G. Chastanet, W. Wernsdorfer, C. E. Anson, C. Benelli, R. Sessoli, A. K. Powell, *Angew. Chem.* **2006**, *118*, 1761 – 1765; *Angew. Chem. Int. Ed.* **2006**, 45, 1729 – 1733; d) J. Luzon, K. Bernot, I. J. Hewitt, C. E. Anson, A. K. Powell, R. Sessoli, *Phys. Rev. Lett.* **2008**, *100*, 247205; e) I. J. Hewitt, J. Tang, N. T. Madhu, C. E. Anson, Y. Lan, J. Luzon, M. Etienne, R. Sessoli, A. K. Powell, *Angew. Chem.* **2010**, *122*, 6496 – 6500; *Angew. Chem. Int. Ed.* **2010**, *49*, 6352 – 6356; f) J. D. Rinehart, M. Fang,W. J. Evans, J. R. Long, *Nature Chem.* **2011**, DOI: 10.1038/nchem.1063; g) M. A. AlDamen, J. M. Clemente-Juan, E. Coronado, C. Mart_- Gastaldo, A. Gaita-Ari_o, *J. Am. Chem. Soc.* **2008**, *130*, 8874 – 8875; h) Y.-N. Guo, G.-F. Xu, Y. Guo, J. Tang, *Dalton Trans.* **2011**, *40*, 9953; l) R. J. Blagg, C. A. Muruyn, E. J. L. McIness, F. Tuna, R. E. P. Winpenny, *Angew. Chem. Int. Ed*. **2011**, *50*, 1-5.

[36] a) R. Sessoli, A. K. Powell, *Coord. Chem. Rev*. **2009**, *253*, 2328-2341; b) Ako, A. M., V. Mereacre, R. Clérac, I. J. Hewitt, Y.-H. Lan, C. E. Anson, A. K. Powell, *Dalton. Trans.* **2007**, 5245; c) G. Abbas, Y. Lan, Y., V. Mereacre, W. Wernsdorfer, R. Clérac, G. Buth, M. T. Sougrati, F. Grandjean, G. J. Long, C. E. Anson, A. K. Powell, *Inorg. Chem*. **2009**, *48,* 9345; d) M. N. Akhtar, V. Mereacre, G. Novitchi, J-P. Tuchagues, C. E. Anson, A. K. Powell, *Chem. Eur. J.* **2009**, *15*, 7278; e) V. Mereacre,D. Prodius, C. Turta, S. Shova, G. Filoti, J. Bartolomé, R. Clérac, C. E. Anson, A. K. Powell, *Polyhedron* **2009**, *28*, 3017; f) A. Baniodeh, I. J. Hewitt, V. Mereacre, Y. Lan, G. Novitchi, C. E. Anson, A. K. Powell, *Dalton Trans.* **2011**, *40(16)*, 4080-4086; g) D. Schray, G. Abbas, Y. Lan, V. Mereacre, A. Sundt, J. Dreiser, O. Waldmann, G. E. Kostakis, C. E. Anson, A. K. Powell, *Angew. Chem. Int. Ed.* **2010**, *49*, 5185-5188; h) V. Mereacre, D. Prodius, Y. Lan, C. Turta, C. E. Anson, A. K. Powell, *Chem. Eur. J.* **2011**, *17*, 123-128.

[37] a) Y.-F. Zeng, G.-C. Xu, X. Hu, Z. Chen, X.-H. Bu, S. Gao, E. E. Sanudo, *Inorg. Chem.* **2010**, *49(21)*, 9734-9736; b) S. Nayak, O. Roubeau, S. J. Teat, L. M. Beaves, P. Gamez, J. Reedjik, *Inorg. Chem*. **2010**, *49(1)*, 216-221.

[38] Examples for 3d-systems; $\{Mn_{10}\}$a) M. Manoli, R. D. L. Johnstone, S. Parsons, M. Murrie, M. Affronte, M. Evangelisti, E. K. Brechin, *Angew. Chem. Int. Ed.* **2007**, *46*, 4456 – 4460; b) $\{Fe_{14}\}$ M. Evangelisti, A. Candini, A. Ghirri, M. Affronte, S. Piligkos, E. K. Brechin, E. J.L. McInnes, *Polyhedron*, **2005**, *24*, 2573–2578; c) for 3d/4f $\{Mn_4Gd_4\}$ G. Karotsis, M. Evangelisti, S. J. Dalgarno, E. K. Brechin, *Angew. Chem. Int. Ed.* **2009**, *48*, 9928 –9931; d)Y.-Z. Zheng, E. M. Pineda, M. Helliwell, R. E. P. Winpenny, *Chem.Eur. J.* **2012**, *18*, 4161-4165.; e) Co-Ln: Y.-Z. Zheng, M. Evangelisti, F. Tuna, and R. E. P. Winpenny, *J. Am. Chem. Soc.*, **2012**, *134* (2), 1057–1065; f) Y.-Z. Zheng, M. Evangelisti, R. E. P. Winpenny, *Chem. Sci.* **2011**, *2*, 99–102; g) Ni-Gd: J.-B. Peng, Q.-C. Zhang, X.-J. Kong, Y.-P. Ren, L.-S. Long, R.-B. Huang, L.-S. Zheng, Z. Zheng, *Angew. Chem. Int. Ed.* **2011**, *50*, 10649 –10652; h) Y.-Z. Zheng, M. Evangelisti, R. E. P. Winpenny, *Angew. Chem. Int. Ed.* **2011**, *50*, 3692 –3695; i) Cu-Dy: S. K. Langley, N. F. Chilton, B. Moubaraki, T. Hooper, E. K. Brechin, M. Evangelisti, K. S. Murray, *Chem. Sci.* **2011**, *2*. 1166; j) $\{Gd_7/Dy_7\}$: J. W. Sharples, Y.-Z. Zheng, F. T., E. J. L. McInnes, D. Collison, *Chem. Commun.* **2011**, *47*, 7650–7652; k) Gd-Ln: T. N. Hooper, J. Schnack, S. Piligkos, M. Evangelisti, E. K. Brechin, *Angew. Chem. Int. Ed.* **2012**, DOI: 10.1002/anie.201200072.

[39] a) M. Evangelisti, E. K. Brechin, *Dalton Trans*. **2010**, *39*, 4672-4676; and others reported therein; b) M. Manoli, A. Collins, S. Collins, S. Parsons, A. Candini, M. Evangelisti, E. K.

Brechin, *J. Am. Chem. Soc*. **2008**, *130*, 11129-11139; c) R. Sessoli, *Angew. Chem. Int. Ed.* **2012***, 51(1)*, 43-45.

[40] a) V. Pecharsky, K. A. Jr. Gschneider, *J. Magn. Magn. Mater*. **1999**, *200*, 44; b) B. F. Yu, Q. Gao, B. Zhang, X. Z. Meng, Z. Chen, *Int. I. Refrig*. **2003**, *26*, 622.

[41] J. Gass, *Rev. Adv. Mater. Sci.* **2005**, *10*, 398-402; b) O. Tegus, E. Brück, K. H. J. Buschow, F. R. de Boer, *Naure* **2002**, *415*, 150-152.

[42] a) J. Bland, © *University of Liverpool* **2003**; b) P. Gütlich, E. Bill, A. X. Trautwein, Mössbauer Spectroscopy and Transition Metal Chemistry: Fundamental and Applications, Springer, **2011**; b) P. Gütlich, *Chemie in unserer Zeit*, **1970**, *4*, 133-144; c) R. L. Mössbauer, *Z. Physik* **1958**, *151*, 124; d) R. L. Mössbauer, *Naturwissenschaften* **1958**, *45*, 538.

[43] A. Baniodeh, *Diplomarbeit*, November **2008**, A. K. Powell, KIT, Karlsruhe (Germany).

[44] For example: A. M. Ako, V. Mereacre, Y. Lan, C. E. Anosn, A. K. Powell, *Chem. Eur. J.* **2011**, *17(16)*, 4366-4370.

[45] J. Robblee, Electron Paramagnetic Resonance Spectroscopy (EPR), Berkley Spectroscopy Club, **2001**.

[46] a) L. Castelli, M. Fittipaldi, A. K. Powell, D. Gatteschi, L. Sorace, *Dalton Trans*. **2011**, *40(32)*, 81455-8455; b) O. Waldmann, A. M. Ako, H. U. Güdel, A. K. Powell, *Inorg. Chem*. **2008**, *47*, 3486-3488.

[47] W. R. Hagen, *Coord. Chem. Rev*. **1999**, *190-192*, 209-229.

[48] http://www.nobelprize.org/nobel_prizes/chemistry/laureates/1999/press.html.

[49] a) A. N. Unterreiner, Ultraschnelle Relaxationsdynamik solvatisierter Elektronen in flüssigem Ammoniak und Wasser, Dissertation, **1998**, Karlsruhe (Germany); b) Y. Liang, Ultrafast dynamics of metalloporphyrins, DNA and iron-lanthanide clusters in the liquid phase, Dissertation, **2012**, KIT, Karlsruhe (Germany).

[50] M. Dantus, P. Gross, *Encyc.of App. Phys*. **1988**, *22*, 431-457.

[51] J. Shah, Ultrafast Spectroscopy of Semiconductors and Semiconductor Nanostrcutures, Second Enlraged Edition from Springer, Berlin Heidelberg New York, ISBN 3-540-64226-9.

[52] a) J. Cobamillas-Gonzalesz, G. Grancini, G. Lanzani, *Adv. Mater*. **2011**, *23*, 5468-5485; b) V. K. Thorsmølle, R. D. Averitt, J. Demsar, D. L. Smith, S. Tretiake, R. L. Martin, X. Chi, B. K. Crone, A. P. Ramirez, A. J. Taylor, *Physica B* **2009**, *404*, 3127-3130; c) J. McGinnes, P. Cory, P. Proctor, *Science* **1974**, *183*, 853-855;A. Mishra, P. Bäuerle, *Angew. Chem. Int. Ed.* **2012**, *51(9)*, 2020-2067.

[53] For example: a) B. Kraabel, D. McBranch, N. S. Sariciftci, D. Moses, A. J. Heeger, *Phys. Rev. B*. **1994**, *50(24)*, 18543-18552; b) H. Hippler, A.-N. Unterreiner, J.-P. Yang, S. Lebedkin, M. M. Kappes, *Phys. Chem. Chem. Phys*. **2004**, *6*, 2387-2390; c) J.-P. Yang, M. M. Kappes, H. Hippler, A.-N.-Unterreiner, *Phys. Chem. Chem. Phys.* **2005**, *7*, 512-517.

[54] R. Berera, R. van Grondelle, J. T. Kennis, *Photosynth Res.* **2009**, *101(2-3)*, 105-118.

[55] R. Bertoni, M. Lorenc, A. Tissot, M. Servol, M.-L. Boillot, E. Collet, *Angew. Chem. Int. Ed.* **2012**, *51(30)*, 7485-7489.

[56] H. Brands, O. T. Ehrler, M. M. Kappes, A.-N. Unterreiner, *Z. Phys. Chem.* **2011**, *225*, 939-956.

[57] H. Brands, Dissertation, Universitätsverlag Karlsruhe, **2008**, ISBN: 978-3-86644-211-5.

[58] R. D. Cannon, P. White, *Prog. Ing. Chem*. **1988**, *36*, 195.

[59] a) S. G. Baca, H. S. Evans, C. Ambrus, S. T. Malinovskii, I. Malaesteam, N. Gerbeleu, S. Decurtis, *Polyhedron* **2006**, *25*, 733-740; b) K. Nakata, A. Nagasawa, Y. Sasaki, A. K. Boudalis, *Dalton Trans*. 2011, 40, 6371-6374; c) G. Novitchi, L. Helm, C. E. Anson, A. K. Powell, A. E. Merbach, *Inorg. Chem*. **2011**, *50(20),* 10402-10416; d) A. N. Georgopoulou, Y. Sanakis, V. Psycharis, C. P. Raptopoulou, A. K. Boudalis, *Hyp. Inter.* **2010**, *198*, 229-241; e) A. N. Georgopoulou, Y. Sanakis, A. K. Boudalis, *Dalton Trans*. **2011,** *40*, 6371-6374; f) R. P. White, N. C. Sa-ard, S. K. Bollen, R. D. Cannon, U. A. Jayasooriya, *Spec. Acta A: Mol. Spec.* **1990**, *46(6)*, 903-910; g) R. N. Puri, R. O. Asplund, S. L. Holt, *J. Coord. Chem.* **1981**, *11*, 125-131.

[60] A. Baniodeh, Synthese und Charakterisierung von mehrkernigen Eisen Komplexe, October **2008**, A. K. Powell, KIT, Karlsruhe (Germany). See ref. **[43]**.

[61] M. Murugesu, K. A. Abboud, G. Christou, *Dalton Trans*. **2003**, 4552-4556.

[62] R. P. White, N. Chai'Sa-ard, S. K. Bollen, R. D. Cannon, U. A. Jayasooriya, S. T. Robertson, U. Steigenberger, J. Tomkinson, *Spectrochem. Acta.* **1990**, *46(7)*, 903.

[63] A. K. Boudalis, N. Lalioti, G. A. Spyroulias, C. P. Raptopoulou, A. Teriz, A. Bousseksou, V. Tangoulis, J.-P. Tuchagues, S. P. Perpeles, *Inorg. Chem*. **2002**, *41*, 6474-6487.

[64] P. Parios, S. A. Moggach, A. R. Lennie, J. E. Warren, E. K. Brechin, M. Murrie, S. Parsons, *Dalton Trans.* **2010**, *39*, 7004-7011.

[65] S. M. Gorun, S. J. Lippard, *Nature*, **1986**, *319*, 666-668.

[66] K. J. Kambe, *J. Phys.Soc.,Jpn.* **1950**, *5*, 48.

[67] a) F. Pointillart, K. Bernot, R. Sessoli, D. Gatteschi, *Chem. Eur. J.* **2007**, *13*, 1602-1609; b) N. Ishikawa, M. Sugita, W. Wernsdorfer, *Angew. Chem. Int. Ed.* **2005**, *44*, 2931.

[68] N. Ishikawa, M. Sugita, T. Ishikita, *Coord. Chem. Rev.* **2011**, *255*, 2124-2148.

[69] For example: S.-L. Zheng, J.-P. Zhang, W.-T. Wong, X.-M. Chen, *J. Am. Chem. Soc.* **2003**, *125*, 6882.

[70] A. Stubna, D. H. Jo, M. Costas, W. W. Brenessel, H. Andres, H.; E. L. Bominaar, E. Munck, L. Que, *Inorg. Chem.* **2004**, *43*, 3067-3079.

[71] Y. Zang, Y. H. Dong, L. Que, K. Kauffmann, E. Munck, *J. Am. Chem. Soc.* **1995**, *117*, 1169-1170.

[72] a) A. N. Buckley, I. R. Herbert, B. D. Rumbold, G. V. H. Wilson, K. S. Murray, *J. Phys. Chem. Solids* **1970**, *31*, 1423; b) A. L. Feig, S. J. Lippard, *Chem. Rev.* **1994**, *94*, 759; c) Y. Zang, G. Pan, L. Que, B. G. Fox, E. Münck, *J. Am. Chem. Soc.* **1994**, *116*, 3653; d) Y. Zang, Y. Dong, Jr. Que, K. Kauffmann, E. Münck, *J. Am. Chem. Soc.* **1995**, *117*, 1169.

[73] a) S. T. Bramwell, M. N. Field, M. J. Harris, I. P. Parkin, *J. Phys. Condens. Matter* **2000**, *12*, 483; b) A. L. Cornelius, J. S. Gardner, *Phys. Rev*. **2001**, *B 64*, 060406.

[74] C. Hansch, A. Leo, R. W. Taft, *Chem. Rev*. **1991**, *91*, 165-195.

[75] E. Geyer, Theorie und Mechanismen in der organischen Chemie, 2. überarbeitete Auflage, I. B. Heim GmbH, **1992**, Art.-Nr. 05-03/13.

[76] a) J. Bartolomé, G. Filoti, V. Kuncser, G. Schinteie, V. Mereacre, C. E. Anson, A K. Powell, D. Prodius, C. Turta, *Phys. Rev. B.* **2009**, *80*, 014430(1); b) M. N. Akhtar, V. Mereacre, G. Novitchi, J.-P. Tuchagues, C. E. Anson, A. K. Powell, *Chem. Eur. J.* **2009**, *15*, 7278.

[77] L. Noodleman, *Journal of Chemical Physics* **1981**, *74*, 5737-5743.

[78] A. Bencini, F. Totti, *International Journal of Quantum Chemistry* **2005**, *101*, 819-825.

[79] T. Onishi, Y. Takano, Y. Kitagawa, T. Kawakami, Y. Yoshioka, K. Yamaguchi, K. *Polyhedron* **2001**, *20*, 1177-1184.

[80] For example: ´O. Rubio-Pons, Y. Luo, *J. Chem. Phys.* **2004**, *121*, 157-162; and others therein.

[81] S. Amiri, H. P. Reisenauer, P. R. Schreiner, *J. Am. Chem. Soc.* **2012**, 10.1021/ja107531y.

[82] a) K. Deleersnyder, H. Mehdi, I. T. Horvath, K. Binnemans, *Tetrahedron.* **2007**, *63*, 9063–9070 ; b) P Parois, S. A. Moggach, A. R. Lennie, J. E. Warren, E.K. Brechin, M. Murrie *Dalton Trans.* **2010**, *39*, 7004–7011.

[83] P. Parois, S. A. Moggach, A. R. Lennie, J. E. Warren, E. K. Brechin, M. Murrie, S. Parsons, *Dalton. Trans*. **2010**, *39*, 7004-7011.

[84] F. E. Hahn, J. Mohr, *Chemische Berichte*. **1990**, *123*, 481-484.

[85] J. K. McCusker, J. B. Vincent, E. A. Schmitt, M. L. Mino, K. Shin, D. K. Coggin, P. M. Hagen, J. C. Huffman, G. Christou, D. N. Hendrickson, *J. Am. Chem. Soc.* **1991**, *113*, 3012-3021.

[86] http://www.chem.wisc.edu/areas/reich/pkatable/index.htm.

[87] S. K. Langley, B. Moubaraki, C. M. Forsyth, I. A. Gass, K. S. Murray, *Dalton Trans.* **2010**, *39*. 1705-1708.

[88] T. Shiga, N. Ito, A. Hidaka, H. Okawa, S. Kitagawa, M. Ohba, *Inorg. Chem.* **2007**, *46*, 3492.

[89] T. Shiga, M. Ohba, H. Okawa, *Inorg. Chem.* 2004, *43*, 4435.

[90] F. Hatert, G. J. Long, D. Hautot, A.-M. Fransolet J. Delwiche, M. J. Hubin-Franskin, F. Grandjean, *Phys. Chem. Minerals* **2004**, *31*, 487–506**.**

[91] N. N. Greenwood, T. C. Gibbs, *Mössbauer Spectroscopy* Chapman and Hall Ltd., London, **1971**.

[92] M. F. Thomas, C. E. Johnson, in *Mössbauer Spectroscopy*, edited by D. P. E Dickson and F. J. Berry, Cambridge University Press, Cambridge, England, **1986**, p. 148–149, D.N.E Buchanan and G.J. Wertheim, *Bull. Am. Phys. Soc*., **1962**, *7*, 227

[93] P. R. Edwards, C. E. Johnson, *J. Chem. Phys.* **1968**, *49*, 211-216.

[94] C. E. Johnson in "Hyperfine Interactions in Excited Nuclei", *G.* Goldring, R. Kalish, Eds., Gordon and Breach, New York, **1971**, p 803.

[95] S. Brooker, *Dalton Trans.***2011**, *40*, 11425.

[96] T. C. Stamatatos, A. G. Christou, S. Mukherjee, K. M. Poole, C. Lampropoulos, K. A. Abboud, T. A. O'Brien, G. Christou, *Inorg. Chem*. **2008**, *47(19)*, 9021-9034.

[97] L. F. Jones, P. Jensen, B. Moubaraki, K. J. Berry, J. F. Boas, J. R. Pilbrow, K. S. Murr

ay, *J. Mater. Chem.* **2006**, *16*, 2690-2697.

[98] A. A. Naini, V. Young, J. G. Verkade, *Polyhedron* **1995**, *14(3)*, 393-400.

[99] For example: the paper describes the determination of the easy axis in a mononuclear Dy system. The radical ligand can interact with The Y^{III} analouge; a) K. bernot, J. Luzon, L. Bogani, M. Etieme, C. Sangregorio, M. Shanmugan, A. Caneschi, R. Sessoli, D. Gatteschi, *J. Am. Chem. Soc.* **2009**, 5573-5579.; b) other examples will be published soon from Powell group.

[100] N. J. Cherepy, *J. Phys. Chem. B*. **1998**, *102*, 770-776.

[101] D. K. Zhong, D. R. Gamelin, *J. Am. Chem. Soc*. **2010**, *132*, 4202-4207.

[102] For example: S. U. M. Khan, J. Akikusa, *J. Phys. Chem. B*. **1999**,7184-7189.

[103] Solar hydrogen production by photo oxidization of water from doped iron oxide (hematite) photoanodes, for example: a) O. Khaselev, J. A. Turner, *Science* **199**8, *280*, 425; b) Doped with TiO_2: A. Fujishima, K. Honda, K., *Nature* **1972**, *37*, 237; c) Doped with ZnO:

T. F. Jaramillo, S. H. Baeck, A. Kleiman-Shwarsctein, K. S. Choi, G. D. Stucky, E. W. McFarland, *J. Com. Chem.* **2005**, *7*, 264; d) Doped with WO_3: S. H. Baeck, K. S. Choi, T. F. Jaramillo, G. D. Stucky, E. W. McFarland, *Adv. Mat.* **2003,** *15*, 1269; e) B. Marsen, E. L. Miller, D. Paluselli, R. E. Rocheleau, *Int. J. Hydrogen Energy* **2007**, *32*, 3110; f) A. Kleiman-Shwarsctein, Y.-S. Hu, A. J. Forman, G. D. Stucky, E. W. McFarland, *J. Phys. Chem. C* **2008**, *20*, 3803; g) Y.-S. Hu, A. Kleiman-Shwarsctein, A. Forman, J.-N. Park, J.-N., E. W. McFarland, *Chem. Mater.* **2008**, *20*, 3803.

[104] T. Fukumara, H. Toyosaki, Y. Yamada, *Semiconductor Science Technology* **2005**, *20(41)*, 103-111.

[105] M. Sheik-Bahae, R. I. Epstein, "progress article" *Nature* **2007**, *1*, 693-698.

[106] Y.-Z. Zheng, M. Evangelisti, R. E. P. Winpenny, *Angew. Chem. Int. Ed.* **2011**, *50*, 3692 –3695.

[107] S. K. Langley, N.F. Chilton, B. Moubaraki, T. Hooper, E. K. Brechin, M. Evangelisti, K. S. Murray, *Chem. Sci.* **2011**, *2*. 1166.

[108] For example: a) L. Games, J. Lousteu, D. Milanese, G. C. Scarpignato, S. D. Jackson, *J. Appl. Phys.* **2012**, *111(6)*; b) G. Lakshmiaryana, J. Qui, M. G. Birk, I. V. Kityk, *J. Appl. Phys.* **2008**, *41(17)*, 175106; c) S. Tanabe, X. Feng, T. Hanada, *Optics Letters* **2000**, *25(11)*, 817-819; d) J. L. Doualan, *Optical Materials* **200**3, *24*, 563-574; f) M. Taher, H. Gebawi, S. Taccheo, L. Jousteau, D. Milanese, N. Peyghambarim, *Optical Components and Materials VIII.* **2011**, *7934*, pp. 793407-793407-6.

[109] A. L. Crumbliss, P. S. Lugg, and N. Morosoff, *Inorg. Chem.* **1984**, *23*, 4701.

[110] T. Uemura, M. Ohba, S. kitagawa, *Inorg. Chem***. 2004**, *43*, 7339.

[111] D. C. Arnett, P. Vöhringer, N. F. Scherer, *J. Am. Chem. Soc.* **1995**, *117*, 12262-12272.

[112] D. Weidinger, D. J. Brwon, J. C. Owrutsky, *J. Chem. Phys*. **2011**, *134*, 12450.

[113] F. Herren, P. Fischer, A. Ludi, W. Hälg, *Inorg. Chem*. **1980**, *19*, 956-959.

[114] C. Shang, E. R. Blatchley, Environ. Sci. Technol. **1999**, *33*, 2218-2223.

[115] G. M. sheldrick, SHELXTL 5.1, Bruker AXS Inc. Madison, WI, USA, **1997**.

[116] G. M. Sheldrick, *Acta Crytsallogr. Sect. A: Found. Cyrstallogr.* **2007**, *64*, 112-122.

[117] WinX^{Pow} 1.07, Stoe & Cie GmbH, Darmstadt (Germany), **2000**.

[118] B. Seeber, T. Fredrich, SQUID- Superconducting Quantum Interference Device, **2009**.

[119] O. Kahn, *Molecular Magnetism*; VCH Publishers, Inc.: New York, Weinheim, Cambridge, **1993**.

[120] P. Pascal, P. *Ann. Chim. Phys.,* **1910**, *19*, 5.

[121] a) F. Yerly, F. Lausanne, Switzerland, **2003**; b)The MathWorks Inc.: **2000**.

[122] M. W. Schmidt, K. K. Baldridge, J. A. Boatz, S. T. Elbert, M. S. Gordon, J. H. Jensen, S. Koseki, N. Matsunaga, K. A. Nguyen, S. J. Su, T. L. Windus, M. Dupuis, M. Montgomery, J. A. *Journal of Computational Chemistry* **1993**, *14*, 1347-1363.

[123] W. J. Stevens, M. Krauss, H. Basch, P. G. Jasien, *Canadian Journal of Chemistry-Revue Canadienne De Chimie* **1992**, *70*, 612-630.

Chapter 8

Appendix: Chapter 2

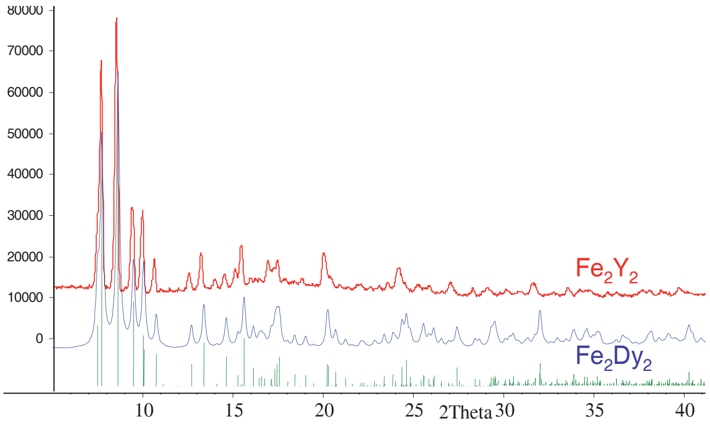

Figure 2.4. Powder diffraction X-ray data for Fe_2Y_2 **2.13** (red line) theoretical powder diffraction for Fe_2Dy_2 **2.8** and **2.11** (green line) and Lorentzian profile powder diffraction for **2.8**.

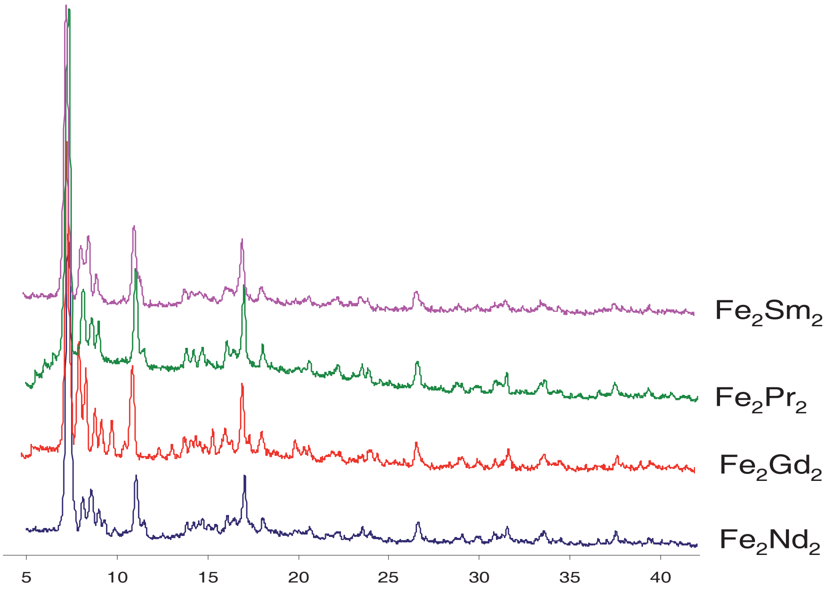

Figure 2.5. Powder diffraction of compounds Fe_2Sm_2 **2.4**, Fe_2Pr_2 **2.2**, Fe_2Gd_2 **2.6** and Fe_2Nd_2 **2.3.**

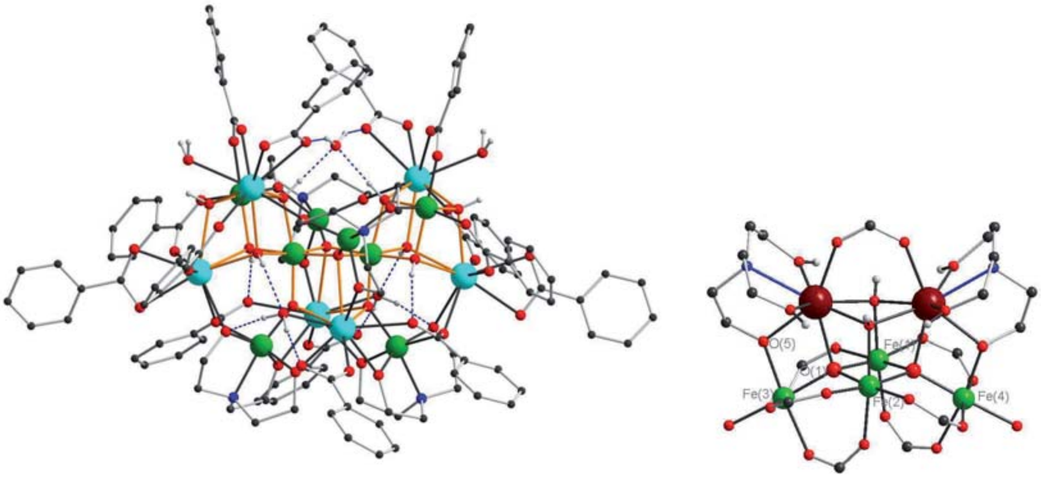

Figure 2.6. The Structures of Fe_8La_6 and Fe_4Lu_2 (**2.14 and 2.15**). Fe (green), La (torques), and Lu (brwon), C(black), O(red), H(white) and N (blue). The dashed lines repersent the hydrogen bondings in **2.14**.

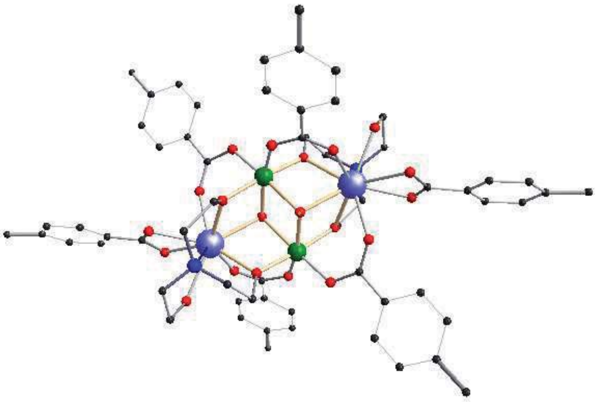

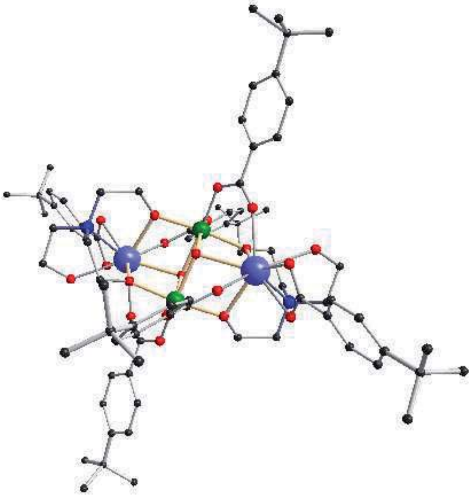

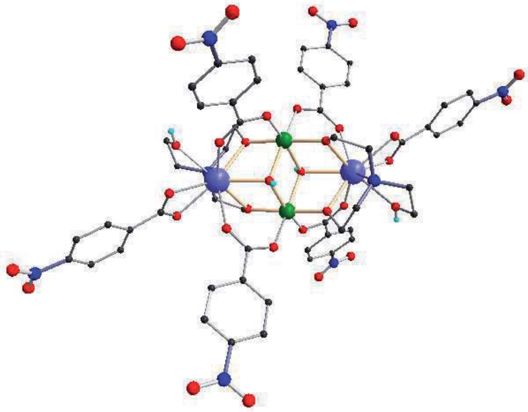

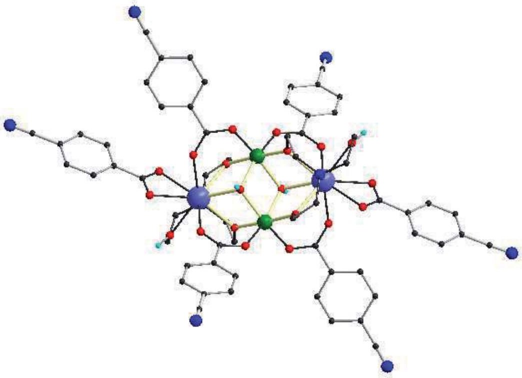

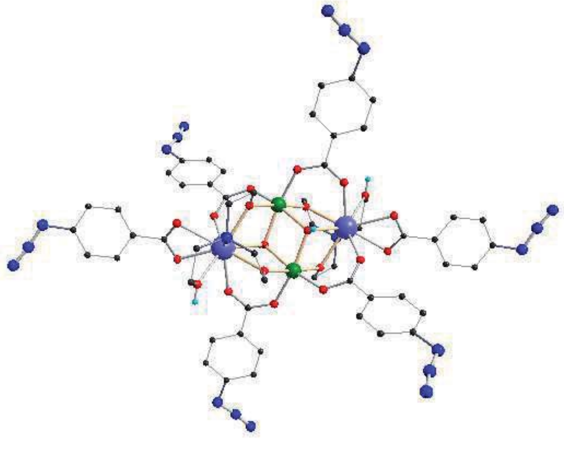

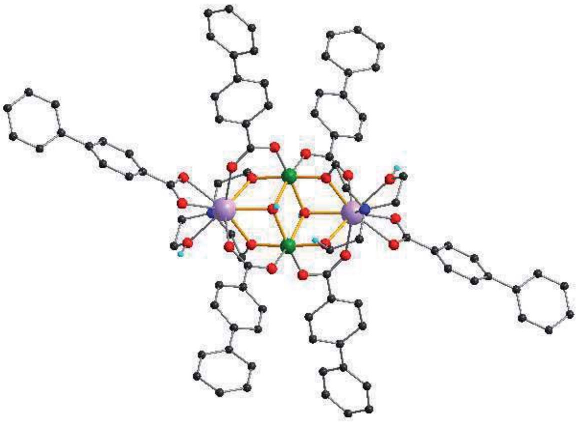

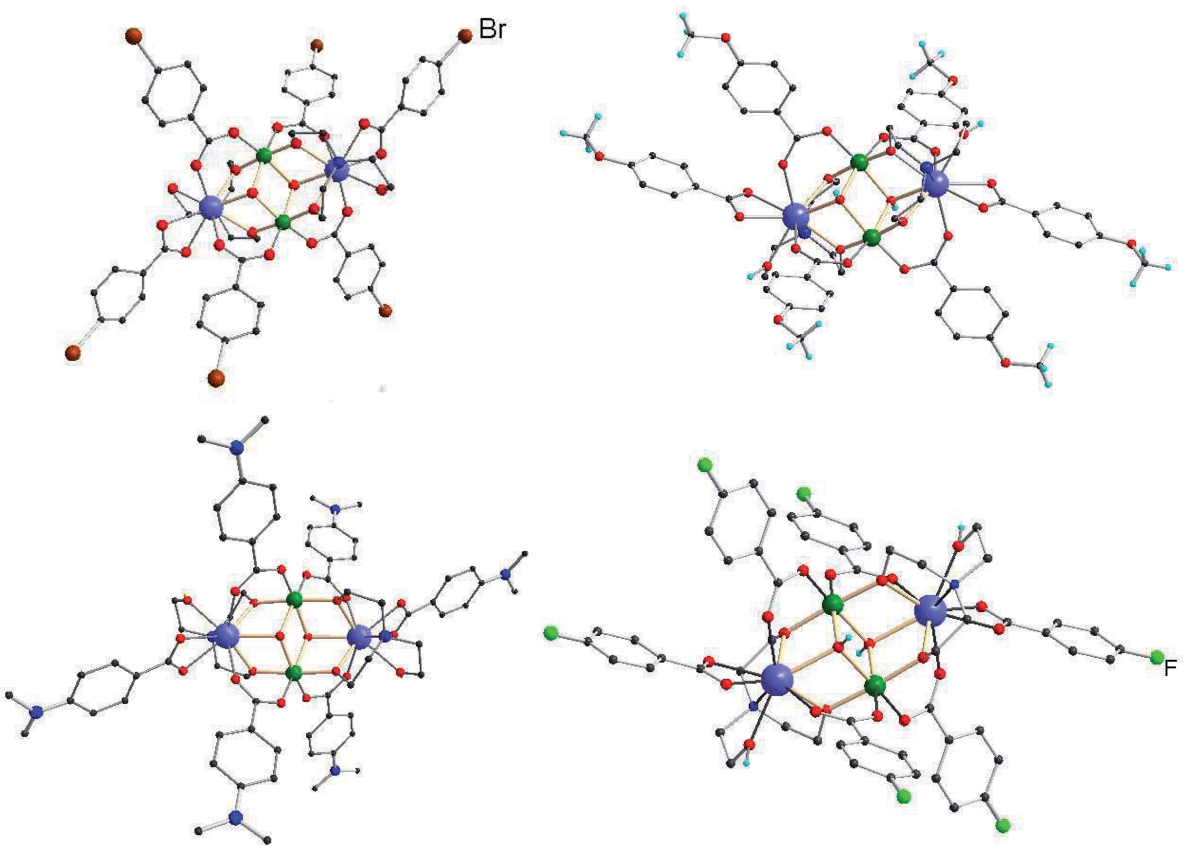

Figure 2.8. The structures of Fe_2Dy_2 complexes with para-substituted benzoates. (Left side) **2.8**$^{\text{teaH-6}p\text{Me}}$, **2.8**$^{\text{teaH-6}p\text{NO2}}$, **2.8**$^{\text{teaH-6}p\text{N3}}$, **2.8**$^{\text{teaH-6}p\text{Br}}$ and **2.8**$^{\text{teaH-6}p\text{N(Me)2}}$. (Riht side) **2.8**$^{\text{teaH-6}pt\text{Bu}}$, **2.8**$^{\text{teaH-6}p\text{CN}}$, **2.8**$^{\text{teaH-6}p\text{Ph}}$, **2.8**$^{\text{teaH-6}p\text{OMe}}$ and **2.8**$^{\text{teaH-6}p\text{F}}$. Fe (green), Dy (shining blue in large), C (grey-black), H(torques), O(red), N(blue, small), Br (brown), F (bright green, see label). The substituents are enlarged. The metal ion core is highlighted in Tan.

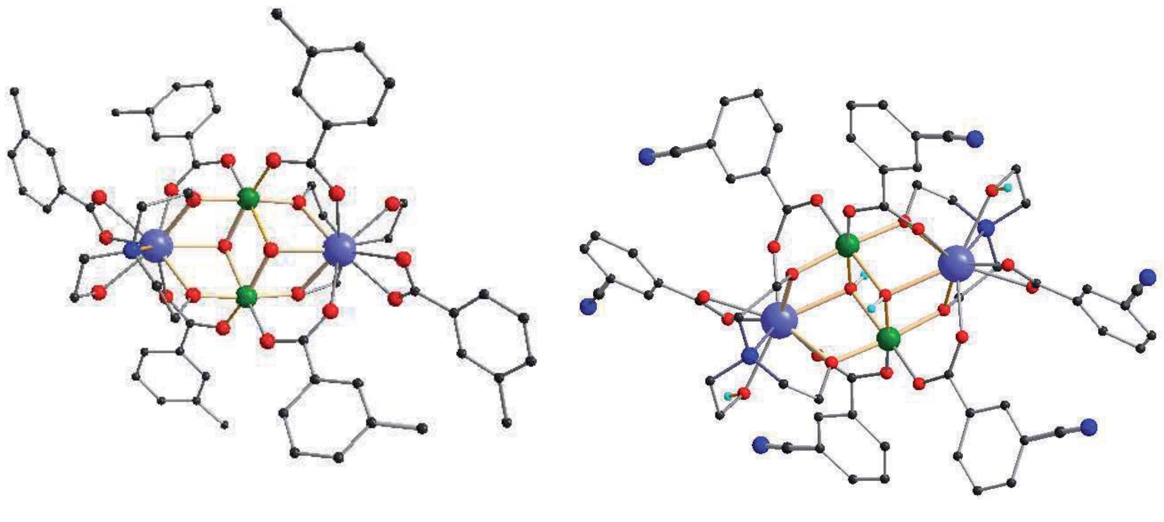

Figure 2.9. The structures of the (six) *meta*-examples: (Left) $[Fe_2Dy_2(\mu_3\text{-}OH)_2(Htea)_2(O_2CC_6H_4\text{-}m\text{CH}_3)_6]$ **2.8**$^{\mathbf{teaH\text{-}6}m\mathbf{Me}}$ and (right) $[Fe_2Dy_2(\mu_3\text{-}OH)_2(Htea)_2(O_2CC_6H_4\text{-}m\text{CN})_6]$ **2.8**$^{\mathbf{teaH\text{-}6}m\mathbf{CN}}$. Fe (green), Dy (shining blue), N (blue, smaller), O (red), C (black). Core is in Tan.

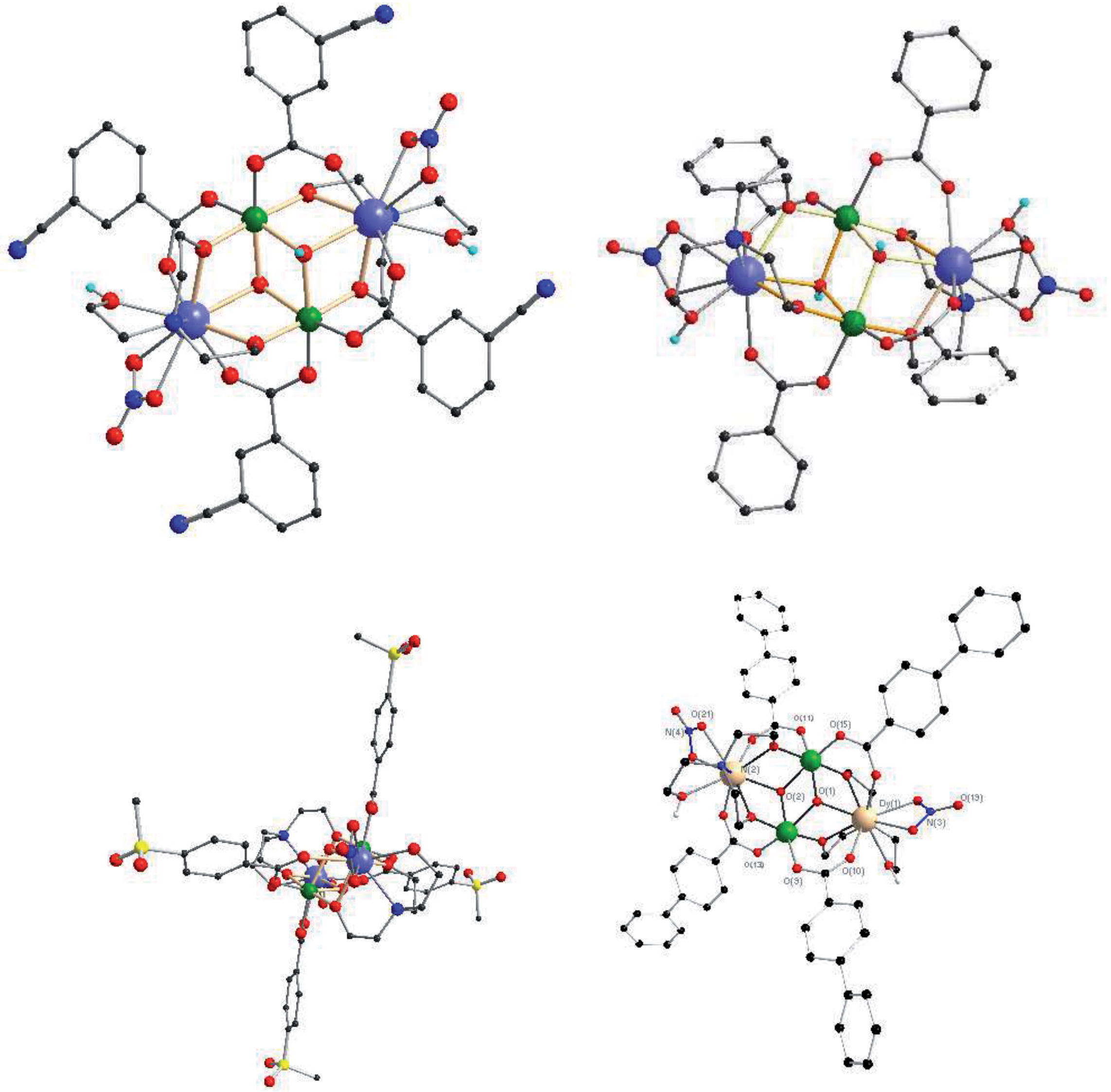

Figure 2.10. The structures of complexes with two chelating nitrates. (Upper, left) **2.8**$^{\mathbf{teaH\text{-}4}m\mathbf{CN}}$ and (upper, right) **2.8**$^{\mathbf{teaH\text{-}4}p\mathbf{H}}$. (Lower, left) **2.8**$^{\mathbf{teaH\text{-}4}p\mathbf{MeSO2}}$ and (lower, right) **2.8**$^{\mathbf{teaH\text{-}4}p\mathbf{Ph}}$. Dy (shining blue), Fe (green), C (black), N (blue), O (red), S (yellow).

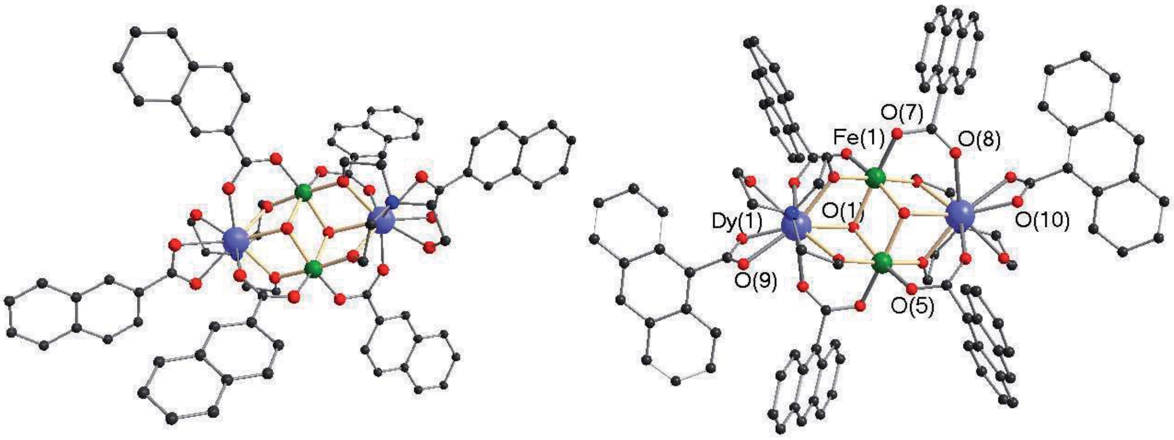

Figure 2.11. The structures of the aromatic-rich examples: [$Fe_2Dy_2(\mu_3\text{-}OH)_2(Htea)_2(2\text{-naphth})_6$] **2.8**$^{\textbf{teaH-6(2-naphth)}}$ (left) and [$Fe_2Ln_2(\mu_3\text{-}OH)_2(Htea)_2(9\text{-anth})_6$] **2.8**$^{\textbf{teaH-6(9-anthr)}}$ (right) .Dy (shining blue), Fe (green), C (grey-black), O (red). Core is in Tan.

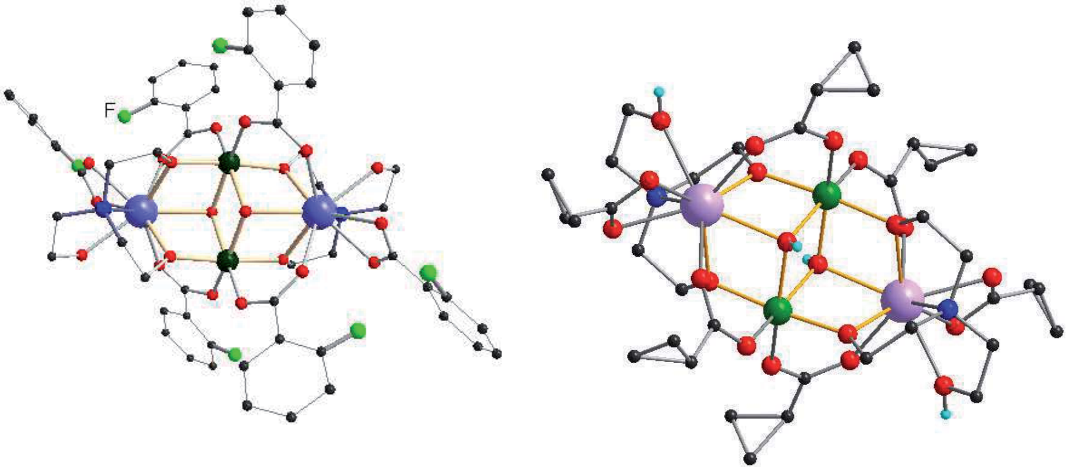

Figure 2.12. (Left) presents the only compound with ortho-position: **2.8**$^{\textbf{teaH-6oF}}$. (Right) The non-aromatic Fe_2Dy_2 compound with six cyclopropane carboxylates **2.8**$^{\textbf{teaH-6cp}}$**.** Dy (lavender), Fe (green), H (torques), C (dark grey), O (red), N (blue).

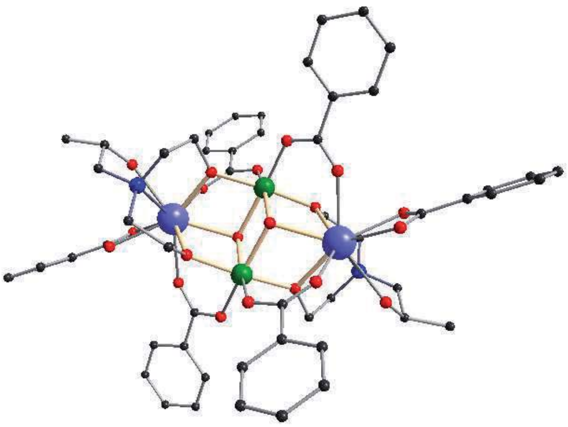

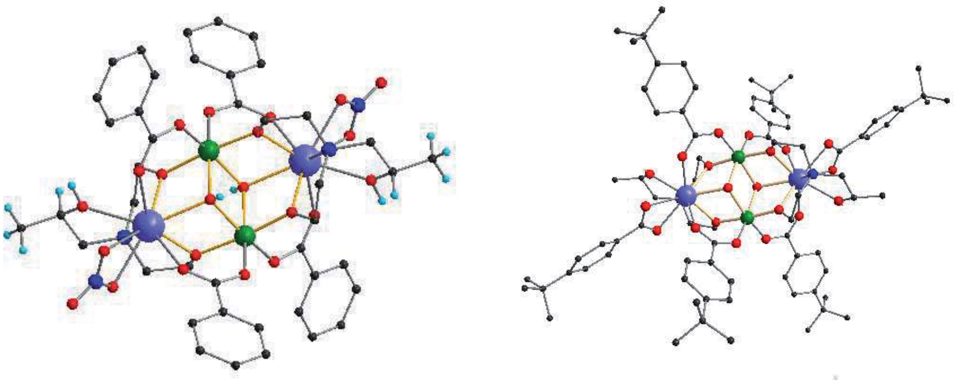

Figure 2.13. The Fe_2Dy_2 structures of the compounds with Me-teaH$_3$. (Upper) $\mathbf{2.}^{\mathbf{8Me\text{-}teaH,\ 6\mathit{p}H.}}$ (Lower, left) $\mathbf{2.8}^{\mathbf{Me\text{-}teaH},\ 4pH}$ and (lower, right) $\mathbf{2.8}^{\mathbf{Me\text{-}teaH,\ 6\mathit{pt}Bu}}$. Dy (shining blue), N (blue), C (grey-black), O (red), H (torques). CH_3 groups on chiral C are shown for $\mathbf{2.8}^{\mathbf{Me\text{-}teaH},\ 4pH}$ as example.

Table 2.1. Crystallographic data for complexes **1**, **6-10**, **12**, **13.**

Compound	**1**	**6**	**7**	**8**
Formula	$C_{60}H_{67}Ce_2Fe_2N_5O_{20}$	$C_{60}H_{67}Fe_2Gd_2N_5O_{20}$	$C_{60}H_{67}Fe_2N_5O_{20}Tb_2$	$C_{60}H_{67}Dy_2Fe_2N_5O_{20}$
FW (g mol^{-1})	1567.11	1604.39	1607.73	1614.89
Crystal system	monoclinic	monoclinic	monoclinic	monoclinic
Space group	C2/c	C2/c	C2/c	C2/c
a (Å)	21.389(2)	21.4105(14)	18.8689(19)	18.7113(9)
b (Å)	12.4258(12)	12.3502(8)	15.9021(18)	15.8961(8)
c (Å)	23.558 (2)	23.3265(15)	21.929(2)	21.8206(11)
α (°)	90	90	90	90
β (°)	90.454(2)	90.210(1)	110.222(7)	110.308(1)
γ (°)	90	90	90	90
V (Å^3)	6260.9(10)	6168.0(7)	6174.4(11)	6086.8(5)
Z	4	4	4	4
T (K)	100(2)	100(2)	200(2)	100(2)
F(000)	3160	3208	3216	3224

ρ_{calc} (g cm^{-3})	1.666	1.728	1.730	1.760
μ (mm^{-1})	1.959	2.663	2.803	2.970
Crystal size (mm)	0.26×0.17×0.15	0.15×0.12×0.03	0.14×0.12×0.10	0.10×0.08×0.07
Data measured	21193	19191	19451	18655
Unique data	7005	6423	5647	6215
R(int)	0.0293	0.0860	0.1064	0.0557
Data with I > 2σ(I)	6384	4791	3189	4794
Parameters	385	378	404	410
wR_2 (all data)	0.1115	0.1120	0.1171	0.0808
S (all data)	1.094	1.029	0.991	1.009
R_1 (I > 2σ(I))	0.0440	0.0467	0.0575	0.0353
Largest diff. peak / hole (e Å^{-3})	+2.31 / -0.57	+2.61 / -1.09	+0.69 / -1.66	+1.50 / -0.67

Table 2.1. (continued)**:** Crystallographic data for complexes **1**, **6-10**, **12**, **13.**

Compound	**9**	**10**	**12**	**13**
Formula	$C_{60}H_{67}Fe_2Ho_2N_5O_{20}$	$C_{60}H_{67}Er_2Fe_2N_5O_{20}$	$C_{60}H_{67}Fe_2N_5O_{20}Yb_2$	$C_{60}H_{67}Fe_2N_5O_{20}Y_2$
FW (g mol^{-1})	1619.75	1624.41	1635.97	1467.71
Crystal system	monoclinic	monoclinic	monoclinic	monoclinic
Space group	C2/c	C2/c	C2/c	C2/c
a (Å)	18.8104(15)	18.6735(7)	18.8025(14)	18.7266(16)
b (Å)	15.9239(13)	15.9092(6)	15.9088(9)	15.8981(11)

c (Å)	22.0043(17)	21.8407(8)	21.9072(15)	22.0196(18)
α (°)	90	90	90	90
β (°)	110.339(1)	110.428(1)	109.900(6)	110.230(6)
γ (°)	90	90	90	90
V (Å^3)	6180.1(9)	6080.4(4)	6161.7(7)	6151.2(8)
Z	4	4	4	4
T (K)	200(2)	100(2)	150(2)	180(2)
F(000)	3232	3240	3256	3008
ρ_{calc} (g/cm^{-3})	1.741	1.774	1.764	1.585
μ (mm^{-1})	3.072	3.280	3.548	2.410
Crystal size (mm)	0.18×0.14×0.07	0.38×0.27×0.25		0.15×0.13×0.08
Data measured	14199	22580	20471	18535
+Unique data	6430	6896	6061	5632
R(int)	0.0400	0.0334	0.0339	0.0924
Data with $I > 2\sigma(I)$	5642	6098	5185	3515
Parameters	410	410	410	410
wR_2 (all data)	0.1143	0.0729	0.1426	0.0711
S (all data)	1.087	1.060	1.070	0.946
R_1 ($I > 2\sigma(I)$)	0.0465	0.0305	0.0520	0.0556
Largest diff. peak / hole (e Å^{-3})	+1.82 / -0.66	+1.74 / -0.57	+0.63 / -2.68	+0.29 / -0.32

Table 2 .2. The crystallographic data of all Fe_2Dy_2 compounds with six *para*-substituted benzoates.

Compound	Fe_2Dy_2 (**2.8**$^{\mathbf{teaH\text{-}6\mathit{p}Me}}$)	Fe_2Dy_2(**2.8**$^{\mathbf{teaH\text{-}6\mathit{pt}Bu}}$)	Fe_2Dy_2 (**2.8**$^{\mathbf{teaH\text{-}6\mathit{p}NMe2}}$)	Fe_2Dy_2 (**2.8**$^{\mathbf{teaH\text{-}6\mathit{p}F}}$)
Formula	$C_{80}H_{92}Dy_2Fe_2N_4O_{24}$	$C_{107}H_{145}Cl_2Dy_2Fe_2N_5O_{24}$	$C_{88}H_{116}Dy_2Fe_2N_{12}O_{24}$	$C_{54}H_{52}Dy_2Fe_2N_2O_{20}F_6$
Mol mass [g/mol]	1930.28	2392.88	2162.63	1763.89
Space group	P-1	P21/c	P-1	P-1
a (Å)	11.5412(10)	18.1723(9)	10.4724(17)	10.7669(17)
b (Å)	14.2757(13)	11.6948(6)	14.098(2)	12.0307(19)
c (Å)	14.4870(12)	26.4638(14)	17.497(3)	14.423(3)
α (°)	61.98(1)		99.182(4)	82.211(13)
β (°)	87.65(1)	96.47(0)	103.905(3)	70.533(13)
γ (°)	80.38(1)		105.498(4)	79.943(12)
V (Å^3)	2075.54(733)	5588.35(80)	2346.2(7)	1728.4(5)
Z	1	2	1	1
T (K)	200	100(2)	150(2)	150(2)
Radiation	Mo Kα	Mo Kα	Mo Kα	Mo Kα
F(000)	976	2464	1104	876
ρ_{cale} (g/cm^{-3})	1.544	1.422	1.531	1.695
μ (mm^{-1})	2.198	1.694	2.686	2.639
Crystal size (mm)	0.26×0.21×0.18	0.21×0.07×0.05	0.21×0.03×0.02	0.28×0.22×0.19
Data meas.	24227	12356	21247	15113
+Unique d	8476	12356	9734	9734
R(int)	0.0458	0.0500	0.0619	0.0786
Data with I>2σ(I)	7303	10946	8239	8239
Parameters	517	635	595	450
wR2 (all data)	0.0956	0.1094	0.1111	0.1251
S (all data)	0.999	1.075	1.049	0.977
R1 (I > 2σ(I))	0.0400	0.0436	0.0487	0.0563

Table 2 .2. The crystallographic data of all Fe_2Dy_2 compounds with six *para*-substituted benzoates (continued).

Compound	**Fe_2Dy_2 (2.8$^{teaH\text{-}6pBr}$)**	**Fe_2Dy_2 (2.8$^{teaH\text{-}6pNO2}$)**	**Fe_2Dy_2 (2.8$^{teaH\text{-}6pCN}$)**	**Fe_2Dy_2 (2.8$^{teaH\text{-}6pN3}$)**
Formula	$C_{70}H_{76}Br_6Dy_2Fe_2N_{10}O_{20}$	$C_{71.40}H_{80.40}Dy_2Fe_2N_{15.70}O_{34,30}$	$C_{72}H_{70}Dy_2Fe_2N_{14}O_{20}$	$C_{62}H_{64}Dy_2Fe_2N_{24}O_{20}$
Mol mass [g/mol]	2293.57	2144.01	1888.12	1902.07
Space group	P-1	P-1	P-1	P-1
a (Å)	10.6946(11)	11.0959(10)	11.9912(6)	10.7750(10)
b (Å)	12.0235(11)	14.0354(12)	12.8733(7)	13.3925(11)
c (Å)	16.8400(2)	14.3715(11)	14.5474(8)	14.6820(12)
α (°)	100.538(9)	85.882(7)	70.567(4)	100.030(7)
β (°)	98.597(9)	89.474(7)	79.101(4)	109.742(7)
γ (°)	99.917(8)	75.941(7)	67.143(4)	103.921(7)
V (Å^3)	2060.1(4)	2165.4(3)	1946.78(18)	1858.4(3)
Z	1	1	1	1
T (K)	180(2)	180(2)	180(2)	150(2)
Radiation	Mo Kα	Mo Kα	Mo Kα	Mo Kα
F(000)	1120	1077	944	948
ρ_{cale} (g/cm^{-3})	1.849	1.644	1.611	1.700
μ (mm-1)	5.120	3.280	3.341	2.410
Crystal size (mm)	0.33×0.29×0.19	0.37×0.33×0.24	0.38×0.33×0.27	0.43×0.37×0.29
Data meas.	20135	15906	56533	26175
+Unique d	8024	9149	10469	8515
R(int)	0.0950	0.0482	0.0261	0.0406

Data with I>2σ(I)	5654	6930	9443	7460
Parameters	400	590	505	504
wR2 (all data)	0.1469	0.0621	0.0593	0.0876
S (all data)	0.976	0.965	1.070	0.997
R1 (I > 2σ(I))	0.0637	0.0363	0.0318	0.0356

Table 2 .2. The crystallographic data of all Fe_2Dy_2 compounds with six *para*-substituted benzoates (continued).

Compound	**Fe_2Dy_2 ($2.8^{teaH\text{-}6pPh}$)**	**Fe_2Dy_2 ($2.8^{teaH\text{-}6pOMe}$)**
Formula	$C_{123.8}H_{114.8}C_{l4.4}Dy_2Fe_2N_{4.8}O_{24}$	$C_{88}H_{104}Dy_2Fe_2N_8O_{32}$
Mol mass [g/mol]	2646.48	2222.49
Space group	P-1	P-1
a (Å)	10.3756(13)	10.9131(9)
b (Å)	15.077(2)	14.6224(14)
c (Å)	19.567(3)	15.7691(14)
α (°)	99.903(2)	94.290(7)
β (°)	104.490(2)	100.465(7)
γ (°)	99.698(2)	108.214(7)
V (Å^3)	2846.8(6)	2327.2(4)
Z	1	1
T (K)	100(2)	150(2)
Radiation	Mo Kα	Mo Kα
F(000)	1342	1128

ρ_{cale} (g/cm^{-3})	1.544	1.586
μ (mm-1)	1.726	1.979
Crystal size (mm)	0.27×0.24×0.18	0.28×0.25×0.23
Data meas.	28637	27155
+Unique d	12465	9514
R(int)	0.0448	0.0532
Data with I>2σ(I)	11851	8010
Parameters	777	597
wR2 (all data)	0.0901	0.1166
S (all data)	1.028	0.988
R1 (I > 2σ(I))	0.0345	0.0486

Table 2.3. The cell parameters of **2.6, 2.8 and 2.13**$^{\textbf{teaH-6pMe}}$

Compound	**Fe$_2$Dy$_2$ (2.8$^{teaH\text{-}6pMe}$)**	**Fe$_2$Gd$_2$ (2.6$^{teaH\text{-}6pMe}$)**	**Fe$_2$Y$_2$ (2.13$^{teaH\text{-}6pMe}$)**
Formula	$C_{80}H_{92}Dy_2Fe_2N_4O_{24}$	$C_{80}H_{92}Gd_2Fe_2N_4O_{24}$	$C_{80}H_{92}Y_2Fe_2N_4O_{24}$
Color	pale yellow	pale yellow	pale yellow
T[K]	200(2)	200(2)	200(2)
Crystal Syst	triclinic	triclinic	triclinic
Space group	P -1(2)	P-1(2)	P-1(2)
a [Å]	11.5412(10)	11.4402(4)	11.6914(21)
b[Å]	14.2757(13)	14.0561(43)	14.4130(23)

c[Å]	14.4870(12)	14.2995(39)	14.6258(22)
α[°]	61.98(1)	62.173(31)	62.099(17)
β[°]	87.65(1)	87.715(38)	87.45(20)
γ[[°]	80.38(1)	80.226(40)	80.106(20)
V [Å^3]	2075.54(733)	2002.0(2.6)	2143.9(1.5)
Z	1	1	1

Table 2.4. The Fe_2Ln_2 (Ln= Gd) compoundof *para*-nitro substituted benzoate.

Compound	**Fe_2Gd_2 (2.6$^{\text{teaH-6}p\text{NO2}}$)**
Formula	$C_{71.40}H_{80.40}Dy_2Fe_2$ $N_{15.70}O_{34.30}$
Color	yellow
T[K]	180(2)
Crystal Syst	triclinic
Space group	P -1
a [Å]	11.0959(10)
b[Å]	14.0354(12)
c[Å]	14.3715(11)
α[°]	85.88(1)
β[°]	89.47(1)
γ[[°]	75.94(1)
V [Å^3]	2165.43(398)
Z	1

Table 2.5. Fe_2Dy_2 compounds prepared with Me-teaH$_3$ as ligand.

Compound	**Fe_2Dy_2 (2.8$^{\text{Me-teaH-6pH}}$)**	**Fe_2Dy_2 (2.8$^{\text{Me-teaH-6}pt\text{Bu}}$)**	**Fe_2Dy_2 (2.8$^{\text{Me-teaH-4}pH}$)**
Formula	$C_{78}H_{80}Dy_2Fe_2N_6O_{24}$	$C_{110}H_{150}Dy_2Fe_2N_6O_{24}$	$C_{50}H_{66}Dy_2Fe_2N_8O_{32}$
Mol mass [g/mol]	1922.18	2377.06	1583.81

Space group	P-1	P 21/c	R-3
a (Å)	11.5295(12)	18.3691(14)	24.818(4)
b (Å)	12.0665(11)	11.8434(6)	24.818(4)
c (Å)	16.9409(18)	26.971(2)	26.453(5)
α (°)	70.010(8)	90.00	90.00
β (°)	77.324(8)	96.328(9)	90.00
γ (°)	65.111(8)	90.00	120.00
V (Å^3)	2001.2(3)	5831.8(7)	14110(4)
Z	1	2	9
T (K)	180(2)	200(2)	293(2)
Radiation	Mo Kα	Mo Kα	Mo Kα
F(000)	966	2456	7110
ρ_{calc} (g/cm^{-3})	1.595	1.354	1.678
μ (mm-1)	2.280	1.579	2.889
Crystal size (mm)	0.25×0.18×0.13		
Data meas.	15451	25881	29833
+Unique d	8439	7126	6143
R(int)	0.0484	0.1052	0.0705
Data with I>2σ(I)	6507	7126	4030
Parameters	515	653	391
wR2 (all data)	0.0555	0.1006	0.733
S (all data)	0.961	0.902	0.965
R1 (I > 2σ(I))	0.0328	0.0486	0.0392

Table 2.6. The Cell parameters of **2.6, 2.8 and 2.13**$^{\text{Me-teaH-6}p\text{H}}$

Compound	**Fe_2Dy_2 (2.8$^{\text{Me-teaH-6}p\text{H}}$)**	**Fe_2Gd_2 (2.6$^{\text{Me-teaH-6}p\text{H}}$)**	**Fe_2Y_2 (2.13$^{\text{Me-teaH-6}p\text{H}}$)**
Formula	$C_{78}H_{86}Fe_2N_6O_{24}Dy_2$	$C_{78}H_{86}Fe_2N_6O_{24}Gd_2$	$C_{78}H_{86}Fe_2N_6O_{24}Y_2$
Color	yellow	yellow	yellow
T[K]	200	200	180(2)
Crystal Syst	triclinic	triclinic	triclinic
Space group	P -1 (2)	P -1 (2)	P -1 (2)
a [Å]	11.5295	11.6801	11.5223(9)
b[Å]	12.0665	12.2321	12.080(1)
c[Å]	16.9409	17.1537	16.9458(15)
α[°]	70.010	69.887	70.15(1)
β[°]	77.329	77.273	77.26(1)
γ[[°]	65.111	64.929	65.09(1)
V [Å^3]	2001.24	2076.5	2003.84(707)
Z	1	1	1

Table 2.7. Fe_2Dy_2 compounds with six *meta*-substituted benzoates.

Compound	**Fe_2Dy_2 (2.8$^{\text{teaH-6}m\text{Me}}$)**	**Fe_2Dy_2 (2.8$^{\text{teaH-6}m\text{CN}}$)**
Formula	$C_{64}H_{70}Dy_2Fe_2N_2O_{20}$),($C_2H_3N$), 2($CH_4O$)	$C_{64}H_{58}Dy_2Fe_2N_{10}O_{20}$
Mol mass [g/mol]	1722.07	1723.90
Space group	P21/c (Nr.14)	P-1
a (Å)	12.4404(8)	9.700(2)
b (Å)	21.4830(15)	12.915(3)

c (Å)	13.7050(9)	14.427(3)
α (°)	90.00	87.159(17)
β (°)	100.532(5)	74.068(18)
γ (°)	90.00	73.135(17)
V (Å^3)	3601.1(4)	1662.2(6)
Z	2	1
T (K)	200(2)	150(2)
Radiation	Mo Kα	Mo Kα
F(000)	1736	856
ρ_{cale} (g/cm^{-3})	1.588	1.722
μ (mm-1)	2.521	2.731
Crystal size (mm)	0.38×0.33×0.25	0.14×0.11×0.05
Data meas.	38489	15190
+Unique d	7652	6039
R(int)	0.0660	0.1076
Data with I>2σ(I)	6012	3726
Parameters	415	449
wR2 (all data)	0.1207	0.1311
S (all data)	1.001	0.984
R1 (I > 2σ(I))	0.0475	0.0616

Table 2.8. Fe_2Dy_2 compounds with $teaH_3$ and only four *para*-carboxylates.

Compound	**Fe_2Dy_2 ($2.8^{teaH\text{-}4pH}$)***	**Fe_2Dy_2 ($2.8^{teaH\text{-}4pPh}$)**	**Fe_2Dy_2 ($2.8^{teaH\text{-}4pMeSO2}$)**
Formula	$C_{52}H_{66}Dy\,Fe_2N_1\,O_{22}$	$C_{75}H_{81}Cl_2Dy_2Fe_2N_9O_{22}$	$Dy_2Fe_2O_{31}H_{56}N_{10}C_{56}S_4$
Mol mass [g/mol]	1619.85	1986.09	1930.06

Space group	P-1	P-1	P-1
a (Å)	12.0501(11)	11.8787(6)	10.4444(21)
b (Å)	12.1666(11)	18.4474(9)	14.5315(29)
c (Å)	12.9001(12)	20.6754(11)	15.3204(31)
α (°)	116.336(1)	116.450(0)	114.18(3)
β (°)	94.679(1)	93.480(0)	96.73(3)
γ (°)	103.009(1)	91.710(0)	106.23(3)
V ($Å^3$)	1615.4(3)	4040.63(836)	1964.16(463)
Z	1	2	1
T (K)	200(2)	150(2)	200(2)
Radiation	Mo Kα	Mo Kα	Mo Kα
F(000)	808	1976	
ρ_{calc} (g/cm^{-3})	1.665	1.618	1.63162
μ (mm-1)	2.806	2.323	
Crystal size (mm)	0.26×0.23×0.16	0.41×0.35×0.27	
Data meas.	13903	32224	
+Unique d	7017	17108	
R(int)	0.0364	0.0163	
Data with I>2σ(I)	6442	14226	
Parameters	405	1030	
wR2 (all data)	0.0758	0.0847	
S (all data)	1.027	1.000	
R1 (I > 2σ(I))	0.0308	0.0344	

* Fe_2Tb_2 and Fe_2Ho_2 have the same cell, see also literature [20a].

Table 2.8. Fe_2Dy_2 compounds with $teaH_3$ and only four *meta*-carboxylates (continued).

Compound	**Fe_2Dy_2 (2.8$^{\text{teaH-4}m\text{Me}}$)**	**Fe_2Dy_2 (2.8$^{\text{teaH-4}m\text{CN}}$)**
Formula		$C_{48}H_{51}Dy_2Fe_2N_{10}O_{22.5}$
Mol mass [g/mol]		1564.69
Space group	C2/c	P-1
a (Å)	13.142(3)	11.1309(19)
b (Å)	10.655(2)	11.5916(17)
c (Å)	21.529(4)	12.9332(18)
α (°)	90.00	82.066(12)
β (°)	91.31(3)	64.549(11)
γ (°)	90.00	74.414(12)
V (Å^3)	3013.7(10)	1450.9
Z		1
T (K)		150(2)
Radiation		Mo Kα
F(000)		773
ρ_{cale} (g/cm^{-3})		1.791
μ (mm-1)		3.122
Crystal size (mm)		0.14x0.11x0.07
Data meas.		19107
+Unique d		5514
R(int)		0.0846
Data with I>2σ(I)		5514

Parameters		384
wR2 (all data)		0.1331
S (all data)		0.975
R1 (I > 2σ(I))		0.0547

Table 2.9. The cell parameters of Fe_2Dy_2 compounds with 3,5-disubstituents.

Compound	**Fe_2Dy_2(2.8$^{teaH-6(3,5-di\mathit{t}Bu)}$**	**Fe_2Dy_2(2.8$^{teaH-6(3,5-diNO2}$)**
Formula		
Mol mass [g/mol]		
Space group	P121/c1	P-1
a (Å)	14.3120	12.6748
b (Å)	28.1983	12.8119
c (Å)	19.8151	14.4280
α (°)		92.782
β (°)	97.208	105.18
γ (°)		103.988
V (Å^3)	7933.7	2178.4

Table 2.10. Fe_2Dy_2 compounds with six 9-anthracene and 2-naphthoate carboxylates.

Compound	**Fe_2Dy_2 (2.8$^{teaH-6(2-naphth)}$)**	**Fe_2Dy_2 (2.8$^{teaH-6(9-anthr)}$)**
Formula	$C_{104}H_{92}Dy_2Fe_2N_4O_{24}$	$C_{110}H_{104}Dy_2Fe_2N_4O_{24}$
Mol mass [g/mol]	2218.52	2302.67
Space group	P-1	P-1

a (Å)	12.8982(12)	13.3514(13)
b (Å)	14.4473(15)	13.9021(14)
c (Å)	14.5807(17)	14.2883(14)
α (°)	61.602(12)	92.621(8)
β (°)	76.184(12)	97.614(8)
γ (°)	84.060(12)	115.053(7)
V (Å^3)	2320.8(4)	2366.0(4)
Z	1	1
T (K)	200(2)	150(2)
Radiation	Mo Kα	Mo Kα
F(000)	1120	1168
ρ_{cale} (g/cm^{-3})	1.587	1.616
μ (mm-1)	1.977	1.943
Crystal size (mm)		
Data meas.	17523	27322
+Unique d	8415	9992
R(int)	0.0947	0.0411
Data with I>2σ(I)	5216	8387
Parameters	623	651
wR2 (all data)	0.941	0.1217
S (all data)	0.941	0.994
R1 (I > 2σ(I))	0.0529	0.0502

Table 2.11. Fe_2Ln_2 compounds with six cyclopropane carboxylates (cp) (Ln= Gd, Dy) and the Fe_2Dy_2 with six ortho-fluorobenzoates.

Compound	**Fe_2Gd_2 (2.6$^{teaH-6cp}$)**	**Fe_2Dy_2 (2.8$^{teaH-6cp}$)**	**Fe_2Dy_2 (2.8$^{teaH-6oF}$)**
Formula		$C_{44}H_{7}0Dy_{2}Fe_{2}N_{6}O_{2}0$	$C_{60}H_{61}Dy_{2}F_{6}Fe_{2}N_{5}O_{20}$
Mol mass [g/mol]		1439.76	1722.84
Space group	P-1	P-1	C2/c
a (Å)	10.96	10.7983(10)	18.5564(18)
b (Å)	12.01	11.8227(11)	16.346(2)
c (Å)	12.21	12.0402(11)	21.919(2)
α (°)	91.97	91.80(1)	90.00
β (°)	115.26	115.46(1)	110.100(7)
γ (°)	102.95	102.62(1)	90.00
V (Å^3)	1340	1340.53(582)	6243.6(12)
Z	1	1	4
T (K)	293	150(2)	150(2)
Radiation	Mo Kα	Mo Kα	Mo Kα
F(000)		720	3416
ρ_{calc} (g/cm^{-3})		1.783	1.833
μ (mm-1)		3.364	2.919
Crystal size (mm)		0.41×0.35×0.28	0.21×0.08×0.06
Data meas.		20611	17688
+Unique d		5687	5698
R(int)		0.033	0.1021
Data with I>2σ(I)		5312	5698
Parameters		342	342
wR2 (all data)		0.0839	0.1387

S (all data)		1.042	0.978
R1 (I > 2σ(I))		0.0334	0.0605

Table 2.12. Crystallographic data of compounds **2.17-2.19**.

Compound	**[Gd_2Fe_2][Gd_2Fe] (2.17)**	**[Dy_2Fe_2][Dy_2Fe] (2.18)**	**[Y_2Fe_2][Y_2Fe] (2.19)**
Formula	$C_{50.4}H_{68.22}Fe_{1.26}Gd_2N_{6.8}O_{23.2}$	$C_{50}H_{67.46}Dy_2Fe_{1.18}N_7O_{23}$	$C_{50.4}H_{68.64}Fe_{1.12}Y_2N_{6.8}O_{23.2}$
FW [g/mol]	1525.41	1525.470	1381.33
Color	orange	orange	orange
T[K]	180(2)	180(2)	180(2)
Crystal Syst	triclinic	triclinic	triclinic
Space group	P -1 (2)	P -1 (2)	P -1 (2)
a [Å]	10.6463(8)	10.6311(4)	10.6345(14)
b[Å]	12.0623(9)	12.0593(5)	12.0265(15)
c[Å]	12.2599(9)	12.2283(5)	12.2005(14)
α[°]	103.773(6)	104.013(3)	103.919(10)
β[°]	106.623(6)	106.575(3)	106.596(10)
γ[[°]	94.004(6)	93.933(3)	94.067(10)
V [$Å^3$]	1449.04(19)	1440.2(1)	1435.0(3)
Z	1	1	1
Radiation	Mo Kα	Mo Kα	Mo Kα
F(000)	765		711
ρ_{cale} (g/cm^{-3})	1.748	1.758	1.598
μ (mm-1)	2.657		2.371
Data meas.	37337		14303
+Unique d	6899		6037
R(int)	0.0667		0.0736
Data with	5944		3880

I>2σ(I)			
Parameters	430		430
wR2 (all data)	0.0527		0.0847
S (all data)	0.994		0.972
R1 (I > 2σ(I))	0.0260	0.034	0.0550

Table 2.13. Crystallographic data for compounds **2.20 and 2.21**.

Compound	**Dy_2-dimer (2.20)**	**Dy-mono (2.21)**
Formula	$C_{40}H_{52}Dy_2N_2O_{16}$	$C_{28}H_{22}DyN_4O_4$
Mol mass [g/mol]	1141.840	1306.01
Space group	P-1	P-1
a (Å)	10.1863(13)	8.2961(14)
b (Å)	10.8877(15)	11.3958(19)
c (Å)	10.9925(14)	16.845(3)
α (°)	74.029(15)	104.148(13)
β (°)	75.225(15)	99.325(14)
γ (°)	67.501(14)	104.378(13)
V (Å^3)	1067.4(2)	1453.2(4)
Z	1	1
T (K)	150(2)	293(2)
Radiation	Mo Kα	Mo Kα
F(000)		644
ρ_{cale} (g/cm^{-3})		1.492
μ (mm-1)		2.609
Crystal size		

(mm)		
Data meas.		14189
+Unique d		5826
R(int)	0.040	0.0976
Data with I>2σ(I)		4945
Parameters		389
wR2 (all data)		0.1471
S (all data)		1.42
R1 (I > 2σ(I))		0.0606

Table 2.14. Crystallographic data of compounds **2.22** and **2.23**.

Compound	**Fe_2Gd_2 (2.22)**	**Fe_2Y_2 (2.23)**
Formula	$C_{60}H_{78}Fe_2Gd_2N_4O_{22}$	$C_{62}H_{80}Fe_2N_6O_{22}Y_2$
Mol mass [g/mol]	1633.46	1550.84
Space group	P 21/n	P 21/n
a (Å)	10.2985(15)	10.113(3)
b (Å)	23.830(3)	96.28(2)
c (Å)	14.145(2)	16.138(4)
α (°)	90.00	90.00
β (°)	102.00(2)	75.225(15)
γ (°)	90.00	90.00
V (Å^3)	3395.46(13)	3576.9(16)
Z	2	2
T (K)	150(2)	150(2)
Radiation	Mo Kα	Mo Kα

F(000)		1600
ρ_{cale} (g/cm^{-3})		1.440
μ (mm-1)		2.079
Crystal size (mm)		
Data meas.		10169
+Unique d		4216
R(int)		0.1235
Data with I>2σ(I)		2365
Parameters		391
wR2 (all data)		0.1961
S (all data)		1.024
R1 (I > 2σ(I))		0.0884

Table 2.15. Crystallographic data of compounds **2.24**.

Compound	**[$\{Fe_2Dy_2\}^{2+}\{Fe_2Dy_2\}^{2-}$] (2.24)**
Formula	$C_{103}H_{118}Dy_4Fe_4N_8O_{46}$
Mol mass [g/mol]	3077.45
Space group	P 21/c
a (Å)	18.437(2)
b (Å)	18.374(2)
c (Å)	18.304(2)
α (°)	90.00
β (°)	104.236(14)
γ (°)	90.00
V (Å^3)	3395.46(13)

Z	2
T (K)	223(2)
Radiation	Mo Kα
F(000)	3056
ρ_{cale} (g/cm^{-3})	1.701
μ (mm-1)	3.011
Crystal size (mm)	
Data meas.	38440
+Unique d	11592
R(int)	0.0724
Data with I>2σ(I)	8256
Parameters	736
wR2 (all data)	0.0692
S (all data)	0.977
R1 (I > 2σ(I))	0.0360

Table 2.16. Crystallographic data of compounds Fe_2Dy_2 (**2.25**) and Fe_6Dy_2 (**2.26**).

Compound	**[Fe_2Dy_2] (2.25)**	**[Fe_6Dy_2] (2.26)**
Formula	$C_{70}H_{100}Dy_2Fe_2N_{16}O_{30}$	$C_{92}H_{126}Dy_2Fe_6N_{10}O_{50}$
Mol mass [g/mol]	2082.36	2832.13
Space group	R -3	P 21/c
a (Å)	37.172(5)	15.420(3)
b (Å)	37.172(5)	22.905(4)
c (Å)	15.936(3)	16.784(3)
α (°)	90.00	90.00

β (°)	90.00	109.735(3)
γ (°)	120.00	90.00
V (Å^3)	19070(5)	5580.0(15)
Z	9	2
T (K)	150(2)	100(2)
Radiation	Mo Kα	Mo Kα
F(000)	9504	2872
ρ_{cale} (g/cm^{-3})	1.632	1.686
μ (mm-1)	2.978	2.176
Crystal size (mm)	0.18x0.16x0.13	0.26x0.24x0.15
Data meas.	37765	43747
+Unique d	10068	12732
R(int)	0.0331	0.0331
Data with I>2σ(I)	9368	10826
Parameters	440	734
wR2 (all data)	0.1212	0.0757
S (all data)	1.039	1.067
R1 (I > 2σ(I))	0.0328	0.0309

Table 2.17. Cyrstallographic data for the two selected trinuclear starting materials with *meta*-tolyate and cycloprpanecarboxylate.

Compound	$[Fe_3O(O_2CPh)_6(OMe)_3]$	$[Fe_3O(_2CC_6H_4$-*m*$CH_3)_6(H_2O)(EtOH)_2]NO_3$	$[Fe_3O(O_2CC_3H_5)_3(HO_2CC_3H_5)(H_2O)_2]Cl$

Formula	$C_{28}H_{39}Fe_3O_{17}$	$C_{56}H_{68}Fe_3O_{21}$	$C_{28}H_{39}Fe_3O_{17}$
Mol mass [g/mol]	815.14	1258.66	815.14
Space group	C2/c	C2/c	P -1
a (Å)	11.625(2)	11.7804(8)	11.625(2)
b (Å)	23.042(5)	24.461(2)	23.042(5)
c (Å)	13.735(3)	21.1750(13)	13.735(3)
α (°)	90.00	90.00	90.00
β (°)	103.140(3)	100.242(7)	103.14(3)
γ (°)	90.00	90.00	90.00
V (Å^3)	3582.77	6004.5(8)	3582.8(12)
Z	4	4	4
T (K)	293(2)	233(2)	293(2)
Radiation	Mo Kα	Mo Kα	Mo Kα
F(000)		2628	1684
ρ_{cale} (g/cm^{-3})	1.51111	1.392	1.511
μ (mm-1)		0.790	1.269
Crystal size (mm)			
Data meas.		24010	18007
+Uniqued		5717	4389
R(int)	0.1116	0.070	2508
Data with I>2σ(I)		4646	4389
Parameters		378	445
wR2 (all data)		0.1586	0.1094

S (all data)		1.037	0.940
R1 (I > 2σ(I))		0.035	0.0539

Table 2.18. Cyrstallographic data for two selected {Fe_8} compounds with 4-fluorobenzoate and cyclopropanecarboxylate.

Compound	$[Fe_8O_3(O_2CC_6H_4F)_9(tea)(teaH)_3]$	$[Fe_8O_3(O_2CC_3H_5)_9(tea)(teaH)_3]$
Formula	$C_{96}H_{100.5}F_9Fe_8N_{8.5}O_{33}$	$C_{62}H_{94}Fe_8N_5O_{33}$
Mol mass [g/mol]	2519.15	1884.22
Space group	P a -3	P-1
a (Å)	27.5070(15)	13.015(8)
b (Å)	27.5070(15)	13.866(7)
c (Å)	27.5070(15)	22.403(14)
α (°)	90.00	81.66(7)
β (°)	90.00	78.15(7)
γ (°)	90.00	78.76(7)
V (Å^3)	20813(2)	3858(4)
Z	8	2
T (K)	150(2)	293(2)
Radiation	Mo Kα	Mo Kα
F(000)	10312	1946

ρ_{cale} (g/cm^{-3})	1.608	1.622
μ (mm-1)	1.183	1.548
Crystal size (mm)		
Data meas.	40451	24128
+Unique d	5013	14028
R(int)	0.0946	0.0943
Data with I>2σ(I)	3236	14028
Parameters	428	977
wR2 (all data)	0.1120	0.2292
S (all data)	0.977	
R1 (I > 2σ(I))	0.0562	0.0875

Table 2.19. The salts, triethanolammonium nitrate and 3,5-dinitrobenzoate triethanommaonium.

Compound	(teaH)$^+$($N_2O_4O_2CC_6H_4$)$^-$	(teaH)$^+$(NO_3)$^-$
Formula	$C_{13}H_{19}N_3O_9$	$C_6H_{16}N_2O_6$
Mol mass [g/mol]	361.31	212.21
Space group	P21/n	P12/c
a (Å)	12.8871(11)	6.4732(5)

b (Å)	7.0860(6)	16.2056(12)
c (Å)	18.0578(15)	9.3201(7)
α (°)	90.00	90.00
β (°)	106.0990(10)	90.693(1)
γ (°)	90.00	90.00
V (Å^3)	1584.3(2)	977.63(13)
Z	4	4
T (K)	100(2)	100(2)
Radiation	Mo Kα	Mo Kα
F(000)	760	456
ρ_{cale} (g/cm^{-3})	1.515	1.442
μ (mm-1)	0.129	0.128
Crystal size (mm)	0.38x0.29x0.22	0.28x0.25x0.19
Data meas.	14340	9259
+Unique d	3533	2210
R(int)	0.0239	0.0358
Data with I>2σ(I)	3031	2029
Parameters	302	192
wR2 (all data)	0.1012	0.0835
S (all data)	1.035	1.075
R1 (I > 2σ(I))	0.0380	0.0328

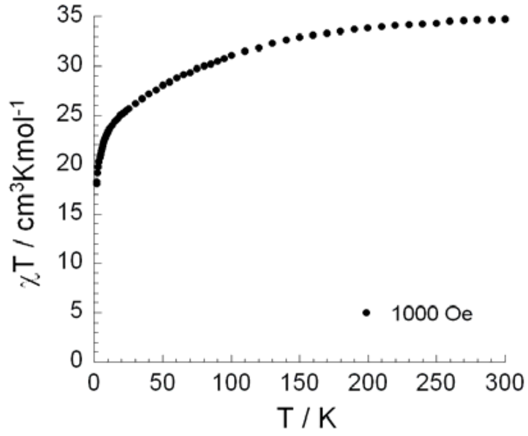
χT / cm³Kmol⁻¹
T / K
● 1000 Oe
0
5
10
15
20
25
30
35
0
50
100
150
200
250
300

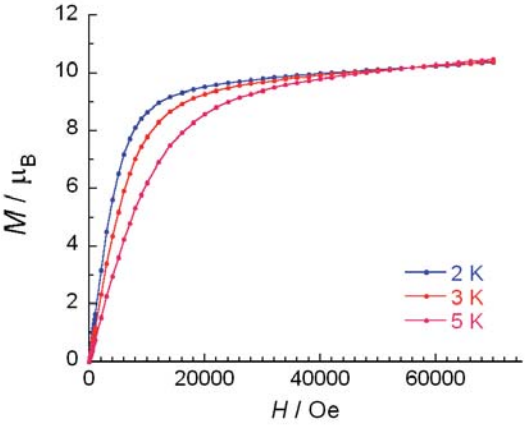
M / μB
H / Oe
2 K
3 K
5 K
0
2
4
6
8
10
12
0
20000
40000
60000

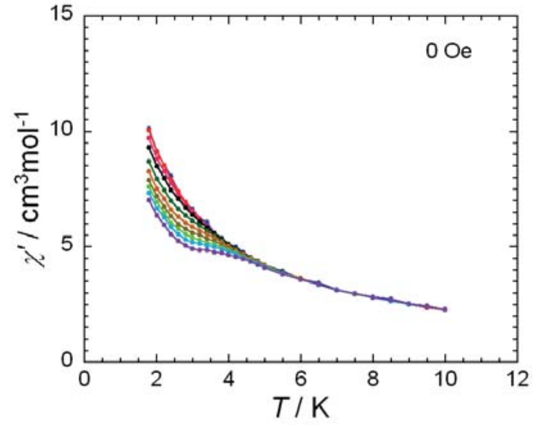
χ′ / cm³mol⁻¹
T / K
0 Oe
0
5
10
15
0
2
4
6
8
10
12

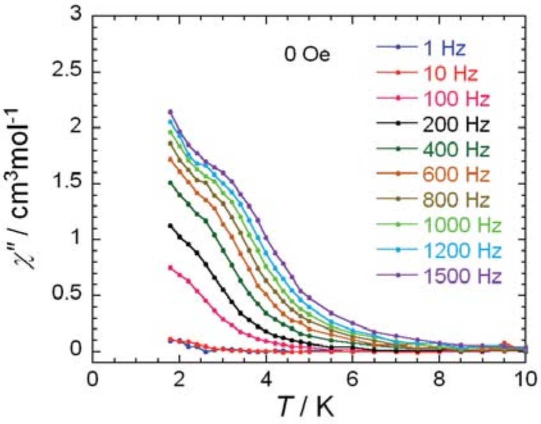
χ″ / cm³mol⁻¹
T / K
0 Oe
1 Hz
10 Hz
100 Hz
200 Hz
400 Hz
600 Hz
800 Hz
1000 Hz
1200 Hz
1500 Hz
0
0.5
1
1.5
2
2.5
3
0
2
4
6
8
10

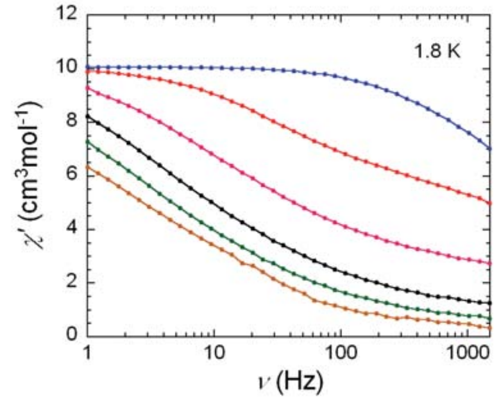
χ′ (cm³mol⁻¹)
ν (Hz)
1.8 K
0
2
4
6
8
10
12
1
10
100
1000

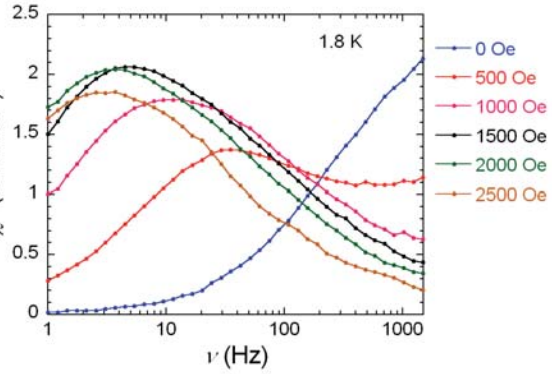
χ″ (cm³mol⁻¹)
ν (Hz)
1.8 K
0 Oe
500 Oe
1000 Oe
1500 Oe
2000 Oe
2500 Oe
0
0.5
1
1.5
2
2.5
1
10
100
1000

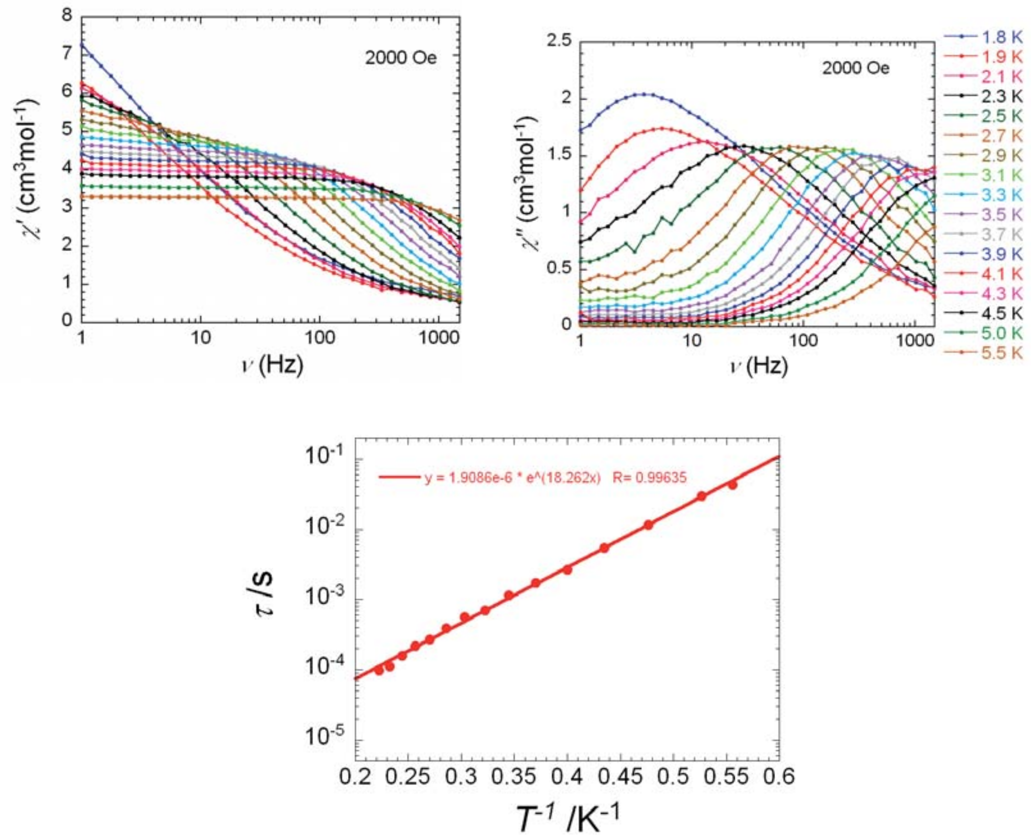

Figure 2. 35. temperature-dependence of the χT product under 0.1 T and the magnetization plots of **Fe$_2$Dy$_2$** compound **2.8$^{\text{teaH-6}p\text{N3}}$,** the plots of in-phase and out-of-phase ac susceptibilities signals vs. temperature at indicated oscillation frequencies as well as signals vs. frequency at 1.8 K and under the indicated dc fields for compounds **2.8$^{\text{teaH-6}p\text{N3}}$** and the Arrhenius plot as lowest.

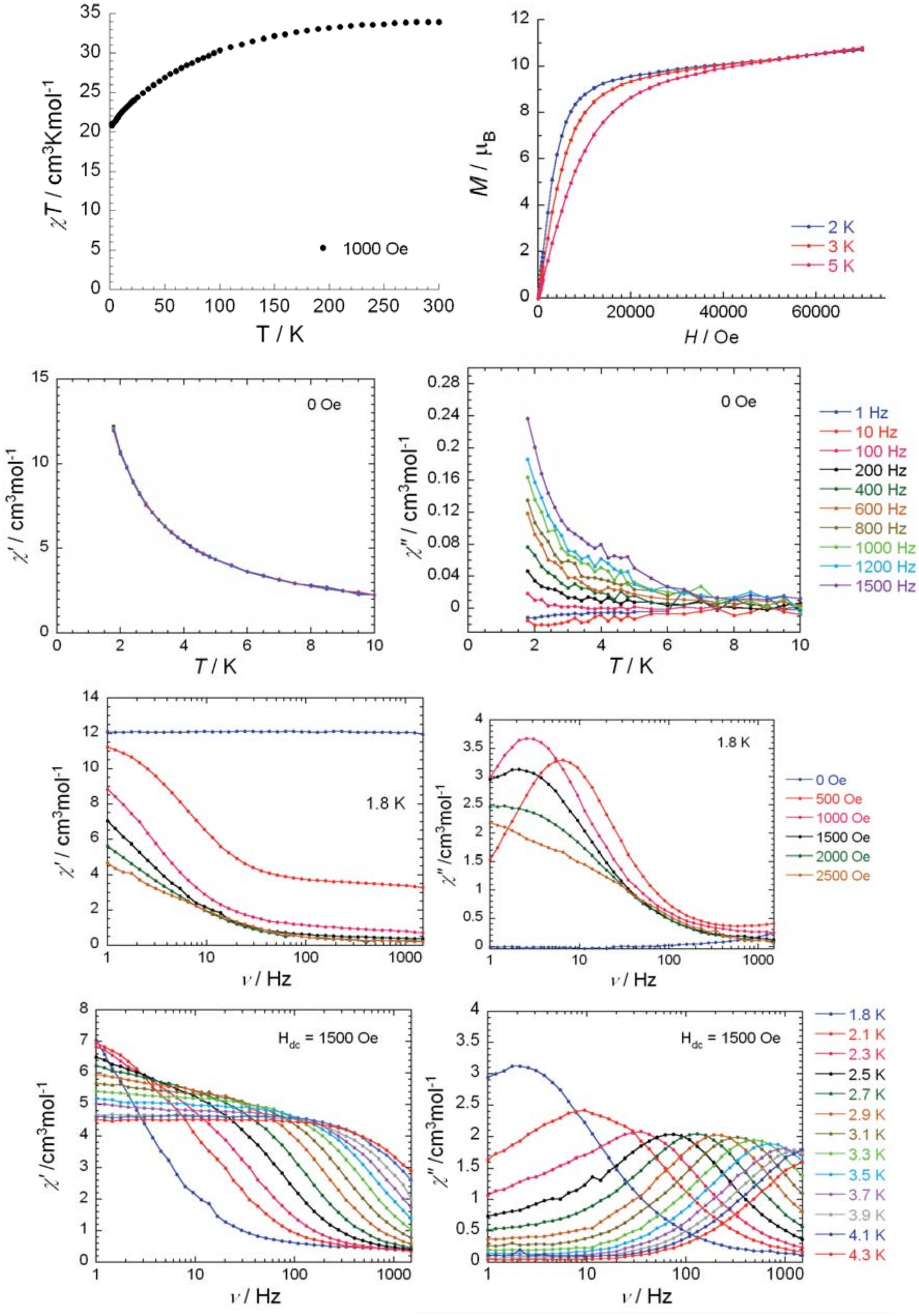
χT / cm³Kmol⁻¹
T / K
1000 Oe
M / μB
H / Oe
2 K
3 K
5 K
χ' / cm³mol⁻¹
T / K
0 Oe
χ'' / cm³mol⁻¹
T / K
0 Oe
1 Hz
10 Hz
100 Hz
200 Hz
400 Hz
600 Hz
800 Hz
1000 Hz
1200 Hz
1500 Hz
χ' / cm³mol⁻¹
ν / Hz
1.8 K
χ'' /cm³mol⁻¹
ν / Hz
1.8 K
0 Oe
500 Oe
1000 Oe
1500 Oe
2000 Oe
2500 Oe
χ' /cm³mol⁻¹
ν / Hz
Hdc = 1500 Oe
χ'' /cm³mol⁻¹
ν / Hz
Hdc = 1500 Oe
1.8 K
2.1 K
2.3 K
2.5 K
2.7 K
2.9 K
3.1 K
3.3 K
3.5 K
3.7 K
3.9 K
4.1 K
4.3 K

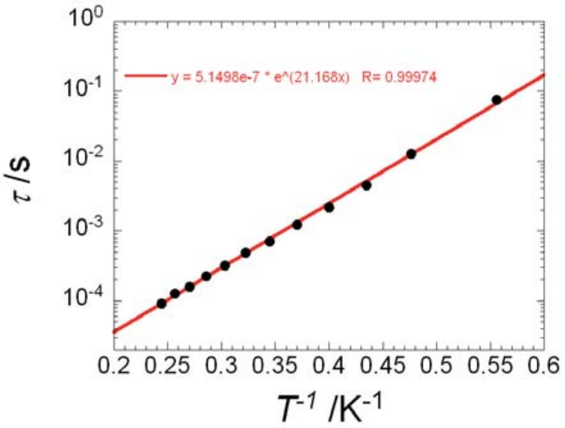

Figure 2. 36. temperature-dependence of the χT product under 0.1 T and the magnetization plots of $\mathbf{Fe_2Dy_2}$ compound $\mathbf{2.8}^{\text{teaH-6}m\text{Me}}$**,** the plots of in-phase and out-of-phase ac susceptibilities signals vs. temperature at indicated oscillation frequencies as well as signals vs. frequency at 1.8 K and under the indicated dc fields for compounds $\mathbf{2.8}^{\text{teaH-6}m\text{Me}}$ and the Arrhenius plot as lowest.

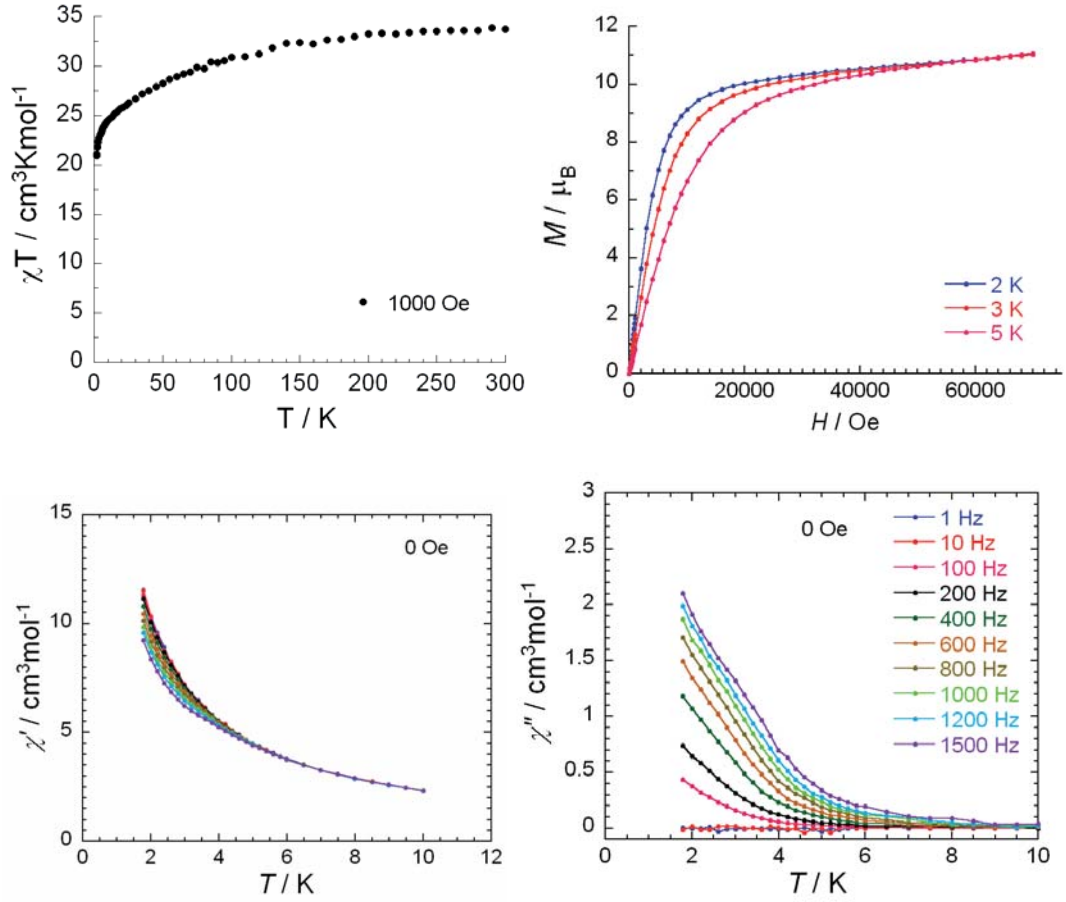

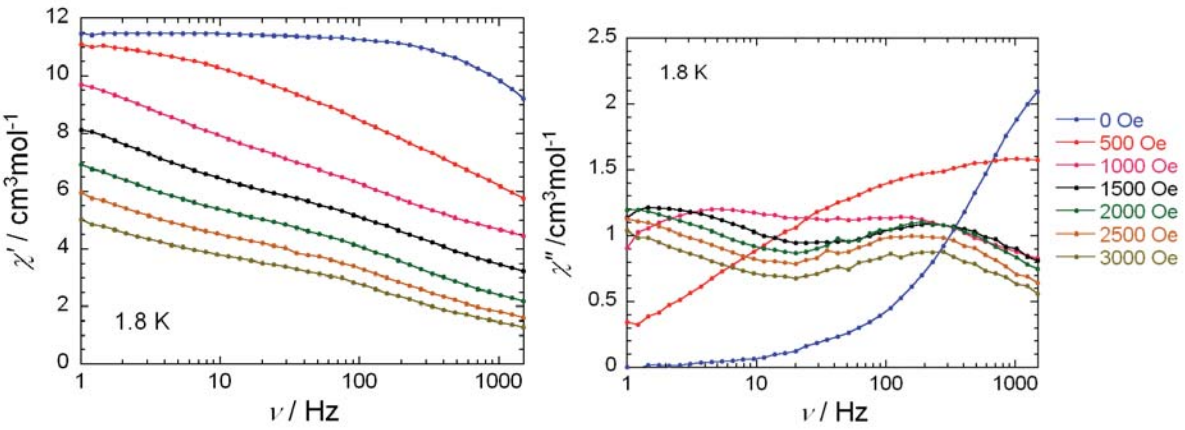

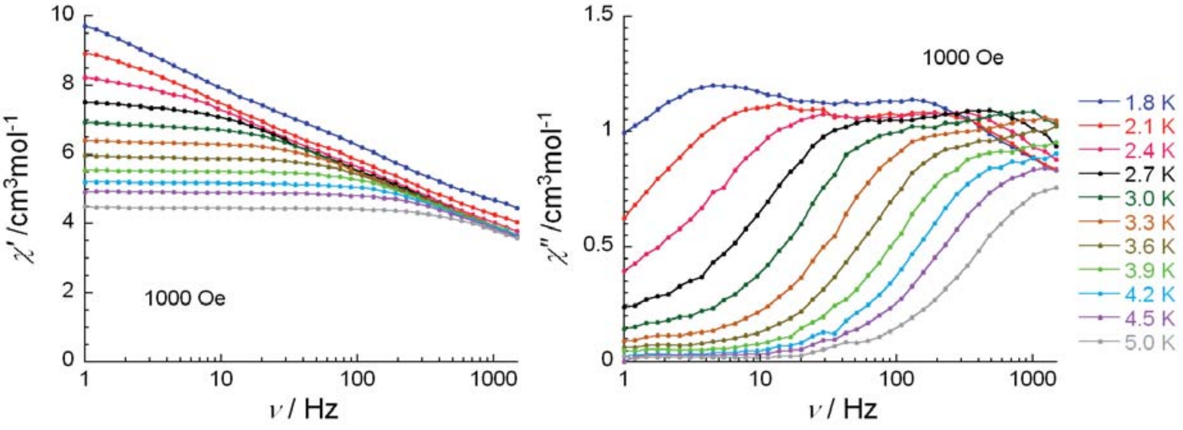

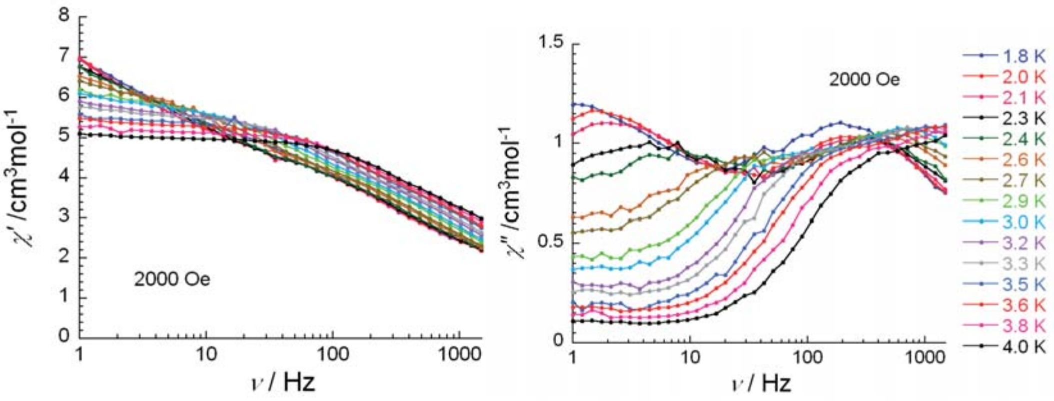

under 2000 Oe

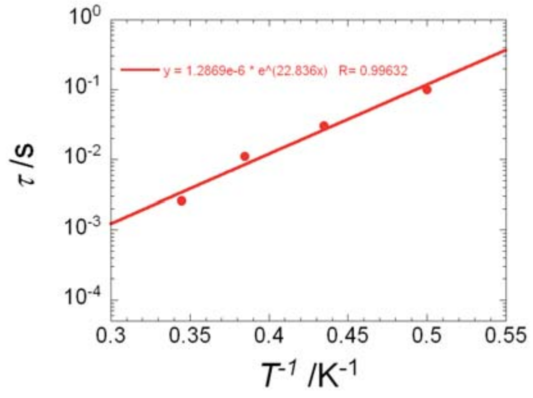

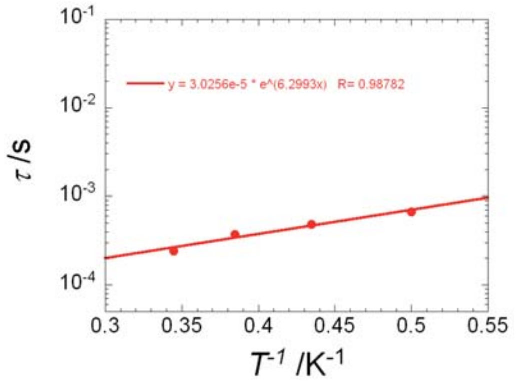

Figure 2. 37. temperature-dependence of the χT product under 0.1 T and the magnetization plots of $\mathbf{Fe_2Dy_2}$ compound $\mathbf{2.8}^{\mathbf{teaH\text{-}6}\boldsymbol{m}\mathbf{CN}}$**,** the plots of in-phase and out-of-phase ac susceptibilities signals vs. temperature at indicated oscillation frequencies as well as signals vs. frequency at 1.8 K and under the indicated dc fields for compounds $\mathbf{2.8}^{\mathbf{teaH\text{-}6}\boldsymbol{m}\mathbf{CN}}$ and the Arrhenius plot as lowest.

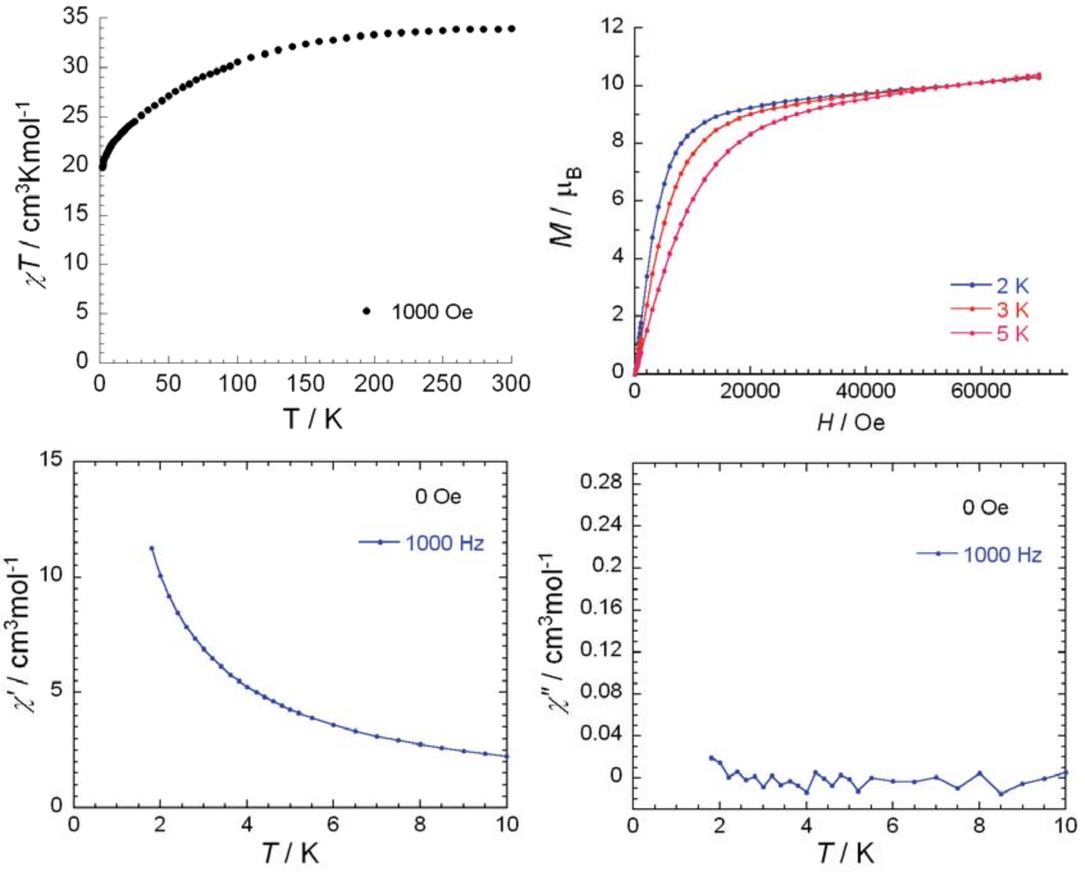

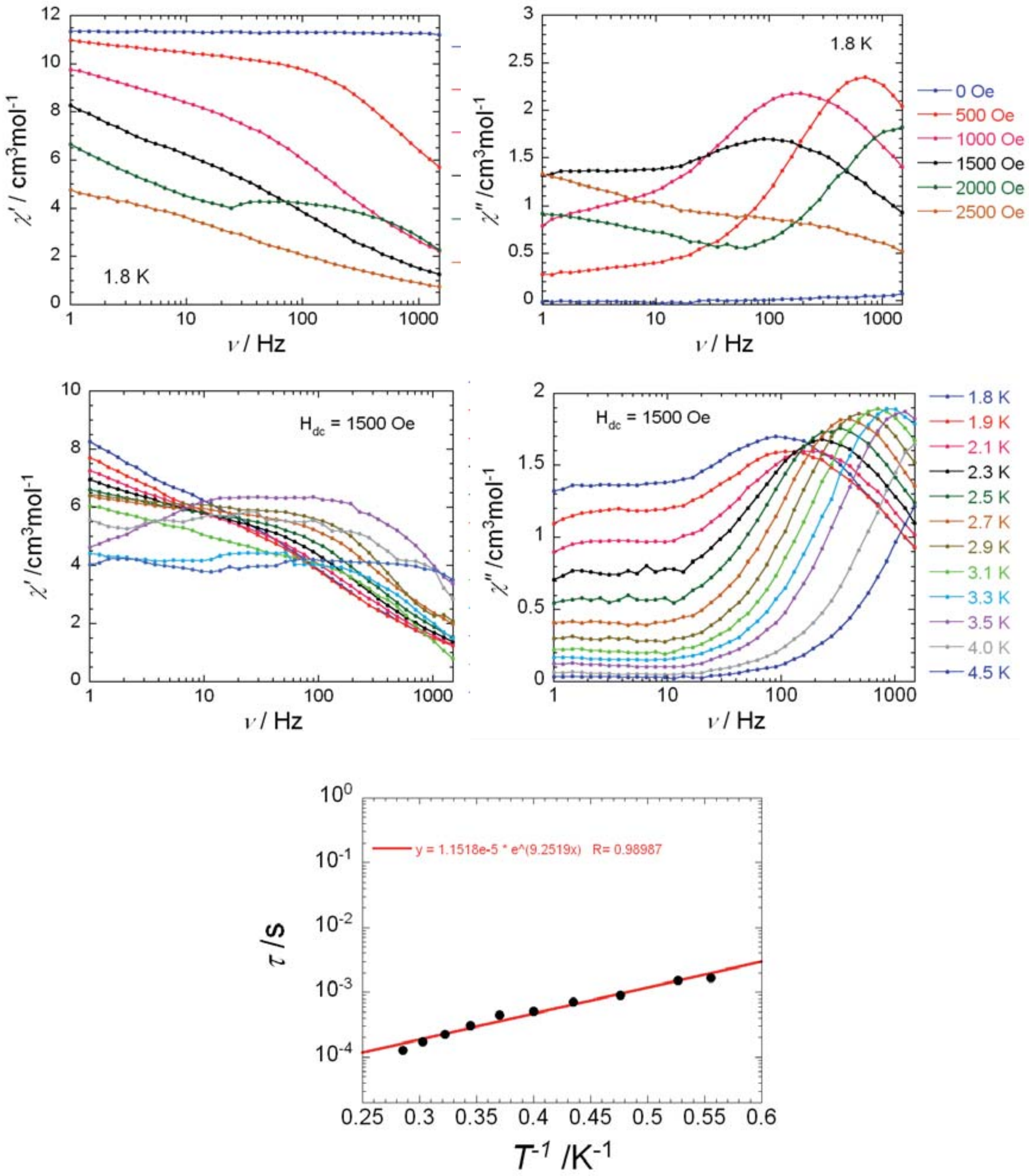

Figure 2. 38. temperature-dependence of the χT product under 0.1 T and the magnetization plots of **Fe_2Dy_2** compound **$2.8^{teaH\text{-}4mMe}$,** the plots of in-phase and out-of-phase ac susceptibilities signals vs. temperature at indicated oscillation frequencies as well as signals vs. frequency at 1.8 K and under the indicated dc fields for compounds **$2.8^{teaH\text{-}4mMe}$** and the Arrhenius plot as lowest.

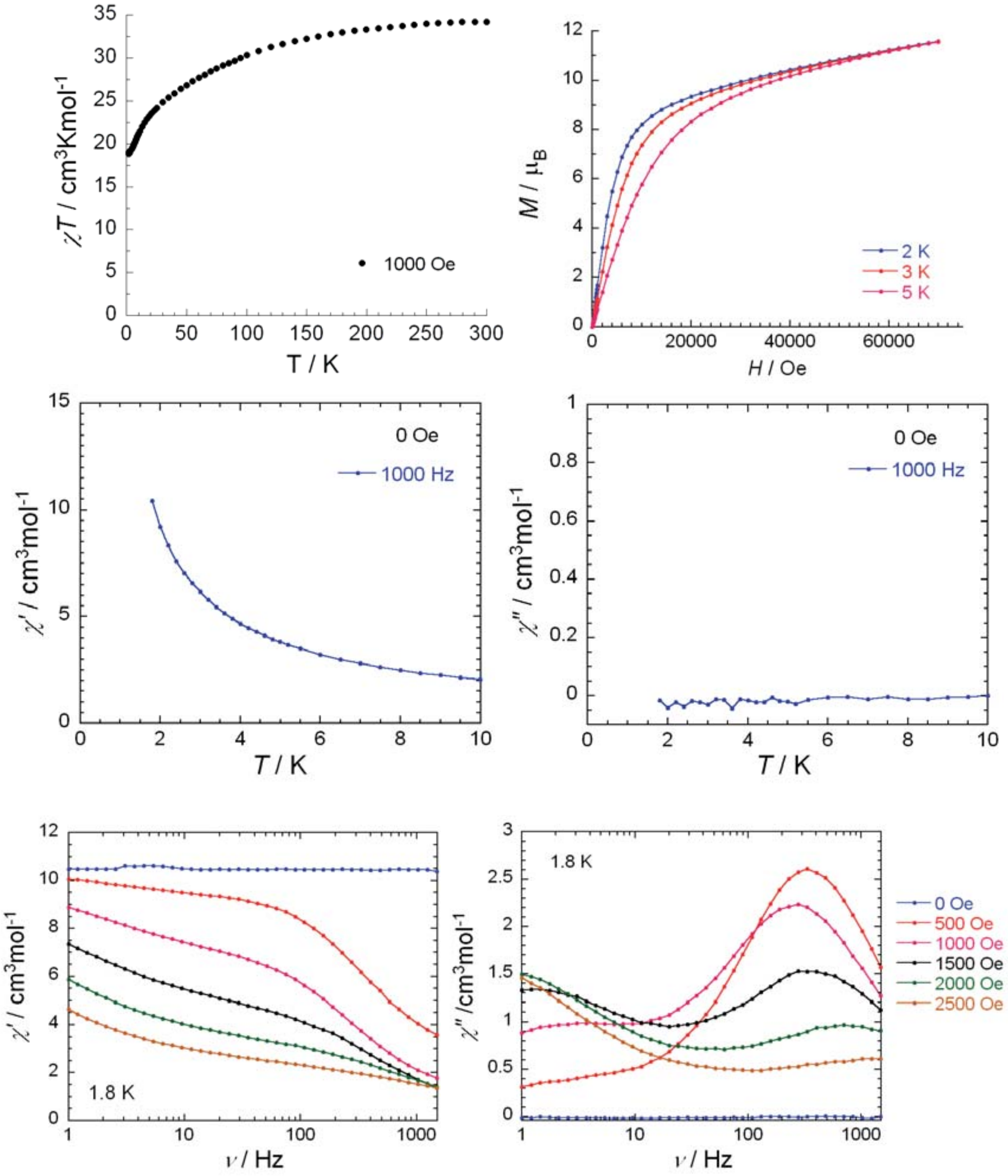
χT / cm³Kmol⁻¹
35
30
25
20
15
10
5
0
1000 Oe
0
50
100
150
200
250
300
T / K
M / μB
12
10
8
6
4
2
0
2 K
3 K
5 K
0
20000
40000
60000
H / Oe
χ′ / cm³mol⁻¹
15
10
5
0
0 Oe
1000 Hz
0
2
4
6
8
10
T / K
χ″ / cm³mol⁻¹
1
0.8
0.6
0.4
0.2
0
0 Oe
1000 Hz
0
2
4
6
8
10
T / K
χ′ / cm³mol⁻¹
12
10
8
6
4
2
0
1.8 K
1
10
100
1000
ν / Hz
χ″ /cm³mol⁻¹
3
2.5
2
1.5
1
0.5
0
1.8 K
1
10
100
1000
ν / Hz
0 Oe
500 Oe
1000 Oe
1500 Oe
2000 Oe
2500 Oe

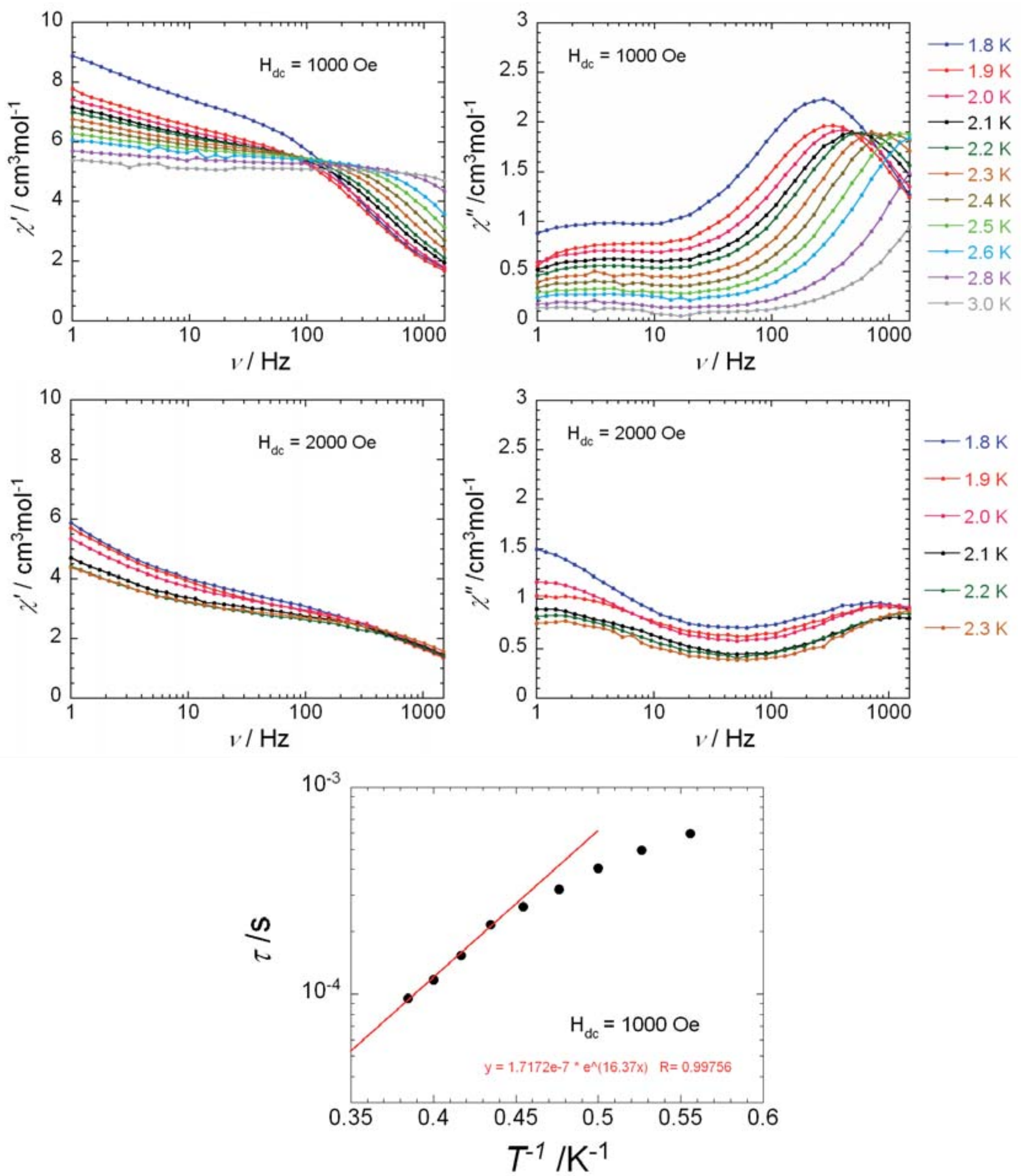

Figure 2. 39. temperature-dependence of the χT product under 0.1 T and the magnetization plots of **Fe_2Dy_2** compound **$2.8^{teaH\text{-}4mCN}$,** the plots of in-phase and out-of-phase ac susceptibilities signals vs. temperature at indicated oscillation frequencies as well as signals vs. frequency at 1.8 K and under the indicated dc fields for compounds **$2.8^{teaH\text{-}4mCN}$** and the Arrhenius plot as lowest.

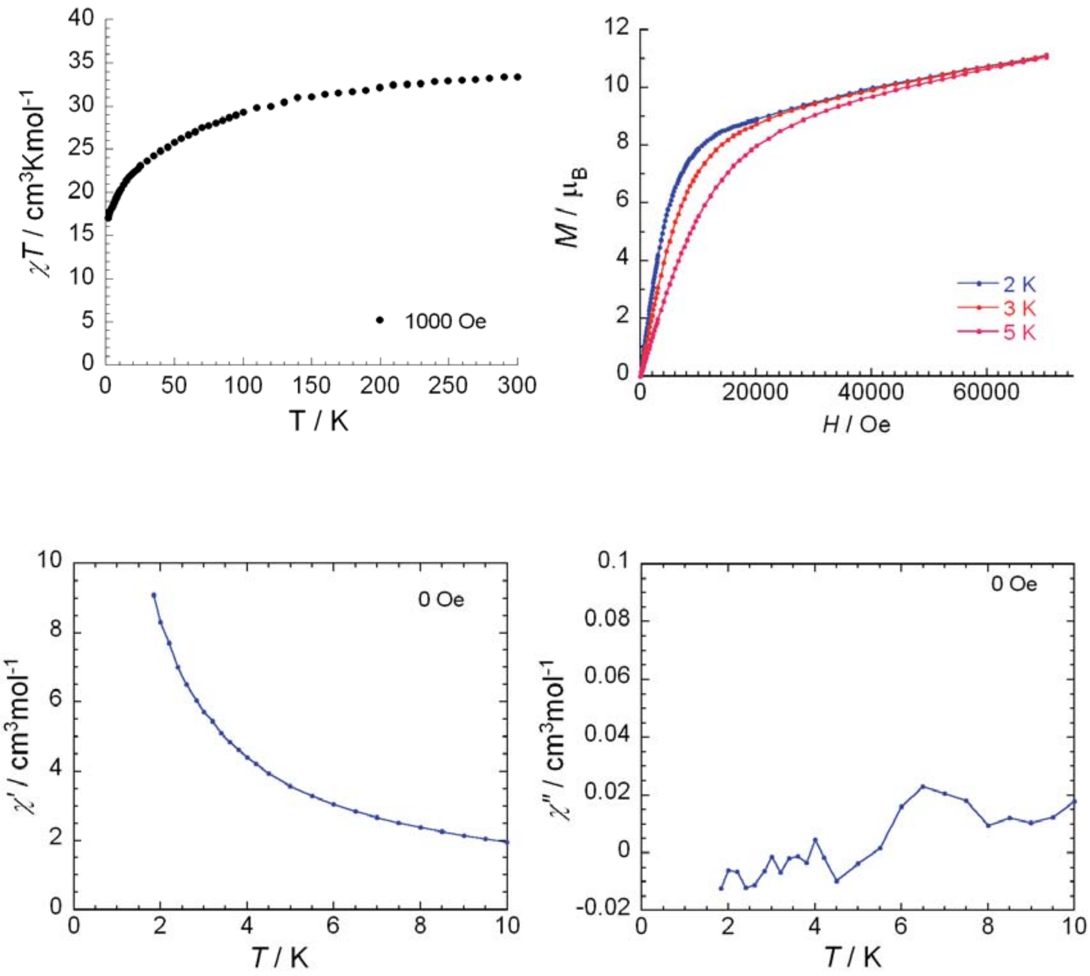

Figure 2. 40. temperature-dependence of the χT product under 0.1 T and the magnetization plots of **Fe_2Dy_2** compound **$2.8^{teaH\text{-}4pPh}$**, the plots of in-phase and out-of-phase ac susceptibilities signals vs. temperature at indicated oscillation frequencies as well as signals vs. frequency at 1.8 K and under the indicated dc fields for compounds **$2.8^{teaH\text{-}4pPh}$** and the Arrhenius plot as lowest.

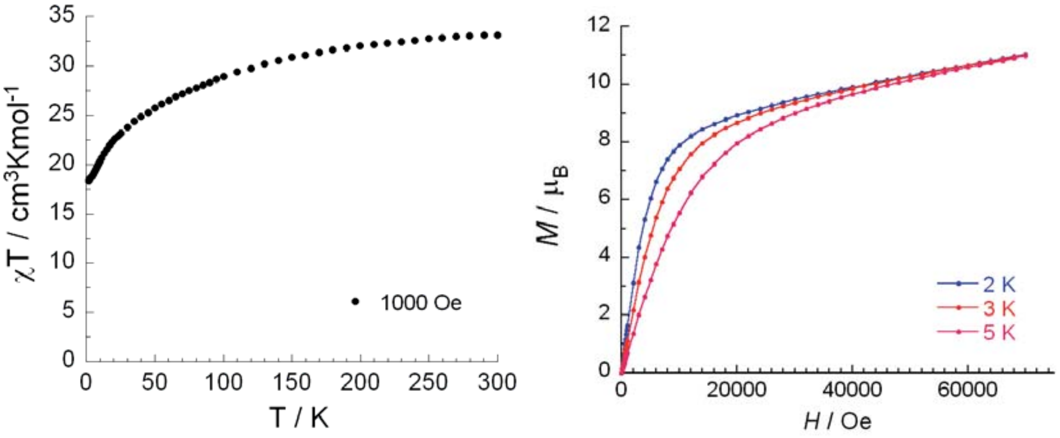

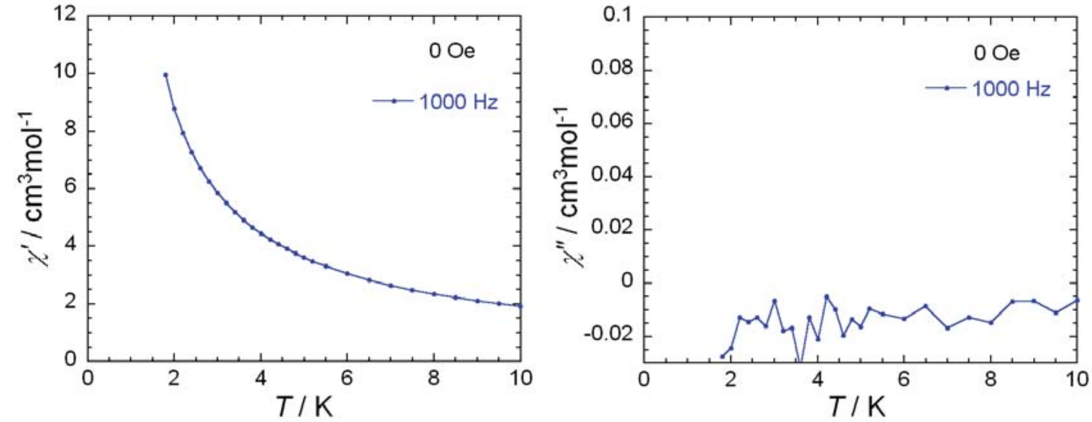
χ′ / cm³mol⁻¹
0 Oe
1000 Hz
T / K
χ″ / cm³mol⁻¹
0 Oe
1000 Hz
T / K

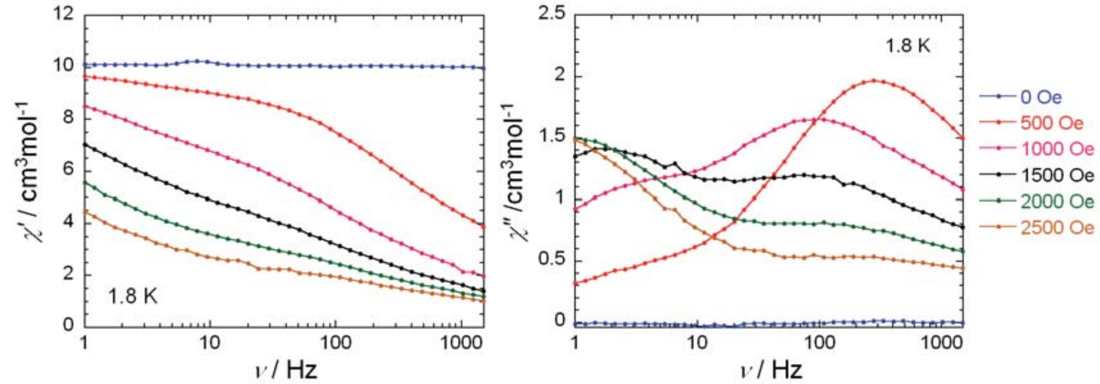
χ′ / cm³mol⁻¹
1.8 K
ν / Hz
χ″ /cm³mol⁻¹
1.8 K
ν / Hz
0 Oe
500 Oe
1000 Oe
1500 Oe
2000 Oe
2500 Oe

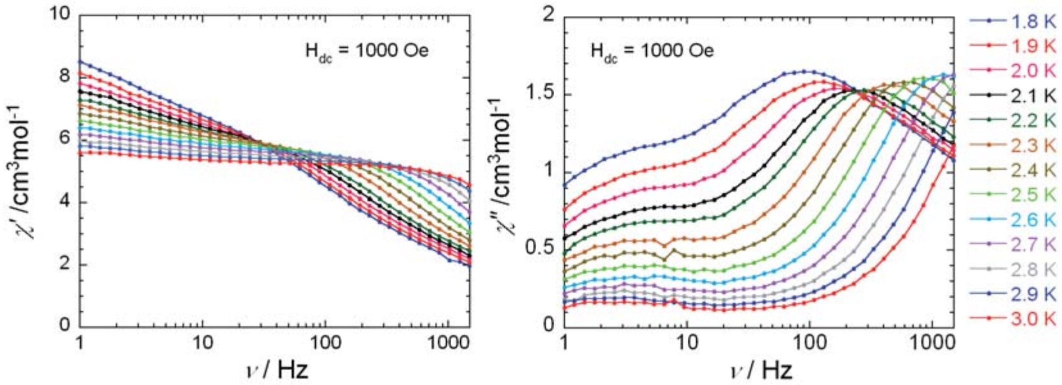
χ′ /cm³mol⁻¹
H_dc = 1000 Oe
ν / Hz
χ″ /cm³mol⁻¹
H_dc = 1000 Oe
ν / Hz
1.8 K
1.9 K
2.0 K
2.1 K
2.2 K
2.3 K
2.4 K
2.5 K
2.6 K
2.7 K
2.8 K
2.9 K
3.0 K

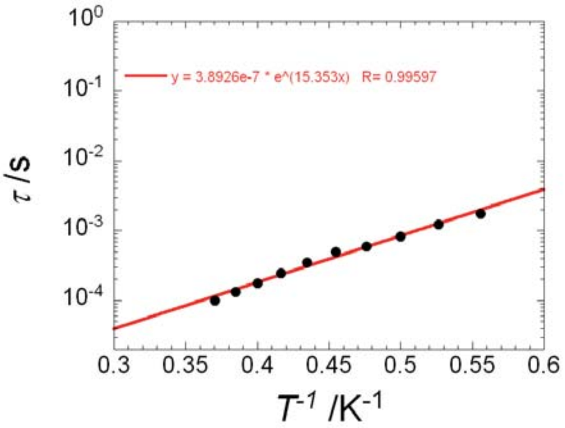
y = 3.8926e-7 * e^(15.353x) R= 0.99597
τ /s
T⁻¹ /K⁻¹

Figure 2. 41. temperature-dependence of the χT product under 0.1 T and the magnetization plots of $\mathbf{Fe_2Dy_2}$ compound $\mathbf{2.8^{teaH\text{-}4\mathit{p}H}}$**,** the plots of in-phase and out-of-phase ac susceptibilities signals vs. temperature at indicated oscillation frequencies as well as signals vs. frequency at 1.8 K and under the indicated dc fields for compounds $\mathbf{2.8^{teaH\text{-}4\mathit{p}H}}$ and the Arrhenius plot as lowest.

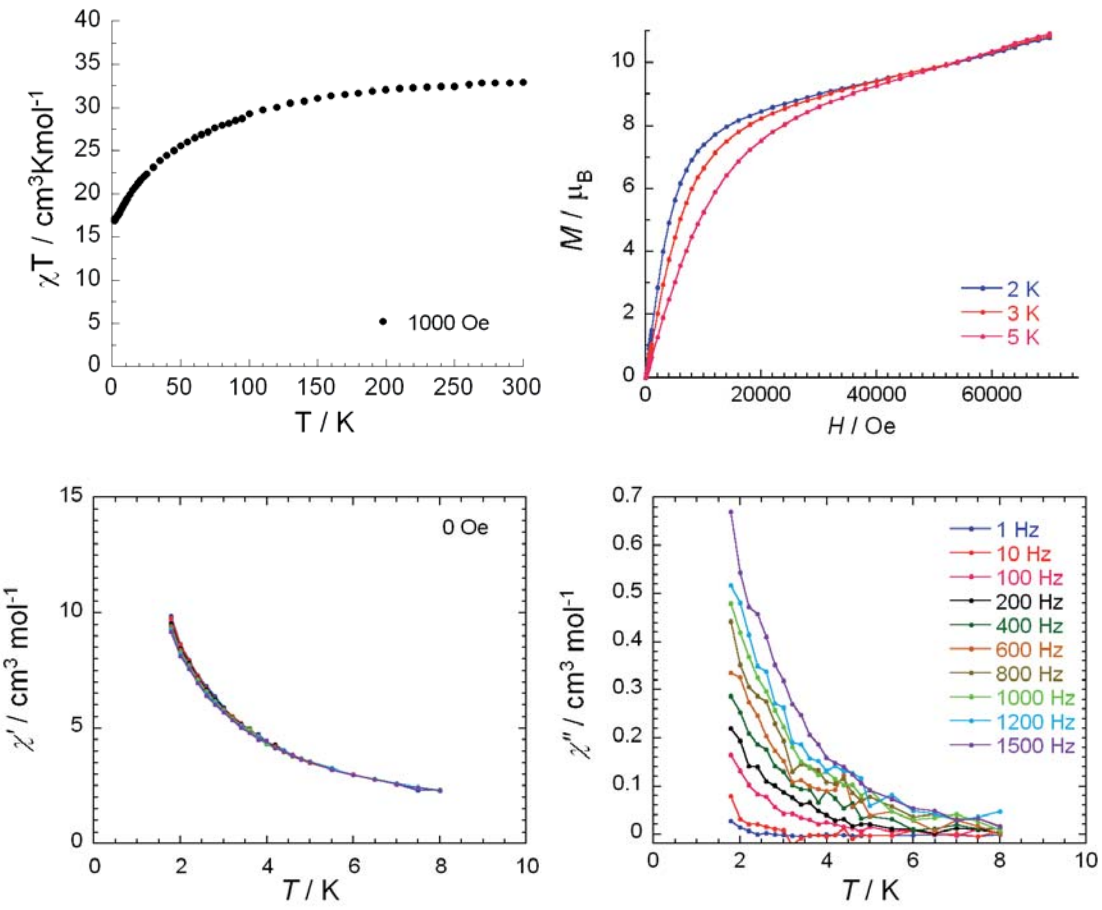

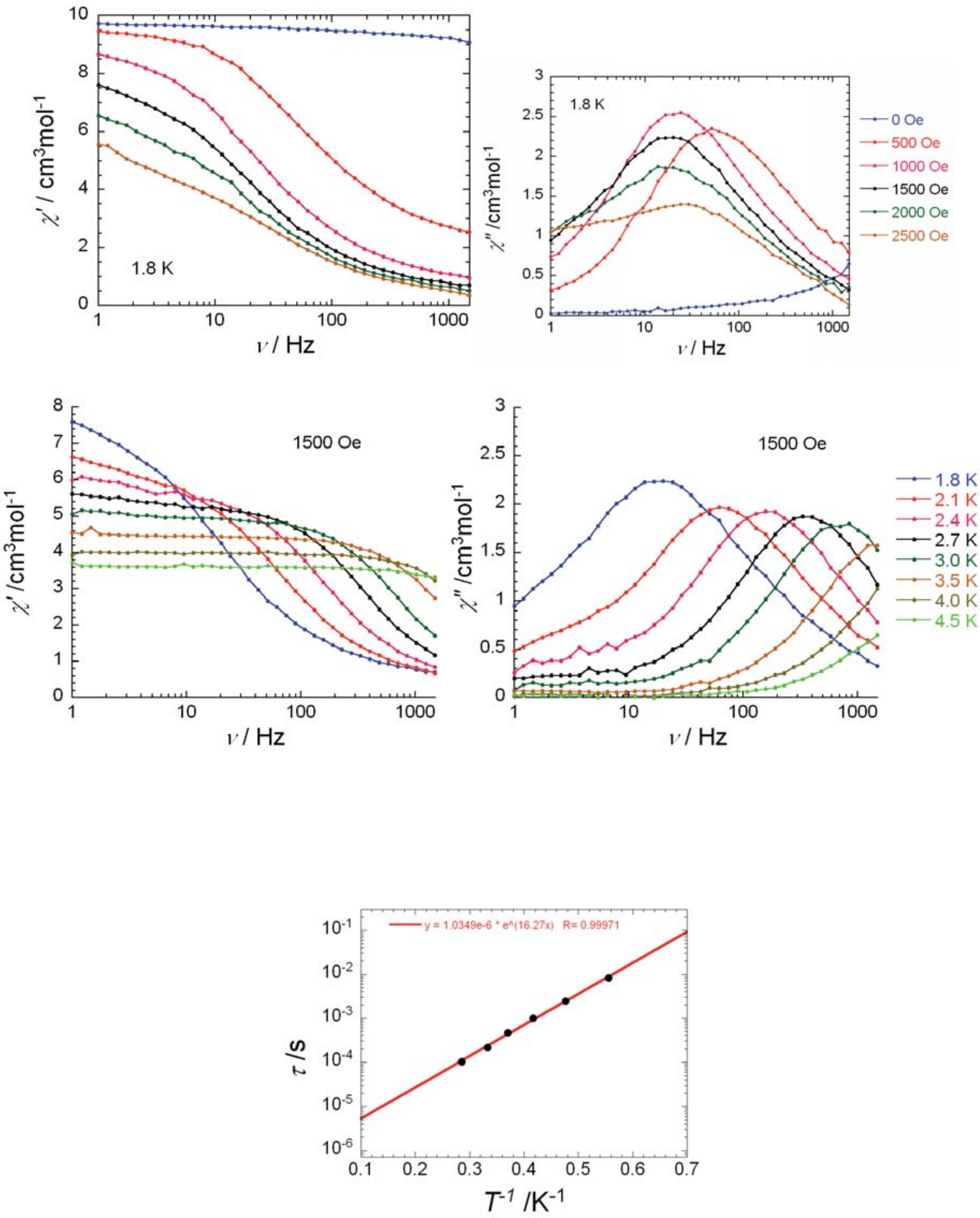

Figure 2. 42. temperature-dependence of the χT product under 0.1 T and the magnetization plots of **Fe_2Dy_2** compound **$2.8^{teaH\text{-}6(9\text{-}anthr)}$,** the plots of in-phase and out-of-phase ac susceptibilities signals vs. temperature at indicated oscillation frequencies as well as signals vs. frequency at 1.8 K and under the indicated dc fields for compounds **$2.8^{teaH\text{-}6(9\text{-}anthr)}$** and the Arrhenius plot as lowest.

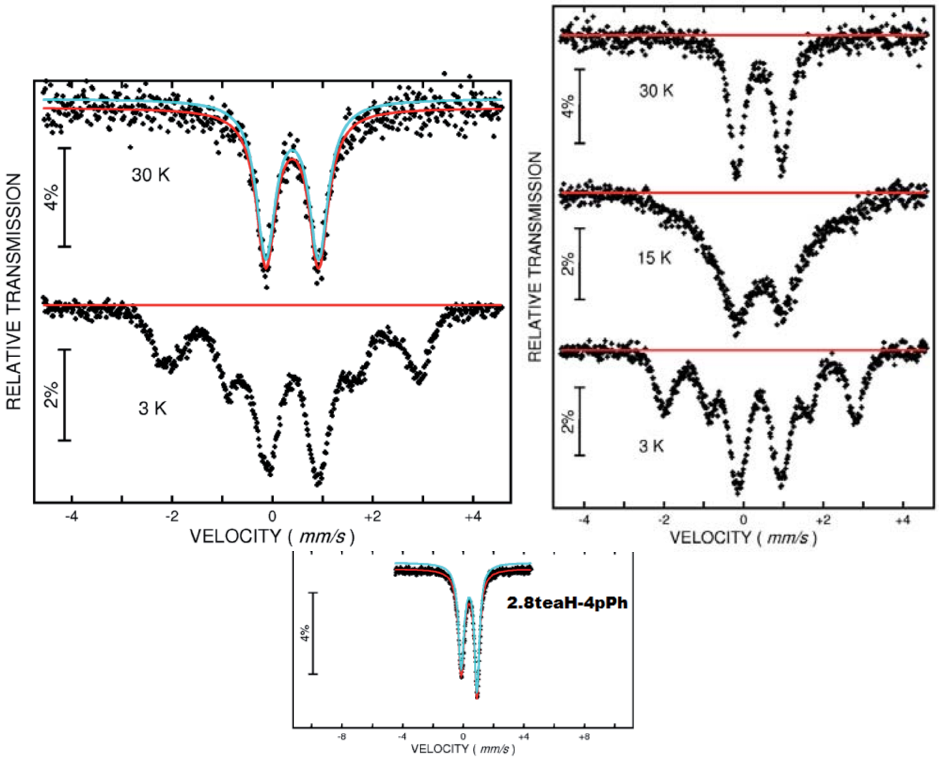

Figure 2.54. (Upper, left) the MS at 30 and 3 K for $\mathbf{2.8}^{\textbf{teaH-6}p\textbf{N3}}$, the MS at 30, 15 and 3K of $\mathbf{2.8}^{\textbf{teaH-6}m\textbf{CN}}$. (Upper, Right) the MS at 3K for $\mathbf{2.8}^{\textbf{teaH-4}p\textbf{Ph}}$**.**

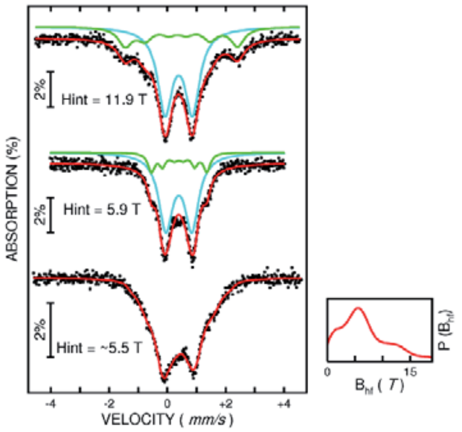

Figure 2.55. The MS at 3K for $\mathbf{2.8}^{\textbf{teaH-6}p\textbf{N(Me)2}}$ compared with $\mathbf{2.8}^{\textbf{teaH-6pt}}$ and the referecnce compound $\mathbf{2.8}^{\textbf{teaH-6}p\textbf{H}}$. (Right) MS of $\mathbf{2.8}^{\textbf{teaH-4}p\textbf{H}}$ at 3K.

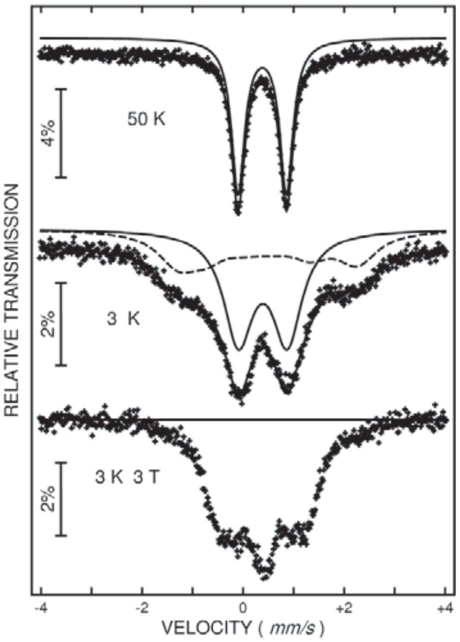

Figure 2.56. (Left) The MS at 50K, 3K and 3K, 3 T for **2.8**$^{\text{Me-teaH-6}p\text{H}}$. (Right) MS of **2.8**$^{\text{Me-teaH-4}p\text{H at 3K.}}$

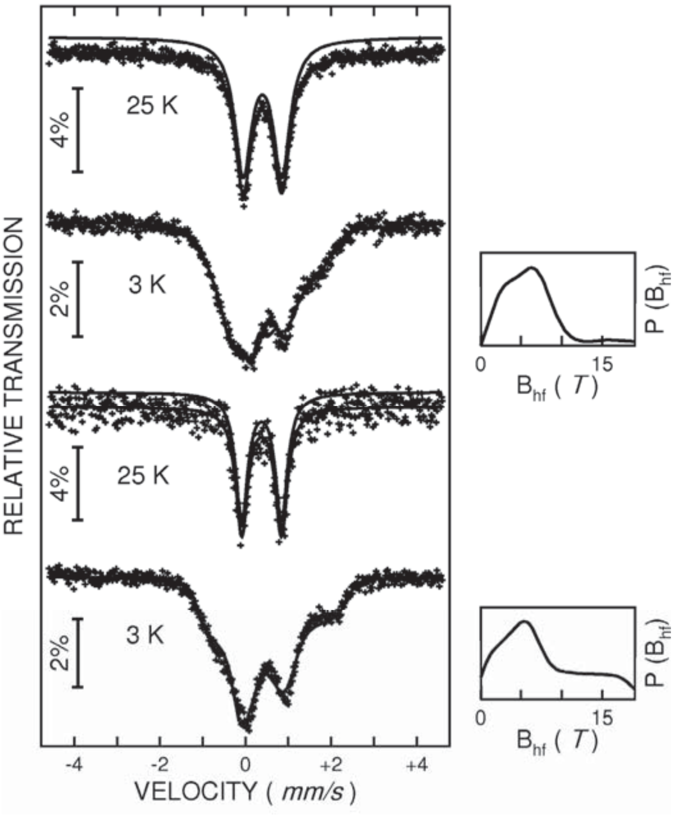

Table 2.58. The first two represent the MS of **2.8**$^{\text{teaH-6(9-anthr)}}$ at 25 K and 3K. The last two represent the MS of **2.8**$^{\text{teaH-6(2-naphth)}}$ at 25K and 3K.

Table 2.26. Summary of electronic effects (based on electro negativity) for selected substituents.

Substituent	I/ M Effect	Hammet Constants[]	Dipolmomnet of substituents [D][]
H	No effect	0.00	0
Me	+I	σ_p (-0.17) σ_m (-0.07)	+0.35
^{t}Bu	+I	σ_p () σ_m ()	
N(Me)$_2$	+I/+M	σ_p (0.23) σ_m (0.39)	
OMe	+M	σ_p (-0.27)	
Ph	+I/-M	σ_p ()	
Br	-I/+M	σ_p (0.23)	-1.52
F	-I/M	σ_p (0.06) σ_m (0.34)	
N$_3$	-I/-M	σ_p (0.37)	Not found
CN	-I/-M	σ_p (0.66) σ_m (0.56)	-3.92**
NO$_2$	-I/-M	σ_p (0.78) σ_m (0.71)	-3.95**

Table 2.27. The calculated Mulliken Charges and dipolmoments for selected susbtituents.

Subst.	Mullik. qO9	Mullik.q O10	dipole moment
H	-0,591674	-0,591651	9,0073
Me	-0,592327	-0,592329	11,3239
^{t}Bu	-0,590709	-0,591146	15,831
N(Me)$_2$	-0,594270	-0,594418	15,3212
NO$_2$	-0,561385	-0,563640	6,1992

Ph	-0,586635	-0,586637	17,3204
3,5-dinitro	-0,559591	-0,559600	7,9297
N_3	-0,584505	-0,584012	10,7059
CN	-0,578139	-0,578139	6,7781

Table 2.28. The x,y and z components of the Dipolmoment and the Polarisability tensor for *meta*-methyl, *para*-methyl, *para*-cyano and *meta*-cyano benzoate ligands.

Anion -X	method	μ_x	μ_y	μ_z	Polarisability tensor		
meta-Me	MP3	11.1164	1.9436	0.0001			
	B3LYP	10.4914	1.7950	-0.0002	139.540	1.660	0.00
						123.360	0.00
							65.770
para-Me	MP3	12.2102	-0.0001	0.0043			
	B3LYP	11.5219	-0.0002	-0.0037	148.894	-0.014	0.736
						116.087	-0.001
							65.662
	MP3	7.3532	0.0001	0.0018			
para-CN	B3LYP	6.7370	0.000	0.0000	175.6099	0.004	0.0025
						110.3159	0.00135
							60.1139
meta-CN	MP3						
	B3LYP	6.2528	5.8255	0.0000	156.2666	10.820	-0.000044
						124.560	0.0000692
	MP3	11.0217	0.0852	0.0013			60.3552

Table 2.29. Dissociation energy calculations for *para* (H and CN) and *meta* (CN) substituents.

MP3						
E	*Para* H	*Para* CN	*Meta* CN			Units
E_0 HF	-417.86079	-509.62466	-509.62425			Hartree
E_{diss} HF	-417.59854	-509.39943	-509.42932			Hartree
ΔE HF	7.14	6.13	5.30			eV
E_0 MP2	-419.22717	-511.280219	-511.278933			Hartree
E_{diss} MP2	-418.86055	-510.96178	-510.969310			Hartree
ΔE MP2	9.98	8.67	8.42			eV
E_0 MP3	-419.23008	-511.2674315	-511.26660			Hartree
E_{diss} MP3	-418.88377	-510.97486	-510.97772			Hartree
ΔE MP3	9.42	7.96	7.86			kJ/mol
Charge of dissociated X	0	-1	0			
Dissociate state of lower energy	triplet	triplet	triplet			Hartree
		Singlet -509.31231 -510.94834 -510.94256	Singlet -509.32210 -510.96865 -510.95611			kJ/mol

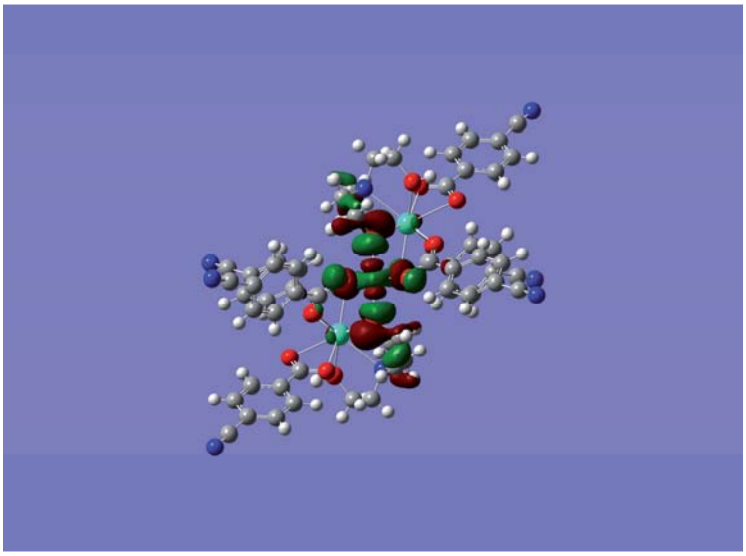

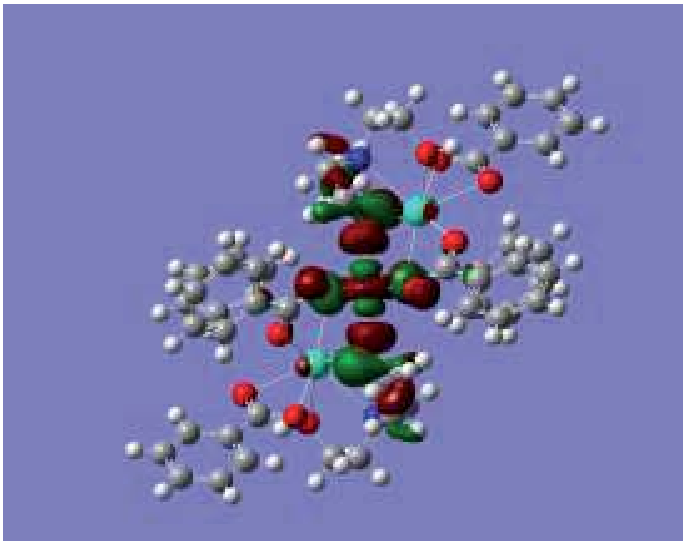

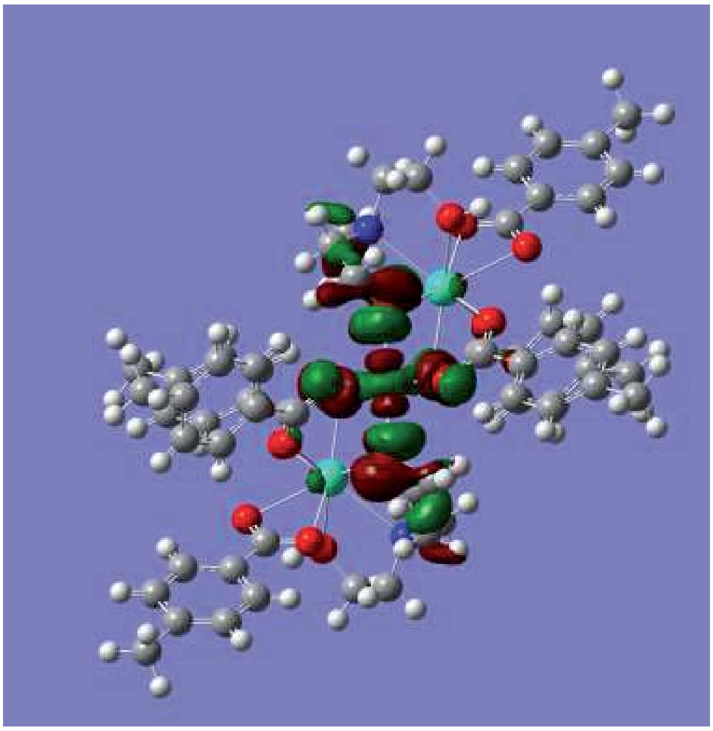

Figure 2.65. Orientation of d-orbitals of Fe.

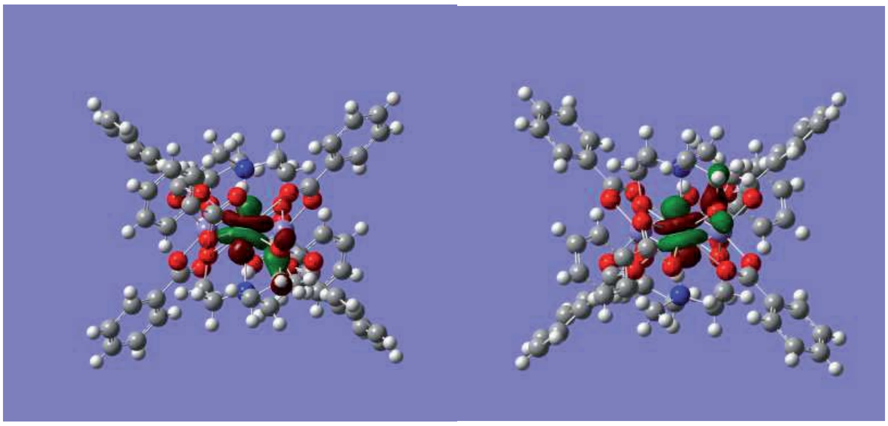

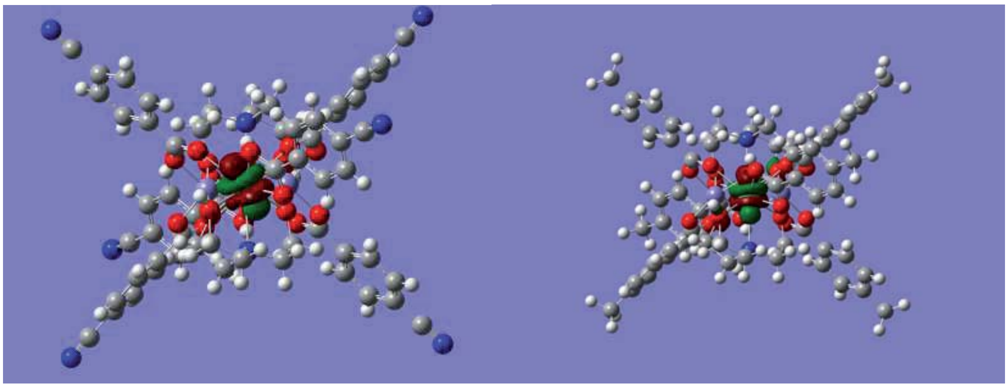

Figure 2.66. Orientations of the orbital f_{z3} of Dy^{III} ions. (upper) for 4H Orb90 and Orb89. (Lower, left) for 4CN and Orb96 and (right) for 4Me and Orb96.

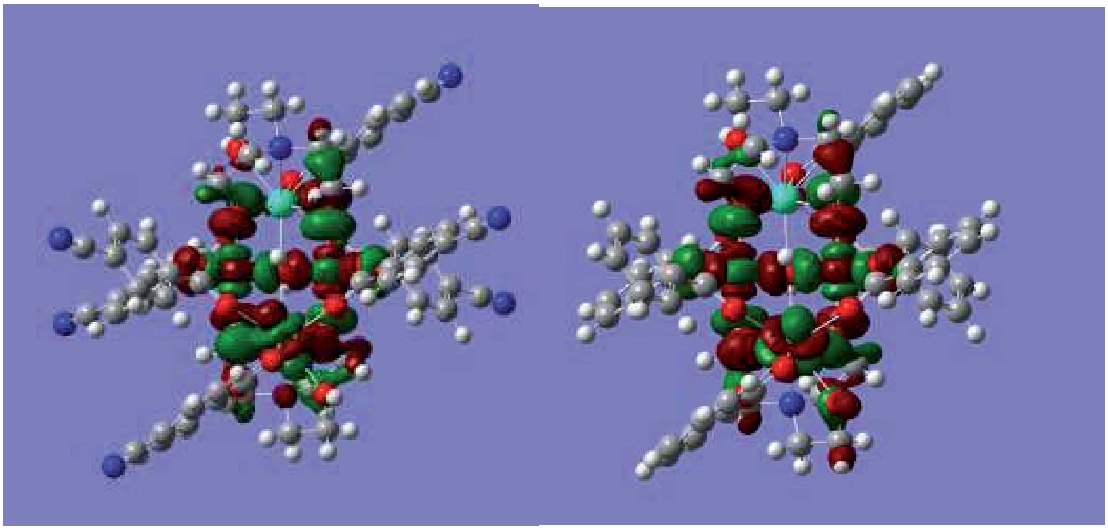

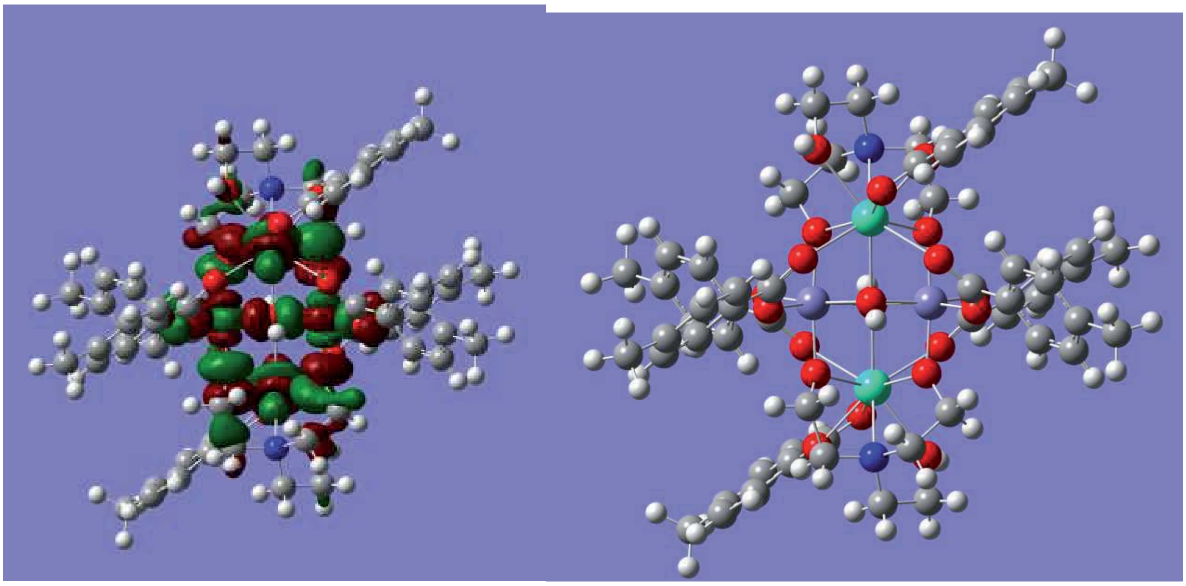

Figure 2.67. Shows how the Dy orbitals oriented toward the Fe orbitals. (Upper, left) HOMO + 96(5) for *p*-CN, (right) HOMO + 90 for *p*-H. (Lower, left) HOMO + 96 for *p*-Me and (right) show how the system oriented in these figures.

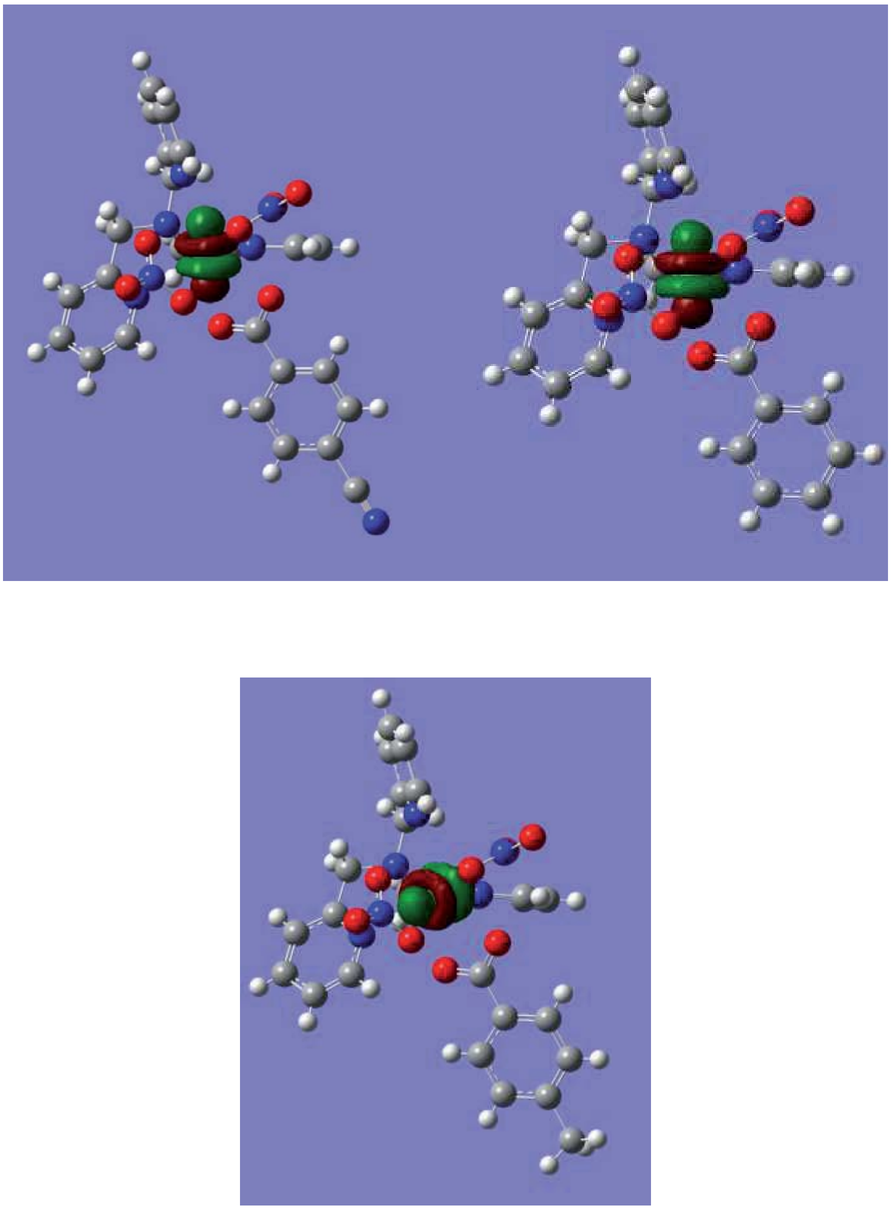

Figure 2.68. Calculations of the mononuclear compound **2.21** for CN, H and Me substituents.

Table 3.1. Crystallographic data of compounds **3.1-3.3.**

Compound	**Fe_5Tm_3 (3.1)**	**Fe_5Yb_3 (3.2)**	**Fe_5Lu_3 (3.3)**
Formula	$C_{110}H_{148.50}F_3Fe_5Tm_3$ $N_{12.50}$ O_{41} S	$C_{108}H_{145.50}F_3Fe_5Yb_3$ $N_{11.50}$ $O_{41}S$	C_{119} H_{162} F_3 Fe_5Yb_3 N_{17} O_{41} S
FW (g mol^{-1})	3177.01	3374.09	3154.08
Crystal system	triclinic	triclinic	triclinic
Color	Pale-yellow	Pale-yellow	Pale-yellow
Space group	P -1	P-1	P-1
a (Å)	16.5406(6)	16.4830(8)	16.5398(11)
b (Å)	19.9598(7)	19.8976(9)	19.9435(12)
c (Å)	20.3517(7)	20.2276(9)	20.2975(13)
α (°)	76.131(3)	76.119(1)	75.95(0)
β (°)	74.346(3)	74.622(1)	74.38(0)
γ (°)	81.272(3)	81.570(1)	81.49(0)
V (Å^3)	6253.9(4)	6185.3(5)	6230.73(16)
Z	2	2	2
T (K)	180(2)	100(2)	123(2)
F(000)	3208	3412	3176
ρ_{calc} (g cm^{-3})	1.573	1.587	1.588

μ (mm^{-1})	2.515	2.630	2.735
Crystal size (mm)		0.28X0.24X0.22	
Data meas.	48836	49751	46052
+Unique d	26538	25848	26298
R(int)	0.0484	0.0781	0.0586
Data with I>2σ(I)	21233	21874	19832
Parameters	1465	1526	1470
wR2 (all data)	0.0784	0.0758	0.0989
S (all data)	1.029	1.042	0.998
R1 (I > 2σ(I))	0.0339	0.0278	0.0266

Table 3.2. Crysallographic data of compounds **3.4-3.7**.

Compound	**Fe_4Er_2 (3.4)**	**Fe_4Tm_2 (3.5)**	**Fe_4Yb_2 (3.6)**	**Fe_4Lu_2 (3.7)**
Formula	$C_{79}H_{102}Er_2Fe_4N_4O_{29}$, $_{3.5}(C_2H_3N)$	$C_{85}H_{111}Fe_4N_7O_{29}Tm_2$, $3(C_2H_3N)$	$C_{85}H_{111}Fe_4N_7O_{29}Yb_2$, $3(C_2H_3N)$	$C_{85}H_{111}Fe_4N_7O_{29}Lu_2$, $3(C_2H_3N)$
FW (g mol^{-1})	2273.25	2256.07	2264.29	2268.15
Crystal system	triclinic	triclinic	triclinic	triclinic

Color	brilliant pale-green	brilliant pale-green	brilliant pale-green	brilliant pale-green
Space group	P -1	P -1	P-1	P-1
a (Å)	14.1941(16)	14.2277(17)	14.2113(9)	14.2470(16)
b (Å)	18.517(2)	18.5879(29)	18.5580(13)	18.44(2)
c (Å)	19.112(2)	19.0796(23)	19.2000(12)	19.187(2)
α (°)	84.696(2)	84.463(16)	84.23(5)	84.003(9)
β (°)	70.795(2)	70.083(14)	70.79(5)	71.211(9)
γ (°)	83.247(2)	81.639(17)	83.144(5)	82.154(9)
V (Å^3)	4703.3(9)	4687.6 (2.5)	4737.34(860)	4744.2(10)
Z	2	2	2	2
T (K)	100(2)	150(2)	150(2)	150(2)
F(000)	2306	2288	2292	3176
ρ_{calc} (g cm^{-3})	1.605	1.573	1.587	1.588
μ (mm^{-1})	2.445	2.515	2.630	2.735
Crystal size (mm)	0.27X0.23X0.18	0.29X0.26X0.22	0.31X0.26X0.18	
Data measured	48988	49254	76472	46052
Unique data	20728	18686	21770	26298
R(int)	0.0530	0.0638	0.0906	0.0874
Data with I > 2σ(I)	15810	11840	15906	19832
Parameters	1121	1027	1014	1470
wR_2 (all	0.0971	0.1098	0.1752	0.1023

data)				
S (all data)	0.994	0.977	1.032	0.998
R_1 (I > 2σ(I))	0.0388	0.0525	0.0686	0.0426

Table 3.3. Crystallographic data of compounds **3.8-3.11**.

Compound	**Fe$_3$Er$_2$ (3.8)**	**Fe$_3$Tm$_2$ (3.9)**	**Fe$_3$Yb$_2$ (3.10)**	**Fe$_3$Lu$_2$ (3.11)**
Formula			$C_{72}H_{94}Fe_3N_5O_{25}Yb_2$	
FW (g mol^{-1})			1943.15	
Crystal system	monoclinic	monoclinic	Monoclinic	See Fig. below
Color	pale yellow	pale yellow	pale-yellow	AND
Space group	P	P	P21/c	PXRD (CD)
a (Å)	19.9511	19.9511	19.9227(15)	ATATCHED
b (Å)	19.7056	19.8037	19.6790(12)	To
c (Å)	22.0819	22.0353	22.0382(15)	THE
α (°)	90.00	90.00	90.00	THESIS
β (°)	108.060	107.914	108.184(8)	
γ (°)	90.00	90.00	90.00	
V (Å^3)	8253.7	8275.7	8208.8(10)	
Z			4	
T (K)	200	200	200(2)	
F(000)				
ρ_{calc} (g cm^{-3})			1.572	
μ (mm^{-1})			3916	
Crystal size (mm)			2.849	
Data measured			47608	
Unique data			15902	
R(int)			0.0847	

Data with I > 2σ(I)			9349	
Parameters			971	
wR2 (all data)			0.1533	
S (all data)			0.981	
R1 (I > 2σ(I))			0.0546	

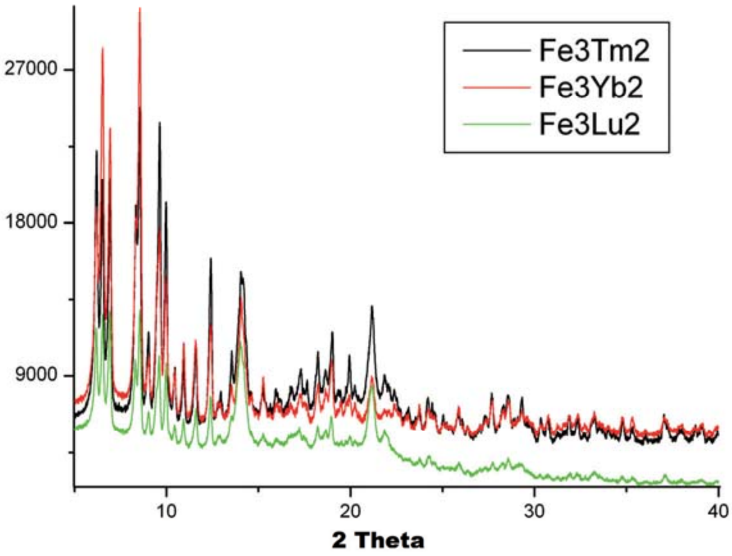

This Figure supports Tab. 3.3 and has no number.

Table 3.4. Crystallographic data of compounds **3.12-3.14**.

Compound	**Tm_2 (3.12)**	**Yb_2 (3.13)**	**Lu_2 (3.14)**
Formula	$C_{46}H_{56}N_2O_{14}Tm_2$	$C_{46}H_{56}N_2O_{14}Yb_2$	$C_{46}H_{56}Lu_2N_2O_{14}$
FW (g mol^{-1})	1202.82	1207.01	1210.87
Crystal system	monoclinic	monoclinic	monoclinic
Color	colourless	colourless	colourless
Space group	P 12/n (14)	P 12/n (14)	P 12/n (14)
a (Å)	14.186(3)	10.0379(9)	10.0586(8)
b (Å)	9.3425(19)	14.3816(8)	14.4229(14)

c (Å)	18.407(4)	17.2087(15)	17.1763(13)
α (°)	90.00	90.00	90.00
β (°)	109.66	94.65	94.408(9)
γ (°)	90.00	90.00	90.00
V (Å^3)	2297.2(8)	2476.07(204)	2484.5(4)
Z	2	2	2
T (K)	290(2)	200(2)	200(2)
F(000)	2288	1196	1200
ρ_{calc} (g cm^{-3})	1.573	1.619	1619
μ (mm^{-1})	2.515	3.817	4.014
Crystal size (mm)	0.29X0.26X0.22		
R(int)		0.097	0.0510
Data with I > 2σ(I)		3287	
S (all data)	1.018	1.011	0.939
R_1 (I > 2σ(I))	0.0525	0.0686	

Table 3.5a. Fe-Fe distances in compounds **3.1-3.3**.

Compound	Fe1····Fe2	Fe3····Fe4	Fe5····Fe1	Fe5····Fe2
3.1	3.0585(7)	3.1162(9)	8.1934(9)	6.1207(9)
3.2	3.0623(7)	3.1249(7)	8.1859(7)	6.1183(6)
3.3	3.0629(9)	3.1267(11)	8.1459(11)	6.0903(10)

Table 3.5a. (continued)

Fe5····Fe3	Fe5····Fe4	Fe1····Fe3	Fe2····Fe4	Compound
7.9519(8)	5.9011(7)	5.7809(8)	7.6556(8)	**3.1**
7.9601(7)	5.8966(7)	5.7409(6)	7.6359(6)	**3.2**
7.9402(12)	5.8813(11)	5.7175(10)	7.6335(10)	**3.3**

Table 3.5b. Selected Fe-O-Fe angles in compounds **3.1-3.3**.

Compound	Fe1···O1···Fe2	Fe1···O2···Fe2	Fe3···O3···Fe4
3.1	102.047(132)	96.913(114)	100.267(118)
3.2	102.109(106)	97.294(95)	100.617(98)
3.3	102.289(160)	96.913(114)	100.722(153)

Table 3.5c. selected Fe-Ln distances for the discussion in compounds **3.1-3.3.**

Compound	Fe1····Ln1	Fe3····Ln1	Fe2····Ln2
3.1	3.3904(5)	3.4279(6)	3.4488(6)
3.2	3.3850(5)	3.4191(5)	3.4491(5)
3.3	3.3807(7)	3.4166(9)	3.4402(7)

Table 3.5d. (continued) selected Fe-Ln distances for the discussion.

Fe4····Ln3	Fe5····Ln2	Fe5····Ln3
3.5800(6)	3.4416(6)	3.4035(5)
3.5745(5)	3.4390(5)	3.3996(4)
3.5739(7)	3.4398(7)	3.3923(8)

Table 3.5e. Selected Ln-O-Fe angles.

Compound	Ln2···Fe5···Ln3	Ln2···O12···Fe5	Ln3···O4···Fe5
3.1	136.589(19)	106.795(116)	106.245(110)
3.2	136.466(13)	107.062(98)	106.357(95)
3.3	137.458(22)	106.992(160)	106.369(150)

Table 3.14. Crystal Data and Refinement Details (only unit cell data are given for **3.15**, **3.18** and **3.20**)

Compound	**3.15**	**3.16**	**3.17**	**3.18**	**3.19**	**3.20**
Formula		$C_{158}H_{341}Eu_4$	$C_{156}H_{338}Fe_{16}$		$C_{156}H_{338}Dy_4$	

		$Fe_{16}N_{33}O_{104}$	$Gd_4N_{34}O_{104}$		$Fe_{16}N_{34}O_{104}$	
Formula weight		5897.10	5877.20		5898.20	
Crystal System	Orthorhombic	Orthorhombic	Orthorhombic	Orthorhombic	Orthorhombic	Orthorhombic
Space Group	*Ccca*	*Ccca*	*Ccca*	*Ccca*	*Ccca*	*Ccca*
a / Å	28.139(6)	27.7369(19)	27.7908(14)	27.8177(9)	27.7714(11)	28.149(5)
b / Å	28.515(8)	28.1589(19)	27.9903(15)	28.0713(10)	28.0818(11)	28.335(6)
c / Å	31.098(6)	30.573(2)	31.269(2)	31.0265(15)	30.6492(13)	31.056(5)
U / Å^3	24953(16)	23879(3)	24324(2)	24227.9(16)	23902.4(17)	24771(14)
Z	4	4	4	4	4	4
T / K	293(2)	100(2)	150(2)	150(2)	100(2)	293(2)
F(000)		12136	12064		12906	
D_c / Mg m^{-3}		1.640	1.605		1.639	
μ(Mo-Kα) / mm^{-1}		2.069	2.090		2.267	
Total Data		84676	77829		70812	
Unique Data		12669	12913		13682	
R_{int}		0.0506	0.0611		0.0332	
Data with $I \geq 2\sigma(I)$		10454	8197		11770	
wR_2 (all data)		0.1586	0.1212		0.1858	
S (all data)		1.201	0.991		1.115	
R_1 [$I \geq 2\sigma(I)$]		0.0496	0.0505		0.0508	
Parameters		724	613		704	

Table 3.15. Crystallographic data of $Fe_{18}Dy_6$ (3.21) and Fe_4Dy_4 (3.22).

Compound	**$Fe_{18}Dy_6$ (3.20)**	**Fe_4Dy_4 (3.21)**
Formula	$Dy_6Fe_{18}O_{124}H_{234}C_{292}N_{44}$	$Fe_4Dy_4N_{10}C_{93}H_{1354}O_{54}$
FW (g mol^{-1})	8323.425	3074.47
Crystal system	Orthorhombic	triclinic
Color	yellow	orange
Space group	P c c n (56)	P-1 (2)
a (Å)	31.0473(34)	17.3293(15)
b (Å)	35.2097(33)	17.3987(15)
c (Å)	36.4720(35)	22.4142(19)
α (°)		75.91(0)
β (°)		81.09(0)
γ (°)		89.98(0)
V (Å^3)	39869.96(690)	6470.59(222)
Z		2
T (K)		100(2)
F(000)		3070
ρ_{calc} (g cm^{-3})		1.578
μ (mm^{-1})		2.800
Crystal size (mm)		0.32x0.25x0.19
R(int)		0.0397
Data with I > 2σ(I)		19250
S (all data)		1.024
R_1 (I > 2σ(I))		0.0708

Table 3.16. Crystallographic data of the Ln_6 compounds **3.23**, **3.24** and **3.28**.

Compound	**Dy_6 (3.23)**	**Dy_6(3.24)**	**Dy_6 (3.27)**
Formula	$C_{44}H_{110}N_{12}O_{44}Dy_6$	$C_{54}H_{108}Dy_6N_{18}O_{36}$	$C_{50}H_{112}Dy_6N_{18}O_{32}$

FW (g mol^{-1})	2486.4	2560.58	2452.58
Crystal system	trigonal	trigonal	trigonal
Color	colourless	colourless	colourless
Space group	R-3	R -3	R -3
a (Å)	16.7756(3)	17.5124(14)	15.778(1)
b (Å)	16.7756(3)	17.5124(14)	15.778(1)
c (Å)	24.9858(3)	24.2551(19)	26.4045(19)
α (°)	90.00	90.00	90.00
β (°)	90.00	90.00	90.00
γ (°)	120.00	120.00	120.00
V (Å^3)	6089.5(3)	6442.1(9)	5692.62(65)
Z	3	3	3
T (K)	123(2)	100(2)	200(2)
F(000)	3618	3726	3570
ρ_{calc} (g cm^{-3})	2.034	1.980	2.146
μ (mm^{-1})	5.549	5.244	5.925
Crystal size (mm)	0.40x0.40x0.20	0.18x.017x.012	
R(int)	0.0207	0.0296	0.0343
Data with I > 2σ(I)	3108	3003	2174
S (all data)	1.081	1.167	1.011
R_1 (I > 2σ(I))	0.0205	0.0182	0.0238

Table 3.16. (continued) The Crystallographic data of Tm_6 (**3.25**) and Ho_6 (**3.26**)

Compound	**Tm_6(3.23)**	**Ho_6 (3.25)**
Formula	$C_{54}H_{108}Dy_6N_{18}O_{36}$	$C_{50}H_{112}Dy_6N_{18}O_{32}$
FW (g mol^{-1})	2560.58	2452.58
Crystal system	trigonal	trigonal

Color	colourless	colourless
Space group	R -3	R -3
a (Å)	17.5124(14)	15.778(1)
b (Å)	17.5124(14)	15.778(1)
c (Å)	24.2551(19)	26.4045(19)
α (°)	90.00	90.00
β (°)	90.00	90.00
γ (°)	120.00	120.00
V (Å^3)	6442.1(9)	5692.62(65)
Z	3	3
T (K)	100(2)	200(2)
F(000)	3726	3570
ρ_{calc} (g cm^{-3})	1.980	2.146
μ (mm^{-1})	5.244	5.925
Crystal size (mm)	0.18x.017x.012	
R(int)	0.0296	0.0343
Data with I > 2σ(I)	3003	2174
S (all data)	1.167	1.011
R_1 (I > 2σ(I))	0.0182	0.0238

Appendix: Chapter 4 (Crystallographic data)

Table 4.1 Crystallographic data for 4.5, 4.7, 4.8.

Compound	**4.5**	**4.7**	**4.8**
Formula	$C_{180}H_{350}Dy_{10}Fe_{10}N_{50}O_{90}$	$C_{180}H_{350}Er_{10}Fe_{10}N_{50}O_{90}$	$C_{176}H_{344}Fe_{10}N_{48}O_{90}Tm_{10}$
Formula weight	6838.60	6886.20	6820.79
Crystal System	triclinic	triclinic	triclinic
Space Group	P-1	P-1	P-1
a / Å	16.678(2)	16.5660(12)	16.5166(8)
b / Å	20.475(3)	20.5294(15)	20.5004(10)
c / Å	21.168(3)	21.0718(14)	21.0621(10)
α[°]	108.198(3)	108.513(6)	108.661(0)
β[°]	101.052(3)	101.198(6)	101.135(1)
γ[[°]	96.705(3)	96.205(6)	96.006(1)
U / $Å^3$	6617.9(16)	6554.2(8)	6522.3(5)
Z	1	1	1
T / K	150(2)	150(2)	100(2)
Crystal size (mm)	0.24X0.13x0.11	0.24x0.13x0.11	0.44x0.22x0.18
F(000)	3420	3440	3406
Radiation	MoKα (λ= 0.8000 nm)/ ANKA	MoKα (λ=0.71073 nm)	MoKα (λ=0.71073 nm)
ρ_{calc} (g cm^{-3})	1.716	1.745	1.737
μ(Mo-Kα) / mm^{-1}	4.681	3.785	3.986

Total Data	64632	55886	84385
Unique Data	27541	23774	28942
R_{int}	0.0818	0.0816	0.0767
Data with $I \geq 2\sigma(I)$	18545	14622	21281
wR_2 (all data)	0.1782	0.1248	0.1771
S (all data)	1.061	0.953	1.071
R_1 [$I \geq 2\sigma(I)$]	0.0590	0.0528	0.0599
Parameters	1262	1262	1262

Table 4.1 Crystallographic data for 4.9 and 4.11 (continued).

Compound	**4.9**	**4.11**
Formula	$C_{182}H_{353}Fe_{10}N_{51}O_{90}Yb_{10}$	$C_{170}H_{335}Fe_{10}N_{45}O_{90}Y_{10}$
Formula weight	6985.05	5897.43
Crystal System	triclinic	triclinic
Space Group	P-1	P-1
a / Å	16.5530(12)	16.621(2)
b / Å	20.5964(13)	20.509(3)
c / Å	21.1312(16)	21.130(3)
α[°]	108.791(5)	108.222(3)
β[°]	101.118(6)	100.792(3)
γ[[°]	95.993(5)	96.803(3)
U / Å^3	6583.9(8)	6598.5(17)
Z	1	1
T / K	150(2)	150(2)

Crystal size (mm)	0.31x0.24x0.20	
$F(000)$	3482	3040
Radiation	MoKα (λ=0.71073 nm)	ANKA
ρ_{calc} (g cm^{-3})	1.762	1.484
μ(Mo-Kα) / mm^{-1}	4.133	1.295
Total Data	62927	73926
Unique Data	25727	27475
R_{int}	0.0785	0.0779
Data with $I \geq 2\sigma(I)$	21281	20629
wR_2 (all data)	0.1101	0.1974
S (all data)	0.959	1.080
R_1 [$I \geq 2\sigma(I)$]	0.0474	0.0628
Parameters	1276	1249

Table 4.1 Cyrstallographic data of Fe$_{10}$Ln$_{10}$ compounds (continued, cells).

Compound	**4.1**	**4.2**	**4.3**	**4.4**	**4.6**	**4.10**
Formula	$Fe_{10}Nd_{10}\cdot 34MeCN$	$Fe_{10}Eu_{10}$	$Fe_{10}Gd_{10}$	$Fe_{10}Tb_{10}\cdot 34MeCN$	$Fe_{10}Ho_{10}$	$Fe_{10}Lu_{10}$
T[K]	150(2)	200	200	150 (2)	200	200
Crystal Syst	triclinic	triclinic	triclinic	triclinic	triclinic	triclinic
Space group	P -1	P -1	P -1	P-1	P -1	P -1
a [Å]	19.0085(18)	16.9283	16.7145	18.8793(32)	16.6763	16.5320
b[Å]	19.6765(19)	20.5131	20.4081	19.5600(28)	20.2091	20.4451

c[Å]	22.099(2)	21.6333	21.3445	22.0598(11)	21.6053	20.9334
α[°]	108.770(2)	108.559	107.720	108.796 (11)	108.551	108.477
β[°]	100.887(2)	101.973	102.074	100.798 (12)	102.781	100.946
γ[[°]	101.703(2)	95.503	96.296	101.630 (12)	96.066	96.233
V [$Å^3$]	6663.5	6859.6	6663.5		6608.7	6479.6
Z	1	1	1	1	1	1

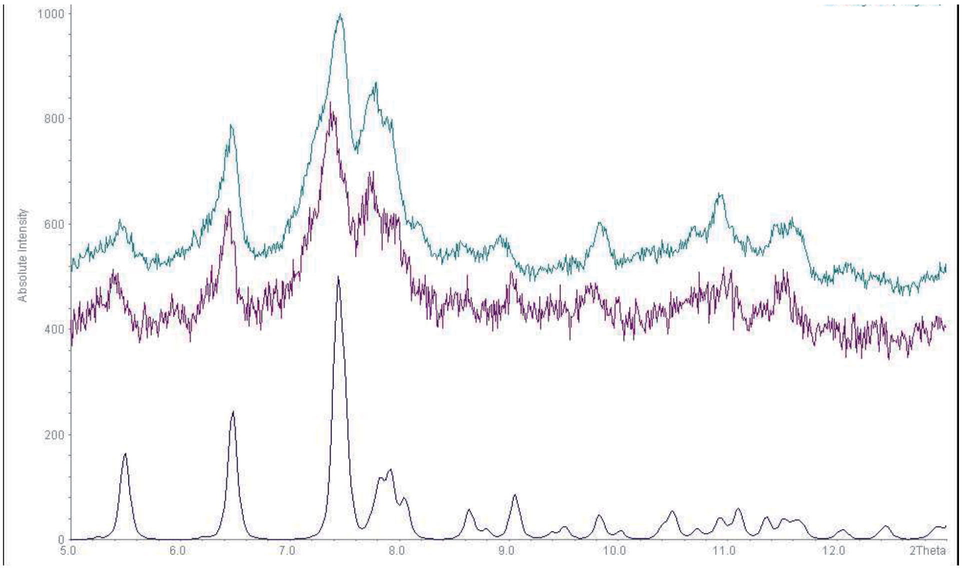

Powder diffraction of complexes **$Fe_{10}Gd_{10}$** (green) and **$Fe_{10}Dy_{10}$** (purple) together with the theoretical pattern for **$Fe_{10}Dy_{10}$** (dark blue). This Figure supports Table 4.1 and has no number.

Table 4.2. Selected bond lengths (Å) and Fe-O-Ln angles (°) for compounds $Fe_{10}Dy_{10}$ and $Fe_{10}Y_{10}$.

$Fe_{10}Dy_{10}$		**$Fe_{10}Y_{10}$**	
Dy1-O4	2.269(4)	Y1-O4	2.256(3)
Dy1-O29’	2.289(4)	Y1-O29’	2.285(3)
Dy1-O2	2.291(5)	Y1-O2	2.279(3)
Dy1-O1	2.293(4)	Y1-O1	2.278(3)
Dy1-O3	2.412(5)	Y1-O3	2.397(3)
Dy1-O32	2.453(6)	Y1-O32	2.435(3)

Dy1-O31	2.488(6)	Y1-O31	2.480(3)
Dy1-N1	2.586(6)	Y1-N1	2.587(3)
Dy2-O7	2.280(5)	Y2-O8	2.272(3)
Dy2-O8	2.287(4)	Y2-O10	2.277(3)
Dy2-O10	2.294(5)	Y2-O7	2.278(3)
Dy2-O5	2.314(5)	Y2-O5	2.290(3)
Dy2-O9	2.410(6)	Y2-O9	2.392(4)
Dy2-O35	2.458(6)	Y2-O35	2.444(4)
Dy2-O34	2.494(7)	Y2-O34	2.458(4)
Dy2-N3	2.539(7)	Y2-N3	2.562(5)
Dy3-O14	2.267(4)	Y3-O14	2.248(3)
Dy3-O16	2.289(6)	Y3-O16	2.283(4)
Dy3-O13	2.301(5)	Y3-O13	2.283(4)
Dy3-O11	2.314(5)	Y3-O11	2.299(3)
Dy3-O38	2.455(6)	Y3-O38	2.430(4)
Dy3-O15	2.452(5)	Y3-O15	2.436(4)
Dy3-O37	2.480(6)	Y3-O37	2.485(4)
Dy3-N5	2.578(7)	Y3-N5	2.566(4)
Dy4-O22	2.270(5)	Y4-O22	2.265(3)
Dy4-O20	2.278(4)	Y4-O20	2.257(3)
Dy4-O19	2.304(5)	Y4-O19	2.296(4)
Dy4-O17	2.315(5)	Y4-O17	2.306(3)
Dy4-O21	2.426(6)	Y4-O21	2.416(4)
Dy4-O41	2.432(5)	Y4-O41	2.425(3)
Dy4-O40	2.457(6)	Y4-O40	2.445(4)
Dy4-N7	2.571(6)	Y4-N7	2.563(4)
Dy5-O28	2.246(5)	Y5-O28	2.240(3)
Dy5-O25	2.265(6)	Y5-O25	2.262(4)

Dy5-O23	2.304(5)	Y5-O23	2.284(3)
Dy5-O26	2.307(5)	Y5-O26	2.288(3)
Dy5-O27	2.441(5)	Y5-O27	2.412(3)
Dy5-O43	2.455(5)	Y5-O43	2.436(3)
Dy5-O44	2.478(6)	Y5-O44	2.462(4)
Dy5-N9	2.622(6)	Y5-N9	2.610(4)
Fe1-O7	1.980(5)	Fe1-O6	1.981(3)
Fe1-O2	1.988(4)	Fe1-O2	1.988(3)
Fe1-O6	1.994(5)	Fe1-O7	1.991(3)
Fe1-O5	2.013(5)	Fe1-O5	2.018(3)
Fe1-O4	2.037(5)	Fe1-O4	2.027(3)
Fe1-N2	2.238(6)	Fe1-N2	2.228(4)
Fe2-O12	1.987(6)	Fe2-O8	1.981(3)
Fe2-O8	1.987(4)	Fe2-O12	1.996(4)
Fe2-O13	1.991(5)	Fe2-O13	1.999(3)
Fe2-O11	2.015(5)	Fe2-O11	2.016(3)
Fe2-O10	2.037(5)	Fe2-O10	2.035(3)
Fe2-N4	2.227(6)	Fe2-N4	2.229(4)
Fe3-O19	1.965(5)	Fe3-O19	1.962(3)
Fe3-O14	1.985(5)	Fe3-O14	1.978(3)
Fe3-O18	1.984(6)	Fe3-O18	1.995(5)
Fe3-O17	2.025(6)	Fe3-O17	2.028(4)
Fe3-O16	2.027(5)	Fe3-O16	2.031(3)
Fe3-N6A	2.145(14)	Fe3-N6A	2.167(10)
Fe4-O20	1.977(5)	Fe4-O24	1.964(5)
Fe4-O20	1.977(5)	Fe4-O20	1.992(3)
Fe4-O24	1.981(8)	Fe4-O25	2.005(3)
Fe4-O23	1.994(6)	Fe4-O23	2.005(4)

Fe4-O25	1.996(5)	Fe4-O22	2.040(3)
Fe4-O22	2.050(5)	Fe4-N8	2.246(5)
Fe4-N8	2.223(9)	Fe5-O30	1.982(4)
Fe5-O26	1.975(5)	Fe5-O26	1.989(3)
Fe5-O30	1.985(5)	Fe5-O1’	2.005(3)
Fe5-O1’	2.005(5)	Fe5-O29	2.017(3)
Fe5-O29	2.011(5)	Fe5-O28	2.049(3)
Fe5-O28	2.038(5)	Fe5-N10	2.220(4)
Fe5-N10	2.207(7)	Fe4-O24	1.964(5)
Fe5-O1-Dy1’	106.07(18)	Fe5-O1-Y1’	106.39(12)
Fe1-O2-Dy1	104.9(2)	Fe1-O2-Y1	104.86(13)
Fe1-O4-Dy1	104.08(19)	Fe1-O4-Y1	104.41(12)
Fe1-O5-Dy2	105.6(2)	Fe1-O5-Y2	106.09(13)
Fe1-O7-Dy2	108.0(2)	Fe1-O7-Y2	107.47(14)
Fe2-O8-Dy2	105.5(2)	Fe2-O8-Y2	105.60(13)
Fe2-O10-Dy2	103.6(2)	Fe2-O10-Y2	103.59(14)
Fe2-O11-Dy3	105.2(2)	Fe2-O11-Y3	105.40(13)
Fe2-O13-Dy3	106.6(2)	Fe2-O13-Y3	106.60(14)
Fe3-O14-Dy3	106.1(2)	Fe3-O14-Y3	106.64(14)
Fe3-O16-Dy3	104.0(2)	Fe3-O16-Y3	103.57(15)
Fe3-O17-Dy4	105.1(2)	Fe3-O17-Y4	105.25(14)
Fe3-O19-Dy4	107.5(2)	Fe3-O19-Y4	107.84(14)
Fe4-O20-Dy4	105.8(2)	Fe4-O20-Y4	105.83(14)
Fe4-O22-Dy4	103.7(2)	Fe4-O22-Y4	103.92(14)
Fe4-O23-Dy5	106.2(2)	Fe4-O23-Y5	106.30(15)
Fe4-O25-Dy5	107.6(2)	Fe4-O25-Y5	107.12(16)
Fe5-O26-Dy5	104.4(2)	Fe5-O26-Y5	104.44(14)

Fe5-O28-Dy5	104.5(2)	Fe5-O28-Y5	104.15(14)
Fe5-O29-Dy1’	106.00(19)	Fe5-O29-Y1’	105.69(12)

Table 4.3. Crystallographic data of **4.12**, **4.16**, **4.17** and **4.18**.

Compound	**4.12**	**4.16**	**4.17**	**4.18**
Formula	$C_{42}H_{96}Fe_6N_6O_{24}$	$C_{61}H_{112}Fe_4N\ O_{27}S_2Yb_2$	$Dy_3Mn_4O_{31}H_{78}N_9C_{42}$	$Dy_4N_{10}C_{32}H_{66}O_{34}$
Formula weight	1404.35	2009.18	1912.36	1784.92
Space Group	R-3	C2/c	R-3	P21/n (Nr.14)
a / Å	24.0344(13)	14.449(2)	23.7885(34)	8.6116(9)
b / Å	24.0344(13)	24.951(4)	23.7885(34)	17.0719(17)
c / Å	8.9649(5)	23.760(4)	20.5652(41)	19.2208(24)
α[°]	90.00	90.00	90.00	90.00
β[°]	90.00	101.820(2)	90.00	90.43(1)
γ[[°]	120.00	90.00	120.00	90.00
U / Å^3	4484.8(6)	8384(2)	6554.2(8)	2825.69(57)
Z	3	4	3	1
T / K	233(2)	150(2)	150(2)	100(2)
Crystal size (mm)	0.35X0.32x0.24	0.15x0.04x0.02		0.27x0.23x0.18
F(000)	2214	4076	3440	
Radiation	MoKα (λ= 0.8000 nm)/ ANKA	MoKα (λ= 0.8000 nm)/ ANKA	MoKα (λ=0.71073 nm)	MoKα (λ=0.71073 nm)
ρ_{calc} (g cm^{-3})	1.560	1.592	1.89038	2.09772
μ(Mo-Kα) / mm^{-1}	1.497	4.063	1.785	3.986
Total Data	11394	30740	10334	

Unique Data	27541	11939	4249	5692
R_{int}	0.0320	0.1180	0.0836	0.0901
Data with $I \geq 2\sigma(I)$	1951	9583	2743	4259
wR_2 (all data)	0.0693	0.2872		
S (all data)	1.040	1.298		1.071
R_1 $[I \geq 2\sigma(I)]$	0.0265	0.0981	0.0516	0.0663
Parameters	131	847	279	358

Table 4.5. The time constants and amplitudes observed for compounds **4.5**, **4.6** and **4.12**.

Property	Time constants τ_i			Relative amplitudes ΣA_i		
Factor	τ_1 (fs)	τ_2 (ps)	τ_3 (ps)	ΣA_1	ΣA_2	ΣA_3
$Fe_{10}Dy_{10}$	201± 19	1.5±0.4	88 ± 21	0.77	0.14	0.09
$Fe_{10}Ho_{10}$	251± 26	2.8±0.4	79 ± 15	0.78	0.12	0.10
Fe_6	363± 75	5.2± 1.4	38 ± 11	0.64	0.23	0.13

For My Family

For Annie

For The Group

For Science

I Have A Problem: I Cannot Give UP!

Thanksgiving

My colleagues and friends told me I have to start thanking the Supervisor either I will fail in the exam. So let me start with the Boss!

I was listening carefully to your lecture in the first semester of my study not only because my German (may yours as well in that time) was weak but because I liked it very much. I liked the way how you explained things. I said to my self when I finish the study I would like to do research in your group. The most important thing i learned from Prof. Annie is to be open mind when it is about science. I also learned from her how to be enthusiastic about nice results. You always told me what one can do with the results and who can help us to understand it further. **Thanks Annie**.

You taught me Inorganic Chemistry from other view, in this you were successful and I would like to thank you very much. You also taught me to be patient when it is about good science.

You supported me in all details of my research: many useful emails and literature and thoughts which you added to my thoughts REALLY helped much. There are no enough places here to say other things ….. **Thanks Annie**. **You are a teacher and friend.**

The solid triangle Yanhua, Chris, and Valeriu is amazing. They are so perfectionists that I could never make a mistake. They found it always. They suggest, they think with you, they criticize and they teach. I thought Chris is the Crystallographer in the group, and then I discovered that he knows almost everything. **Thanks Chris** for your support and your jokes which I understood mostly one day later …because they were typical English!

Thanks for all what you taught me about X-ray measurements and refinement but also your fluoro or other tips, tricks and advices … **Thanks Chris**.

Well, at least from Yanhua one can hear some nice motivation words which I cannot say about the Russian Boxer. I have never heard "halt die Klappe" so often in my life ……

Thanks to Yanhua for her patience and for great discussions about magnetism. **Thanks Yanhua.**

Thanks Valeriu for all what you taught me about the magic of Mössbauer spectroscopy and giving me so many literatures. I could not read all but I will!… Look we will never agree everything but this is good for research…. My explanations sound sometimes nicer than yours but they might be wrong. **Thanks Valeriu** for your great support. **Thanks Valeriu** for the nice time, you are a good friend. **Thanks Valeriu.**

Actually there are no enough places here to thank the four above so again **thanks Annie, Yanhua, Chris and Valeriu.**

A **special great super thank to Ghenadie** for teaching me so many important things in the Diploma work and his support after that per Skype! His nice music videos he keep sending me to keep relaxed. You are a friend **Gehnadie, thanks**.

A Giga special thank to Dr. Nicola Magnani plus WOW for great discussions and teaching me new things in theoretical calculations and for "REALLY" funny time. For checking the English of chapter 2 which resulted in Italian English and I have had to correct it again…..For unlimited support. For great science we are doing … **Thanks Nicola, you are a friend.** It is really nice to have you in the group and imagine very important as well.

The best thing was always the Friday meeting with you people. Special **thanks to Dr. Ali Malik** for his support and collaboration. **Thanks to the collaborators** (from other groups) who with me studied and studying or going to study all these systems, some of them since the begin of this work: **Prof. V. Voronkova, Dr. A. Sukhanov, PD Dr. Andreas N. Unterreiner , Dr. Yu Liang (Special thank**, we have done a good job**), Prof. M. Kappes, Prof. L. Bogani, Dr. Karin Goss, Dr. Konstantis, Prof. E. Collet, Prof. C. Mckenzie, Dr. M. Ferbinteau and Prof. van Slageren, Dr. L. Chibotaru, Dr. Ion P. and Dr. Oscan…….. Thanks to Dr. J. Wolny and Prof. V. Schuenemann.**

Thanks to Andreas again for the great scientific discussions and to the introduction in the world of Femtosecond Spectroscopy.

Special thank to Getraud. She is great! And sorry for making you stress by different things.

We all had a difficult time in our group! We survived this time because we are together. This in memory of **my friend Dr. Ian Hewitt** who taught so many important things about synthetic chemistry and who left great results which are great achievements in this field. I would like to thank here **Dr. Julia Rinck** for her great support for all in that time.

A super special **thank** to my friend **Markus** for his much appreciated support. **Markus you are a friend.** We had really interesting time!!

I would like also to give a special thank to **Dr. Konstantis** for his support by measurements and for being my worst collaborator. **Thanks Blond-Konstantis!, you are a friend!**

Many thanks to the Doctors: **Tapas, Ako, George, Anindita and Konstantin**. In particular for **Ako** for scientific discussions and many other tips about how to make good syntheses. and for **George** for his support by literature and other things …

Thanks Dr. Sven, Dirk and Dr. Julia for support especially in the first year. For **Dirk** for his support and help by computer problems and for **Dirk and Sven** by X-ray measurements in the first year …

Thanks for Amin for so many good things ..he always reminded me about important things in this life… shokran Akhi! **Thanks to Zeeshan** for being kind to me even if I stressed him sometimes…shokran Akhi! Thanks for all other people I met in my three and half years research time in the group the ex-members…..

Thanks to Rebecca (car-service and chemistry discussions as well), **for Nicole** and **Irina** for the nice and funny time in the lab. **Thanks** for **Ayse** for the great time and discussions about chemistry in the breaks. **Thanks to the group** members for the kind atmosphere and many **thanks for Martin, Thomas, Sihuai and Peng. Special thank for Kartik.**

A super **special thank** to **Vanessa**!

A **special thank** for **Shasha** for her unlimited support by so many things. **Special thank** to **Lena**! **Thanks to Gabi and Lehman** for being helpful and all **other** technician stuff.

A super special **1000 thanks for Michael** for all years of studying together and great time till the end of the promotion time. …..Many thanks to all my friends….Thanks to all Professors (**specially: Prof. Arlichs, Prof. Schnöckel, Prof. Bräse)** and to **Dr. Nattland** who were teaching chemistry from all fields in my study. **Thanks to Germany** and **KIT** for giving me the chance to study here because I could not at my home… because of war.

Thanks you all

Forgive me if I forgot any one!!